Proceeding of MAMIP2012
Asian International Conference on Materials, Minerals and Polymer
23rd – 24th March 2012, Vistana Hotel, Penang

PROCEEDING

PART 2

Asian International Conference on Materials, Minerals and Polymer (MAMIP 2012)

23rd – 24th March 2012, Vistana Hotel, Penang, MALAYSIA

Proceeding of MAMIP2012
Asian International Conference on Materials, Minerals and Polymer
23rd – 24th March 2012, Vistana Hotel, Penang

Published by:
School of Materials and Mineral Resources Engineering
Universiti Sains Malaysia

Editorial:
Ahmad Zahirani Ahmad Azhar
Muhammad Ghaddafy Affendy
Maryam Irani
Mohamad Salleh Gorji
Kee Chia Ching
Wan Fahmin Faiz Wan Ali
Mohd Fariz Abd Rahman

For bibliograrphic purposes, this document may be cited as:

Asian International Conference on Materials, Minerals and Polymer (MAMIP 2012)
Universiti Sains Malaysia…

Background of Institution

Established as the second university in the country in 1969, University Sains Malaysia (USM) was first known as the University of Penang, before the University's Act came into effect on 4th October 1971.

The university has been developing and expanding since its inception, which started with the enrolment of 57 science based students. Now, USM offers courses at undergraduate and postgraduate levels to approximately 20,000 students. USM has also become a well-known university locally and internationally.

USM was founded after an agreement made on a resolution approved by the Penang State Legislative Council in 1962, which suggested that a university college be established in the state. An area in Sungai Ara was identified and later the foundation stone was placed by the then Prime Minister, Y.T.M Tunku Abdul Rahman Putra Al-Haj on the 7th of August 1967.

In 1969, the University of Penang was established in response to the need for a larger campus with a more conducive environment, appropriate to the needs of the future of the country.

Since its beginning, USM has implemented a school system, as opposed to the traditional faculty system. What is unique about this system is that each school could fulfil the needs of a more focused degree in the chosen area of study and at the same time, students could have the opportunity to explore other areas of study offered by another school. The interdisciplinary approach ensures that USM, the first in the country to adopt this system, would produce trained, multi-skilled graduates.

USM main campus is located within a tropical island of Penang, Malaysia with a land area of 591.72 acres (240.13 hectares). There are two USM branch campuses, one at Kubang Kerian in Kelantan (approximately 300km from the main campus) known as Health Campus and the other at Nibong Tebal (approximately 50km from the main campus), known as Engineering Campus. The former houses the School of Medical Sciences, School of Health Sciences and School of Dental Sciences, while the latter houses the six Engineering Schools. To date, the total enrolment is more than 30,000 students.

Vision

Transforming Higher Education for Sustainable Tomorrow

Mission

USM is a pioneering, transdisciplinary research intensive university that empowers future talents and enables the bottom billions to transform their socio-economic well-being.

School of Materials and Mineral Resources Engineering

School of Materials and Mineral Resources Engineering started its programme since 1984 in USM, Penang under the School of Industrial Technology and Engineering Sciences. With the advancement of technology and market demand for skilled engineers in the country, USM took the initiative to fulfil the requirement by having its own engineering school separated from other disciplines of applied sciences. School of Materials and Mineral Resources Engineering started its programme since 1984 in USM, Penang under the School of Industrial Technology and Engineering Sciences.

With the advancement of technology and market demand for skilled engineers in the country, USM took the initiative to fulfil the requirement by having its own engineering school separated from other disciplines of applied sciences. In March 1986, the engineering disciplines under the School of Industrial Technology were separated to form their own schools, which include the formation of the School of Materials and Mineral Resources Engineering. USM had then housed the new campus at Ipoh before moving to Seri Iskandar, Perak. However, a lapsed of 15 years, in May 2001, the campus was moved to the new site situated at Seberang Perai Selatan, Penang. Compared to other schools or faculty in other Institutes of Higher Learning in Malaysia, the School of Materials and Mineral Resources Engineering is unique because it offers three programmes, these are Materials Engineering, Mineral Resources Engineering and Polymer Engineering at bachelor degree (honours) level for each programme. Polymer Engineering programme is the latest addition to the school that commenced in April 2002. The programme is an upgrading of polymer technology that was originally under the School of Industrial Technology in USM Penang.

In principal, Universiti Sains Malaysia, upholds the mission among which to build a greater understanding and strive to provide quality education as well as efficient and professional services through vast knowledge, innovation and latest expertise while upholding common ethical values. With that, SMMRE through its three programmes have one similar objective that is to produce materials, mineral resources and polymer engineers that are professionally qualified, knowledgeable and matured, highly skilled, capable and able to compete at national and international level and giving ideas and solution towards engineering crisis through analytic, innovative and proactive thinking. With these philosophies, SMMRE programmes curriculum have been design to fulfill the government aspiration towards vision 2020, industrial needs and at par with the growth of world globalisation technology.

Mission of SMMRE

To be globally recognized as a dynamic engineering school that produces creative, innovative and resourceful intellectuals with an ethos towards life-long learning that will contribute towards the creation of a knowledge based society.

Vision of SMMRE

To be an established and respectable world class academic and research school of excellence based on current technology.

MAMIP 2012

INTRODUCTION

Since its inception in 1984, the School of Materials and Mineral Resources Engineering (SMMRE), Universiti Sains Malaysia (USM) has always been at the forefront in the research and development of materials, mineral resources and polymer engineering. SMMRE's vision is to be an established and respectable world class academic and research school of excellence.

On September 3rd 2008, USM has been chosen to implement the Accelerated Programme for Excellence (APEX). USM has outlined its efforts in advocating the process of a sustainable development in ascertaining a more lasting future. In line with this, SMMRE has embraced the concept whole fully in its researches and operations. Thus, numerous publications and inventions have been produced with great emphasis on environment conservation and human development. By organizing an international conference, the knowledge can be shared to everyone not only in Malaysia but to the rest of the world.

The Asian International Conference on Materials, Minerals, and Polymer (MAMIP) is well known as a suitable platform for postgraduate students, researchers, academicians, and industrial experts worldwide to pool their knowledge and achievements for the benefits of mankind. This year, MAMIP will be organized by the Postgraduate Students Club (PGSC) under SMMRE which offers an excellent opportunity for USM postgraduate students to create an effective network among participants from various fields of expertise.

By achieving its objectives, MAMIP should be able to be a highlight event for SMMRE and USM in the years to come. Researchers and students worldwide will want to take part in MAMIP to learn and share novel, innovative, and efficient researches for a sustainable future.

OBJECTIVES

The objectives of this international conference are as follows:
   a) To provide a suitable platform for researchers and postgraduate students to showcase and share their respective researches from all around Asia.

   b) To facilitate and develop future research collaborations and networks between postgraduate students and professionals.

   c) To promote the events and achievements of SMMRE and USM to fellow participants from different parts of Asia.

Patron: Prof. Dato' Omar Osman

Advisor :   1) Prof. Hanafi Ismail
                                         2) Prof. Ahmad Fauzi Mohd Noor

Vice – advisor :   Mohd Firdaus Omar

Director :   Muhammad Ghaddafy Affendy

Deputy Director :   1) Wong Yew Hoong
                                         2) Mathialagan a/l Muniyadi

Secretary :   1) Ashraf Rohaniza Asari
                                         2) Khairul Arifah Saharudin

Treasurer :   Chang Boon Peng

Sponsorship :   1) Shazlin Mohamed Shaari
                                         2) Siti Rohana Yahya
                                         3) Ong Pek Ling

Scientific :   1) Ahmad Zahirani Ahmad Azhar
                                         2) Maryam Irani
                                         3) Mohamad Salleh Gorji
                                         4) Kee Chia Ching

Publicity and Website :   1) Hiew Jie Su
                                         2) Ng Chai Yan
                                         3) Mohamad Kahar Ab Wahab

Technical and Logistics :   1) Lai Chin Wei
                                         2) Muhammad Azwadi Sulaiman
                                         3) Mohamad Johari Abu
                                         4) Wan Fahmin Faiz Wan Ali

Food and Accommodation :   1) Nurul Hidayah Ismail
                                         2) Siti Shuhadah Md Saleh
                                         3) Norshahida Sarifuddin
                                         4) Farah Diana Mohd Daud

Protocol and Events: 1) Nor Fasihah Zaaba
                                         2) Komethi a/p Muniandy
                                         3) Sheril Rizal Vincent

Special tasks   1) Cheah Wee Keat
                                         2) Sarah Ishak
                                         3) Lee Ting

MESSAGE FROM
Prof. Dato' Omar Osman
Vice-Chancellor
Universiti Sains Malaysia

First and foremost I would like to extend my heartiest congratulations to Universiti Sains Malaysia (USM) for their success in organizing the Asian International Conference on Materials, Minerals, and Polymer (MAMIP) 2012.

Apart from the success of organizing this conference, this program outshines the ability of our university students excelling in sustainability researches. This conference has also generated greater awareness and interest among students on the significance of the usage of science, technology and engineering knowledge so as to benefit the country and at the same time to maintain sustainability of its resources.

The Asian International Conference on Materials, Minerals, and Polymer or MAMIP 2012, is an appropriate platform to encourage postgraduate students, researchers, academicians, and industrial experts worldwide to pool and share their knowledge, works and experiences in the field of Materials Science and Engineering. This is in line with this year's MAMIP theme; 'Bridging Notions, Sustaining Innovations'.

We need to understand the concept of sustainability through researches and apply them in our innovations and future products as a way to develop our beloved country while maintaining the resources available for the next generations.

MAMIP 2012 wouldn't be a success without the cooperation from all the participants, sponsorship and the organizing committee of MAMIP 2012. It takes the effort from all parties involved to make MAMIP 2012 a success. I therefore would like to express my gratitude and heartiest congratulation to the USM committee for their determination and sacrifice for this marvellous event.

On behalf of the university, I would like to acknowledge the contributions and efforts to all the participating universities for realizing this event.
Thank you.

Prof. Dato' Omar Osman
Vice-Chancellor
Universiti Sains Malaysia

MESSAGE FROM
Director
School of Materials & Mineral
Resources Engineering
MAMIP 2012

Assalamualaikum and greetings to everyone,

On behalf of the committee, it is my utmost pleasure to welcome all of the participants to the Asian International Conference on Materials, Minerals, and Polymer (MAMIP) 2012. We are proud to host MAMIP, a highlight event for the School of Materials and Mineral Resources Engineering (SMMRE), Universiti Sains Malaysia. Now, in its fifth time, MAMIP 2012 is spreading its wings to the international stage.

As technology and devices keep improving by the day, the need for better materials is apparent. Hence, developments in the research and engineering world can be seen significantly. However, it is equally important as well to ensure that our researches do incorporate sustainable elements. Preserving today's natural resources is a must, so that future researches in materials, minerals, and polymer can prosper for centuries to come. This matter suits the theme for MAMIP 2012: "Bridging notions, Sustaining innovations".

The success of MAMIP 2012 is the result of great support and contributions from Universiti Sains Malaysia, School of Materials and Mineral Resources Engineering, sponsors and our fellow participants. I would like to take this opportunity to thank and congratulate the entire MAMIP 2012 organizing committee for their tremendous hard work, sacrifices and commitment towards MAMIP 2012.

Have a great conference, and all the best.

Thank you very much.

Muhammad Ghaddafy Affendy
Director
MAMIP 2012

Table of Contents

Proceeding of MAMIP2012
Asian International Conference on Materials, Minerals and Polymer
23rd – 24th March 2012, Vistana Hotel, Penang

THE INFLUENCES OF ALPHA AND BETA NANO-SCALED NUCLEATING AGENTS ON CRYSTALLIZATION BEHAVIOR AND THERMAL PROPERTIES OF POLYPROPYLENE

Panjapong Sripanya[1], Sirijutaratana Covavisaruch[1,*], and Nawadon Petchwattana [2]

[1] Department of Chemical Engineering, Faculty of Engineering,
Chulalongkorn University, Payathai Road, Patumwan, Bangkok 10330, Thailand

[2] Division of Polymer Material Technology, Faculty of Agricultural Product Innovation and
Technology, Srinakharinwirot University, Sukhumvit 23, Bangkok 10110, Thailand

*Corresponding author: fchscv@hotmail.com

Abstract: *The influences of alpha and beta nano-scaled nucleating agents (NA) on isotactic polypropylene (iPP) were investigated. The crystallization temperature was raised with the addition of each NA. The crystalline melting temperature of the PP/α-NA exhibited only one peak but that of the PP/0.15wt% β-NA did two peaks; the lower one reflected the melting of the β crystals. PP crystals grew slowly to sizes of 100 to 200 µm. The addition of α-NA led to rapid crystal growth with spherurite radius from 1 to 2 µm. X-Ray Diffraction detected a fraction of the β crystal at 0.85 when only 0.10wt% β-NA was applied.*

Keywords: Polypropylene, Crystallization behavior, Thermal properties, alpha nano scaled nucleating agent, Beta nano scaled nucleating agent.

1.   INTRODUCTION

Polypropylene (PP) is widely used as commercial commodity plastic. Its versatility is reflected in its wide range of applications both in the industrial and consumer goods such as packaging, automotive parts, textiles, filament and electrical appliance [1,2].

PP is a semi-crystalline polymer consisting of two main parts; amorphous and crystalline. Each part is directly related to the PP's properties. The high amorphous part tends to be more flexible, tough, the molecules are more susceptible to elongate. In contrast the crystalline part gives PP stiffness and high modulus. The process of crystallization generally consists of two stages namely the nucleation and spherulite growth [2,3]. The nucleation is basically the formation of nuclei as a focal center around which the lamellae can arrange themselves as spherulite and grow. The process of crystallization can be induced more rapidly by addition of a nucleating agent (NA). The added NA helps by enhancing the number of nucleating or crystallization sites, reducing the size of spherulite and enhancing the growth rate. Some improvement of mechanical, thermal properties and physical properties can be expected when the degree of crystallinity is enhanced [4,5].

Usually, the spherulites which crystallize in iPP have various structures according to crystallization conditions. iPP can crystallize in to different crystalline modifications namely monoclinic (α-form), hexagonal (β-form) and orthorhombic (γ-form) [6,7]. The alpha form or monoclinic crystalline unit cell is the most common phase of iPP. It's predominant under standard processing condition over 95% of crystals in the PP commercial parts are typical of α-type. This form seems to be the most thermodynamically stable (melting crystalline point at 160°C) [6,8].

Formation of the β-modification or hexagonal form is less common form, generally found less than 5% of the crystal in common processing conditions. The β-form can be

obtained under some specific conditions such as crystallization in high temperature gradients, melts exposed to shear stress and the most common and higher promotion way for produce β-form is the application of selective β-nucleating agent [4,6,8].

Many researches are interested in β-phase properties because their have several advantages such as Romakiewize, A. et al. [4] and Xu, L. et al. [5] were found the T_m of β-form is lower than α-form 5 to 10 ^oC. This effect is directly related to the processing time in the injection molded. Tjong, S.C. et al. [9] found the tensile test and elongation at break is enhanced by addition of beta NA. Zhang, P. et al. [10] were found the impact strength and elongation at break were improved that reason of the materials is controlled by the microstructure, spherulite and crystallinity.

The objective of the present study is to investigate and to compare the effects of alpha and beta nano-scaled nucleating agents on the crystallization behavior and thermal properties of iPP. The formation and transformation of the crystalline alpha and beta phase upon melting subsequent and solidification is characterized by using X-ray diffractometer, Differential scanning calorimeter (DSC) and Polarized optical microscope.

2.   EXPERIMENTION

2.1   Material Preparations

The polymer in this study was a commercial grade isotactic homo-polypropylene powder (PP1100NK, produced by IRPC Co., Ltd., Thailand). The manufacture characterizes the material by melt flow index (MFI) of 11 g/min. The specific alpha and beta nano-scaled nucleating agents selected for the present study have an average particle size in range form 20 to 90 nm (VP101B and VP101T, Siam Extek Co., Ltd., Thailand). Each was compounded with the iPP powder by firstly dry-blending using a high speed mixing machine at the speed of 1,000 rpm for 20 sec. Each nucleating agent was applied at various contents from 0.0 to 0.5 wt%. The compounded pellets of PP were prepared by melt extrusion using a co-rotation twin screw extruder with the length to diameter ratio at 38:1. The temperatures of the screw were set at 200, 210, 220, 230 and 220 ^oC. The extruder screws rotated at the speed of   110 rpm.

2.2   Characterization
Thermal test

The crystallization behavior and the thermal properties namely the melting crystalline temperature (T_m), the crystallization temperature (T_c), and the degree of crystallinity ($\%X_c$) of the iPP and the iPP modified with various NA contents were determined by using a differential scanning calorimeter (DSC, Mettler Toledo star^e system Thermal Analyzer). Each sample with an average weight from 5 to 10 mg was used to investigate under non-isothermal condition in nitrogen atmosphere. First, it was firstly heated at a rate of 10 ^oC/min from -30^oC to 210^oC and held at 210 ^oC for 5 min to remove previous thermal history. Subsequently, the sample was cooled to -30 ^oC in order to observe the T_c and $\%X_c$. Thus second heating was conducted to 210 ^oC again for investigating of the T_m.

Crystal structure

Determination of the crystalline structure and the fraction of β-phase of the modified iPP, the specimens was conducted by using X-Ray Diffractometer (XRD, Bruker AXS, Germany Model D8 Advance) with Cu Kα radiation (λ = 0.154 nm) operated in a reflective mode at voltage of 50 kV and the filament current of 30 mA. Radiation scans of intensity versus differential angle 2θ were recorded in the region of 5° to 30°. The iPP with beta NA

each sample was determined from the peak area and the relative proportion of the β-form in the crystalline part. The specimens with thickness of 1 cm, and 5x5 cm were in length and width prepared by compression molding at 190°C with a force of 1,200 kN. The XRD was used for characterizing the alpha and the beta phase.

Observation of crystallization

The compression molding was used to prepare specimens for investigation on the crystallization behaviors of iPP and the iPP with NA. A thin film with 2 cm diameter and 35±5 μm in thickness were prepared for crystalline behavior observation by preheating the PP compound for 5 min and compressed from 50 kN to 200 kN within 5 min at 190 °C. The Polarized Optical Microscope with a heated-stage (POM) was used to observe the crystallization behavior of PP. The samples were crystallized under non-isothermal from 50°C to 200°C for elimination of thermal and mechanical history, then they were cool down and heated again. For the second cooling with isothermal conditions at 135°C, the POM micrographs were recorded by using a digital camera and an Image-Pro plus photo editor software. Both heating and cooling rate was 10 °C/min.

3. RESULTS AND DISCUSSION

3.1 The degree of crystallinity

The degree of crystallinity of the iPP modified with various alpha and beta NA contents were evaluated from the DSC scan as shown in Figure 1. The degree of crystallinity of the pure iPP was 43.8±0.25%. The degree of crystallinity of the iPP modified with alpha NA clearly increased from 44.04% to 48.69% at the initial addition and become quite stable with greater NA. In the case of iPP modified with beta NA, was stable at 43.8±0.20% and it tended to decrease when more than 0.1% of beta NA was added.
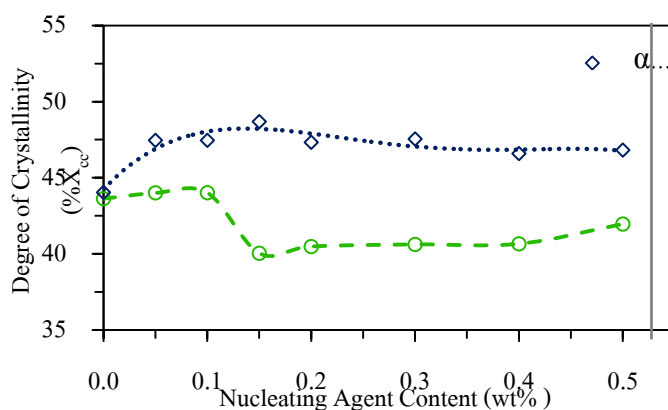
Figure 1. The Crystallinity of iPP modified with alpha and beta nucleating agents

3.2 The crystalline structure

The morphology, crystalline structure and the fraction of the β-phase of the modified iPP were characterized by XRD. The alpha and the beta phase were analyzed by different deflection angles. The XRD pattern shows the characteristic of various phases in pure iPP as shown in Figure 2(a). There are (110) (300) (040) (130) (301) (111) (400) peaks with the

Proceeding of MAMIP2012
Asian International Conference on Materials, Minerals and Polymer
23rd – 24th March 2012, Vistana Hotel, Penang

corresponding 2θ at 14.0^{o}, 16.0^{o}, 16.9^{o}, 18.6^{o}, 21.0^{o}, 21.8^{o} and 25.5^{o}, respectively. In the case of iPP modified with alpha NA, the XRD pattern shows that the peaks of α-phase at (110) (040) (130) (111) clearly increased while that of the iPP with beta NA shows the peak at (300) and (301) at 2θ of 16.0^{o} and 21.0^{o}. The beta peak observed were significantly greater intensity with increasing NA content. These results imply that the alpha phase was observed mainly in the iPP and the iPP modified with alpha NA, and that the beta NA effectively provided the β-phase in the modified iPP. The fraction of β-phase was calculated by applying the Tuner-Jounes et. al. equation as shown in Equation (1). The K value was determined to range from 0.05 to 0.85 when 0.10wt% of beta NA was added. The fraction of the β-phase remains rather constant at around 0.72±0.02 when more than 0.3wt% added.

$$K \text{ value} = \frac{H_{\beta 1}}{H_{\beta 1} + H_{\alpha 1} + H_{\alpha 2} + H_{\alpha 3}} \qquad (1)$$

Where $H_{\alpha 1}$, $H_{\alpha 2}$, and $H_{\alpha 3}$ are intensity of the three α-diffraction peaks (110), (040) and (130), respectively, and $H_{\beta 1}$ is the intensity of the strong single β-peak (300) at 2θ of 16.2^{o}.

(a)   (b)
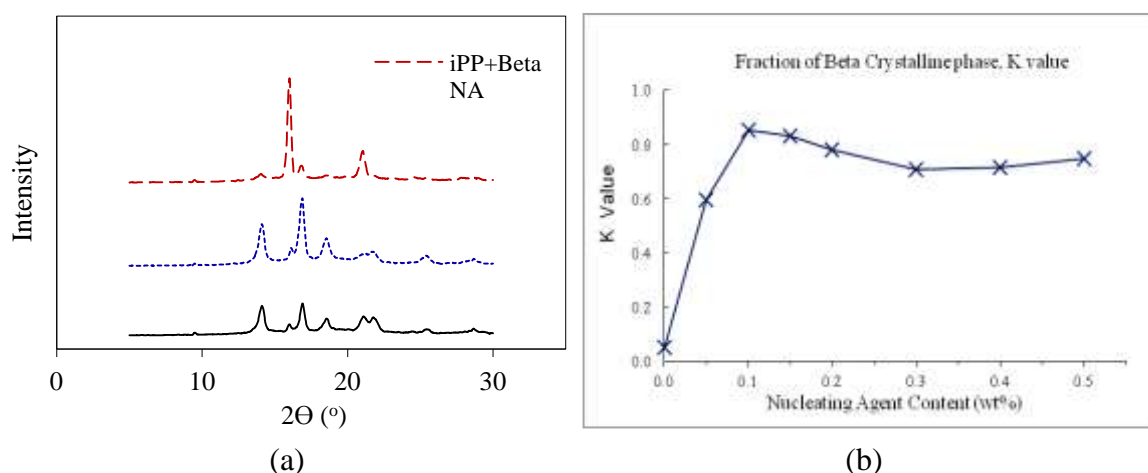
Figure 2. (a) The XRD patterns of the iPP and the iPP modified with alpha and beta NA
(b) the fraction of beta phase in the iPP modified with beta NA.

3.3 Thermal properties

The effects of Non-isothermal crystallization on the formation of alpha and beta crystallites in iPP with different contents of NA were investigated by DSC. The crystalline temperature (T_c) of the iPP modified with each nano-scaled nucleating agent was found to increase with the NA contents; that of the modified iPP was raised by 3.34^{o}C from 120.33 ^{o}C to123.66 ^{o}C when alpha NA was added at 0.05wt%. In the case of iPP with beta NA, the T_c was found to increase from 113 ^{o}C to 117 ^{o}C and 128 ^{o}C when beta NA was added at 0.05wt% and 0.03wt% respectively as show in Figure 3(a).

The melting crystalline temperature (T_m) of iPP and the iPP modified with 0.15wt% alpha NA each appeared as only one peak at around at 165 ^{o}C, it increased slightly to 166 ^{o}C when 0.20wt% of alpha NA was added. The iPP with beta nucleating agent more than 0.15wt% exhibited two melting crystalline peaks at 167°C and 147°C, as shown in Figure 3(a). The higher peak corresponds to the melting of the alpha phase as it was found in both the

pure iPP and the iPP modified with alpha NA while the lower one represents the beta crystalline characteristic. The trend of melting alpha crystalline temperature and the melting beta crystalline temperature was slightly increased with greater NA contents.

(a)   (b)
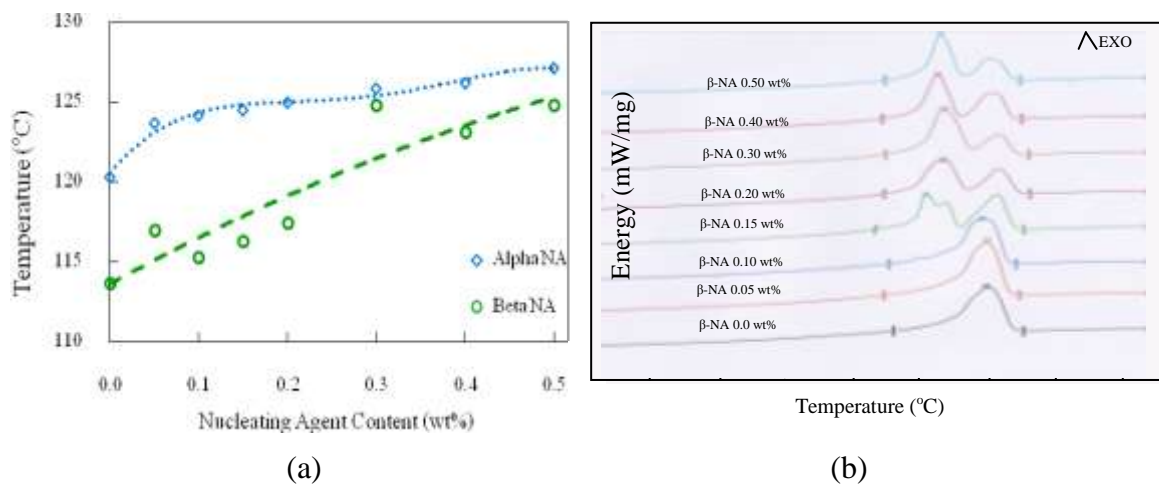
Figure 3. (a) The crystallization temperature of iPP with alpha and beta nucleating agents. (b) The melting crystalline temperatures of the iPP with various β-NA contents.

3.4   Crystallization behavior

The POM micrographs illustrating the crystallization under isothermal condition at 135°C of pure iPP, iPP with alpha NA and iPP with beta NA after 2 min are illustrated in Figures 4. Microscopic observation revealed that the pure iPP crystal grew slowly, the spherulite were well define with clearly visible boundaries. The diameter size of spherulites iPP at 5 min was 20.5±10.19 μm, crystallization still progressed to full solidification at around 20 min range from 100 to 200 μm.

The addition of both nano-scaled nucleating agents decreased significantly the spherulite dimensions as shown in Figure 5. In the case of iPP with 0.05wt% alpha NA, the crystal grew rapidly, leading to very fine morphology with spherulite diameter at 0.79±0.07 μm within 1 min and the boundary grew to impingement with the size of the spherulite at 1.24±0.15 μm within 3 min. At greater than 0.05wt% alpha NA contents, the spherulites were nucleated and grew very rapidly. The sizes of the spherulites at 2 min were 1.01±0.27, 0.89±0.23, 0.95±0.18 and 0.79±0.07 μm when the NA was added at 0.10, 0.15, 0.20, and 0.40wt% respectively.

The sizes of the spherulites of the iPP with beta NA decreased significantly to 1.10±0.14 μm at 2 min with the addition of only 0.05wt%. At greater than 0.10wt% of beta NA, the crystals were very fine and grown very rapid.

(a) iPP 2 min   (b) iPP 10 min

Figure 4. The optical micrographs illustrating the spherulite of iPP
at (a) 2 min and (b) 10 min respectively.

(a) iPP/α-NA 0.05wt% 2 min   (b) iPP/β-NA 0.05wt% 2 min

(c) iPP/α-NA 0.40wt% 2 min   (d) iPP/β-NA 0.15wt% 2 min
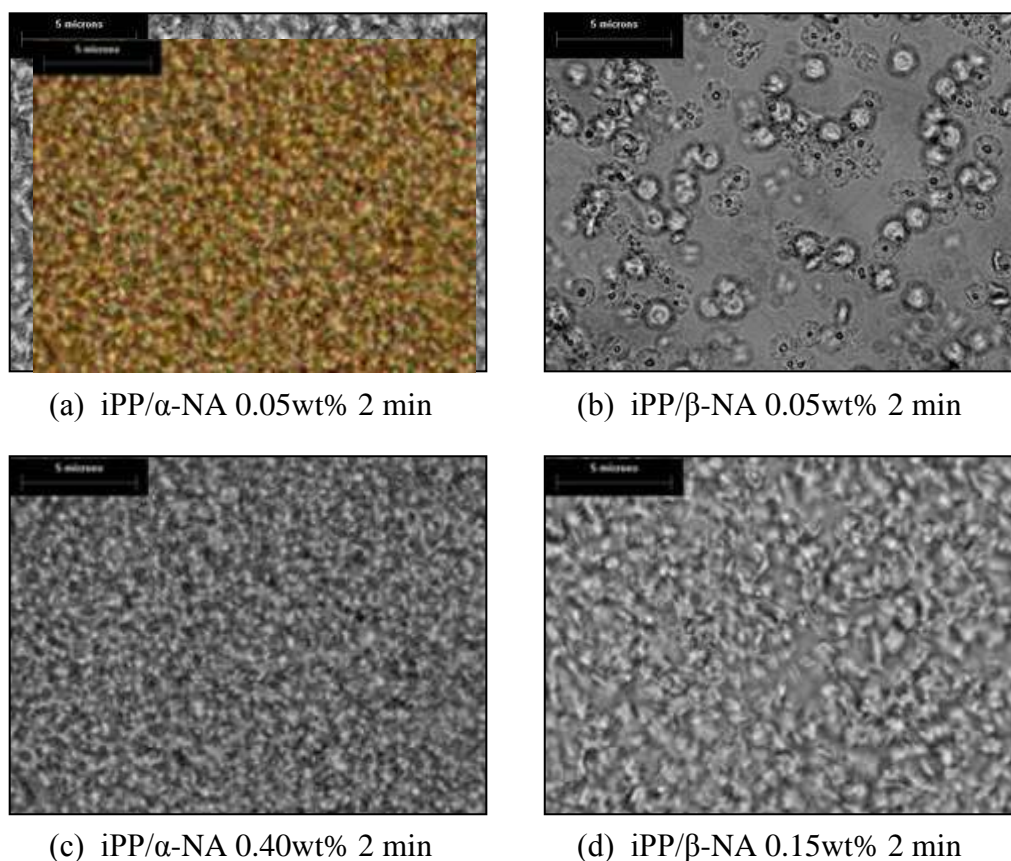
Figure 5. The optical micrographs illustrating the crystallization of iPP
and iPP with alpha and beta NAs at 0.05 and 0.15wt% at 2 min.

4.   CONCLUSIONS

The degree of crystallinity of iPP with alpha NA was significantly higher than that of the iPP with beta NA because the α-form is a simpler form of iPP spherulite, generated in normal conditions and it has high thermal stability. The iPP and the iPP modified with alpha NA exhibited mainly α-phase. The β-phase was detected when beta NA was added more than 0.05wt%. A large fraction of the β-phase was found at 0.85 when 0.01% of beta NA was added.

The melting crystalline temperature of the iPP and the iPP modified alpha NA with α-phase appeared as only one peak at around $165^{o}C$. The iPP modified with beta NA exhibited

two peaks at 167°C and 147°C, of which the lower one corresponded to beta phase. The crystallization temperature increased with initial addition of both NAs.

The iPP crystallized slowly to form spherulite in sizes ranged from 100 to 200µm. The addition of nano-scaled NAs increased vastly the nuclei, and reducing the sizes of the spherulite. The crystal size was in the range from 1 to 2µm, the higher NA content led more rapid crystal growth to extremely fine sizes.

5. ACKNOWLEDGEMENTS

6. REFERENCES

1   Nagarajan, K., & Levo K., & Myerson A.S. (2000). Nucleating agents in polopropylene. *Journal of Thermal Analysis and Calorimetry*, 59, 497-508.
2   Raab, M., & Scudla J., & Kolarik J. (2004). The effect of specific nucleation on tensile mechanical behaviour of isotactic polypropylene. *European Polymer Journal*, 40, 1317-1323.
3   Kotek J., & Raab M., & Baldrian J., & Grellmann W. (2002). The effect of specific β-Nucleation on Morphology and Mechanical Behavior or Isotactic Polypropylene. *Journal of Applied Polymer Science*, 85, 1174-1184
4   Moore, E. P. (1996). *Polypropylene Handbook.* Munich: Carl Hanser Verlag.
5   Karian, H. G. (2003). *Handbook of Polypropylene and Polypropylene composites*. (2nd ed.). New York: Marcel Dekker.
6   Karger-Kocsis, J. (1999). *Polypropylene: An A-Z reference*. Dordecht: Kluwer Academic Publishers.
7   Romankiewicz, A., & Sterzynski T., & Brostow. W. (2004). Structural characterization of α- and β-nucleated isotactic polypropylene. *Polymer International*, 53, 2086-2091.
8   Xu, L., & Xu, K., & Chen, D., & Zheng, Q., & Lui, F., & Chen, M. (2009). Thermal behavior of isotactic polypropylene in different content of β-nucleating agent. *Journal of Thermal Analysis and Calorimetry*, 96, 733-740.
9   Tjong, S.C., & Shen, J.S., & Li., R.K.Y. (1996). Mechanical behavior of injection molded β-crystalline phase polypropylene. *Polymer Engineering and Science*, 36, 100-105.
10   Zhang, P., & Liu, X. & Li, Y. (2006). Influence of b-nucleating agent on the mechanics and crystallization characteristics of polypropylene. *Material Science and Engineering*, A 434, 310-313.

Surface Characteristic of Mesostructured Cellular Foam (MCF) Silica and Nickel Supported on the MCF Materials

Lilis Hermida[1,2], Ahmad Zuhairi Abdullah[1]*, Abdul Rahman Mohamed[1]
[1]School of Chemical Engineering, Universiti Sains Malaysia,
14300 Nibong Tebal, Penang, Malaysia.
[2]Department of Chemical Engineering, Universitas Lampung,
Bandar Lampung 35145, Lampung, Indonesia.
*Corresponding authors: chzuhairi@eng.usm.my

Abstract: *Surface characteristics of mesostructured cellular foam (MCF) silica materials prepared at an aging temperature of 80 ^{o}C and different aging times were investigated. The effect of nickel nanoparticle incorporation into these structures was also examined in terms of surface area, pore volumes and cell size and window pore size which were obtained from nitrogen adsorption-desorption measurements. The structures properties were also characterized using TEM and SEM analysis. The nitrogen adsorption-desorption measurements show that the window pore size increased with the aging time in the MCF silica synthesis. The window pore size of MCF silica material significantly affected the nickel nanoparticle incorporation.*

Keywords: MCF silica, Nickel catalyst, Pore structure, Surface characteristic

1. INTRODUCTION

Supported nickel catalysts have attracted research attention as heterogeneous catalysts because of their application in many important petrochemical industries such as hydrogenation, methanation, reforming, and hydrocracking. Besides nickel particle dispersion in catalyst support, it is found that pore size was a crucial variable affecting the catalyst performance, as the catalytic reactions rely on the presence of active centres located on the pore structures of the catalysts. Larger-pore sizes of catalyst provide better diffusion of reactants and products during the course of reactions. Therefore, well-dispersed the active centres on the high pore size are always desirable. Catalyst support may play a more active role in increasing the dispersion and stability of metal particles[1]. The main function of catalyst support is to keep up a fine dispersion of nickel particles and prevent the particle from aggregating relying on its confining nanosized environments [2].

Mesoporous silicas (such as MCM-4, SBA-15, HMS) having high surface area and high porosity (pore size of up to 10 nm) have been widely studied as a catalyst support for incorporation of sulphated metal oxides[3,4], platinum nanoparticles [5] and propyl sulfonic acid[6-8]. The mesoporous silicas have also been extensively used as supports for incorporation of nickel particles. Nickel functionalized mesoporous silicas hav been successfully applied for hydrochorination of chlorobenzene[9], catalytic reforming of methane with carbondioxide to produce synthesis gas (syngas)[10], hydrogenation of naphthalene[11], etc.

Mesostructured cellular foam (MCF) silica is a class of three-dimensional (3D) hydrothermally robust materials with ultra-large mesopores (up to 50 nm) [12-14]. In terms of the textural and framework structure, the MCF materials are composed of uniform spherical cells interconnected by window pores with a narrow size distribution [12]. Owing to their 3D mesopore system with pore sizes substantially larger than those of MCM-41 or SBA-15 mesostructures, MCF materials are known to have advantages in terms of better diffusion of reactants and products. This allows them to better overcome mass transfer limitations in many

reactions[14,15] . However, there has been quite limited information about the utilization of MCF silica as supports for loading of catalytically active component and there is no report in the literature dealing with dispersion of nickel particle on mesostructured cellular foam (MCF) silica so far.

In the present study, MCF silica materials with different mesostructure characteristics were prepared at various conditions in terms of aging time and used as support for nickel catalyst. Incorporation of nickel particle in the MCF silica was carried out using deposition and precipitation (DP) method followed by reduction process. Surface characteristics of the MCF silica materials prepared and their functionalization with nickel particle were examined by nitrogen adsorption-desorption measurements, TEM and SEM analysis.

2.   EXPERIMENTAL

2.1.   Preparation of MCF silica material

MCF silica materials with different structures were synthesized according to previously reported procedure [16] except the amount of acidic solution, the use of $NH_4F.HF$, the use of a lower aging temperature (80 ^oC) and various aging times. In a typical synthesis 4 g of P123 was dissolved in 70 ml of 1.6 M HCl. Then, 6.8 ml of TMB was added, and the resulting solution was heated to 40 ^oC with rapid stirring to synthesis of microemulsion (template). After stirring for 2 h, 9,2 ml of TEOS was added to the solution and stirred for 5 min. Then the solution was transfered into a poly-ethylene bottle at 40 ^oC in an oven for 20 h for formation of pre-condensed silica foam. After that, the mixture was removed from the oven and then $NH_4F.HF$ (92 mg in 10 ml DI water) was added to the mixture with slow mixing. Then the mixture was aged at 80 ^oC in the oven for certain aging time. Three samples were prepared for such mixtures, MCF-1D was aged for 1 day, MCF-2D was aged for 2 days and MCF-3D was aged for 3 days. After cooling, the mixture was filtered and then dried at 100 ^oC for 12 h. After that, calcination was carried out in static air at 300 ^oC for 0.5 h and 500 ^oC for 6 h to remove the template. The calcined MCF silica materials were used as support for Ni catalyst.

2.2.   Incorporation of nickel catalyst on MCF silica materials

MCF-1D, MCF-2D and MCF-3D materials were then functionalized with nickel using deposition precipitation method adopted from Nares et al[11]. In the functionalization reaction. 250 ml of an aqueous solution containing 10.156 g of $Ni(NO_3)_2.6H_2O$ and 0.3 ml of HNO_3 69% wt/wt was prepared. In a typical preparation, 40 ml of the aqueous solution was used for dissolving 6.3 g urea at room temperature to produce a urea solution and 210 ml of the aqueous solution was mixed with 1.9 g of MCF silica materials to make a suspension. The suspension was heated at 40 ^oC, and then mixed with the urea solution under rapid mixing. After that, the mixture was heated to 90 ^oC for 2 h under static condition. After cooling, the mixture was filtered and the solid was washed three times with 20 ml distilled hot water (~50 ^oC), then dried at 100 ^oC for 12 h. Then, the solid was calcined in static air at 300 ^oC for 6 h. The calcined solids were designated as NiMCF-1D(C), NiMCF-2D(C) and NiMCF-3D(C). Then the samples were reduced at 550 ^oC for 2.5 h in hydrogen stream, and then cooled to room temperature under nitrogen flow. The reduced samples were designated as NiMCF-1D(R), NiMCF-2D(R) and NiMCF-3D(R).

2.3.   Characterization

Nitrogen adsorption–desorption isotherms were measured using a Quanta-chrome Autosorb 1C automated gas sorption analyzer at liquid nitrogen temperature. Prior to the experiments, samples were degassed (P < 10^{-1} Pa) at 270 ^oC for 6 h. The amount of nitrogen

gas adsorbed over a range of partial pressures at a single temperature was measured to obtain a graph known as an adsorption isotherm, whilst desorption isotherm was obtained by measuring the quantities of gas desorbed from the sample as the relative pressure was lowered. Specific surface areas were calculated using BET method (S_{BET}), while pore size distributions were obtained using the Barrett-Joyner-Halenda (BJH) model applied to adsorption and desorption isotherms data for cell and window pore sizes.

SEM images were capture using an Leo Supra 50 VP field emission SEM. TEM images were provided by Philips CM 12 transmission electron microscope. Before the TEM analysis, sample of about 0.08 g was first dissolved in a 5 ml of 100 % ethanol. Then, the solution was shaken for a moment; and subsequently a small amount of the solution was taken using a micropipette and dropped on a metal grid for the analysis.

3.   RESULT AND DISCUSSION

Table 1 summarizes textural properties of various MCF silica supports prepared at different aging times and the corresponding nickel functionalized MFC catalysts after the reduction process. The textural properties were derived from nitrogen adsorption-desorption data using BJH method for cell and window pore size, and using BET method for total pore volume and surface area. For the MCF silica supports, window pore size generally increased with increasing aging time whilst cell size remained stable as can be seen from Table 1. The window pore sizes (from 125 A to 158 Å) were within mesoporous range. This result could be attributed to that the 'soft silica" –coated TMB/P123 microemulsion droplets (composite droplets) increased in size and expanding the window pore size in the composite droplets during the aging step at 80 ^{o}C. At the same time, condensation of silica in the walls continuously took place with the formation of Si-O-Si linkages solidifying inorganic network, and the materials with increased pore size gradually rigidified [17,18]. The longer duration of aging was attempted, the bigger increase of window pore size in MCF structure would be formed.

Table 1. Summary of the nitrogen-sorption results

Sample	S_{BET} (m^2/g)	V_{pore}(cm^3/g)	d_{cell} (Å)	$d_{window\ pore}$ (Å)
MCF-1D	394	1.85	235	125
MCF-2D	375	2.24	232	130
MCF-3D	378	2.12	235	158
NiMCF-1D(R)	253	0.93	233	153
NiMCF-2D(R)	281	1.02	184	125
NIMCF-3D(R)	307	1.09	234	90

d_{cell} and $d_{window\ pore}$ are the cell and window pore diameters, respectively, determined by the BJH method,13 S_{BET} is the surface area determined by the BET method, and V_{pore} is the total pore volume determined at a relative pressure of 0.9948

The table also shows that total surface area decreased from 394 to 375 cm^2/g if the aging time was increased from 1 day to 2 days. The reduction of the BET surface areas with increased aging time might be related to the enlarged window pore sizes and denser framework walls [17,18]. However, the total surface area slightly increased from 375 to 378 cm^2/g if the aging time was increased from 2 days to 3 days. The increase in aging time from 1 day to 2 days resulted in an increase in total pore volume from 1.85 to 2.24 cm^3/g. Further increase in aging time to 3 days caused a slight decrease of the total pore volume to 2.12 cm^3/g. Moreover, incorporation of nickel particle on MCF silica materials resulted in a decrease in textural parameters like total surface area, total pore volume, cell size and window pore size.

The reduction of total pore volume of MCF materials after the functionalization can be confirmed by pore size distribution curves. The pore size distributions of cells and connecting window pores of MCF silica materials and nickel species functionalized MCF materials are shown in Figure 1. The figure shows strong evidences of pore volume reductions in which cell and window pore size distribution curves in nickel species functionalized MCF materials (NiMCF-1D(R), NiMCF-3D(R), and NiMCF-3D(R)) were smaller compared to those in MCF materials. Furthermore, functionalization of MCF-1D resulted in a bimodal window pore size distribution with maximum peaks at around 30 Å and 150 Å. The maximum peak in window pore size distribution of MCF-1D parent material was at around 150 Å. Meanwhile, the maximum peak of cell size distribution (at about 230 Å) in MCF-1D did not change after the functionalization. Functionalization of MCF-2D resulted in a decrease in the maximum peak of cell size distribution from about 230 to 200 Å but the maximum peak of window pore size distribution (at about 130 Å) in MCF-2D was about the same as that in the nickel functionalized MCF-2D material. Different observation was made for MCF-3D material, in which maximum peak in window pore size distribution was much lower after the functionalization with nickel species. The observed reduction of pore volume, cell and window pore sizes of nickel species functionalized MCF materials were attributed to the attachment of the desired nickel species to the pore surface.
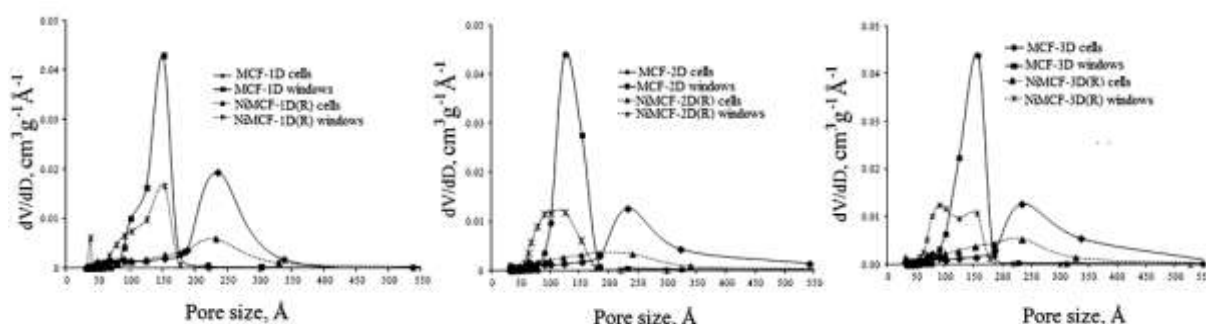
Figure 1. Cell and window pore size distribution of MCF silica materials and nickel species functionalized MCF silica after reduction process

Nitrogen adsorption-desorption isotherms for MCF silica materials shown in Figure 2 are of type IV as hysteresis occurs in multilayer range of physisorption isotherms. This hysteresis is often associated with capillary condensation (the pore filling process) in mesopore structure [19]. The nitrogen adsorption-desorption isotherms are in close agreement with those published previously [12,13,17,18] and exhibit a large H1 hysteresis loop, which suggests that the MCF material possesses cell-type mesopores connected by smaller window pores. According to IUPAC (International Union of Pure and Applied Chemistry) recommendation, pores with diameter not exceeding 20 Å are defines as micropores, while mesopores are pores with diameter between 20 and 500 Å, and macropores represent pores with diameter greater than 500 Å [19]. Type IV adsorption isotherms usually flatten at high P/P0 indicating that the mesopore filling was complete [20]. However, final upward turn was observed for all the isotherm curves as shown in Figure 2. This was due to capillary condensation in macropores or in interstices between grains as reported in the literature [21].
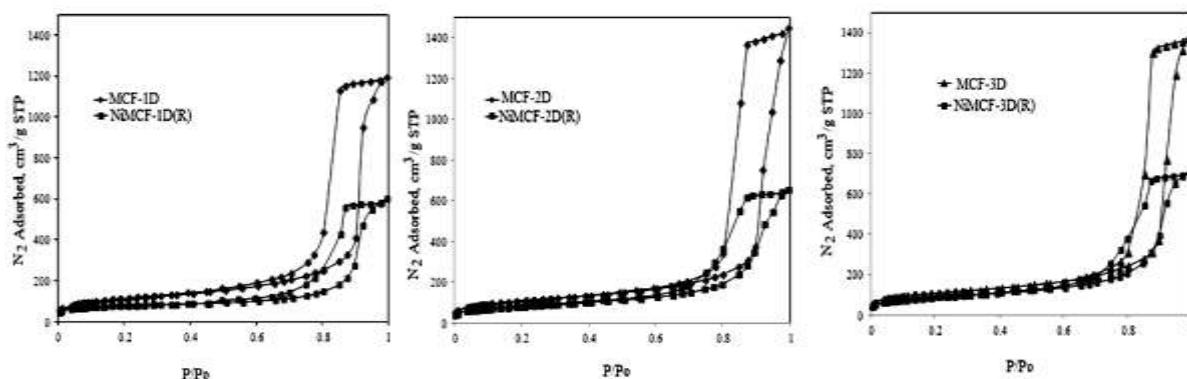
Figure 2. Nitrogen adsorption-desorption isotherm of MCF silica materialand nickel species functionalized MCF silica after reduction process.

Surface functionalization of MCF silica materials with nickel species followed by reduction process in hydrogen flow at 550 $^\circ$C, i.e. NiMCF-1D(R), NiMCF-2D(R), NiMCF-3D(R), resulted in lower isotherm curves but no appreciable change in the form of the isotherms (Figure 2). This indicates that total pore volume decreased but the mesoporosity of the MCF materials was maintained after functionalization. Furthermore, it can be noted that, for MCF-3D material, the functionalization resulted in the highest isotherms compared to MCF-1D and MCF-2D materials, possibly indicating the lowest densification of the silica walls.
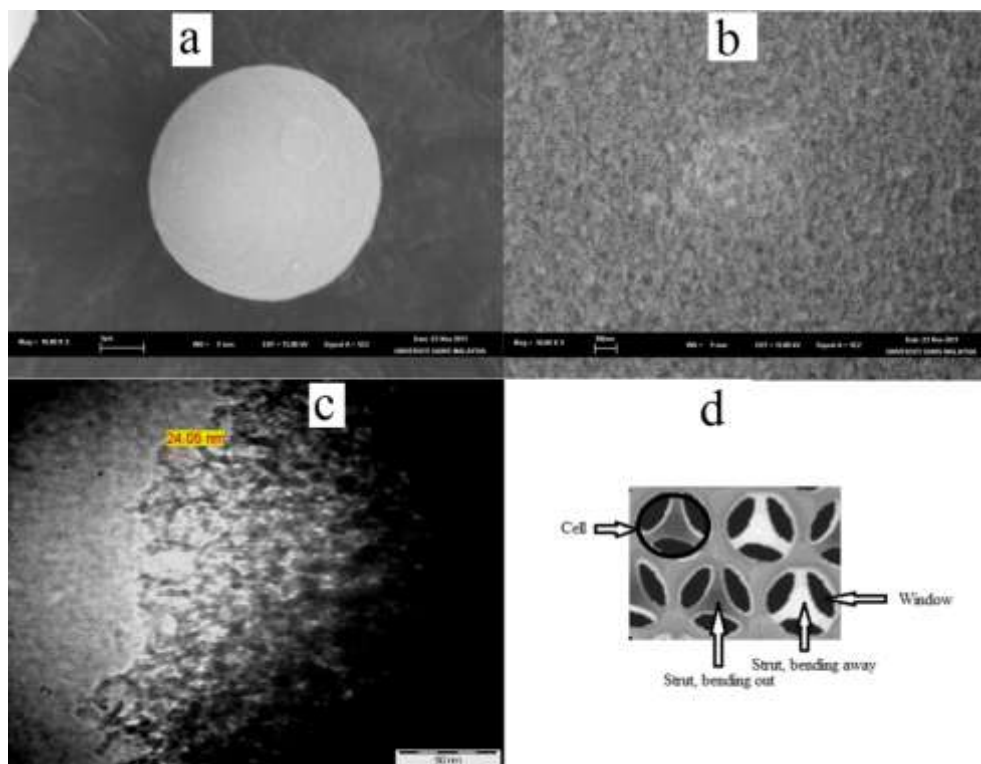
Figure 3, (a) SEM image of MFC-3D morphology, the scale bar represents 1μm. (b) A higher magnification image showing the morphology of the MCF-3D surface. (c) TEM image of MCF-3D, the scale bar represents 50 nm. (d) Schematic cross section of MCF material[18].

Figure 3(a) shows scanning electron microscope (SEM) image of MCF-3D material that clearly confirmes a spherical particle of MCF-3D with a size of about 5 μm in diameter. A higher magnification SEM image (Figure 3(b)), and transmission electron microscopy (TEM) image (Figure 3(c)) show that MCF-3D possessed a mesoporous structure with cell size of about 240.5 Å (24.05 nm), which was consistent with the average cell size (235 Å) obtained from nitrogen adsorption-desorption data (Table 1). The TEM image also confirmed a disordered array of silica struts composed of uniform-sized spherical cells interconnected by window pores with a narrow size distribution, which is the characteristic structural feature of MCF material [12,18]. It has been reported in the literature that schematic cross section of MCF material is of strutlike structure, as given in Figure 3 (d), showing that the cells of the MCF structure are framed by the silica struts [18]. The wall thickness of the MCFs estimated by TEM is about 5 nm, in agreement with the thick, robust framework walls observed in MCF-type mesoporous silica as reported in the literature [18].
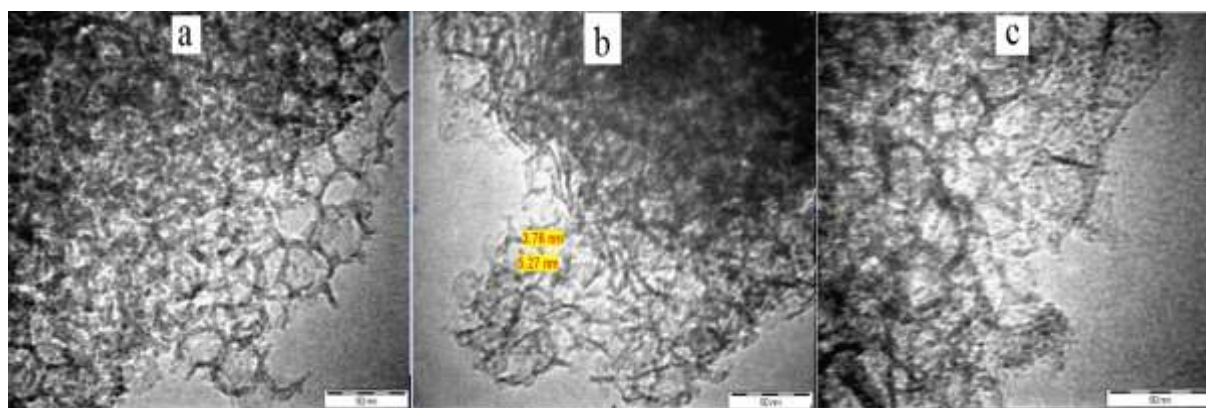
Figure 4. TEM images of (a) NiMCF-1D(R), (b) NiMCF-2D(R) and (c) NiMCF-1D(R)

Functionalization of MCF silica materials with Ni that were prepared at different aging times (MCF-1D, MCF-2D and MCF-3D) with nickel species followed by reduction process resulted in dispersed nickel particles on the MCF silica materials, as shown though TEM images in Figure 4. The figure clearly shows that nickel nanoparticles visible as dark spots were successfully distributed inside the pore of MCF materials and their mesostructures were preserved after the functionalization. This result was consistent with that reported by Na-Chiangmai et al.[22] who observed that functionalization of MCF material with Pd nanoparticles had no significant influent on structure of the mesoporous host material. For NiMCF-1D(R) and NiMCF-2D(R) prepared using MCF host with aging time for 1 and 2 days, respectively, spherical Nickel particles with sizes about 3.76 – 5.27 nm and irregular shape were found to be dispersed on the MCF supports as shown in Figure 4 (a) and 4 (b). However, for NiMCF-3D(R) prepared using MCF host with aging time for 3 days, a narrow nickel particle size distribution and much smaller nickel particles with a mean particle size about 1-2 nm were observed. Through the TEM images it can be noted that the amount of nickel nanoparticles particles observed in NiMCF-3D(R) was the highest compared to that in NiMCF-1D(R) and NiMCF-2D(R). The amount of nickel nanoparticles dispersed on the MCF materials seems to decrease in the order NiMCF-3D(R) > NiMCF-2D(R)> NiMCF-1D(R).
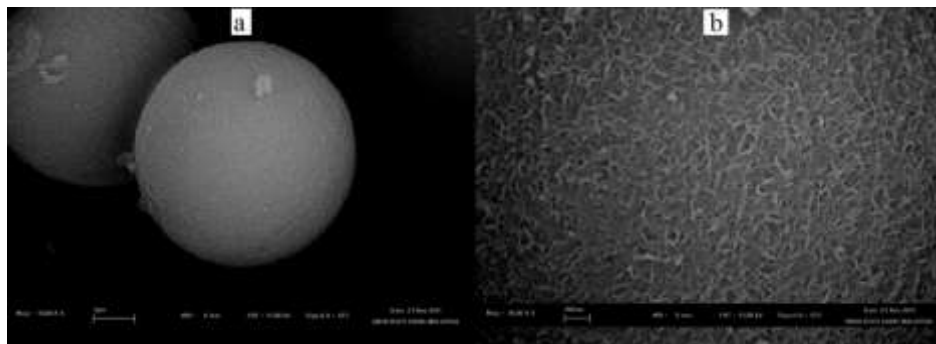
Figure 5. SEM image of NiMFC-3D(R) morphology, the scale bar represents 1μm. (b) A higher magnification image showing the morphology of the NiMFC-3D(R) surface,

It could be envisioned that window pore size of MCF material used as a host was the main factor that influenced the nickel nanoparticle incorporation. The window pore size of MCF host prepared using aging time of 3 days (MCF-3D) was the highest among the others and window pore size of MCF-2D was higher than that of MCF-1D, as presented in Table 1. As such, most of nickel nanoparticle could be easily introduced through the window pore size of MCF-3D host. This results in the highest amount of nickel nanoparticles in the NiMCF-3D(R). It can be concluded that larger window pore size of MCF host resulted in the easier incorporation of nickel nanoparticle with smaller sizes. Figure 5 (a) showing SEM image of NIMCF-3D(R) particles clearly confirms their spherical shape of about 5 μm in diameter which was maintained after nickel nanoparticle incorporation. A higher magnification SEM image in Figure 5 (b) shows that the uniform nickel nanoparticles in the form of nanoworms were well dispersed in the framework of the MCF-3D host. Hence, a suitable host was necessary for obtaining a high dispersion of nickel species with small size into the mesoporous framework

4.   CONCLUSIONS

Incorporation of nickel nanoparticles into MCF silica materials prepared at aging temperature of 80 $^{\circ}$C and various aging times (1, 2 and 3 days) was successfully carried out. The increase in aging time resulted in increase in window pores size in the MCF materials. Meanwhile, total surface area and pore volume tended to decrease. The nickel nanoparticle incorporation into the MCF silica materials was prepared using deposition-precipitation method at 90 $^{\circ}$C for two hours followed by reduction process for 2.5 h at 550 $^{\circ}$C. The window size was deemed the critical dimension controlling for the nickel nanoparticle incorporation. Among the MCF silica with various window pore sizes used in this study, MCF-3D with the highest window pore size was the best host for the nickel nanoparticle incorporation as most of nickel particles with small sizes were easily introduced as confirmed in TEM analysis results.

5.   REFERENCES

1. Taylor, W. F., Yates, D. J. C., and Sinfelt, J. H. (1964). Catalysis over supported metals II. The effect of the support on the catalytic activity ofnickel for ethane hydrogenolysis. *J. Phys. Chem.,* 68, 2962- 2966.
2. Niu, K., Shi, D., Dong, W., Chen, M., Zhongbin. N. (2011). Chelating template-induced encapsulation of NiO cluster in mesoporous silica via anionic surfactant-templated route. *J. Colloid Interface Sci.,* 362, 74–80.

3. Hermida, L., Abdullah, A.Z., Mohamed, A.R. (2010). Post synthetically functionalized SBA-15 with organosulfonic acid and sulphated zirconia for esterification of glycerol to monoglyceride. *J. App. Sci.*, 10 (24), 3199–3206.

4. Degirmenci, V., Yilmaz, A., Uner, D. (2009). Selective methane bromination over sulfated zirconia in SBA-15 catalysts. *Catal. Today.* 142, 30–33.

5. Huang, T., Tu, W. (2009). Modification of functionalized mesoporous silica on the formation and the catalytic performance of platinum nanocatalysts. *Appl. Surf. Sci.,* 255, 7672–7678.

6. Hermida, L., Abdullah, A.Z., Mohamed, A.R. (2011). Synthesis of monoglyceride through glycerol esterification with lauric acid over propyl sulfonic acid post-synthesis functionalized SBA-15 mesoporous catalyst. *Chem. Eng. J.*, 174, 668– 676.

7. Kureshy, R.I., Ahmad, I., Pathak, K., Khan, N.H., Abdi , S.H.R., Jasra, R.V.(2009). Sulfonic acid functionalized mesoporous SBA-15 as an efficient and recyclable catalyst for the synthesis of chromenes from chromanols. *Catal. Commun.,* 10, 572–575.

8. Hermida, L., Abdullah, A.Z., Mohamed, A.R. Effects of functionalization conditions of sulfonic acid grafted SBA-15 on catalytic activity in the esterification of glycerol to monoglyceride: a factorial design approach. *J. Porous Mater.* in press.

9. Chen, J., Zhou, J., Wang, R., Zhang, J. (2009). Preparation, characterization, and performance of HMS-supported Ni catalysts for hydrodechlorination of chorobenzene. *Ind. Eng. Chem. Res.*, *48,* 3802–3811.

10. Liu, D., Lau, R., Borgna, A., Yang Y. (2009). Carbon dioxide reforming of methane to synthesis gas over Ni-MCM-41 catalysts. *Appl. Catal. A.*, 358, 110–118.

11. Nares, R., Ramırez, J., Gutierrez-Alejandre, A., Cuevas, R. (2009).Characterization and hydrogenation activity of Ni/Si(Al)- MCM-41 catalysts prepared by deposition-precipitation. *Ind. Eng. Chem. Res. 48,* 1154–1162.

12. Schmidt-Winkel, P., Lukens Jr., W.W., Zhao, D., Yang, P., Chmelka, B.F., Stucky, G.D. (1999). Mesocellular siliceous foams with uniformly sized cells and windows. *J. Am. Chem. Soc.,* 121 254-255.

13. J.S. Lettow, Y.J. Han, P. Schmidt-Winkel, P. Yang, D. Zhao, G.D. Stucky, J.Y. Ying, Hexagonal to mesocellular foam phase transition in polymer-templated mesoporous silicas. *Langmuir,* 16 (2000) 8291-8295.

14. On, D.T., Kaliaguine, S. (2003). Zeolite-coated mesostructured cellular silica foams. *J. Am. Chem. Soc.*,125, 618-619.

15. Han, Y.J., Watson, J.T., Stucky, G.D., Butler, A. (2002). Catalytic activity of mesoporous silicate-immobilized chloroperoxidase . *J. Mol. Catal, B.*, 17, 1-8.

16. Han, Y., Lee, S. S., Ying, J. Y. (2010). Siliceous mesocellular foam for high-performance liquid chromatography: Effect of morphology and pore structure. *J. Chromatogr. A.* 1217, 4337–4343

17. Schmidt-Winkel, P, Glinka, C.J, Stucky, G.D. (2000).Microemulsion templates for mesoporous silica. *Langmuir,* 16, 356- 361.

18. Schmidt-Winkel, P, Lukens,W.W, Yang, P., Margolese, D.L., Lettow, J.S., Ying, J.Y., Stucky, G.D. (2000). Microemulsion templating of siliceous mesostructured cellular foams with well-defined ultralarge mesopores. *Chem Mater.*, 12, 686-696.

19. Sing, K.S.W. (1998). Adsorption methods for the characterization of porous materials. *Adv. Colloid Interface Sci.,* 76 – 77, 3-11.

20. Barton, T. J., Bull, L. M., Klemperer, W. G., Loy, D. A., McEnaney, B., Misono, M., Monson, P. A., Pez, G., Scherer, G. W., Vartuli, J. C., and Yaghi, O. M. (1999). Tailored porous materials. *Chem. Mater.,* 11, 2633-2656.

21. Sing, K.S.W., Everett, D.H., Haul, R.A.W., Moscou, L., Pierotti, R.A., Rouquerol J., Siemieniewska, T. (1985). Reporting physisorption data for gas/solid systems with special reference to the determination of surface area and porosity. *Pure Appl. Chem.,* 57, 603–619.

22. Na-Chiangmai, C., Tiengchad, N., Kittisakmontree, P., Mekasuwandumrong, O., Powell, J., Panpranot, J. (2011). Characteristics and catalytic properties of mesocellular foam silica supported Pd nanoparticles in the liquid-phase selective hydrogenation of phenylacetylene. *Catal. Lett.,* 141, 1149–1155.

Synthesis and characterization of polymer hydrogel composites based on poly (acrylic acid) grafted cotton microfiber

Waham Ashaier Laftah[1,*], Shahrir Hashim[2], [c]Akos N. Ibrahim[3]

[1, 2, 3] Department of Polymer Engineering, Faculty of Chemical Engineering, Universiti Teknologi Malaysia

*Corresponding author: waham2007@yahoo.com

Abstract: *The effect of cotton micro- powder (CTN), initiator (APS), cross-linker (MBA), sodium hydroxide (NaOH) on water absorption capacity were optimized using central composite design method (CCD). Swelling rate, water release rate and re-swelling capacity were studied. The affect of cotton microfiber on thermal stability of PHG was investigated using thermal gravimetric analysis (TGA). The function group of PHG was characterized using FTIR. Morphology study of PHG was carried out using scanning electromagnetic (SEM). The highest WAC was obtained at 1.28, 0.15, 13.09 and 13.54 wt. % of APS, MBA, NaOH and CTN respectively. Grafted PHG had better swelling rate, absorption and holding capacity than unfilled PHG.*

Keywords: polymer hydrogels, water absorption capacity, swelling properties, hydrogel composites

1.   INTRODUCTION

Polymer hydrogels (PHGs) are visco-elastic loosely crosslink hydrophilic three dimensional networks of flexible polymer chains with dissociated ionic functional groups, that can absorb large amount of water or other biological fluid in a short time and retain them under pressure [1, 2, 3, 4, 5]. PHGs have been abundantly used in disposable diaper industry for the past 35 years. PHGs applications are still being expanded to many fields including agriculture, horticulture, sealing composites, artificial snow, drilling fluid additives, medicine for drug delivery system and more. Recently, the preparation of polymer hydrogels composites (PHGCs) received great attention because of their relatively low production cost and high water absorbency. There is a wide range of organic and inorganic materials available for preparation of PHGCs such as kaolinite, montmorillonite (MMT), hectite, saponite , synthetic mica, used paper (UP), oil palm empty fruit bunch (OPEFB) , and wheat strew (WS). Some of these materials are used in Nanosize to prepare Nanocomposite of PHG such as fabrication of silver or zinc nanoparticles. PHGC materials find many new applications beyond those of PHG such as catalysis, optics, electronics, bio-medicals and quantum-sized domain applications. Also, there are some potential applications of PHGC in water treatments which have already been described [6, 7].

2. SYNTHESIS OF POLYMER HYDROGELS

2.1 Materials

Acrylic acid (AA) is a product from Merck, USA, Ammonium persulphate (APS), *N,N'*-Methylene-bis-acrylamide (*N,N'*-MBAAm), Sodium Hydroxide (NaOH), sodium chloride (NaCl) are products of Sigma-Aldrich, Natural cotton ball (CTN) is a product by Nibong Tebal Enterprise SDN BHD.

2.2 Preparation of PHGs

Response surface methodology and quadratic model were used for experiments designing and optimization. Certain amount of AA was mixed with 10 ml water in three-neck flask equipped with magnetic stirrer, thermometer, condenser and nitrogen line. The flask was placed in a thermostat water bath. NaOH was added and allowed to stay for 10 min at room temperature. Temperature was increased gradually till 60 ^{o}C after which CTN Micro-fiber, MBA and APS were added under nitrogen atmosphere and constant stirring (NaOH, APS and MBA was diluted by distilled water before added). The mixture in the flask was made up to constant volume using distilled water. Thick and viscose products were observed after 15 min. The product was finally washed several times with distilled water and dried at 60°C to constant weight.

2.3 Experimental Design and Statistic Analysis

Four independent variables were used in this study (X1, APS % ; X2, MPA %; X3, NaOH, %; X4, CTN) with high and low levels as shown in table1. The complete design consisted 27 runs (24 are factorial points and 3 are central points). Central composite design (CCD) data were analyzed via multiple regressions to fit equation 1 of quadratic polynomail model.

$$Y = \beta_{k0} + \sum_{i=1}^{4} \beta_{ki} x_i + \sum_{i=1}^{4} \beta_{kii} x_i^2 + \sum_{i<j=2}^{4} \beta_{kii} x_i x_j \qquad (1)$$

Where Y is the response function; β_{k0} is an intercept; $\beta_{ki}, \beta_{kii} \, and \, \beta_{kii}$ are the coefficients of quadratic terms; $x_i \, and \, x_j$ are the coded independent variables respectively. Design of Expermants (DOE) version 8.0.6 softwere was used to analyze the experimental data and visualize the factors effect on WAC.

Table 1: Independent variables and their high and low leveles

Factor	Name	Units	Minimum	Maximum
A	APS	wt. %	0.4	4
B	MBA	wt. %	0	0.4
C	NaOH	wt. %	0	20
D	CTN	wt. %	0	40

3.   TESTING AND CHARACTERIZATION

3.1   Measurement of WAC

Certain amount of dried PHG samples were placed in weighed tea bags and immersed into excess distilled water and allowed to soak at room temperature to achieve swelling equilibrium. The swollen samples were filtered using sieves to remove non-absorbed water and weighed again. The water absorbency was calculated using the following equation:

$$WAC = (M - M_0)/M_0 \qquad\qquad (2)$$

Where M and M_0 denote the weight of swollen and dry sample respectively, and WAC is the water absorption capacity g/g.

3.2   Swelling Rate and Reswelling

Convinced amount of PHG sample of 10-20 size mesh was placed in weighed tea bags and then immersed in 200 ml distilled water. For 30 min time intervals, the samples were weighted and WAC was calculated using equation 3. Re-swelling capacity measurements were carried out by immersed certain amount of PHG sample in excess distilled water to achieve swelling equilibrium and then the swollen sample was placed in an oven to dehydrate at 70°C. After thorough drying, sample was immersed in distilled water to reach swelling equilibrium again. Similar procedures were used to evaluate the samples re-swelling capability by calculating WAC after each step using equation 2.

3.3   Water Release From PHGs

Definite amount of PHG sample of 10-20 size mesh were placed in a weighted tea bag and immersed in distilled water. After the equilibrium swelling capacity was reached the sample was sieved and weighed for interval time at room temperature. Water release rate (WRR) was calculated using equation 3.

$$WRR\% = \frac{W_{i-1} - W_i}{W_{i-1}} \times 100 \qquad\qquad (3)$$

Where WRR % is the water release rate, W_{i-1} is sample initial weight and W_i is sample weight at certain time.

3.4   FTIR Spectroscopy

PHG samples were characterized using Fourier-transform infrared (FTIR) spectroscopy to identify the functional groups. Samples were ground along with dried KBr powder. An FTIR spectrum was subjected from 4000 to 375 cm^{-1}.

3.5   Thermal Stability
Thermogravimetric analysis was used to study the thermal stability of PHGs. A Perkin Elmer Thermogravimetric Analyzer (TGA 7) was utilized to study the thermal stability in terms of temperature decomposition. Approximately 8 mg of PHG sample was heated from 35 to 700

°C at a heating rate of 10 °C/min under nitrogen atmosphere. Sample stability and weight loss were estimated accordance to ASTM D 3850-2000.

3.6   Morphology Analyses

Morphology quality of CTN fiber, PHG and PHG-g-CTN samples were examined using TM3000 scanning electron microscopy (SEM). PHG and PHG-g-CTN Samples were immersed in distilled water for 24 hours and then scanning by SEM with magnification of 250X.

4.   Result and Discussion
4.1   Statistic Analysis and Model Fitting

According to factorial design, maximum WAC (570 g/g) was recorded at (1.28 APS, 0.15 MBA, 13.09 NaOH and 13.54 CTN) wt.% content. Experimental data were analyzed using multiple regression analysis, the response and independent variables were related by following second- order polynomial equation:

$$Y = 545.2 - 29.05*X_1 - 55.93*X_2 + 26.7*X_3 - 37.95*X_4 - 1.36*X_1*X_2 + 1.92*X_1*X_3 + 12.36*X_1*X_4 + 0.15*X_2*X_3 + 11.89*X_2*X_4 - 43.58*X_3*X_4 - 17.22*X_1^2 - 63.07*X_2^2 - 44.51*X_3^2 - 60.72*X_4^2$$

ANOVA of the quadratic regression model shows that the determination coefficient $R^2 = 0.9321$ which means the model is significant and only 6.79 % of total variations were not explained by this model. P-value of less than 0.05 is an indication of significant model terms and the smaller is the more significant. P-values in table 3 indcated that the model is significant. X_1, X_2, X_3, X_4, X_2X_4, X_2^2, X_3^2, X_4^2 are significat variables in this model and X_2 X_4^2 X_2^2 are the most sagnfacant variables which means they are the most effective values in this model.

Table 2: Response surface central composite desing and water absorption capasity results

Run	APS wt. %	MBA wt. %	NaOH wt. %	CTN wt.%	WAC g/g
1	0.4	0.2	10	20	512.1
2	3.1	0.1	5	30	347.4
3	1.3	0.1	15	10	570.5
4	3.1	0.3	15	30	219
5	2.2	0.2	10	20	511.9
6	1.3	0.1	5	10	492.3
7	2.2	0.2	10	20	591
8	3.1	0.3	5	10	235
9	2.2	0.4	10	20	204.6
10	1.3	0.3	15	10	488.4
11	1.3	0.3	15	30	265
12	3.1	0.1	15	10	543
13	2.2	0.2	20	20	408
14	3.1	0.3	15	10	345
15	3.1	0.3	5	30	286.2
16	1.3	0.3	5	10	290
17	2.2	0.2	10	20	535.7
18	1.3	0.3	5	30	298
19	2.2	0.2	0	20	294.6
20	2.2	0	10	20	349.5
21	1.3	0.1	15	30	371
22	2.2	0.2	10	0	321.5
23	3.1	0.1	15	30	358
24	3.1	0.1	5	10	374
25	4	0.2	10	20	408.8
26	2.2	0.2	10	40	251.4
27	1.3	0.1	5	30	423

Table 3: Regression cofficient of the quadratic polynomial model

P-value	Parameter
< 0.0001	**Model**
0.0070	X_1
< 0.0001	X_2
0.0115	X_3
0.0012	X_4
0.9032	$X_2\,X_4$
0.8636	$X_1\,X_3$
0.2817	$X_1\,X_4$
0.9893	$X_2\,X_3$
0.2997	$X_2\,X_4$
0.0018	$X_3\,X_4$
0.0949	X_1^2
< 0.0001	X_2^2
0.0005	X_3^2
< 0.0001	X_4^2

4.2   Effect of Initiator and Cross Linker Content on WAC

The results in Figure 1 indicate that WAC is low at low percentage of APS and starts to increase and reached the maximum at 1.28 wt. %. With further increase in APS percentage WAC starts to decline. These results can be explained via the effect of APS on polymer molecular weight and polymerization rate. Low percentage of initiator leads to low polymerization rate and high molecular weight distribution (MWD) and that is the main reason for large network space volume and low WAC. In contrast to high percentage of initiator, the probability of termination step is high which led to low molecular weight distribution and more chain ends therefore the produced hydrogels have loose network structure and low WAC [8, 9]. Therefore, 1.28 of APS was the optimum content to get the higher WAC. MBA was affecting WAC by the same of ABS as shown in Figure 1. The results indicated that the highest WAC was at 0.15wt. %. of MBA. Cross linking density is mainly depended on percentage of cross linking agent. Therefore, WAC was low at high and low percentage of MBA. Low MBA wt. % led to produce weak wobbly network. This kind of structure is not strong to hold and trap water molecules. High content of MBA led to decrease WAC as a result of increased number of cross linking point (ties) inside the network structure and left no space for water molecules to enter the structure. Furthermore, high percentage of MBA led to produce additional network by adding a large number of growing polymer chains into structure and that led to concentrated network which led to decrease in final WAC of PHG [10].
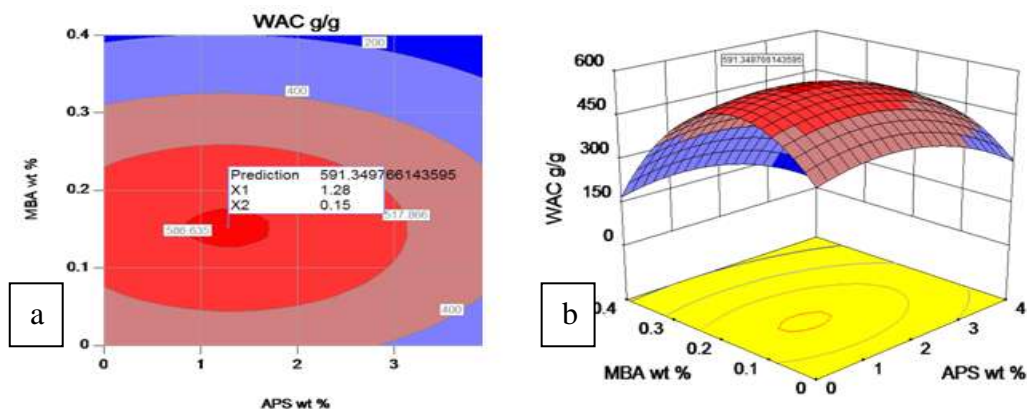
Fig 1: Effect of APS and MBA on WAC; a) Contour structure, b) Three dimensions structure

4.3   The Effect of Sodium Hydroxid and Fiber Content on WAC

Figure 2 shows that WAC of PHGs enhanced by increasing degree of neutralization (DON) to reach the maximum at 13.09 wt % of NaOH. Further increase in NaOH content led to decrease WAC. At low content of NaOH, networks electrostatic repulsion force (ESF) is less than polymer chains elastic force and that allows the chains to contract each other and don't allow water to enter the structure. Enhancing ESF via increased in NaOH content led to increase in WAC till the ESF becomes equal to the polymer chains elastic force.   Further increase in DON led to decrease in WAC as a result of increase in chain stiffness and counterion condensation (screening effect). In addition increase in Na^+ led to shielding of carpoxylate anions of PAA chains and inhibits the anion anion repulsion force which means decrease in ESF and WAC [11]. WAC gets higher initially with increase in CTN percentage. This is attributed to the enhancement of network affinity of PHG to water via high affinity material (CTN). High affinity of CTN is due to high percentage of cellulose (85-99 %) [12, 13, 14, 15]. Decrease in WAC was observed after 13.54 wt. % of CTN. That can be due to increase in cross-linking ties of PHG (CTN act as cross linker) therefore high percentage of CTN led to high cross linking density and decrease WAC.
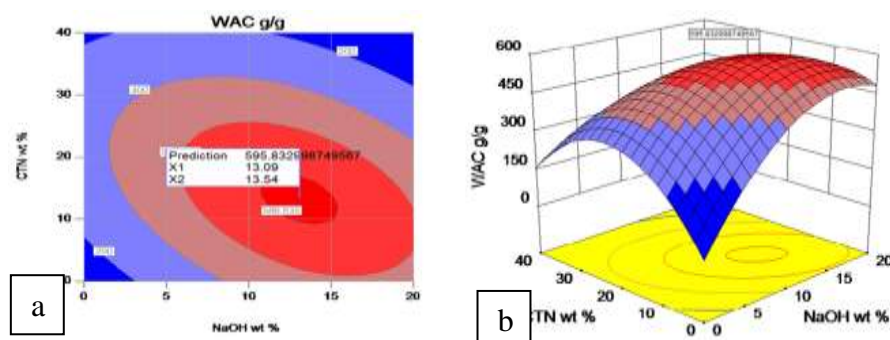
Fig 2: Effect of NaOH and CTN on WAC; a) contour structure, b) three dimension structure

4.4   Swelling Rate and Reswelling Capasity

Results in Figure 3 showed that the swelling rate of water uptake sharply increases initially and then start to level up for both samples (a, b). When the curve becomes flat this means the samples under swelling equilibrium state. The high swelling rate is observed to be with

polymer hydrogel composite (PHG-g CTN) as a result of high affinity network. High affinity makes the sample to reach the maximum swelling capacity faster due to high rate of diffusion. The result of high affinity of sample (a) is due to high content of hydrophilic material (CTN).
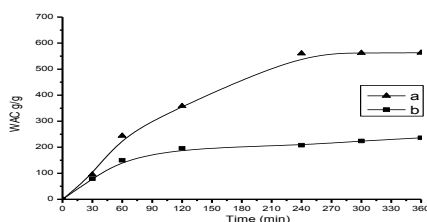
Fig 3: Swelling rate of PHG a) PHG-g-CTN (1.28 APS, 0.15 MBA, 13 NaOH and 13.5 CTN) wt.%, b) PHG (1.28 APS, 0.15 MBA, and 13 NaOH) wt.%

Figure 4 showed that PHG samples have high re-swelling capacity with no significant change in WAC of sample (a) after six runs of swelling and de-swelling. A little change in WAC was observed with unfilled PHG might be as a result of loose structure network due to swelling and de-swelling process which means PHG network becomes weaker after each run and led to decrease in WAC. In this case CTN acts as a supporting substance for the network structure and helps to stabilize the network structure of PHG.
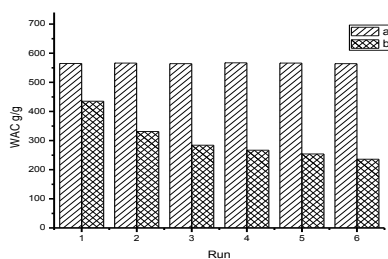
Fig 4: Re-swelling capacity of PHG a) PHG-g-CTN (1.28 APS, 0.15 MBA, 13 NaOH and 13.5 CTN) wt.% , b) PHG (1.28 APS, 0.15 MBA, and 13 NaOH) wt.%

4.5   Absorbency in Salt Solution

This test was carried out by immersing PHG samples in NaCl solution with concentrations of 0.01, 0.1, 1, 2, 3 M for 24 hrs. The results illustrated in Figure 5 indicated that WAC of PHG samples were highly affected by the concentration of NaCl in absorbed fluid. Increase in ionic strength of absorbed fluid led to decrease in PHG absorbency as a result of decrease in the difference of osmotic pressure in and outside the network structure. This result can be explained using Donnan equilibrium theory. This theory considers that the ESF is a result of osmotic pressure that depends on concentration of mobile ions in and outside the network. Therefore, the higher difference of mobile ion concentrations leads to enhance in ESF and increase in WAC. However, increase in saline concentration of absorbed fluid leads to decrease the different of mobile ions inside and outside the structure and decrease in WAC [16].
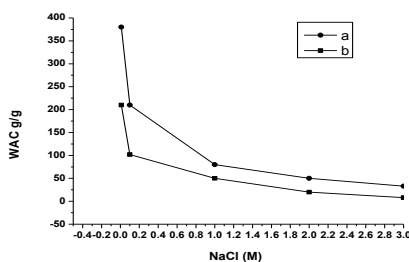
Fig 5: The effect of salt concentration on WAC of PHG; a) PHG-g-CTN (1.28 APS, 0.15 MBA, 13 NaOH and 13.5 CTN) wt.% , b) PHG (1.28APS, 0.15 MBA, and 13 NaOH) wt.%

4.6   Water Release Rate

The results in Figure 6 show that the release rate was higher in first five hours and starts declined after that. This is attributed to the high percentage of free water inside the network structure of PHGs. After the free water was released at the first hours the bonded water starts to leach out of the structure. This analysis is based on the idea of "most trapped water within the network structure is free water" [17]. Grafted polymer hydrogel sample (a) shows low releasing rate than unfilled PHG although it has bigger porous size than unfilled sample (b). The reason for that might be the high holding capacity of grafted sample as a result of hydrogen bonds between the fiber and water molecules which have to be more in number than that of unfilled polymer hydrogel.
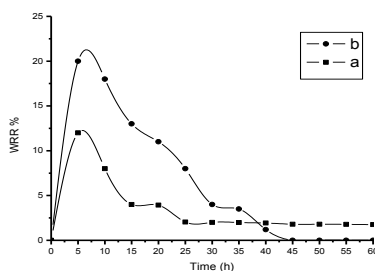
Fig 6: Water release rate from PHG; a) PHG-g-CTN (1.28 APS, 0.15 MBA, 13 NaOH and 13.5 CTN) wt.% , b) PHG (1.28 APS, 0.15 MBA, and 13 NaOH) wt.%

4.7   FTIR Analysis

FTIR spectrums in Figure 7 show a broad band at 3300-3500 cm^{-1} corresponded to O-H and N-H stretching from cellulose and MBA respectively. In addition this band might be assigned to hydrogen bonds of cellulose and carboxylic groups of PAA. The bands at 2895.18 and 2923.51 cm^{-1} in sample A and CTN are corresponding to C-H stretching vibration from cellulose molecules. The spectrum of sample B shows a broad band from 1450-1700 cm^{-1} this band may be corresponded to N-H binding and C=O of MBA and AA respectively and same band can be seen in sample A shafted to 1650-1800 cm^{-1}. In addition the bands in sample A and CTN at 1405.72 and 11410 cm^{-1} in that order are assigned to symmetric CH_2 bending vibration. The spectrum of grafted hydrogel sample (A) shows a broad band at 1063.31 might be crossponding for C-O-C bond between AA and the cellulose. Depending on FTIR spectrums analysis the main evidence of cellulose grafted AA is the bands at 2895.18, 2923.51   and 1063.31 cm^{-1} in sample CTN and A as they are not found in sample B.

311
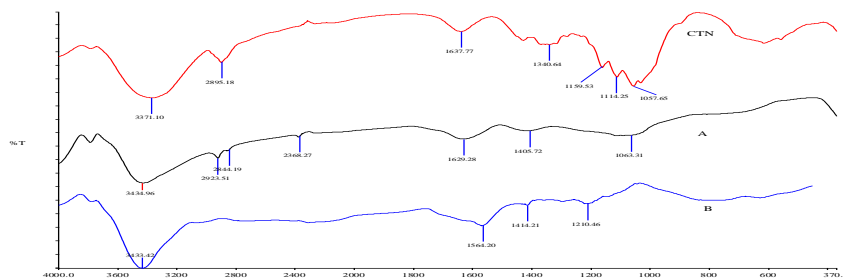
Figure 7: FTIR spectrums of; a) PHG-g-CTN (1.28 APS, 0.15 MBA, 13 NaOH and 13.5 CTN) wt.% , b) PHG (1.28 APS, 0.15 MBA, and 13 NaOH) wt.%, c) Cotton fiber

4.8   Thermal stability

The result of thermogravimetric analysis of plain CTN, PHG and grafted PHG-g-CTN are shown in Figure 8. The result indicated that CTN fiber begin to decomposed at 300 ^{o}C with rapid thermal degradation and the sample lost more than 90% of its weight at 400 ^{o}C. Samples of PHG and grafted PHG exhibited initial decomposition temperature of 150 ^{o}C. The thermogram of PHG and grafted PHG show multiphase decomposition in contrast with CTN thermogram. Multiphase degradation is attributed to decomposition of different groups of the composite. Moreover, grafted PHG shows higher thermal resistant than PHG as a result of enhancement of thermal stability via using CTN fiber.
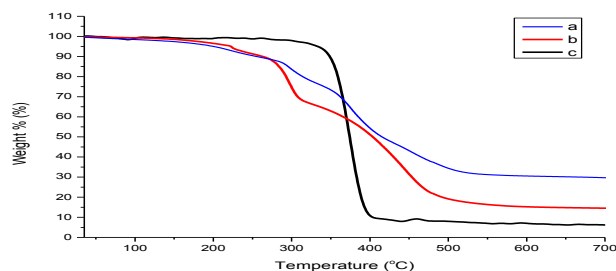
Fig 7: Thermogravimetric analysis (TGA); a) PHG-g-CTN (1.28 APS, 0.15 MBA, 13 NaOH and 13.5 CTN) wt.% , b) PHG (1.28 APS, 0.15 MBA and 13 NaOH) wt.%, c) Cotton fiber

4.9   Morphology study

Surface morphology study result indicated that the grafted PHG with CTN has bigger porous size approximately 100-200 µm than that of unfilled PHG (20-70 µm) as shown in Figure 8 (a and b). Bigger porous size maybe allowed more water to penetrate the network and enhance the final swelling rate and absorption capacity. In addition, Figure 8 (c and d) shows the micro size of cotton fibers.
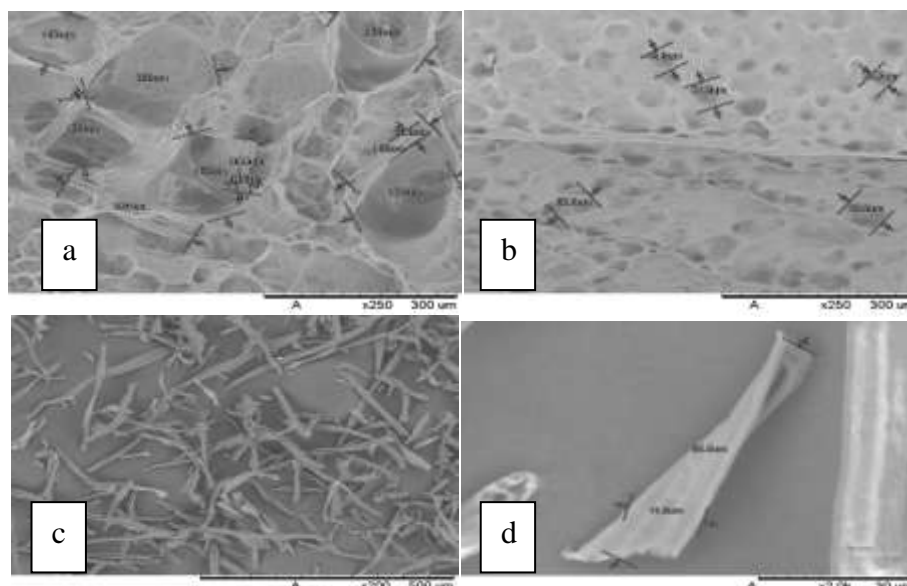
Fig 8: SEM images of; PHG-g-CTN (1.28 APS, 0.15 MBA, 13 NaOH and 13.5 CTN) wt.% , b) PHG (1.28 APS, 0.15 MBA, and 13 NaOH) wt.%, c,d) Cotton fiber

5.   CONCLUSION

The optimum contents of APS, MBA, NaON and CTN for higher absorption capacity sample were 1.28, 0.15, 13.09 and 13.54 respectively. WAC was low at low contents of APS, MBA, NaOH, and CTN WAC and started to increase with further increase in there percentages till the optimum point and then started to decline. PAA-g-CTN shows higher swelling rate, re-swelling capability and absorption capacity than polymer hydrogel. WAC was found to be negatively affected by saline concentration in water.

6.   REFERENCES

1.   H. Omidian, J.G. Rocca & K. Park. (2005). Advances in superporous hydrogels. *Journal of Controlled Release*. 102 (1), 3-12.
2.   K.M. El Salmawi. (2007). Application of polyvinyl alcohol (PVA)/carboxymethyl cellulose (CMC) hydrogel produced by conventional crosslinking or by freezing and thawing. *Journal of Macromolecular Science, Part A: Pure and Applied Chemistry*. 44 (6), 619-624.
3.   S. Ouchi, O. Yoshihito, K. Kanji, F. Takao, I. Okihiko, H. Yoshitsugu, M. Tsutomu, S. Tadao, W. Lin & I. Hatsuo, in: Gels Handbook, (Academic Press, Burlington, 2001).
4.   Y.K. Li, T.W. Xu, Z.Y. Ouyang, X.C. Lin, H.L. Liu, Z.Y. Hao & P.L. Yang. (2009). Micromorphology of Macromolecular Superabsorbent Polymer and its Fractal Characteristics. *Journal of Applied Polymer Science*. 113 (6), 3510-3519.
5.   L.C. Davies, J.M. Novais & S. Martins-Dias. (2004). Influence of salts and phenolic compounds on olive mill wastewater detoxification using superabsorbent polymers. *Bioresource Technology*. 95 (3), 259-268.
6.   V.K. Gupta & Suhas. (2009). Application of low-cost adsorbents for dye removal - A review. *Journal of Environmental Management*. 90 (8), 2313-2342.
7.   K.M. Smith, G.D. Fowler, S. Pullket & N.J.D. Graham. (2009). Sewage sludge-based adsorbents: A review of their production, properties and use in water treatment applications. *Water Research*. 43 (10), 2569-2594.

8. J. Lin, Q. Tang & J. Wu. (2007). The synthesis and electrical conductivity of a polyacrylamide/Cu conducting hydrogel. *Reactive and Functional Polymers*. 67 (6), 489-494.

9. L. An, A.Q. Wang & J.M. Chen. (2004). Studies on poly(acrylic acid)/attapulgite superabsorbent composites. II. Swelling behaviors of superabsorbent composites in saline solutions and hydrophilic solvent-water mixtures. *Journal of Applied Polymer Science*. 94 (5), 1869-1876.

10. J. Xie, X. Liu, J. Liang & Y. Luo. (2009). Swelling Properties of Superabsorbent Poly(acrylic acid-co-acrylamide) with Different Crosslinkers. *Journal of Applied Polymer Science*. 112 (2), 602-608.

11. W.A. Laftah, S. Hashim & A.N. Ibrahim. Polymer Hydrogels: A Review. *Polymer-Plastics Technology and Engineering*. 50 (14), 1475-1486.

12. N. Rjiba, M. Nardin, J.-Y. Dréan & R. Frydrych. (2007). A study of the surface properties of cotton fibers by inverse gas chromatography. *Journal of Colloid and Interface Science*. 314 (2), 373-380.

13. M.S. Sreekala, M.G. Kumaran & S. Thomas. (1997). Oil palm fibers: Morphology, chemical composition, surface modification, and mechanical properties. *Journal of Applied Polymer Science*. 66 (5), 821-835.

14. A. Hebeish, M. Hashem, N. Shaker, M. Ramadan, B. El-Sadek & M.A. Hady. (2009). New development for combined bioscouring and bleaching of cotton-based fabrics. *Carbohydrate Polymers*. 78 (4), 961-972.

15. K.T. Meilert, D. Laub & J. Kiwi. (2005). Photocatalytic self-cleaning of modified cotton textiles by TiO2 clusters attached by chemical spacers. *Journal of Molecular Catalysis A: Chemical*. 237 (1-2), 101-108.

16. T. Yoshimura, K. Matsuo & R. Fujioka. (2006). Novel biodegradable superabsorbent hydrogels derived from cotton cellulose and succinic anhydride: Synthesis and characterization. *Journal of Applied Polymer Science*. 99 (6), 3251-3256.

17. A.S. Hoffman. (2002). Hydrogels for biomedical applications. *Advanced Drug Delivery Reviews*. 54 (1), 3-12.

OIL PALM FIBER REINFORCED POLY (ε-CAPROLACTONE) AND POLY (LACTIC ACID) COMPOSITES: EFFECT ON MECHANICAL PROPERTIES.

Akos Noel Ibrahim[1], Mat Uzir Wahit[2]* Rahmah Mohamed[3]

[1]Department of Science Laboratory Technology, School of Science and Technology, Federal   Polytechnic P.M.B 1012 Kaura-Namoda; Nigeria

[2]Department of Polymer Engineering, Faculty of Chemical Engineering, Universiti Teknologi Malaysia 81310 Skudai Johor Bahru

[3]Polymer Composites Research Laboratory, Institute of Science, Universiti Teknologi MARA, Malaysia

*Corresponding author: mat.uzir@cheme.utm.my

Abstract: *Developing poly (ε-caprolactone) (PCL) and poly (lactic acid) (PLA) palm press fiber composites with enhanced mechanical properties using twin screw extruder have been studied. Injection molding of composites produced specimens for mechanical properties test. Results show remarkable increase in Young's modulus from 604MPa for PCL/PLA (90:10) blend to 4275MPa for palm press reinforced PCL/PLA (90:10) at 25Wt. % fiber load. Tensile strength decreased from 29.7MPa for blends to 15MPa for PCL/PLA (90:10) composite at 10Wt. % fiber load. Impact strength decreased from 6.5KJ/m² for blend to 4.9KJ/m² for composite. These results indicate the composite potential in wider outdoor application fields.*

Keywords: Palm press fibers; PCL/PLA composites; Mechanical properties

1.   INTRODUCTION

Attention over the century has been focused on polymer composites due to their mechanical, thermal properties and degradation advantages over homo-polymers. Polymer composites are prepared using polymers combined with compatible natural or synthetic fibers by different methods and conditions. The preparation and processing of polymer composites depends on the starting materials. Twin-screw extrusion and solution casting methods are commonly used to process natural fiber composites. These techniques have the potential of better mixing and dispersion of the fillers in the system thereby giving better interaction between the fiber and matrix[1-6].

Natural fibers are materials extracted from substances made in nature. They have been used to enhance polymers in the last three decades as alternatives to wood and synthetic fibers. Natural fibers can be classified into three main categories: vegetables (plant fibers), animals and minerals fibers. In view of recent global environmental issues and inadequate fiber sources, scientists worldwide have began to show interest in exploiting the full potentials of plant fibers and several attempts have been made to prepare and evaluate natural fiber composites for various applications. This is because natural fibers offer low density, low cost, environmentally friendly and have good mechanical properties [7-9].

The development of biocomposites from biodegradable polymers and natural fibers is attracting interest because of growing environmental awareness and pressure on the world's petroleum resources [2, 10, 11]. Also, the growing use of biodegradable polymers is on the increase because they degrade naturally in soil without releasing toxic components, can be used in special products especially in the medical field, packaging and also be easily disposed[10, 12, 13].

Biodegradable poly (lactic acid), (PLA) is a linear aliphatic thermoplastic polyester. It can be synthesized from renewable resources such as sugar feedstock, corn e.t.c. It is one of the promising biopolymer that has attracted researchers [2, 11, 14]. The market for this polymer is promising in areas like household plastic bags, sanitary and diapers barrier and other important application fields. Even though the polymer is considered expensive and requires modification to make it useful, it has some good mechanical properties, is biodegradable and insoluble in water [2, 10, 14]. Poly (ε-caprolactone), (PCL) is a petroleum based linear polymer recognized as one of the few synthetic polymers that are completely biodegradable. It's biodegradability depends on its chemical structure and not the raw material source [15]. PCL has some similar mechanical properties like PLA but the low glass transition temperature (Tg) and melting point (Tm) reduces its chances of application in some fields. In view of the above, different approaches to enhance properties and also expand application fields has led to blending [16-19] and addition of fibers as reinforcements [20-22].

2.1 EXPERIMENTAL
2.2 Materials

PCL (BGH800C) is a commercial product of Shenzhen Esun Industrial Co. Ltd China. It has Molecular weight, Mwt = 120,000; Melting point, Tm = 60-62°C; Glass Transition Temperature, Tg = -60°C and Melt Flow Index, MFI at 190°C, 2.16 kg, g/10min =7.29. PLA is also a product of the same company with the following properties. Mwt = 80,000; Tm = 150°C; and MFI = 7. Sodium hydroxide (NaOH) and glacial acetic acid (CH$_3$COOH) are products of Sigma-Aldrich. They were used as received. Unprocessed palm press fibers (PF) were supplied by Sedenak Oil Mill Kulaijaya, Malaysia.

2.3 Processing of Fibers and Preparation of Composites

The unprocessed palm oil fibers were cleaned by thorough washing with hot water to remove left over particles, oil and other debris materials. The fibers were soaked in 5% NaOH solution for 24hrs. After the treatment they were thoroughly rinsed with water containing few drops of acetic acid. Finally, water was used to rinse the fibers after which they were dried in hot air oven at 105°C for 24hrs to remove moisture. The dried fibers were pulverized and then sieved to obtain 400 μm maximum size fillers using Endcotts (EFL 2MK3) sieving machine. These were used to produce the natural fiber composites.

To prepare the composites PCL, PLA and treated palm oil fibers were dried to remove moisture. Appropriate quantities were measured and poured into a container that has cover and then mixed by shaking. A Brabender PL 2000 twin-screw extruder was used to extrude composites at temperature between 100°C feed zone to 180°C at die head and 40 rpm screw speed to achieve enough shear mixing. The JSW injection molding machine was used to inject the extruded composites between 150°C to 180°C to obtain standard tensile, flexural and impact test specimens. These standard specimens were used to carry out tensile and impact test using LLOYD instrument Ltd universal tensile tester and Toyoseki impact tester respectively.

3.1 Results and Discussion

Table 1 shows mechanical properties of neat PCL and PLA. The neat PLA has slightly higher tensile strength (32.9MPa) and a remarkably high Young's modulus (4612MPa) than neat PCL which has 32.4MPa tensile strength and 1680MPa Young's modulus. The neat PCL however has very high impact strength (22.99KJ/m^2) than neat PLA (2.21KJ/m^2).

Table 1: Mechanical properties of neat PCL and PLA

Sample	Tensile strength (MPa)	Young's modulus (MPa)	Impact strength

			(KJ/m^2)
Neat PCL	32.4	1680	22.99
Neat PLA	32.9	4612	2.21

The graphical presentation of results obtained for some of the mechanical properties are as shown below. The tensile strength of the blends as shown in figure 1 decreased steadily from 29.7MPa at 10Wt. % PLA to 6.3MPa at 40Wt. % PLA content. The reason adduced to the steady decrease in tensile strength is the brittle nature of PLA.
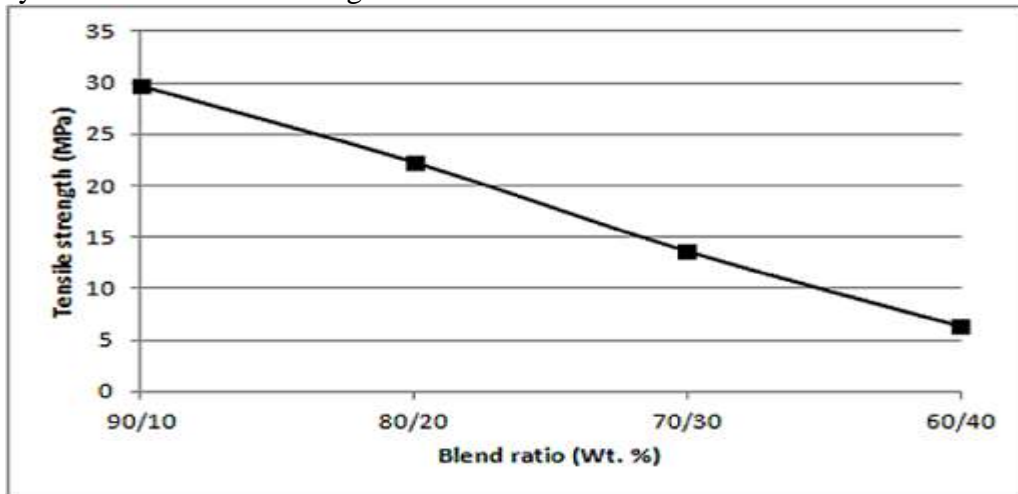
Fig. 1: Tensile strength of PCL/PLA blends.

Figure 2 is the tensile strength profile of PCL/PLA (90:10) composite as fiber load increases. The tensile strength decreased from 15.3MPa to 13.5MPa as fiber loading increased from 10Wt. % to 25Wt. %. The natural fibers were observed to reduce the tensile strength of the blends.
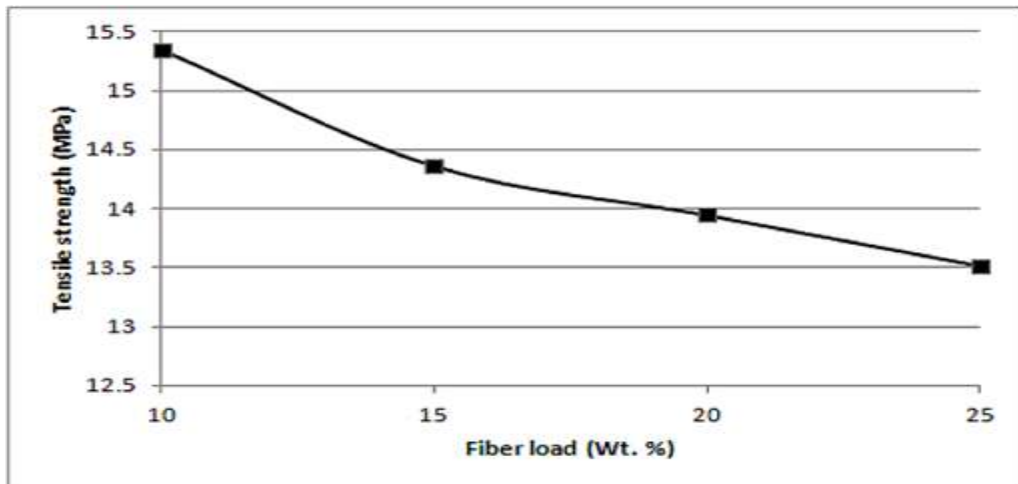
Fig. 2: Tensile strength of PCL/PLA/Fiber composite.

The Young's modulus of PCL/PLA blends is as shown in figure 3. Steady increase in modulus from 604.2MPa to 1205.9MPa was observed as the quantity of PLA increased from 10Wt. % to 40Wt. % in the blends. This is because of the high modulus of the neat PLA.
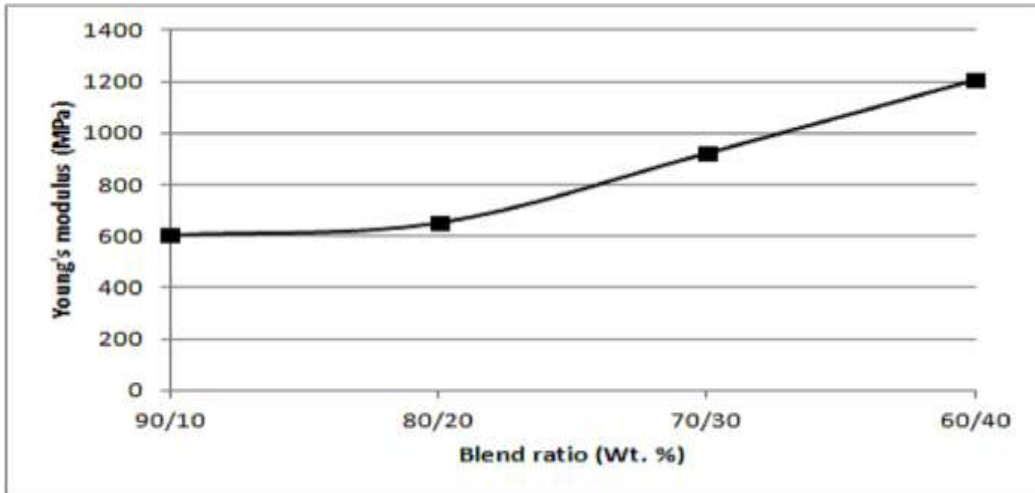
Fig. 3: Young's modulus of PCL/PLA blends.

Figure 4 is a presentation of the Young's modulus of PCL/PLA (90:10) composite with different percentage of fiber loading. An increase in modulus from 951.1MPa to 4275.5MPa was obtained when fiber loading increased from 10Wt. % to 25Wt. %. The increase in modulus is due to increase in fiber load. The natural fibers increased the modulus of the composites but decrease their tensile strength as shown in figure 2.
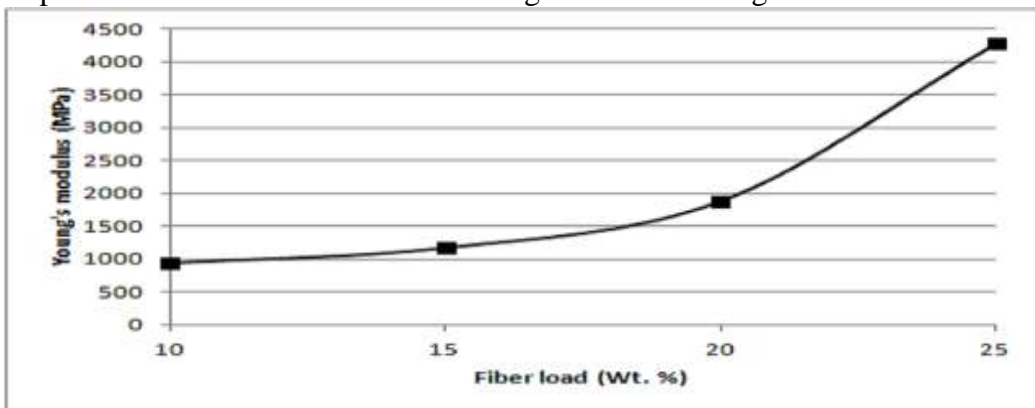
Fig. 4: Young's modulus of PCL/PLA/Fiber composite.

The impact strengths of PCL/PLA blends are as shown in figure 5. The blend with 10Wt. % PLA had 6.5KJ/m^2 impact strength which is the highest when compared to blends with PLA content of 15Wt. % and above. The high impact strength observed is attributed to the toughness of PCL. Also, the brittleness of PLA reduces impact strength of the blends as PLA content increased.
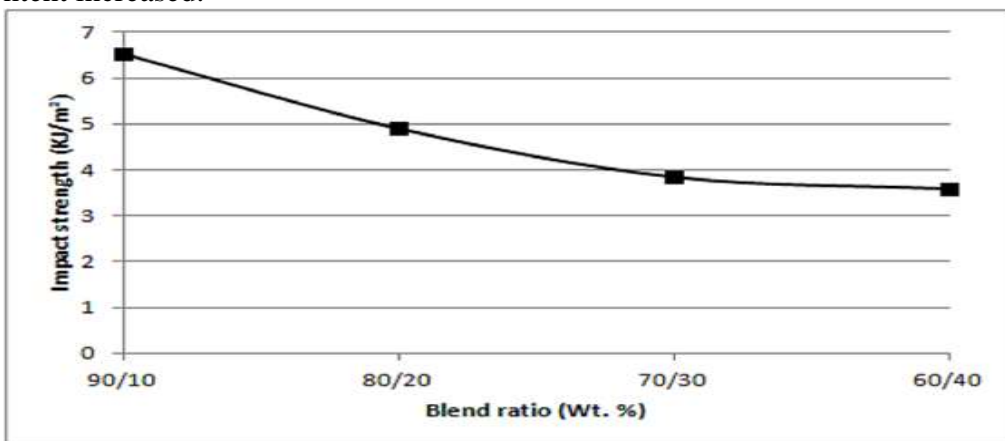
Fig.5: Izod impact strength of PCL/PLA blends.

Figure 6 shows the impact strength of PCL/PLA (90:10) composite with different fiber loading. The impact strength increased from 4.8KJ/m^2 to 4.9KJ/m^2 at 15Wt. % fiber load but decreases as fiber load increased. The initial increase in strength is due to the good distribution of the external force to the fibers by the fiber/matrix interface. This agrees with Maya and Anandjiwala in their review [23]. They posited that the fiber/matrix interface in fiber-reinforced composites transfers externally applied load to fibers themselves. The drop in impact strength as fiber load increases may be due to stress concentration. Increase fiber load can result in the formation of fiber bundles which act as barriers to transfer of stress, resulting in impaired properties.
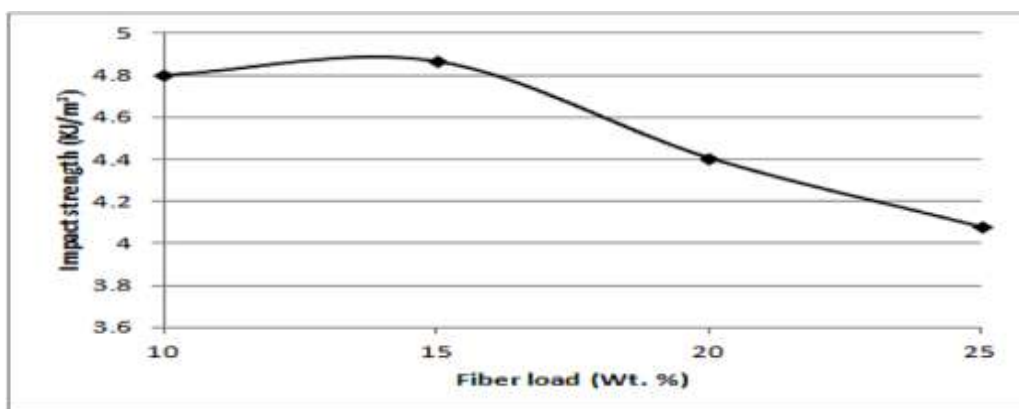
Fig. 6: Izod impact strength of PCL/PLA/Fiber composite.

4.1   CONCLUSION

The exploration of PCL/PLA blends and their palm press fiber composite in an effort to enhance their mechanical properties is ongoing. Results obtained for the uncompatibilised composites show that the treated palm press fibers used as reinforcement enhanced the Young's modulus of the composites. The tensile and impact strength of the composites slightly dropped when compared with the blends.

REFERENCES

1.   Sinha Ray, S., Bousmina, Mosto. Biodegradable polymers and their layered silicate nanocomposites: In greening the 21st century materials world. *Progress in Materials Science*. 2005. 50(8): 962-1079.
2.   Yussuf, A. A., I. Massoumi and A. Hassan. Comparison of polylactic Acid/Kenaf and polylactic Acid/Rice husk composites: The influence of the natural fibers on the mechanical, thermal and biodegradability properties. *Journal of Polymers and the Environment*. 2010. 18(3): 422-429.
3.   Lee, B.-H., H.-S. Kim, S. Lee, H.-J. Kim and J. R. Dorgan. Bio-composites of kenaf fibers in polylactide: Role of improved interfacial adhesion in the carding process. *Composites Science and Technology*. 2009. 69(15-16): 2573-2579.
4.   Lijun Qin., J. Q., Mingzhu Liu., Shenglong Ding., Liang Shao., Shaoyu., Guohong Zhang., Yang Zhao., Xie Fu. Mechanical and thermal properties of poly(lactic acid) composites with rice straw fiber modified by poly(butyl acrylate). *Chemical Engineering Journal*. 2011. 166: 772-778.

5. Sahoo, S., M. Misra and A. K. Mohanty. Enhanced properties of lignin-based biodegradable polymer composites using injection moulding process. *Composites Part A: Applied Science and Manufacturing*. 2011. 42(11): 1710-1718.

6. Pradeep K Kushwaha., R. K. Influence of chemical treatments on the mechanical and water absorption properties of bamboo fiber composites. *Journal of Reinforced Plastics and Composites*. 2011. 30(1): 73-85.

7. Araújo, J. R., W. R. Waldman and M. A. De Paoli. Thermal properties of high density polyethylene composites with natural fibres: Coupling agent effect. *Polymer Degradation and Stability*. 2008. 93(10): 1770-1775.

8. Mohanty, A. K., Misra Manjusri, Drzal Lawrence. T ed. *Natural fibers, Biopolymers and Biocomposites*.(pp1-286) Boca Raton: CRC Press. 2005

9. Joshi, S. V., L. T. Drzal, A. K. Mohanty and S. Arora. Are natural fiber composites environmentally superior to glass fiber reinforced composites? *Composites Part A: Applied Science and Manufacturing*. 2004. 35(3): 371-376.

10. Plackett, D., T. Løgstrup Andersen, W. Batsberg Pedersen and L. Nielsen. Biodegradable composites based on l-polylactide and jute fibres. *Composites Science and Technology*. 2003. 63(9): 1287-1296.

11. Sawpan, M. A., K. L. Pickering and A. Fernyhough. Improvement of mechanical performance of industrial hemp fibre reinforced polylactide biocomposites. *Composites Part A: Applied Science and Manufacturing*. 2011. 42(3): 310-319.

12. Lee, S.-H. and S. Wang. Biodegradable polymers/bamboo fiber biocomposite with bio-based coupling agent. *Composites Part A: Applied Science and Manufacturing*. 2006. 37(1): 80-91.

13. Mensitieri, G., E. Di Maio, G. G. Buonocore, I. Nedi, M. Oliviero, L. Sansone and S. Iannace. Processing and shelf life issues of selected food packaging materials and structures from renewable resources. *Trends in Food Science & Technology*. 2011. 22(2-3): 72-80.

14. Siracusa, V., P. Rocculi, S. Romani and M. D. Rosa. Biodegradable polymers for food packaging: a review. *Trends in Food Science & Technology*. 2008. 19(12): 634-643.

15. Goldberg, D. A review of the biodegradability and utility of polycaprolactone. *journal of Environment and Polymer Degradation*. 1995. 3(2): 61-67.

16. Sivalingam, G., S. P. Vijayalakshmi and G. Madras. Enzymatic and thermal degradation of poly(ε-caprolactone), poly(D,L-lactide), and their blends. *Industrial and Engineering Chemistry Research*. 2004. 43(24): 7702-7709.

17. Singh, R. P., J. K. Pandey, D. Rutot, P. Degée and P. Dubois. Biodegradation of poly(ε-caprolactone)/starch blends and composites in composting and culture environments: the effect of compatibilization on the inherent biodegradability of the host polymer. *Carbohydrate Research*. 2003. 338(17): 1759-1769.

18. Tait, M., A. Pegoretti, A. Dorigato and K. Kalaitzidou. The effect of filler type and content and the manufacturing process on the performance of multifunctional carbon/poly-lactide composites. *Carbon*. 2011. 49(13): 4280-4290.

19. Takayama, T., M. Todo and H. Tsuji. Effect of annealing on the mechanical properties of PLA/PCL and PLA/PCL/LTI polymer blends. *Journal of the Mechanical Behavior of Biomedical Materials*. 2011. 4(3): 255-260.

20. Tsimpliaraki, A., I. Tsivintzelis, S. I. Marras, I. Zuburtikudis and C. Panayiotou. The effect of surface chemistry and nanoclay loading on the microcellular structure of

porous poly(d,l lactic acid) nanocomposites. *The Journal of Supercritical Fluids*. 2011. 57(3): 278-287.

21. Zhao, Y.-Q., H.-Y. Cheung, K.-T. Lau, C.-L. Xu, D.-D. Zhao and H.-L. Li. Silkworm silk/poly(lactic acid) biocomposites: Dynamic mechanical, thermal and biodegradable properties. *Polymer Degradation and Stability*. 2010. 95(10): 1978-1987.

22. Abdul Hamid, M. Z., N. A. Ibrahim, W. Md Zin Wan Yunus, K. Zaman and M. Dahlan. Effect of grafting on properties of oil palm empty fruit bunch fiber reinforced polycaprolactone biocomposites. *Journal of Reinforced Plastics and Composites*. 2010. 29(18): 2723-2731.

23. Maya Jacob John., R. D. A. Recent developments in chemical modification and characterization of natural fiber-reinforced composites. *Polymer Composites*. 2008. 29: 187-207.

An investigation on microstructure and mechanical properties of Al7075/Ti-6Al-4V TLP bonded joint

[1]Mohammad Saleh Kenevisi, [1]Seyed Mohammad Mousavi Khoie*

[1]Full Department of mining and metallurgy Engineering, Amirkabir University of Technology (Tehran Polytechnic), Tehran, Iran

*Corresponding author: mmousavi@aut.ac.ir

Abstract: *Transient Liquid Phase (TLP) bonding of two dissimilar alloys Al7075 and Ti-6Al-4V has been done at 500°C. Cu was electrodeposited on Al7075 and Ti-6Al-4V surfaces, 50µm thick Sn-4Ag-3.5Bi foil was used as interlayer and bonding process was carried out at several bonding times. The microstructure of the joints was evaluated by Scanning Electron Microscopy (SEM), Energy Dispersive Spectroscopy (EDS) and X-Ray Diffraction (XRD). The intermetallics formation at joint interface was responsible for joint formation. Hardness of the joints increased with increasing bonding time. The study showed that the highest bond strength was 36 MPa which was obtained for the samples joined for 60 minutes.*

Keywords: transient liquid phase, diffusion bonding, aerospace alloys, joint properties

1. INTRODUCTION

The aluminum alloy Al7075 and titanium alloy Ti-6Al-4V are used in a variety of applications in aerospace and chemical industries because of their properties such as high strength to weight ratio and good corrosion resistance [1-3]. The ability to join Al7075 alloy to Ti-6Al-4V alloy can provide a product that is less costly, but retains the high strength and light weight properties which is necessary for the aerospace industry [4]. There are two main challenges in joining Al to Ti, large differences in the physical properties between Al and Ti such as melting point and the presence of stable oxide layer in the both Al and Ti surfaces. Therefore, conventional fusion welding processes are not applicable for joining these metals [2,5] and also special surface preparation should be done to bond aluminum to titanium. Transient Liquid Phase (TLP) bonding is an advanced solid state joining process which has an ability to join similar and dissimilar metals [5,6]. Generally, the quality of the joint is affected by the chemical composition, microstructure and mechanical properties of the joint region. So, process parameters such as temperature, pressure and bonding time should be optimized to obtain a good joint. Moreover, interlayer composition and thickness plays an important role in bonding process. Previous works on solid state and liquid stare diffusion bonding of Al/Ti has been reported [7-12]. Coating the Al and Ti surfaces with Cu prevent the oxide formation on Ti/Al interface and form intermetallics at the joint interface [11]. Lead-free Sn-based alloys are widely used to join dissimilar alloys [13]. Addition of Ag to Sn improves the alloy mechanical properties [14]. Bi enhances the wettability and strength of the Sn-Ag eutectic system [15,16]. In this work, the diffusion bonding of the Al7075 and Ti-6Al-4V alloys was investigated using 50 µm thick Sn-4Ag-3.5Bi as interlayer.

2. EXPERIMENTAL PROCEDURE

The Ti-6Al-4V and Al7075 alloys were investigated for liquid state diffusion bonding experiment using interlayer with a thickness of 50 μm. Compositions of the Al and Ti alloys and the interlayer are listed in **Table 1**.

Table 1. Chemical compositions of the metals used in this study

Alloys	Elements (wt.%)							
	Ti	Al	V	Cu	Mg	Sn	Ag	Bi
Ti-6Al-4V	Bal.	6.43	4.16	-	-	-	-	-
Al7075	-	Bal.	-	1.52	2.30	-	5.87	-
Interlayer	-	-	-	-	-	Bal.	3.78	3.34

The base metals were received as plates of 3 mm thickness for Ti alloy and 10mm thickness for the Al alloy. The samples were cut into dimensions of 12×12×3 mm. SiC papers down to 1000 were used for samples preparation. Oxide films of Ti and Al could form easily on each surface, so to eliminate the oxide layer from the joining surface, Ti-6Al-4V sample were immersed in 3% HF + 30% HNO_3 solution, then water flushed and dried. Also Al7075 surfaces immersed firstly in 6% NaOH, water flushed, and then immersed in 40% HNO_3, water flushed and dried [7]. After that, samples and 50 μm thick Sn-10Zn-3.5Bi foils were ultrasonically cleaned in acetone for 15 minutes. A solution from 17.5 g copper sulfate ($CuSO_4$) and 175 g sulfuric acid (H_2SO_4) in a liter of distilled water was prepared for electrodepositing Cu onto samples surfaces [17]. Samples immersed in solution as cathode and the anode was 99.99% Cu. The Sn-Zn-Bi interlayer was placed between the surfaces of the samples being joined and the assembly moved into the diffusion bonding chamber. Once a vacuum of $5×10^{-4}$ torr was achieved, samples were heated. The bonding temperature was set to 500˚C and bonding process was carried out at several bonding time up to 60 minutes. Transverse sections were made by cutting the bonded samples through the joint region. Samples were polished down to 1μm diamond suspension. The etchant for Al7075 was Keller's reagent (1.5 ml HCl, 2.5 ml HNO_3, 1 ml HF, and 95 ml distilled water) and for Ti-6Al-4V was Kroll's reagent (5 ml HNO_3, 5 ml HF, and 90 ml distilled water) [18]. The microstructures of the joints were observed using light optical microscope (LOM) and Philips XL30 scanning electron microscope (SEM). Microhardness measurements were made with a load of 50 g. Shear strength of the joints was measured by Santam STM-600 machine with a cross head speed of 1mm/min.

3.   RESULTS AND DISCUSSION

3.1   Microstructure evaluations

Samples bonded at 500˚C with different holding times were studied in order to understand the microstructural changes in the diffusion zone. Fig. 1-a shows a cross-section representative of bond with a short bonding time of 30 min. A eutectic phase can be seen along the Al7075 grain boundaries. From the calculated Al7075-Cu phase diagram [19], it can be predicted that Cu diffuses into Al and Al_2Cu eutectic phase was formed along the Al7075 grain boundaries. As bonding time increases, homogenous microstructure can be seen at the joint interface (Fig. 1-b).
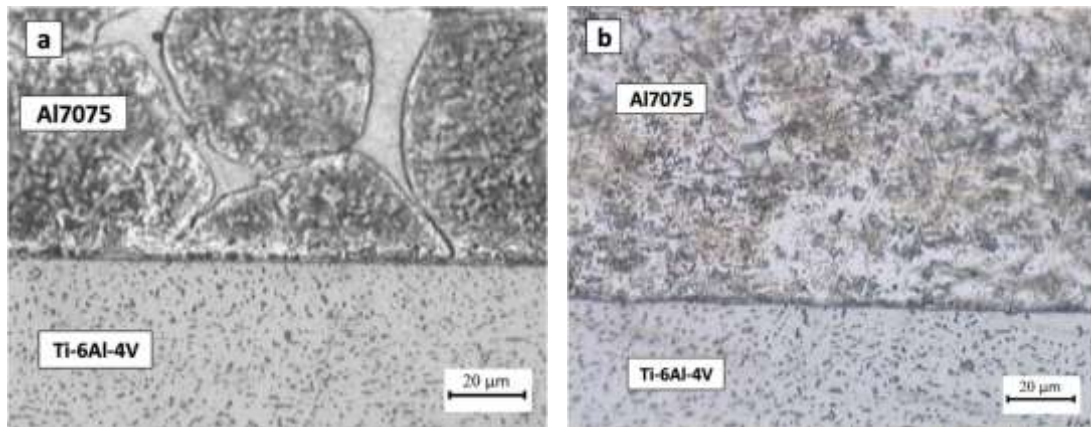
Fig. 1. Light micrographs of joint interface at bonding time of (a) 30 min, (b) 60 min.

To investigate the microstructure more precisely, SEM micrographs from the bonded joints were taken (Fig. 2). It is obviously clear that the joint structure is highly dependent on the bonding time. The bond made for 30 minutes (Fig. 2-a) shows the absence of the interlayer, however eutectic phase is formed which is along the Al7075 grain boundaries as seen in light micrographs. Also, small bright regions can be seen along the grain boundaries. Fig. 2-b represents a completed joining process.
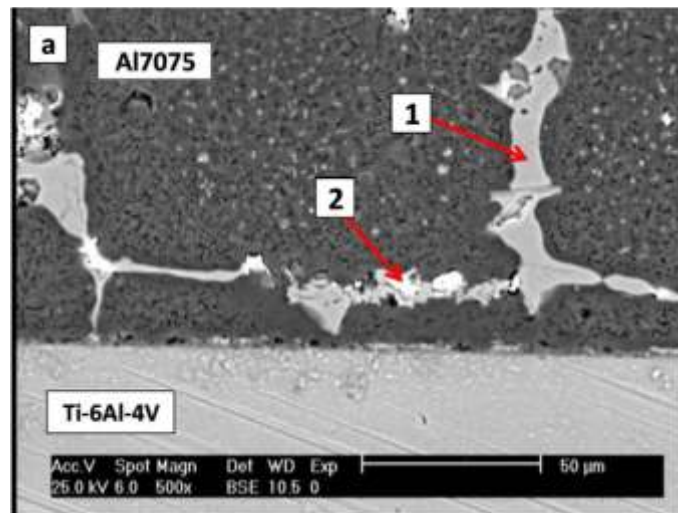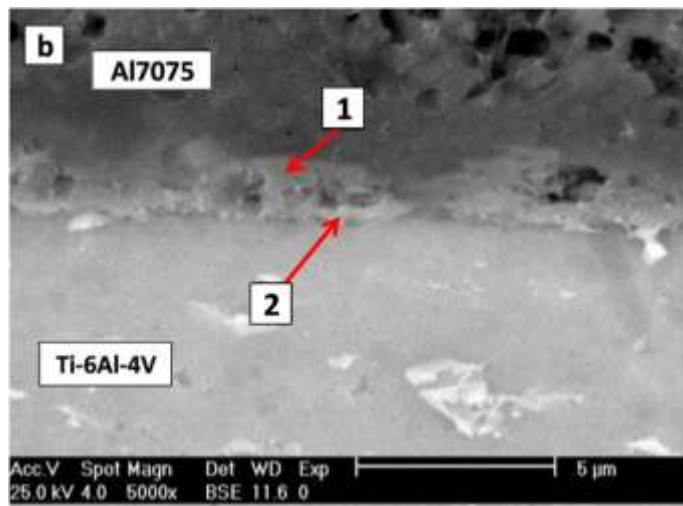
Fig. 2. SEM micrographs of joint interface at bonding time of (a) 30 min, (b) 60 min.

For further investigation and in order to determine the elemental composition across the joint region, EDS analysis was applied and different regions in bonds are shown in Fig. 2 and marked as 1 and 2 in each bond. The elemental composition of marked regions is shown in Table 2.

Table 2. EDS analysis [wt%] of selected regions for bonds shown in Fig. 2.

	Region	Al	Ti	Cu	Sn	Ag	Bi
30 min	1	53.4	0.5	44.6	0.6	-	-
	2	2.3	0.9	2.7	89.2	0.8	0.3
60 min	1	34.8	59.3	2.7	0.5	-	-
	2	16.2	81.5	1.9	-	-	-

At 30 minutes bonded joint, it was illustrated that the major elements in region 1 are Al and Cu. Considering the elemental composition, it is clear that the $\theta(Al_2Cu)$ eutectic phase is formed in this region. Also, region 2 is Sn reach region that remains at grain boundaries. In the bond made for 60 minutes, region 1 and 2 are TiAl and Ti_3Al intermetallics respectively. Moreover, according to the elemental composition it is believed that the intermetallics can be formed between Ti and Cu which was demonstrated by Geng et al. [20].

3.2 Mechanical properties of the joint

The mechanical properties of the joints were characterized by microhardness and tensile-shear tests. Fig. 3 shows the hardness test results obtained from the bonded joints made at different bonding times.
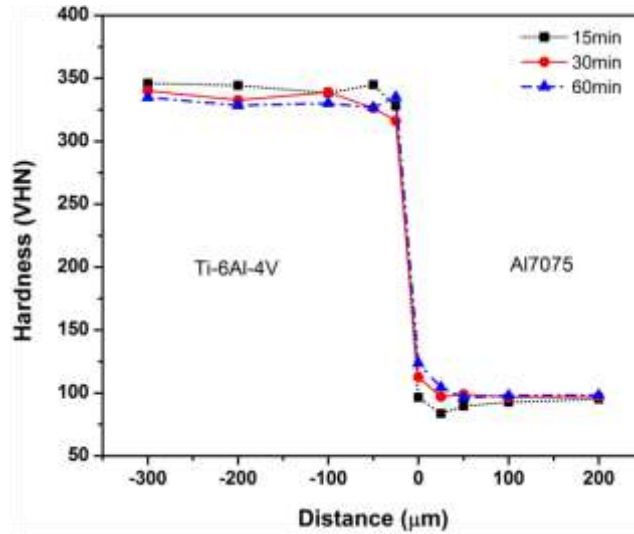
Fig. 3. Microhardness profile of diffusion zone at different bonding times

As seen, hardness values at joint region taken from the 15 minutes bonded sample are lower than the values taken from the 2 other samples. This decrease in hardness values can be attributed to the existence of interlayer at joint interface. As bonding time increases, the hardness values of the joint interface increases. This increase in hardness values is due to formation of intermetallic compounds at the joint center. In addition, it can be concluded that the width of the joint region was reduced with increasing time.

The interfacial bond strength of bonded joints was evaluated by the single lap shear test with varying bonding time and the results are shown in Fig. 4.
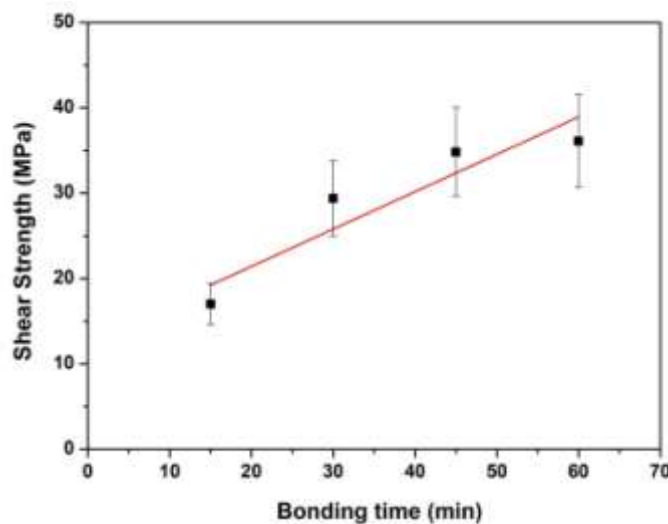
Fig. 4. Tensile-shear strength of joints as a function of bonding time.

The shear strength increases with the increase of bonding time. The increase of bond strength was caused by the intermetallics formation at the joint interface such as TiAl and Ti_3Al during the bonding process. Furthermore, the rate of the strength increasing is high at the first stages of the process and then slows down as bonding time increases. After 45 minutes, no noticeable changes in the joint strength were occurred with increasing time and the maximum shear strength obtained at 60 minutes which was 36 MPa.

4.   CONCLUSION

(1) Final Relatively good bond is attained in TLP bonding between Cu coated surfaces of Al7075 and Ti-6Al-4V using Sn-4Ag-3.5Bi as interlayer under the condition of 500°C bonding temperature, a vacuum of 5×10^{-4} torr and 60 minutes bonding time.

(2) Diffusion of Ti, Al and Cu atoms resulted in formation of intermetallic compounds which produced metallurgical bond at the interface.

(3) As bonding time increases, the hardness of the interface increases due to intermetallic compounds formation.

(4) The joint strength depends on the eutectic and intermetallic phases percentage and metallurgical structure in the diffusion zone. The strength of the bonds increases with increasing bonding time and reaches to 36 MPa at 60.

5.   REFERENCES

1.   J. R. Davis. (1993). *Aluminum and Aluminum Alloys*. New York: ASM International.
2.   ASM Handbook. (1990). *Properties and Selection: Nonferrous Alloys and Special-Purpose Materials*. 10th ed. vol. 2.
3.   C. Leyens. (2002)*Titanium and Titanium Alloys; Fundamentals and Applications*. WILEY-VCH GmbH & Co.
4.   J.R. Williamson. (1982). *Superplastic forming of structural alloys*. Warrendale.
5.   AWS Handbook. (1997). *Diffusion Welding and Brazing*. 8th ed. vol. 2.
6.   ASM Handbook. (1993). *Welding Brazing and Soldering*. vol. 6.
7.   Yao Wei, Wu Aiping, Zou Guisheng, Ren Jialie. (2008). Formation process of the bonding joint in Ti/Al diffusion bonding. *Mat Sci Eng A* 480, 456-463.
8.   J-G. Lou, V. L. Acoff. (2000). Interfacial Reactions of Titanium and Aluminum during Diffusion Welding. *Welding Journal*, 239-243.
9.   Ren Jiangwei, Li Yajiang, Feng Tao. (2002). Microstructure characteristics in the interface zone of Ti/Al diffusion bonding. *Mater Lett*, 56, 647-652.
10.   Woong H. Sohn, Ha H. Bong, Soon H. Hong. (2003). Microstructure and bonding mechanism of Al/Ti bonded joint using Al-10Si-1Mg filler metal. *Mat Sci Eng A*, 355, 231-240.
11.   A. Alhazaa, T.I. Khan. (2008). Diffusion bonding of Al7075 to Ti-6Al-4V using Cu coatings and Sn-3.6Ag-1Cu interlayers. *J Alloy compd*, 494, 351-359.
12.   A. Alhazaa, T. I. Khan, I. Haq. (2010). Transient liquid phase (TLP) bonding of Al7075 to Ti–6Al–4V alloy. *Mater Charact*, 61, 312-318.
13.   J. H. Vincent, G. Humpston. (1994). Lead-free Solders for Electronic Assembly. *GEC journal of research*, 11, 76-89.
14.   M. McCormac, H. S. Chen, G. W. Kammlott, S. Jin. (1997). Significantly improved mechanical properties of Bi-Sn solder alloys by Ag-doping. *J Electron Mater*, 26, 954-958.
15.   H.L. Lai, J.G. Duh. (2003). Lead-free Sn-Ag and Sn-Ag-Bi solder powders prepared by mechanical alloying. *J Electron Mater*, 32, 215-220.
16.   P.T. Vianco, J.A. Rejent. (1999). Properties of ternary Sn-Ag-Bi solder alloys: wettability and mechanical properties analyses. *J Electron Mater*, 28, 1138-1143.
17.   F. A. Lowenheim. (1974). *Modern electroplating*. 3rd ed. New York: Wiley-Interscience publication.
18.   ASM Handbook. (1998). *Metallography and Microstructures*. vol. 9.
19.   Yan X, Chang Y, Xie F. (2001). Calculated phase diagrams of aluminum alloys from binary Al–Cu to multicomponent commercial alloys. *J Alloys Compd*, 320, 151-160.
20.   J. Geng, P. Oelhafen. (2000). Photoelectron spectroscopy study of Al–Cu interfaces. *Surf Sci*, 452, 161–171.

Composite Material based on Natural Wood Fibre: Preparation and Properties

Dr Yong Kok Chong[1,*] and Asrul bin Mustafa[1]

[1] Technology & Engineering Division, Rubber Research Institute of Malaysia, Malaysian Rubber Board, 47000 Sungai Buloh, Selangor, Malaysia.

*Corresponding author: kcyong@lgm.gov.my

Abstract: *Composite material based on natural rubber compound and natural wood fibre was successfully prepared using the economical and practical lamination technique. Epoxy resin based adhesion system was chosen for enhancing the bonding strength between the layers of rubber compound and fibre. It was found that the natural wood fibre based laminate composite possessed high penetration resistance (up to 25.5 Joule), good tensile properties (tensile strength up to 16.5 MPa) and also strong adhesion strength. As a result, this particular type of composite material may be used for the low level body armor-anti stab application.*

Keywords: laminate composite; natural wood fibre; penetration resistance; tensile properties; adhesion strength

1. INTRODUCTION

The use of natural fibre in composites manufacturing has increased recently due to their relative cheapness compared to conventional materials such as glass and aramid fibres, their ability to recycle and for the fact that they compete well in terms of strength per weight of material [1]. In terms of strength and modulus, the natural fibres compare quite well with glass, but are not as strong as both polyaramid and carbon [2-3].

The main objective of this project was to produce high impact strength and flexible composite by using at least 70 total wt % of 'green' and sustainable raw materials via the economical and practical lamination technique [4], which targeted for the body armor-anti stab application. The lamination technique has been successfully applied by various workers [5-6] in order to acquire high strength composite materials. When manufacturing composite materials, compatibility of the matrix and the fibres is always stated as a problem. As a result, epoxy resin based adhesion system was chosen in order to enhance the bonding strength between the laminated layers of natural rubber compound and natural wood fibre. Apart from the adhesion strength studies (via both tensile pulling and solvent swelling tests), penetration resistance (via an *in house* developed penetration test system) and some basic tensile properties of the produced laminate composites were also performed.

2. EXPERIMENTAL

2.1 Raw Materials and Chemicals

Masterbatch compound of 100.0 p.h.r. (parts per hundred rubber) natural rubber (Standard Malaysian Rubber 20) and 30.0 p.h.r. fillers was prepared using a two roll-mill at temperature 30°C. 2.0 p.h.r. sulfur, 2.0 p.h.r. zinc oxide and 5.0 p.h.r. stearic acid were added to the masterbatch compound as vulcanizing agents. Random fibre mat was prepared from cellulose-rich material obtained from a source of mixed natural woods (supplied by Flexsys Chemicals Sdn. Bhd.). The cellulose content of the material is at least 70 weight %. Wetted fibres were compressed under 5 tonnes compression and dried sufficiently to obtain their fibre mats as shown in Fig. 1. The selected type of adhesive system here was the mixture of epoxy resin and its curing agent.

Fig.1. Random Fibre Mat comprising of Cellulose-Rich Material from Natural Woods

2.2 Test Samples Preparation

The produced fibre mats were used in rubber lamination together with epoxy resin in order to obtain reinforced laminates. The fibre mats were adequately bleached (in order to remove contamination) followed by incorporation of lamination adhesive. The fibre mats with adhesive system were then laminated alternately with layers of rubber compound (i.e. 6 layers of rubber compound and 5 layers of fibre mat in order to achieve a '*sandwich*' structure with total thickness of about 11.0 mm). Curing of the laminates was performed by using a metal clamp (see Fig. 2) at temperature of 100°C for 60 min. Control sample (without any fibre mats) was also prepared using the same technique for comparison purpose.

2.3 Penetration Energy Determination

Penetration resistance of a laminate composite can be estimated from its determined penetration energy (obtained via a simple penetration test). As a rule of thumb, the higher the penetration energy, the bigger the penetration resistance. In this part of work, an in house developed penetration energy test system was used for the penetration energy determination. This test system consisted of two main parts, i.e. the mechanical (a sample holder and an *US National Institute of Justice Standard-S1* [7] complied tungsten carbide knife) and the electro-hydraulic parts (modified from an existing hydraulic press machine, featured a 0-60 bars pressure transducer and a Gwinstek-GDS 1000 Series digital oscilloscope). Voltage outputs from the transducer were recorded by the oscilloscope while the knife penetrating a test sample (5 test pieces were repeated for each type of adhesive system based composite) and later calculated as penetration energy based on Eq. 1.

$$E = 0.5 \left(\text{Fmax} \right) \left(s \right) \qquad (1)$$

where; F_{max} is the maximum force achieved during the penetration process and 's' is the length from the blade tip to the marking point, i.e. 4 cm.
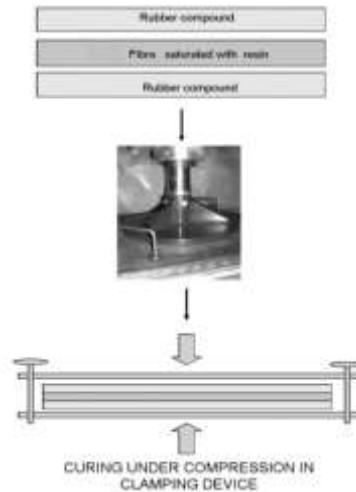
Fig.2. Flow of Natural Rubber Compound-Natural Wood Fibre Composite Lamination

2.4 Tensile Properties Measurement

Basic tensile properties (i.e. tensile strength and elongation percentage at break [EB %]) test was performed according to BS ISO standard [8]. Different test pieces (consisted sandwich of two rubber compound layers with one fibre mat layer, thickness about 3.0 mm) were prepared here. Six test pieces of each laminate composite were used to repeat each test in order to define the final result as the mean value of a total of six measurements. Control sample (without any fibre mats) was also prepared using the same technique for comparison purpose.

2.5 Adhesion Strength Determination

Two methods (i.e. the solvent swelling test and the tensile pulling test) were applied here in order to determine the adhesion strength of the resulted laminate composites and their control samples.

In the solvent (i.e. toluene) swelling test, adhesion strength of each laminate composite (with test piece in cylindrical shape, diameter 22.0 mm x thickness 11.0 mm) was determined based on the mean percentage value of test piece's volume swelling (repeated for 5 test pieces before and after submerged in solvent) for 72hr at 23°C. The degree of volume swelling % of a test piece ($Q\%$) was calculated using the following Eq. 2; where $W1$ is the weight of rubber after swelling (gram) and $W2$ is the weight of rubber before swelling (gram).

$$Q\% = \left(\frac{W1 - W2}{W2} \right) \left(100 \right) \qquad (2)$$

Meanwhile for the tensile pulling test, it was carried out by using an Instron 5567 tensile machine (with an applied constant straining rate, 200 mm/min). Different test pieces (consisted sandwich of two rubber compound layers with one fibre mat layer, thickness about 3.0 mm, repeated for 5 test pieces of each adhesive system type) were also prepared here for the pulling test purpose (as illustrated by Fig. 3). About 20 mm of each opposite edge of the test piece was delaminated (with only one rubber compound layer left) as the place for the tensile machine jig's clamping purpose. For this pulling test, tensile strength at where the full delamination (between any layers of laminated material) occurred was recorded.
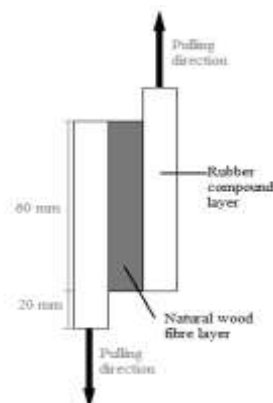
Fig. 3. A Simple Schematic of Tensile Pulling Test for the Laminate Composite

2.6 Microscopy Study

All laminated composite samples were sent for microscopy study (scanning electron microscope, JOEL JSM-6701F, at 2 keV with magnification 100 times) in order to study their fractured intersection surfaces. All samples were nitrogen-frozen before fractured (without any prior coating) in the hope to obtain a perfect intersection surface for the microscopy analysis purpose.

3. RESULTS & DISCUSSION

3.1 Penetration Energy Determination

All results are summarized in Table 1. Test sample based on epoxy resin-adhesive system showed high penetration energy (E) value. The introduction of natural wood based fibre did enhance the composite's penetration resistance from the sharp projectile up to about 56% if compared to the control sample. This phenomenon indicates that the natural wood based fibre may be used as the penetration resistance reinforcing material just likes other types of synthetic fibre [2-3].

Table 1: Calculated Mean Penetration Energy (E) Value of Natural Rubber Compound-
Natural Wood Fibre Laminate Composite and Its Control Sample

Sample	Mean E (Joule)
Control (without fibre mat)	*17.1 ± 0.50*

Test sample (with fibre mat)	*25.5 ± 0.50*

3.2 Tensile Properties Measurement

Results (in mean values) of the tensile strength and elongation at break (EB%) of the prepared laminate composite and its control sample are presented in Figs. 4 and 5 respectively for comparison purpose.
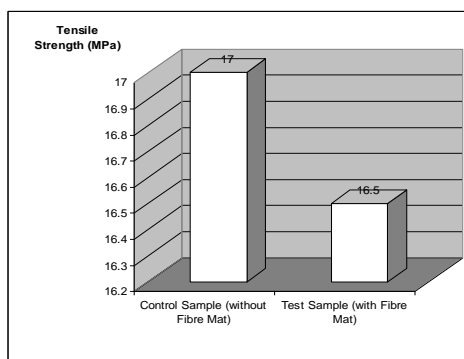
Fig. 4. Tensile Strengths (Error, ±0.5 MPa) of Natural Rubber Compound-Natural Wood Fibre Laminate Composite and Its Control Sample
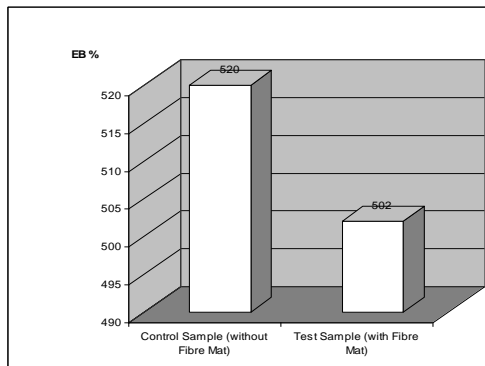
Fig. 5. Elongation at Break (EB%, Error ±20.0%) of Natural Rubber Compound-Natural Wood Fibre Laminate Composite and Its Control Sample

It was found that the epoxy resin-adhesive system based laminate composite showed comparable tensile properties with its control sample. This finding is in agreement with the results from section 3.3, where both materials also had comparable bonding strength via the applied epoxy resin-adhesive system. From this observation, it is able to say that the produced laminate composite did have a structure as flexible as the vulcanized rubber compound itself.

3.3 Adhesion Strength Determination

Samples of natural rubber compound-natural wood fibre laminate composite and its control were analyzed. All results from toluene swelling test are summarized in Table 2. Test

sample with natural wood based fibre showed a similar volume swelling mean percentage value to its control sample. For the tensile pulling test, results are summarized in Table 3. Test sample with natural wood based fibre again showed a comparable recorded tensile strength value to its control sample. From this finding, it is proposed that the epoxy resin based adhesive system can be used to bind up both natural rubber compound and natural wood based fibre effectively.

Table 2: Mean Percentage Values of Volume Swelling (in Toluene) of Natural Rubber Compound-NaturalWood Fibre Laminate Composite and Its Control Sample

Sample	Mean % value of volume swelling
Control sample (without fibre mat)	*8.0 ± 0.5*
Test sample (with fibre mat)	*8.2 ± 0.5*

Table 3: Mean Values of Tensile Strength at Full Delamination of Natural Rubber Compound-Natural Wood Fibre Laminate Composite and Its Control Sample

Sample	Mean value of tensile strength (MPa)
Control sample (without fibre mat)	*9.5 ± 0.5*
Test sample (with fibre mat)	*9.2 ± 0.5*

3.4   Microscopy study

Test sample of laminate composite based on the epoxy resin-adhesive system featured a compact and well interacted sandwiched structure (see Fig. 6 for an example). This leads to the explanation why the natural rubber compound-natural wood based fibre laminate composite showed good penetration resistance and adhesion strength as discussed before.
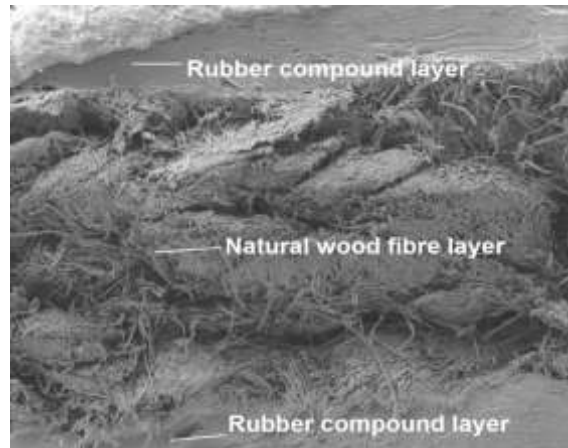
Fig. 6. Example of Intersectional Surface Micrograph of Natural Rubber Compound-Natural Wood Fibre Laminate Composite

4. CONCLUSION

It is able to conclude that the laminated natural rubber compound-natural wood fibre composite with epoxy resin based adhesive system possessed high penetration resistance and good tensile properties. The epoxy resin based adhesive system also provided strong adhesion strength for the purpose of natural rubber compound and natural wood fibre laminating. As a result, this particular type of laminate composite will be selected for further study as one of the potential materials for the low level body armor-anti stab application.

5. REFERENCES

[1] Robson, D., Hague, J., Newman, G., Jeronomidis, G. & Ansell, M. (1996). *Survey of Natural Materials for Use in Structural Composites as Reinforcement and Matrices*. Abingdon: Woodland Publishing Ltd.

[2] Eichhorn, S.J., Baillie, C.A. & Zafeiropoulo, N. (2001). Review: current international research into cellulosic fibres and composites. *J. Mater. Sci.,* 36, 2107-2131.

[3] Bisanda, E.T.N. & Ansell, M.P. (1992). Properties of sisal-CNSL composites. *J. Mater. Sci.*, 27, 1690-1700.

[4] Bledzki, A.K. & Gassan, J. (1999). Composite reinforced with celluose based fibres. *Prog. Polym. Sci.*, 24, 221-274.

[5] United State Patent No. 5,145,727. (1992). *Multilayer Nonwoven Composite Structure*.

[6] United State Patent No. 4,820,568. (1989). *Composite and article using short length fibre*.

[7] National Institute of Justice Standard-0115.00. (September 2000). *Stab Resistance of Personal Body Armor*, Washington DC: National Institute of Justice.

[8] British Standards ISO 37. (2005). *Rubber, Vulcanised or Thermoplastic-Determination of Tensile Stress-Strain Properties*.

Proceeding of MAMIP2012
Asian International Conference on Materials, Minerals and Polymer
23rd – 24th March 2012, Vistana Hotel, Penang

Glass transition temperatures of binary and ternary copolymers from butyl acrylate, glycidyl methacrylate, and tetrahydrofurfuryl acrylate

Ahmad Danial Azzahari[1,*], Rosiyah Yahya[1]

[1]Department of Chemistry, University of Malaya, 50603, Kuala Lumpur, Selangor, Malaysia

*Corresponding author: o_danny@siswa.um.edu.my

Abstract: *Poly(glycidyl methacrylate-co-tetrahydrofurfuryl acrylate) copolymers and poly(butyl acrylate-co-glycidyl-co-methacrylate-co-tetrahydrofurfuryl acrylate) terpolymers were synthesized using free radical polymerization. The glass-transition temperatures (T_g's) were determined by differential scanning calorimetry. Polymers with high content of glycidyl methacrylate comonomer units showed higher T_g's whereas those with high content of tetrahydrofurfuryl acrylate and butyl acrylate comonomer units showed lower T_g's. The relations of T_g's of the varying ratios of incorporated comonomer units were investigated by the widely used Fox equation and Johnston equation, as well as a new equation by Liu et al. which considers contributions of mole fractions of triads to the T_g of the copolymer.*

Keywords: Glass transition; T_g vs. composition; Glycidyl methacrylate; Tetrahydrofurfuryl acrylate

1. INTRODUCTION

Acrylic copolymers have achieved prime importance in various avenues of industrial application [1-8]. Glycidyl methacrylate (GMA), which is of interest to us, is used to provide epoxy functionalization to our acrylate resin. On its own, the homopolymer of GMA would have a rather narrow range of applications. However, its properties can be manipulated by copolymerization with other monomers to give products with desired physicomechanical properties. Polymer glass transition temperature (T_g), which represents the molecular mobility of polymer chains, is an important phenomenon that influences the material properties and potential applications of a given polymer. Knowing this important intrinsic parameter would serve as a useful tool towards optimizing the utility for the tailored copolymers. In this work, poly(glycidyl methacrylate-*co*-tetrahydrofurfuryl acrylate) copolymers and poly(butyl acrylate-*co*-glycidyl-*co*-methacrylate-*co*-tetrahydrofurfuryl acrylate) terpolymers were synthesized and its qualitative and quantitative T_g–composition relationships are discussed.

2. EXPERIMENTAL

2.1 Materials

GMA (Merck), *n*-butyl acrylate (*n*BA) (Merck) and tetrahydrofurfuryl acrylate (THFA) (Aldrich) were purified by distillation under reduced pressure. Benzoyl peroxide BPO (Merck) was recrystallized from ethanol and dried under vacuum at 40 °C. All the other solvents were purified by distillation prior to their use.

2.2 Polymerization procedure

Each of the free radical polymerization reactions was carried out with predetermined ratios of monomers in toluene at 70±1°C under N_2 atmosphere. Polymeric material was

precipitated twice in excess of *n*-hexane and dried in vacuum at ambient temperature. Copolymer compositions were calculated by ^{1}H NMR measurements performed with a JEOL-Lambda 400 MHz spectrometer. Thermal data were obtained using a PerkinElmer HyperDSC instrument. The DSC analysis procedure used consisted of first heating the polymer from –50 to 150°C, then cooling it to –50°C at a rate of 100°C min^{-1}, and holding at –50°C for 5 minutes before the next heating cycle to erase thermal history. All reported T_g values are from the second heating cycle using the Half Cp Extrapolated method.

3. RESULTS AND DISCUSSION

3.1 Synthesis of polymers

The results of the synthesized copolymers are shown in Table 1. f_1 and F_1 corresponds to the initial feed and the mol fraction of incorporated GMA units respectively (Complimentarily, $f_2=1-f_1$ and $F_2=1-F_1$ for THFA). In the case of the terpolymer shown in Table 2, f_i and F_i for $i=1$, 2, 3 refers to *n*BA, GMA and THFA respectively. The polymers obtained were colourless solids with intermediate properties of poly(GMA): hard solid; poly(THFA): soft adhesive; and poly(*n*BA): viscous resin.

Table 1: Composition data along with experimental
and predicted T_g values of poly(GMA-*co*-THFA)

f_1	F_1	T_g [K]		
		Experimental	Fox	Extended Gibbs-DiMarzio
0.102	0.214	270.5	278.6	267.7
0.151	0.285	270.0	282.9	269.9
0.201	0.329	269.9	286.3	272.5
0.249	0.429	271.1	289.0	275.5
0.397	0.478	288.9	295.7	287.6
0.553	0.526	314.9	301.9	304.9
0.600	0.554	311.4	304.0	311.0
0.751	0.661	331.9	312.0	332.5
0.793	0.693	336.5	315.1	338.6
0.849	0.776	338.9	320.1	346.0

Table 2: Composition data along with experimental and
predicted T_g values of poly(*n*BA-*co*-GMA-*co*-THFA)

f_1	f_2	f_3	F_1	F_2	F_3	T_g [K]	
						Experimental	Fox
0.200	0.398	0.402	0.175	0.586	0.239	302.0	296.1
0.150	0.699	0.152	0.153	0.805	0.043	311.0	316.7
0.374	0.448	0.178	0.287	0.642	0.071	299.0	294.4
0.152	0.155	0.693	0.156	0.319	0.526	273.9	277.4
0.374	0.175	0.451	0.344	0.342	0.314	267.4	269.4
0.594	0.202	0.204	0.441	0.411	0.148	273.4	268.9
0.240	0.242	0.518	0.194	0.437	0.368	282.3	283.7

Proceeding of MAMIP2012
Asian International Conference on Materials, Minerals and Polymer
23rd – 24th March 2012, Vistana Hotel, Penang

0.243	0.514	0.243	0.216	0.681	0.104	294.3	301.8
0.387	0.305	0.307	0.295	0.517	0.188	275.2	284.1
0.747	0.127	0.126	0.637	0.278	0.085	262.2	250.6

3.2 Glass transition temperature
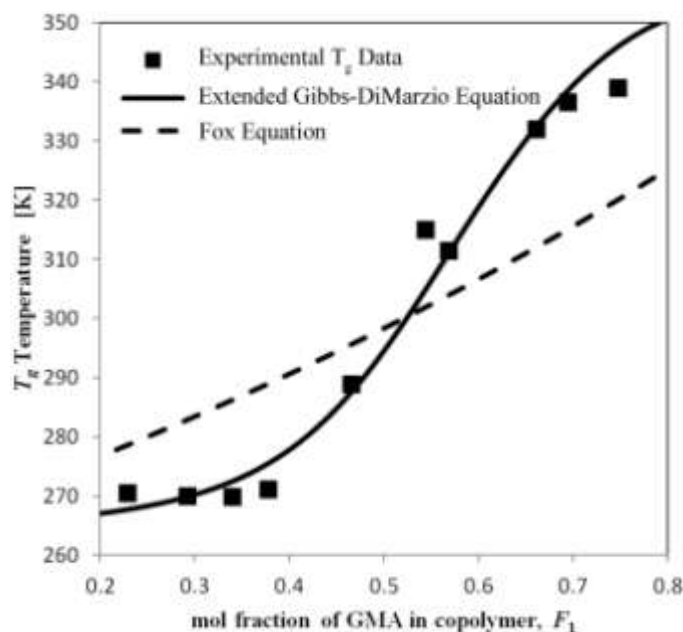
Figure 1: Experimental and predicted T_g's of poly(GMA-*co*-THFA)

Figure 1 portrays the T_g values for the poly(GMA-*co*-THFA) samples. In general, T_g values measured has an S-shaped T_g versus composition relation. The THFA unit does not significantly influence the T_g of the copolymer until it reaches about 43% mol GMA. From that point onwards, T_g are seen to increase in a relatively linear manner up to about 66% mol GMA, where a plateau is achieved. High T_g of the copolymers indicates substantial decrease of chain mobility of the copolymer due to α-CH$_3$ from the GMA unit.

One of the most well-known methods to predict the T_g's of copolymers are given by the linear relations of Gordon–Taylor (Eq. 1) and Gibbs–DiMarzio (Eq. 2) equations which only considers copolymer composition contribution [9-11]:

$$T_g = \frac{w_1 T_{g1} + K w_2 T_{g2}}{w_1 + K w_2} \qquad (1)$$

$$T_g = n_1 T_{g1} + n_2 T_{g2} \qquad (2)$$

where T_g is the glass transition temperature of the copolymer; w_i and n_i are the weight and molar fractions of the component i in the copolymer; T_{gi} is the glass transition temperature of the homopolymer (in the case of Eq. 1, T_{g1} and T_{g2} are assigned such that $T_{g1} < T_{g2}$) ; K is a parameter specified by the model. The volume additivity of repeating units in the copolymer was the assumption basis of Eq. 1. On the other hand, Eq. 2 was based on the additivity of the chain stiffness energy. By further assuming the validity of the Simha–Boyer rule ($\alpha T_g =$ constant) [12] that the parameter K is equal to T_{g1}/T_{g2} , then Eq. 1 can be reformulated as the well-known Fox relation [13]:

$$\frac{1}{T_g} = \frac{w_1}{T_{g1}} + \frac{w_2}{T_{g2}} \qquad (3)$$

A curve fit was applied to Eq. 3 to compare with the experimental data in Table 1. Here, T_{g1} = 347.2 K and T_{g2} = 264.5 K corresponds to the homopolymers of PGMA and PTHFA respectively [14]. As can be seen from Figure 1, large deviations from the experimental T_g's occurred when the T_g's were predicted by using Eq. 3. To accommodate the deviations of experimental results from the linear equations, the effects of sequence distribution should be considered. For the diad sequence, the Barton equation (Eq. 4) and Johnston equation (Eq. 5) are mostly used [15, 16]:

$$T_g = n_{11}T_{g11} + n_{22}T_{g22} + n_{12}T_{g12} + n_{21}T_{g21} \tag{4}$$

$$\frac{1}{T_g} = \frac{w_1 P_{11}}{T_{g1}} + \frac{w_2 P_{22}}{T_{g2}} + \frac{w_1 P_{12} + w_2 P_{21}}{T_{g12}} \tag{5}$$

where $T_{g\ ij}$ is the additive temperature associated with the diad sequence ij ; n_{ij} and P_{ij} are the mole fraction and the probability of forming the respective diad ij from the end group of unit i, respectively. The diad probabilities P_{11}, P_{12}, P_{22}, and P_{21} are calculated from the reactivity ratios r_1=0.379 and r_2=0.266 [17] and are given as [18]:

$$P_{11} = \frac{r_1}{r_1 + f_2/f_1} \tag{6}$$

$$P_{12} = 1 - P_{11} \tag{7}$$

$$P_{22} = \frac{r_2}{r_2 + f_1/f_2} \tag{8}$$

$$P_{21} = 1 - P_{22} \tag{9}$$

However, discrepancies between experimental data and theoretical results still exist when these equations are adapted to describe the S-shaped T_g versus composition relations such as the difficulty in solving out $T_{g\ 12}$ by data regression. Figure 2 below portrays an example of Eq. 5 being applied. Here, five different curve fittings using T_{g12} values that were incrementally raised from between T_{g1} =264.5 K to T_{g2} =347.2 K to demonstrate that even if any other combinations of T_{g12} were to be used, none would likely fit into the S-shaped profile of the experimental data.
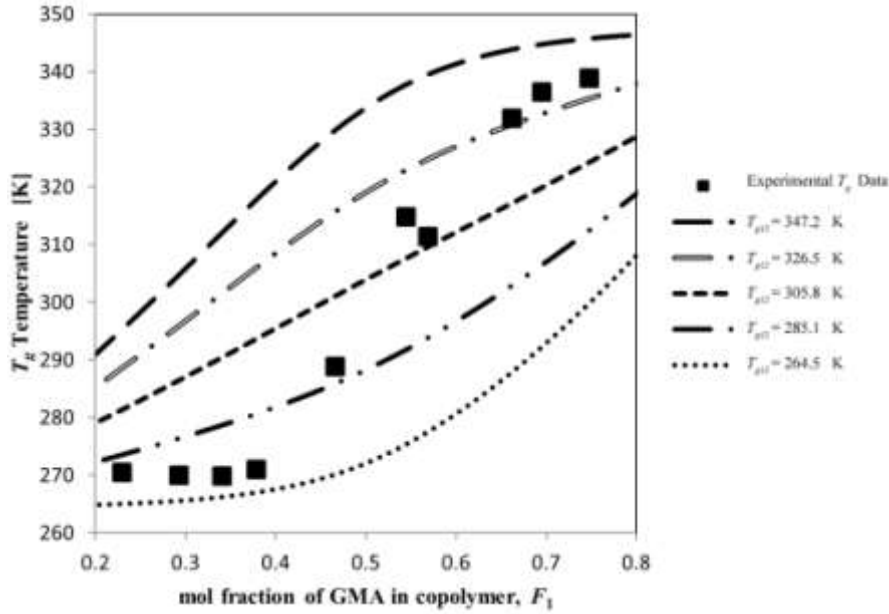
Figure 2: Experimental and predicted T_g's of poly(GMA-*co*-THFA) using Eq. 3

Significant improvements in the fitting results can be observed when the triad sequence effect is taken into consideration for most copolymer T_g versus composition relations [19, 20]. Ham extended the Barton equation as:

$$T_g = n_{111}T_{g111} + n_{222}T_{g222} + n_{112}T_{g112} + n_{211}T_{g211}$$
$$+ n_{122}T_{g122} + n_{221}T_{g221} + n_{121}T_{g121} + n_{212}T_{g212} \qquad (10)$$

where $T_{g\ ijk}$ and n_{ijk} are the additive temperature and mole fraction of the triad sequence *ijk*. However, there are six unknown parameters in this equation. In a recent article by Liu et al [21], they proposed a copolymer T_g –composition equation by incorporating assumptions of bond rotation flexibility and the additivity of stiff energy to form an extension of Eq. 2 thereby reducing the number of intractable parameters in Eq. 8 to just three:

$$T_g = n_{111}T_{g1} + n_{222}T_{g2} + 2(n_{121} - n_{112})T_{g[12]} + 3n_{112}T_{g[112]} + 3n_{221}T_{g[221]} \qquad (11)$$

where $T_{g\ [12]}$, $T_{g\ [112]}$ and $T_{g\ [221]}$ are T_g's of periodic copolymers poly[12], poly[112] and poly[221] respectively. The mole fractions of triads were calculated from the reactivity ratios and are given as [21]:

$$n_{111} = F_1 P_{11} P_{11} \qquad (12)$$
$$n_{222} = F_2 P_{22} P_{22} \qquad (13)$$
$$n_{121} = F_1 P_{12} P_{21} \qquad (14)$$
$$n_{112} = F_1 P_{11} P_{12} \qquad (15)$$
$$n_{221} = F_2 P_{22} P_{21} \qquad (16)$$

The T_g contributions of the periodic copolymers were solved out by data regression [22, 23] and the fitted values obtained were 253.3 K, 375.7 K and 267.5 K for $T_{g\ [12]}$, $T_{g\ [112]}$ and $T_{g\ [221]}$ respectively. Figure 1 shows the Eq. 11 being applied. The Table 1 shows the comparison

of the experimental data with the methods used, with Eq. 11 being the best choice to predict the curve fits. Since the regression of Eq. 11 minimizes the orthogonal distance to the tangent of the curve, it can be expected that there will be slightly larger deviations in the region where the slope is steep. Comparison with Eq. 5 is not shown since no combination of T_{g12} into it could match the T_g versus composition profile of the copolymer system that could further improve the curve fit of Eq. 3.

The treatment methods mentioned above for the prediction of T_g can be readily extended to multicomponent polymer systems. For example, the Fox, Barton and Johnston general forms become [24]:

$$\frac{1}{T_g} = \sum_i \frac{w_i}{T_{gi}} \tag{17}$$

$$T_g = \sum_{i,j} n_{ij} T_{gij} \tag{18}$$

$$\frac{1}{T_g} = \sum_{i,j} \frac{w_i P_{ij}}{T_{gij}} \tag{19}$$

Table 2 gives the glass transitions as determined by DSC for the poly(nBA-co-GMA-co-THFA) samples. The T_g contributions from each of the three types of repeating units in the terpolymer can be better visualized in Figure 3 below.
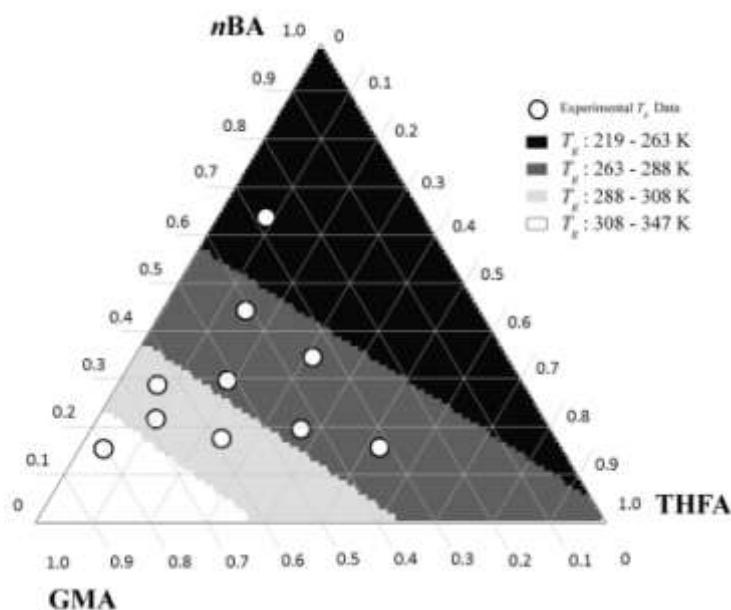
Figure 3: Experimental and predicted T_g's of poly(nBA-co-GMA-co-THFA)

The treatment method such as Eq. 18 and Eq. 19 which takes into consideration of the diad sequence distribution of the terpolymer requires information on the intermediary $T_{g\ ij}$ values. Since the scope of this work is only on poly(GMA-co-THFA) and poly(nBA-co-GMA-co-THFA), $T_{g\ ij}$ values for poly(nBA-co-GMA) and poly(nBA-co-THFA) would be unavailable. Here, the Fox equation (Eq. 17) was applied to group the experimental data into an approximate trend of four regions: from 219-263 K, 263-288K, 288-308K, and 308-347K. The contribution of T_{g3} for poly(nBA) in Eq. 17 was 219.2K [14]. The Table 2 gives the comparison of the experimental data with the predicted T_g values which, unlike the copolymer system, shows slightly less deviation when the Fox equation (Eq. 17) is applied. This would be most likely due to the terpolymer system only having one out of three of its unit types that has an α-CH$_3$ substitution on its polymer backbone. The α-CH$_3$ substitution could be a source

of dissymmetry in the polymer backbone that influences the T_g greatly by its sequence distribution [24].

4.   CONCLUSION

The concluding remark of the T_g behaviour of the poly(GMA-*co*-THFA) system is that it is very dependent on the triad sequence distribution, most likely due to the α-CH$_3$ from the GMA unit. Unlike the copolymer system, the T_g of the terpolymer system shows slightly less deviation when the Fox equation (Eq. 15) is applied. The GMA unit is most likely the largest contributor to the T_g deviating from the linearity of the Fox equation.

5.   ACKNOWLEDGMENT

6.   REFERENCES

1.   Hall C.E., Datta D. & Hall E.A.H. (1996). Parameters which influence the optimal immobilisation of oxidase type enzymes on methacrylate copolymers as demonstrated for amperometric biosensors. *Analytica Chimica Acta,* 323(1-3), 87-96.

2.   Yang W., et al. (1999). Dispersion copolymerization of styrene and glycidyl methacrylate in polar solvents. *Colloid and Polymer Science,* 277(5), 446-451.

3.   Malmsten M. & Larsson A. (2000). Immobilization of trypsin on porous glycidyl methacrylate beads: effects of polymer hydrophilization. *Colloids and Surfaces B: Biointerfaces,* 18(3-4), 277-284.

4.   Bayramoglu G., Akgöl S., Bulut A., Denizli A., & Yakup ArIca M. (2003). Covalent immobilisation of invertase onto a reactive film composed of 2-hydroxyethyl methacrylate and glycidyl methacrylate: properties and application in a continuous flow system. *Biochemical Engineering Journal,* 14(2), 117-126.

5.   ArIca M.Y., Bayramog, lu G. & Biçak N. (2004). Characterisation of tyrosinase immobilised onto spacer-arm attached glycidyl methacrylate-based reactive microbeads. *Process Biochemistry,* 39(12), 2007-2017.

6.   Adhikari B. & Majumdar S. (2004). Polymers in sensor applications. *Progress in Polymer Science,* 29(7), 699-766.

7.   Nino G.D., et al. (2004). Catalytic activity of bovine lactoperoxidase supported on macroporous poly(2-hydroxyethyl methacrylate-co-glycidyl methacrylate). *Reactive and Functional Polymers,* 61(3), 411-419.

8.   Pérez J.P.H., López-Cabarcos E. & López-Ruiz B. (2006). The application of methacrylate-based polymers to enzyme biosensors. *Biomolecular Engineering,* 23(5), 233-245.

9.   Gordon M. & Taylor J.S. (1952). Ideal copolymers and the second-order transitions of synthetic rubbers. i. non-crystalline copolymers. *Journal of Applied Chemistry,* 2(9), 493-500.

10.   Dimarzio E.A. & Gibbs J.H. (1959). Glass temperature of copolymers. *Journal of Polymer Science,* 40(136), 121-131.

11.   Penzel E., Rieger J. & Schneider H.A. (1997). The glass transition temperature of random copolymers: 1. Experimental data and the Gordon-Taylor equation. *Polymer,* 38(2), 325-337.

12.   Simha R. & Boyer R.F. (1962). On a General Relation Involving the Glass Temperature and Coefficients of Expansion of Polymers. *The Journal of Chemical Physics,* 37(5), 1003-1007.

13.   Fox T. (1956). Influence of diluent and of copolymer composition on the glass temperature of a polymer system. *Bulletin of the American Physical Society,* 1, 123-135.

14.   Brandrup J., Immergut E.H. & McDowell W. (1975). *Polymer Handbook* (2nd Ed). Wiley Interscience, New York.

15.   Barton J.M. (1970). Relation of glass transition temperature to molecular structure of addition copolymers. *Journal of Polymer Science Part C: Polymer Symposia,* 30(1), 573-597.

16.   Johnston N.W. (1973). Sequence Distribution-Glass Transition Effects. III. α-Methylstyrene-Acrylonitrile Copolymers. *Macromolecules,* 6(3), 453-456.

17.   Azzahari A.D., Yahya R., Hassan A. & Sheikh M.R.K. (forthcoming). Synthesis and characterization of new copolymers from glycidyl methacrylate and tetrahydrofurfuryl acrylate: Determination of reactivity ratios. *Fibers and Polymers*.

18.   Odian G.G. (2004). *Principles of polymerization* (4th Ed). Wiley-Interscience, New Jersey.

19.   Ham G.E. (1975). Role of Triad Concentration in Glass Transition Temperatures of Copolymers. *Journal of Macromolecular Science: Part A - Chemistry,* 9(3), 461-467.

20.   Liu G., Zhang L., Yao Y., Yang L., & Gao J. (2003). Glass-transition temperatures and rheological behavior of methyl methacrylate–styrene random copolymers. *Journal of Applied Polymer Science,* 88(13), 2891-2896.

21.   Liu G., Meng Z., Wang W., Zhou Y., & Zhang L. (2008). Sequence Distribution Effects on Glass Transition Temperatures of Copolymers: An Extended Gibbs−DiMarzio Equation in View of Bond Rotation Flexibility. *The Journal of Physical Chemistry B,* 112(1), 93-99.

22.   Reilly P.M. & Patino-Leal H. (1981). A Bayesian Study of the Error-in-Variables Model. *Technometrics,* 23(3), 221-231.

23.   Reilly P.M., Reilly H.V. & Keeler S.E. (1993). Algorithm AS 286: Parameter Estimation in the Error-in-Variables Model. *Journal of the Royal Statistical Society. Series C (Applied Statistics),* 42(4), 693-701.

24.   Bonardelli P., Moggi G. & Turturro A. (1986). Glass transition temperatures of copolymer and terpolymer fluoroelastomers. *Polymer,* 27(6), 905-909.

An Investigation of Expanded Austenite Formation on Duplex Stainless Steels Treated by Low Temperature Carburizing in a Tube Furnace Atmosphere

N.F.M Yusof[1], M. N Berhan[1], M.S. Adenan[1], E. Haruman[2],

[1]Faculty of Mechanical Engineering, University Technology of MARA, Selangor, Malaysia.
[2]Faculty of Industrial Engineering, Bakrie University, Jakarta, Indonesia
Email: farhanayusof126@gmail.com;

Abstract: *A low temperature thermochemical carburizing technique has recently been developed on the surface of duplex stainless steels to achieve combined improvement in hardness and wear resistance. The carburized layer is free from chromium carbide precipitates and contains austenite phase supersaturated with carbon. An attempt was conducted in various process parameters by adding 3 - 5% CH_4 in gas mixtures with N_2 at temperature 450°C – 550°C for 14h. Structure and properties of the carburized layer was investigated by various tests such as X-ray diffraction (XRD), scanning electron microscopy (SEM), optical microscope and testing for microhardness and wear. The surface hardness and wear resistance of the carburized layer was significantly increased compared to that of the untreated one.*

Keywords: duplex stainless steels, expanded austenite, carburizing, methane (CH_4), low temperature

1.   INTRODUCTION

Duplex stainless steels (DSS) represent an important class of materials that widely used in chemical, petrochemical, food, paper, pharmacy, marine and many other fields. Although DSS is widely used in many applications, there are some drawbacks for certain properties of this material. These include poor wear properties and low surface hardness which constrains the materials for wider applications and thus, might cause problem to an enhanced application especially for fitting and piping connection. [1-4]. General methods being used to increase the surface properties of steels and alloys, for the improvement of wear properties and increasing the wear hardness are by surface engineering techniques. A few journal papers have been reviewed [2, 4-8] discussing about performing low temperature themochemical treatment is one of surface engineering methods that has been proven to be a useful technique for increasing the hardness and wear resistance of austenitic stainless steel without reducing the corrosion resistance of this alloy [6] . T. Christiansen et. al [8-9] have been performed thermochemical treatments, carried out in carbon and/or nitrogen gases with temperatures above 400°C on austenitic stainless steels without developing chromium carbide on the surface. In addition, a recent research by E. Haruman et.al, Triwiyanto et.al [7-8] on low temperature surface treatment can improve the surface hardness and wear resistant. This method maintains the corrosion resistance of the steel by preventing the gases applied to react with chromium content at the steel mainly due to the processing temperature below 500°C. Despite their promising results the above works mostly based on austenitic stainless steels. By performing low temperature, basically, it is applicable to obtain carbon EA without any undesired phase developed during the treatment. As discussed earlier by previous wokrs [6-11], temperature above 550°C will creates carbide layer at the surface which will deteriorate the corrosion resistance of the steel.

2.   MATERIALS AND EXPERIMENTAL TECHNIQUES

The material used in the experiments is round bar rolled products of duplex stainless steel UNS 31803. The 22% Chromium and 5% Nickel of these solution-annealed duplex stainless steels with 25mm diameter. Prior to the treatment, the specimens were cleaned by acetone and immersed into hydrochloric acids (HCl) for 15 minutes to remove oxide before being put into tube furnace for carburizing process. Investigation on the effect of austenite (γ), ferrite (α) structures on the formation of expanded austenite (S-phase), different carburizing treatment temperatures (450°C, 500°C, 550°C) for 14 hours and different gas composition with N_2 and 3 - 5 % CH_4 addition for carbon sources [5, 7] was employed in relation to the resulting mechanical properties [7, 10-12]. These parameters were based on studies [6-8] have proven that at 500°C with optimum duration 14 h low temperature carburizing can produce hard and thick expanded austenite layer free from chromium precipitates. To validate the formation of expanded austenite on duplex feritic-austenitic substrate, the Rigaku Model Diffractometer was used. The 2θ degree diffraction scans were employed at speed 1 degree/min with sampling step at 0.05deg, in the range 30 – 100 degrees. Specimens for metallographic evaluation were extracted from cross-sectional area of carburized layer. Polished samples were etched with Kalling's reagent no. 2 (100ml ethanol, 100ml 32% HCl, 100ml H_2O and 4.5g $CuCl_2$) which has been used to reveal the structure of stainless steels grades [7-8]. The image of cross-sectional area of carburized thin layer was done by Scanning Electron Microscope (SEM). The hardness profile of carburized specimen was measured by using Vickers microhardness tester with an applied load of 25g according to ASTM E384. The wear

resistant of samples was tested using pin-on-disk tribometer. Tribological behaviors were evaluated with a dry slide tribo-tester model Ducom TR 20LE using steel ball as mate material.

3. RESULT AND DISCUSSION

3.1 XRD Analysis

Attempt were come out until 14 hours and expected result to produce the thicker layer of carbon. Figure 1.0 is clearly shows XRD patterns of the samples which having a mixed of ferrite and austenite at it structure. The surface of the carburized samples consisted of ferrite, austenite, and an expanded austenite (S phase). The expanded austenite is considered to be a supersaturated solid solution of carbon on the surface and its diffusion into the structure of austenitic phase which called carbon expanded austenite. Previous reported by other researchers [3, 7, 13-14], the peaks are slightly shifted to lower 2θ angles than those for normal austenite and the peaks become broader, indicating an expansion of the lattice due to carbon EA reaches at great amount of carbon, compare to the untreated DSS. Increasing the temperature to 450°C resulted in the formation of a relatively thick carburized layer without precipitation of chromium carbide due to shifted angle and higher peak after 14 hours carburizing comparing to the substrate DSS peak. At the temperature 550°C at 14 hours by adding 3% CH_4, the chromium carbide, Cr_3C_2 starts produce on the DSS surface and continuously produces until temperature 550°C at 14 hours for 5% CH_4 level. Increasing the CH_4 level until 5%, the C-enriched layer thickness such that the total layer thickness is increased due to the great amount of carbon penetration on the surface[5, 7]. The position of higher peak depends on the process parameters (temperature, gas mixture composition and treatment duration time) are observed the samples of carburizing thermochemical treatment compare with untreated DSS.
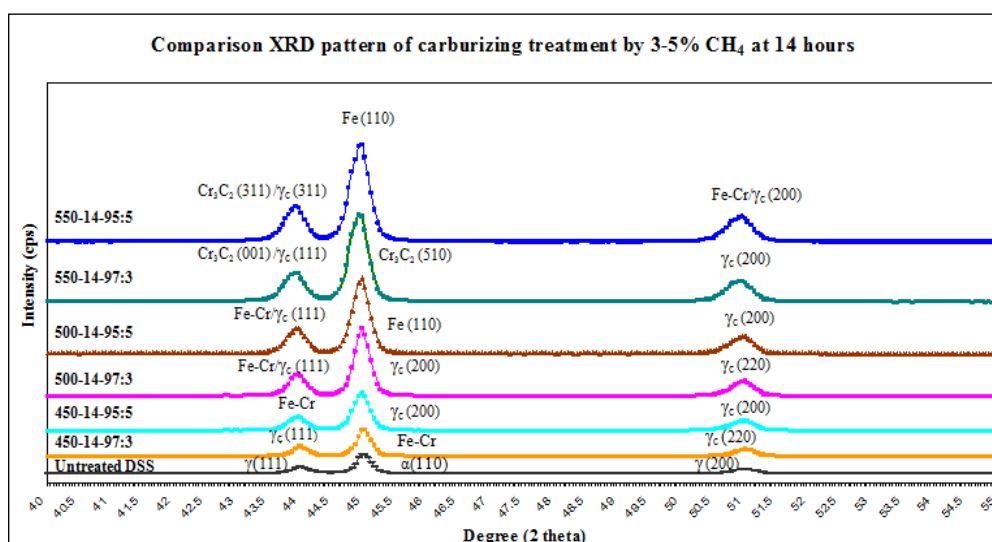
Figure 1.0 summarizes the phase compositions in the treated specimens as determined by XRD pattern from the specimen treated at 450°C, 500°C and 550°C for 14 hours.

3.2   Layer Morphology and hardness profile

Figure 2.0 shown different layer of carburized thickness layer at different temperature and gas compositions. Refer to the Figure 2.0 (c), as confirmed by XRD, the treatment up to 14 hours for temperature 500°C by adding 5% CH_4 shows the highest thickness of producing carbon EA about 78.85μm. It also leading to a significant increase in surface hardness about 703.0 $HV_{0.025}$ which indent on the top surface. Figure 2.0 (d) shows the chromium precipitation was produced along the surface and Figure 2.0 (e), the chromium carbide precipitation were continuous and the thickness reduced about 8.5-15%. However at temperature 550°C, the dark phase on the surface which shown in Figure 2d and 2e is associated with the formation of chromium carbide precipitates in the carbide layer, as confirmed by XRD analysis [9]. In oppositions to the hardness trend, it was found that increasing the percent of CH_4, it gives the effect to thicknesses where significantly increased 6% due to the presence of carbon EA.

a) 450-14-95:5   b) 500-14-97:3   c) 500-14-95:5

d) 550-14-97:3   e) 550-14-95:5
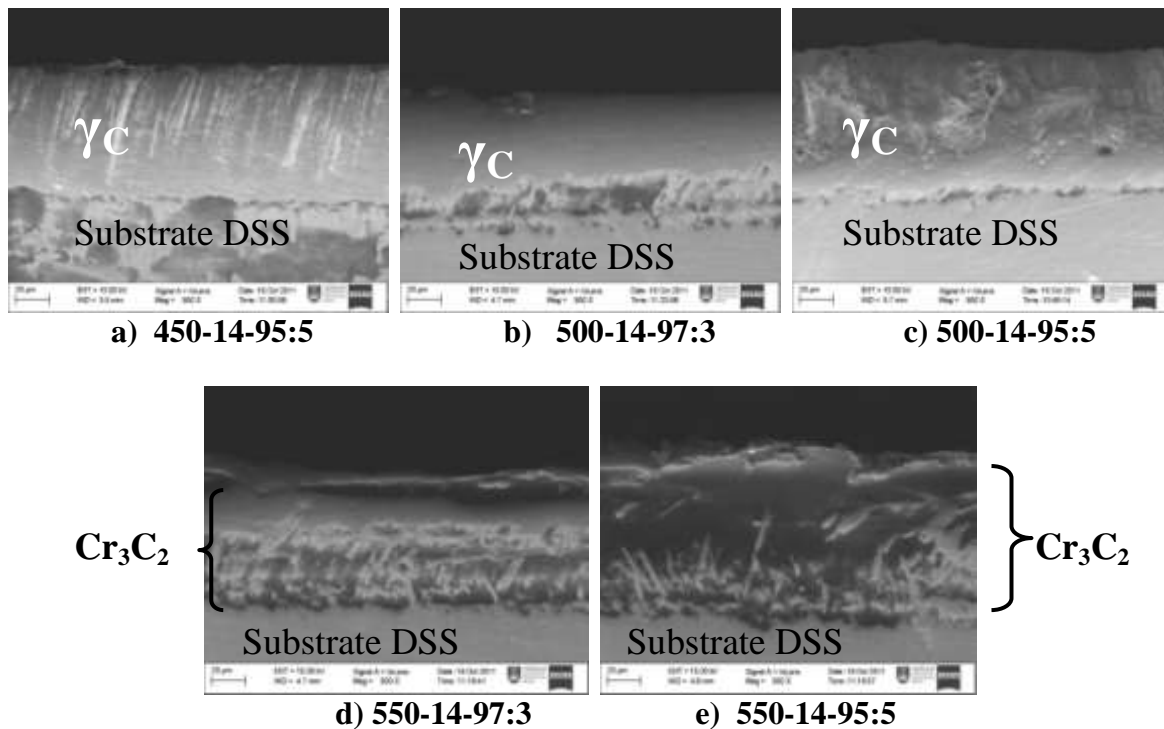
Figure 2.0 cross sectional microstructure hardened carbon EA layers produced on duplex stainless steel by gaseous thermochemical carburizing in various process parameters at 500x magnification for a) 450-14-5%, b) 500-14-3%, c) 500-14-5%, d) 550-14-3%, e) 550-14-5%

The carbon EA with different morphologies were observed as a result of the various treatment conditions and the thicknesses of the layers produced in different conditions are shown in Table 1.0.

Table 1.0 Treatment conditions and their corresponding layer thicknesses by selected samples.

No.	Name of samples	Thickness layer (μm)	Microhardness ($HV_{0.025}$)

	Untreated DSS	-	222.5
a	450-14-5%	34.46	382.2
b	500-14-3%	67.23	524.8
c	**500-14-5%**	**78.85**	**703.0**
d	550-14-3%	59.19	376.0
e	550-14-5%	68.12	444.9

The hardness profile curves of layers of carbon expanded austenite were observed with different morphologies at various conditions. The effects of different parameters hardness profile for 6 specimens during 14 hours are shown in Figure 3.0. The carburized specimens at temperature 500°C at 14 hours with 3% CH_4 have developed a highest hardness on the top surface of about 703.0 $HV_{0.025}$ respectively. It was increasing about 68.35% compare to the untreated one. However, the surface hardness of carbon EA slightly decreased when temperature up to 550°C where chromium carbide precipitation has been produce. Mostly, the hardness of treated samples was slightly increases with increasing the processing time until 14 hours. By addition of CH_4 at 5%, the thickness of carbon EA layer was increased as increasing of CH_4 addition. With increasing carburizing temperatures, the surface hardness increased and the hardness profile became shallower. It should be noted that the core hardness increased substantially with increasing temperature of carburizing treatment. By performing at longer duration treatments for all various processing temperature, it led to increase in surface hardness. However, prolong treatment for up to 550°C and above for both gas compositions will caused the chromium carbide precipitation obtained respectively.
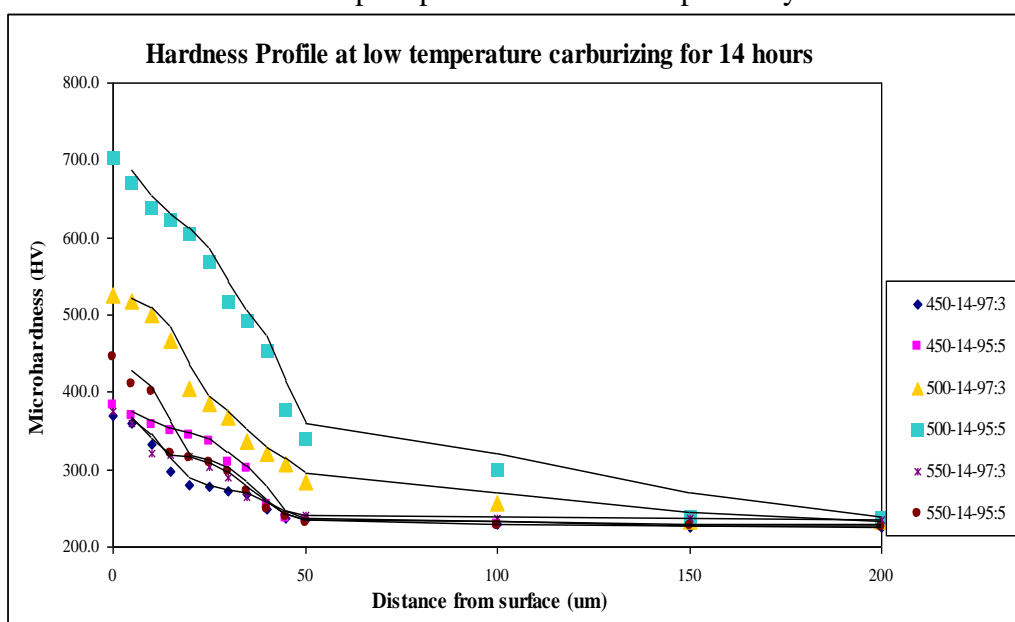
Figure 3.0 Depth profile of microhardness of gaseous thermochemical carburizing treatment for 14h at temperature 450°C – 550°C

3.2   Wear Results

The wear resistance of carburized was strongly related to the surface hardness of the carburized region and was dependent on the applied normal load. Figure 4.0 shows the result of wear tests with applied 20N load for selected samples for the thickest carbon EA and greatest hardness. The figure also shows the wear track appearance of the samples. Wear test results presented have correlate well with the hardness test and it indicate the improvement in

wear resistance comparing to the untreated DSS. The sample which in temperature 500°C at 14 hours by adding 5% CH_4 exhibited the lowest cumulative wear loss about 0.4 mg, followed by sample which is in same temperature but in 3% CH_4. The treated samples, 550-14-97:3 which produce the chromium carbide precipitation had poor wear resistance due to low hardness. It also noted that the weight loss of treated samples decreases with increasing the carburized layer thickness and hardness. For similar treatment, the wear result is reported [7, 11] which is concluded that the wear resistance of carburized layer increases with the increasing layer hardness.
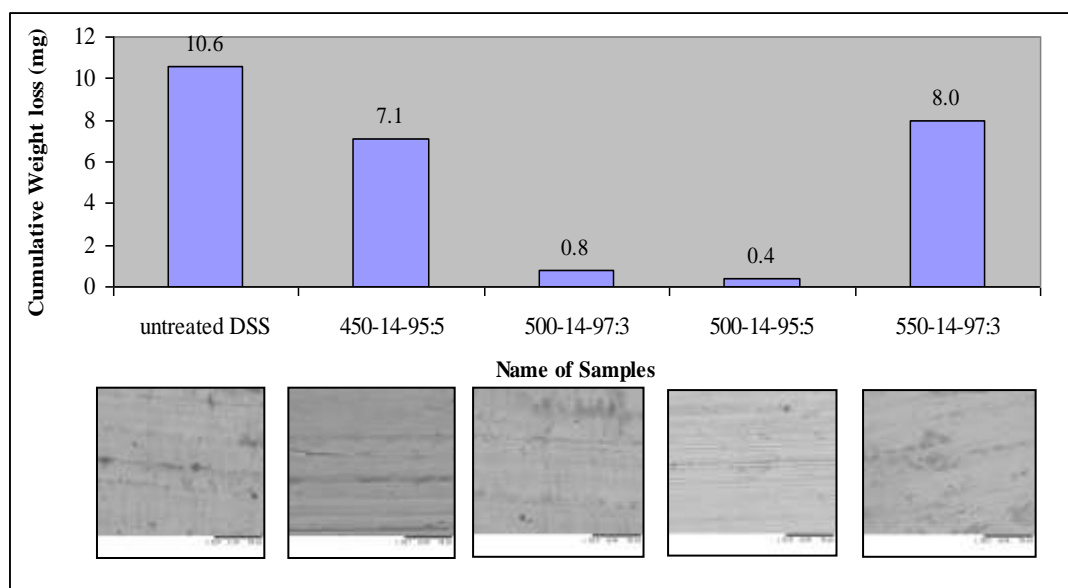
Figure 4.0 Wear test results on various samples low-temperature carburizing on DSS

4.   CONCLUSION

The thermochemical treatments of duplex stainless steel in tube furnace at 450-500°C demonstrate that it is possible to produce carbon expanded austenite (EA) layer with free precipitation of chromium carbide. Carbon EA development on DSS through low temperature gaeous treatment at 450°C, 500°C and 550°C for 14 hours by addition 3-5% CH_4 have been studied. Observation have shown the thickest layer carbon EA has been obtained during 500°C for 14h at 5% CH_4. Nevertheless, it has been found that at 14 hours processing time at 550°C, the chromium carbide precipitation has been produced on the carbon EA and continously produce at highest CH_4 level at 5%. In conclusion, it is effect mechanical properties by producing any precipitation on the surface where it reduce the microhardness. Generally, the hardness of carbon EA is depending on the longer processing time, process temperature and high level of CH_4 to the great amount of carbon diffusion on the surface. So that, it concluded that the process parameters have a strong influence during gaseous treatment to create optimum layer of carbon EA.

5.   REFERENCES

1. K.H. Lo, C.H. Shek, J.K.L. Lai, (2009).Recent developments in stainless steels, Materials Science and Engineering R 65 39–104
2. Frechard, S., Martin, F., Clement, C. and Cousty J. (2006). AFM and EBSD combined studies of plastic deformation in a duplex stainless steel, Materials Science and Engineering: Structural Materials: Properties, Microstructure and Processing A 418, 312-319
3. Dong, H., Sun, Y. and Bell, T. (1997), Enhanced corrosion resistance of duplex coatings, Surface and Coatings Technology 90, 1-2, 91-101
4. Villanueva, D. M. E., Junior, F. C. P., Plaut, R. L. and Padilha, A. F. (2006): Comparative study on sigma phase precipitation of three types of stainless steels: austenitic, superferritic and duplex, Materials Science and Technology 22, 9, 1098-1104
5. M.S. Adenan, E.H., N.F.M Yusof, (2010). *A View on Performing Low Temperature Thermochemical Heat Treatment on Duplex Stainless Steels*., Faculty of Mechanical Engineering, Universiti Teknologi MARA: Shah Alam, Selangor, Malaysia. p. 1-5.
6. Bell, T. and Sun, Y. (1998). Process for the treatment of austenitic stainless steel articles UK Patent 9715180.7
7. Triwiyanto, S.M., E. Haruman And M. Bin Sudin,(2009). Thermochemical Treatments Of Austenitic Stainless Steel in Fluidized Bed Furnace For Improved Mechanical And Ribological Properties. International Journal Of Mechanical And Materials Engineering (Ijmme), Vol. 4, No. 2, 197-203.
8. Y. Sun, E.H., (2006). *Effect of carbon addition on low-temperature plasma nitriding characteristics of austenitic stainless steel* Science Direct, Vacuum 81 114–119.
9. Somers, T.C.M.A.J. (2005). *Low temperature gaseous nitriding and carburising of stainless steel.* Department of Manufacturing Engineering and Management, Technical University of Denmark, VOL 21, NO 5–6
10. Thomas Christiansen and Marcel A. J. Somers, (2006) *Characterization low temp surface hardened Stainless Steels.* Struers Journal of Materialography.
11. E. Haruman, Y.S., H. Malik, A.G.E Sutjipto, (2006). *Low Temperature Fluidized Bed Nitriding of Austenitic Stainless Steel,*. Solid State Phenomena, Vol. 118 pp.125-130.
12. Carlos Eduardo Pinedo, A.P.T. (2010). *LOW TEMPERATURE PLASMA CARBURIZING OF AISI 316L AUSTENITIC STAINLESS STEEL AND AISI F51 DUPLEX STAINLESS STEEL.*, University of Mogi das Cruzes: Brazil. p. 1-8.
13. Liu-Ho Chiu, F.-S.C., Yang-Yu Su, (2005). *Effect of CH_4 Addition on Low Temperature Plasma Nitrocarburizing of Duplex Stainless Steel,*. Department of Materials Engineering: Tatung University, Taiwan
14. Zhao Cheng, X. Li, H. Dong, T. Bell (2005) *Low temperature plasma nitrocarburising of AISI 316 austenitic stainless steel*. Surface & Coatings Technology 191, 195– 200.

Tensile and Oxidative Degradation Properties of Polyvinyl alcohol/Chitosan/Polyethylene Glycol Blend

W. S. Khoo[1,]*, H. Ismail[1], and A. Ariffin[1]

[1]School of Materials and Mineral Resources Engineering, Universiti Sains Malaysia (USM)
Seri Ampangan,14300 Nibong Tebal, Penang, Malaysia

*Corresponding author: weeshen24@gmail.com

Abstract: *Polyvinyl alcohol (PVA)/Chitosan (CS)/Polyethylene glycol (PEG) blend films were prepared using wet casting method. The blend films were characterized for tensile, morphology and oxidative degradation properties. Tensile strength and Young's modulus decreased whereas elongation at break increased when the content of PEG increase in the blend films. The blend films were degraded using Fenton reagent. The degradation of blend films improved as the content of PEG increased.*

Keywords: Polyvinyl alcohol; Chitosan; Polyethylene glycol

1.   INTRODUCTION

Plastic has been available since 1907. Since then, wide variety of applications uses plastic. The raw materials used to make most plastic are from petroleum. Plastic are macromolecules, thus it takes ages to degrade the plastic. Furthermore, it is pointed out that plastic produced from petroleum takes 106 years to degrade [1]. The worldwide consumption of polymeric materials and plastics rises annually by around 7 to 10% [2]. To further optimize the properties of plastic, polymer blend are develop by researchers. Polymer blend has at least two polymers blended together to create a new material with different properties. It increase engineering resins performance, improves mechanical strength, increase solvent resistance while reducing the cost [3].

PVA is the largest synthetic water soluble polymer produced in the world and has been available since 1924. PVA is an odorless and tasteless, translucent, white granular powder [4]. PVA has excellent aroma and oxygen barrier properties, have antistatic properties and show good heat sealability [5]. CS (β-(1→4)-2-amino-2-deoxy-d-glucose) is the second most abundant natural polymer from shrimp, crab shell, fungi and other crustaceans. CS is a cationic polymer product of chitin deacylation. CS contains reactive amino and hydroxyl

groups. Moreover, it has good film forming properties, good mechanical strength, biocompatible, biodegradable and low cost [6]. PEG is a water soluble polymer and it is widely used in biomedical application. PEG has a simple chain with ester linkage [7]. PEG is a biocompatible polymer with excellent biocompatibility and nontoxicity [8]. PEG presents unique physico chemical properties, such as high hydrophilicity and very good solubility in water. In this research, PVA/CS/PEG blend films were prepared. Effect of PEG content on the tensile, morphology and oxidative degradation properties of blend films were investigated.

2.   MATERIALS AND METHODS

2.1   Materials

Polyvinyl alcohol, 99+ % hydrolyzed, Mw= 89,000 – 98,000 was supplied by Sigma Aldrich Chemistry. On the other hand, CS of degree of deacytylation > 90.0% was supplied by Hunza Nutriceuticals Sdn Bhd. PEG with a tradename of LIPOXOL 6000 MED powder, supplied from Euro Chemo Parma Sdn Bhd, Malaysia. Besides that, glacial acetic acid solution 99%, 50% glutaraldehyde (GA) solution and hydrogen peroxide 30% solution were obtained from Merck. Furthermore, ferrous sulphate, 0.1 mol was supplied by Fixanal Sigma.

2.2   Method

Prior to the preparation of the blend films, 2.5 wt% of PEG solution was prepared. Later, PVA/CS 80/20 solution was prepared by mixing 2.5 wt% of PVA and CS solution together. After preparing both PVA/CS 80/20 and PEG solution, both solutions were homogenised together according to Table 3.5 at room temperature for 30 minutes under magnetic stirring. Then, the blend solution was cast on a 14 cm x 7 cm glass plate. The solution was air-dried for 2 days under room temperature to cure the film. Finally, PVA/CS blend films were peeled off the glass plate and stored in desiccator. The obtain films has a thickness of 0.12 ±0.05 mm.

Table 1: Formulation for PVA/CS/PEG blend

Sample ID	Composition (wt%)	
	PVA/CS	PEG
PVA	100	0
PEG 2	98	2
PEG 4	96	4
PEG 6	94	6
PEG 8	92	8
PEG 10	90	10

2.3   Tensile properties

Dumb bell shaped samples were punched from the blend films by a tensile specimen cutter. Tensile strength, elongation at break, Eb and Young's modulus were tested according to ASTM D638. Universal tensile testing machine Instron 3366 was used to record the tensile

results at room temperature (25±2 °C) with crosshead speed of 20 mm/min. The test was repeated five times for each sample.

2.4 Morphology properties

The tensile fractured surfaces of blend films were investigated by using a Supra-35VP SEM. To prevent the electrostatic charging during observation, the samples were coated by a thin layer of a Pd–Au alloy.

2.5 Oxidative degradation properties

2.8 M of hydrogen peroxide solution and 0.1 M of ferrous sulphate solution were prepared beforehand. Also, pH of the ferrous sulphate solution was adjusted to 4.2 by pH meter. Rectangular shaped sample were cut with dimension of 30×20×0.12 mm and the initial weight of the sample were weighted. The degradation begins by adding 5 ml of hydrogen peroxide solution and 5 ml of ferrous sulphate solution into a small glass cup. Photograph of the degradation reaction was taken at 10 second, 2 minute, 1 hour and 5 hour. After the fifth hour, the solution were filtered with filter paper and weight of the final degrade product were measured. The percentage of degradation was calculated.according to the eq. 1 below:

$$\%D = \frac{Wo - W1}{W0} \times 100 \qquad \text{(eq. 1)}$$

Where W_1 is the final weight of the sample at every interval and W_0 is the initial weight of the sample

3. RESULT AND DISCUSSION

3.1 Tensile properties

Tensile strength of the films decreased as the percentage of PEG in the films increased. As portrayed in Fig. 1, tensile strength was at 40.73 MPa without the addition of PEG. After addition of 2% PEG, tensile strength dropped to 38.98 MPa. It decreased to 32.06 MPa after addition of 10% of PEG. The decrease in tensile strength was due to the partial replacement of PVA/CS 80/20 blend with PEG. Besides that, the presence of PEG will lead to reduced intermolecular interaction between PVA and CS. PEG act as a plasticizing agent that reduced the tensile strength of the film. Plasticizer agent are known to develop polymer plasticizer hydrogen bonds replacing the polymer polymer interaction in the films [9]. The plasticizing effect is not prominent due to the higher molecular weight PEG used. The higher increase molecular weight means decrease in the number of PEG end group. The number of end group is an important factor which will determine the plasticizing effect [10].

Contrary to the tensile strength, elongation at break, E_b of the blend film values increase as the PEG increased as shown in Fig. 2. PVA films show the highest E_b at 144.83% while addition of 10% of CS leads the Eb to decrease by 48.6%. The increase in E_b show the plasticizing effect occurred in the films. The increasing PEG content reduced the Young's modulus of the blend films as illustrated in Fig. 3. The Young's modulus recorded without the addition of PEG was 950.38 MPa while the Young's modulus dropped to 353.8 MPa after addition of 10% PEG. The decreased in Young's modulus in the films were attributed to the partial replacement of PVA/CS with PEG. Besides that, plasticising effect in the blend films also play a role in the reduction of Young's modulus which lead to lesser interaction between PVA and CS.
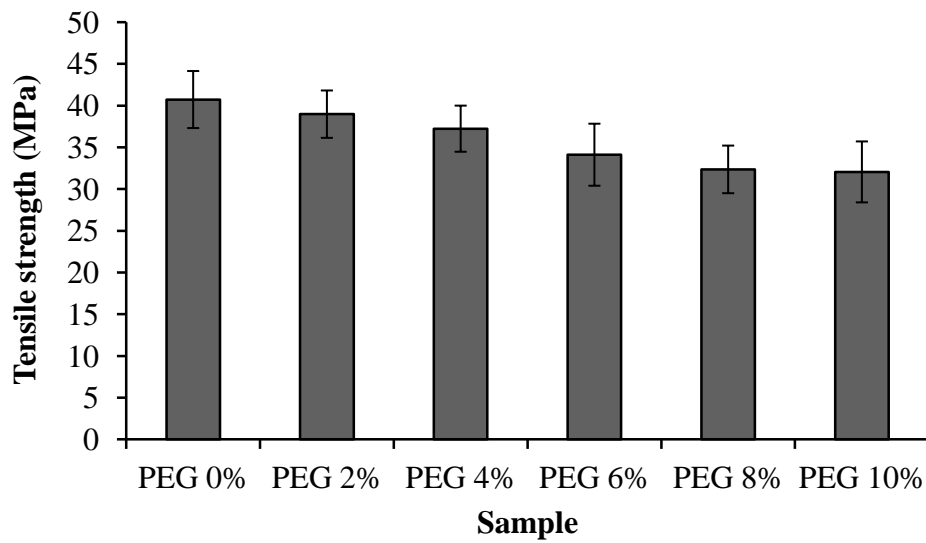
Fig 1. Tensile strength of PVA/CS/PEG blend films
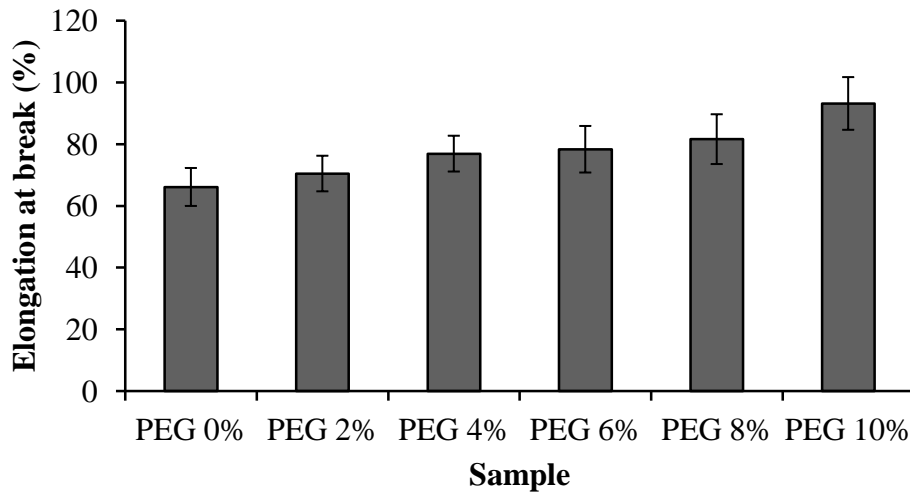
Fig 2. Elongation at break of PVA/CS/PEG blend films
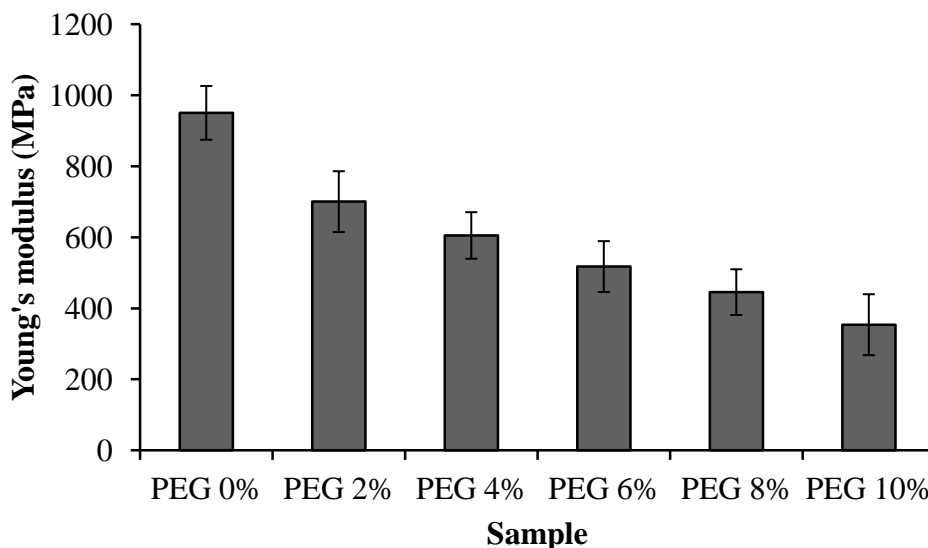
Fig 3. Young's Modulus of PVA/CS/PEG blend films

3.2   Morphology properties

Fig 4 illustrates the fracture surface morphology of blend films at magnification of 800X. The morphology at 0% and 2% PEG were smooth without obvious phase separation. After addition of 2% PEG, the fracture morphology became rougher. There were obvious phase separations after addition of 6% of PEG. Zeng et al [11] reported that phase separation occurred in CS/PEG blend membranes. These results indicate that CS and PEG were not very compatible although it formed hydrogen bonding interaction. After addition of 10% PEG, agglomeration of CS were observed due to the The phase separation lead to lower load were needed tearing shows that higher load needed to break the film. This observation was in agreement with the tensile strength discussed previously.

(a)   (b)

(c)   (d)
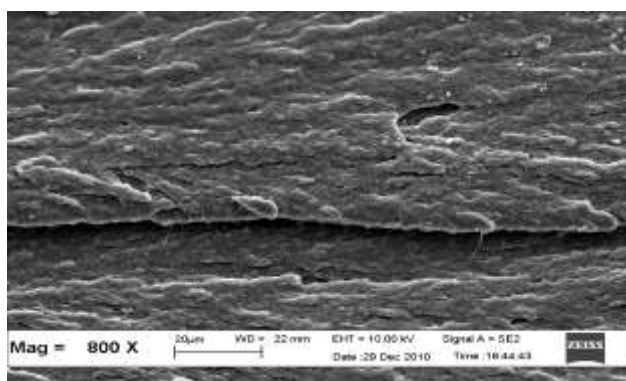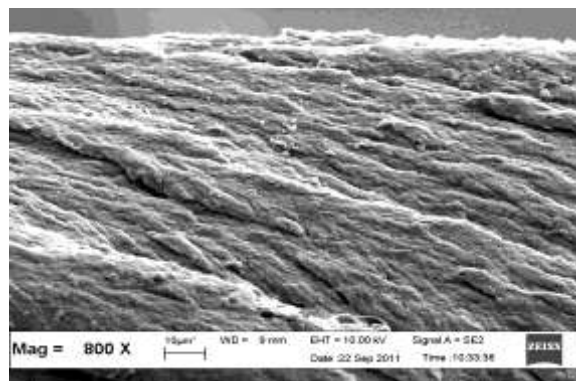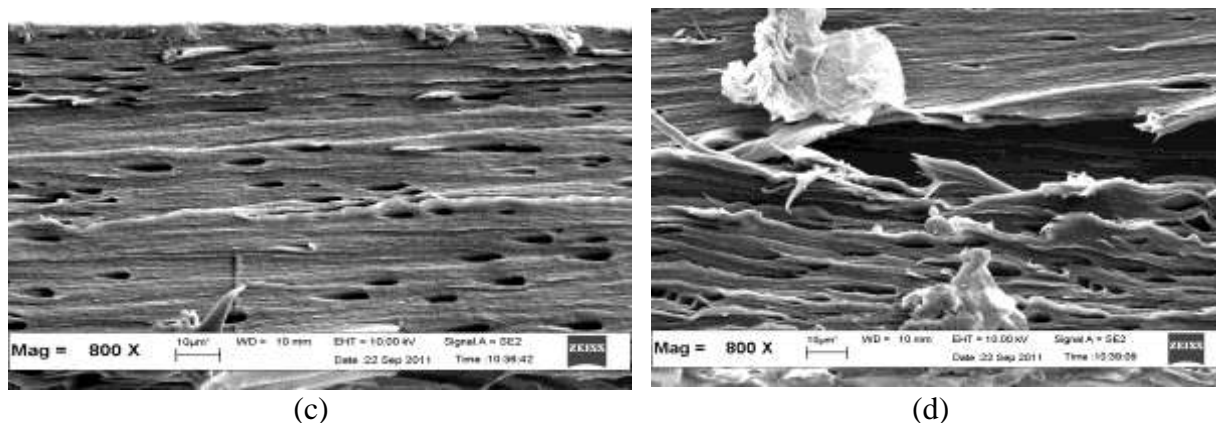
Fig 4. Fracture morphology of the blend films (a) PEG 0% (b) PEG 2% (c) PEG 6% (d) PEG 10%

3.3   Oxidative degradation properties

The degradation process started after dark red brown coloured solution was formed Fenton reagent was added into the sample. This was due to the formation of Fe^{3+} from the redox reaction between hydrogen peroxide and ferrous sulphate. Therefore, gaseous were formed within the solution and become more vigorous after the reaction last for 2 minute. This is due to the chain scission of the polymer backbone. More PVA, CS and PEG macromolecules were broken into smaller molecule. Degraded product such as carbon dioxide, oxygen and water were produced. Shan et al. reported that PVA macromolecules are broken into smaller molecules such as aldehydes, ketone, acid, polyalcohols or conjugate group compounds. After 2 minutes, orange solution was formed. This phenomenon is due to the reduction of Fe^{3+} to Fe^{2+} leading to the continuous generation of hydroxyl radicals. The degradation process occurs very fast as minimal degradation occurs after it reacted for first hour.

Almost no gaseous were emitted from the solution indicating the reaction stopped at fifth hour. Overall, the solution coloured change from dark brown solution to light green yellowish solution. At the fifth hour, the film is fragmented into small pieces due to the chain scission of carbon backbone of the polymer and reduction of molecular weight of PVA and CS. After degradation process of the films, the leftover in the solution was filtered to measure the final weight of the leftover.   Fig. 5 shows the percentage of degradation of the PVA/CS/PEG blend films. Higher content of PEG lead to the higher degradation percentage. PEG 10% films showed the highest degradation at 75%. This trend indicates that the network become more open after the addition of PEG as more hydroxyl radical were able to break the polymer chains in the blend films. On top of that, PEG also reduced the physical interaction between PVA and CS which contributes to the increasing degradation percentage. Partially substitutes of PVA/CS with PEG were the main reason for the increasing degradation percentage as the low molecular weight of PEG was venerable to hydroxyl radicals attack.
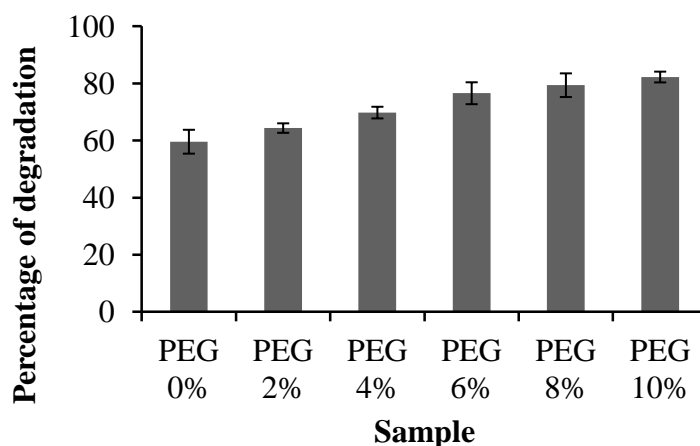
Fig 5. Percentage of degradation of PVA/CS/PEG blend films after 5 hours of Fenton reaction

3.   CONCLUSION

Partially substitute of PEG in PVA/CS blend films resulted in improved elongation at break but reduced tensile strength and Young's modulus. Fractured surface morphology showed phase separation as the PEG content increased. Thereby lower load was needed to break the sample. Degradation properties of the blend films showed that percentage degradation increased as the content of PEG increased. The reduction in tensile strength and increased degradation properties were attributed to the partially substitute and plasticizing effect of PEG.

4.   REFERENCES

1. Satyanarayana, K. G., Arizaga, G. G. C., & Wypych, F. (2009). Biodegradable composites based on lignocellulosic fibers—An overview. *Prog Polym Sci*, 34(9), 982-1021.

2. Chiellini, E., Cinelli, P., & Corti, A. (2007). Developments and Future Trends for Environmentally Degradable Plastics. *Plastics and Materials from Renewable Resources*, 63-118.

3. Utracki, L. A. (2002). Polymer blends handbook, Volume 1. Technology & Engineering, Springer, SpringerLINK ebook collection, 1442.

4. Zainuddin, Hill, D. J. T., & Le, T. T. (2001). An ESR study on γ-irradiated poly(vinyl alcohol). *Radiat Phys Chem*, 62, 283-291.

5. Moore G. F., & Saunders S. M. (1998). Advances in Biodegradable Polymers. iSmithers Rapra Publishing, C R C Press LLC.

6. Pillai, C. K. S., Paul, W., & Sharma, C. P. (2009). Chitin and chitosan polymers: Chemistry, solubility and fiber formation. *Prog Polym Sci*, 34(7), 641-678.

7. Sionkowska, A. (2006). The influence of UV light on collagen/poly(ethylene glycol) blends. *Polym Degrad Stabil*, 91(2), 305-312.

8. Zhang M., Li, X. H., Gong, Y.D., Zhao, N. M., & Zhang, X. F. (2002). Properties and biocompatibility of chitosan films modified by blending with PEG. *Biomaterials*, 23(13), 2641-2648.

9. Cao, N., Yang, X., & Fu, Y. (2009). Effects of various plasticizers on mechanical and water vapor barrier properties of gelatin films. *Food Hydrocolloids*, 23(3), 729-735.

10. Sun, G., Zhang, X.-Z., & Chu, C.-C. (2008). Effect of the molecular weight of polyethylene glycol (PEG) on the properties of chitosan-PEG-poly(N-isopropylacrylamide) hydrogels. *J Mater Sci-Mater M*, 19(8), 2865-2872.

11. Zeng, M., Fang, Zhengping, & Xu, Chengwei. (2004). Effect of compatibility on the structure of the microporous membrane prepared by selective dissolution of chitosan/synthetic polymer blend membrane. *J Membrane Sci*, 230(1-2), 175-181.

Effect of SEBS-g-MAH on the Mechanical, Thermal and Morphological Properties of Poly(lactic acid)/Halloysite Nanocomposites

W.L. Tham[1], W.S. Chow[1,*], Z.A. Mohd Ishak[1]

[1]School of Materials and Mineral Resources Engineering,
Engineering Campus, Universiti Sains Malaysia, 14300 Penang, Malaysia.

*Corresponding author: chowwenshyang@yahoo.com

Abstract: *Poly(lactic acid) (PLA)/halloysite nanocomposites were prepared using melt compounding followed by compression molding. Effects of maleic anhydride grafted styrene-ethylene/butylene-styrene (SEBS-g-MAH) on the mechanical, thermal and morphological properties for the PLA/halloysite nanocomposites were determined and discussed. The properties of PLA nanocomposites were characterized using tensile tests, scanning electron microscopy (SEM), and differential scanning calorimetry (DSC). It was found that the toughness of PLA/halloysite nanocomposites was increased by the addition of SEBS-g-MAH. The brittle-like morphology of PLA/halloysite transformed to ductile-like in the presence of SEBS-g-MAH. Crystallization temperature and degree of crystallization of PLA was affected by the halloysite and SEBS-g-MAH content.*

Keywords: poly(lactic acid), halloysite, SEBS-g-MAH, nanocomposites

1.   INTRODUCTION

Poly(lactic acid) (PLA) derived from renewable resources has become popular owing to their sustainability, biodegradability and superior transparency. PLA is potential to be used in food packaging, automotive parts, disposable tableware, sutures and drug delivery device [1-4]. Among the disadvantages, the low temperature resistance of PLA and its brittle behavior has to be mentioned. Efforts have been carried out to modify the properties of PLA using various fillers and fibers, e.g. starch [5], kenaf fibers [6], montmorillonite [7], bentonite and hectorite [8] and talc [9].

Halloysite is a type of mineral clay with the chemical composition $Al_2(OH)_4Si_2O_5(2H_2O)$. Common form of halloysite is fine, tubular particles with high aspect ratio. The external surface of halloysite is composed by Si-O-Si groups, while, its internal surface consisting of Al-OH groups [10]. Halloysite nanoclays can act as reinforcing agent for polymer due to its high aspect ratio [11-13]. It has been documented that the addition of halloysite improved the mechanical and thermal properties of linear low density polyethylene [14], poly(vinyl alcohol) [12], polypropylene [15], polyamide [16].

A straightforward strategy to improve the toughness of polymer/filler composites is by introducing a suitable rubber toughener or impact modifier. Maleic anhydride grafted styrene-ethylene/butylene-styrene copolymers (SEBS-g-MAH) has been used as polymeric compatibilizer, interfacial modifier and toughening agent [17]. In our previous works, it was found that the addition of SEBS-g-MAH improved the impact strength and thermal stability of PLA/organo-montmorillonite [18]. In this work, we attempted to produce PLA/halloysite clay nanocomposites in the absence and presence of SEBS-g-MAH. Mechanical, thermal and morphological properties of the PLA nanocomposites are investigated and discussed.

2.   EXPERIMENTAL
2.1   Materials

PLA (Ingeo[TM] 3051D) was purchased from NatureWorks LLC®, USA. The specific gravity and melt flow index of the PLA are 1.25 and 25 g/10 min (2.16 kg load, 210°C). Halloysite nanoclays (HNC) were supplied by Sigma-Aldrich (Malaysia). The dimension of HNC is approximately (30-70) nm x (1-3) µm (diameter x length) with specific gravity of 2.53. SEBS-g-MAH with a MAH grafting level of 1.4–2.0 wt% and styrene/rubber ratio of 30/70 (wt/wt) was purchased from Shanghai Jianqiao Plastic Co. Ltd., (Shanghai, China). The melt flow index and specific gravity of the SEBS-g-MAH are 1.0 g/10 min (2.16 kg load, 230°C) and 0.91, respectively.

2.2   Preparation of PLA nanocomposites

Prior compounding, all the materials used (i.e. PLA, SEBS-g-MAH, HNC) were dehumidified in an oven for 24 h at 60°C. The melt compounding was carried out by using an internal mixer (Haake PolyDrive R600, Karlsruhe, Germany) at 180°C for 10 min. The rotor speed was set at 50 rpm. The compression molding was performed at 185°C using a hot press machine (Go Tech, Taichung city, Taiwan). The preheating time, compression molding time and cooling time was 7 min., 3 min., and 3 min., respectively. Table 1 shows the materials designation and composition of PLA/HNC nanocomposites.

Table 1: Materials designation and composition of PLA nanocomposites

Materials designation	PLA (wt%)	Halloysite nanoclay (wt%)	SEBS-g-MAH (wt%)
PLA	100	-	-
PLA/2-HNC	98	2	-
PLA/2-HNC/5-SEBS-g-MAH	93	2	5
PLA/2-HNC/10-SEBS-g-MAH	88	2	10
PLA/2-HNC/15-SEBS-g-MAH	83	2	15
PLA/2-HNC/20-SEBS-g-MAH	78	2	20

2.3   Measurements
2.3.1   Tensile tests

Tensile tests were performed using an Instron machine model 3366 (Norwood, USA) at room temperature and 50% relative humidity according to ASTM D638. The gauge length and crosshead speed was set at 50 mm and 1 mm/min respectively. Tensile modulus, tensile strength and elongation at break were determined from the stress-strain curves.

2.3.2   Thermal tests

Differential scanning calorimetry was performed using DSC 1 (model Mettler Toledo STAR[e], Schwerzenbach, Switzerland). The specimens are approximately 10 mg sealed in aluminum pan were scanned from 30°C to 200°C at a heating rate of 10°C/min. Then, they were cooled from 200°C to 30°C at a cooling rate of 10°C/min. Second scanning was performed similar to the first scanning in order to erase the thermal history. The glass

transition temperature (T_g), melting temperature (T_m), and crystallization temperature (T_c) were determined. The degree of crystallinity (χ_c) of PLA nanocomposites was calculated according to Equation 1:

$$\chi_c = [\Delta H_m/(\Delta H_f \text{ x } w_{PLA})] \text{ x } 100\% \hspace{2cm} \text{Equation 1}$$

where χ_c is the degree of crystallinity; ΔH_m is the heat of fusion of the sample; ΔH_f corresponds to the heat of fusion for 100% crystalline material, and w_{PLA} is the net weight fraction of the PLA. The heat of fusion of 100% crystalline PLA (ΔH_f) is approximately 93.6 J/g.

2.3.2 Morphological analysis

The fractured surface of PLA/HNC nanocomposites was investigated by using a field emission scanning electron microscope (FESEM, Zeiss Supra 35VP, Gemini) at an accelerator voltage of 5 kV. The specimen surfaces were coated with gold alloy prior FESEM examination.

3.   RESULTS AND DISCUSSION

Table 2 shows the tensile properties of PLA and its nanocomposites. It can be seen that the tensile modulus of PLA increased significantly by the addition HNC. This is attributed to the reinforcing-ability of HNC. However, incorporation of SEBS-g-MAH reduced the tensile modulus and strength of PLA/HNC gradually. From Table 2, one may observe that the elongation at break of PLA/HNC nanocomposites increased markedly in the presence of elastomeric nature of SEBS-g-MAH, which implying an improvement in ductility for the PLA nanocomposites. Similar finding has been reported by Denac et al [19], that the ductility of polypropylene/talc composites increased profoundly by the addition of SEBS-g-MAH. The SEBS-g-MAH is capable to induce energy dissipation mechanism in nanocomposites during tensile deformation [20].

Table 2: Tensile properties of PLA/HNC nanocomposites.

Material designation	Tensile modulus (MPa)	Tensile strength (MPa)	Elongation at break (%)
PLA	1610	40.6	3.76
PLA/2-HNC	1852	43.8	4.28
PLA/2-HNC/5-SEBS-g-MAH	1648	35.3	4.25
PLA/2-HNC/10-SEBS-g-MAH	1560	29.1	4.68
PLA/2-HNC/15-SEBS-g-MAH	1367	24.3	5.30
PLA/2-HNC/20-SEBS-g-MAH	1162	20.5	5.62

Figure 1 shows the FESEM micrographs taken from the tensile fractured surface of PLA and its nanocomposites. Figure 1a & 1b displays the brittle fracture surface of PLA and PLA/2-HNC nanocomposites. Figure 1c & 1d, on the other hands, shows different morphology for the PLA/2-HNC/5-SEBS-g-MAH and PLA/2-HNC/15-SEBS-g-MAH. Numerous microvoids were observed in Figure 1c which can be due to the pulling-out of SEBS-g-MAH from PLA matrix – this can lead to the energy dissipation during tensile deformation process. The incorporation of 15% SEBS-g-MAH (Figure 1d) in PLA

nanocomposite showed more fibrillated morphology, which implying a higher elongation at break of the material.
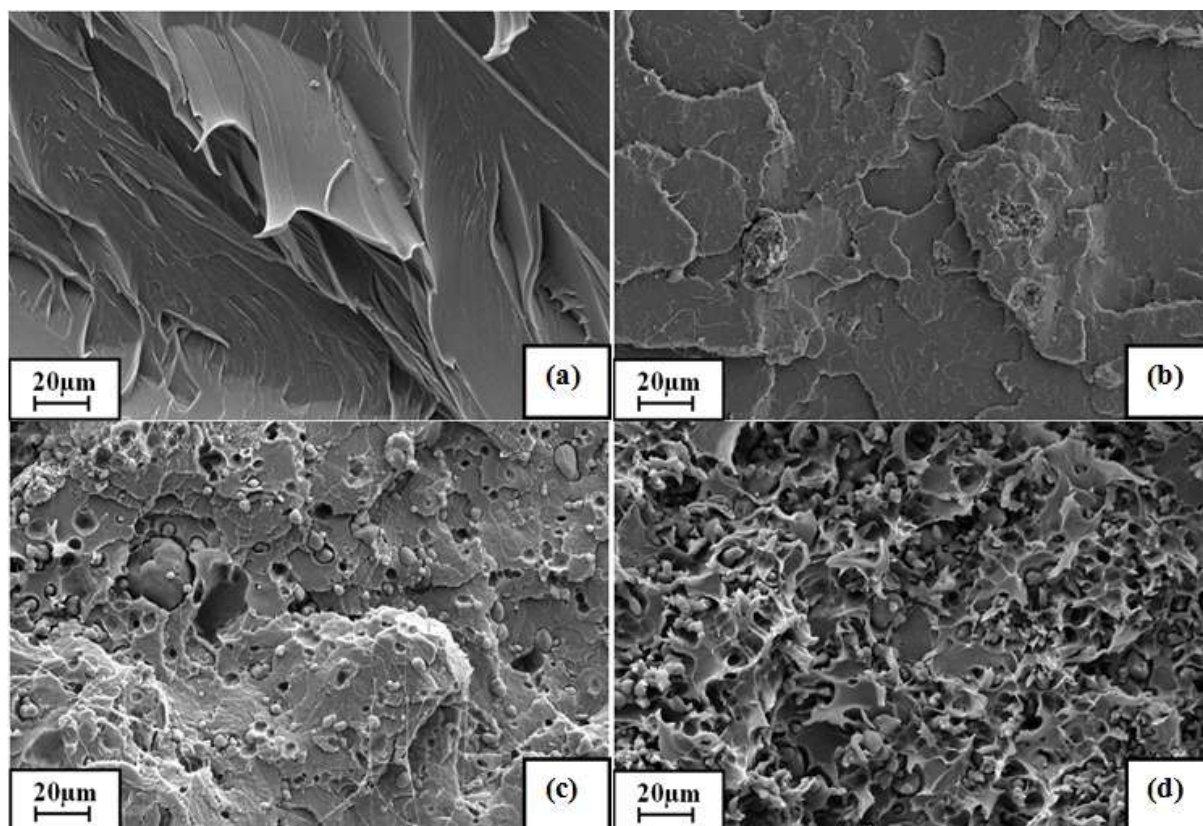
Figure 1: FESEM micrographs taken from the tensile fractured surface of (a) PLA, (b) PLA/2-HNC, (c) PLA/2-HNC/5-SEBS-g-MAH, and (d) PLA/2-HNC/15-SEBS-g-MAH.

Table 3 summarizes the glass transition temperature (T_g), crystallization temperature (T_c), melting temperature (T_m), and degree of crystallinity (χ_c) of PLA/HNC nanocomposites. It can be seen that the T_g and T_m of PLA is close to PLA/HNC nanocomposites (both with and without SEBS-g-MAH). Addition of HNC shifted the T_c of PLA to lower temperature, implying that the nucleating effects of the HNC nanoclay. On contrary, the T_c of PLA/HNC shifted to higher temperature in the presence of SEBS-g-MAH. This is may be attributed to the nucleation barrier for crystallization [21]. Bimodal melting peaks are observed in all PLA/HNC nanocomposites containing SEBS-g-MAH. Multiple melting behaviour of PLA is depends on crystallization conditions and T_c value. Double melting endotherms are commonly found in PLA which crystallized at T_c in the temperature range of 110-130°C. The multiple melting endotherms can be attributed to the melt-recrystallization mechanism. The present of T_{m1} is due to the lamellar rearrangement during crystallization of PLA. Also, it has been documented that, during the slow rate scanning, the imperfect crystals can re-melt at higher temperature to reorganize into perfect crystals [1, 22-24].

Table 3: Thermal characteristics of PLA/HNC nanocomposites recorded from DSC.

Material designation	T_g (^{o}C)	T_c (^{o}C)	T_m (^{o}C)		X_c (%)
			T_{m1}	T_{m2}	
PLA	58.6	109.1	-	168.7	30.0
PLA/2-HNC	59.5	105.9	-	168.5	31.2
PLA/2-HNC/5-SEBS-g-MAH	58.7	113.9	162.4	169.5	32.2
PLA/2-HNC/10-SEBS-g-MAH	58.9	113.2	162.2	169.6	25.8
PLA/2-HNC/15-SEBS-g-MAH	59.2	114.1	162.9	170.4	24.2
PLA/2-HNC/20-SEBS-g-MAH	58.5	114.1	162.6	169.6	13.7

4.   CONCLUSIONS

The elongation at break of PLA/HNC nanocomposites increased profoundly in the present of SEBS-g-MAH. The fracture morphology of PLA/HNC transformed from brittle-like to ductile-like by the addition of SEBS-g-MAH. Bimodal melting peaks are observed in all PLA/HNC nanocomposites containing SEBS-g-MAH. The crystallization temperature and degree of crystallinity of PLA was affected by the HNC and SEBS-g-MAH.

ACKNOWLEDGEMENTS

REFERENCES
1. Martin, O. and Averous, L. (2001). Poly (lactic acid): plasticization and properties of biodegradable multiphase systems. *Polym.,* 42, 6209-6219.
2. Krikorian, V. and Pochan, D. J. (2003). Poly (L-lactic acid)/layered silicate nanocomposite: fabrication, characterization, and properties. Chem. Mater.*,* 15, 4317-4324.
3. Arroyo, O., Huneault, M., Favis, B. and Bureau, M. (2010). Processing and properties of PLA/thermoplastic starch/montmorillonite nanocomposites. Polym. Compos., 31, 114-127.
4. Shin, B. Y., Jang, S. H. and Kim, B. S. (2011). Thermal, morphological, and mechanical properties of biobased and biodegradable blends of poly (lactic acid) and chemically modified thermoplastic starch. *Polym. Eng & Sci.,* 51, 826-834.
5. Orozco, V.H., Brostow, W., Chonkaew, W., and Lopez, B.L. (2009) Preparation and characterization of poly(lactic acid)-g-maleic anhydride + starch blends. *Macromolecules Sym.,* 277, 69-80.
6. Srebrenkoska, V., Gaceva, G.B., and Dimeski, D. (2009) Preparation and recycling of polymer eco-composites I. Comparison of the conventional molding techniques for preparations of polymer eco-composites. *Macedonian J. Chem.& Chem. Eng.*, 28(1), 99-109.
7. Pluta, M., Jeszka, J. and Boiteux, G. (2007). Polylactide/montmorillonite nanocomposites: Structure, dielectric, viscoelastic and thermal properties. *Euro. Polym. J.*, 43, 2819-2835.
8. Petersson, L., Oksman, K., and Mathew, A.P. (2006) Using maleic anhydride grafted poly(lactic acid) as a compatibilizer in poly(lactic acid)/layered-silicate nancomposites. *J. Appl. Polym. Sci.*, 102, 1852-1862.
9. Fowlks, A. C. and Narayan, R. (2010). The effect of maleated polylactic acid (PLA) as an interfacial modifier in PLA talc composites. *J. Appl. Polym. Sci.*, 118, 2810-2820.

10. Cavallaro, G., Lazzara, G. and Milioto, S. (2011). Dispersions of nanoclays of different shapes into aqueous and solid biopolymeric matrices. *Extended Physicochem. Study. Langmuir,* 27, 1158-1167.

11. Hedicke-Höchstötter, K., Lim, G. T. and Altstädt, V. (2009). Novel polyamide nanocomposites based on silicate nanotubes of the mineral halloysite. *Comp. Sci & Technol.,* 69, 330-334.

12. Zhou, W. Y., Guo, B., Liu, M., Liao, R., Rabie, A. B. M. and Jia, D. (2010). Poly (vinyl alcohol)/halloysite nanotubes bionanocomposite films: Properties and in vitro osteoblasts and fibroblasts response. *J. Biomed. Mater. Res. A,* 93, 1574-1587.

13. Carli, L. N., Crespo, J. S. and Mauler, R. S. (2011). PHBV nanocomposites based on organomodified montmorillonite and halloysite: the effect of clay type on the morphology and thermal and mechanical properties. *Comp. A: Appl. Sci. & Manufac.,* 42, 1601-1608.

14. Jia, Z., Luo, Y., Guo, B., Yang, B., Du, M. and Jia, D. (2009). Reinforcing and flame-retardant effects of halloysite nanotubes on LLDPE. *Polym.-Plast. Technol. & Eng,* 48, 607-613.

15. Liu, M., Jia, Z., Liu, F., Jia, D. and Guo, B. (2010). Tailoring the wettability of polypropylene surfaces with halloysite nanotubes. *J. Colloid & Interface Sci.,* 350, 186-193.

16. Lecouvet, B., Gutierrez, J., Sclavons, M. and Bailly, C. (2010). Structure-property relationships in polyamide 12/halloysite nanotube nanocomposites. *Polym. Degrad. & Stab*, 96, 226-235.

17. Liu, S. P., Ying, J. R., Zhou, X. P., Xie, X. L. and Mai, Y. W. (2009). Dispersion, thermal and mechanical properties of polypropylene/magnesium hydroxide nanocomposites compatibilized by SEBS-g-MA. *Compos. Sci. & Technol.,* 69, 1873-1879.

18. Leu, Y., Mohd Ishak, Z. and Chow, W. (2012). Mechanical, thermal, and morphological properties of injection molded poly (lactic acid)/ SEBS-g-MAH/organo-montmorillonite nanocomposites. *J. Appl. Polym. Sci.,* 124(2), 1200-1207.

19. Denac, M., Musil, V. and Smit, I. (2005). Polypropylene/talc/SEBS (SEBS-g-MA) composites. Part 2. Mechanical properties. *Comp. A: Appl. Sci. & Manufac.,* 36, 1282-1290.

20. Tjong, S. and Bao, S. (2007). Fracture toughness of high density polyethylene/SEBS-g-MA/montmorillonite nanocomposites. *Comp. Sci. & Technol.,* 67, 314-323.

21. Na, Y. H., He, Y., Shuai, X., Kikkawa, Y., Doi, Y. and Inoue, Y. (2002). Compatibilization effect of poly (ε-caprolactone)-b-poly (ethylene glycol) block copolymers and phase morphology analysis in immiscible poly (lactide)/poly (ε-caprolactone) blends. *Biomacromolecules,* 3, 1179-1186.

22. Li, B., Dong, F. X., Wang, X. L., Yang, J., Wang, D. Y. and Wang, Y. Z. (2009). Organically modified rectorite toughened poly (lactic acid): Nanostructures, crystallization and mechanical properties. *Euro. Polym. J.,* 45, 2996-3003.

23. Wang, Y. L., Hu, X., Li, H., Ji, X. and Li, Z. M. (2010). Polyamide-6/poly(lactic acid) blends compatibilized by the maleic anhydride grafted polyethylene-octene elastomer. *Polym.-Plast. Technol. & Eng.,* 49, 1241-1246.

24. Nijenhuis, A., Colstee, E., Grijpma, D. and Pennings, A. (1996). High molecular weight poly (L-lactide) and poly (ethylene oxide) blends: Thermal characterization and physical properties. *Polym.*, 37, 5849-5857.

Kenaf Fibers Reinforced Recycled Polypropylene/Recycled Polyamide 6 Composites

Nur Liyana Suradi*, Agus Arsad, and Abdul Razak Rahmat

Polymer Engineering Department, Faculty of Chemical Engineering, Universiti Teknologi Malaysia 81310 Skudai, Johor, Malaysia

*Corresponding author: nurliyanasuradi@gmail.com

Abstract: *The environmental non-degradation of plastics materials has prompted the research on recycling of these materials. Therefore, the objective of this study is to develop recycled composites based on recycled polypropylene (rPP)/recycled polyamide 6 (rPA6) reinforced with kenaf fibers, potentially to be used for electronic and automotive applications. Polypropylene (PP) reinforced by kenaf were less sensitive to reprocessing cycles compared to PP reinforced of other natural fibers. Chemical modification is required to improve its compatibility with thermoplastics such as PP. The investigations were undertaken by collecting of rPP from the nearest landfill and prepared rPA6, chemical modifications of kenaf, composites preparation using twin screw extruder and samples prepared for testing using injection molding machine. Composition selected rPP/rPA6, 70/30 with different the compositions by weight of kenaf. The physical and mechanical properties were determined by tensile and flexural tests. These composites processing behavior and morphological study were determined by Melt Flow Index (MFI) and Scanning Electron Microscopy (SEM). From the study, the mechanical properties of the composites were improved as the compositions of kenaf were increased. For processing behavior, when the kenaf composition was increased, the MFI decreased, and the processing became difficult. SEM micrograph shows better dispersion of kenaf in polymer matrix when kenaf compositions were increased. The suitable parameter was investigated to be adapted with the desired applications.*

Keywords: Recycled blending, chemical modification, kenaf fibers, recycled polypropylene, recycled polyamide 6

1.   INTRODUCTION

Recently, the use of natural fibers reinforced polymeric materials has become more favorable. The environmental significance and effectiveness as the reinforcement agent induce the use of natural fibers for significant improvement of the composites properties. The research on recycling of plastic materials is carried out because of high cost of virgin materials, high volume percentage in domestic wastes of plastics materials, and environmentally non-degradable of plastic materials itself. Hence, the tendency of using the recycled polymeric materials to replace the virgin polymeric materials has gained interest [2,4,9]. It is because, the use of recycled polymeric materials is more economically and environmentally friendly, and reduces the amount of solid waste in the landfills. Since polyolefin's polymers such as polypropylene (PP) are being used widely in electronic and automotive applications, hence this study is focusing on producing composites from plastic waste based on PP. Blending of polyolefin with engineering plastics has been one of the focuses of polymer engineering for many years. Blending PP and PA6, provided materials with balanced properties including low moisture absorption, reasonable mechanical and thermal properties, and improved processability and acceptable price [14].

Proceeding of MAMIP2012
Asian International Conference on Materials, Minerals and Polymer
23rd – 24th March 2012, Vistana Hotel, Penang

A few natural fibers are suitable for automotive applications and one of most commonly used is kenaf due to good properties and higher strength. Advantages of natural fibers over man-made fibers are low density, low cost, recyclability and biodegradability [7]. However, low interfacial properties between fibers and polymer matrix often reduce their potential as reinforcing agent, then chemical modifications are considered to optimize the interface of fibers [7]. In this study, kenaf surface was modified with chemical modification to increase effective interaction and adhesion between kenaf and polymer matrix. Chemical modification would activate the hydroxyl group (OH) in fibers and enhance effective blending between fibers and polymer matrix. In general, chemical coupling agents function in two ways which are first react with the hydroxyl group in cellulose and second react with the functional group of polymer matrix [7]. From the previous researcher [10,11,15], alkaline treatment was preferred for chemical modifications. The alkaline treatment is very effective to increase surface roughness and possible reaction sites for blending [7].

The study of kenaf reinforced with both recycled materials, rPP/rPA6 compatibiliser by the Maleic Anhydride-graph-Polypropylene (MAPP) was carried out to investigate the effect of kenaf fibers compositions in mechanical, processing properties, and morphology study.

2.   EXPERIMENTAL
2.1   Materials

In this study, the rPP collected from industrial waste with MFI of 23.7 g/10 min and rPA6 was prepared by extruding virgin polymer once to produce PA6 with recycled properties, the MFI of the rPA6 was 42.9 g/10 min. Both MFI testing were carried out at 230°C with standard weight, 2.16 kg. The kenaf fibers from the bass part were planted in Kelantan with bulk density of 0.19806 g per cm^3 after pre-treatment with alkaline treatment. The MAPP supplied from China with MFI 120 g/10 min, sodium hydroxide (NaOH) for alkaline treatment supplied by Quality Reagent Chemical (QReC) with molecular weight of 40.0 gram/mol.

2.2   Chemical Modification of Kenaf Natural Fibers

The raw materials of bass part of kenaf were soaked in the 5% concentration of NaOH AT room temperature (RT) in range of 27-30 °C [10,11]. The kenaf was soaked for 4 hours [11], before washing with distilled water 3 times. Then, kenaf was washed once with dilute acetic acid, in order to neutralize and remove the remaining NaOH at the surface of kenaf before washing again with distilled water. The last step of washing with distilled water was to remove excess acetic acid at the surface area of kenaf fibers surface area. Washed kenaf was then dried in the open air for 24 hours before being dried again in the oven for another 24-48 hours at 110°C. Treated kenaf was ground to powder. Ground kenaf was sieved for 10 minutes using sieve with 75 μm mesh size.

2.3   Blending of Kenaf Natural Fibers Reinforced rPP/rPA6

Blending of treated kenaf and polymeric materials were conducted with four different formulations 0 – 30 % compositions by weight of kenaf fibers (wt. %) in the blends, labeling with A, B, C, and D respectively. The rPP/rPA6 blend consisted of 70 wt. % of rPP and 30

wt. % of PA6, respectively. When MAPP was introduced at 3 wt. %, the rPP compositions were stated at 67 wt. % in order to maintain the 30 wt. % of rPA6 in the blends as mentioned by Rosch and Mulhaupt[12].

2.4 Preparation and Characterization for Mechanical and Thermal Test
2.4.1 Mechanical Testing

The mechanical tests included tensile test and 3 point bending flexural. The samples for the tests were prepared using JSW N100 BII Injection Mounding machine. Each formulation was prepared with 10 samples, which were samples for 3 point bending flexural test and tensile test. The thickness of each sample was measured and used during 3 point bending test (flexural test). Tensile test was conducted as stated in ASTM D638, with speed 50mm/min and flexural test using standard ASTM D790, with speed 10mm/min. Both tests were performed at RT. Every formulation test was repeated five times and the average then was determined.

2.4.2 MFI Test

This test was conducted to study the melt flow of the composites, which provided necessary properties for processing process. MFI test were conducted at 230 °C, with plunger weight 2.16 kilogram (kg) for all formulations. The method was described in similar standards ASTM D1238. Even though there is no specific method for recycled materials, these conditions were chosen based on the nearest properties with the recycled materials.

2.4.3 Morphology Test

The morphology of composites was studied using scanning electron microscopy (SEM). The samples were frozen in liquid nitrogen for 30 minutes and then impact-fractured for SEM analysis. The fractured surface was gold-sputtered before SEM observation. The acceleration voltage was 20 kV [14]. These tests were conducted with a magnification of 100 times in average.

3. RESULTS AND DISCUSSION

3.1 Tensile Test

Pretreatment of fibers in kenaf-reinforced composites usually shows improvement in tensile properties compared with untreated fibers by increased fiber-matrix adhesion and dispersion of the fiber in the polymer matrix [5]. Hence, all used kenaf was treated by alkaline treatment in order to reduce the hydrophilic properties of kenaf natural fibers, provided better adhesion with polymer matrix. The efficiency of MAPP as dispersing agent depends on the dispersion of rPA6 in rPP matrix, the formation of elastomer/rPA6 copolymer [12].
Figure 1 shows the tensile strength versus kenaf composition by wt. % in the rPP/rPA6/MA-g-PP (67/30/3) composites. The tensile strength of composites without kenaf (0 wt. %) had significant tensile strength with 31 MPa, since this composite content of rPP is the dominant material. The compatibilizer (MA-g-PP) was well miscible with PP matrix [8], which promotes better adhesion between rPP and rPA6 polymer matrix. Other than that, when 10 wt.% of kenaf fibers added to the composites, the tensile strength drastically drops to 27 MPa. This may be caused by poor dispersion of kenaf fibers in the recycled polymer matrix, and also

attributed by the presence of impurities together with recycled polymer. The effects of poor dispersion of kenaf in polymer matrix towards tensile strength have been studied by other researchers [3,9].

Otherwise, increasing the kenaf to 20% slightly increases the tensile strength (29 MPa) compared with 10% kenaf in the composites. However, this value is still lower than the composites without kenaf. The reason of tensile strength reduction, may be attributed to the properties of PA6 itself which easily absorb water. Other than that, the properties of bass kenaf that easily absorb moisture from the environment also influence the composites tensile strength. Then, high content of the moisture in the composites caused the composite to slip when mechanical stress is applied to it, therefore reducing the tensile strength. Previous researchers stated that rPA6 exhibited solid-like property with long relaxation time as compared to the rPP, reinforcing the moisture influence [2].

Finally, with 30% of kenaf, a significant increase in tensile strength to 32 MPa, which is better tensile strength compared with composites without kenaf (0%). The better tensile strength achieved with better dispersion and adhesion of kenaf reinforced polymer matrix [1]. The void areas in the blends are fully occupied by the kenaf. Hence, closer arrangement of the molecules causes stress to be easily absorbed by composites, producing better tensile strength. When the kenaf compositions in the composite increased, the better tensile strength with good mechanical properties achieved [1].

Fig. 2 shows the Young's modulus of composites versus kenaf compositions by weight (%). From the figure, the Young's modulus of composites increases proportionally with the increasing kenaf percentage in the composites. From Fig. 2, without kenaf (0%), 1.8 GPa Young's modulus was recorded, where the young's modulus increased to 13 percent to 2.1 GPa when 10% of kenaf was added. The reason of the increasing Young's modulus was the presence of fibers that occupy the void area in the blending polymers, increased stiffness hence increasing the Young's modulus of composites. Further addition of kenaf with 20% and 30%, the young's modulus increased directly proportionally with the increased kenaf. This is similar with other researchers [6], the composites increased tensile strength and young modulus by adding kenaf. The hypotheses that can be made were higher composition of kenaf, higher Young's modulus of composites, producing good mechanical properties.

3.2   Flexural Test

From the flexural test, flexural strength and flexural modulus were calculated. Fig. 3 shows the flexural strength versus kenaf compositions by weight (%). Referring to Fig. 3, without kenaf (0%), the flexural strength recorded was 43 MPa, which then reduced to 37 MPa with 10% of kenaf. The flexural strength dropped because of poor adhesion between kenaf and polymer matrix [3]. Other than that, when kenaf composition was increased to 20%, the flexural strength drastically increased to 45 MPa which was slightly higher than the flexural strength of composites without kenaf. The reason of this increase was better adhesion of kenaf and polymer matrix, which reduced the unoccupied area in the composites, then later on increased the flexural strength towards load/stress applied to it. Further increasing of kenaf composition to 30% with slightly reduce the flexural strength of composites but still higher than the composites without kenaf. The best flexural strength was with 20% of kenaf.

Similar to the mechanical properties in Young's modulus, the flexural modulus increased proportionally with the kenaf compositions in the composites. Fig. 4 shows the flexural modulus versus kenaf compositions in the composites. The flexural modulus recorded without kenaf (0%) was 1.6 GPa, which was slightly lower than the composites with kenaf with any compositions. When, 10% of kenaf was added to the composites, significant increase of flexural modulus was recorded which is 23 percent higher than the composites without kenaf with flexural modulus of 2.0 GPa. Then, further increase of kenaf with 20% and 30% also increased the flexural modulus. The flexural moduli achieved were 2.6 GPa and 3.1 GPa respectively. The reasons of proportional increase of the flexural modulus were void areas in the blends are occupied by the kenaf, causes composites become more stiff than the composites without kenaf. Similar observation was also stated by others, higher improvement of mechanical properties attributed to the efficiency transfer stress from polymer matrix to the kenaf which increased the composites stiffness [1].
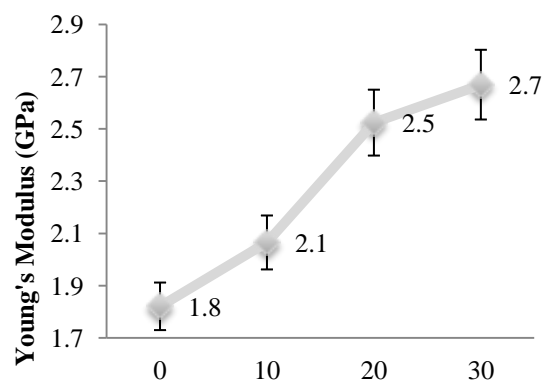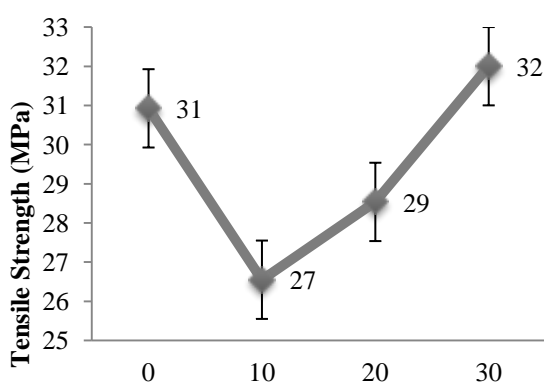
Fig. 5 shows the MFI versus kenaf compositions by weight (%). From the figure, the MFI of the composites were inversely proportional to the increases of kenaf compositions by weight (%). The composite without kenaf (0%) gives higher MFI, which was 12.0 g/10 min. The high values of MFI make the further processing process easy since these composites easily flow at temperature of 230 °C. However, this value is still lower than the rPP and rPA6 itself alone with MFI 23.7 g/10 min and 42.9 g/10 min respectively. The reason of the different MFI between rPP, rPA6 and blends of rPP/rPA6/MA-g-PP is because the void areas in the rPA6 matrix were occupied by the rPP polymers. The presence of MA-g-PP compatibilizer ensures the effective blends occurred, polymer matrix bind tightly between each other, which reduces the flow of the composites. Other observations [4], include the presence of MA-g-PP compatibilizer, the copolymer tends to interfere with PA6 polymer, binds both PP and PA6 effectively.
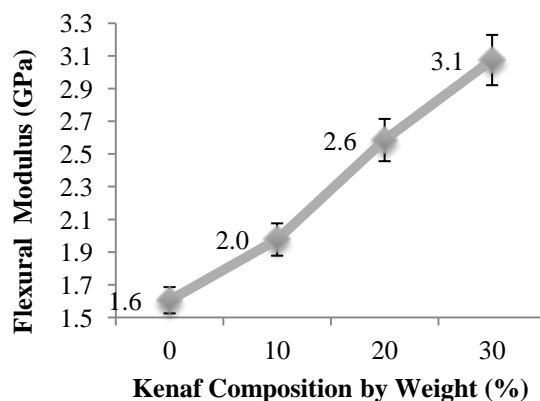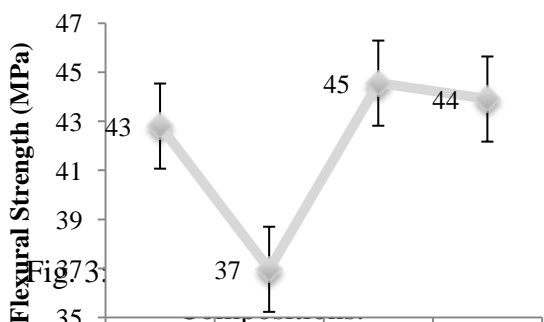
Fig. 4: Flexural Modulus versus Kenaf Compositions

When 10% of kenaf is added to the composites, there is drastic MFI drop to become 7.8 g/10 min. Further increasing of kenaf compositions to 20% and 30% slightly decrease MFI of composites, to become 7.4 g/10 min and 7.3 g/10 min respectively. The reasons were when kenaf is added, the composites become packed, void areas occupied by the kenaf, then increasing temperature to break the bond between polymer matrix and kenaf, reducing MFI values, hence composites difficult to process. Similar observations were also recorded [4], where high crystallinity reduced the flows of composites.
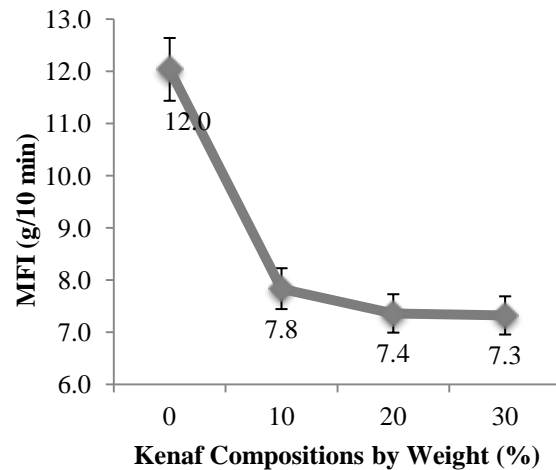
Fig. 5: MFI versus Kenaf Compositions.

3.4 Morphological Analysis

Fig. 6 shows the rPP/rPA6/MA-g-PP SEM micrographs of facture surface with different kenaf compositions by weight (%). From Fig. 6) a), micrographs show without kenaf (0%) fine dispersion facilitates good adhesion between rPP/rPA6 by the presence of MA-g-PP compatibilizer in the composites. Huda *et al.* reported thatthe coupling agent/compatibilizer causes a significant better wetting of the kenaf fibers through the polymer matrix [3]. Good dispersion avoids unoccupied area of the blending, hence gives desired mechanical strength when stress or strain is applied to it, better mechanical strength compared to composites without compatibilizer. This is proven by the mechanical test applied to the composites, from Fig. 1 to Fig. 4, mechanical properties show that without kenaf, composites have significant strength.

Then, when10% kenaf was added, Fig. 6) b) shows that there are some void areas in the composites fracture, meaning that with 10% of kenaf, it not enough to occupy all empty area of the polymer blending. Hence, there are still some empty spaces in the composites, reducing the efficiency of transferring stress to the composites, lowering mechanical properties. However, the occupied area of polymer matrix shows good adhesion and dispersions of kenaf, shows that the use of kenaf is compatible with these polymers. Other researchers stated that good adhesion between polymer matrix and kenaf is shown with alkali treated kenaf [6].

Further increase of kenaf to 20% by weight is shown in Fig. 6) c). The figure shows that the unoccupied area is reduced. The kenaf occupied more empty space in the polymer matrix, Better mechanical strength was recorded, with better dispersion of the kenaf. Less moisture took place in the polymer matrix and increased the stiffness of the composites. According to Figs. 2 and 4, there is increasing of mechanical properties compared with 10%

kenaf. It shows that better dispersion in SEM micrograph proportional with the mechanical properties of the composites.

Finally, the micrograph with 30% of kenaf added is shown in Fig. 6) d). In the figure, the best dispersion in the polymer matrix for kenaf is shown. Less unoccupied area can be seen which means that most of the void areas already are occupied by the kenaf. The best kenaf dispersion is shown with 30% of kenaf. From Fig. 6, increasing the kenaf composition to the composites result in better dispersion and adhesion of composite.
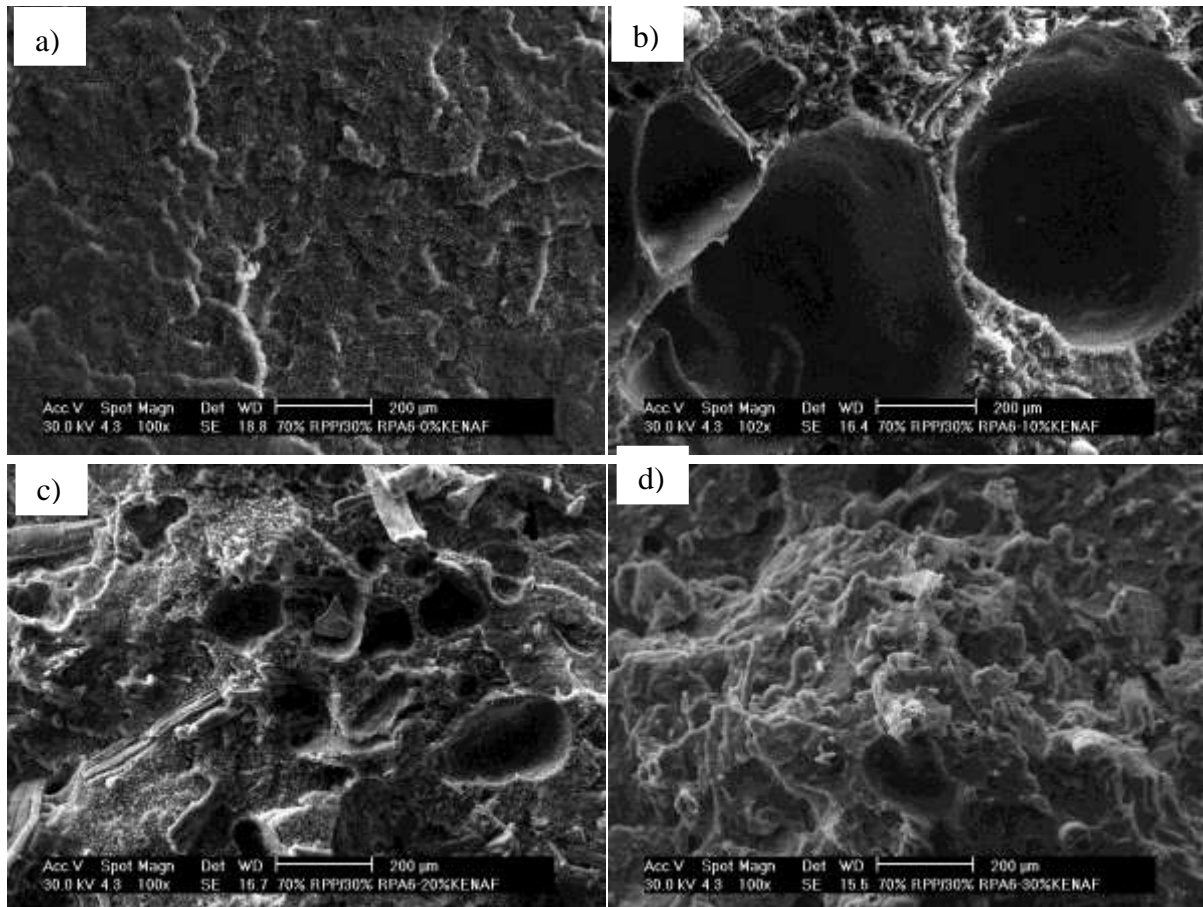
Fig. 6: The rPP/rPA6/MA-g-PP morphology with kenaf fiber by weight percents, a) 0wt.%; b) 10 wt.%; c) 20wt.%; d) 30 wt.%.

4.   CONCLUSION

The best Young's modulus and flexural modulus are with 30% kenaf added to blends of rPP/rPA6/MA-g-PP (67/30/3), and the best tensile strength and flexural strength recorded with 20% of kenaf. When the kenaf compositions in the composites are increased, MFI decreases and the composites become difficult to process. Other than that, the best dispersion and adhesion of kenaf in the polymer matrix is shown with 30% of kenaf. The best composition for the blend rPP/rPA6/MA-g-PP (67/30/3) is with 30% kenaf.

5.   ACKNOWLEDGEMENT

6.   REFERENCES

1. Gao H., Xie Y., Qu R., and Wang Q. (2011). Grafting Effects of polypropylene/polyethylene blends with maleic anhydride on the properties of the resulting wood-plastics composites. *Composites: Part A*. 43, 150-157.

2. Hong S.M., Hwang S.S., Jeon B.H., Choi J.S., Kim H.B., Lim S.T., and Choi H.J. (2005). Polypropylene/polyamide 6 blends based on commingled plastic wastes. *Journal of Materials Science*. 40, 3857-3859.

3. Huda M.S., Drzal L.T, Mohanty A.K., and Misra M. (2007). Effect of fiber surface-treatments on the properties of laminated biocomposite from poly(lactic acid) (PLA) and kenaf fibers. *Composites Sciences and Technology*. 68, 424-432.

4. Jaziri M., Barhoumi N., Massardier V., and Melis F. (2007). Blending PP with PA6 Industrial Wastes: Effect of the Composition and the Compatibilization. *Journal of Applied Polymer Science*. 107, 3451-3458.

5. Kalia S., Kaith B.S, and Kaur I. (2009). Pretreatment of Natural Fibers and their Application as Reinforcing Materials in Polymer Composites-A Review. *Polymer Engineering and Science*. 49 (7), 1253-1268.

6. Lee C.K., Cho M.S., Kim I.H., and Lee Y. (2010). *Macromolecular Research*. 8(6), 566-570.

7. Li X., Tabil L.G., Panigrahi S. (2007). Chemical Treatment of Natural Fiber for Use in Natural Fiber-Reinforced Composites: A Review. *Journal of Polymer Enviroment*. 15, 25-33.

8. Li Y., Wang D., Zhang J.M., Xie X.M. (2010). Influences of component ratio of minor phases and charge sequence on the morphology and mechanical properties of PP/PS/PA6 ternary blends. *Polymer Bulletin*. 66, 841-852.

9. Lin Z., Chen C., Guan Z., Tan S., and Zhang X. (2011). A Compatibilized Composites of Recycled Polypropylene Filled with Cellulosic Fiber from Recycled Corrugated Paper Board: Mechanical Properties, Morphology, and Thermal Behavior.

10. Mishra S., Misra M., Tripathy S.S., Nayak S.K., and Mohanty A.K. (2001). Graft Copolymerization of Acrylonitrile on Chemically Modified Sisal Fibers. *Macromolecule Material Engineering*. 286 (2), 107-113.

12. Ray D., Sarkar B.K., Rana A.K., and Bose N.R. (2001). Effect of alkali treated jute fibers on composite properties. *Bulletin of Material Science*. 24 (2), 129-135.

13. Rosch J. and Mulhaupt R. (1994). The role of core/shell-micro particle dispersions in polypropylene.polyamide-6 blends. *Polymer Bulletin*. 32, 697-704.

14. Wang Q., Liu C., and Chen Z. (2001). Pan-Milling Preparation of Polypropylene-graft-Maleic Anhydride and Its Compatibilizing Effect on Polyamide 6/Polypropylene Blend. *Polymer Journal*. 33(7), 522-527.

15. Yang W., Tang X.G., Xie B.H., Zhu Y.P., Yang M.B., and Hou M. (2008). Heterogeneous Dispersion of the Compatibilizer in the Injection Molding of

Polyamide 6/Polypropylene Blends. *Journal of Applied Polymer Science*. 113, 299-305.

16. Yussof A. A., Massoumi L., Hassan A. (2010). Comparison of Polylactic Acid/Kenaf and Polylactic Acid/Rice Husk of Composites: The Influence of Natural Fibers on Mechanical, Thermal and Biodegrability Properties. *Journal of Polymer Enviroment*. 18, 422-429.

Studies of Cellulose Solution produce from Palm Oil Empty Fruit Bunch Pulp and Cellulose from Filter Paper

Nur Fazlinda Razali[*], Sarani Zakaria., Hatika Kaco, and Chin Hua Chia

School of Applied Physics, Faculty of Science and Technology,
Universiti Kebangsaan Malaysia, 43600 UKM Bangi,
Selangor, Malaysia.

*Corresponding author: lyn_faz2@yahoo.com

Abstract: *Cellulose solution system was used to dissolve palm oil empty fruit bunch (EFB) pulp and filter paper (FP) in mixture of NaOH/urea/thiourea. The produced dissolved cellulose solution of the pure cellulose and the EFB pulp were analyzed using X-ray Diffraction (XRD) to determine the crystallinity index and Fourier transform infrared-attenuated total reflectance (FTIR-ATR) to analyze the functional group. Concentration of NaOH, urea and thiourea solvent ratio was (8/8/6.5) for the dissolution of EFB pulp and FP. The results showed that the percentage of cellulose dissolution of FP is higher than the EFB pulp, whereas the crystallinity of dissolved cellulose of FP was lower than the EFB pulp.*

Keywords: Cellulose, cellulose solution, EFB

1. INTRODUCTION

Cellulose is the most abundant polysaccharide material available worldwide and it has been considered as an unlimited renewable organic material. It is well known of its environmental friendly and biocompatible with approximately production rate of 10^{11} - 10^{12} ton/year. In cellulose molecular structure, β-(1→4)-D-glucanvallows chain packing by strong inter and intra-molecular hydrogen-bonding [1]. Due to stiff molecules and close chain packing via the numerous inter- and intra molecular hydrogen bonds, it is extremely hard to dissolve cellulose using water [2]. However, it was found that cellulose can be dissolved using specific solvents, i.e., N_2O_4/N,N-dimethylformamide (DMF), SO_2/amine, Me_2SO/ paraformaldehyde (PF) and LiCl-DMAc [3].

To date, there are several solvent systems, including N-methylmorphorine-N-oxide (NMMO), aqueous solution of 8-10 wt% NaOH [4], NaOH/urea [5] and NaOH/thiourea [6], which have used to dissolve cellulose. Cellulose in alkaline solution such as NaOH possesses a homogeneous solid structure in the swollen state and created ion-pair interaction favouring, compared with the original native and regenerated cellulose [4]. Other research shows rapid dissolution behaviour in aqueous NaOH/thiourea/urea at 8/6.5/8 to dissolve the cellulose fiber

at low temperature. The effects of NaOH concentration on cellulose dissolution shows solubility of 7% cellulose improved significantly with increasing NaOH concentrations and peaked at 8% NaOH with 91% solubility [7].

Cellulose II can be prepared by two distinct routes: mercerization (alkaline treatment) and regeneration (solubilization and subsequent recrystallization) [8]. Ionic liquids have been focused as solvents for cellulose processing and derivatization to produce regenerated cellulose. The most common ionic liquid is 1-butyl-3-methylimidazolium chloride ([C4mim]Cl). However, study showed this solvent required long period of time (10 h) to completely dissolve cellulose fibres [9]. Recently, addition to liquid ionic solvents, research efforts have been made on the elaboration of cellulose film forming solution using cheap and non-polluting direct solvent such as alkaline solvent. [5].

Malaysia is the second world largest palm oil producer after Indonesia in the year 2009. EFB fibres are waste by-products that are being investigated for further uses. Up to that time, EFB fibres disposed by burning due to low commercialization value. Oil palm fibre is rich in cellulose and lignin. Extraction of EFB fibres can produce raw cellulose, hemicelluloses and lignin with the compositional percentage of cellulose (44.2%), hemicelluloses (33.5%), and lignin (20.4%) [10].

EFB fibres consist of high lignin content, which is unattractive to further process. Bleaching is a process required to remove the lignin in EFB fibres to produce pure cellulose. Lignin will turn into darker colour when exposed to UV light due to activation of chromophorm. There are few stages of bleaching, occupied some alkaline and acid treatment.

Lignin content in EFB pulp can be determined using a standard Tappi method (TAPPI-222) for unbleached and bleached pulps. This method describes a procedure which can be applied to determine acid-insoluble lignin in wood and all grades of unbleached pulps.

In this present work, we attempt to prepare the cellulose solution and study the solubility and crystallinity between the two cellulose fibres obtained from EFB pulp and FP. Both cellulose were dissolved in an alkaline solution system (NaOH/thiourea/urea) to obtain regenerated cellulose. The cellulose solutions functional group were analyzed using Fourier-transformed infrared spectroscopy (FTIR) and the crystallinity of cellulose was analyzed by X-ray diffraction (XRD).

2. MATERIALS AND METHOD

2.1 Materials

(EFB pulp) was obtained from a pulping mill after the soda pulping. The pure cellulose fibres were obtained from quantitative filter papers ashless grades (Whattman). EFB pulp through some process to become cellulose and dried at 105 °C for 24 h and stored in a

desiccators before used. NaOH, thiourea, urea (99> purity were analytical grade purchased from Sigma Aldrich.

2.2   Preparation of EFB fibre

EFB pulp immerse in excessive water and disintegrate before produce EFB fibre. For bleaching process, there were four stages to bleach the EFB fibre in this work. EFB pulp were bleached with chlorine dioxide (D stage), chlorine dioxide produced through reaction between sodium chloride and water where as the sodium chloride molarity 1M at 60 °C for 2 h using waterbath shaker. Then, the process was followed by E stage with 4% NaOH solution at 60 °C for 30 min. EFB pulp was washed with excess distilled water to remove all the impurities and unreacted NaOH/thiourea/urea. Pretreatment continued with second stage with 6% NaOH (E stage) at 70 °C for 30 min. Last stage for bleaching treatment is using chlorine dioxide at 70 °C for 1.5 h. Removed lignin was washed with excess distilled water and dried at 105 °C for 24 h.

2.2   Preparation of cellulose solution

A 100 ml solution of NaOH (8 wt%), urea (8 wt%) and thiourea (6.5 wt%) was prepared in a beaker. The solvent prepare were pre-cooled to -10 $^{\circ}$C for 24 h. About 1 g of cellulose sample was added into the solvent and stirred to obtain transparent cellulose solution. The temperature of the solvent was maintained using a salt ice bath. After vigorous stirring the temperature of solution was increased to approximately 0 $^{\circ}$C. Previous study concluded that low temperature break the overcoat layer because of the rapid thermal escape motion of small molecules, which exposes hydroxyl groups of cellulose to each other.

The cellulose solution was then centrifuged at 10000 rpm for 10 min to separate the undissolved fraction. The undisolved fraction was washed with exceed distilled water to remove excess NaOH/urea/thiourea to determine the percentage of dissolution. The dissolved fraction (cellulose solution) was then dried in an oven at 105 $^{\circ}$C and kept for further characterizations.

2.3   Characterization

The cellulose powder was analyzed using a X-ray diffractometer (Bruker, D8-Advance) in the chamber with the temperature at which it can perform X-ray diffraction techniques on sample at high temperature up to 2300 $^{\circ}$C and low until 263 $^{\circ}$C. The radiation used in the XRD pattern was Cu Kα (1.5406 x 10-10 m) at 40 kV and 30 mA was recorded in the range of 9–77° at a scanning speed of 2°/min.

Fourier transform infra red-attenuated total reflectance (ATR) model Perkin Elmer Spectrum 400 GX to characterize the functional groups in the determined sample. The sample was taken at random from cellulose solution in deionized water. The residual water on the surface of samples was removed using FP. In direct contact with Ge crystal, data of the

sample were collected over 32 scans at 4 cm^{-1} resolution using a variable-angle ATR at a nominal incident angle of 45°.

3. RESULT AND DISCUSSION

3.1 Comparison of Solubility EFB and FP

The solubility of EFB and FP in NaOH/urea/thiourea systems is shown in Table 1. The results show that solubility of NaOH/urea/thiourea system for FP is higher than the EFB, this is because the FP is pure cellulose meanwhile EFB might still consists of small amount of lignin of lignin 0.3% after the bleaching process. For each determination, calculate the lignin content in the test specimen as follows:

$$Lignin,\% = A\frac{100}{W} \tag{1}$$

where A is the weight of lignin, g and W is the weight of the specimen after oven dry, g. Meanwhile, the solubility was calculated from the following formula:

$$S_a = \frac{1-F_1}{1} \times 100\% \tag{2}$$

Where F_1 denotes the weight (g) of the insoluble cellulose fibre [11]. All the experiments were done in duplicate.

Table 1: The solubility of EFB and FP.

	EFB	FP
Weight fibre used (g)	1g	1g
Percentage of dissolving (%)	40%	99%

3.2 Crystallinity of Cellulose Fibre and Regenerated Cellulose

In this work, the change of crystalline structure of cellulose due to regeneration from different type of cellulose source was analysis using XRD. To determine the Crystalline Index (CI) of cellulose from the XRD spectra, CI was calculated from the height ratio between the intensity of crystalline peak (I_{002}- I_{am}) [12] by using following equation :

$$CI\,(\%) = \frac{I_{002} - I_{am}}{I_{002}} \times 100\% \tag{3}$$

375

Where I_{002} is the peak intensity from the (0 0 2) lattice plane ($2\theta = 22.6\ \theta$) and I_{am} the peak intensity of amorphous phases ($2\theta = 18.5\ \theta$).

The CI of regenerated result shows a significant change in crystallinity, (Table 2). Higher crystallinity was recorded for regenerated cellulose from EFB pulp (Fig. 1c). The XRD pattern sharper peaks than pure FP (Fig. 1a). This means that the mechanism of dissolution affects the reordering of cellulose chains upon their precipitate and crystallization. Other research had concludes the interaction between cellulose and aqueous alkali hydroxide and water onto the fibres resulting in a decrease of NaOH concentration in the surrounding medium [13].

Table 2: Crystallinity index of EFB and FP.

Crystallinity index	Pure cellulose	Cellulose solution
EFB	62.64	66.76
FP	70.13	61.93
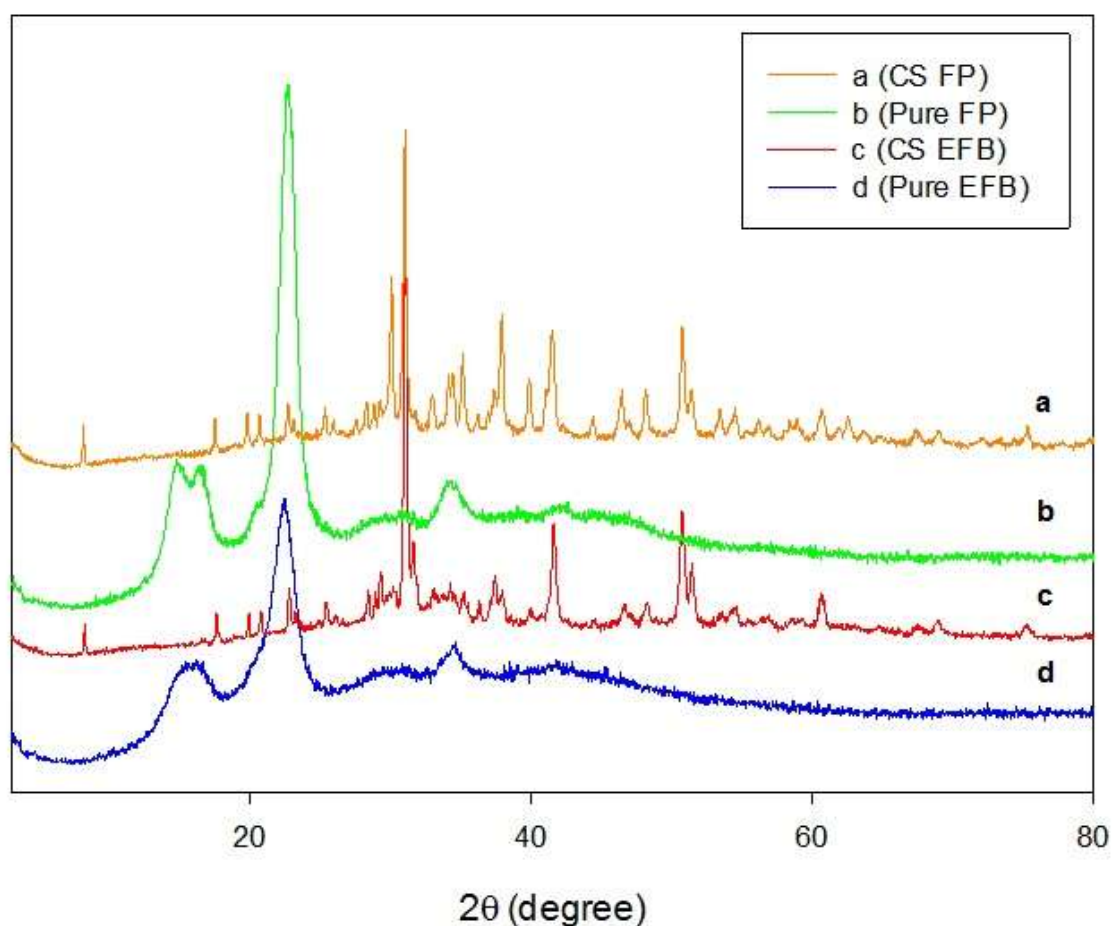
Fig. 1: XRD of (a) CS FP, (b) Pure FP, (c) CS EFB, (d) Pure EFB samples.

Fig. 1 shows the XRD diffraction patterns of (Fig. 1a) cellulose solution for FP, (Fig. 1b) pure FP, (Fig. 1c) cellulose solution for EFB and (Fig. 1d) pure EFB. The diffraction

376

peaks at 2θ= 14.8˚, 16.5˚, and 22.8˚ for (1 Ī 0), (1 1 0) and (2 0 0) planes are characteristic for cellulose I crystal. The amorphous peak at 18° can also be attributed to cellulose I and the cellulose crystallinity is determined according to usual area method [14]. Intensity profiles of all the treated cellulose become sharper than the original cellulose and the shoulder of the peak around 2θ = 22° has been shifted to 28-29 for EFB and FP (Fig. 1a & 1c).
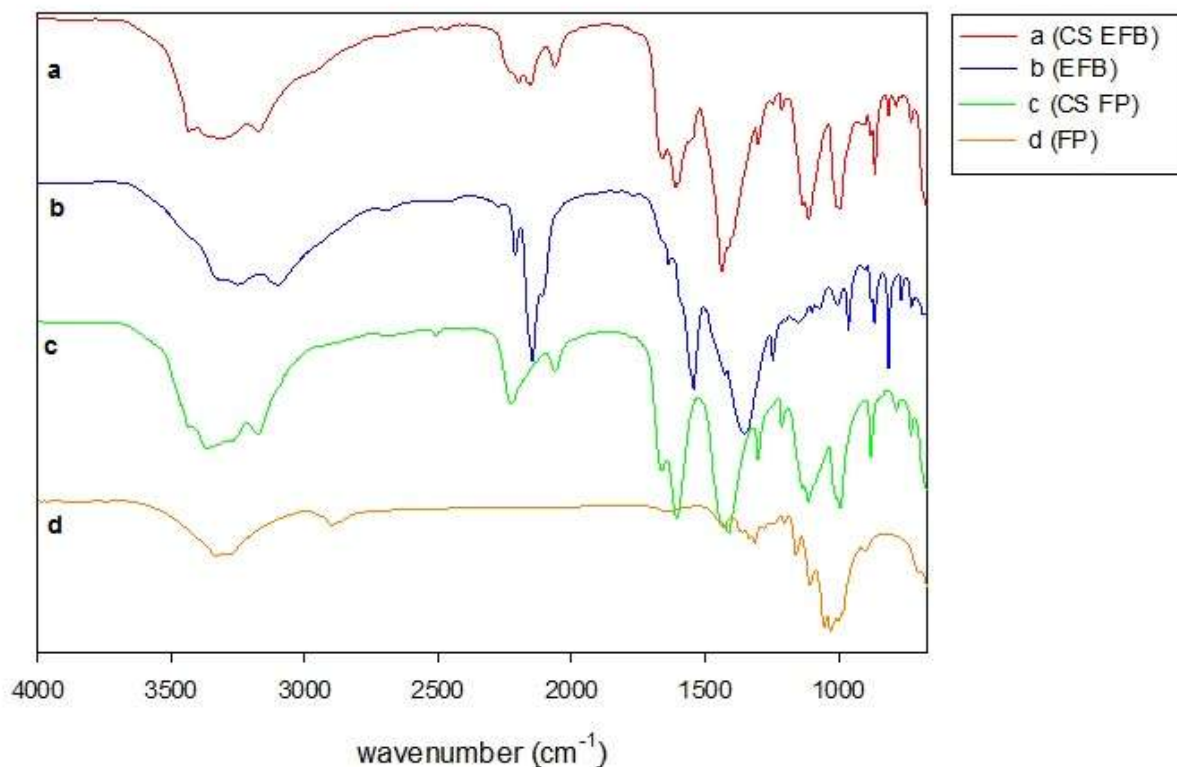
Fig. 2: FTIR spectra of (a) CS EFB, (b) Pure EFB, (c) CS FP, (d) Pure FP samples.

Fig. 2 shows the FTIR spectra of cellulose of EFB and FP. The broad absorption band of cellulose at 3100-3300 (Fig. 2b & 2d) was assigned to the stretching of the large number of hydroxyl group cellulose chain for EFB and FP. The major peak for pure cellulose centered at 3435 cm⁻¹ is corresponding to stretching vibration of –OH [15]. But to differentiate between EFB and FP, there are peak shows aromatic ring at peak 3100-2900 cm⁻¹ (Fig. 2d). For regenerated cellulose EFB and FP at 3200-3300 cm⁻¹ (Fig. 2a & 2c) corresponding to the stretching vibration of –NH [16]. Peak 1600-1700 cm⁻¹ appear on cellulose solution for EFB and FP compare to pure EFB and FP appear because existent of primary amine that attach on C6 of cellulose. Significant to reactivity of C-6 OH (linked to primary carbon), followed by C-2 OH is less reactive and the C-3 OH is the weakest for bending due to formation of hydrogen bond with the neighboring oxygen molecule [17].

Table 3 : Wave Numbers of the FTIR Bands.

Wave number (cm⁻¹)	Band
3200-3400	Urea N-H stretch
3320-3360	Monosubstituted urea N─H stretch

3400-3440	Asymmetric monosubstitued urea –NH$_2$ stretch
1656-1660	C=O stretch, primary amide ─NH$_2$ (urea)
1644	C=O stretch, secondary amine ─NH─ (methylol and methylene urea)

Source: Kandelbauer [18]

4. CONCLUSION

NaOH/urea/thiourea was proposed to dissolve EFB pulp and FP to compare the solubility and regenerated cellulose at low temperature. Low temperature condition for dissolution of cellulose avoids the evaporation of the chemical agents and qualifies this aqueous NaOH/urea/thiourea system as a green solvent. From the dissolution, results show that EFB fibers can get up to 40% solubility compare to FP used as pure cellulose. EFB as waste material can be benefit to produce useful product. The crystallinity index of EFB pulp cellulose is increased in crystallinity from cellulose I to cellulose II after treated in NaOH/urea/thiourea system. Moreover, FTIR results showed there are some lignin attached on EFB pulp that respond to decrease solubility.

5. REFERENCES

1. C. Chang, L. Zhang, J. Zhou, L. Zhang & J. F.Kennedy. (2010). Structure and properties of hyrogels prepared from cellulose in NaOH/urea aqueus solutions *Carbohydrate Polymers*. 82 122-127.

2. Y. Chen, L. Zhang, J. Gu & J. Liu. (2004). Physical properties of microporous membranes prepared by hydrolyzing cellulose/soy protein blends. *Journal of Membrane Science*. 241 393-402.

3. B. Lindman, G. Karlstrom & L. Stingsson. (2010). On the mechanism of dissolution of cellulose. *Journal of Molecular Liquids*. 156 76-81.

4. A. Isogai. (1997). NMR analysis of cellulse dissolved in aqueous NaOH solutions. *Cellulose*. 4 99-107.

5. X. Chen, X. Xu, L. Zhang & J.F. Kennedy. (2009). Flexible chain conformation of (1 → 3)-β-d-glucan from Poria cocos sclerotium in NaOH/urea aqueous solution. *Carbohydrate Polymers*. 75 (4), 586-591.

6. E.V.R. Almeida, E. Frollini, A. Castellan & V. Coma. (2010). Chitosan, sisal cellulose, and biocomposite chitosan/sisal cellulose films prepared from thiourea/NaOH aqueous solution. *Carbohydrate Polymers*. 80 (3), 655-664.

7. S. Zhang, F.X. Li, J.y. Yu & Y.L. Hsieh. (2010). Dissolution behaviour and solubility of cellulose in NaOH complex solution. *Carbohydrate Polymers*. 81 668-674.

8. S. Park, J.O. Baker, M.E. Himmel, P.A. Parilla & D.K. Johnson. (2010). Cellulose crystallinity index: measurement techniques and their impact on interpreting cellulase performance. *Biotechnology for Biofuels*. 3 (10), 1-10.

9. W. Lan, C.F. Liu, F.X. Yue, R.C. Sun & J.F. Kennedy. (2011). Ultrasound assisted dissolution of cellulose in ionic liquid. *Carbohydrate Polymers*. 86 672-677.

10. S. Shinoj, R. Visvanathan, S. Panigrahi & M. Kochubabua. (2011). Oil palm fiber (OPF) and its composites: A review. *Industrial Crops and Products*. 33 7-22.

11. X. Hu, Y. Du, Y. Tang, Q. Wang, T. Feng, J. Yang & J.F. Kennedy. (2007). Solubility and property of chitin in NaOH/urea aqueous solution. *Carbohydrate Polymers*. 70 451-458.

12. S. Park, J.O. Baker, M.E. Himmel, P.A. Parilla & D.K. Johnson. (2010). Cellulose crystallinity index: measurement techniques and their impact interpreting cellulase performance. *Biotechnology for Biofuels*. 3 10.

13. N.A. El-Wakil & M.L. Hassan. (2008). Structural Changes of Regenerated Cellulose Dissolved in FeTNa, NaOH/thiourea, and NMMO Systems. *Journal of Applied Polymer Science*. 109 2862-2871.

14. H. Jin, C. Zha & L. Gu. (2007). Direct dissolution of cellulose in NaOH/thiourea/urea aqueous solution. *Carbohydrate Research*. 342 851-858.

15. J. Wu, S. Liang, H. Dai, X. Zhang, X. Yu, Y. Cai, L. Zhang, N. Wen, B. Jiang & J. Xu. (2010). Structure and properties of cellulose/chitin blended hydrogel membranes fabricated via a solution pre-gelation technique. *Carbohydrate Polymers*. 79 (3), 677-684.

16. C. Chang, B. Duan, J. Cai & L. Zhang. (2010). Superabsorbent hydrogels based on cellulose for smart swelling and controllable delivery. *European Polymer Journal*. 46 (1), 92-100.

17. J. Rojas & E. Azevedo. (2011). Functionalization and crosslinking of microcrystalline cellulose in aqueous media : A safe and economic approach. *International Journal of Pharmaceutical Science Review and Research*. 8 (1), 28-36.

18. A. Kandelbauer, A. Despres, A. Pizzi & I. Taudes. (2007). Testing by Fourier Transfrom Infrared Species Variation During Melamine-Urea-Formaldehyde Resin Preparation. *Journal of Applied Polymer Science*. 106 2192-2197.

Glass Fiber and Nanoclay Reinforced Polypropylene Composites: A Study of the Morphological, Thermal and Dynamic Mechanical Behaviors

Normasmira A. Rahman*, Aziz Hassan, R. Yahya, R.A. Lafia-Araga

Department of Chemistry, Faculty of Science
University of Malaya, Kuala Lumpur, Malaysia

*Corresponding author: nmmira@um.edu.my

Abstract: *Polypropylene (PP), E-glass fiber (GF) and nanoclay (NC) were compounded with a twin-screw extruder and injection molded. The morphology, thermal and dynamic mechanical behaviors of PP/GF/NC nanocomposites were investigated. Transmission electron microscopy (TEM) results revealed an intercalated morphology. DSC results showed that the melting temperature (T_m) and the degree of crystallinity (X_c) was deeply influenced by the presence of the GF and NC in the matrix. Dynamic mechanical analysis (DMA) showed an increase in storage modulus (E') in PP/GF/NC composites. The tan δ spectra presented a strong influence of GF and NC content on the magnitude of tan δ_{max} value.*

Keywords: Microstructural, DSC, DMA, hybrid polypropylene/glass fiber/nanoclay

1.   INTRODUCTION

Fiber reinforced polymer (FRP) composites have been developed as an alternative to thermoset fiber composites with a wide variety of matrix polymers. Polypropylene (PP) is a semi-crystalline engineering thermoplastic with many potential applications in automobiles and commercial products for its well-balanced physical and mechanical properties and its easy processability at a relative low cost [1]. Glass fiber reinforced polymers have been widely use in the automotive and aerospace industries for their high strength and low weight properties. However, due to stress concentration and poor fiber-matrix adhesion, it has repeatedly been shown that an incorporation of short glass fiber (SGF) in PP increases tensile modulus, yet decrease the strength and toughness [2].

Recently, it has been observed that by incorporating nanoparticles into the matrix of fiber reinforced composites (hybrid), synergistic effect may be achieved [3]. It has been observed that by incorporating filler particles into the matrix of fiber reinforced composites, synergistic effects may be achieved in the form of reduction in material costs, increase modulus, heat resistance and biodegradability of biodegradable polymers, decrease gas permeability and flammability, yet decrease the strength and impact toughness [4].

Hybrid reinforced composites form a complex system, and there is inadequate data available about the phenomena behind the property changes due to the addition of particulate fillers to the fiber-reinforced thermoplastic composites. Thus, the present paper is an attempt to clarify the thermal and dynamic mechanical behaviors of hybrid composites based on PP matrix, SGF reinforcement and nanoclay particulate filler. The micro structural, thermal and dynamic mechanical properties of PP/NC and PP/GF/NC were investigated by transmission electron microscopy (TEM), differential scanning calorimetry (DSC) and dynamic mechanical analysis (DMA), respectively.

2. MATERIALS AND METHOD

PP (Propelinas H022) was supplied by Petronas, Malaysia. The neat PP was in the form of pellets with a melt flow index of 11 g/10 min and a density of 910 kg.m^{-3}. Chopped E-glass fiber, surface-treated with silane and having a density of 2,550 kg.m^{-3}, diameter of 14 μm and length of 6 mm, obtained from KCC Corporation, Korea and used as the principal reinforcement. The nanoclay (NC, type PGV), is a natural untreated montmorillonite clay, with a density of 776 kg.m^{-3} and a particle size of about 16 μm and manufactured by Nanocor, USA.

Table 1: Designation, compositions and DSC data of glass fiber composite specimens.

Sample	Fiber weight fraction ,W_f (%)	Clay content (phr)	DSC data				
			T_m (ºC)	ΔH_m (J/g	X_c (%	T_c (ºC)	ΔH_c (J/g)
NC (clay)	-	-	-	-	-	-	-
PP	-	-	163.0	75.07	35.9	121.7	93.11
PP85/G15	15	-	161.6	71.67	34.3	121.7	91.86
PP100/NC3	-	3	162.0	53.10	25.4	121.4	67.61
PP100/NC6	-	6	163.5	67.92	32.5	121.6	93.15
PP100/NC9	-	9	163.6	73.35	35.1	122.8	94.12
(PP85/G15)/NC3	15	3	163.8	70.83	33.9	125.5	96.02
(PP85/G15)/NC6	15	6	165.5	85.35	40.8	130.3	96.09
(PP85/G15)/NC9	15	9	164.9	82.14	39.3	129.7	98.68

PP/GF and PP/NC composites were prepared with different ratios of PP/chopped GF and PP/clay powder, respectively as shown in Table 1. Compositions were physically pre-mixed and then compounded using a Brabender, KETSE 20/40 (Germany) twin screw extruder with the screw diameter and aspect ratio of 20 mm and 40, respectively. The temperature profile was set to 185°C - 190°C. For the PP/GF composites, the screw speed was set to 100 rpm, whereas for the PP/NC composites, the screw speed used was 800 rpm. The materials extruded from both formulations were pelletized into length of about 6 mm. In order to produce PP/GF/NC composites, the different ratios of the PP/NC and chopped GF were physically mixed and re-compounded in a twin screw extruder, using the same temperature

profile and screw speed of 100 rpm. The dumb bell-shaped tensile specimens, according to ASTM standard D638 [5], were then injection molded using a Boy® 55M (Germany), a 55 tonne clamping force injection molding machine. The processing temperature was set between 175°C – 185°C and the mould temperature was set at 25°C. The screw speed was maintained at 30 – 50 rpm. List and abbreviation of specimens prepared are given in Table 1.

The microstructure of the PP/NC and PP/GF/NC were analyzed with a Hitachi H-600 (Japan) transmission electron microscope (TEM). The samples were ultra-microtomed with a diamond knife on a Leica Ultracut UCT (UK) microtome at room temperature to give section with a nominal thickness of 200 nm. Sections were transferred to 400-mesh Cu grids. Bright-field TEM images of the composites were obtained at 300 kV under low-dose conditions.

DSC experiments were performed with a Perkin-Elmer Diamond DSC (USA). Each sample was subjected to heating and cooling treatments at a scanning rate of 10°C.min^{-1} under nitrogen atmosphere with the nitrogen flow rate of 20 ml.min^{-1} in order to prevent oxidation. A test sample of 5 – 10 mg was crimped in an aluminum pan and tested over a temperature range of 0°C to 190°C.

The dynamic mechanical properties of specimens were analyzed with a Thermal Analysis Instrument, TAI Q800 (USA) dynamic mechanical analyzer (DMA). Test specimens were taken from the middle section of the injection molded dumb-bell test bar and were subjected to a three-point bending mode with a support span of 50 mm. Measurements were conducted over a temperature range of -100°C to 110°C with a heating rate of 3°C.min^{-1} at a constant frequency of 1.0 Hz.

3. RESULTS AND DISCUSSION

3.1 Transmission Electron Microscopy (TEM)

To gain insight into the morphology of nanocomposites, characterization using TEM was conducted at lower and higher magnification for 3 and 9 phr NC based nanocomposite samples, as shown in Fig. 1. Nanocomposites containing 3 and 9 phr of NC show heterogeneous dispersion, presence of aggregates, as well as resin-rich areas in the matrix without clay. However, there are regions where completely delaminated sheets are dispersed individually, showing as average dark lines of 1 – 2 nm thickness (Fig. 1 (a1 and b1)). It appears that the clay exists as expanded aggregates. The size of aggregates and the number of platelets in them increase with the percentage of clay within the PP matrix. Farzana et al. [6] in their study suggest that the degree of intercalation or exfoliation depends on type and surface modification of NC, presence of compatibilizing agent, as well as the processing condition. Within this scope of study, untreated NC has been used. Therefore, a homogenous dispersion of layered silicates is difficult to attain as the NC has strong tendency to agglomerate and interaction between PP and NC may be poor as no compatibilizer has been added.

| (a1) | (a2) | (b1) | (b2) |
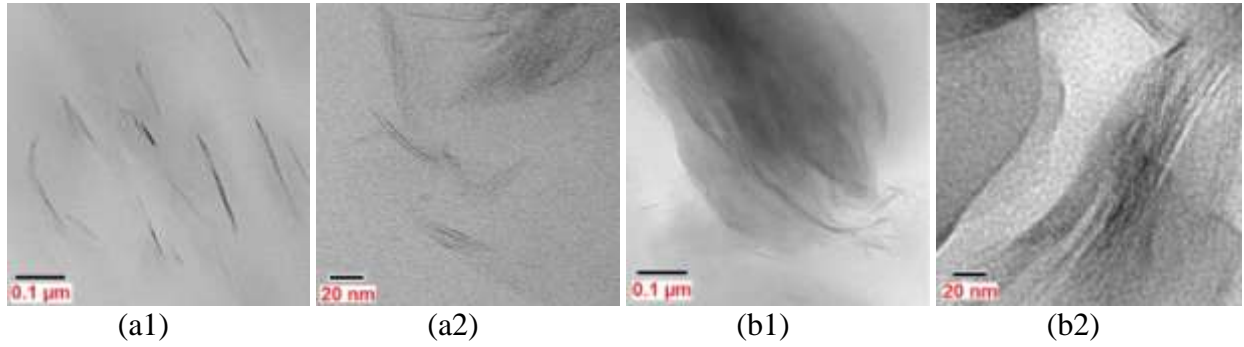
Fig. 1: TEM images of PP/NC as a function of NC concentration. (a1), (a2): PP/NC3; (b1), (b2):PP/NC9.

In Fig. 1 (a2 and b2), the average distance between clay platelets for PP/NC3 and PP/NC9 nanocomposites are 1.6 nm and 1.1 nm, respectively. It is of interest to mention that the interlayer spacing for NC in PP/NC3 composite is expanded compared with composites with 9 phr NC loading. The PP/GF/NC hybrid composites were also examined by TEM, where structure and orientation of NC was unclear. The hybrid composites therefore analyzed with scanning electron microscopy.

3.2   Differential Scanning Calorimetry (DSC)

The DSC thermograms allow one to get information on the melting temperature (T_m), crystallization temperature (T_c), enthalpy of melting (ΔH_m), enthalpy of crystalline (ΔH_c). The degree of crystallinity (X_c) of the specimens can also be calculated using the following equation [2],

$$X_c = \frac{\Delta H_m}{\Delta H_m^*} \times 100\% \qquad (1)$$

where ΔH_m^* is enthalpy of melting of fully crystalline PP, taken as 209 J/g [7]. The ΔH_m, ΔH_c and X_c values of PP, PP/GF, PP/NC and PP/GF/NC may be computed according to the actual PP content in the composites, as seen in Table 1.

DSC thermograms show the presence of single peaks for both heating and cooling scans of the composites (Figs. 2 and 3). The melting temperature of pure PP is 163°C. DSC thermograms from Fig. 2 show that the increasing the level of clay loading in PP/NC (PP/NC3-9) has an insignificant effect on the melting temperature of the nanocomposites. Meanwhile, for PP/GF composite, incorporation of 15 wt% GF into the system slightly

reduced the T_m value (Fig. 3 and Table 1). However, in the hybrid composite systems, the T_m value increased by up to 2.5°C with increasing NC content.

Results from Table 1 show that the X_c values of these composites are slightly reduced, relative to that of neat PP (35.9%). Meanwhile, as for hybrid composites, the addition of clay in 15 wt% GF composite show some increment in the degree of crystallinity. An insignificant change (0.8% reduction) in X_c was observed with the addition of 3 phr of clay into PP/GF15 composite. Further addition of 6 phr clay in the matrix ((PP:G15)/NC6) increases the X_c value to 40.8%. As the clay content in the hybrid composite increases to 9 phr ((PP:G15)/NC9), the X_c value is slightly reduced to 39.3%, probably because this degree of crystallinity is very close to the maximum that the PP can achieve according to its stereoregularity [8].
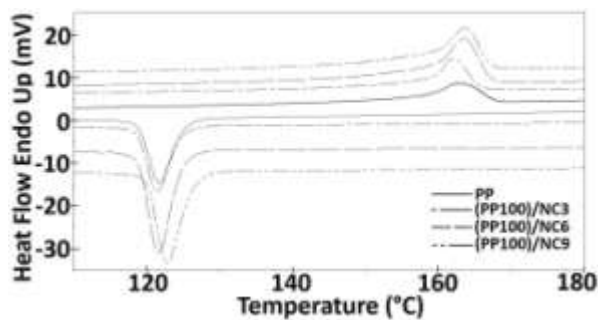
Fig. 2: The DSC thermograms of injection-molded PP/NC composites.
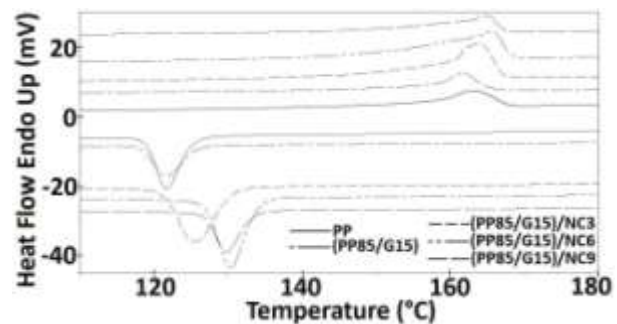
Fig. 3: The DSC thermograms of injection-molded PP/GF/NC hybrid composites.

As for the crystalline peak temperature (T_c), no significant changes in T_c values are observed with incorporation of glass fiber and nanoclay (PP/GF and PP/NC) into the system (Table 1, Figs. 2 and 3). By contrast, the T_c of the hybrid composites were enhanced to higher temperatures (Fig. 3). The T_c of the hybrids increase by about 3.8°C, 8.6°C and 8.0°C for (PP:G15)/NC3, (PP:G15)/NC6 and (PP:G15)/NC9, respectively, compared to that of PP (121.7°C). These increments indicate the nucleating effect of the nanoclay in the crystallization of PP [9]. Incorporation of both NC and GF may accelerate the crystallization of PP, thereby making it crystallize at higher temperature, and they will shorten the molding cycle in practical production [7]. The same trend was observed for the crystalline enthalpy ΔH_c.

3.3 Dynamic Mechanical Analysis (DMA)

3.3.1 Storage Modulus (E')
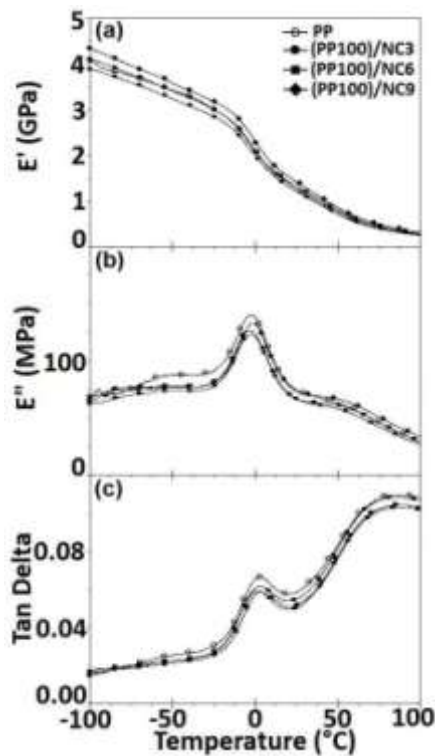
Fig. 4: The DMA curves of injection-molded PP/NC composites.
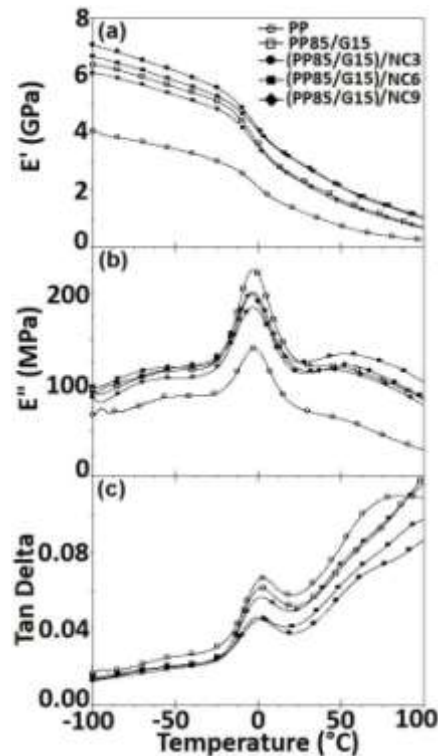
Fig. 5: The DMA curves of injection-molded PP/GF/NC hybrid composites.

The storage modulus (E') is closely related to the load bearing capacity of a material and is analogous to the flexural modulus measured as per ASTM Standard D790 [2,10]. Variation of E' as a function of temperature for virgin PP, PP/GF, PP/NC and PP/GF/NC composites are graphically enumerated in Figs. 4 (a) and 5 (a). From these figures, a decreasing trend in the storage modulus over the whole temperature range is observed. Fig. 4 (a) illustrates that storage modulus of PP/NC composites show a dependence on the NC loading below the T_g, while insignificant variation of E' between the composites is seen above the T_g. Generally, composites with higher NC loading (PP/NC6-9) possessed higher storage modulus than pure PP through all the temperature range. It is evident from Table 2 and Fig. 4 (a), that there is a notable increase in the modulus of PP/NC (at -100°C) with incorporation of NC, probably due to increase in the stiffness of the matrix because of the restriction of molecular motions imparted by the NC [11]. The addition of 9 phr NC gives increment of about 6% in the storage modulus (at -100°C) relative to PP.

As for PP/G15 composite, incorporation of 15 wt% GF greatly increases the E' value (at -100°C) by 56% higher compared with PP (Fig. 5 (a)). The incorporation of NC into PP/GF system further enhances this property. E' of (PP/G15)/NC6 and (PP/G15)/NC9 composites (at -100°C) were increased by 63% and 73%, respectively, relative to PP, as NC was added to the PP/GF system. It is suggested that the improvement of E' in the hybrid

composites (PP/GF/NC) is mainly attributed to the improvement of the matrix E' from particulate filler dispersion. By contrast, as for (PP/G15)/NC3, a slight decrement of E' relative to PP/G15 is observed for the whole temperature range. It is suggested that the reinforcement effect is not effective at lower NC contents and the NC only act as plasticizer in the composites.

3.3.2 Loss Modulus (E")

The variation in E" of virgin PP, PP/NC and PP/GF/NC hybrid composites as a function of temperature are shown in Figs. 4 (b) and 5 (b). In this work, $T_{\alpha}^{E"}$ is referred to temperature at the maximum value of loss modulus in α-transition region. As observed from Figs. 4 (b) and 5 (b), PP/NC and PP/G15 composites show insignificant changes in the $T_{\alpha}^{E"}$ value relative to PP. By contrast, $T_{\alpha}^{E"}$ of PP/GF/NC hybrid composites shifts to lower temperatures compared to the PP. The decrease of $T_{\alpha}^{E"}$ in this system indicates that the amorphous molecules become mobile at lower temperature than that of PP matrix. This may be due to the existence of low molecular weight intercalants [9]. The magnitude of $T_{\alpha}^{E"}$ value of PP ($E_{max}^{"}$) was measured to be 140 MPa as shown in Table 2. The presence of NC in the system reduces $E_{max}^{"}$ to 123 MPa – 133 MPa for PP/NC3 – PP/NC9. Meanwhile, the addition of 15 wt% of GF in PP/G15 increases the $E_{max}^{"}$ to 226 MPa. However, $E_{max}^{"}$ value for hybrid systems was found to be lower compared with PP.

Table 2. DMA thermomechanical data of glass fiber composites.

Sample	Storage modulus, E' (GPa)		Loss modulus, E"		Tan δ	
	at -100˚C	at 25˚C	E"$_{max}$ (MPa)	T$_{\alpha}^{E"}$ (˚C)	tan δ$_{max}$ (x 10^{-2})	T$_g$ (˚C)
PP	4.07	1.28	140	-3	6.67	3
(PP100)/NC3	3.88	1.21	123	-3	6.15	2
(PP100)/NC6	4.11	1.33	127	-4	5.93	2
(PP100)/NC9	4.33	1.42	133	-1	5.88	3
(PP85:G15)	6.36	2.39	226	-3	6.16	2
(PP85:G15)/NC3	6.08	2.32	202	-4	5.63	1
(PP85:G15)/NC6	6.65	2.93	185	-3	4.50	1
(PP85:G15)/NC9	7.06	2.98	199	-5	4.63	-1

3.3.3 Loss Tangent (tan δ)

The ratio of loss modulus to storage modulus is measured as the mechanical loss or damping factor (tan δ). The damping properties of the material give the balance between the elastic phase and viscous phase in a polymeric structure [2]. The variations of tan δ as a function of temperature are represented in Figs. 4 (c) and 5 (c). The transition region as indicated by damping maxima is usually known as α-transition.

By analyzing the tan δ curves for PP/GF, PP/NC and PP/GF/NC composites, no significant difference in T_g value can be observed. The same trend has been reported by Modesti et al. [8]. It is suggested that the T_g is not sensibly affected by the presence of glass fiber and nanoclay. However, the presence of the GF reduces the magnitude of tan δ_{max} values dramatically. Higher reduction for composite with higher filler loading is believed to be due to the strengthening effect by the GF and limiting the mobility of polymer matrix. In this case, the incorporation of GF act as barriers to the mobility of polymer chain, leading to lower degree of molecular motion and hence lower damping characteristics [12]. Another possible reason is that there is less matrix by volume to dissipate the vibration energy. Incorporation of NC in PP/GF composite further reduced this value. Tan δ_{max} of (PP/G15)/NC6 show a maximum decrease of about 32% compared to the pure matrix (0.0667 to 0.0450). A decline in the tan δ values with addition of NC indicates an improvement in interfacial adhesion in composites [13].

4. CONCLUSIONS

Introducing the NC into the PP matrix results in no significant changes on the melting temperature of the composite. By contrast, for hybrid composites, the T_m value seems to be increase. For PP/NC and PP/GF/NC systems, it was observed that generally the X_c of composites increased with increasing clay content. In addition, the T_c value of hybrid composites are enhances to a higher degrees compare with conventional PP/GF and PP/NC composites.

Generally, composites with higher NC loading possess higher storage modulus (E') than PP matrix through all the temperature range. Temperature at maximum loss modulus ($T_{\alpha}^{E''}$) of the PP/NC and PP/G15 composites show insignificant changes relative to PP. By contrast, for PP/GF/NC hybrid composites, $T_{\alpha}^{E''}$ shift to lower temperature and its magnitude reduce compared with PP. Incorporation of NC and GF reveal no significant difference on T_g value. On the other hand, the presence of the GF reduces the magnitude of tan δ_{max} values dramatically. A decline in this value is more prominence in the PP/GF/NC hybrid systems.

5.   ACKNOWLEDGEMENTS

6.   REFERENCES

1.   Seo, M.K., Lee, J.R. & Park, S.J. (2005). Crystallization kinetics and interfacial behaviors of polypropylene composites reinforced with multi-walled carbon nanotubes. *Mater. Sci. Eng. A.,* 404(1-2), 79-84.

2.   Hassan, A., Normasmira, A.R. & Yahya, R. (2011). Extrusion and injection-molding of glass fiber/MAPP/polypropylene: Effect of coupling agent on DSC, DMA and mechanical properties. *J. Reinf. Plast. Compos.,* 30(14), 1223-1232.

3.   Kornmann, X., Rees, M., Thomann, Y., Necola, A., Barbezat, M. & Thomann, R. (2005). Epoxy-layered silicate nanocomposites as matrix in glass fibre-reinforced composites. *Compos. Sci. Technol.,* 65(14), 2259-2268.

4.   Acosta, J.L., Rocha, C.M., Ojeda, M.C., Linares, A. & Arroyo, M. (1984). The effect of several modified sepiolites on the transition temperatures and crystallinity of filled propylene. *Angew. Makromol. Chemie.,* 126, 51-57.

5.   ASTM Standard D638-03. Standard Test Method for Tensile Properties of Plastics, *ASTM International, West Coshoshocken, PA, 2003, DOI 10.1520/D0638-03, www.astm.org.*

6.   Hussain, F., Roy, S., Narasimhan, K., Vengadassalam, K. & Lu, H. (2007). E-glass - polypropylene pultruded nanocomposite: Manufacture, characterization, thermal and mechanical properties. *J. Thermoplast. Compos. Mater.,* 20(4), 411-434.

7.   Cui, Y.H., Wang, X.X., Li, Z.Q. & Tao, J. (2010). Fabrication and properties of nano ZnO/glass fiber reinforced polypropylene composites. *J. Vinyl. Addit. Technol.,* 16(3), 189-194.

8.   Modesti, M., Lorenzetti, A., Bon, D. & Besco, S. (2006). Thermal behaviour of compatibilised polypropylene nanocomposite: Effect of processing conditions. *Polym. Degrad. Stabil.,* 91(4), 672-680.

9.   Lei, S.G., Hoa, S.V. & Ton-That, M.T. (2006). Effect of clay types on the processing and properties of polypropylene nanocomposites. *Compos. Sci. Technol.,* 66(10), 1274-1279.

10.   Saha, A.K., Das, S., Bhatta, D. & Mitra, B.C. (1999). Study of jute fiber reinforced polyester composites by dynamic mechanical analysis. *J. Appl. Polym. Sci.,* 71(9), 1505-1513.

11.   Bozkurt, E., Kaya, E. & Tanoglu, M. (2007). Mechanical and thermal behavior of non-crimp glass fiber reinforced layered clay/epoxy nanocomposites. *Compos. Sci. Technol.,* 67(15-16), 3394-3403.

12.   López-Manchado, M.A., Biagiotti, J. & Kenny, J.M. (2002). Comparative study of the effects of different fibers on the processing and properties of polypropylene matrix composites. *J. Thermoplast. Compos. Mater.,* 15(4), 337-353.

13.   Nayak, S.K. & Mohanty, S. (2010). Sisal glass fiber reinforced PP hybrid composites: Effect of MAPP on the dynamic mechanical and thermal properties. *J. Reinf. Plast. Compos.,* 29(10), 1551-1568.

Effect of Stearic Acid on Properties of Aluminium – Zinc Oxide Composites

A.R. Nurul Razliana[*], H. Salmah , and J.B. Shamsul

School of Material Engineering, University Malaysia Perlis (UniMAP),
Kompleks Taman Muhibbah, Jejawi 2, Perlis, Malaysia

*Corresponding author: nrazliana@gmail.com

Abstract: *Stearic acid was used as a binder in Aluminium (Al)/Zinc oxide (ZnO) composites. The composites with and without binder were mixed by ball mill and compacted under pressure at 200 MPa. The composites sintered at 750°C for two hours. The results show that density and hardness of Al/ZnO composites increased with increasing of ZnO content. The composites with stearic acid exhibit higher density and hardness than composites without stearic acid.*

Keywords: Aluminium, zinc oxide, stearic acid, composites

1. INTRODUCTION

Nowadays, composites have become one of the essential materials in variety applications. This happen due to the physical and mechanical properties of the composites which are better that exist material. As known, composite is a material that consists of two of more different materials, which are produced via a physical combination to obtain a new material that have a unique properties when compared to the original material [1]. The possibility of combining different materials such as metal, ceramic and non metal gives the opportunity for unlimited variation and properties of these new materials. One of the main composites that have been developed recently was metal matrix composites (MMC) and it's been apply for various applications of industry. These innovative materials open up unlimited possibilities for modern material science and development; the characteristic of MMC's can be designed into the material, custom made, dependent on the application [2].

Aluminium metal matrix composites is one of the most popular composites due to the low density, greater strength, improved stiffness, improved high temperature properties and thermal/heat management [3]. The aluminium was selected to combining with ZnO particulates to form Al/ZnO composites. In this study, the physical and mechanical properties of the Al metal matrix composite with inorganic material of ZnO were investigated. The using ZnO was chosen as filler due to one of its applications which is catalyst, by using simple method; powder metallurgy.

Powder metallurgy is one of most common production technique for MMC's. It is done by blending element of pre-alloyed powders together, compacting the blend in a die and

sintering /heating the pressed part to bond the particles. this manufacturing method have several advantages which are it can obtain homogenous microstructures among matrix and the reinforcement, have a wider choices of alloy composition that make it possible to obtain tailored properties, better thermal properties, lower production cost and can obtain composite that can use particles/whiskers as reinforcement more easily compare to other method [4-6].

During mixing, it is a common practice to mix lubricant to minimize the wear facilitates the ejection from the die after compaction and some powders binder to achieve a high green strength. Binder was also added to powder to increase the fluidity during forming or to improve the green strength of the compact or to cementing together powder particles. This binder and lubricant are usually burn out of the compacts. Binders are thermoplastic mixtures such as waxes, polymers, oils, lubricants and surfactants [4, 7].

2. EXPERIMENTAL

Aluminium (Al) and stearic acid was supplied by HmbG Chemicals, Germany and zinc oxide was supplied by Metaoxide Sdn Bhd, Malaysia. The density of the Al is 2.7 g/cm³ and ZnO is 5.6 g/cm³, respectively. Malvern particle analyzer was used to measure particle size Al and ZnO, particle size of the Al is 35.5 μm and ZnO was 7 μm.

a)   Mixing Procedure

The Al/ZnO composites were prepared using powder methodology method. Unidirectional mould was used to compress the pellet into cylindrical shape. At first, the Al/ZnO composites without stearic acid composites were mixed with amount of ZnO was varying from 10 wt% to 40 wt%. The mixtures were mixed in the container by ball mill with ball to powder weight ratio was 10:1. The mixing was carried out for 60 minutes and the speed of the roll mil 131 rpm. After mixing, the powder mixtures were compacted into cylindrical shape with 15mm diameter mould. The mixtures were pressed under pressure 200 MPa for 2 minutes. The green body samples were sintered in a muffle furnace for two hours at 750°C. The composites sintered under atmosphere environment. The similar procedure was done for Al/ZnO composites with stearic acid. The amount of stearic acid added in Al/ZnO composites was 2wt%. The formulation of Al/ZnO composites with and without stearic acid is show in Table 1.

Table 3: The formulation of Al/ZnO composites with and without stearic acid.

Materials	Composites without stearic acid	Composites with stearic acid
Al (wt%)	90, 80, 70, 60	90, 80, 70, 60
ZnO (wt%)	10, 20, 30, 40	10, 20, 30, 40
Stearic acid (wt%)	-	2

b)   Density Test

The density of composites was measured by using equipment Accupyc II 1340 Gas Displacement Pycnometer according to ASTM B 962 – 08. Samples with weight about 5 ± 1g were placed in the instrument 10 cm³ chamber and the volume were measured using helium gas at temperature between $22 - 23°C$. The equilibration rate was 0.005 psig/min with 10 cycles of purge.

c)   Hardness test

The hardness test was carried out using ASTM Designation B 933 – 09: Standard Test Method for Microindentation Hardness of Powder Metallurgy (PM) Materials. Vickers's hardness tester (Future Tech, model: FV – 700e) was used with an applied load 10N and the dwell time was 8 seconds. The indentation was done for five times at different location on the sample surface. The average value of five indentation value was recoded.

d)   Microstructure

The microstructures of composites were carried out by using Scanning electron microscope (SEM) JEOL JSM-6460LA. The microstructure was observed at magnification 500X using secondary image.

3.   RESULT AND DISCUSSION

Fig. 1 shows the density of the Al/ZnO composites with and without stearic acid when sintered at 750°C. The density of Al/ZnO composites without stearic acid was increased with the increasing of ZnO wt%. The increasing density of Al/ZnO composites without stearic acid composites due to addition of the ZnO in Al matrix influences the density of mixing Al/ZnO composites. This is due to the density of ZnO higher than density of Al.

The density of composites Al/ZnO composites with stearic acid binder also increase with the increasing of the ZnO content, however, it is slightly lower compared to density of the Al/ZnO composites without stearic acid binder. Presence of the stearic acid binders influences the density of the Al/ZnO with binders, because the binders probably had deleterious effect on sintered density, mainly owing to its wide burn of range and hence incomplete removal during sintering [8].
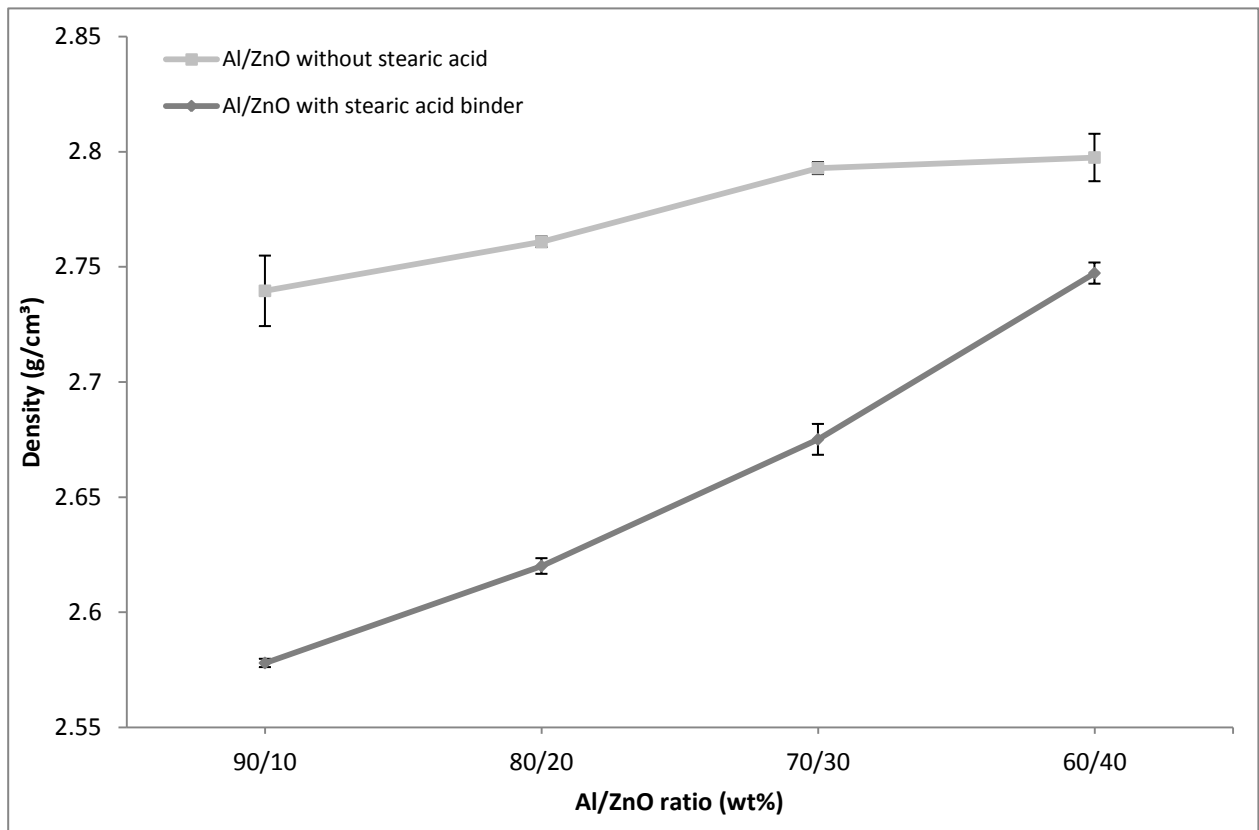
Fig. 1: The density of the Al/ZnO composites with and without stearic acid.

Fig. 2 shows the hardness of Al/ZnO composites with and without stearic acid at sintered 750°C. From the graph, it shows that the hardness of both composites was increased with the increasing of ZnO content. The addition of smaller size of ZnO particle in Al matrix, gives an effect on the hardness of the composites. The ZnO have smaller particle size than Al, thus the smaller particle size lead to greater interfacial area between the filler and the matrix [4] and cause the increase in hardness of composites.

From the result showed the composites Al/ZnO composites with stearic acid gives higher hardness compared to Al/ZnO composites without stearic acid. This result show that the stearic acid binder playing a role to strengthen the composites. The stearic acid was playing a role in order to strengthen the composites which lead to higher hardness compared to Al/ZnO composites without stearic acid. The presence of the stearic acid binder, can improved the surface interaction between ZnO and Al matrix.
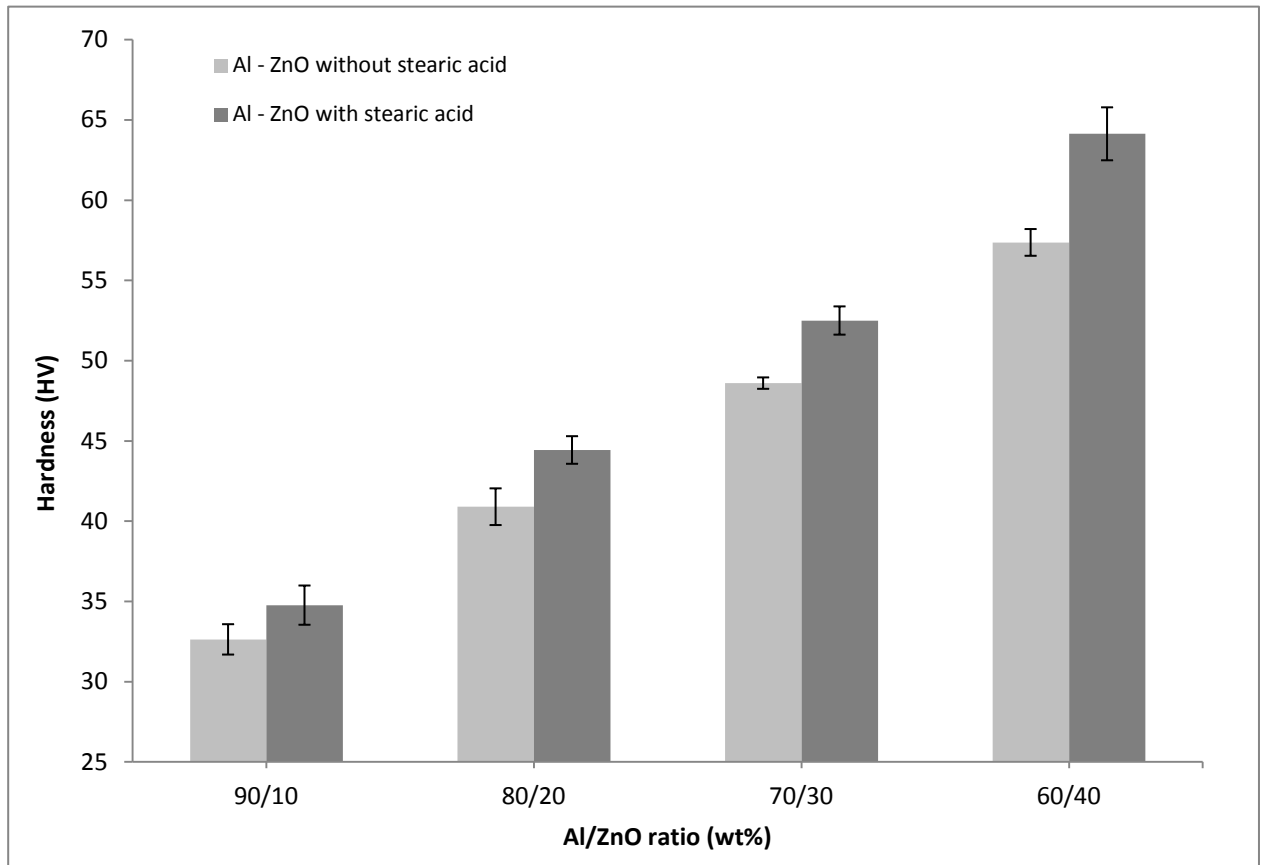
Fig. 2: The hardness result of Al/ZnO composites with and without stearic acid.

Figs. 3 and 4, show SEM microstructure of the Al/ZnO composites without stearic acid at ratio 80/20 and 60/40 Al/ZnO composites at sintered temperature 750°C. From this, show that the ZnO not well dispersed in Al matrix. The presence many hole was occurred between ZnO and Al matrix. This attributed the poor interaction between ZnO and Al matrix. The increasing of ZnO content indicates less hole and agglomeration of ZnO, this evidence that higher ZnO wt% showed higher hardness.
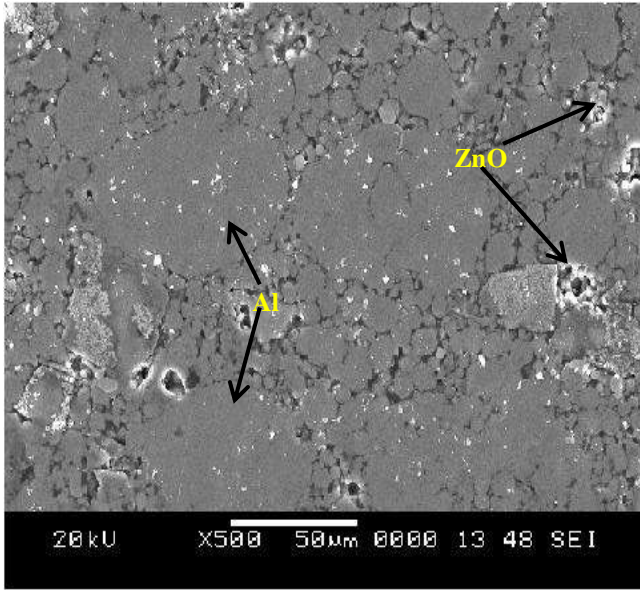
Fig. 3: SEM micrograph of Al/ZnO
composites without stearic acid
(80/20 : Al/ZnO).
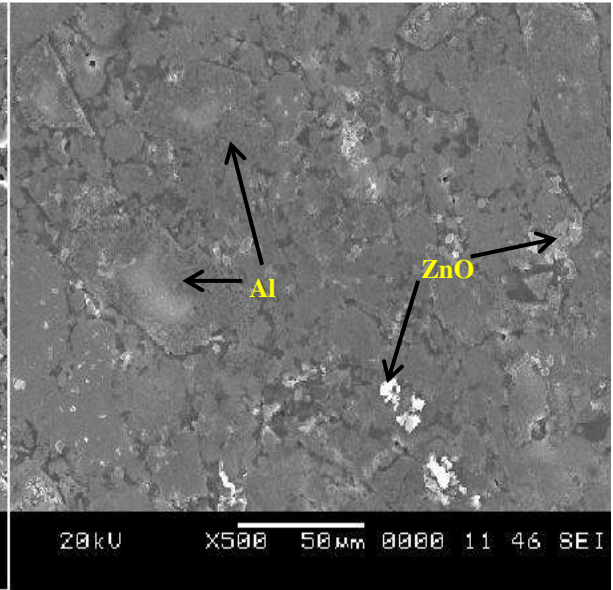
Fig. 4: SEM micrograph of Al/ZnO
composites without stearic acid
(60/40 : Al/ZnO).

Fig. 5 and 6 indicates the SEM micrograph of Al/ZnO composites with stearic acid with ratio 80/20 and 60/40 Al/ZnO composites with stearic acid. From the figure shown, the ZnO was dispersed well in between the Al in the composite and with the presence of stearic acid in the Al/ZnO, it reduce pore between ZnO and Al and then lead to better surface interaction between them. The better surface interaction between Al and ZnO resulting better hardness compared to Al/ZnO without stearic acid.
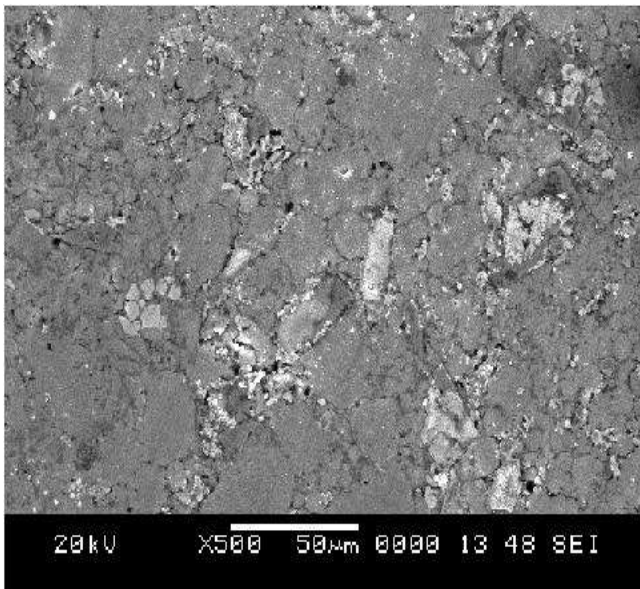
Fig. 5 : SEM microstructure of Al/ZnO
composites with stearic acid
(80/20 : Al/ZnO)
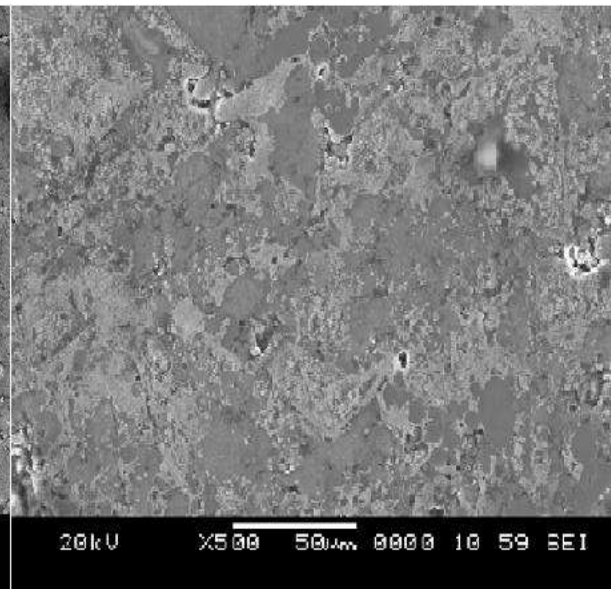
Fig. 6 : SEM microstructure of Al/ZnO
composites with and stearic acid
(60/40 : Al/ZnO)

4.   CONCLUSION

The increasing of the ZnO content, have increased the hardness and density of the Al/ZnO composites. The addition of the stearic acid has enhanced the hardness of the Al/ZnO composites with stearic acid than Al/ZnO composites without stearic acid. The microstructure study showed the better interaction between ZnO and Al was improved with the presence of stearic acid.

5.   REFERENCES

1. Cayron, C. (2000). TEM study of interfacial reactions and precipitation mechanisms in Al2O3 short fiber or high volume fraction SiC particle reinforced Al-4Cu-1Mg-0.5Ag squeeze-cast composites. University of Leuven, Belgium.
2. Kainer, K. U. (2006). Basics of Metal Matrix Composites. In Karl U Kainer (Ed.), *Metal Matrix Composites: Custom-made Materials for Automotive and Aerospace Engineering* (pp. 1-50). WILEY-VCH Verlag GmbH & Co. KGaA, Weinheim.
3. Surappa, M. K., & Rohatgi, P. K. (1981). Preparation and properties of cast aluminium-ceramic particle composites. *Journal of Materials Science*, *16*(4), 983-993. Springer Netherlands. DOI : 10.1007/BF00542743
4. Rahimian, M., Ehsani, N., Parvin, N., & Baharvandi, H. reza. (2009). The effect of particle size, sintering temperature and sintering time on the properties of Al– Al2O3 composites, made by powder metallurgy. *Journal of Materials Processing Technology*, *209*, 5387–5393.
5. Verlinden, B., & Froyen, L. (1994). Aluminium Powder Metallurgy. Belgium: European Aluminium Association (Training in Aluminium Application Technologies).
6. Torralbaa, J. M., Costab, C. E. da, & Velascoa, F. (2003). P/M aluminum matrix composites: an overview. *Journal of Materials Processing Technology*, *133*, 203–206.
7. Setasuwon, P., Bunchavimonchet, A. & Danchaivijit, S. (2008). The effects of binder components in wax/oil systems for metal injection molding. *Journal of Materials Processing Technology*, *196*(1-3), 94-100. doi:10.1016/j.jmatprotec.2007.05.009
8. Gökçe, A., & Findik, F. (2008). Mechanical and physical properties of sintered aluminum powders. *Journal of Achievements in Materials and Manufacturing Engineering*, *30*(2), 157–164.

Electrical Properties of ZnO-Bi₂O Varistor Ceramics

Noor Azira Mohd Noor[*], Mohd Nazree Derman, and Muhamad Asri Idris

PPK Bahan, Universiti Malaysia Perlis, Pusat Pengajian Jejawi 2, Taman Muhibah,
02600 Jejawi, Arau, Perlis

*Corresponding author: noorazira @unimap.edu.my

Abstract: *A comparative study of varies speed of milling during mixing of ZnO-Bi₂O₃ varistor using planetary ball mill is reported in this paper. The samples were prepared through conventional mixing technique. The microstructure of the sintered samples were characterised with X-ray diffraction. The electrical behaviour of the samples was studies on the basis of the current versus voltage (I-V) characteristics. The milling process ensures the homogeneity in the distribution of additives, the new phases formed obtained through out X-ray diffraction. The optimum parameter for milling speed was 300 rpm with non-linear coefficients, α of 23.4.*

Keywords: Varistor, ZnO, milling speed, planetary mill and I-V

1. INTRODUCTION

Zinc oxide varistor are polycrystalline ceramics containing minor additive and dopants. They are highly non-ohmic resistors, i.e. voltage-dependent switching devices. At low electric fields, varistors behave like high value Ohmic resistors. As applied fields are increase, varistors exhibit nonlinear Ohmic characters often expressed empirically by the relation $J= kE^{\alpha}$, where E and J are the electric field and current density, respectively, and k is a materials constant. The exponent α is called the nonlinearity coefficient. Desirable varistor properties generally include high resistance at low fields and a large coefficient at high fields [1].

Ceramic processing results in semiconducting ZnO grains, with intergranular bismuth-rich oxide phases. The non-linear current-voltage characteristics are governed by the interfaces between the ZnO grains. The voltage –dependent resistivity result from Schottky barriers at ZnO-ZnO boundaries, but the Bi-rich phases present at multiple grain junctions also has a significant effect on the overall resistivity. The ability to control E_b and α are both important for device applications, and this may be achieved by the addition of multiple dopants and by control of the ceramic fabrication conditions. Although the electronic properties of the grain boundaries and their effect on varistor properties are firmly established, there continues to be some variation in the literature as to the exact phase composition and

397

physical distribution of the intergranular phase, which originates from liquid-phase sintering [2].

Effective grain boundary effects tend to control the electrical properties of ZnO-based varistors. From the work of numerous investigators, it is known that the device nonlinear and breakdown field are dependent on the number of effective boundaries per volume and conductivity of ZnO grains [2]. In the present work, the influence of the milling speed during milling process on the electrical properties has been investigated.

2.   EXPERIMENTAL PROCEDURE

The detail of the varistor powder compositions is given in table I.

Table 1: The composition of varistor.

	ZnO	Sb_2O_3	Bi_2O_3	CoO	MnO_2	Cr_2O_3
mol %	97	1	0.5	0.5	0.5	0.5

For conventional route, the powder was weighting according to the mol% and mixed together. The composition was prepared by milling a mixture in varies speed; 200, 300, 400 and 500 rpm. Particle analysis was done using particle analyzer (Malvern Mastersizer 2000). The mixed powders were calcined at 750°C for 2 hours. Then the powder was press into pellet before sintered at 1200°C for 2 hour. The crystalline phases of the samples were identified by Lab X XRD-600 Shimadzu.

To measure the electrical properties the samples were contacted with silver paste on the both surfaces and heated at 120°C for 20 minutes. The electrical characteristic was measured by taking: the voltage current at a current 1 mA and 10 mA. Then the nonlinear coefficient α can be estimated by the following equation:

$$\alpha = \frac{1}{\log\left(V_{10mA}/V_{1mA}\right)}$$

(1)

where V_{1mA} and V_{1mA} represent the voltages at 1 and 0.1 mA respectively.

3.   RESULTS AND DISCUSSION

XRD patterns of the investigated samples are given in Fig.1. For all sample, five phases were indentified: the ZnO phase, $Mn_{1.5}Cr_{1.25}Sb_{0.25}O_4$ phase, $CrMn_{1.5}O_4$ phase, $CoCr_2O_4$ phase and $BiMnO_3$ phase. The intensity was similar for all samples. Therefore the milling speed not affects the phase composed as was confirmed by XRD.
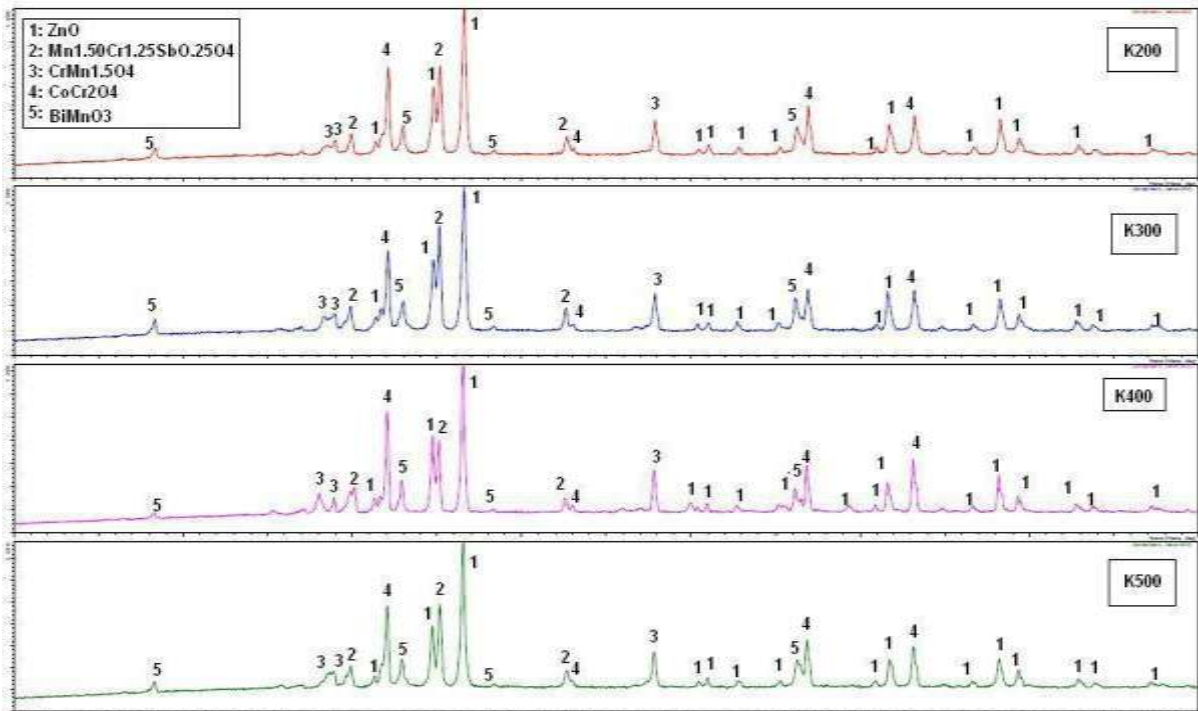
Fig 1: XRD pattern of ZnO- Bi_2O_3-based varistor ceramics milled at 200 rpm, 300 rpm, 400 rpm and 500 rpm.

Fig 2 shows I-V characteristics of the sample for each milling speed. For the sake of comparison, data are presented in voltage-current relation. It is clearly shown that the breakdown curve shift to higher voltage with increasing milling speed but at 400 rpm, the curve decrease. In the present varistor system, as the chemical properties of the grain boundaries in relation to double Schottky barriers can be regarded as essentially consistent irrespective of the composition, breakdown voltage data are thought primarily related with the grain size [3]. Therefore the higher milling speed, the particle size formed decrease but at 400 rpm the varistor tends to formed agglomerate and the particle size not homogenous.
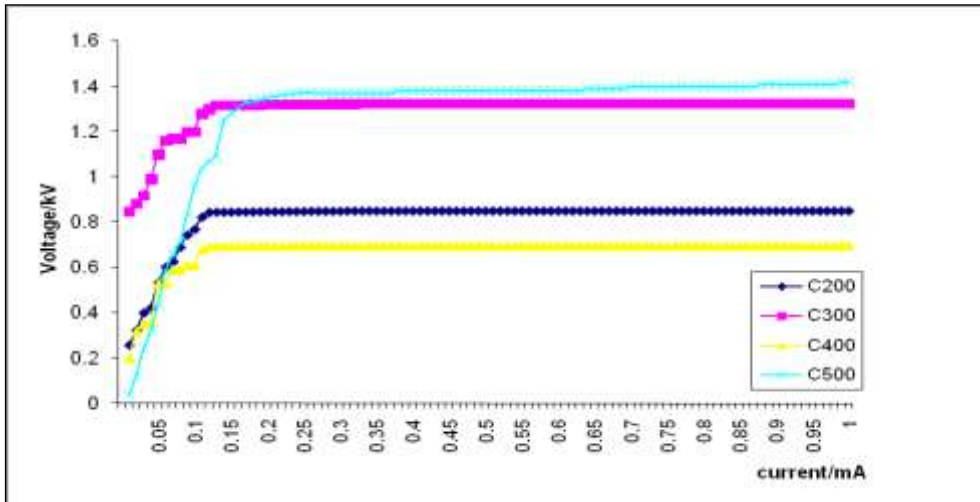
Fig. 2: I-V characteristic of ZnO- Bi_2O_3-based varistor ceramics milled at 200 rpm, 300 rpm, 400 rpm and 500 rpm.

Breakdown voltage and nonlinear coefficient (α) evaluated from the results of I-V measurement are presented as functions of nonlinear coefficient (α) and milling speed (rpm) shows in Fig. 3. Nonlinear coefficient was decrease with the increasing milling speed because it strongly dependent on grain size. The ability to control breakdown voltage and α are important for device applications, and this may be achieved by the addition of multiple dopants and by control of the ceramic fabrication conditions [4]. So by controlling the milling speed during mixing process, varistor with good nonlinear coefficient can be produce. The optimum milling speed for produce a good varistor was at 200 rpm and 300 rpm which is 23.4 and 23.4. The value not much different shows that the varistor powder can mix homogenously at low speed compare to high speed. At 500 rpm, the α value is the lowest value.
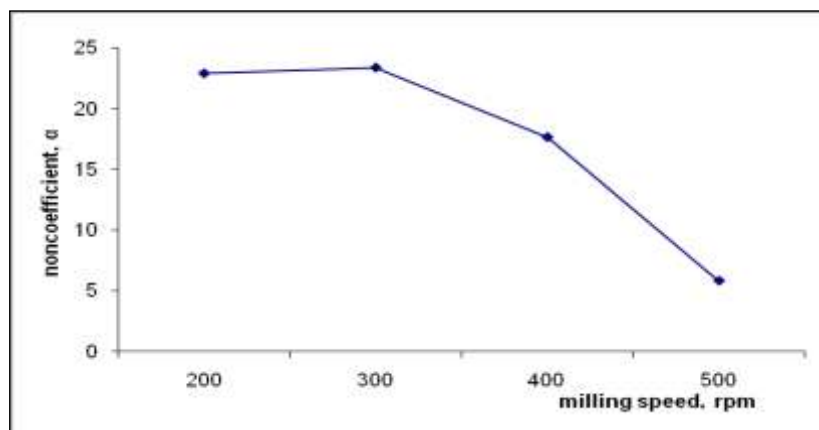
Fig. 3: Nonlinear coefficient for varistors milling at 200 rpm, 300 rpm, 400 rpm and 500 rpm.

4.   CONCLUSION

The studied milling speed at lower milling speed which are 200 rpm, 300 rpm n 400 rpm led to desired α. At the lower milling speed the α value was higher and decrease with increasing milling speed. The explanation proposed here is that varistor powder can mix homogenously at lower speed using planetary mill and the new phase composed not affect by the milling speed.

5.   REFERENCES

12.   Lin, C.C., Lee, W.S., Sun, C.C., & Whu, W.H. (2007). The influences of bismuth antimony additives and cobalt manganese dopants on the electrical properties of ZnO-based varistors. *Composites part B:engineering,* 38, 338-344.

13.   Onreabroy, W., Sirikulrat, N., Brown, A.P., Hammond, C. And Milne, S.J. (2006). Properties and intergranular phase analysis of a $ZnO\text{-}CoO\text{-}Bi_2O_3$ varistor. *Solid State Ionics,* 177, 411-420.

14.   Kim, C.H and Kim, J.H. (2004). Microstructure and electrical properties of $ZnO\text{-}ZrO_2\text{-}Bi_2O_3\text{-}M_3O_4$ (M=Co, Mn) varistors. *Journal of the European Ceramic Society,* 24, 2537-2546

15.   Onreabroy, W., Sirikulrat, N., Brown, A.P., Hammond, C. and Milne, S.J. (2006). Properties and intergranular phase analysis of a $ZnO\text{-}CoO\text{-}Bi_2O_3$ varistor. *Solid State Ionics,* 177, 411-420.

16.   Bernik, S., Macek, S. and Ai, B. (2001). Microstructural and electrical characteristics of Y_2O_3-doped ZnO- Bi_2O_3-based varistor ceramics. *Journal of the European Ceramic Society,* 21, 1875-1878

17.   Viswanath, R.N., Ramasamy, D., Ramamoorthy, R, Jayavel, P. and Nagarajan, T. (1995). Preparation and characterization of nanocrystalline ZnO based materials for varistor applications. *NonoStructured Materials,* 6, 993-996

18.   Rubia de la, M.A., Peiteado, M., Fernandez, J.F. and Calallero, A.C. (2004) Compact shape as a relevant parameter for sintering ZnO- Bi_2O_3-based varistor. *Journal of the European Ceramic Society,* 24, 1209-1212

The Effects of Cellulose and Cellulose Acetate as Fillers on the Properties of Biodegradable Low Density Polyethylene (LDPE) Composite

Halimatuddahliana, M. W. Adnin[*], D. M. Putri, and E. Eliana

Department of Chemical Engineering, Faculty of Engineering, Universitas Sumatera Utara
Jalan Almamater Kampus USU Padang Bulan Medan 20155 Sumatera Utara, Indonesia

*Corresponding author: wahyu.adnin@yahoo.com

Abstract: *The effects of cellulose and cellulose acetate as fillers on the properties of biodegradable low density polyethylene (LDPE) composite were investigated. Composites were prepared in several filler loading viz. 5, 10, and 15% using an extruder at processing temperature of 125^0C. Results indicate that the use of 10% of filler loading have shown the highest tensile and impact strengths of composites for cellulose acetate filler and the use of 5% of filler loading have shown the highest tensile and impact strength of composite for cellulose filler. In term of type of filler, the use of cellulose acetate shows higher tensile strength, elongation at break, and impact strength in all filler loading compared to similar cellulose/LDPE composites. It is also shows that the rates of degradation cellulose acetate/LDPE composites were faster than the cellulose/LDPE composites in all filler loading.*

Keywords: Cellulose, cellulose acetate, biodegradable

1. INTRODUCTION

Increasing number of natural fillers as reinforcement of polymer composites in recent years was strongly influenced by environmental issues, production costs and high competition. This increases the interest to conduct a research in the use of industrial and agricultural wastes, which is have great benefits. The unification of several types of fillers, into a polymer matrix of composites can be used to produce polymers with different properties. Today, researches using fillers derived from agricultural products or industrial waste as an alternative to inorganic fillers in rubber and plastic become a big attention.

Polymer composites are growing today, competing with the metal and ceramic matrix composites. Variety of composite processing continues to be driven and directed to the targets products are as expected. Commercial polymer composites have been generally using thermoset polymer materials. Limited supply of raw materials results this material is relatively expensive compared to thermoplastic polymers that are available. Thermoplastic polymers, such as low density polyethylene (LDPE) is a commercial polymer composite which is relatively cheaper compared to thermoset polymers that are available. LDPE is a

thermoplastic polyolefin that is, inexpensive, and can be recycled, but in the mixing process requires heat. The excess of LDPE as a matrix, include : easy processing, lower temperature processing compared to other polymers as well as more applicable in their use[1].

The use of natural filler in composite materials evolve along with development in technology, economic factors, and environmental issues. In Indonesia, cellulose and cellulose acetate can be obtained from various sources, especially of raw materials derived from oil palm empty fruit bunches[2].

In this era, the ability of composites to decompose in nature become very important. Composite wastes are very difficult to decompose naturally and this cause composites become the biggest waste on this earth. Therefore, researches to discover a composite with high rate of biodegradation become a great challenge to all researches, particularly in material or polymer[3].

The process of blending LDPE with cellulose (C) are less likely to take place homogeneously because of the nature of the two materials having different in polarity. Meanwhile, the use of cellulose acetate (CA) as filler in LDPE is expected to take place homogeneously because of the nature of both materials having the same polarity, which is hydrophobic. Furthermore, to produce a composite with good mechanical properties, it should not be given or added coupling agent on composite mixture of LDPE and cellulose acetate. In addition, cellulose acetate is good to be used as filler in LDPE due to cellulose acetate has good color, good clarity, and good durability of plastic film[4].

Based on the above, comes the desire to conduct a research on the effects of cellulose and cellulose acetate as fillers on the properties of biodegradable low density polyethylene (LDPE) composite.

2.   EXPERIMENTAL

2.1   Materials

Low density polyethylene was purchased from PT. Surya Batam Plastik. Cellulose and cellulose acetate used was supplied by Pusat Penelitian Kelapa Sawit (PPKS), Medan, Indonesia. Cellulose contains 1,15% lignin, 73,91% holocellulose and 49,75% α-cellulose. In the other hand, cellulose acetate as another filler, has 1.761 of degree of substitution and 32.098 % of % acetil[5].

2.2   Preparations and processing

Composites were prepared in several filler loading viz. 5, 10, and 15% using an extruder at processing temperature of 125^{0}C. Table 1 shows the detailed composition of LDPE/Cellulose/Cellulose Acetate blends in this study.

Table 1: Blend Ratio of LDPE/Cellulose/Cellulose Acetate.

Blend No.	LDPE (% wt)	Cellulose (% wt)	Cellulose Acetate (% wt)
1	100	0	0
2	95	5	0
3	90	10	0
5	95	0	5
6	90	0	10
7	85	0	15

Low density polyethylene and cellulose in all filler loading were first loaded into an extruder at processing temperature 125°C. Composites for testing were compression molded using hot press. The press was pre-heated at 125°C for 5 minutes prior for moulding and this was followed by 5 minutes compression time at the same temperature. The specimens were allowed to cool under pressure for another 5 minutes. The same procedure was adopted for low density polyehylene and cellulose acetate in all filler loading.

2.3   Tensile properties

Tensile tests were carried out according to ASTM D638 using a Testometric tensometer. 6 mm width and 1 mm thick dumbbell specimens were cut from the moulded sheets with a dumbbell cutter. The tensile test was performed at constant rate (20 mm/min) at room temperature (25°C). The results were quoted based on the average value of three specimens for each blend system.

2.4   Impact properties

Impact teste were carried out according to ISO 180 using an Izod impact tester (notched izod). Specimen from moulded for impact test is 80 x 10 x 4 mm with the depth of the notch is 8 mm. the resulst were quated based on the average value of three specimens for each blend system.

2.5   Degredation properties

Degredation properties from the moulded sheets were cut with a dumbbell cutter. Specimen for degredation test is 3 x 3 x 1 cm. Degredation analysis of the resulting composites with all loading is done by planting in the soil with depth 20 cm and it is also done by hanging in open environment.

The rates of degradation composites were observed based on the weight reduction and confirmed by analysis of changes in functional groups with FT-IR.

3. RESULT AND DISCUSSION

3.1 Tensile Properties

The effect on the tensile strength of LDPE/Cellulose/Cellulose Acetate blends is shown in Fig. 1. The maximum tensile strength of cellulose filler of LDPE/Cellulose composite was obtained from ratio of 95/5 and for the cellulosa acetate filler of LDPE/Cellulose Acetate composite, the maximum tensile strength was obtained from ratio 90/10. Both of those value was above the tensile strength of LDPE without any content filler.
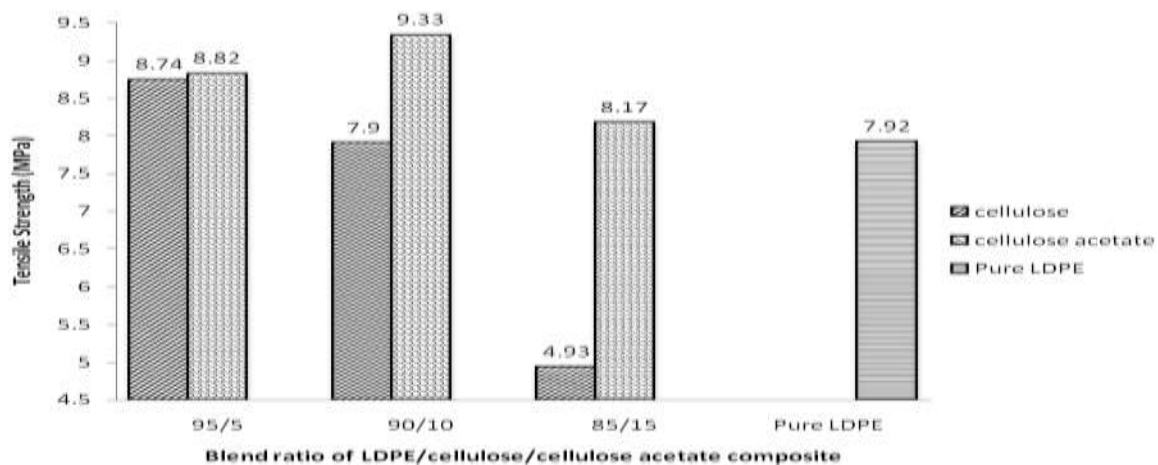
Fig. 1: The effect of fillers addition on tensile strength of LDPE/Cellulose/Cellulose Acetate blends.

The tensile strength of composites with cellulose filler decreased significantly with increasing filler content. The reduction is due to the present of lignin contains in cellulose that effects the less interaction between LDPE and cellulose and gives poor stress transfer between phases. It is also caused by low interfacial adhesion between the constituent phases in the blend. Another thing that can effects the decreasing in tensile strength is the distribution of filler content less evenly or the composites is less homogeneous[6]. On the other hand, the increase of tensile strength of LDPE/Cellulose Acetate compositewas obtained at ratio of 95/5 and 90/10. The enhancement in tensile strength was due to a same hidrophobicity properties of matrix and filler, which resulted in increased of interfacial bond of LDPE and cellulose acetate. The improvement of interfacial bond between LDPE and cellulose acetate produces a good distribution of stress transfer during stretching[7]. But at ratio 85/15, the tensile strenght of composite was having a reduction. It is because the amount of filler is excessive and trigger the agglomeration process itself so that the distribution of filler in matrix becomes non homogeneous.

The enhancement in tensile strenght of LDPE/cellulose acetate composites compared with LDPE/cellulose can be supported by FT-IR spectrum for both types of composites such as shown in Figure 2 and Figure 3.
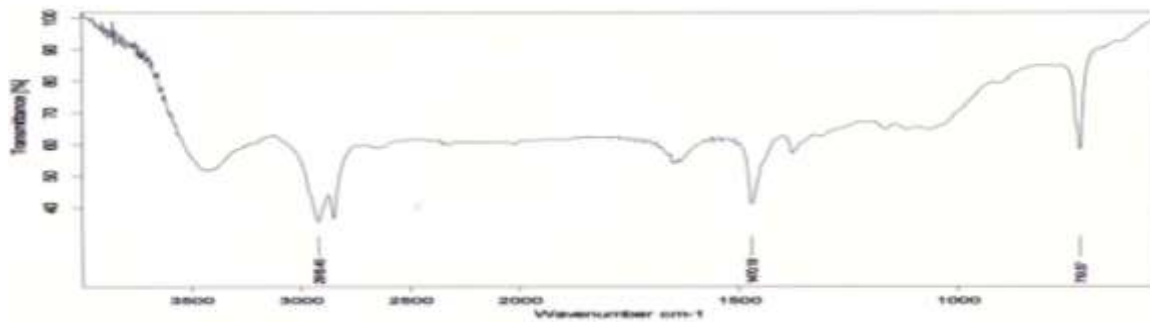
Fig. 2: FT-IR spectrum of LDPE/cellulose composite.
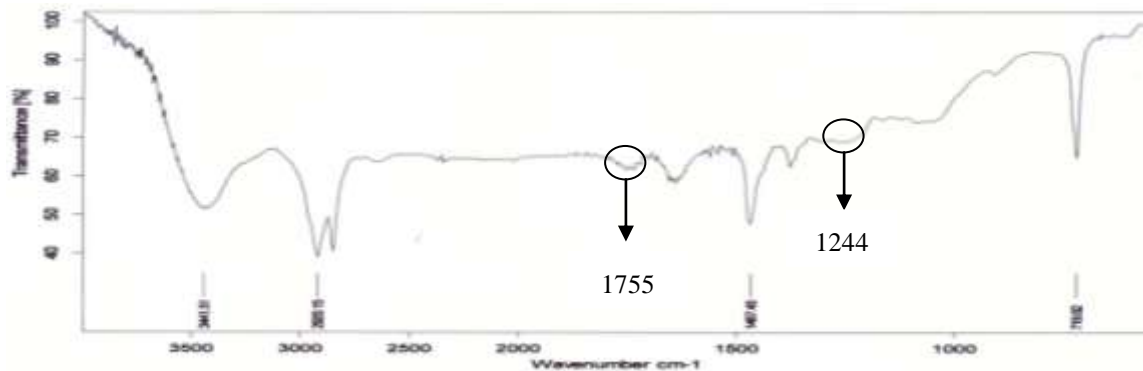
1755

1244

Fig. 3: FT-IR spectrum of LDPE/cellulose acetate composite.

In Fig. 3, appear functional group of acetate (C-C-O) at wave number 1244 cm^{-1} and also functional group of ester carbonyl (C=O) at wave number 1755 cm^{-1}, which is not shown in Fig. 2. This indicates that the properties of cellulose had changed in polarity. Cellulose was a polar compound, but after the acetylation process, cellulose became cellulose acetate, which is a non-polar compound.

Fig. 4(a) shows the SEM micrographs of surface breaking of LDPE/ cellulose composite of ratio 90/10 as well as Fig. 4(b) shows the SEM micrographs of surface breaking of LDPE/cellulose acetate composite of ratio 90/10.
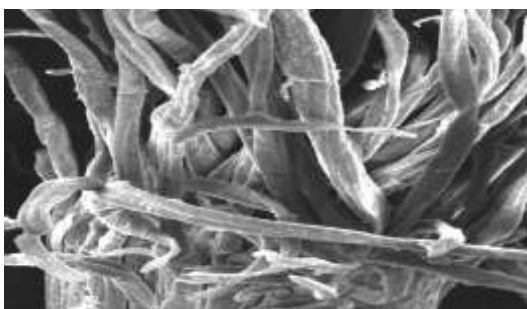
Fig. 4(a): SEM micrographs of surface breaking of LDPE/cellulose composite of ratio 90/10.
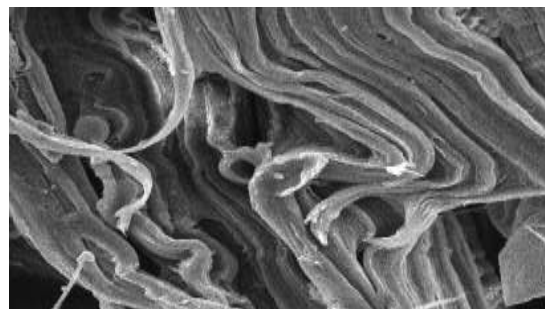
Fig. 4(b): SEM micrographs of surface breaking of LDPE/cellulose acetate composite of ratio 90/10.

Fig. 4(b) shows that the LDPE/cellulose acetate composite indicates a rejection at the time of tensile test occured. This suggest that this composite shows the increase of interfacial

bond. In Fig. 4(a), the LDPE/cellulose composite had no resistance at the time of tensile test occured. This is caused by the LDPE/cellulose composite shows less increase of interfacial bond compared with LDPE/cellulose acetate.

Fig. 5 shows the effect of elongation at break for LDPE/Cellulose/Cellulose Acetate blends. Both of the composites with cellulose and cellulose acetate as fillers are having reduction along with addition of fillers content. The reduction in elongation at break at LDPE/cellulose composite is higher against at LDPE/cellulose acetete. It is again due to poor compatibility between LDPE/Cellulose composite compared with LDPE/Cellulose Acetate. The lowest elongation at break for cellulose was obtained in ratio 85/15. This is due to the nature of cellulose which has a high stiffness properties then LDPE. The properties of high stiffness is caused by a considerable amount of lignin in the cellulose content. The higher content of cellulose with in the composite, the more it will increase the stiffness properties of composites so that will decreased the deformabilty of the LDPE/Cellulose blends[8].
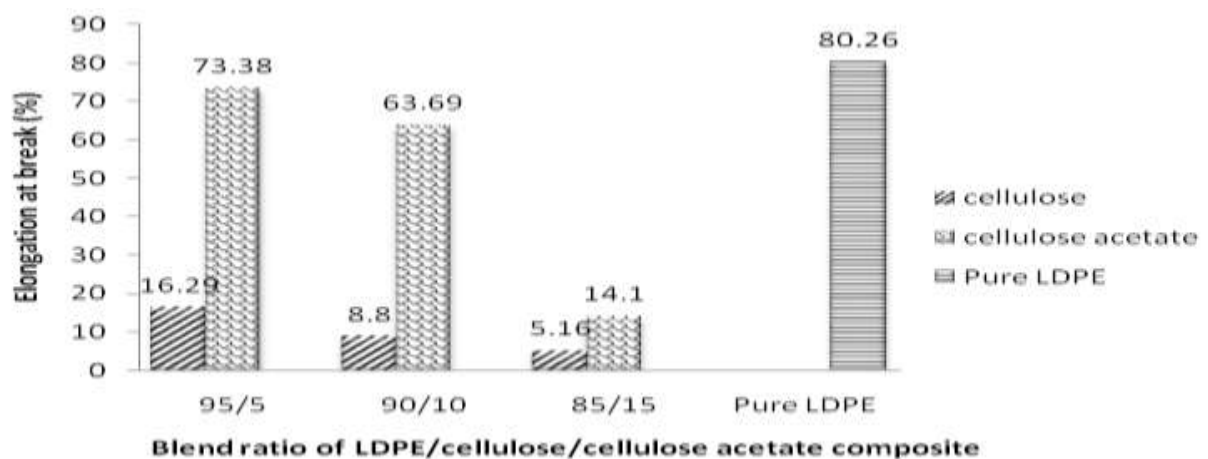
Fig. 5: The effect of fillers addition on elongation at break of LDPE/Cellulose/Cellulose Acetate blends.

Meanwhile the lowest elongation at break of LDPE/cellulose acetate was obtained in ratio 85/15. Cellulose acetate has higher percentage of elongation campared with cellulose in all loading of fillers. It is due to the least amount of lignin content in cellulose acetate. The acetylation process of cellulose makes cellulose acetate having same polarity with the matrix so that produce a high interaction of surface[9].

3.2   Impact properties

Fig. 6 shows the effect of fillers content on the impact strenght of LDPE/Cellulose/Cellulose Acetate blends. The maximum impact strength of LDPE/cellulose composite was obtained from ratio 95/5.
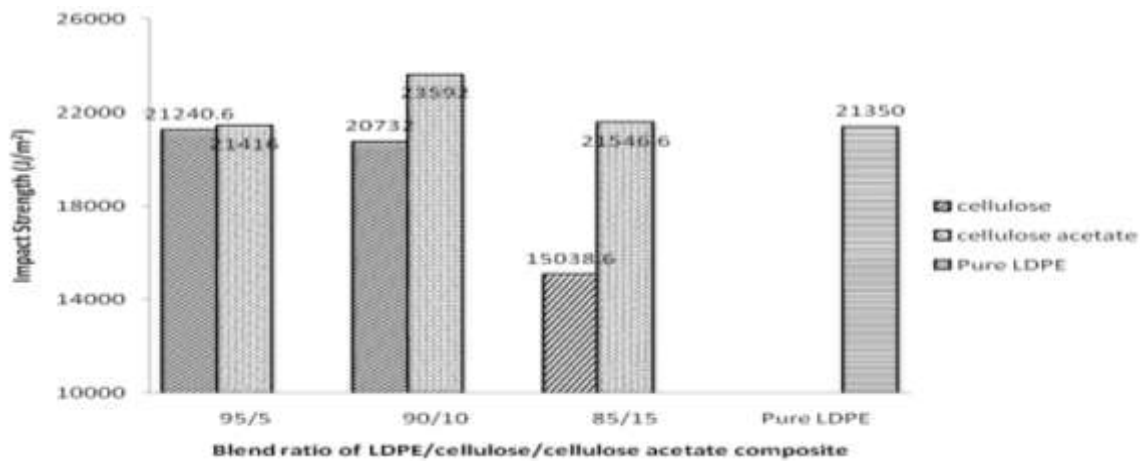
Fig. 6: The effect of fillers addition on impact strength of LDPE/Cellulose/Cellulose Acetate blends.

The impact strength of LDPE/cellulose composites is decreasing along with addition of cellulose as filler. The lignin in cellulose is believed to decrease the degree of cristallinity. Organic material such as lignin and hemicellulose which has an amourphous structure can reduce the degree of cristallinity in the composites (wikberg dan mauna). The effect of chemical structure on the polymer properties in which the crystalline polymers (in this case : LDPE) are generally harder, stronger and more resistant than amorfous polymers (in this case : cellulose)[1].

In addition of cellulose acetate filler, the maximum impact strength of was obtained in ratio 85/15. The impact strength of LDPE/cellulose acetate composite is increasing with addition of celluluse acetate as filler until the ratio 90/10. But on the ratio 85/15, the impact strengh was lower than that of ratio 90/10, but still, higher than that of ratio 95/5. It is due to the reduction amount of matrix whereas the amount of filler was increasing so that the interface of matrix and filler was no longer optimal[1].

3.3 Degradation properties

Degradation tests for the resulting composites were done in two ways, they were planting in the soil and hanging in open environment. Table 3 shows the percentage decrease in mass of speceimens after grown in soil and hanged on exposed environment.

Table 3: Percentage of decrease in mass of specimens after dagradation process.

Type of filler	Ratio (LDPE/filler)	Grown in soil (%)			Hanged on exposed environment (%)		
		10 days	20 days	30 days	10 days	20 days	30 days
Cellulose	95 : 5	0.356	0.446	0.448	0.400	0.536	0.573
	90 : 10	0.486	0.488	0.669	0.618	0.799	0.896
	85 : 15	0.526	0.625	0.678	0.718	0.964	1.217
Cellulose acetate	95 : 5	0.435	0.568	0.659	0.556	0.656	0.881
	90 : 10	0.575	0.801	0.897	0.663	0.713	1.121
	85 : 15	0.613	0.822	1.036	0.817	1.236	1.459

By hanging on exposed environment, the rate of degradation was faster compared by planting in soil. The main stage of degradation is the termination on the main chain to form fragments with low molecular weight (oligomers) that can be assimilated by microbes. Decrease in molecular weight caused by the chain termination of hydrolysis and oxidative. Hydrolysis occurs using the aquatic environment with the addition of enzymes or non-enzymatic coonditions. In this case, auto-catalysts, heat, or metal catalysts also cause hydrolysis. Oxidative terminations occurs because of the presence of oxygen, metal catalysts, UV light or enzymes[9]. It is clear that by hanging on exposed environment would cause the faster rate of degradation than by planting in soil because of all the factors that trigger the degradation of composite contain in an open environment[10]. Also, from the table we can see that LDPE/cellulose acetate composite shows higher percentage of decrease in mass of all ratio compared with LDPE/cellulose composite. This shows that cellulose acetate, use as a filler in LDPE, are more degradable than cellulose.

FT-IR characterization was done as well to support the explanation earlier. Figure 7 and 8 show FT-IR spectrum of LDPE/cellulose acetate composite of ratio 90/10 after degradation process.
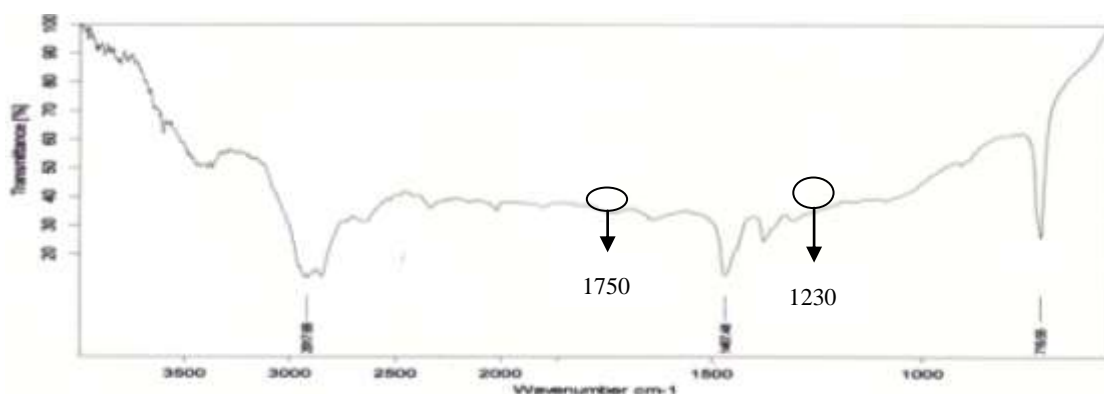
Fig. 7: FT-IR spectrum of LDPE/cellulose acetate composite of ratio 90/10 after hanging for 30 days.
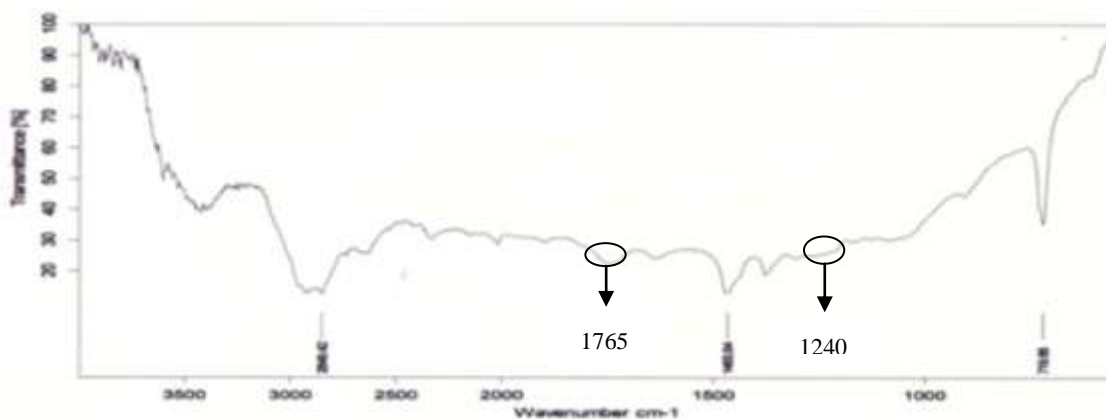
Fig. 8: FT-IR spectrum of LDPE/cellulose acetate composite of ratio 90/10 after planting for 30 days.

The functional groups that changed after degradation process in LDPE/cellulose acetate are ester (C=O) and acetates (C-C-O). The ester functional groups were shown at wavenumber of wavenumber of 1750 cm^{-1} (Fig. 7) and wavenumber of 1765 cm^{-1} (Fig. 8). The acetate functional groups were shown at wavenumber of 1230 cm^{-1} (Fig. 7), and wavenumber of 1240 cm^{-1} (Fig. 8).

The intensity of a functional group can be seen from the FT-IR spectrum of functional group itself, where the high intensity of a functional group is shown by the form of a sharp peak, whereas a blunt peak indicates that the intensity of a functional group had been reduced[11]. The overall FT-IR spectrum figures of LDPE/cellulose acetate composites of ratio 90/10, LDPE/cellulose acetate composite which was hanged in exposed environment shows the highest rate of degradation compared with LDPE/cellulose acetate composite which was planted. This can be seen from the blunt peak of two functional groups – esters and acetate – of the FT-IR spectrum in LDPE/cellulose acetate composite.

4.   CONCLUSIONS

The use of 5% of filler loading have shown the highest tensile and impact strength of composite for cellulose filler and the use of 10% of filler loading have shown the highest tensile and impact strength of composite for cellulose acetate filler. The higher result of tensile strength was shown by the composite with cellulose acetate as filler rather than cellulose, supported by FT-IR spectrum and SEM micrographs. For degradation test, LDPE/cellulose acetate composite shows faster rate of degradation than LDPE/cellulose composite in all filler loading. Also, degradation process by hanging on exposed environment are better than planted in soil.

5.   REFERENCES

1.   COWD, M. A., (1991), *KIMIA POLIMER*, TERJEMAHAN OLEH FIRMAN, H., ITB BANDUNG

2.   FIRDAUS, "*STUDI PEMBUATAN PULP DARI TANDAN KOSONG SAWIT DENGAN PROSES ETANOL*", TESIS MAGISTER, TEKNIK KIMIA ITB, 1998.

3.   SCHNABEL, W. (1981), BIODEGRADATION DALAM *POLYMER DEGRADATION, PRIINCIPLES AND PRACTICAL APPLICATIONS*, MACMILLAN PUBLISHING CO, INC., NEW YORK; 154 -176.

4.   KIRK, OTHMER (1964), *KIRK-OTHMER ENCYCLOPEDIA OF CHEMICAL TECHNOLOGY* 4TH ED. VOL 22, JOHN WILEY & SONS, INC. NEW YORK, 1964.

5.   Research Centre of Coconut Palm (2010), Medan, Indonesia.

6.   JOSEPH P.V., JOSEPH, K., THOMAS, S., PILLAI, C.K.S., PRASAD, V.S., GROENICKS, G. AND SARKISSOVA, M. 2003. THE THERMAL AND CRYSTALLIZATION STUDIES OF

SHORT SISAL FIBER REINFORCED POLYPROPYLENE COMPOSITES. *COMPOSITE APPLIED SCIENCE AND MANUFACTURING*. 34: 253-266.

7. KIM, H, S., LEE, B, H., CHOI S, W., KIM, S., DAN KIM, H, J., (2007). THE EFFECT OF TYPES OF MALEIC ANHYDRIDE-GRAFTED POLYPROPYLENE (MAPP) ON THE INTERFACIAL ADHESION PROPERTIES OF BIO-FLOUR-FILLED POLYPROPYLENE COMPOSITES, *COMPOSITES*, 38 (A) : 1473 – 1482.

8. OKSMAN, K., DAN CLEMONS, C., (1998), MECHANICAL PROPERTIES OF IMPACT MODIFIER POLYPROPYLENE-WOOD FLOUR COMPOSITES, *JOURNAL APPL. POLYM. SCI*, 67 : 1503 – 1513.

9. SAIN, M., P., SUHARA, S., DAN LAW, A. B., (2005), INTERFACE MODIFICATION AND MECHANICAL PROPERTIES OF NATURAL FIBER-POLYOLEFIN COMPOSITE PRODUCTS, *JOURNAL OF REINFORCED PLASTIC AND COMPOSITES*, 24 (2) : 121-130.

10. SMITH, (2005). *BIODEGADABLE POLYMER FOR INDUSTRIAL APLICATIONS*, WOODHEAD PUBLISHING. LTD AND CRC PRESS. CAMBRIDGE: ENGLAND.

11. HALIMATUDDAHLIANA, (2005), *CHARACTERIZATIONS AND PROPERTIES OF POLYPROPILENE/ETHYLENE – PROPYLENE DIENE TERPOLYMER/NATURAL RUBBER (PP/EPDM/NR) TERNARY BLENDS*, UNIVERSITI SAINS MALAYSIA.

Comparison between Friction Stir Spot Welding and Riveting in Aluminum Alloy

M. Zemri[1,*], B. Bouchouicha[1], M. Mazari[1] and A. Imad[2]

[1]Materials Laboratory - University Djillali Liabes, BP89, Larbi Ben Mhidi, 22000 Sidi Bel Abbes - Algeria
[2]Mechanical Laboratoty of Lille, Cité Scientifique 59655 Villeneuve d'Ascq- France

*Corresponding author: mzemri@univ-sba.dz, mzemri@gmail.com

Abstract: *Several studies have been conducted for the comparison between riveting and conventional spot welding of structures. Since its invention by TWI in 1991, the Friction Stir Welding (FSW) process has involved users of aluminum alloys, because without melting, it enables welding of high strength alloys, previously unusable due to their difficult weldability with traditional methods. The main sectors concerned are; aerospace industry, shipbuilding, rail and automotive.*

The first of this work is the determination of optimal parameters for a Friction Stir Welding and the second is to examine and compare the mechanical properties and fatigue behavior of structures using riveting and Spot Friction Stir Welding.

It was found that the mechanical properties and fatigue behavior were better for welding FSW compared to a conventional riveting. More, this technique is simple, and physically clean. Its low energy requirement low running costs give it advantages in joining thin materials, and eventual recycling is much easier than with riveting joints.

Keywords: Experimental study, aluminum alloy, spot friction stir welding, riveting

1.   INTRODUCTION

In aerospace industry, shipbuilding, rail and automotive, we always seek for weight saving, a better corrosion resistance and improved characteristics. This led to making of new aluminum alloys and the development of new methods of assembly.

Many elements produced from these aluminum alloys, by stamping, moulding, extrusion, forging…, must be joined to make structures but unweldable with traditional methods. Therefore aluminum alloys with very high mechanical strength or the molded alloys were mainly assembled in a mechanical way by bolting or riveting.

Friction Stir Welding (FSW) is a solid-state joining process developed. Since its invention by The Welding Institute [1] (TWI) in 1991, the process has involved users of

aluminum alloys, because without melting, it enables welding of high strength alloys, previously thought to be unweldable with traditional methods.

Compared to traditional fusion welding techniques, FSW offers higher mechanical properties, simplified processing, fewer weld defects, and reduced weld distortion and residual stresses [2, 3].

Recently, a new technology of spot welding was developed by Mazda Motors Corporation and Kawasaki [4,5], using the Friction Stir Welding technique and was called Friction Stir Spot Welding (FSSW) or Friction Spot Joining (FSJ) [6,7,8]. Since, riveting was replaced by this process for, initially, all the advantages which it has and, then, for lightening in weight of the assembled structures.

Several studies have been conducted for the comparison between riveting and conventional Spot Welding of structures (RSW) [9, 10].

To evaluate the potential of friction Spot Stir Welding (FSSW) as a replacement for conventional spot welding for construction, a study of comparison between Friction Stir Spot Welding and riveting in aluminum alloy was conducted after the determination of optimal parameters.

The shape of the tool and specially the probe has a great influence on the mechanical strength of the joint of welding, due to thermal and mechanical stresses suffered by the material during welding. These stresses depend on the material and the choice of parameters such as geometry, positioning and inclination of the tool (1 à 3°), speed, depth of penetration and the force applied by the probe and its shoulder.

FSSW was performed using a welding tool designed in figure 10.We conducted experiments under *quasi-static* and *cyclic loading* conditions.

2.   PRESENTATION OF THE PROCESSES

2.1.   FSW process

2.1.1.   Principle

The welding process "Friction Stir Welding" takes again the principle of welding friction in rotation but it however has the effect of applying to all the types of parts, punts, sheets or massive. It is composed in three stages. First of all, a specific tool is put in fast rotation and comes to rub on the two parts to assemble. The friction of the tool on the parts causes a "softening" of matter which enters a pasty phase. The tool penetrates then in the mating plane, the interface between the parts to be welded and closely mixes the matters of the two parts by a combined operation of forging and extrusion of metal. After a time, the tool

advances linearly along the joint. Schematic diagram of the FSSW process is given in figure 1.
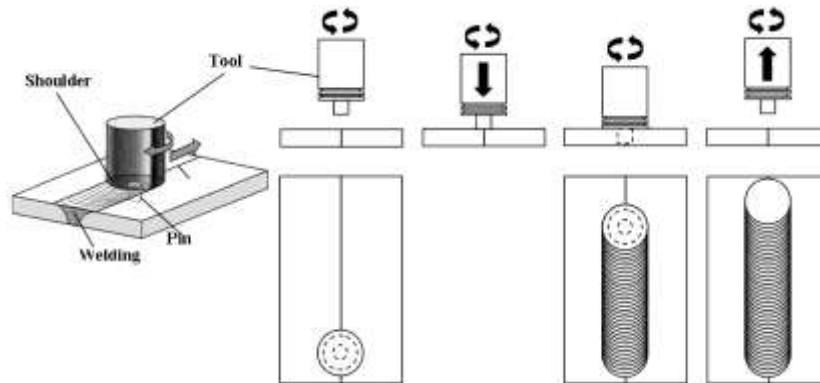
Fig. 1: Schematic diagram of the FSW process.

By making a transverse section we will notice three zones:
The Heat Affected Zone (HAZ), the Thermo-Mechanically Affected Zone (TMAZ) and finally the Dynamically Recrystallized Zone (DXZ).
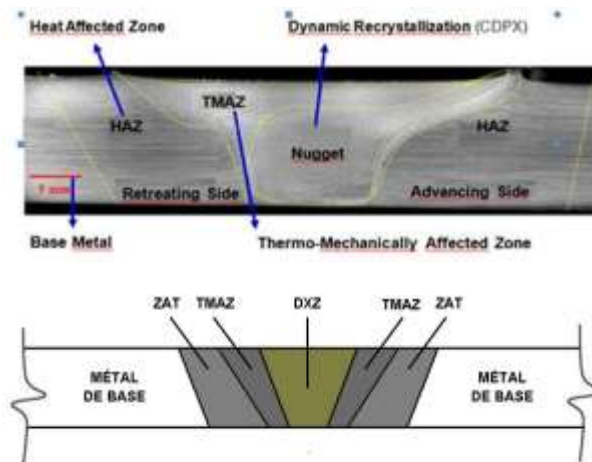
Fig. 2: Cross section of a welded joint.

2.1.2. Advantages of the process
- The process is ecological; it does not generate smoke or radiation.
- Operating in pasty phase, there is no fusion of the matter and the deformations are weak. The problems encountered during welding by the traditional processes (blisters, hot cracking, inclusions) are decreased considerably, even disappear completely.
- Since the temperatures reached remain lower than the melting point we have good mechanical properties compared to the majority of the traditional processes of welding
- Simple and effective process

414

- Welding of aluminum alloys not easily weldable by the traditional processes
- Welding of copper and its alloys, alloys of magnesium, zinc, titanium and its alloys, steels….
- Possibility of heterogeneous assemblies; Aluminum/copper, Aluminum/Steel….

2.2   FSSW process

The Friction Stir Welding Spot (FSSW) or Friction Joining Spot (FJS) is the FSW process but in specific use. Schematic diagram of the FSSW process is given in Fig. 3.
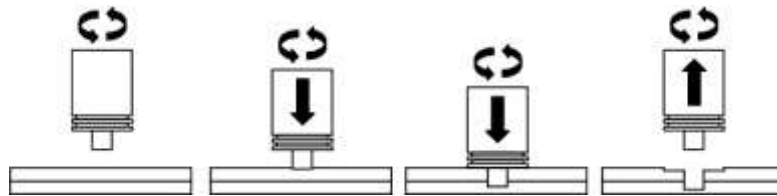
Fig.3: Schematic diagram of the FSSW process.

A tool with a pin in fast rotation is initially plunged in sheet, when the shoulder is in contact with the upper surface we apply a load from top to bottom. The load and the speed are maintained during a time to produce heat of friction, the material becomes soft. Finally, the tool is extracted.

This process allows an assembly by solid way, which removes the defects related to solidification and gives lower internal stresses lower. However, one of the *disadvantages of FSSW* joint is that probe *hole* inevitably remains at the centre of the weld nugget.
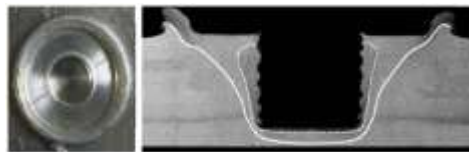
Fig. 4: Macroscopic aspect of *FSSW* joint with the hole left by the pin.

2.   EXPERIMENTAL PROCEDURES

The experiments were undertaken under static and cyclic loading. The assembly by FSSW process was carried out on a vertical milling machine, Fig. 5.
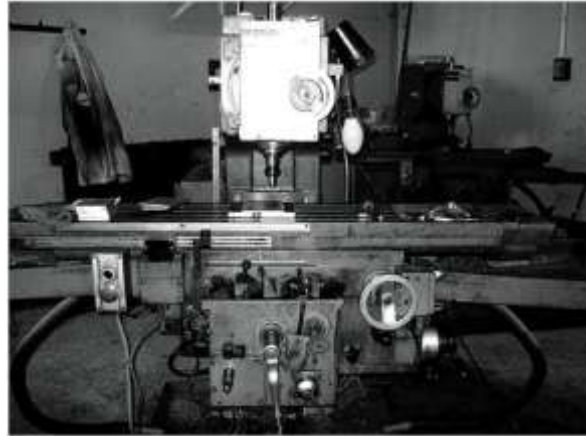
Fig. 5: Milling machine.

Lap-shear specimens are two 20x140 mm sheets with 20x20 mm overlap area, shown in figure 6. Figures 7 and 8 show a lap-shear specimen with a spot friction weld and rivet.
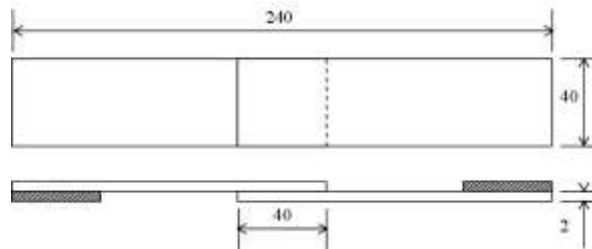
Fig. 6: Dimensions of lap-shear specimen (D1002).

Fig. 7: Lap-shear specimen with a spot friction weld.

Fig. 8: Lap-shear specimen with rivet.

Fatigue and quasi-*static tests* were carried out using an Instron Universal Testing Machine 8516. The first tests with a frequency of 10 Hz and a stress ratio, R = 0.1 and stopped with separation of sheets or even before when the displacement of the grips exceeds 5 mm then we have *Nr,* the number of cycle to *fatigue failure*. The second tests at crosshead speed of 0.5 mm/min and terminated when sheets separated. The load and displacement were simultaneously recorded during the testing.

2.1   Materials used

The material used is aluminum alloy 6060-T5. This alloy has very good welding characteristics and could be welded by all of the common welding techniques. Mechanical properties and chemical composition are given in tables 1 and 2.

Table 1: Chemical composition of 6060-T5 Aluminium alloy.

6060T5	%	Si	Fe	Cu	Mn	Mg	Cr	Zn	Ti
	Min	0.03	0.10	0.10	0.10	0.35	0.05	0.15	0.10
	Max	0 60	0.30			0.60			

Table 2: Mechanical properties of 6060-T5 Aluminium alloy.

Youg's Modulus (MPa)	Tensile Strength (MPa)	Ultimate Tensile (MPa)	Elongation (%)	Poisson's Ratio
69500	110	150	14	0.33

Density (g/cm^3)	Melting Range (°C)	Thermal conductivity (W/M°C)	Specific Heat Capacity (J/Kg°C)	Hardness (HV)
2.70	605-665	200	945	90

We used a standard rivets in aluminum alloy with 8 mm diameter, Fig. 9.

Fig. 9: Standard rivet.

2.2. Welding Tool

A tool of X210CR12 steel with a shoulder of 14 mm diameter and a pawn of 3.95 mm length and 5 mm diameter was used, Fig. 10.

Fig. 10: Welding tool.

2.3. Welding parameters

The welding parameters used in this investigation are the results of M. Merzoug [11]; 16 mm/mn for the welding feed rate and 1000 rpm for the tool rotating speed.

3. RESULTS AND DISCUSSIONS

The aim of this work is to make a comparative study between Friction Stir Spot Welding and riveting in the same material.

We conducted experiments under quasi-static and cyclic loading conditions based on the experimental observations.

3.1. Tensile strength test

The experiments were conducted on several specimens. The tensile tests gave the following results:
The corresponding load to σ_e, Fe = 3.0 kN for the welded joint and 2.5 kN for the riveted joint and the corresponding load to σ_m, Fm = 3.6 kN for the welded joint and 3.2 kN for the riveted joint.

Fig. 11 shows the specimens after tensile tests.

Fig. 11: Specimens after tensile tests.

Fig. 12 shows a typical load–displacement curve of a spot friction weld and riveting. The average failure load for tested specimens is 3.58 kN for a spot friction weld.
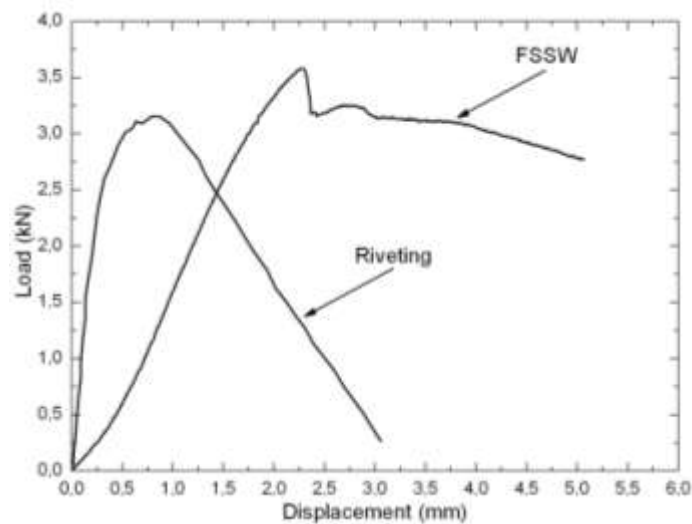
Fig. 12: Load vs displacement curve of FSSW and riveting.

3.2. Cyclic loading test

Starting from tensile tests, the fatigue tests were carried out with four loading rates (50, 60, 70 and 80% of Fe).

Figure 13 shows the specimens after cyclic loading tests.

Figure 13: Specimens after cyclic loading tests.

The failed spot friction welds under cyclic loading conditions with the fatigue lives from 1×10^5 to 6×10^6 for a maximum load of 1.5 kN, show a different failure mode.

Fig. 14 shows the experimental results for the spot friction welds in lap-shear specimens under cyclic loading conditions.
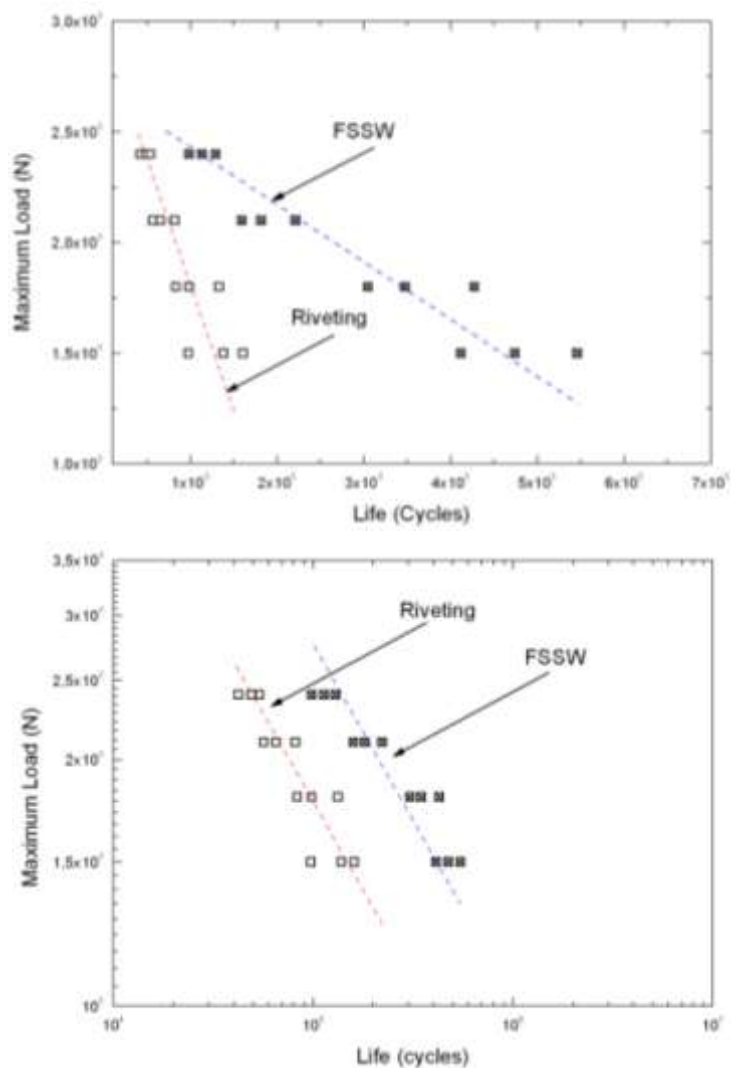
Fig. 14: Experimental results for the Spot Friction welds and riveting in lap-shear specimens under cyclic loading conditions.

4. CONCLUSION

419

After the determination of the optimum parameters of welding of aluminium alloy 6060-T5 for the resistance in static loading conditions, the aim of this work is to make a comparative study between Friction Stir Spot Welding with these parameters and riveting in the same material.

Based on the results obtained from the tensile and fatigue tests in the present investigation, the following conclusion can be drawn:
For our material, the structure assembled by the Friction Stir Spot Welding process has a better behavior in strength and fatigue than riveting method.

5. REFERENCES

1. Thomas, W.M. and al. (Dec. 1991). Friction Stir Butt Welding, *International Patent Appl.* No. PCT/GB92/02203 and GB Patent Appl. No. 9125978.8, U.S. Patent No.,460,317.
2. Knipstrom, K, E, & Pekkari, B. (Sept. 1997). Friction Stir Welding Process Goes Commercial, *Welding Journal*, vol. 76, pp. 55-57.
3. Anderson, C.G. & Andrews, R.E. (June 14-16, 1999). Fabrication of Containment Canisters for Nuclear Waste by Friction Stir Welding", *1st International Symposium of Friction Stir Welding,* Los Angeles, CA, (2005). Friction Joining, *JSAE Annual Congress.*
4. Sakano, R. Murakami, K. Yamashita, K. Hyoe, T. Fujimoto, M. Inuzuka, M. & al. (September 27–28, 2001). Development of Spot FSW robot system for automobile body members. In: *Proceedings of the 3rd international symposium of friction stir welding*, Kobe, Japan,
5. Iwashita, T. (August, 5, 2003). Method and apparatus for joining. *US Patent 6601751B2.*
6. Sakano, R, Murakami, K, Yamashita, K, Hyoe, T, Fujimoto, M, Inuzuka, M, & al. (2004). Development of spot FSW robot system for automobile body members. *Proceedings of the 3rd international symposium of friction stir welding*.
7. Fujimoto, M. Inuzuka, M. Nishio, M. Nakashima, Y. (2004). Development of friction spot joining (Report 1). Cross sectional structures of friction spot joints. *Preprint of the Natio Meet of Japan Weld Soc* (74): 4-5.
8. Fujimoto, M. Inuzuka, M. Nishio, M. Nakashima, Y. (2004). Development of friction spot joining (Report 2). Mechanical properties of friction spot joints. *Preprint of the Natio Meet of Japan Weld Soc*. (74): 6-7.
9. Krause, A. (1995). A Comparative Study of the Fatigue Behaviour of Spot Welded and Mechanically Fastened Aluminium Joints, *SAE Technical Paper 950710*.
10. Blundell, N. & Han, L. (2005). A Comparative Study between Self-Pierce Riveting and Spot Friction Joining", JSAE Annual Congress.
11. Merzoug, M. & al. (2009). Parametric studies of the process of friction spot stir welding of aluminum, *Materials and Design*.

Tensile and Flexural Properties of Rice Husk Reinforced Polyester Composites

Syed Azuan Syed Ahmad[1,*], Mohd Fahmi Abdullah[1], and Mohamad Juraidi Jamal[1]

[1] Department of Mechanical and Manufacturing, Universiti Kuala Lumpur Malaysia France Institute, 43650, Bandar Baru Bangi, Selangor, Malaysia

*Corresponding author: syedazuan@mfi.unikl.edu.my

Abstract: *Rice husk which is relatively inexpensive and abundantly available has the potential to be used as reinforcement in polymer composite. In this paper, tensile and flexural properties of rice husk polyester composites were evaluated by using different volume fractions of rice husk. The untreated rice husks were used as reinforcements in the polyester matrix. Composites plate with four different volume fractions of rice husk was fabricated by using hand-lay up techniques. The results showed the decreased tensile and flexural strength properties when increasing volume of rice husk, which indicates that ineffective stress transfer between the fibre and matrix.*

Keywords: Rice husk, tensile properties, flexural properties, polyester composites

1.   INTRODUCTION

The use of natural fiber as a reinforcement in polymer matrix composites has received increasing attention both by the academic sector and the industry. Natural fibers have many significant advantages over synthetic fibers. Currently, many types of natural fibers [1] have been investigated for use in plastics including flax, hemp, jute straw, wood, rice husk, wheat, barley, oats, rye, cane (sugar and bamboo), grass, reeds, kenaf, ramie, oil palm empty fruit bunch, sisal coir, water, hyacinth, pennywort, kapok, paper mulberry, banana fiber, and pineapple leaf fiber. They are environmentally friendly, fully biodegradable, abundantly available, renewable and cheap and have low density.

Mechanical properties of plant fibers are much lower when compared to those of the most widely used competing reinforcing glass fibers [2]. However, because of their low density, the specific properties (property-to-density ratio), strength, and stiffness of plant fibers are comparable to the values of glass fibers [3]. Unsaturated polyesters are extremely versatile in properties and applications and have been a popular thermoset used as the polymer matrix in composites [4]. They are widely produced industrially as they possess many

advantages compared to other thermosetting resins including room temperature cure capability, good mechanical properties and transparency.

Rice husk is one of the biomass materials abundantly available in Malaysia. Rice husk can be obtained easily from the rice mill plants which are rendered as a waste and can be explored as a potential reinforcement. Rice husks makes up about 20% of the rice (paddy) weight. Nowadays almost 70% of the rice husks are not commercially used [5]. According international estimates the rice demand by 2020 will growth to 780 million tons.The uses for rice husk are continually growing. Today it is increasingly used as biomass to fuel and co-fuel power plants. Other uses are in horticulture (soil aeration), animal bedding, and composites (WPC decking, materials & furniture).

The first such as a project in Malaysia using rice husk bio-composite was made possible by the Techno Fund grant, awarded by the Ministry of Science, Technology and Innovation in late 2007 [6]. In this project, natural fibre materials are compounded in larger composition and extruded with a certain amount of thermoplastics, while additives are used for ease of processing and for promoting the bonding between the otherwise incompatible natural fibre and thermoplastic components. Research in rice husk normally used in ground size / powder / filler form rather than used it directly like other natural fibers[7,8]. Therefore, in this paper, the main objective is to investigate the uses of ungrounded rice husk by addresses it performance by analyzing the effect of volume fractions on the composite tensile and flexural properties.

2. MATERIALS AND METHODS

Rice husk is the outermost layer of protection encasing a rice grain. It is a yellowish colour and has a convex shape. It is slightly larger than a grain of rice, thus length up to 7 mm are possible. Typical dimensions are 4 mm - 6 mm and it is lightweight in density. Rice husk was obtained from the rice mill located at Simpang Empat, Perlis, Malaysia.. The rice husk subsequently washed by using water to remove the dirt and later dried in the sunlight until all the moisture is removed from the rice husk. No chemical treatment has been made to the rice husk in an attempt to simulate the original strength of the rice husk. Polyester resin is obtained from Luxchem polymer under the trade name of Polymal 820-1-WPT(P). It appears as clear yellow colour liquid with viscosity of 400 cps and specific gravity of 1.13.

The composites with rice husk loading 5%, 10%, 15% and 20% of volume fraction were fabricated using hand lay up method with size mould of 200 mm (length, L) $\times$ 150 mm (width, W) $\times$ 3 mm (thickness, T). Initially, polyester resin and hardener were mixed with ratio 200 : 2 to form a matrix. Then, fibres were spread into mould and covered with the matrix. The composites were compressed until thickness of 3 mm was achieved. The curing time was about 24 hours applied near room temperature (25-30°C). Finally, composites plates were cut into the tensile and flexural specimens based on ASTM standard D638 – Type 1 and D790.

Fig.1: Rice husk.

3.   RESULTS AND DISCUSSION

3.1   Tensile Properties

Fig. 2 and 3 show the results of tensile strength and tensile modulus with the increase in percentage of rice husk volume fraction, respectively. Fig. 2 result showed that the tensile strength of pure polyester is much higher than reinforced composites. There is a decrease trend in the ultimate strength of the composite with the increase in the rice husk volume fraction. There was not much difference in tensile strength value from 5 vol% to 20 vol%. The highest tensile strength for rice husk reinforced polyester composites is obtained at 5 vol% with value of 10 MPa, in average. It was 75% reduction of tensile strength value compared to the pure polyester. The result from this current study is similar to the result obtained from by Ishak et al.,[7] which used ground rice husk /polyester composites. It has been observed that the increasing ground rice husk (sieved size of 120 -200 um) volume fraction resulted in 68% reduction tensile strength but not at tensile modulus whereby it showed increasing trends.
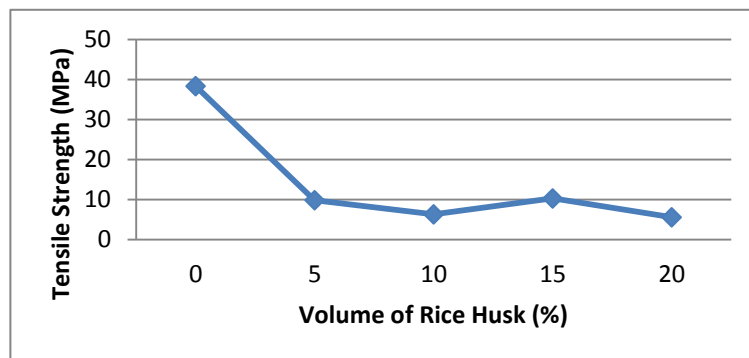
Fig. 2: Effect of rice husk volume fraction on tensile strength.

Fig. 3 shows the tensile modulus for the rice husk reinforced polyester composites. It shows the decreasing trend when increasing the rice husk volume content. From the two figures, the strength and modulus decreased as in increasing of rice husk volume fraction. The

decrement is due to poor interfacial bonding between rice husk and matrix. The brittleness of the rice husk also contributed to low mechanical strength because higher fibers contain higher possibilities of the fibers to sustain load. The concave shape of rice husk also contributed to the incomplete wettability or bonding between rice husk and polyester resin and also poor in their capability to support stress transmission in form of the matrix.
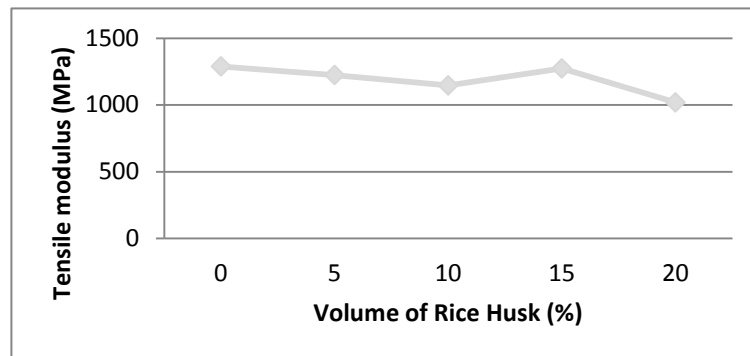
Fig. 3: Effect of rice husk volume fraction on tensile modulus.

Rozman et al.,[8] investigated the effect of rice husk loading, percentage of rice husk hydroxyl and rice husk size on the mechanical properties of rice husk / polyurethane composites found that the increased of rice husk loading also increased the tensile strength. It also mentioned that the size of rice husk also played a significant role in the properties, where smaller size RH produced composites with higher strength. However, based on the reduced size of rice husk in the previous study[7] the result of tensile strength is similar to the originally size / ungrounded rice husk in this present study.

3.2. Flexural properties

Fig. 4 shows that the flexural strength of all volume fractions used in rice husk polyester composites is lower than flexural strength of pure polyester resin. This indicates a poor adhesion between the rice husk and the resin. It can be found that 10 vol% of rice husk has the highest average value of flexural strength, which is 17 MPa, while rice husk with 5 vol% has the lowest average value of flexural strength, which is 14 MPa. It is also found that the composites have a lower flexural strength then the polyester alone and there is no significant effect on the rice husk content to the flexural strength of composites.
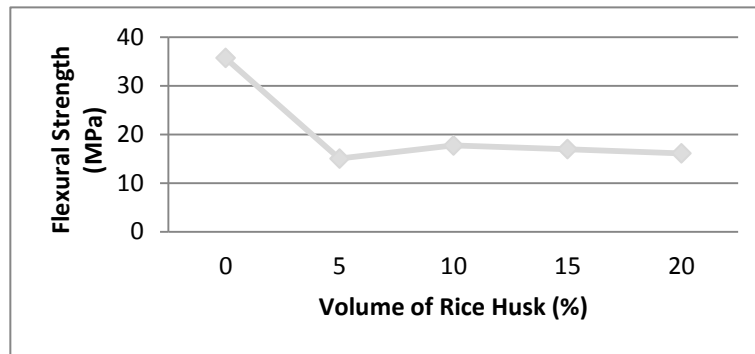
Fig. 4: Effect of rice husk volume fraction on flexural strength.

Fig. 5 shows the flexural modulus of the rice husk reinforced polyester composites. Flexural modulus tends to be decreased as the rice husk content is increased. This trend is also similar to the flexural strength of the rice husk reinforced polyester composites where by addition of rice husk, the value of flexural modulus is decreased. The reason is due to the alignment of the fibers and the interaction between rice husk – matrix. Nielsen [9] has reported that in the particulate filled composites due to poor stress-transfer at the filled-polymer interphases, discontinuities are created which generates weak structure.
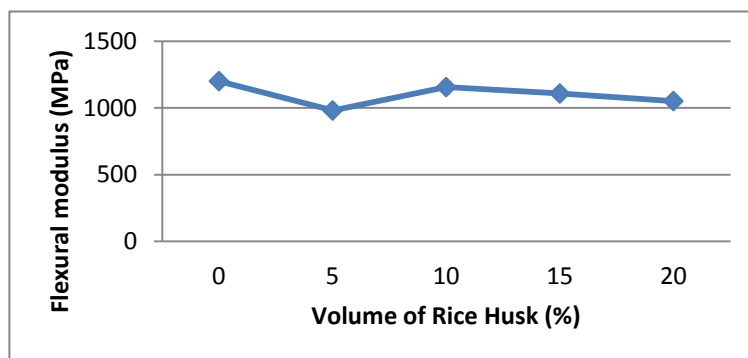
Fig. 5: Effect of rice husk volume fraction on flexural modulus.

4.   CONCLUSION

Tensile and flexural properties of rice husk reinforced polyester composites were investigated and presented. The results showed that tensile and flexural properties decreased as the rice husk volume increased. The optimum percentage of rice husk in polyester resin to obtain the highest tensile properties was found at 5 vol% but there was no significant effect of addition more than 5 vol% to the flexural properties of composites. The role of the matrix in a fiber reinforced composite is to transfer stress between the fibers, to provide a barrier against an adverse environment and to protect the surface of the fibers from mechanical abrasion. For rice husk cases, polyester resin didn't play it role in transferring the stress due to the adhesion problem. Beside that poor rice husk matrix interactions and rice husk dispersions are believed to be responsible for the poor ultimate strength properties. The fact that the strength of the composites specimens are not as strong as other natural fibers (jute, sisal, coir, hemp, flax)

reinforced polyester composites[10] it doesn't mean to necessarily exclude the potential use of rice husk as reinforcement in composites. Therefore, more studies are needed to determine the beneficial and cost effective applications of rice husk in composites.

5.   REFERENCES

19.   Bledzki, A.K. and Gassan, J. (1999). Composites reinforced with cellulose based fibers. *Prog. Polym.Sci.* 24, 221-274.

20.   Amar, K.M., Manjusri, M. and Lawrence, T.D. (2005). *Natural Fibers, Biopolymers, and Bio-composites. CRC Press,* Tailor & Francis.

21.   Wambua, P., Ivens, U. and Verpoest, I. (2003). Natural fibers: can they replace glass in fiber-reinforced plastics? *Compos. Sci. Technol.* 63, 1259- 1264.

22.   Sharifah, H.A., Martin, P.A., Simon, T.C. and Simon, R.P. (2005). Modified polyester resins for natural fiber composites. *Compos. Sci. Technol,* 65, 525-535.

23.   Rice husk Technology. Retrieved Nov 2011, from http://www.poerner.at.

24.   Ruhil, A. First-of-its-kind green furniture using *rice husk* set to enter market in 2010. Retrieved Nov 2011, from http://www.sirim.my/press.

25.   Ishak, A., Dayang, R.A.B., Siti, N.M. and Anita, R. (2007). Direct Usage of Products of Poly(ethylene terephthalate) Glycolysis for Manufacturing of Rice Husk/Unsaturated Polyester Composite. *Iranian Polymer Journal*. 16(4), 223 -239.

26.   Rozman, H.D., Ang, L.G., Tay, G.S.and Abu Bakar. A.(2003). The mechanical properties of rice husk–polyurethane composites. *Polymer – Plastic Technology Engineering, 42(3)*, 1237–1247.

27.   Neilsen, L.E.(1974). *Mechanical Properties of Polymers and Composites*, Marcel Dekker, New York.

28.   Ticoalu, A., Aravinthan, T., and Cardona, F. (2011). Experimental investigation into gomuti fibres/polyester composites. Centre of Excellence in Engineered Fibre Composites, Faculty of Engineering and Surveying, University of Southern Queensland, Toowoomba, Queensland, Australia. Retrieved Nov 2011, from http://www.usq.edu.au/ceefc.

Effects of MAPE Content on the Mechanical Properties of Red Balau (*Shorea Dipterocarpaceae*)/ LDPE Composites

Ruth Anayimi Lafia-Araga*, Aziz Hassan, Rosiyah Yahya, and Nor Masmira Abd. Rahman

Department of Chemistry, Faculty of Science, University of Malaya,
50603 Kuala Lumpur, Malaysia

*Corresponding author: rutharaga@yahoo.ca

Abstract: *One major problem with wood thermoplastic composites is the inherent incompatibility between the polar wood and the non polar matrix. To checkmate this shortcoming, maleic anhydride grafted polyethylene (MAPE) was employed as coupling agent in the compounding of Red Balau sawdust with low density polyethylene (LDPE). Tensile and flexural tests were conducted to assess the effects of MAPE content on the mechanical properties of the composites. Result revealed that MAPE enhances the properties of LDPE/Red Balau sawdust composites as better interfacial adhesion was achieved. Therefore, this presents a way of extending the applications of LDPE beyond its traditional uses.*

Keywords: Wood thermoplastic composites, coupling agents, interfacial adhesion, mechanical properties

1.   INTRODUCTION

Wood thermoplastic composites (WTC) have attracted a great deal of attention in recent times because of the specific advantages they offer over the classic mineral fillers. The need to have alternative low cost material with the attendant cut in manufacturing costs while improving the material properties are some of the driving forces behind the current trend. In addition, natural fillers have an added advantage of being environmentally friendly, abundantly available, renewable and relatively cheap. Furthermore, they have good strength to weight ratio because of their low density and posses good tribological properties [1].

Among the varieties of natural fillers, wood flour has drawn significant attention in the field of both fundamental research and industrial applications. However, due to the hygroscopic nature of wood arising from the presence of OH groups in their chemical components such as the cellulose and hemicellulose, water sensitivity and poor dimensional stability becomes a challenge [2]. In addition, as a result of the hydrophilic nature of wood, their compatibility with relatively hydrophobic polymer matrix is reduced. The consequence of this is a poor filler/matrix interfacial adhesion leading to poor mechanical properties, meaning that the resultant composites cannot be utilized to full capacity. This makes WTC

427

vulnerable to environmental attacks that can weaken it and reduce the lifespan. Therefore the use of WTC in structural/moisture challenging applications is limited.

In order to checkmate these problems, compatibilizers were used in WTC processing. This helps to induce bond formation between the wood particles and the polymer, thereby improving the interfacial adhesion [3]. Compatibilizer chemically links the hydrophilic lignocellulosic filler on one side while enhancing the wetting of the hydrophilic polymer on the other hand. Many studies have been conducted on the use of maleic anhydride polypropylene (MAPP) as compatibilizers in polypropylene-wood composites [4, 5, 6]. Meanwhile, research on the use of low density polyethylene (LDPE) in WTC has not received much attention. Nevertheless, polyethylene (PE) presents the highest volume of plastics used worldwide [7]. In addition, LDPE possesses desirable processing characteristics, such as low melting temperature, high melt strengths and relatively low viscosities [8]. Furthermore, red balau (balau merah) , a heavy hard wood, is one of the timber species that is abundantly available in Malaysia used in the construction and building industries [9]. Waste from this wood either from harvesting or processing can be useful when incorporated as fillers in WTC. Composites from red balau compounded with LDPE will extend the applications of LDPE beyond the traditional use in films and packaging. To the knowledge of the authors, research on WTC using red balau saw dust as fillers in LDPE has not been published. This work is therefore intended to compound red balau sawdust with LDPE using maleic anhydride polyethylene (MAPE) as compatibilizer for enhanced interaction between the non polar matrix and the polar wood particles.

2.   EXPERIMENTAL

2.1   Materials

Red Balau (*Shorea dipterocarpaceae*) saw dust was obtained from a local saw mill in the Klang Valley, Selangor, Malaysia. It was milled to between 40-100 mesh (400-150 µm) sizes using a locally fabricated mill. Commercially available LDPE (Titanlene LDI300YY), with a density of 920 kg/m^3, molecular weight of 350,000 – 380,000 g/mol and MFI 20 g/10 min as measured by ASTM D-1238, supplied by Titan Petchem (M) Sdn Bhd, Malaysia, was used as the matrix [10]. Maleic anhydride grafted linear low density polyethylene, MAPE (Orevac 18302N), 0.8% grafting, with a density of 920 kg/m^3 supplied by Arkerma, USA, was used as the compatibilizer.

2.2   Specimen Preparation

2.2.1   Compounding

LDPE, wood flour and MAPE were pre-mixed in different compositions in 200 g portions and compounded in a twin screw co-rotating extruder (Brabender KETSE 20/40 Lab Compounder, Germany, with screw diameter of 20 mm and L/D ratio of 40). Temperatures

were set between 150°C and 155°C along the barrel zones and the screw speed used was 250 rpm. The melt pressure varied between 34-39 bar depending on the wood content, while the die temperature was between 164-178°C. Vacuum venting was used to extract volatile compounds. The samples were extruded out through a circular die of 3 mm in diameter. The extruded strand was cooled in a water bath and pelletized. The pellets were then oven dried at 80°C for 24 hours and stored in sealed plastic bags for injection molding. Composites were prepared at 37% by weight wood flour loading based on the total weight of the composite and 0, 2, 4, 6, 8 and 10 wt % MAPE based on the total weight of LDPE in the composite.

2.2.2 Injection Molding

The pellets were injection molded into tensile (ASTM D-638) [11] test pieces using the BOY 55M injection molding machine at a barrel temperature of between 150°C and 155°C, an injection pressure of 100-120 bar and mould temperature of 25°C.

2.3 TESTING

2.3.1 Tensile Testing

Tensile tests were carried out using a universal testing machine (Instron 5569) equipped with a load cell of 50 kN and a mechanical extensometer according to ASTM D-638 [11]. Unconditioned specimens were tested at ambient conditions at a cross-head speed of 5 mm/min (10%/min). A zero span of 50 mm was chosen for the extensometer. The averages of at least five reproducible results were reported. The tensile modulus was calculated at 0.5% strain.

2.3.2. Flexural Testing

The same instrument used for tensile testing was used for the flexural testing but in three point bending according to ASTM D-790 [12]. Unconditioned tensile test specimens were tested at ambient conditions with a span of 50 mm. Samples were tested to a maximum deflection of 30 mm at a crosshead speed of 1.28 mm/min. Reported values are the average of at least five reproducible results.

3. RESULTS AND DISCUSSION

3.1 Tensile properties

The tensile properties of composites at 37 wt% wood loading with varying MAPE content are shown in Figs. 1 and 2. Incorporation of wood seems to improve the tensile properties of LDPE. Tensile modulus of neat LDPE increases from 0.23GPa to 0.96 GPa on loading 37 wt% wood without compatibilizer. This is due to the reinforcing effect of wood

particles. Addition of MAPE further improved the tensile modulus of the composites steadily up to 8% MAPE content, beyond which no appreciable increase is observed (Fig. 1). This improvement is expected because of the ability of MAPE to induce an enhanced interfacial adhesion between the wood particles and the LDPE [13].

Tensile strength of the uncompatibilized composites (8.24 MPa) decreases slightly relative to the neat matrix (9.14 MPa). This may be due to weak interfacial adhesion and low compatibility between the hydrophilic wood flour and the hydrophobic LDPE. In addition, at high wood content, wetting problems becomes prominent and a higher possibility of wood-wood contact results.

| Fig. 1: Tensile strength and modulus of red balau sawdust/LDPE composites with varying MAPE content. | Fig. 2: Tensile strain of red balau sawdust/LDPE composites with varying MAPE content. |
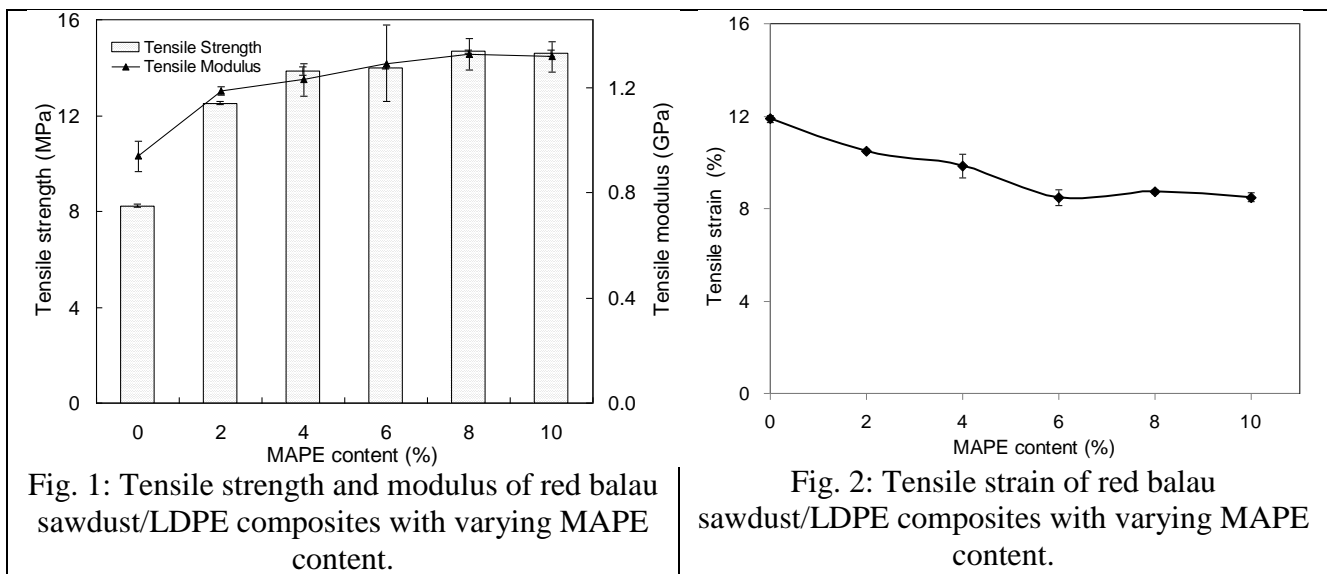
During testing, especially in the tensile mode, unwetted wood particles could constitute stress concentration areas, leading to premature failure and consequently, lower strength [14]. However, on addition of MAPE, a significant improvement in tensile strength is observed. Furthermore, improvement in tensile strength is achieved minimally up till 6% MAPE content. The degree of improvement became significant at 8% MAPE loading beyond which no additional effect is observed (Fig. 1). This may mean that at 8% MAPE content, better wettability of the wood particles by the matrix was achieved that provided the maximum interfacial adhesion needed for effective stress transfer between the wood particles and the matrix. Additional MAPE loading (10%) seems to be of no effect in strengthening the system.

Tensile strain (Fig. 2) decreased drastically in the composites (8.49 %) compared to the neat matrix (91.41 %). This is may be because of the embrittlement imparted by the filler which can act as notches thereby reducing the strain. This behaviour has also been attributed to the restrained chain mobility of the matrix on addition of fillers leading to increased rigidity and drastic reduction of strain at failure [5]. This trend is maintained with the addition of MAPE at all levels.

430

3.2   Flexural properties

The flexural properties of composites with different MAPE content are presented in Figs. 3 and 4.
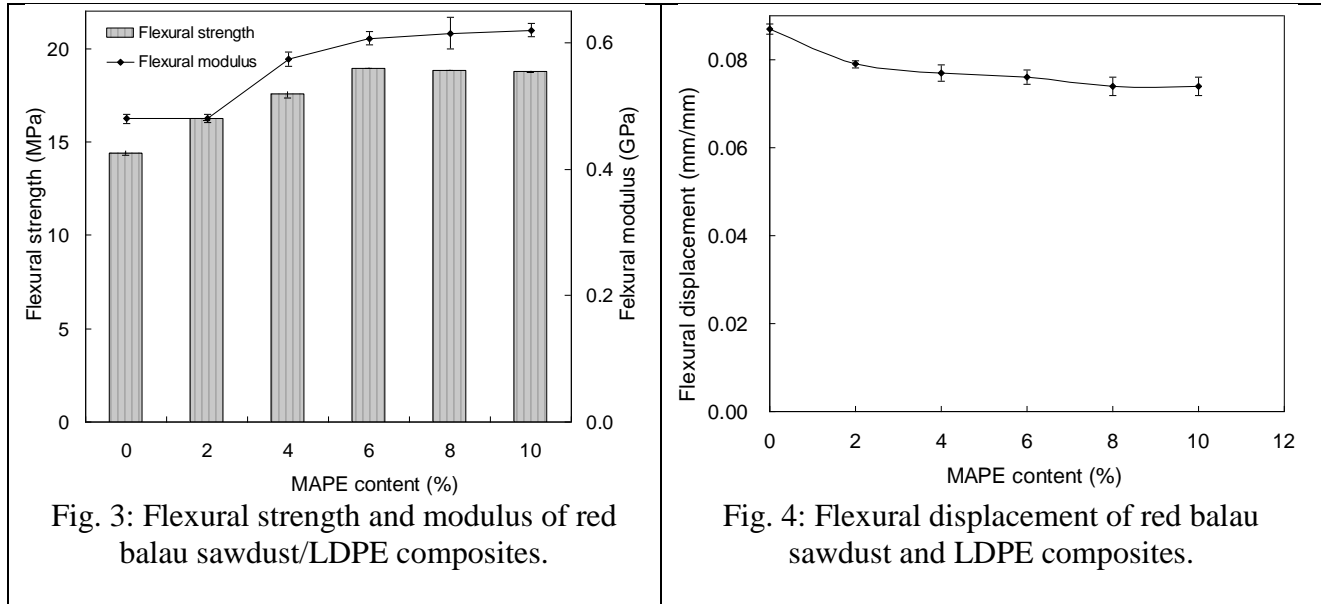
Fig. 3: Flexural strength and modulus of red balau sawdust/LDPE composites.

Fig. 4: Flexural displacement of red balau sawdust and LDPE composites.

Without coupling agents, addition of woodflour improves the flexural strength of the neat LDPE from 7.13 MPa to 14.41 MPa. However, further enhancement in flexural strength is observed with varying amount of MAPE. Flexural strength increases steadily throughout the range of MAPE content used in this study (Fig. 3). Better interfacial adhesion between the wood particles and the matrix could be responsible for this trend. A significant increase is observed between 0% and 4% MAPE content. Beyond this MAPE content, the degree of improvement in strength is observed to be marginal up to 10% MAPE.

Flexural modulus of the composites (0.48 GPa) increases relative to the neat matrix (0.12 GPa). However, addition of 2% MAPE seems to have no effect on the flexural modulus of the composites (Fig. 4). It is possible that 2% MAPE could not provide the needed coupling required for better interaction between the filler and the matrix. As the MAPE content increases to 6% loading, a steady improvement is observed. Additional MAPE content (8 and 10%) did not seem to effect any further improvement in flexural modulus. The flexural displacement reduces generally with MAPE loading (Fig. 4). This may result from improved adhesion between the filler and the matrix which tends to stiffen the composite system.

4.   CONCLUSION

Based on the results of these investigations, the mechanical properties of red balau/LPDE composites can be improved to various extents by the addition of MAPE. 8% MAPE content provides the highest tensile strength and modulus values of the composites,

indicating that this MAPE content is appropriate for imparting the needed interfacial adhesion for better stress transfer between the filler and the matrix. A significant improvement in flexural strength was achieved at 4% MAPE loading whereas 6% MAPE content was observed to be appropriate to attain maximum enhancement of flexural modulus. In view of these results, it is pertinent to note that tensile properties require higher MAPE content relative to flexural properties. Moreover, these results have demonstrated that the mechanical properties of LDPE can be significantly improved by addition of red balau sawdust as filers with adequate level of MAPE content. Therefore, this presents a way of extending the applications of LDPE beyond its traditional uses.

5. ACKNOWLEDGEMENT

6. REFERENCES

1. Zhang, M. Q., Rong, M. Z and Lu, X. (2005). Fully biodegradable natural fiber composites from renewable resources: All plant fiber composites. *Compos Sci Technol*, 65; 2514.
2. Mehta, G., Drzal, L. T., Mohanty, A. K. and Misra, M. (2006). Effect of fiber surface treatment on the properties of biocomposites from nonwoven industrial hemp fiber mats and unsaturated polyester resin. *J Appl Polym Sci*, 99(3), 1055-1068.
3. Li, Q. and Matuana, L. M. (2003) *J Thermoplast Compos Mater*. (16) 551-564
4. Myers, G. E., Chahyadi, I. S., Coberly, C. A. and Ermer, D.S. (1991). Woodflour/polypropylene composites: Influence of maleated polypropylene and process and composition variables on mechanical properties. *Int J Polymeric Mater*. 15; 21-44.
5. Correa, C. A., Razzino, C. A. and Hage Jr, E. (2007). Role of maleated coupling agents on the interface adhesion of polypropylene-wood composites. *J Thermoplast Compos Mater*. 20; 323-339.
6. Nourbakhsh, A., Karegarfard, A., Ashori, A. and Nourbakhsh, A. (2010). *J Thermoplast Compos Mater*. 23; 169-174.
7. Andrady, A. L. (2003). Common plastic materials. In: A. L. Andrady (Ed.), (pp 77-121). *Plastics and the environment*. John Wiley & Sons.
8. Peacock, A. J. (2000). *Hand book of polyethylenes, structures, properties and applications*. USA: Mercel Dercker, 537.
9. Lee,Y. H. and Chu,Y. P. (1979). *Commercial Timbers of Peninsular Malaysia*. Department of Forestry, Peninsular Malaysia and the Malaysian Timber Industry Board.
10. Product data sheet. (2007) Titanlene LDI300YY. Titan Petchem (M) Sdn Bhd. Malaysia.
11. ASTM Standard D-638 (2003.) Standard test method for tensile properties of plastics. *ASTM International,* West Coshoshocken, PA.

12.   ASTM standard D-790. (2003). Standard method for flexural properties of unreinforced and reinforced plastics and electrical insulating materials. *ASTM International,* West Coshoshocken, PA.

13.   Kim, H-S., Lee B-H, Choi., S-W, Kim Sumin and Kim, H-J (2007). The effect of types of maleic anhydride–grafted polypropylene(MAPP) on the interfacial adhesion properties of bio-flour-filled polypropylene composites. *Compos Part A*: 38; 1473-1482.

14.   Lafia-Araga, A. R., Hassan, A., Yahya, R., Abd.Rahman, N., Hornsby, P. and Heinderian, J. (2012). Thermal and mechanical propertiesof treated and untreated Red balau(Shorea dipterocarpacea)/LDPE composites. *J Reinf Plast Compos.* DOI: 10.1177/0731684411433913

Study of Fatigue Crack Propagation by the Energy Method

M. Mazari[*], M. Benguedia, B. Bouchouicha, and M. Zemri

Djillali Liabes University of Sidi Bel Abbes,
Laboratory of Materials and Reactive Systems,
BP 89 Cite Larbi Ben M'hidi, 22000 Sidi Bel Abbes, Algeria

*Corresponding author: mazari_m@yahoo.fr

Abstract: *Plasticity effects at the crack tip had been recognized as ''motor'' of crack propagation. The growth of cracks is related to the existence of a crack tip plastic zone, whose formation and intensification is accompanied by energy dissipation. In the actual state of knowledge, fatigue crack propagation is modelled using crack closure concept. Recent studies demonstrated that closure effects and the role of plasticity-induced crack closure are more pronounced at the early stage of the crack growth at low stress ratio R.*

Keywords: Fatigue crack growth, correction factor, energetic approach, plasticity, crack closure

1.   INTRODUCTION

Material resistance to fatigue depends on many parameters such as chemical composition, mechanical properties, heat treatment conditions, applied loads and environmental conditions.

The knowledge of crack mechanisms has known a significant evolution since Paris and Erdogan [1] proposed a law relating crack growth rate to the stress intensity factor.

There is no evidence of the effects of mechanical parameters in Paris' relation. Elber [2] had shown that a crack stays closed during a certain period of a cycle (even if it is in tension) due to the existence of residual stresses in the plastic core at the crack tip expressed by ΔK_{eff}, the period of a cycle where the crack is totally open. Elber proposes the following relation:

$$\frac{da}{dN} = c(\Delta K_{eff})^n \tag{1}$$

where

$$\Delta K_{eff} = K_{max} - K_{op} \tag{2}$$

434

a, is the length of the crack (mm); N, is the number of cycles; $\frac{da}{dN}$, the crack growth rate (mm/cycles); ΔK_{eff}, the amplitude of the effective stress intensity factor (MPa m$^{1/2}$); K_{max}, the maximum stress intensity factor; and K_{op}, the stress intensity factor to the opening.

Besides this mechanically based concept, other approaches based on energy consideration [3] or on micro- mechanisms acting at the crack tip had been developed.

In these approaches certain authors attempted to express the crack growth rate by explaining the effects of different parameters by means of theoretical models based on the crack tip opening theory and cyclic hardening.

The initial model son materials behaviour are based on the determination of strain amplitude and damage accumulation in the crack tip plastic zone.

A new approach was proposed by Weertman [3] who considers that the crack advances when the accumulated plastic energy at the crack tip reaches a critical value. Weertman proposed to relate the crack growth rate to this energy by a law type:

$$\frac{da}{dN} = \frac{A\Delta K^4}{\mu\sigma_c^2 U}$$
(3)

With $\frac{da}{dN}$ being the crack growth rate; ΔK, the stress intensity factor range; μ, the shear modulus; σ_c, the cyclic elastic limit; U, the surface energy creation; and A, the non-dimensional constant.

This model has gained a high interest, many authors have attempted to verify its validity and many experimental techniques had been developed to measure the energy of surface creation U, which represents the dissipated energy in the plastic zone by unit created surface.

For ductile material, the energy of plastification is much higher than the theoretical surface energy creation γ. Ikeda et al. [4] had measured the quantity for steel of low carbon content and for high resistance aluminum alloy from hysteresis loops in the plastic zone using strain micro gages. Davidson et al. [5] had developed a method to evaluate the plastic energy from sub grain size measures. Liaw et al.[6] had compared the results by micro gage technique to those obtained by the sub grain size measure technique.

In the first experiment, these authors were led to make extrapolation in order to obtain a value for plastic deformation for r < 100 μm due to finite size of the gages.

The authors realized that the sub grain size technique gives a value of the plastic work which differs only by 15% from their estimation. Other measuring techniques had been

435

developed such as micro calorimetry [7]. Ranganathan et al. [8, 10] had measured the work in the hysteresis loop U using CT specimens slightly modified in order to be able to measure the crack opening displacement (COD) in the loading axial direction. The work in the hysteresis loop U can be directly evaluated by the compliance measure according to the relation:

$$U = \frac{\text{Area hysteresis loop } (P, \delta')}{2B(\frac{da}{dN})} \qquad (4)$$

where B is the specimen thickness.

On the basis of these results, the authors show that over certain value of ΔK called ΔK$_{cr}$ (amplitude of the critical stress intensity factor), the value of U is constant and independent on both the ratio R and the environment.

Recently Klingbeil [11] had modified Weertman's relation [3] by introducing the total plastic energy dissipated per cycle dW/dN and had expressed the crack growth rate by:

$$\frac{da}{dN} = \frac{A\Delta K^4}{E\sigma_c^2 G_c} \frac{dW}{dN} \qquad (5)$$

In this relation, the crack growth rate is expressed in terms of energy restitution ratio, the modulus of elasticity and the material resistance.

The constant A of Eq. (5) had been determined on the basis of experimental results of specific energy U and Klingbeil [11] in this model assumed it to be equal to the restitution energy ratio G$_C$ and by neglecting the surface energy creation γ (for the case of ductile materials).

Following this assumption Klingbeil found A to be equal to 2.23×10^{-3}, a closer value to that found elsewhere [12, 6].

2. EXPERIMENTAL STUDY

The study had been conducted on a high strength aluminum alloy 2024-T351 whose chemical composition and mechanical properties are given, respectively, in tables 1 and 2.

Table 1: Chemical composition of aluminum alloy 2024 T351.

Elements	Si	Fe	Cu	Mn	Mg	Cr	Zn	Ti	Al
Percentage	0.10	0.22	4.46	0.66	1.50	0.01	0.04	0.02	Remain

Table 2: Mechanical properties of aluminum alloy 2024 T351.

Material	$\sigma_{0.2}$ [MPa]	σ_R [MPa]	A (%)	K	N

2024 T351	318	524	12.8	652	0.104

The experimental tests had been conducted at LMPM ENSMA – Poitiers by Ranganathan on CT specimens of two different thicknesses 4 and 10 mm and two types of experimental tests were conducted:
- Constant amplitude loading with threshold test in ambient air at stress ratio R = 0.5,
- Constant amplitude loading in vacuum at stress ratio R = 0.5.

The threshold tests under ambient air and vacuum had been conducted with a frequency of 20 Hz with decreasing ΔK. The crack propagation in air had been observed by optical method by means of a magnifying binocular (X25). For the case under vacuum condition, the crack propagation had been followed by the method of potential variation.

3.   EXPERIMENTAL RESULTS AND DISCUSSIONS

3.1.   Relations between the crack growth rate and the stress intensity factor amplitude

The crack growth rate da/dN with respect to ΔK at R = 0.5 for threshold tests under two different environments (air and vacuum) is given in Fig. 1. It shows the existence of different regimes of crack growth separated by transitions.

Regime I corresponds to the behavior at low crack growth rates ($<10^{-6}$ mm/cycle) which decreases rapidly till the threshold value is reached.
The transition T1 points out the beginning of the rapid decrease of da/dN. The value of this transition is 3×10^{-7} mm/cycle under vacuum and has a value of 2×10^{-6} mm/cycle under aggressive environment (air).

Another transition T2 appears for a value of da/dN=4×10^{-6} mm/cycle which is located in the range of $3.6 < \Delta K < 5.6$ MPa m$^{1/2}$. This transition appears only for the tests conducted under ambient air.
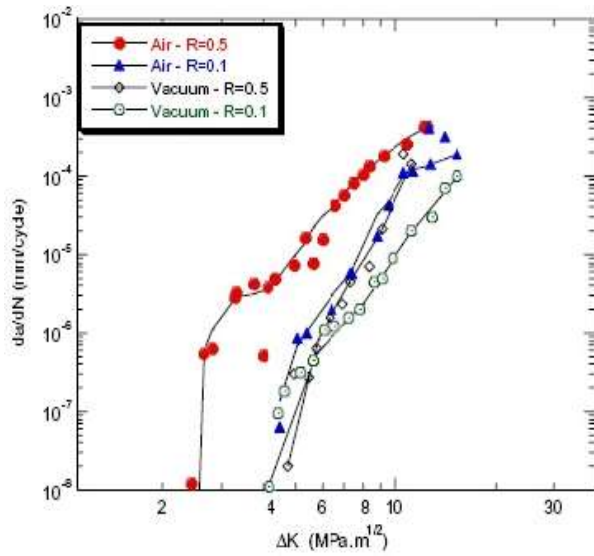
Fig. 1: Evolution of da/dN versus ΔK
for alloy 2024 T351 [8, 13].
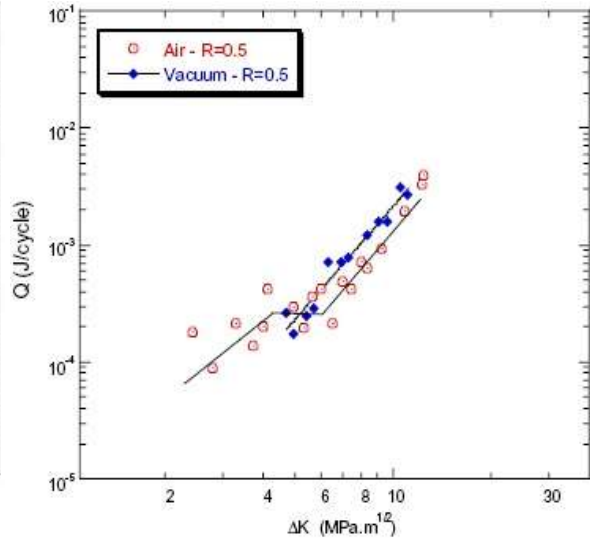
Fig. 2: Evolution of Q with respect to ΔK
for 2024 T351.

3.2. Relations between hysteretic energy Q and ΔK

Fig. 2 shows the evolution of the dissipated hysteretic energy per cycle Q with respect to the stress intensity factor range ΔK for R = 0.5 under both vacuum and air.

The hysteretic energy Q dissipated through one cycle is obtained by integration of the (P–δ') curves, and the specific energy U is given by relation (4).

3.3. Relations between specific energy U and ΔK

It is observed in Fig. 3 that under air environment and for R = 0.5, the specific energy U is constant for $\Delta K > 7.8$ MPa m$^{1/2}$, its critical value Ucr ≈ 2.6x10^5 J/m^2.
However under vacuum, the phenomenon is not highly noticed.
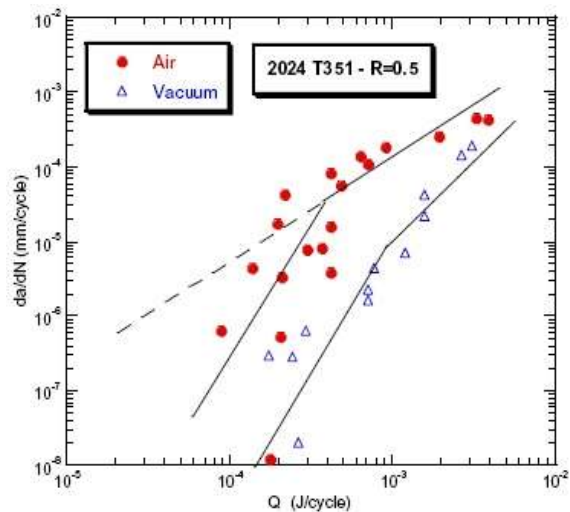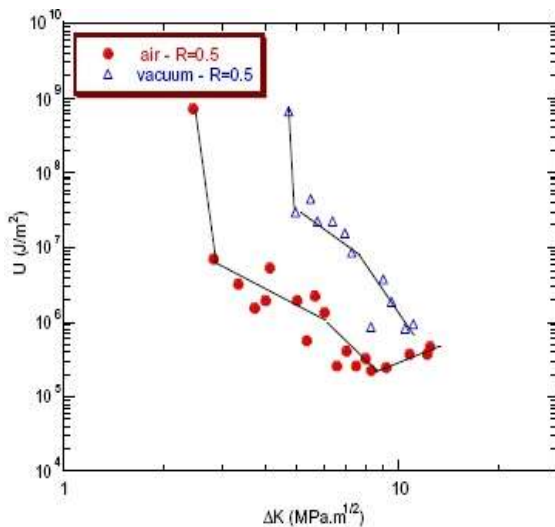
Fig. 3: Evolution of U with respect to ΔK   Fig. 4: Evolution of da/dN with respect to Q
              for 2024 T351.   for 2024 T351(R = 0.5).

3.4. Relations between crack growth rate and the dissipated energy per cycle Q

Fig. 4 shows the evolution of crack growth rate da/dN with respect to the hysteretic energy per cycle Q under air and vacuum for R = 0.5.

It is observed that under air and for da/dN > 4×10^{-5} mm/cycle a linear relation can be determined between these two parameters and is of the form:

$$\frac{da}{dN} = A.\,Q \text{ with } A \approx 0.166 \tag{6}$$

These values are slightly different from those obtained elsewhere [8, 9]. The obtained relation corresponds to the range where the specific energy U is constant and is equal to U_{cr}. For da/dN < 4×10^{-5} mm/cycle under air, there is a higher decrease of the crack growth rate with the dissipated energy per cycle.

Under vacuum, the transition described above is marked and is less apparent and is around 10^{-5} mm/cycle. From the obtained results, it is observed that the evolution of da/dN with respect to the dissipated energy per cycle Q varies according to a power law of the type:

$$\left(\frac{da}{dN}\right)_p = B.\,Q_p^n \tag{7}$$

where Q_p is the power part of Q; n is an exponent.

For growth rates lower than 4×10^{-5} mm/cycle, it has the following linear form:

$$\left(\frac{da}{dN}\right)_l = A.\,Q_l \tag{8}$$

where Q_l is a linear form of Q.

It was also observed that for lower crack growth rates, different factors contribute to the increase of crack closure such as roughness or oxidation [2]. Thus, the dissipated energy Q during one cycle is not useful for surfaces creation; a part of this energy will be lost.

From these conditions, we can establish an energetic model based on the correction of the evolution of crack growth rates da/dN_ with respect to Q. Considering that there is a continuity of the crack growth rate at the transitions, this continuity allows to equalize relations (7) and (8) which gives

$$A. Q_l = B. Q_p^n$$

Thus

$$Q_l = \frac{B}{A} . Q_p^n$$

The equivalent energy dissipated per cycle Q_{eq} has the form:

$$Q_{leq} = K. Q_p^n \text{ with } K = B/A$$

The experimental results at R = 0.5 in air and the corrections obtained are shown in Figs 5 and 6. It is observed that the evolution between da/dN and Q is linear with a coefficient K =$5.88.10^{-2}$.
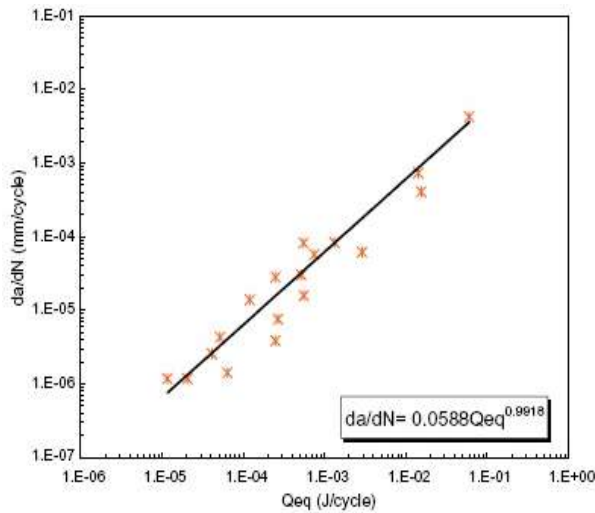
Fig. 5: Evolution of da/dN with respect to Q of 2024-T351 at R = 0.5 with correction. correction.
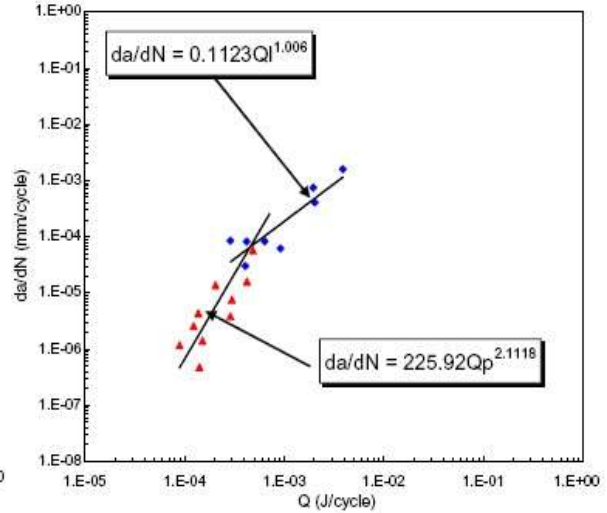
Fig. 6: Evolution of da/dN with respect to Q of 2024 T351 at R = 0.5 after

4. ENERGETIC MODEL

The crack growth rate da/dN can be formulated in terms of the total dissipated plastic energy per cycle Q_P as:

$$\frac{da}{dN} = \frac{1}{G_c} . Q_p \quad (9)$$

G_C is the energy release rate related, in mode I, to the critical stress intensity factor K_I by:

$$G_c = \frac{K_I^2}{E_T} \tag{10}$$

with $E_T = E$ being in plane stress conditions; and $E_T = \frac{E}{1-\upsilon^2}$ being in plane strain conditions. After substitution of (10) in (9), the propagation law becomes:

$$\frac{da}{dN} = \frac{E_T}{K_I^2} \cdot Q_p \tag{11}$$

This relation requires the determination of the parameters $Q_p = \iint_{rp} \oint \sigma_{ij} \cdot d\varepsilon_{ij}^p \cdot dA$ (rp being the radius of the plastic zone ahead of the crack tip), either by finite element method [11] or experimentally by calculating the area of the hysteresis loop (P,δ') [13].

Following the phenomena experimentally observed concerning the existence of a transition due to the environment and which give rise to two propagation regimes and according to the approach suggested by Newman [14], it is necessary to determine an energetic correction factor which allows us to determine the equivalent dissipated energy per cycle obeying Weertman's model [3], thus eliminating the effects observed during threshold tests at constant DP. To do this, we have proceeded as follows: a parameter Q_{ad} calculated using the relation

$$Q_{ad} = \frac{\sigma^2 E}{\Delta K^m} Q \tag{12}$$

where σ, is the elastic limit of the material; E, Young's modulus; ΔK, the stress intensity factor range; Q, the hysteresis energy per cycle; and m, Paris' exponent.
Then, an energetic correction factor has been determined, which is expressed as:

$$\zeta_M = \frac{\sum_{i=1}^n Q_{ad}}{n} \tag{13}$$

where n is the number of iterations on crack length.
The equivalent specific energy becomes:

$$U_{eq} = \frac{\Delta K^m}{\frac{da}{dN} \sigma^2 E} \zeta_M \tag{14}$$

From relations (8) and (14), we determine the equivalent energy Q_{eq} dissipated per cycle:
• *In plane stress*:

$$Q_{eq} = \frac{1}{A} \frac{da}{dN} \text{ and } A = \left(\frac{2B}{2(1+\upsilon)} \right) \zeta_M$$

$$Q_{eq} = \left(\frac{2(1+\upsilon)}{2B}\right)\frac{da}{dN}\frac{1}{\zeta_M} \tag{15}$$

• *In plane strain*:

$$Q_{eq} = \left(\frac{2B}{2(1-\upsilon)}\right)\frac{da}{dN}\frac{1}{\zeta_M} \tag{16}$$

The crack growth rate is given by:

$$\frac{da}{dN} = \frac{\zeta_M}{\sigma^2 E}\cdot\frac{\Delta K^m}{U_{eq}} \tag{17}$$

This expression is similar to that proposed by Weertman [3] and other authors [15–18] as:

$$\frac{da}{dN} = \frac{A}{\sigma^2 \mu}\cdot\frac{\Delta K^4}{U} \tag{18}$$

where μ, represents the shear modulus; U, the specific energy which is equal to G_C (in this study); and A, a non-dimensional constant.

The results obtained from the model proposed in this study by (15) and (16) are represented in Figs. 7 and 8. The results are compared to the experimentally obtained results and to those obtained, respectively, by Klingbeil's [11] model and Tracey's model [19].

We can observe that the present model also gives the energy with respect to ΔK^4; it conforms to the other theoretical models and the crack growth rate da/dN is well a linear function of energy [11, 14 and 19].
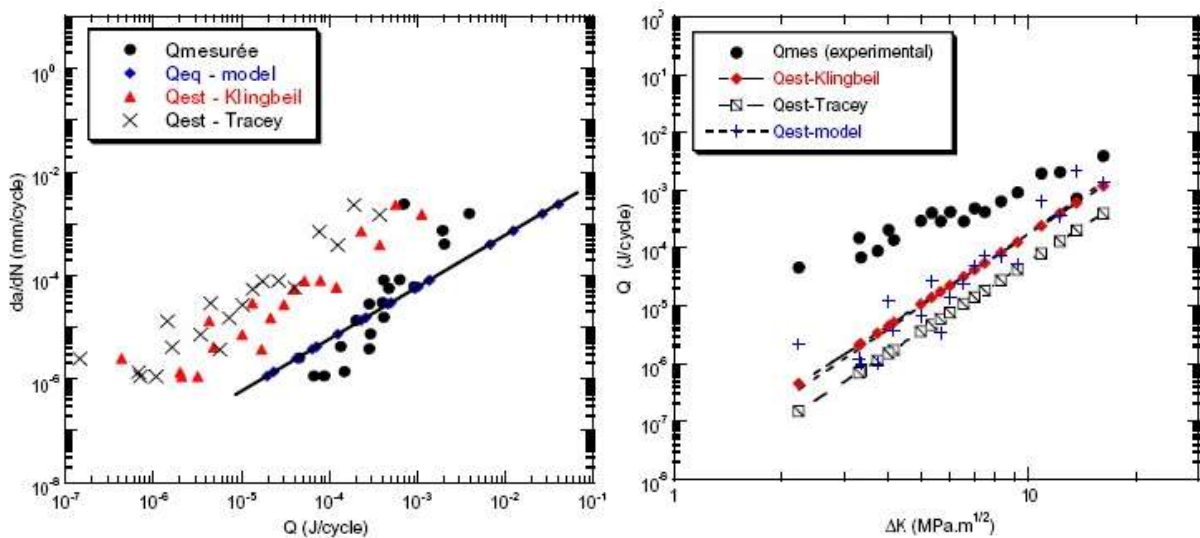
Fig. 7: Evolution of Q_{eq} with respect to ΔK Qeq and comparison with other models.

Fig. 8: Evolution of da/dN with respect to and comparison with other models

5. CONCLUSION

The proposed model that has been developed and which is based on Weertman's concept allows to describe the evolution of crack growth rate in terms of energy consideration.

Where ζ_M is the average energetic correction coefficient obtained from the experimental results. Its inclusion in the model allows to linearise the relation between the crack growth rate and the hysteretic energy per cycle Q in all the ΔK ranges under study.

6. REFERENCES

1. P.C. Paris, F. Erdogan, Trans. ASME Series D. J. Bas. Eng. 85 (1963)
2. W. Elber, Am. Soc. Testing Mats. (1971) 230–242.
3. J. Weertman, Int. J. Fracture 9 (1973) 125–131.
4. S. Ikeda & al., Eng. Fracture Mech. 9 (1977) 125–136.
5. D.L. Davidson& al., in: Proc. Symp. Env. Sens. Frac. Eng. Matls., TMS ASME, Warendale PA, USA, 1980, p. 59.
6. P.K. Liaw & al., Frac. Eng. Mater. Structure 3 (1980) 59.
7. T.S. Gross, J. Weertman, Metall. Trans. A 13 (1982) 2165.
8. N. Ranganathan, Contribution au développement d'une approche énergétique à la propagation d'une fissure de fatigue. Thèse de doctorat, Université de Poitiers, 1985.
9. M. Benguediab, Thèse de doctorat de l'Université de Poitiers, 1988.
10. K. Jendoubi, Thèse de doctorat de l'Université de Poitiers, 1989.
11. N.W. Klingbeil, Int. J. Fracture 25 (2003) 117–128.
12. Y. Isumi, M. E Fine, T. Mura, Eng. Fracture Mech. 11 (1979) 791.
13. M. Mazari, These de doctorat, Universite de de Sidi Bel Abbes, 2003.
14. J.C. NEWMAN Jr., in: An evaluation of plasticity – induced crack closure concept and measurement methods, ASTM STP, vol. 1343, PA, 1999, pp. 128–144.
15. T. Mura & al., Int. J. Fracture Mechan. 10 (1974) 284–287.
16. S.R. Bodner & al., Eng. Fracture Mechan. 17 (n_2) (1983) 189–191
17. P.K. Liaw & al., Metall. Trans. A 12 (1981) 49–55.
18. N. Ranganathan et al., Energy required for fatigue crack propagation 7th Int. Conf. on strength of Metals and Alloys, Montreal, Canada, 1986, pp. 1267–1272.
19. D.L. Tracey, J. Matls. Tech. 98 (1971) 146.

Reinforcement of Natural Rubber Latex Films through Surface Modified Silica with Macromolecular Coupling Agent

M C W Somaratne[1,*], N M V K. Liyanage [2], and S. Walpalage [3]

[1]Institute of Technology Univesity of Moratuwa, Sri Lanka
[2]Department of Materials, University of Moratuwa, Sri Lanka
[3]Department of Chemical Engineering, University of Moratuwa, Sri Lanka

*Corresponding author: chandani.mcw@gmail.com

Abstract: *The surface of precipitated silica particles was modified by reacting with a macromolecular coupling agent containing both hydrophilic and hydrophobic monomer units. Inter facial interactions between -OH groups of silica and -COOH groups of macromolecule were created through H-bonds and covalent bonds confirmed by Fourier Transform Infrared Spectroscopy. Two different dispersions of unmodified/modified silica were prepared and incorporated to natural Rubber Latex (NRL). Physical properties of NRL films containing modified silica fillers were compared with those of films containing unmodified filler. Even distribution of modified filler was seen in microstructures of film cross sections obtained from Scanning Electron Microscope.*

Keywords: Reinforcement, natural rubber latex, silica, surface modification, macromolecular coupling agents

1. INTRODUCTION

For certain natural rubber latex (NRL) products like condoms, medical strips, exercising bands and latex cloths, the existing tensile and tear strength of the films are not adequate, particularly for ultra thin film products like condoms and physiotherapy exercising bands. Therefore, the thickness of the product or film is increased without disturbing its elasticity or modulus to bear up the mechanical force applied on it during usage. One good example for that corrective action is, exercising band. However, such practices are not very encouraging as they will not get the maximum use of raw material. Therefore, the latex products manufacturers are interested in reinforcement of NRL.

On the other hand, the reinforced latex film with its increased product properties reduces the percentage of rubber used. At present, NR latex market is fluctuated at very high prices, as a result some industries are compelled to cut down their production. As such, a systematic investigation on the use of various types of fillers to improve the extent of reinforcement of NRL films will be very beneficial to the NRL based-products manufacturing industries.

444

Several attempts have been made to improve strength properties of NR latex films with the use of reinforcing fillers but with very little success. Considerable amounts of research have been carried out on ultra fine / nano $CaCO_3$[1,2] clay material [3]and silica[4] to improve the mechanical properties of latex films.

Surface activity is conveyed to a particle by means of the functional groups attached to the surface and thereby generates true bonding sites. Silica is one good example for active filler and therefore the surface bound hydroxyl groups create the surface activity. Hence, it is utilized in various applications, among them dry rubber industry is well-known. Even though silica is superior active filler its hydrophilic nature weakens the compatibility with hydrophobic rubber. In recent years much research interest had been paid on surface modification of silica particles. Silane coupling agents that accomplished to convert hydrophilic silica into rubber-philic are widely used in dry rubber industry. The other reported novel techniques are in situ graft polymerization [5,6], admicellar polymerization [7,8] and make use of macromolecular coupling agents [9,10] to modify the surface of silica.

Even if the surface of silica is successfully modified it is still a challenging task to disperse it uniformly in NRL which is a stable colloidal dispersion of rubber particles in an aqueous medium. Thus, the modified filler is also essential to incorporate in a stable aqueous dispersion form to make it compatible with the NRL.

This paper, the reinforcement of NRL is discussed by means of surface modified silica with macromolecular coupling agent (MCA), containing both hydrophilic and hydrophobic groups.

2. EXPERIMENTAL

2.1 Materials

A concentrated Low Ammonia NRL sample obtained from Leefern Laboratory (Pvt) Limited and Silica (Ultrasil VN3) obtained from Chemical Industries Colombo Ltd were used throughout this study. All other chemicals and reagents were obtained from local chemical suppliers.

2.2 Methods

Synthesis of macromolecular coupling agent

The MCA was synthesized by following solution polymerization process by using appropriate amounts of a hydrophobic monomer and a hydrophilic monomer [molar ratio hydrophobic to hydrophilic is 40:60] in xylene at 90˚C with benzoyl peroxide as the initiator. Resultant polymer was isolated by filtration and vacuum dried for 10hrs before use.

Surface modification

10g of silica powder [Ultrasil VN3] was mixed with 60ml of xylene. MCA synthesized above (5% w/w of silica) was added to the same mixture. The mixture was heated to 100˚C and maintained at 100˚C for 3hrs while stirring. The modified filler was filtered out and vacuum dried for 10hrs. It was then divided into four portions and three of them were washed with 200ml of tetrahydrofuran in a Soxhelt apparatus for 12, 48 and 72 hours respectively. Finally the modified, washed filler samples were vacuum dried.

Fourier Transform Infrared (FTIR) spectra of filler samples i.e. unmodified, modified, modified/washed and combined dry powder mixture of unmodified filler and MCA (5%w/w of silica) were obtained using [Alpha] FTIR spectrophotometer to confirm the possible chemical and physical interactions between MCA and silica.

Preparation and incorporation of dispersions into NRL

Two separate sets of 15% aqueous dispersions of silica i.e. unmodified (UM) and modified (MF) were prepared by grinding in a pot mill for10hrs. The stability of dispersions was observed by increasing the pH of them up to7 and 10. The dispersions at neutral pH were mixed with vulcanized and un-vulcanized latex at different levels of additions i.e. 3phr, 5phr, 8phr, 10phr and 20phr.

Thin films [thickness < 0.5mm] of the filler added NRL were cast and tensile and tear strength of them were measured by using [Hounsfield H10KT] tensile testing machine as per the standard test method for latex films [ISO 37, 2005] , [ISO 34-1, 2004].

Microstructures of cast film cross-sections were also examined by using scanning electron microscope (Leo 1420 VP). The filler (20phr) added films were used for this study.

2.3   Results and Discussion

FTIR spectroscopy

FTIR spectrums of unmodified filler (a), modified unwashed filler (b), modified washed; 12hrs (c), 48hrs (d), 72hrs (e), combined dry powder mixture of unmodified filler and macromolecule (f) and macromolecule (g) are shown in **Figure: 1**. The strong peak at the range 1709-1736cm^{-1}of polymer is corresponding to the carbonyl groups of ester (1736cm^{-1}) and carboxyl (1709cm^{-1}) stretching vibrations, equivalent peaks at identical points are showed by the same functional groups of the combined dry powder mixture of MCA and filler. However; modified unwashed filler shows a broad peak at the same region corresponding to hydrogen bonds plus covalent bonds between carboxyl groups and silanol groups. Thus, by washing the modified filler, the corresponding broad peak gradually shifts towards 1736cm^{-1}, as well broadness is reduced with washing time. That may due to the covalently bonded ester groups are prominent while the H-bonds disappear.

The peaks in the region 2800cm^{-1} - 3000cm^{-1} of the FTIR spectra of modified washed fillers correspond to the stretching vibration of -CH$_2$-, -CH$_3$ groups of the covalently bonded macromolecules to the surface of silica filler.

Stability of filler Dispersion

At the time of unloading, both UM filler and MF dispersions were at pH range 4.5-6.5 and it was observed that the stability of each was very poor. While adjusting their pH up to 7 viscosity of MF sample was increased showing better dispersibility. However the behaviour of UM filler dispersion was different and particle settling was observed at pH 7. When pH was increased up to 10 both dispersions displayed particle settling with time.
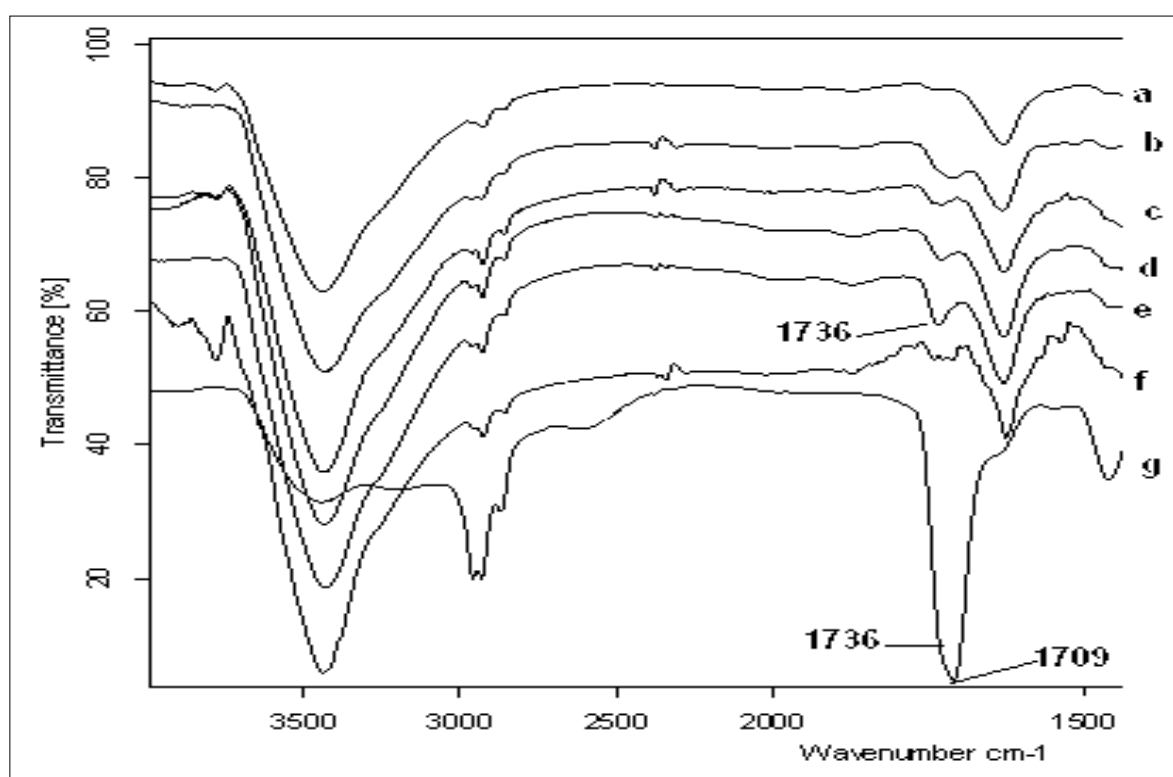
Fig. 1: FTIR results of unmodified filler (a), modified unwashed filler (b), modified washed; 12hrs (c), 48hrs (d), 72hrs (e), combined dry powder mixture of unmodified filler and macromolecule (5% polymer /filler) (f) and macromolecule (g).

Silica with macromolecular coupling agent in acidic aqueous medium forms hydrogen bonds with surface hydroxyl groups. Modification reaction of the filler surface involves formation of both covalent and hydrogen bonds. When pH of the dispersions is increased, surface attached macromolecules have a tendency to ionize and dissolve, thus the macromolecular chains get expanded at pH close to 7, and therefore the dispersion stability is improved. However, the hydrophilic groups may be totally ionized at pH 10 disappearing the hydrogen bonds and breaking filler-polymer hybrid complex. Subsequently, the strength of

447

covalent bonds alone may not enough to drag the filler as a colloid to the aqueous medium, as a result, the filler starts to settle down with time. It points out that the hydrogen bonds contribute towards dispersion stability mainly by forming a network like structure.

Filler rubber compatibility

UM filler in NRL settled down to the bottom of the container ensuring the compatibility of UM filler with NRL was very poor, the cast films also showed two separate layers of rubber and UM filer. However, the MF incorporated samples showed excellent dipersibilty of filler particles certifying its improved compatibility with NRL, cast films also conferred uniformed structure from top to bottom.

The filler particles, of which the surface hydroxyl groups have interacted chemically and physically forming hydrogen bonds and covalent bonds with hydrophilic groups of MCA, in NRL create interactions with rubber particles through the hydrophobic groups of the surface attached MCA. Hence the compatibility and therefore the dispersibity of MF particles in NRL are improved as shown in Fig. 2.
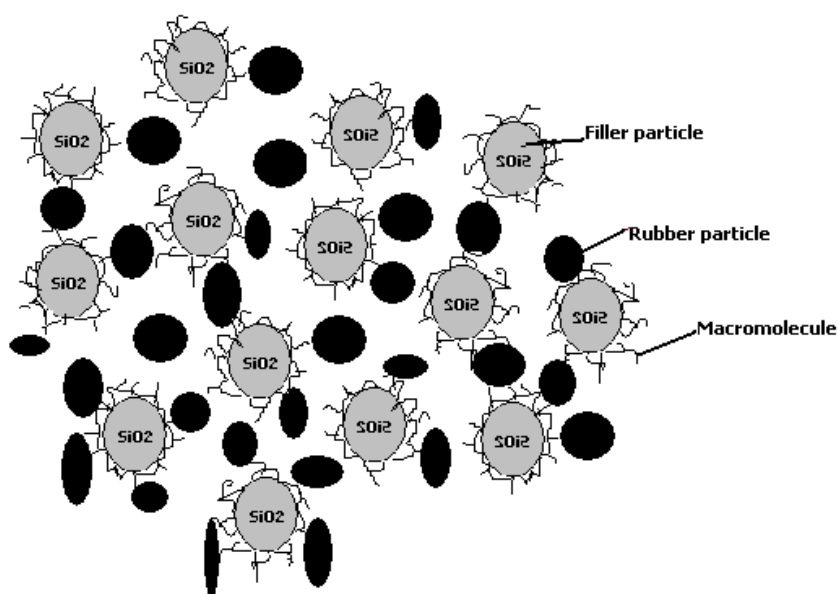
Fig. 2: Interactions between silica filler and rubber particles via macromolecular coupling agent.

Scanning Electron Microscopic analysis

Scanning Electron Microscopic (SEM) images of cross sections of unfilled latex film (a), UM filler added latex film (b) and MF added latex film (c) are given in Fig. 3. The image of unfilled latex film shows an amorphous polymer structure of pure natural rubber while the UM filler added film shows a clear separation of layers; the bottom layer is loaded with UM

filler where as the top layer is mainly with rubber. The image of MF added latex film displays an even distribution of filler particles throughout the rubber matrix.

Physical properties of cast films

The variation of tensile strength of un-vulcanized NRL cast films, including different levels of UM and MF are shown in Fig. 4. UM filler added films at low filer concentrations up to 5phr level show improved tensile values than the unfilled latex film. The films with high filler concentrations from 8phr on wards show reduced tear values than it for 5phr level. Almost similar pattern is given by the vulcanized latex films with UM filler for tensile strength values as given in Fig. 5.

At low filler concentration levels, the possibility to form larger filler aggregates is very low, the smaller size, individual aggregates are formed and entrapped in the rubber matrix, hence, the tensile strength may improve. However, when the concentration is increased, higher number of particles collapses together and increases the size of aggregates, as a result, the settling of UM filler occurs rapidly while reducing the tensile strength.
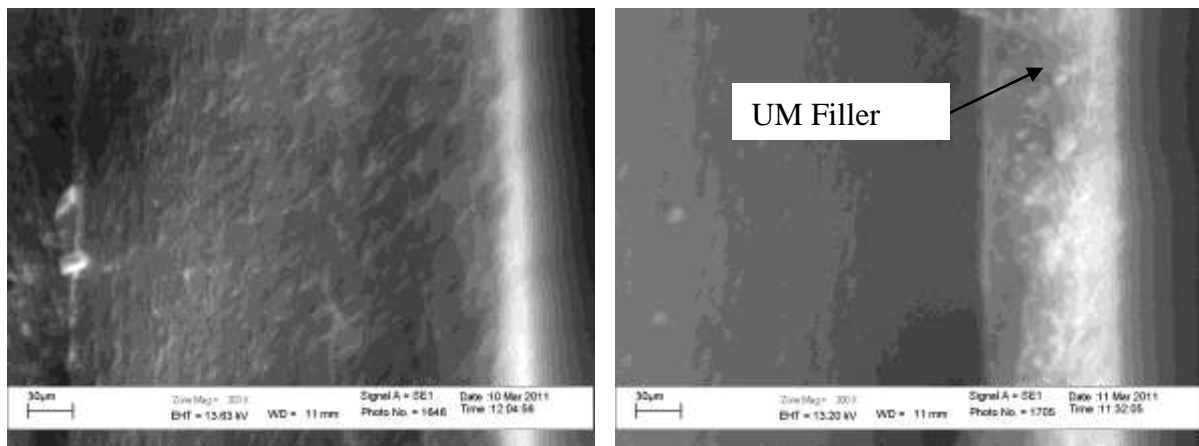
a   b
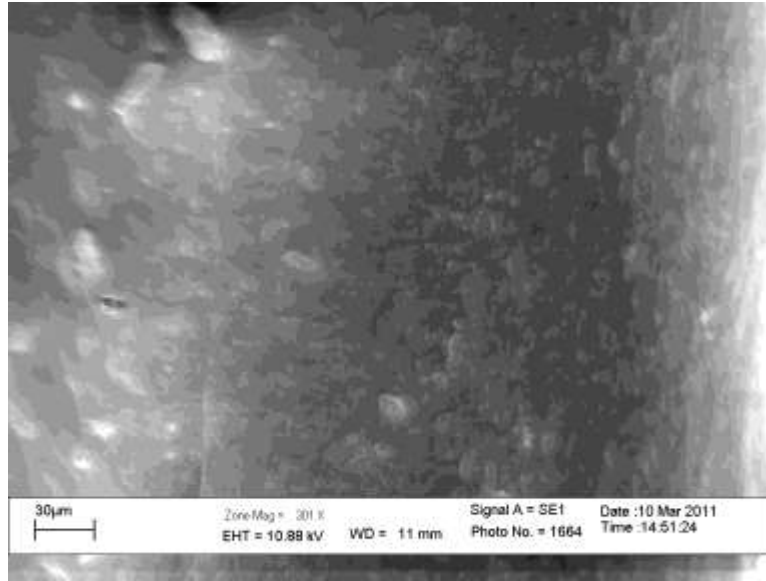
c

Fig. 3: SEM images of a- unfilled latex lilm, b- unmodified filler incorporated latex film, c- modified filler incorperated latex film.

MF filler added films of un-vulcanised NRL in Fig. 4 and vulcanised NRL in Fig. 5 show continuous improvements of tensile properties with the concentration of MF is increased. The created interactions between filler and rubber via MCA improve the tensile properties of MF added latex films.
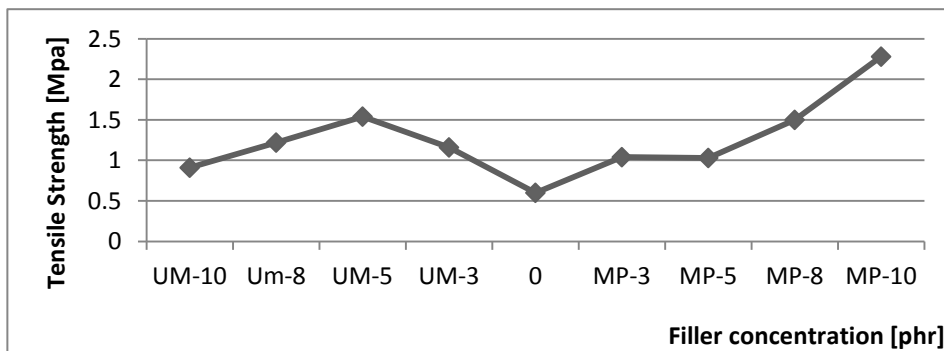
Fig. 4: Tensile properties of UM and MP filler added un-vulcanized cast films.
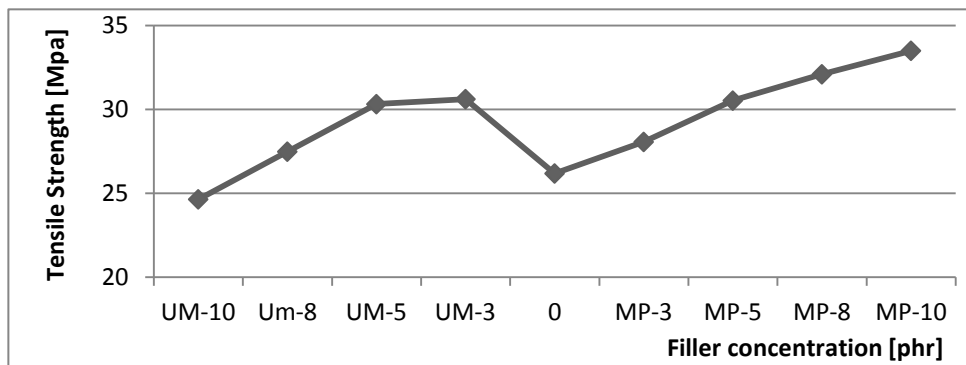
Fig. 5: Tensile properties of UM and MP filler added vulcanized cast films.

Tear strength of UM filler added, un-vulcanized latex films is increased gradually with the dosage of filler is increased as in Fig. 6. The entrapped filler aggregates may act as a barrier to the propagation of tearing. That of MF added samples initially, at low concentration levels do not show significant change however the samples containing filler levels above 5phr show improved tear strength. The increment of MF added films is higher than that of UM filler added films containing equivalent phr levels.

The tear strength of vulcanised films is varied in different manner. At low concentration levels of UM as well MF added sample films in Fig. 7 show lower tear strength values than that of unfilled latex film. However the tear strength is increased in both samples from 5phr level onwards and the increment of MF added films is higher than that of UM filler added films.
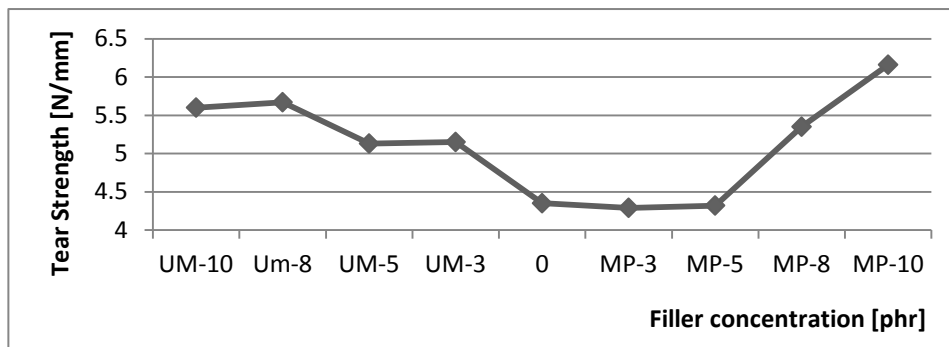
Fig. 6: Tear properties of UM and MP filler added un-vulcanized cast films.
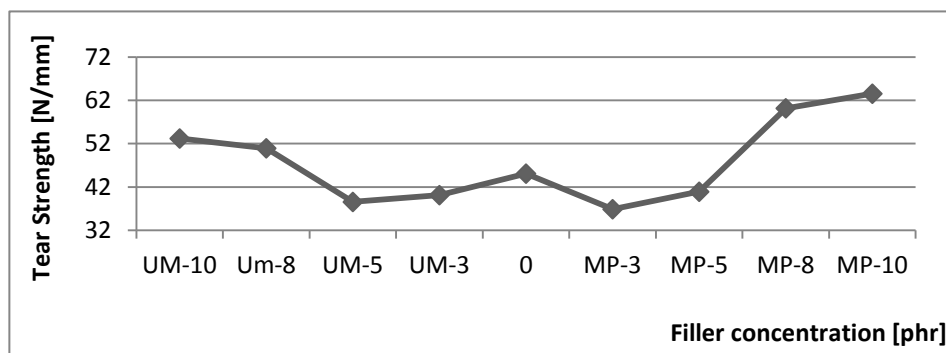
Fig. 7: Tear properties of UM and MP filler added vulcanized cast films.

3. CONCLUSION

The enhanced compatibility, through interfacial interactions between surface modified silica particles and NRL, results better dispersibility of filler particles throughout the rubber matrix and improves physical properties of filled latex cast films.

4. REFERENCES

1. Cai, H., et al., (2003). Reinforcement of natural rubber latex film by ultra fine calsium carbonate. *Journal of Applied Polymer Science., 87, 952-985.*

2. Deng, C., et al., (2006). CaCo3/natural rubber latex nanometer composite and its propertties. *Journal of Applied Polymer Science,. 101, 3442-3447.*

3. Claramma, N.M., L. Vaghese, and N.M. Mathew, 1999. Effect of the fillers on the properties of prevulcanized nathural rubber latex film. *Elastomers and Plastics, 31, 130-142.*

4. Peng, Z., et al., 2007. Self asssembled natural rubber/ silica nano composites: Its preparation and characterization. *Composite science and technology, 67, 3130-3139.*

5. Nguyen, V., W. Yoshida, and Y. Cohen, 2003.Graft Polymerization of Vinyl Acitate on Silica *Jornal of Applied Polymer Science, 87, 300-310.*

6. Suzuki, K., et al., 2000. Modification of Porus Silica Paticles with Poly(acrylic Acid). *Polymers for Advanced Technologies, 11, 92-97.*

7. Nontasorn, P., et al., 2005. Admicellar polymerization modified silica via a continuous stirred-tank reactor system: Comparative properties of rubber compounding. *Chemical engineering, 108, 213-218.*

8. Rangsunvigit, P., et al., 2008. Mixed surfactants for silica modification by admicellar polymerization using a continiuous stirred tank reactor. *Chemical Engineering, 136, 288-294.*

9. Tai, Y., J. Qian, and Y. Zhang, 2008. Study of Surface Modification of Nano-SiO$_2$ with Macromolecular Coupling Agent. *Chemical Engineering, 141, 354-361.*

10. Xia, R., et al., 2008. Surface modification of nano-sized silicon nitride with BA-MAA-AN terpolymer. *Applied polymer science, 107, 562-570.*

Effect of Acrylic Acid on Thermal Properties of Coconut Shell Powder Filled Polylactic Acid Biocomposites

Koay Seong Chun*, Salmah Husseinsyah, and Hakimah Osman

School of Materials Engineering
Universiti Malaysia Perlis

*Corresponding author: koayseongchun@hotmail.com

Abstract: *The effect of filler content and acrylic acid on thermal properties of polylactic acid (PLA)/coconut shell powder (CSP) biocomposites were studied. The studies of thermal properties of PLA/CSP biocomposites were carried out by using Differential scanning calorimetry (DSC) and thermogravimetric analysis (TGA). From DSC curve shown, incorporation of CSP increased the glass transition temperature (T_g) and percentage of crystallinity (X_c) of PLA/CSP biocomposites at 30 php CSP content. The increasing of X_c of PLA/CSP biocomposites was due to the nucleating effect from CSP and it was proven by the present of temperature peak of crystallization (T_c). The treatment with acrylic acid was increased the T_g and X_c of PLA/CSP biocomposites, due to the improved of filler-matrix interaction. However, melting temperature T_m of PLA/CSP biocomposites was not significantly effect by filler content and acrylic acid. Total weight loss at 600 ^{o}C and decomposition temperature of maximum rate (T_{dmax}), thermal stability of PLA/CSP increased with increasing of CSP content. The thermal stability of PLA/CSP biocomposites was enhanced with acrylic acid treatment.*

Keyword: Polylactic acid, coconut shell powder, acrylic acid, biocomposites

1.   INTRODUCTION

Nowadays, biocomposites materials have shown remarkable interest among the researchers and industries, as the demand of biocomposites increased with the increasing of environment concern. Generally, biocomposites were composites materials made from natural filler/fiber and fossil based plastic or biodegradable bioplastic (e.g, polylactic acid (PLA)). Previously, researchers made biocomposites by incorpoting natural filler into fossil based polymer, but those biocomposites were not fully biodegradable. Therefore, many researchers today were efforts on developing a new class of fully biodegradable "green" composites (biocomposites) by combining natural filler/fiber with biodegradable bioplastic [1].

PLA was one of the bioplastics, which polymerized from lactic acid obtained agricultural product such as corn, sugarcane and sugar beet [2]. PLA was very suitable in short life cycle product (e.g., packaging tray, and food container), since it can degrades after a period of time in soil and enzymatic environment [2]. PLA was also great in mechanical properties, thermal stability and wide processability, for example injection moulding,

extrusion and film blowing [4-5]. There was many advantage of PLA compared to commercial plastic, but it was not widely used in plastic industry because of its high cost [2,4,6]. Formerly, PLA can become priceless by mixing with low cost natural filler to become PLA biocomposites.

Coconut shell was lignocellulosic filler, which was which is agriculture co-product abundanced in Malaysia, since Coconut (Cocos nucrifera) in Malaysia is the fourth important crop in term of acreage, after oil palm, rubber and paddy. The lignocellulosic filler exhibit some excellent properties compare to mineral filler (e.g., calcium carbonate, kaolin , mica, and talc), as low cost, renewable, high specific strength to weight ratio, minimal health hazard, low density, less abrasion to machine, certainly biodegradability and environmental friendly [7]. However, the present of strong polarized hydroxyl groups on the surface of lignocellulosic fillers make the difficulty in forming a strong interfacial bonding with a non polar polymer matrix, as the hydrogen bonds tend to prevent the wetting of the filler surfaces [8-9]. In result, lignocellulosic fillers were shown poor mechanical properties in polymer composites as lack of good interfacial adhesion. Alternatively, the interfacial adhesion better filler and matrix can be improved by surface modification of filler. Currently, these was many of method to promote the interfacial adhesion between the lignocellulosic filler and polymer matrix, such as alkaline treatment [10], esterification [11-12], silane treatment [13], and using compatibilizer [14].

This research study was focus to investigate the effect of filler content and acrylic acid treatment on thermal properties of PLA/CSP biocomposites. The thermal properties of PLA/CSP biocomposites were investigated by using differential scanning calorimetry (DSC) analysis and thermogravimetric analyzer (TGA).

2.   EXPERIMENTAL

2.1   Materials

The polylactic acid (PLA) was supplied by TT Biotechnologies Sdn. Bhd., Penang. The coconut shell was obtained from market, Perlis and cleaned manually. After cleaned, the coconut shell was crushed and grinded into powder. The coconut shell powder (CSP) was dried at 80°C for 24 hours. The average particle size of the CSP was 38μm, by using Malvern Particle Size Analyzer Instrument. The acrylic acid (grade 01730) and ethanol was supplied by Fluka.

2.2   Filler Treatment

The acrylic acid was dissolved into ethanol (3 % (v/v)). The CSP was added slowly into the solution and stirred for 1 hour for completed esterificaition. The CSP was filtered and dried in oven at 80°C for 24 hours.

2.3   Preparation of Biocomposites

The PLA/CSP biocomposites was prepared by using Brabender Plastograph mixer Model EC PLUS at temperature 180°C and rotor speed of 50 rpm. Firstly, PLA was charged into mixing chamber for 1 minute until it completely melts. After 1 minute, CSP was added and mixing continued for 7 minutes. The total mixing time was 8 minutes. The biocomposites was compressed into 1 mm thin sheet by using compression moulding machine model GT 7014A. The compression procedure involved preheating at 180°C for 1 minute follow by compressing for 1 minute at the similar temperature and subsequent cooling under pressure for 5 minutes. The formulation of PLA/CSP biocomposites was shown in Table 1.

Table 1: Formulation of PLA/CSP biocomposites.

Materials	PLA/CSP untreated	PLA/CSP treated with AA
PLA (php)	100	100
CSP (php)	0, 30, 60	0, 30, 60
Acrylic acid (%)*	-	3

*3% based on weight of CSP [12].

2.4   Differential Scanning Calorimetry (DSC) Analysis

DSC analysis was particularly useful in determining glass transition temperature (T_g), crystallization temperature (T_c), melting temperature (T_m) and percentage of crystallinity of biocomposites (X_c). The DSC analysis was carried by using DSC Q10, Research Instrument. The sheet of PLA/CSP biocomposites was cut into small piece and placed in close aluminum pan with sample weight in range 7-8mg. The specimen was heated from 30˚C to 200˚C with a heating rate of 20˚C/min under nitrogen atmosphere. The nitrogen gas flow rate was 50 ml/min. The degree of crystallinity of biocomposites (X_c) can be evaluated from DSC data by using the following Eq. 1.

$$X_c = (\Delta H_f / \Delta H_f^0) \times 100 \tag{1}$$

Where ΔH_f was the heat fusion of the PLA biocomposites, and ΔH_F^0 was the heat fusion for 100% crystalline PLA ($\Delta H_{100} = 93.7$ J/g).

2.5   Thermogravimetric Analysis (TGA)

The thermal stability of biocomposites can studied through decomposition temperature at maximum rate (T_{dmax}), total weight loss at temperature 300°C and 600°C by using TGA. The thermal analysis was carried out by using TGA Pyris Diamond Perkin-Elmer apparatus. The sample was undergoes thermal scan from 30°C to 600°C in open platinum pan at heating rate of 20 ^{o}C/min under nitrogen atmosphere. The nitrogen flow rate was 50 ml/min.

3.   RESULT AND DISCUSSION

3.1   Differential Scanning Calorimetry (DSC)

DSC curve of virgin PLA, untreated and treated PLA/CSP biocomposites at different filler content were shown in Fig 1 and those DSC data was summarized in Table 2. The T_g and X_c of PLA/CSP biocomposites were increased at 30 php of CSP content compared to virgin PLA. However, T_g and X_c of PLA/CSP biocomposites decreased at 60 php CSP content. The increment of T_g can be explained by the reducing of chain mobility of non-crystalline chains were constrained by being anchored to the immobile crystallites. However, less constraint on the non-crystalline chain segments resulting more mobility to non-crystalline chains, causing decreasing in T_g [11]. The nucleating effect from lignocellulosic filler causes the X_c of PLA/CSP biocomposites increased. The decrement X_c of PLA/CSP biocomposites can be explained by explained by retraction of filler agglomerates to PLA chain to rearrange for crystallization. The T_c peak appear in PLA/CSP biocomposites around temperature 115° and it was indicated as nucleating effect of lignocellulosic filler [15]. The T_g and X_c of treated PLA/CSP biocomposites was higher than untreated PLA/CSP bicomposites. The increasing of T_g and X_c with the present of AA due to the nucleating effect was enhanced by strong filler-matrix interaction. The T_c and T_m of PLA/CSP biocomposites were not significantly effect by CSP content and AA treatment.
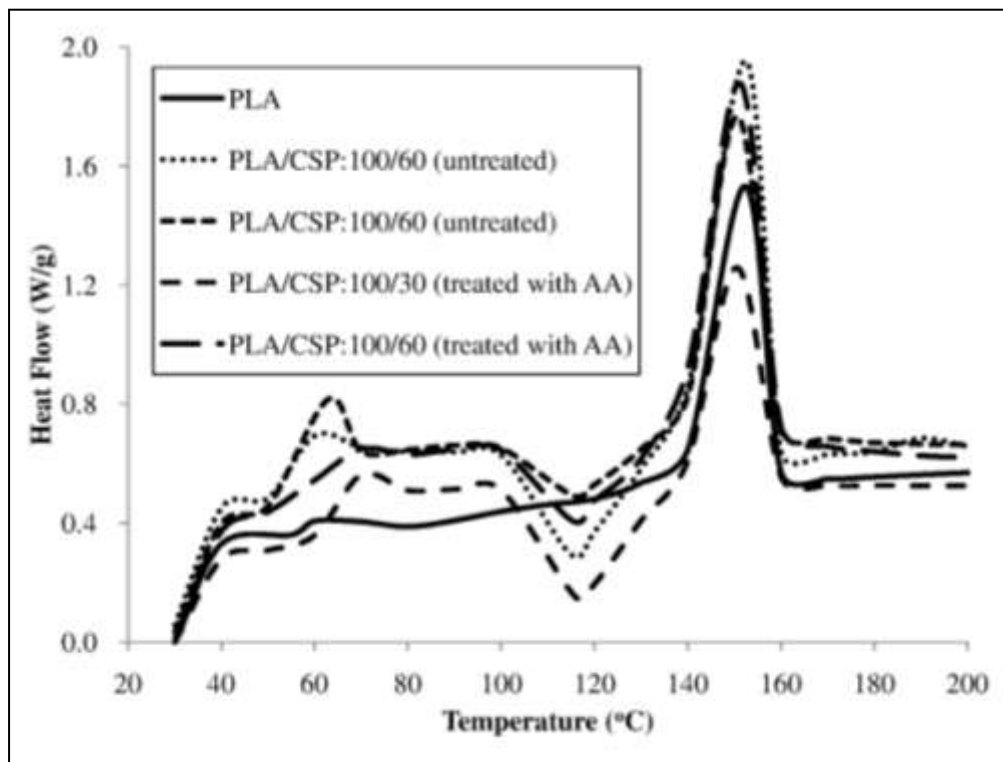
Fig. 1: DSC curves of PLA, untreated and treated PLA/CSP biocomposites at different filler content.

Table 2: Data DSC of PLA, untreated and treated PLA/CSP biocomposites.

Materials	T_g (^{o}C)	T_c (^{o}C)	T_m (^{o}C)	X_c (%)
PLA	57.7	-	151.8	30.2
PLA/CSP :100/30	62.9	115.4	150.1	31.3

456

untreated				
PLA/CSP:100/60 untreated	61.6	115.2	150.7	25.0
PLA/CSP :100/30 treated with AA	63.4	115.8	150.6	35.3
PLA/CSP :100/60 treated with AA	62.5	115.3	151.2	30.2

3.2 Thermogravimetric Analysis (TGA)

DTG curves of CSP, virgin PLA, untreated and treated PLA/CSP biocomposites with AA were shown in Fig 2. The data of DTG and TGA was summarized in Table 3. The CSP was decomposed at two stages in temperature range 200-400°C, and the decomposition involved: i) decomposition of hemicelluloses at 200-350°C and ii) decomposition of lignocelluloses at 350-400°C. The neat PLA, untreated and treated PLA/CSP biocomposites were decomposed in one stage above temperature 300°C. Figure 3 shown TGA curves of neat PLA, CSP, untreated and treated PLA/CSP biocomposites at different CSP content. The data from TGA curves is summarized into Table 3. At 300°C shown that total weight loss of PLA/CSP biocomposites decomposed early than virgin PLA. It was attributed to thermal decomposition of hemicelluloses in CSP at temperature range 250-300°C. The addition of CSP increased the thermal stability of PLA/CSP biocomposites, whereas the T_{dmax} of PLA/CSP biocomposites were higher compared to neat PLA. The total weight loss of PLA/CSP biocomposites at 600°C was decreased with increasing of CSP content. This that indicated the present of CSP enhanced the thermal stability of biocomposites and it might be attributed by the char formation from the pyrolysis of CSP, which act as protective layer preventing PLA matrix from thermal decomposition [15]. The CSP treated with AA was enhanced the thermal stability of PLA/CSP biocomposites, since the T_{dmax} of AA treated PLA/CSP biocomposites was increased along with decreasing of weight loss at temperature 300°C and 600°C. It can be explained by present of AA enhanced filler-matrix interaction and better dispersion of CSP particle in PLA matrix, resulting more homogenous of char layer to providing better thermal protection of biocomposites.
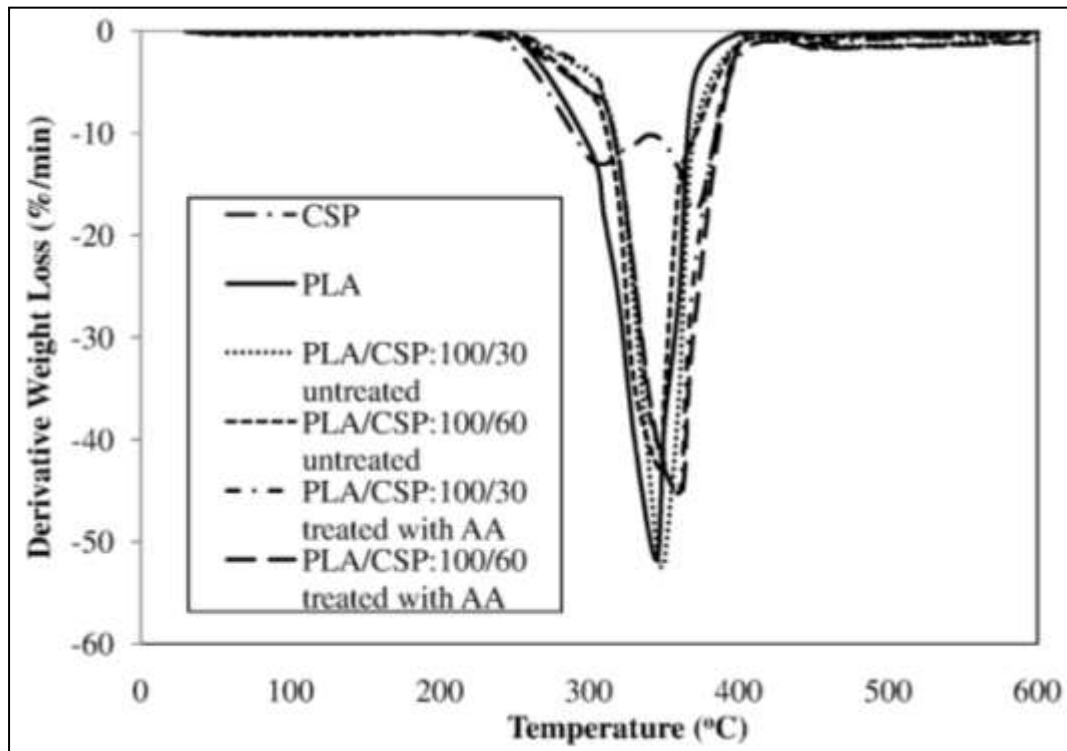
Fig. 2: Derivative thermogravimetric analysis curves of PLA, CSP, untreated and treated PLA/CSP biocomposites at different filler content.
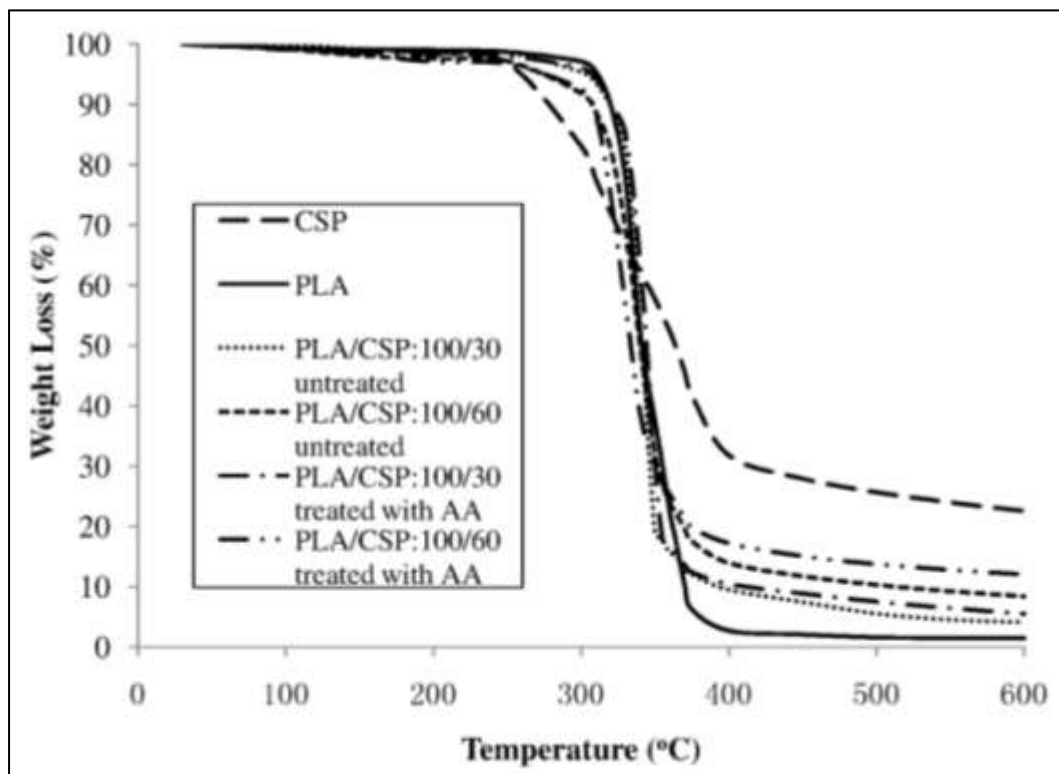
Fig. 3: Thermogravimetric analysis curves of PLA, CSP, untreated and treated PLA/CSP biocomposites at different filler content.

Table 3: Data TGA of CSP, PLA untreated and treated PLA/CSP biocomposites at different filler content.

Materials	T_{dmax}	Weight loss (%)

	(^{o}C)	300°C	600°C
PLA	344.63	2.90	98.52
PLA/CSP:100/30 untreated	346.32	4.63	95.92
PLA/CSP:100/60 untreated	348.28	8.16	91.59
PLA/CSP:100/30 treated with AA	360.76	3.91	94.50
PLA/CSP:100/60 treated with AA	362.17	7.51	87.93

4.   REFERENCES

1.   Averous, L., & Digabel, F. L. (2006). Properties of biocomposites based on lignocellulosic fillers, *Carbohydrate Polymers.,* 66, 480-493.
2.   Wu, C. S. (2009). Renewable resource-based composites of recycled natural fibers and maleated polylactide bioplastic: Charecterization and biodegradability, *Polymer Degradation and Stability.,* 94, 1076-1084.
3.   Yu, L., Dean, K., & Li, L. (2006). Polymer blends and composites from renewable resources, *Progress In Polymer Science., 31*, 576-602.
4.   Carrosco, F., Pages, P., Gamez, P. J., Satana, O. O., & Maspoch, M. L. (2010). Processing of poly(lactic acid): Charecterization of chemical structure, thermal stability and mechanical properties, *Polymer Degradation and Stability.,* 95, 116-125
5.   Schwark, F. (2009). Influence factors for scenario analysis for new environmental technologies - the case for biopolymer technology, *Journal of Cleaner Production.,* 17, 644-652.
6.   Madhavan, N. K., Nair, N. R., & John, R. P. (2010). An overview of the recent developments in polylactide (PLA) research, *Bioresource Technology., In Press*.
7.   Xie, Y., Hill, C. A. S., Xiao, Z., Militz, H., & Mai, C. (2010). Silane coupling agents used for natural fiber/polymer composites: A review, *Composites: Part A.,* 41, 806-819.
8.   Tserki, S., P. Matzinos, S. Kokkou, and C. Panayiotou. (2005). Novel Biodegradable composite based on treat lignocellulosic waste flour as filler. Part I. Surface chemical modification and characterization of waste flour, *Composites: Part A.*, 36, 965-974.
9.   John, M. J., & Anandjiwala, R. D. (2009). Chemical modification of flax reinforced polypropylene composites. *Composites: Part A.,* 40, 442-448.8.
10.   Fronaco, H. P. J., & Gozalez, V. A. (2005). A study of the mechanical properties of short natural-fiber reinforced composites. *Composites: Part B.,* 36, 597-608.
11.   Arif, M. F., Megat-Yusoff, P. S. M., & Ahamad, F. (2009). Effect of chemical treatment on oil palm empty fruit bunch reinforced high density polyethylene composites, *Journal of Reinforced Plastics and Composites.,* 29, 2105-2118.
12.   Salmah, Ismail, H., & Abu Bakar, A. (2006). The effect of chemical modification of paper sludge filled Polypropylene (PP) / Ethylene Propylene Diene Terpolymer (EPDM) composites, *Journal Reinforced Plastic & Composites.,* 25, 43-58
13.   Pickering, K. L., Abdalla, A., Ji, C., McDonald, A. G., & Franich, R. A. (2003). The effect of silane coupling agents on radiata pine bibre for use in thermoplastic matrix composites, *Composites: Part A.,* 34, 915-926

14.   Danyadi, L., Moczo, J., & Pukanszky, B. (2010). Effect of various surface modifications of wood flour on the properties of PP/wood composites. *Composites: Part A., 41*, 199-206

15.   Perinovic, S., Andricic, B., and Erceg, M. (2010). Thermal properties of poly($_L$-lactic)/olive stone flour composites. *Thermochimica Acta., 510*, 97-102.

A Study on FTIR Spectroscopy and Thermal Analysis of Palm based Polyurethane

Maisara Shahrom[*], Wong Chee Sien, and Khairiah Hj. Badri

School of Chemical Sciences and Food Technology, Faculty Science and Technology, Universiti Kebangsaan Malaysia, 43600 Bangi, Selangor Darul Ehsan, Malaysia

*Corresponding author: maisarashahrom@hotmail.com

Abstract: *The palm kernel oil based polyurethane (PU) was synthesized through the reaction of palm-based monoester-OH with 2,4-diphenylmethane diisocyanate (MDI). Four compositions of PU were prepared using prepolymerization method by varying the ratio between monoester-OH and MDI and labeled as PU1 (100:200), PU2 (100:150), PU3 (100:100) and PU4 (100:75). The presence of urethane bond was observed in all the Fourier Transform Infrared Spectroscopy (FTIR). The carbonyl peak (C=O) was identified at 1702 cm^{-1} and amide peak (N-H) at 3293 cm^{-1}. Thermal analysis were carried out by using Differential Scanning Calorimetry (DSC) and Thermogravimetric Analysis (TGA). Optimization of PU showed that PU1 gave the best thermal properties (T_g 74℃ and stable temperature 195℃) and the highest gel content (66%) than PU2, PU3 and PU4.*

Keywords: Palm based polyurethane, FTIR, TGA, DSC

1.   INTRODUCTION

In recent years, the use of renewable resources mainly from forest products has attracted the attention of many technologists as potential substitutes of using petrochemical-based where crude oil and coal are used as starting materials. These materials are very expensive, higher rate of depletion and require high technology processing systems. By using renewable resources such as palmeri oil, soya bean oil, palm oil, vernodia oil have been synthesize to replace the petrochemical based polyol [1]. In this research polyurethane was produced by using palm kernel oil as polyurethane based since Malaysia is globally known as the major producer of palm oil.

Polyurethane is a versatile polymer due to some excellent chemical and physical properties which suit to a wide range of applications including elastomers, fibers, foams, surface coatings and adhesive products [2]. They are becoming increasingly important as engineering materials. Polyurethane can be prepared by a simple polyaddition reaction of polyol, isocyanate and a chain extender which is usually low molecular weight diols [3]. The mechanical and thermal properties are mainly depends on the stoichiometric ratios of isocyanate-to-hydroxyl groups and the amount of chain extender used. These stoichiometric contribute significant effects on the polyurethane properties.

Polyurethane are block copolymers containing of low molecular weight polyester covalently bonded by a urethane group (-NHCO=O). The polyurethane been produced in this research is undergo prepolymerization method which undergo by the reaction of an excess of diisocyanate with a polyol. One of the isocyanate groups (NCO) reacts with a hydroxyl group (OH) of the polyol. Another isocyanate group reacts with the second OH group. The prepolymer is formed by addition polymerization and there are no by-products formed that have to be removed. The mole reaction ratio of the diol to diisocyanate is normally kept in the range 1.6 to 2.5 mole of the diisocyanate. The chemical reaction proceeds with the prepolymer end group isocyanate react with the available hydroxyl groups of the diol from

chain extender and then formation of polyurethane finally occured [4]. This is illustrated in Fig. 1.
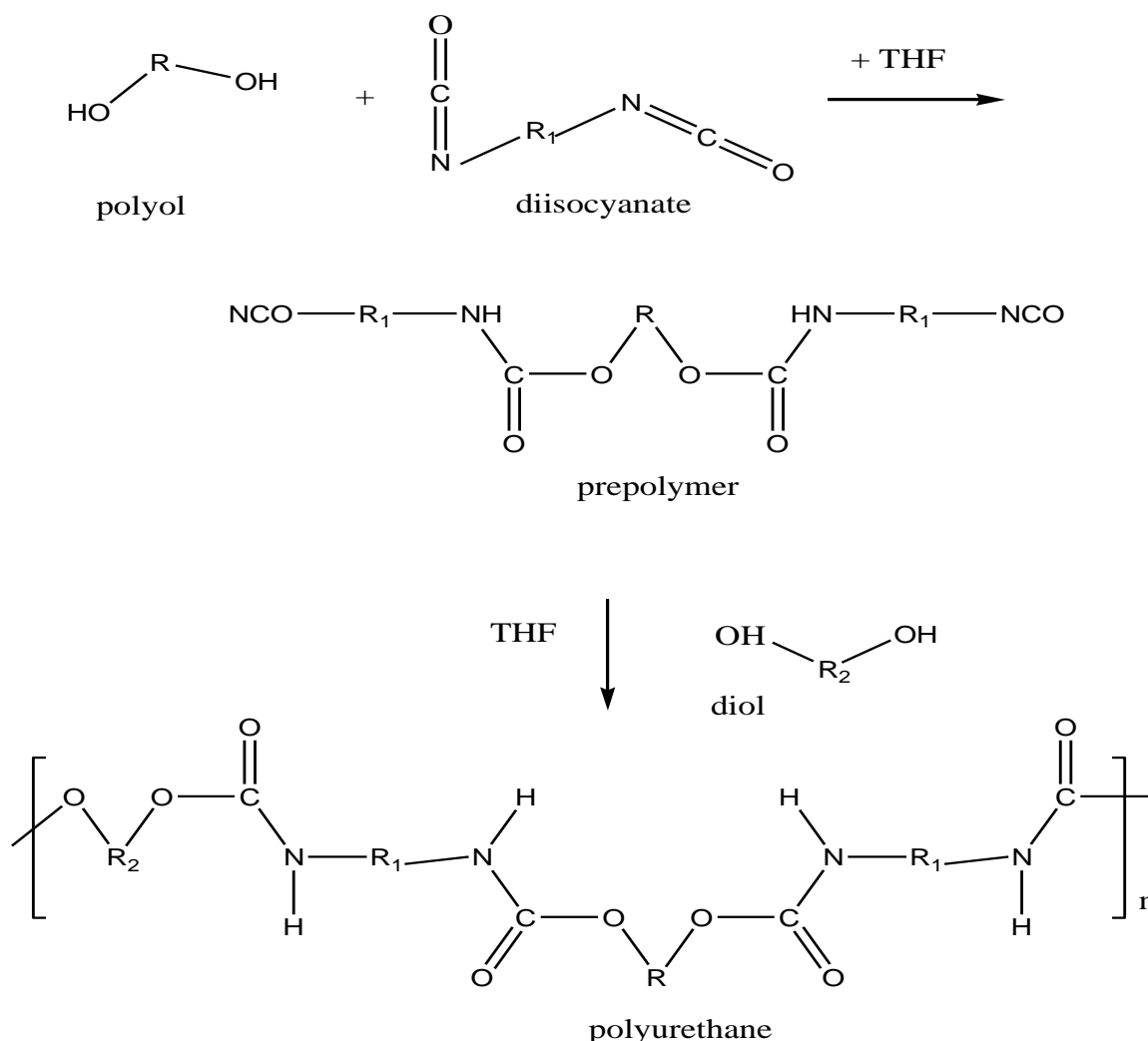
Fig. 1: Mechanism of polyurethane.

Polyurethane has block-segmented structure and consists of alternating hard and soft segments [5]. The polyurethane main chain includes both soft and rigid segments. The soft segments, which arise from high-molecular- weight polyols, provide rubbery properties and the hard segments, which provide crosslinking agents and rigid properties which arise from diisocyanate [6]. In this paper, it describes a significant investigation of isocyanate / hydroxyl group ([NCO/OH]) ratio on the FTIR spectrum and thermal analysis on polyurethane film.

2. MATERIALS AND METHOD

2.1 Materials

In this research, polyol was produced by using palm kernel oil via the method which describes in studies of Badri and her partners [1]. 4,4-diphenylmethane diisocyanate (MDI) gained from Cosmo polyurethane (M) Sdn. Bhd., Klang, Malaysia. Tetrahydrofuran (THF) were gained from Merck Sdn Bhd, Malaysia. Diethylene glycol (DEG) was purchased from Fluka Chemie Sdn. Bhd, Malaysia.

2.2 Methods

Polyurethane (PU) film was prepared by the reaction of polyol and MDI. The polyol dissolve in in THF was mixed with MDI in different ratios which follow [(OH:NCO)] (100:200, 100:150, 100:100 and 100:70) respectively denoted as PU1, PU2, PU3 and PU4. The preparation were prepared in the round-bottomed flask under nitrogen atmosphere at ambient temperature to form urethane prepolymer and then added with DEG as chain extender. Then the solution was agitated at 200 rpm in 1 hour for the polymerization. Then the mixture was cast on Teflon plate with 1 mm thickness film. The cast film was dried in vacuum oven at 55°C for 24 hours.

3. RESULTS AND DISCUSSION

3.1 FTIR Spectroscopy

Fourier Transform Infrared Spectrum recorded was obtained from FTIR spectroscopy Perkin Elmer Spectrum BX Spectroscopy model. This analysis is important to detect the functional group of PU.
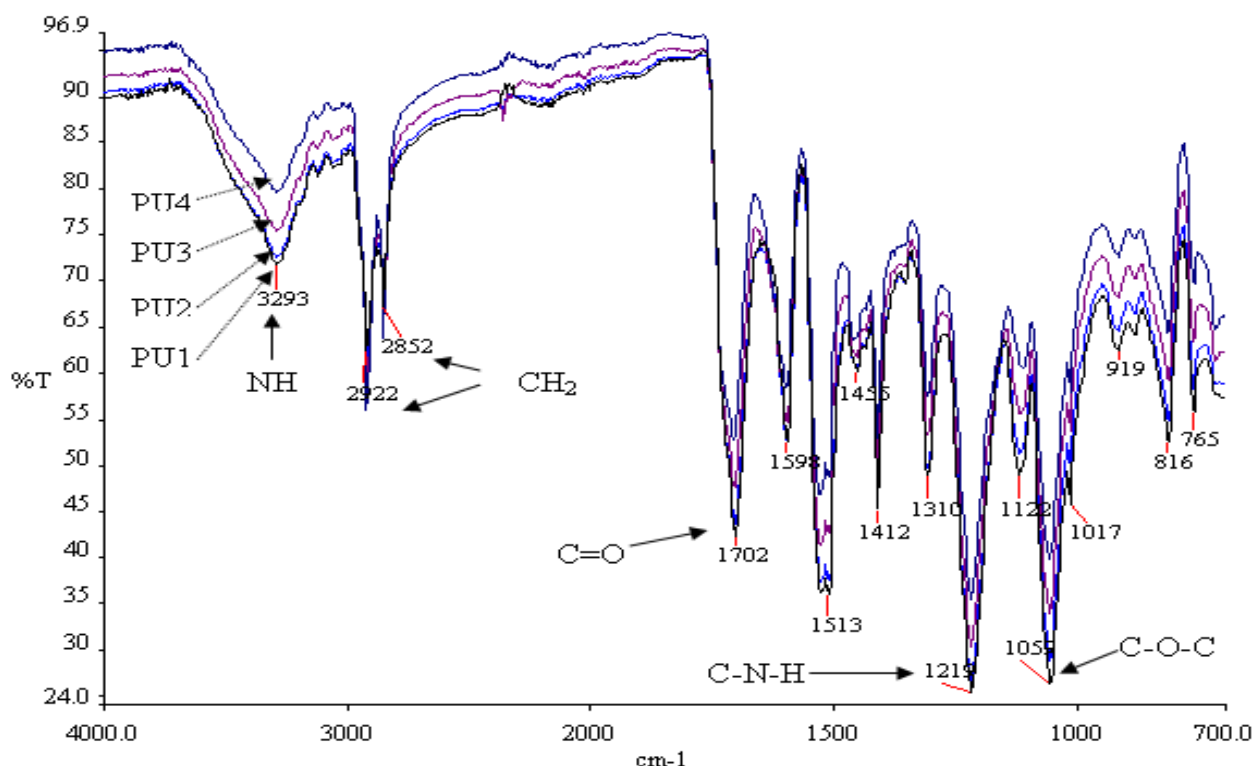
Fig. 2: FTIR spectrum for PU1, PU2, PU3 and PU4.

Fig. 2 showed the IR spectrum for PU1, PU2, PU3 and PU4. Ratio OH: NCO for PU1 is 100:200, PU2 is 100:150, PU3 is 100:100, and PU4 is 100:70. PU1 has the highest amount of MDI compared to PU2, PU3 and PU4 which has the lowest amount of MDI. From Fig.2, we can see that the existence of amide peak (N-H) at 3293 cm^{-1}, carbonyl urethane group (C=O) at 1702 cm^{-1}, carbamate group (C-N) at 1219 cm^{-1} proved the formation of urethane in the PU above. The wave number for N-H and C=O peak are at 3293 cm^{-1} and 1702 cm^{-1} respectively. The absence of isocyanate peak at 2270 cm^{-1} showed complete reaction between

NCO and OH. According to Pavia et al. (2009) [7], the free C=O is at 1730 cm^{-1} meanwhile C=O from the Fig. 2 showed at 1702 cm^{-1}. This is proved that C=O was a hydrogen bonded carbonyl group. Hence, the FTIR proved that hydrogen bonding was occurred in this prepolymerization method. The hydrogen bonding was occurred between functional group C=O and N-H urethane group. Fig. 3 showed the illustration of the formation of hydrogen bonding in polyurethane.
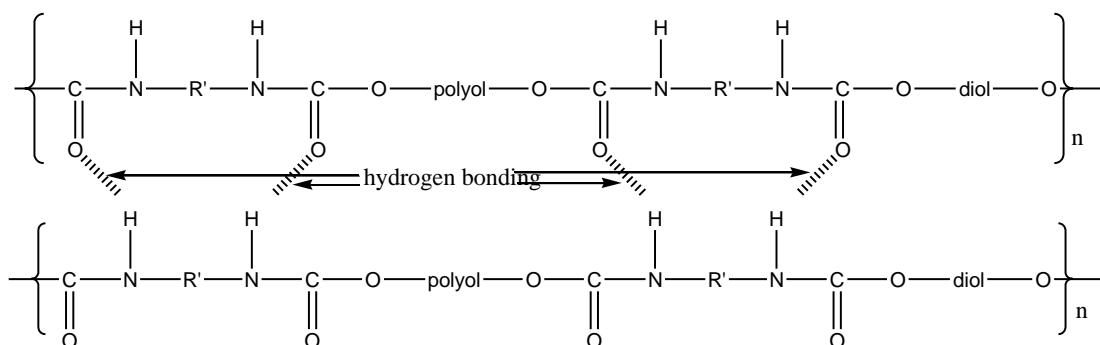
Fig. 3: Formation of hydrogen bonding in polyurethane.

According to Oprea et al. (1999) and Ho et al. (1999) [8,9], the existence of hydrogen bonding at C=O and N-H will shifted the peak to lower frequency and increase the transmittance. When the formation of hydrogen bonding occurred, N-H group acting as proton donors, while C=O acts as a receiver that receives the proton from N-H. This interaction between the molecules forming hydrogen bonds formed. Mohaghegh et al. (2006) [10] stated that, crosslinking can be formed if the resulting hydrogen bonds are strong and this restricted the movement of polymer chain. Carbonyl stretching peak at wave numbers around 1690-1660 cm^{-1} is a carbonyl group of urea. Figure 2 shows no peak of urea, and this clearly shows that urethane is the main group in polyurethane above.

3.2 Differential Scanning Calorimetric (DSC)

DSC analysis carried out to study the nature of PU polymer chain mobility when subjected to heat energy by heating. Table 1 showed the glass transition temperature (T_g) for PU1, PU2, PU3 and PU4.

Table 1: Glass transition temperature (T_g) for PU1, PU2, PU3 and PU4.

PU sample	Glass transition temperature, T_g (^{o}C)
PU1	74
PU2	67
PU3	61
PU4	51

From Table 1, we can see that PU1 gives the highest T_g with 74 ^{o}C compared with PU2 (67 ^{o}C), PU3 (61 ^{o}C) and PU4 (51 ^{o}C). The higher the ratio of NCO/OH is used, the higher the T_g PU. According to Chattopadhyay et al. (2006) [11], T_g temperature and thermal stability will increase with increasing ratio of NCO/OH. T_g can give an indication of the effect of hard segment in PU. PU with higher T_g is influenced by the hard segments in PU that restrict the movement of PU chain. This is proved that amount of isocyanate plays an important role on determining T_g PU. This is because of hard segments formed from the

reaction between OH and NCO while soft segment consist of polyester flexible chain. So, PU1 has the highest amount of isocyanate so it provides more hard segment compared to soft segment so that the T_g increased in PU1. Compared with PU4 which has lesser amount of isocyanate and give more soft segment than hard segment, so the T_g for PU4 is decreased [12]. In addition, the influence of stearic effect also influencing because of the aromatic ring in the structure of PU and limit the chain mobility of PU. Figure 4 is the illustration of hard segment and soft segment in polyurethane. From Fig. 4, we can see that the hard segment consists of isocyanate, urethane group and chain extender meanwhile soft segment consists of polyol flexible chain. So, increasing amount of isocyanate may influence the amount of hard segment in PU.
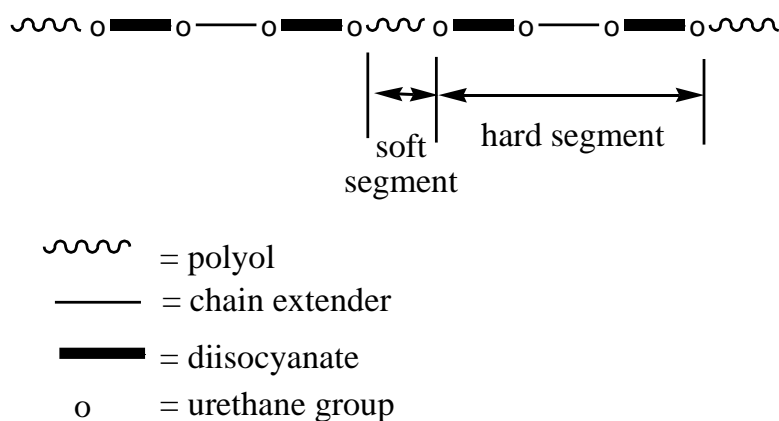
Fig. 4: Illustration of hard segment and soft segment of polyurethane.

3.3   Termogravimetry analysis (TGA)

TGA analysis was carried out to see the thermal stability and the percentage loss of mass. TGA is suitable method to evaluate the thermal properties of several types of polyurethane. Figure 5 is a TGA termogram of PU1, PU2, PU3 and PU4. Two-step degradation can be observed in all curves. The first was associated with the hard segments degradation and the second one with the soft segments.
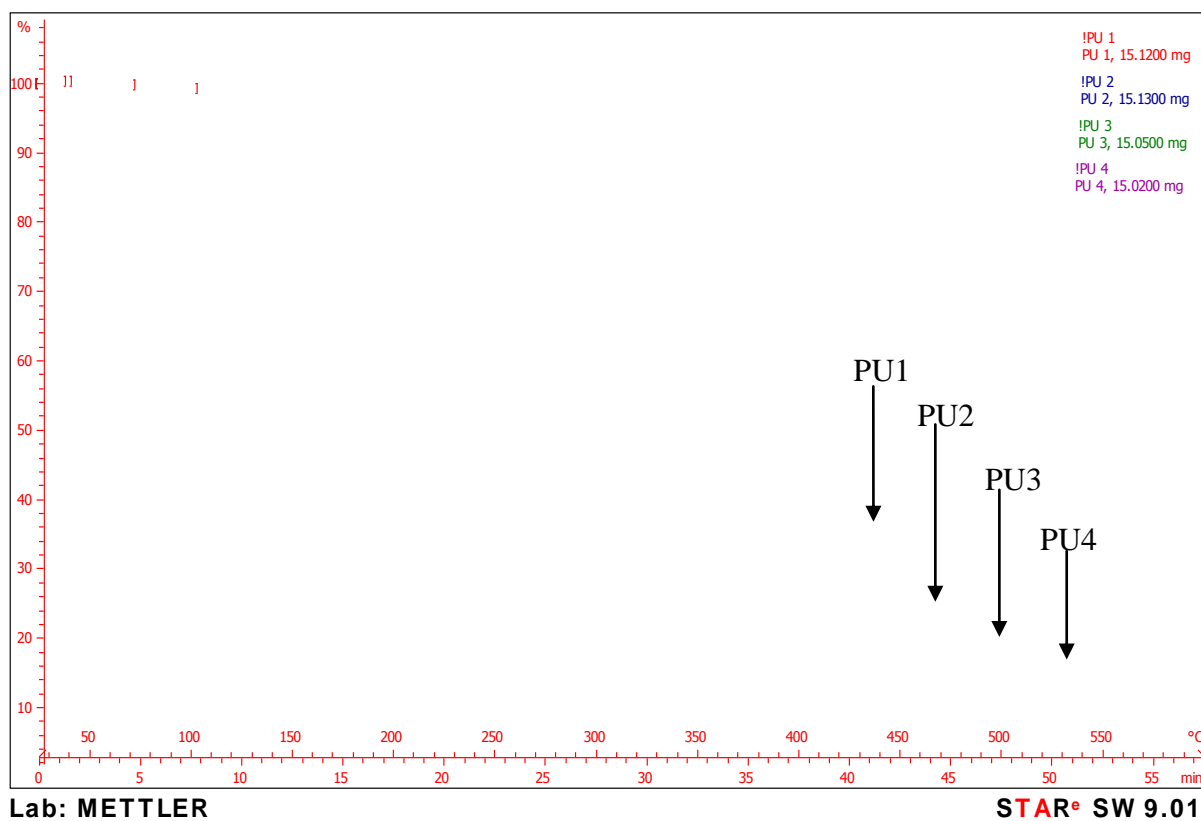
Fig. 5: TGA thermogram for PU1, PU2, PU3 and PU4.

Table 2: TGA result for PU1, PU2, PU3 and PU4.

PU	T_{stable}, T_1 (^{o}C)	% mass loss for T_1	T_2 (^{o}C)	% mass loss for T_2	% Total mass loss
PU1	195	52.2%	390	40.7%	94.2%
PU2	190	46.6%	392	47.9%	95.2%
PU3	185	41.5%	395	54.4%	96.3%
PU4	180	39.0%	397	56.3%	96.6%

From the Table 2 we can see that PU1 gives the highest stability temperature with 195 ^{o}C compared to PU2 (190 ^{o}C), PU3 (185 ^{o}C) and PU4 (180 ^{o}C). The initial degradation temperature is due to the hard segments. An increasing tendency in mass loss values can also be observed as NCO/OH increase in hard segment content. More isocyanate content in PU1, allow complete reaction between isocyanate and OH occurs and increasing the degree of crosslinking in PU [13]. Thus the higher temperatures required for the degradation of the hard segment chains. PU4 has lower isocyanate content, so the reaction between OH and isocyanate are limited. This gives the degree of crosslinking of PU4 is lower than PU1. TGA analysis also provides the percentage mass loss after heating to 600 ^{o}C of maximum temperature. The percentage of mass loss at initial degradation for PU1 also higher at 52.2% compared to PU2 (46.6%), PU3 (41.5%) and PU4 (39.0 %). This is because the amounts of isocyanate in PU1 are much compared to PU2, PU3 and PU4 and this contribute to the much more formation of hard segments in PU1 [14].

Following the initial degradation in the hard segments, the second stage of degradation was related to the soft segments and started at about 390 ^{o}C. This soft segments was influenced by the content of OH that did not react with the isocyanate. PU4 gives the

highest temperature with 397 ^{o}C compared to PU3 (395 ^{o}C), PU2 (392 ^{o}C) and PU1 (390 ^{o}C). However, the difference is not significant. The significant differences can be seen in the percentage of mass loss of the second stage refers to the soft segments, where PU4 shows the percentage of the highest mass loss of 56.3% compared to PU3 (54.4%), PU2 (47.9%) and PU1 (40.7%).

Total percentage of mass loss for PU4 (96.6%) is the highest while PU1 (94.2%) is the lowest total percentage of mass loss. From this analysis showed that PU1 provide the thermal stability higher than PU2, PU3 and PU4.

4.   CONCLUSION

FTIR results proved the prepolymerization occurred in PU. The polymerization of urethane bond was proved by the disappearance of the peak of isocyanate 2270 - 2250 cm^{-1} in FTIR result. PU1 has the highest NCO/OH ratio and gives the highest T_g value at 74 ^{o}C and decreased to PU4 at 51 ^{o}C in DSC analysis. The degradation of polyurethane occurred in two stages. The first one associated with the hard segments and the second one associated with the soft segments. The TGA curved showed that the hard segment content had a strong influence on the thermal profile of the sample. TGA curved shows that PU1 also gives the highest stable temperature at 195 ^{o}C compared to PU2, PU3 and PU4.

5.   REFERENCES

29.   Badri, K.H., Othman, Z. & Ahmad, S.H. (2004). Rigid polyurethane foams from oil palm resources. *Journal of Materials Science*. , 39, 5541-5542.

30.   Badri, K.H., Ahmad, S.H. & Zakaria, S. (2001). Production of a high-functionality RBD palm kernel oil-based polyester polyol. Journal of Applied Polymer Science. , 81, 384-389

31.   Deligoz, H., Yalcinyuva, T. & Ozgumus, S. (2005). A novel type of Si-containing poly(urethane-imide)s: synthesis, characterization and electrical properties. *European Polymer Journal*. , 41, 771-781.

32.   Clemitson, I. (2008). *Castable Polyurethane Elastomers.* Boca Raton: CRC Press.

33.   Chattopadhyay, D.K., Mishra, A.K., Sreedhar, B. & Raju, K.V.S.N. (2006). Thermal and viscoelastic properties of polyurethane-imide/clay hybrid coatings. Polymer Degradation and Stability. , 91 ,1837-1849.

34.   Lin, C.Y., Liao, K.H., Su, C.F., Kuo, C.H. & Hsieh, K.H. (2007). Smart temperature-controlled water vapour permeable polyurethane film. Journal of membrane science. , 299 , 91-96.

35.   Pavia, D.L., Lampman, G.M., Kriz, G.S. & Vyvyan J.R. (2009). *Introduction to Spectroscopy*. (Ed. ke-4) Belmont: Brooks/ Cole Cencage Learning.

36.   Oprea, S., Vlad, S., Stanciu, A., Ciobanu, C. & Macoveanu, M. (1999). Synthesis and characterization of poly(urethane-urea-acrylate)s. *European Polymer Journal* , 35 , 1269-1277.

37.   Ho, K.S., Hsieh, K.H., Huang, S.K. & Hsieh, T.H. (1999). Polyurethane-based conducting polymer blends: I. Effect of chain extender. *Synthetic Metals* , 107, 65-73.

38.   Mohaghegh, S.M.S., Barikani, M. & Entezami, A.A. (2006). The effect of grafted poly(ethylene glycol monomethyl ether) on particle size and viscosity of aqueous polyurethane dispersions. *Colloids and Surfaces A: Physicochem Eng. Aspects* ,276, 95-99.

39. Chattopadhyay, D.K., Mishra, A.K., Sreedhar, B. & Raju, K.V.S.N. (2006). Thermal and Viscoelastic properties of polyurethane-imide /clay hybrid coatings. *Polymer Degradation and Stability* ,91, 1837-1849

40. Drobny, J.G. (2007). *Handbook of Thermoplastic Elastomers*. New York: PDL Plastic Design Library.

41. Cautinho, F.M.B., Delpech, M.C. (2000). Degradation profile of film cast from aqueos polyurethane dispersion. *Polymer Degradation and Stability* ,70, 49-57.

42. Chuayjuljit, S., Sangpakdee, T. & Saravari, O. (2007). Processing and properties of palm oil –based rigid polyurethane foam. *Journal of Metals, Materials, Minerals* ,17, 17-23.

Effect of Sodium Dodecyl Sulfate on Mechanical and Morphological Properties of Chitosan Filled Polypropylene Composites

Faisal Amri[*], Salmah Husseinsyah, and Kamarudin Hussin

School of Materials Engineering, Division of Polymer Engineering
Universiti Malaysia Perlis, 02600, Jejawi, Perlis, Malaysia

*Corresponding author: icalamri@gmail.com

Abstract: *In this article, effect of sodium dodecyl sulfate (SDS) on mechanical and morphological properties of polypropylene (PP)/chitosan composites was investigated. From mechanical point of view, results showed the treated PP/chitosan composites had higher tensile strength and Young's modulus than untreated ones, but lower in elongation at break in the same filler loading. Scanning electron microscopy (SEM) and fourier transform infrared (FTIR) studies revealed less detachment of filler from matrix on the tensile surface of treated PP/chitosan composites as an evidence of enhanced interfacial adhesion between filler and matrix due to the formation of covalent bonding between chitosan and SDS.*

Keywords: Polypropylene, chitosan, sodium dodecyl sulfate, properties, composites

1. INTRODUCTION

Research in the use of materials from renewable sources as filler or reinforcing agent in plastic composites is growing. Chitosan is known as the second most abundant natural fiber after cellulose. It is extracted from crustaceous shells such as crabs, shrimp and prawns[1]. Currently, active researches have been conducted on the application of chitosan as biomaterials due to its biodegradability, biocompatibility and non toxicity[2], etc. in spite of low cost, resource abundances, lightness and non abrasive nature[3].

In this study, polypropylene (PP) was used as the matrix and chitosan as natural filler in manufacturing the plastic composites. PP is used due to its excellent mechanical and thermal properties[4]. A large number of studies have reported the use of PP in natural fiber reinforced composites[5,6], however its study in composite materials filled with chitosan was less reported. From our knowledge, chitosan is a polysaccharide possesses the hydroxyl (–OH) and amine (–NH_2) groups along the chain[7]. The existence of these groups contributes the hydrophilic character of chitosan which decrease the interfacial adhesion with hydrophobic matrix leads to reduce mechanical properties. Therefore, several chemical modification methods have been developed in order to hydrophobize the chitosan and enhance the interfacial adhesion[8,9].

The interest in the use of chemical modification method is mainly due to the appearance of polar groups of chitosan which contribute a substitution reaction with modifying agent[10]. Sodium dodecyl sulfate (SDS) is known as anionic surfactant and widely used in synthesizing of biomaterials [11]. The presence of SDS onto chitosan chain is expected decrease the hydrophilic character as a result of the formation of chemical interaction between polar head groups of SDS and polar groups of chitosan. The current study was devoted to investigate the effect of SDS on mechanical and morphological properties of PP/chitosan composites.

2.   EXPERIMENTAL

2.1   Materials

Polypropylene (PP) homopolymer used in this study was injection molding grade S11232 G112, from Polypropylenas Sdn. Bhd., Malaysia with MFI value of 45 g/10 min at 230°C. Chitosan (Hunza Nutriceuticals Sdn Bhd., Malaysia) with average size of 80 μm and degree of deacetylation (DD) of 90% was dried in an oven for 24 hours at 80°C to eliminate moisture content. Table 1 shows the properties of chitosan. Ethanol (98%.v/v) and sodium dodecyl sulfate (SDS) in powder form were obtained from Aldrich, Penang, Malaysia.

Table 1: Physical and chemical properties of chitosan.

Item	Specification	Test Method
Appearance	Off-white powder	Visual
Solubility of 1% chitosan in 1% acetic acid	>99.0 %	Dissolution & Filtration
Viscosity	150 – 200 mPa.s	Ubbelohde Viscometer
Moisture content	< 10.0 %	Infra-red drying
Ash content	< 1.0 %	Inceneration

2.2   Chemical Modification of Chitosan

SDS solution was prepared by dissolving SDS powder in ethanol at temperature of 40°C. The amount of SDS used was 3% by weight of filler. The solution was then cooled down to room temperature. Afterward, chitosan was gradually added to the solution while slowly stirred. The mixture was mechanically stirred for 2 hours in order to be homogenized and stayed overnight. The precipitate was filtered and then dried in the oven at 80°C for 24 h to remove ethanol residue.

2.3   Mixing Procedure

PP/chitosan composites were prepared in a Z-blade Mixer at 190°C and rotor speed 50 rpm. PP was first charged to start the melt mixing. After 12 min, the chitosan was added. Mixing was continued for another 3 min. At the end of 15 min, the PP/chitosan composites were taken out and sheeted through a laboratory mill at 2.0 mm nip setting. The sample of PP/chitosan composites were compression molded in an electrically heated hydraulic press. Hot-press procedures involved preheating at 190°C for 9 min followed by compressing for 3 min at the same temperature and subsequent cooling under pressure for 3 min. Table 2 shows the formulation of untreated and treated PP/chitosan composites at different filler loading.

Table 2: Formulation of untreated and treated PP/chitosan composites.

Materials	Untreated PP/Chitosan Composites	Treated PP/Chitosan Composites
PP (php)	100	100
Chitosan (php)	0; 10; 20; 30; 40	10; 20; 30; 40
Sodium dodecyl sulfate (SDS) (%wt.)	-	3

php = part per hundred of polymer

2.4 Tensile Testing

Tensile tests were carried out according to ASTM D 638-91 on an Instron 5582. Five dumbbell specimens of each composition with thickness 1 mm were cut from the molded sheets with a Wallace die cutter. A cross head speed of 50 mm/min was used and the test was performed at $25 \pm 3\,^{0}$C.

2.5 Morphology Study

Study on the morphology of tensile fractured surface of PP/chitosan composites was carried out using a scanning electron microscope (SEM), model JSM 6260 LE JEOL. The fracture ends of specimens were mounted on aluminium stubs and sputter coated with a thin layer of palladium to avoid electrostatic charging during examination.

2.6 Fourier Transform Infrared (FTIR) Spectroscopy

Fourier transform infrared (FTIR) spectroscopy analysis of untreated and treated chitosan was carried out in ATR mode (Perkin-Elmer 1600 Series) scanned from 650 to 4000 cm^{-1} with resolution of 4 cm^{-1}.

3. RESULTS AND DISCUSSION

Fig. 1 shows effect of filler loading on tensile strength of untreated and treated PP/chitosan composites. The tensile strength of untreated and treated PP/chitosan composites decreases with the increase of filler loading due to the lack interaction between chitosan and PP matrix on the interface resulted from the different polarity between hydrophilic chitosan and hydrophobic PP matrix. As the filler loading increases, thereby increasing the interfacial area, the worsening interfacial bonding between chitosan filler and PP matrix decreases the tensile strength. However, the tensile strength of treated PP/chitosan is higher as compared to untreated PP/chitosan composites. The presence of SDS onto the surface of chitosan reduces significantly the hydrophilicity. This might be due to the formation of intermolecular bonding between polar group of chitosan and polar group of SDS through the covalent bond.
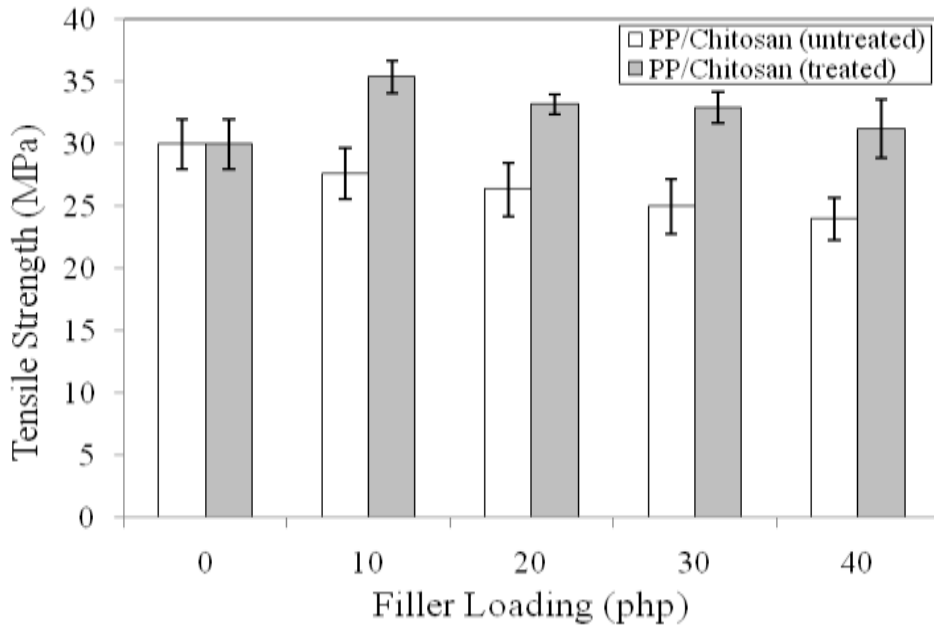
Fig. 1: Effect of filler loading on tensile strength of untreated and treated PP/chitosan composites.

Fig. 2 shows effect of filler loading on elongation at break of untreated and treated PP/chitosan composites. The increase of filler loading decreases significantly the elongation at break of untreated and treated PP/chitosan composites due to the formation of rigid interface between chitosan and PP matrix that hinder the mobility of PP molecular chain leading to loss of flexibility of PP matrix. At a similar filler loading, the treated PP/chitosan composites show lower elongation at break compared to the untreated PP/chitosan composites. On the contrary, the increase of filler loading increases the Young's modulus of untreated and treated PP/chitosan composites as shown in Fig. 3. The stiffness of PP/chitosan composites is apparently stronger at a higher filler loading. The treated PP/chitosan composites exhibit higher Young's modulus than untreated PP/chitosan composites.
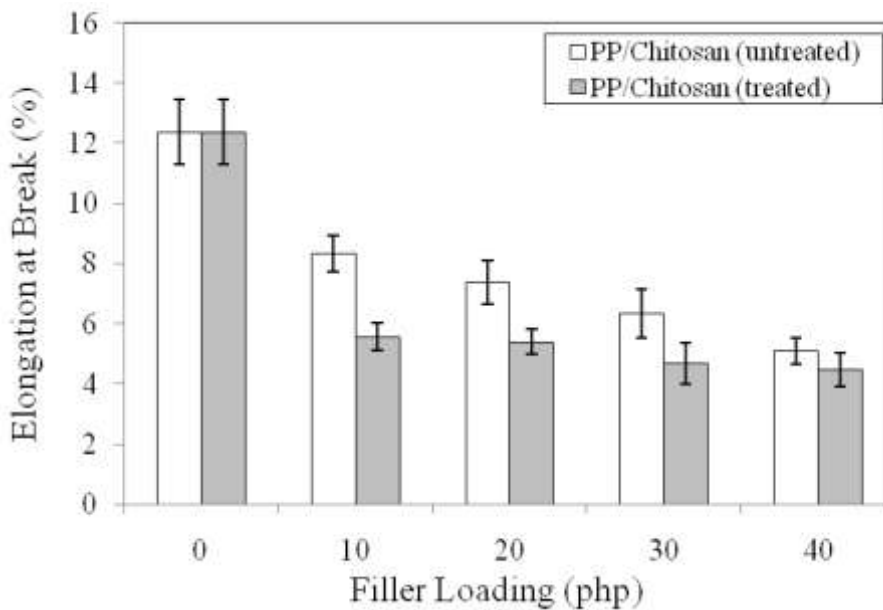
Fig. 2: Effect of filler loading on elongation at break of untreated and treated PP/chitosan composites.
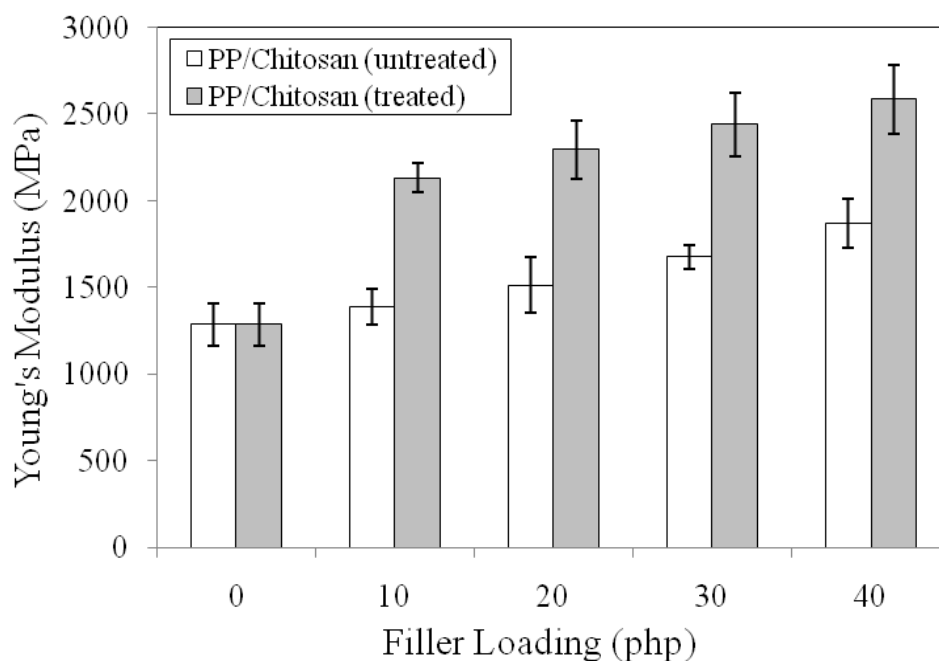
Fig. 3: Effect of filler loading on Young's modulus of untreated and treated PP/chitosan composites.

Figs. 4(a) – (d) show SEM micrographs of tensile fractured surface of untreated and treated PP/chitosan composites. The micrographs of untreated PP/chitosan composites (Figs. 4(a) and (b)) show the appearance of voids indicates to pulled out filler from the matrix. This is mainly due to poor wetting of the filler by the matrix. The fracture occurred at the interface between chitosan and PP matrix. The different polarity between filler and matrix leads to lack interaction on the interface especially at a higher of filler loading. However, the less appearance of voids is observed on the tensile surface of treated PP/chitosan composites (Figs. 4(c) and (d)). A good wetting of the filler by the matrix is related to the presence of SDS which is hydrophobically modified the chitosan leads to enhanced interfacial adhesion with PP matrix.

Fig. 5 illustrates the FTIR spectra of untreated and treated chitosan. As can be seen, the IR spectrum of untreated chitosan, the main characteristic peaks of chitosan are at 3358 cm^{-1} (O – H stretch), 2872 cm^{-1} (C – H stretch), 1675 cm^{-1} (N – H bend) and 1590 cm^{-1} (C = O stretch). The IR spectrum of treated chitosan exhibits a significant absorption on band of hydroxyl group from 3358 cm^{-1} to 3251 cm^{-1} indicating the reduction of hydrophilic character of chitosan. This is attributed to the presence of covalent bonding between polar head group of SDS and hydroxyl group of chitosan as identified by the presence of the absorption band at 1722 cm^{-1}. The formation of this bonding is also supported by the reduction of bands at 1675 cm^{-1} to 1645 cm^{-1} and 1590 cm^{-1} to 1565 cm^{-1} indicating of N – H bending vibration and amide I (C = O) stretching vibration of chitosan chain. The schematic reaction between chitosan and sodium dodecyl sulfate (SDS) is shown in Fig. 6.
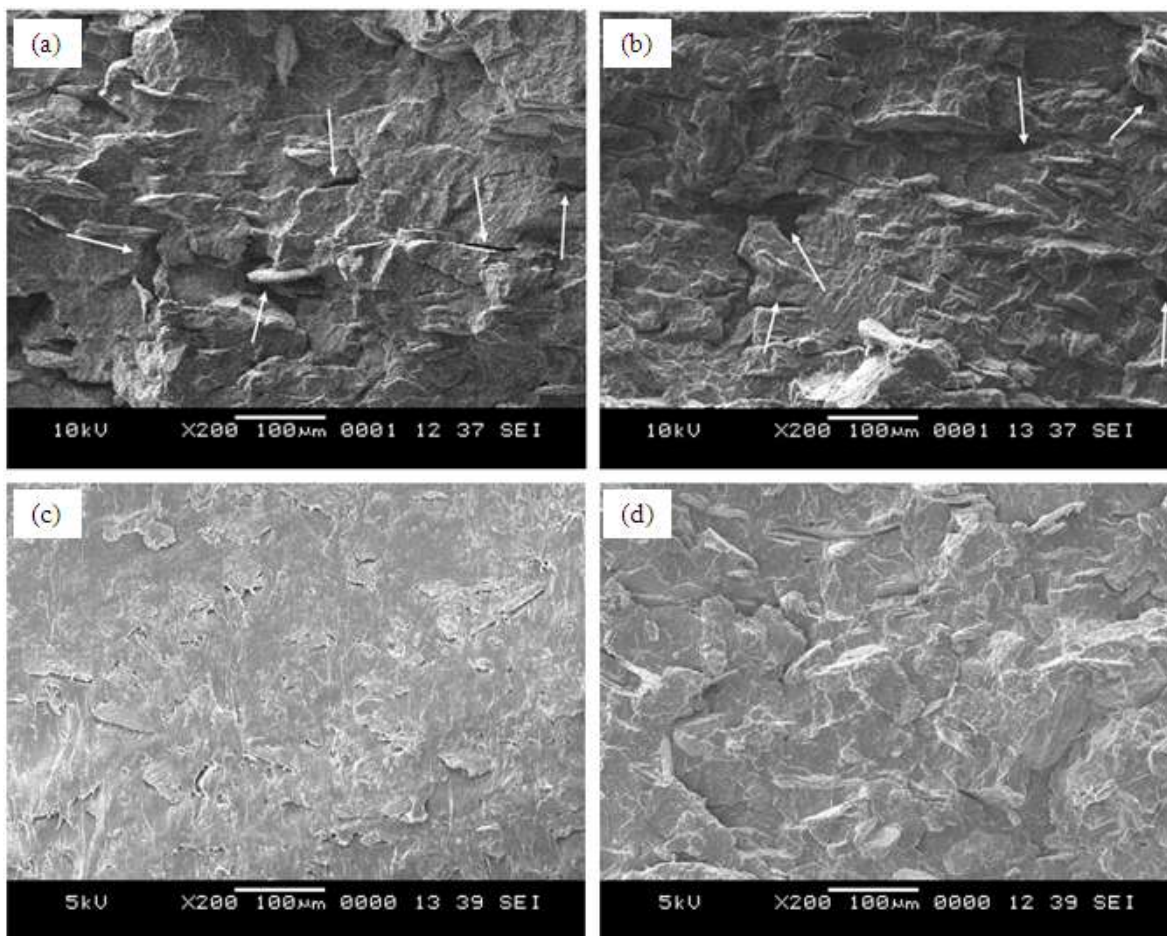
Fig. 4: SEM micrograph of tensile fractured surface; (a) untreated PP/chitosan composite (20 php), (b) untreated PP/chitosan composite (40 php), (c) treated PP/chitosan composite (20 php), (d) treated PP/chitosan composite (40 php) at magnification 200X, respectively.
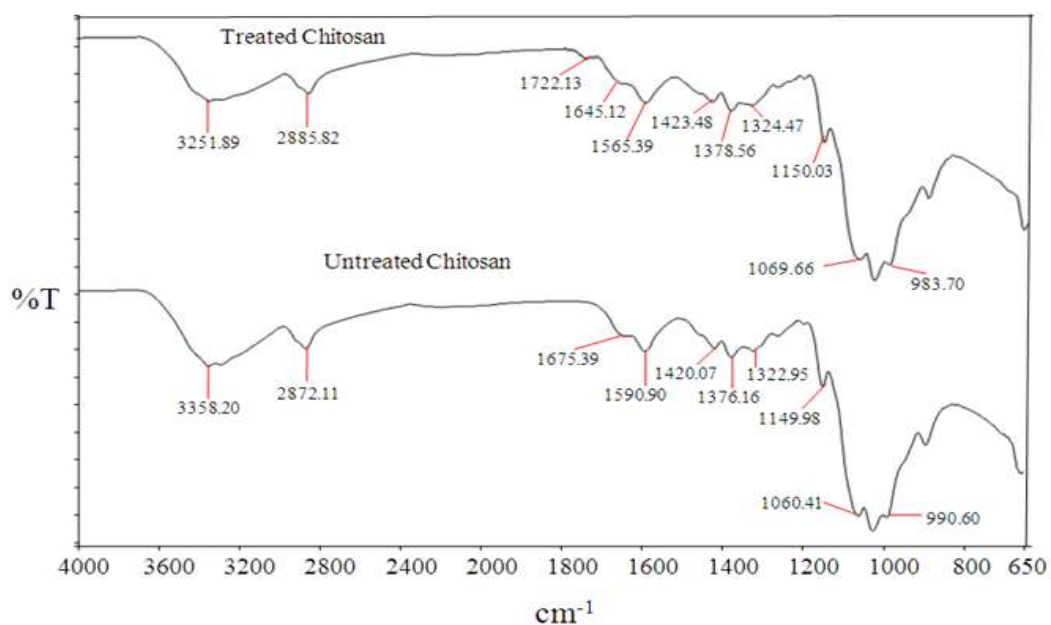
Fig. 5: FTIR spectra of untreated and treated chitosan with SDS.
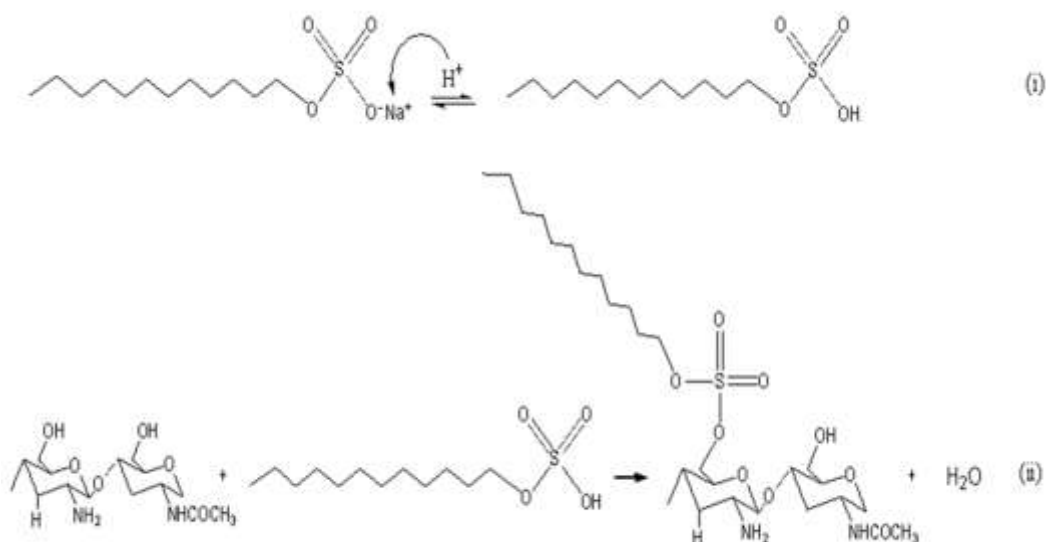
Fig. 6: The proposed schematic reaction between chitosan and SDS.

4.   CONCLUSION

The effect of sodium dodecyl sulfate (SDS) on mechanical and morphological properties of polypropylene (PP)/chitosan composites has been studied. The results of tensile properties showed that the incorporation of chitosan filler into PP matrix reduced the tensile strength and elongation at break, but increased the Young's modulus. The treated PP/chitosan composites were observed have higher tensile strength and Young's modulus but lower elongation at break than untreated composites. FTIR spectra and SEM micrographs revealed that sodium dodecyl sulfate (SDS) was successfully bonded onto the chitosan surface led to enhanced interfacial adhesion with PP matrix.

5.   REFERENCES

1.   Vargas, M., Albors, A., Chiralt, A., & Gonzalez-Martinez, C. (2009). Characterization of chitosan-oleic acid composite films. *Food Hydrocolloids,* 23: 536-547.
2.   Prashanth, K., & Tharanathan, R. (2007). Chitin/chitosan modifications and their unlimited application potential - an overview. *Trends Food Sci. Technol.,* 28:117 - 131.
3.   Nitayaphat, W., Jiratumnukul, N., Charuchinda, S., & Kittinaovarat, S. (2009). Mechanical properties of chitosan/bamboo charcoal composite films made with normal and surface oxidized charcoal. *Carbohyd. Polym.*, 78: 444–448.
4.   Spoljaric, S., Genovese, A., & Shanks, R.A. (2009). Polypropylene-microcrystalline cellulose composites with enhanced compatibility and properties. *Composite A,* 40: 791-799.
5.   Bledzki, A.K., Mamun, A.A., & Volk, J. (2010). Physical, chemical and surface properties of wheat husk, rye husk and soft wood and their polypropylene ccomposites. *Composite A,* 41: 480-488.
6.   Brahmakumar, M., Pavithran, C., & Pillai, R.M. (2005). Coconut fibre reinforced polyethylene composites: effect of natural waxy surface layer of the fibre/matrix interfacial bonding and strength of composites. *Comp. Sci. Technol.,* 65: 563-569.

7.   Martinez-Camacho, A.P., Cortez-Rocha, M.O., Ezquera-Brauer, J.M., Graciano-Verdugo, A.Z., Rodriguez-Felix, F., Castillo-Ortega, M.M., Yepiz-Gomez, M.S., & Plascencia-Jatomea, M. (2010). Chitosan composite films: thermal, structural, mechanical and antifungal properties. *Carbohyd. Polym.,* 82: 305 - 315.

8.   Salmah H., Faisal, A., Kamarudin, H., & Ismail, H. (2011). Mechanical and thermal properties of chitosan filled popypropylene composites: the effect of acrylic acid. *J. Vinyl Add. Technol.,* 17: 125–131.

9.   Salmah, H., Faisal, A., & Kamarudin, H. (2011). Chemical modification of chitosan filled polypropylene (PP) compoites: the effect 3-aminopropyltriethoxysilane on mechanical and thermal properties. *Int. J. Polym. Mat.,* 60: 429–440.

10.   Onisippe, C., & Lagerge, S. (2008). Study of the complex formation between sodium dodecyl sulfate and chitosan. *Coll. Surf. A,* 317: 100-108.

11.   Schmidt,V., Giacomelli, C., & Soldi, V. (2005). Thermal stability of films formed by soy protein isolate-sodium dodecyl sulfate. *Polym. Degrad. Stab.,* 87: 25-31.

Preliminary Study of Biodegradation of Natural Rubber Latex Products Filled with Peroxide Bleached Banana Skin Powder

Hamidah Harahap[*] and Erick Kamil

Chemical Engineering Department, Faculty of Engineering, University of Sumatera Utara, Medan, Indonesia

*Corresponding author: hamidah_usu@yahoo.com

Abstract: *Banana skin powder that was used as natural rubber latex filler was bleached by immersion in an 6% H_2O_2 solution. The bleached powder was made into a dispersion system. This dispersion system was mixed with natural rubber latex and curative agent with composition from 5 phr to 20 phr with 5 phr increment. This latex compound was pre-vulcanized at 70^oC and vulcanized at 100^oC for 15 minutes by dry dipping method. Product was investigated and biodegradation process was carried by burying samples in soil, and fertilized soil for a certain time.*

Keywords: Biodegradation, bleaching, banana skin, natural rubber latex, hydrogen peroxide

1.   INTRODUCTION

Natural rubber latex is a stable colloidal dispersion of cis-1,4-polyisoprene of high molecular mass in aqueous medium. Natural rubber latex is produced by tapping rubber tree (*Hevea brasiliensis*)[1,2].

Biodegradability of rubber products plays important role disposal and recycling rubber waste. As natural product, natural rubber is subjected to biological cycles. Natural rubber is relatively resistant to microbial decomposition compared with many natural polymer. Despite natural rubber is relatively resistant to microbial decomposition, many report of biodegradation on natural rubber products by microorganism have been published [3,4,5,6]. Natural rubber is consist of minimum 90% rubber hydrocarbon and small amounts of protein, sugar, resin, fatty acid and mineral[7].

The usage of banana skin powder a renewable and biodegradable as filler is in order to produce natural rubber products which can decompose in soil. Composition of banana skin is presented in Table 1.

The breakdown of polymer is it may occur by microbial action, photo degradation, chemical degradation. All these three methods are classified under biodegradation [9]. Natural rubber filled with bleached banana skin is buried in soil in order to break down by microbial present in soil.

Table 1: Composition of Banana Skin [8].

Parameter	Concentration [%]
Moisture	6.70
Ash	8.50
Organic Matter	91.50
Protein	0.90
Crude Lipid	1.70
Carbohydrate	59.00
Crude Fiber	31.70

2. MATERIALS AND METHODS

2.1 Filler preparation

Filler is prepared by chipping banana skin into 1 cm length and dried at 100°C for 24 hours. The dried banana skin was crushed into 100 mesh size and bleached by hydrogen peroxide. Bleaching system was made by dilution of 50% hydrogen peroxide to 6% hydrogen peroxide, the pH was increased to 11 by adding 10% sodium hydroxide solution and heated to 80 ^{o}C for 1 hour. Bleached banana skin was washed with water and made into dispersion system. The dispersion system was made by bleached banana skin, water, and polyvinyl pyrrolidone with ratio of 15, 83, and 2 respectively, and mixed in a ball mill for 24 hour.

2.2 Pre-vulcanization and vulcanization

High ammonia latex and curative agent were mixed and pre-vulcanized for 15 minutes at 70°C. Pre-vulcanized latex was mixed with filler dispersion system. Latex compound was vulcanized by dry dipping method at 100°C for 15 minutes. Films were made by using stainless steel plates as formers.

Table 2: Formulation of curatives.

Ingredients	Weight (g)
50% Sulphur	3
50% ZDEC	3
30% ZnO	0.83

2.3 Biodegradation Process

Biodegradation process of natural rubber latex was carried by burying samples into soil and fertilized soil. Fertilized soil was added with NPK fertilizer. Samples were buried in 15 cm depth. The rates of degradation were observed based on the weight reduction.

3. RESULT AND DISCUSSION

The result is presented by Figure 1 and Figure 2. Latex products filled with bleached banana skin powder showed greater weight loss than pure latex products.
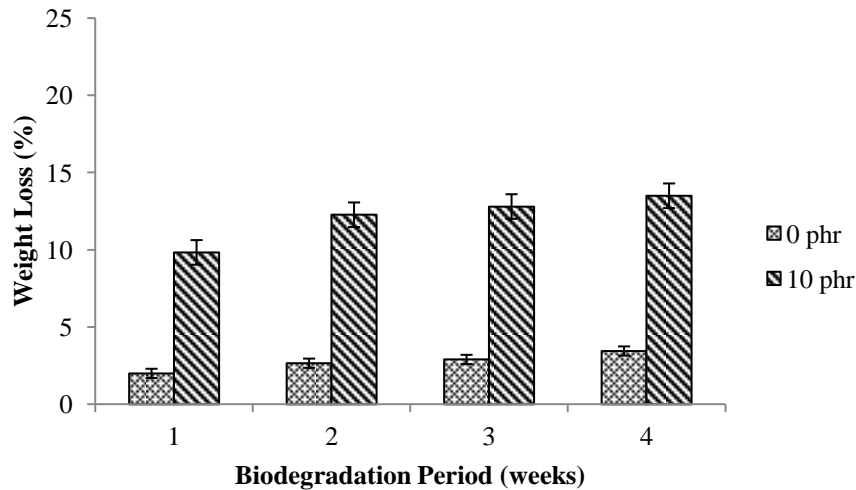
Fig. 1: The effect of filler loading of NR latex films biodegradation without fertilizer, 0 phr and 10 phr loading.

Fig. 1 shows that the longer the samples were buried in soil, the greater the weight loss was. Natural rubber (NR) latex film with 0 phr loading didn't show significant weight loss. From the first week until the fourth week of biodegradation, NR latex film with 0 phr filler loading only shows weight loss not more than 5%. This was because NR is relatively resistant to microbial decomposition [10]. While NR latex film with 10 phr filler loading showed significant weight loss compare to NR latex film with 0 phr loading. At the first week, NR latex film with 10 phr loading shows weight loss 10%, and the fourth week its weight loss increased to 15 %. The increase in weight loss is due to organic filler. Banana skin powder which contains carbohydrate can increase adhesion of microorganisms to surface of polymer[11], in this case to the surface of NR latex film.
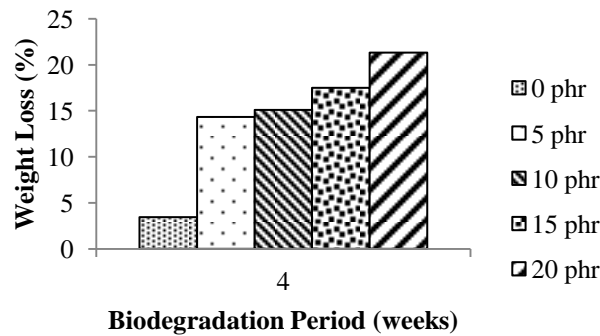
Fig. 2: The effect of filler loading of NR latex films biodegradation without fertilizer at 4th week.

Fig. 2 shows the effect variation of filler loading to weight loss. The more the filler was added, the more significant the weight loss was. At fourth week of biodegradation period, NR Latex film with 0 phr filler loading showed the least weight loss. Increasing the filler loading to 5 phr will increase the biodegradability of NR latex film, this was shown that weight loss of NR latex film with 5 phr filler loading is more than film with 0 phr filler loading. While NR latex film with 10 phr filler loading showed a slight more weight loss compare to NR latex with 5 phr filler loading. Increasing filler loading to 15 phr and 20 phr will increase the weight loss of NR latex films. The more filler that was loaded, the less the matrices of NR latex were. This means the NR latex films become more biodegradable as the filler loading increase.
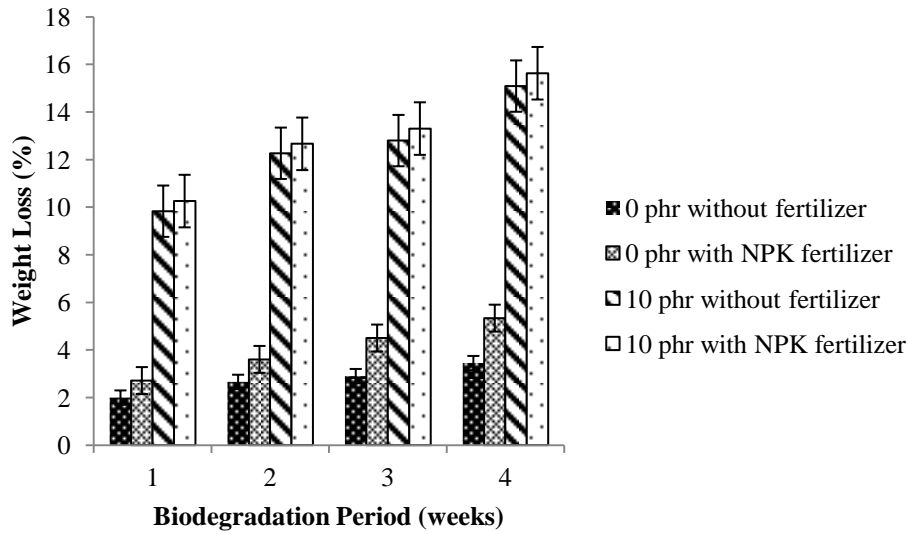
Fig. 3: The effect of filler loading of NR latex films biodegradation with NPK fertilizer compare to biodegradation without fertilizer, 0 phr and 10 phr loading.

Fig. 3 shows comparisons of burial of 0 and 10 phr Loading NR latex film without fertilizer to burial with NPK fertilizer. Biodegradation of NR latex with 0 phr filler loading with NPK Fertilizer films showed significant weight loss compare to biodegradation of 0 phr loading films without fertilizer. Biodegradation of NR latex films with 10 phr filler loading with NPK fertilizer showed greater weight loss compare to biodegradation of NR latex film with 10 phr filler loading films without fertilizer. This means adding fertilizer will increase weight loss rate compare to without fertilizer.
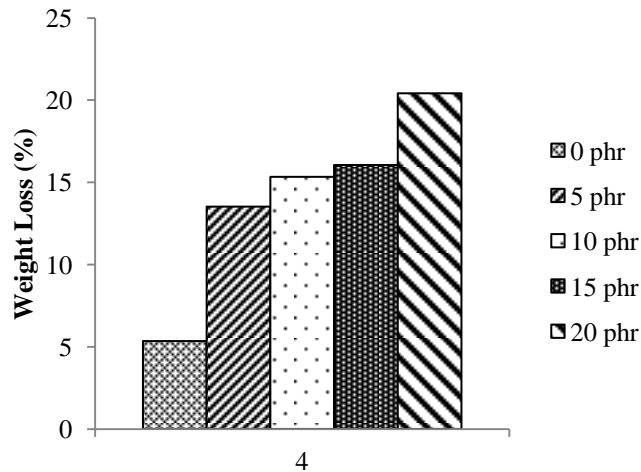
Fig. 4: The effect of filler of NR latex films biodegradation with NPK fertilizer, 4th week.

Fig. 4 shows the effect variation of filler loading to weight loss. The least weight loss at the fourth week was NR latex film with 0 phr loading. Increasing the filler loading to will increase the weight loss. NR latex film with 20 phr loading showed the greatest weight loss.

4.   CONCLUSION

480

Biodegradation of NR latex films with filler loading showed significant weight loss compare to films without filler. Biodegradation of NR latex film with 0 phr filler loading with NPK fertilizer showed more weight loss than without fertilizer.

5. REFERENCES

1. Blackley, D.C. (1997). *Polymer Latices Science and Technology*. London: Chapman & Hall. 1.
2. Kent, James A. (2007). *Kent and Riegel's Handbook of Industrial Chemistry and Biotechnology* (11th ed.). New York: Springer. 696.
3. Linos, A. et al. (2000). *Biodegradation of cis-1,4-Polyisoprene Rubbers by Distinct Actinomycetes: Microbial Strategies and Detailed Surface Analysis*. Applied and Environmental Microbiology, 66(4), 1639-1645.
4. Tsuchii, A. et al. (1985). *Microbial Degradation of Natural Rubber Vulcanizates*. Applied and Environmental Microbiology, 50(4), 965-970.
5. Cherian E. and Jayachandran K. (2009). *Microbial Degradation of Natural Rubber Latex by a Novel Species of Bacillus sp. SBS25 isolated from Soil*. Int. J. Environ. *Res.*, 3(4), 599-604.
6. Berekaa, Mahmoud M. et al. (2005). *Degradation of Natural Rubber by Achromobacter sp. NRB and Evaluation of Culture Conditions*. Polish Journal of Microbiology, 54(1), 55-62.
7. Zyska, B.J. (1981). *Economic Microbiology*, *In Rose A.H. ed. vol.6.* New York: Academic Press, Inc.
8. Anhwange, B.A. et al. (2009). *Chemical Composition of Musa Sapientum (Banana) Peels*. EJEAFChe, 8(6), 437-442.
9. Kolybaba, M. et al. (2003). *Biodegradable Polymer: Past, Present, and Future*. ASAE Paper No. RRV03-0007.
10. Rifaat, H. M. and M. A. Yosery. 2004. *Identification and Characterization of Rubber Degrading Actinobacteria*. Applied Ecology and Environmental Research (1), 63-70.
11. Arutchelvi, J. et al. 2007. *Biodegradation of Polyethylene and Polypropylene*. Indian Journal of Biotechnology (7), 9-22.

Preliminary study of Biodegradation of Natural Rubber Latex Products Filled with Banana Skin Powder Bleached with Hydrogen Peroxide

Hamidah Harahap[*] and Emelya Khoesoema

Department of Chemical Engineering, Faculty of Engineering, University of Sumatera Utara, Medan, Indonesia

*Corresponding author: hamidah_usu@yahoo.com

Abstract: *Banana skin powder that has been bleached with peroxide is used as filler in natural rubber latex products. Banana skin powder was bleached with 6% peroxide solution for 1 hour at 80 °C. Banana skin powder was made into dispersion system. Natural rubber latex is mixed with the curatives and banana skin powder as filler for mastication. Prevulcanised latex compound at a temperature of 70 °C and the dipping process was done. Dipping process was performed by the method of dipping dry and samples were dried at vulcanized temperature at 100 ºC for 15 minutes. The process of biodegradation is carried by hanging samples in the air. Products were investigated to prove that the NR latex film have biodegraded.*

Keyword: Banana skin powder, biodegradation, dry dipping method, hydrogen peroxide, natural rubber latex

1. INTRODUCTION

Natural rubber latex is a stable colloidal dispersion of cis-1,4-polyisoprene of high molecular mass in aqueous medium. Natural rubber latex is produced by tapping rubber tree (*Hevea brasiliensis*)[1,2].

The breakdown of polymer may occur by microbial action, photo degradation, and chemical degradation. All these three methods are classified under biodegradation. Photodegradable polymers undergo degradation from the action of sunlight. In many cases, polymers are attacked photochemically, and broken down to small pieces [3]. Biodegradability of rubber products plays important role disposal and recycling rubber waste.

Significant oxidation can occur if natural rubber latex is exposed to ozone. Other factors that contribute to the effects of ozone on natural rubber latex deterioration include sources of heat and light. Excessive exposure of gloves to heat can accelerate the oxidation process and cause cracks to appear sooner than would occur if exposed to ozone alone. Ultraviolet light from sunlight also accelerate natural rubber latex deterioration. They produce photochemical reactions in rubber that can promote the oxidation of the surface of the rubber resulting in discoloration and a loss in mechanical strength [4].

Natural rubber is consist of minimum 90% rubber hydrocarbon and small amounts of protein, sugar, resin, fatty acid and mineral[5]. The usage of banana skin powder as a renewable and biodegradable filler is in order to see the effect of filler to natural rubber. Composition of banana skin is presented in Table 1.

Table 1: Composition of banana skin [6].

Parameter	Concentration [%]
Moisture	6.70
Ash	8.50
Organic Matter	91.50
Protein	0.90
Crude Lipid	1.70
Carbohydrate	59.00
Crude Fiber	31.70

2. MATERIALS AND METHODS

2.1 Filler preparation

Filler is prepared by chipping banana skin into 1 cm length and dried at 100°C for 24 hours. The dried banana skin was crushed into 100 mesh size and bleached by hydrogen peroxide. Bleaching system was made by 6% hydrogen peroxide, the pH was increased to 11 by adding 10% sodium hydroxide solution and heated to 80 ^{o}C for 1 hour. Bleached banana skin was washed with water and made into dispersion system. The dispersion system was made by bleached banana skin, water, and polyvinyl pyrrolidone with ratio of 15, 83, and 2 respectively, and mixed in a ball mill for 24 hour.

2.2 Pre-vulcanization and vulcanization

High ammonia latex and curative agent were mixed and pre-vulcanized for 15 minutes at 70°C. Pre-vulcanized latex was mixed with filler dispersion system. The filler variations are 5 phr (per hundred rubber), 10 phr, 15 phr, and 20 phr. Latex compound was vulcanized by dry dipping method at 100°C for 15 minutes.

Table 2: Formulation of curatives.

Ingredients	Weight (g)
50% Sulphur	3
50% ZDEC	3
30% ZnO	0.83

2.3 Biodegradation Process

Biodegradation process of natural rubber latex film was carried by hanging samples in air. Samples were hung at place exposed to sunlight and rain. The rates of degradation were observed based on weight reduction.

3. RESULT AND DISCUSSION

The result is presented by Figure 1. Latex products filled with bleached banana skin powder show greater weight loss than pure latex products.
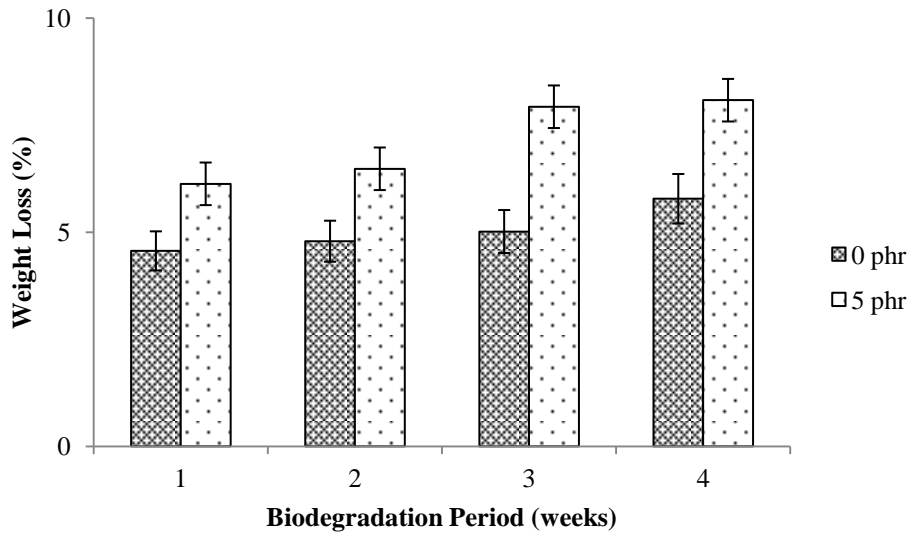
Fig. 1: The effect of filler of NR latex films biodegradation, 0 phr and 5 phr loading.

The longer the films were hung, the greater the weight loss was. From the first week until the fourth week of biodegradation, natural rubber (NR) latex film with 0 phr filler loading shows weight loss over 5%. Increasing filler loading will increase weight loss. This can be seen from NR latex films with 5 phr loading have greater weight loss. From the first week to the fourth week, NR latex films with 5 phr loading showed significant weight loss compare to 0 phr NR latex films.

NR Latex film with 0 phr loading after 4 weeks of exposure to weather and sun, the films became sticky and soften. This is usual behavior of unfilled NR vulcanizates[7]. Figure 2 shows samples of 0 phr NR Latex Film after hung at open air for 3 weeks. The below sample had become sticky as can be seen the lower left end has stuck to the center of sample. While small crack can also be observed on the surface of NR film filled with banana skin powder filler. In contrary to NR Latex 0 phr loading, samples filled with banana skin powder tend to become brittle, but not sticky. This is because ozone attack the unsaturated bond of NR. Ozone can cause surface crack on filled NR latex[7].

Fig. 2: NR latex film 0 phr loading after hung for 3 weeks.
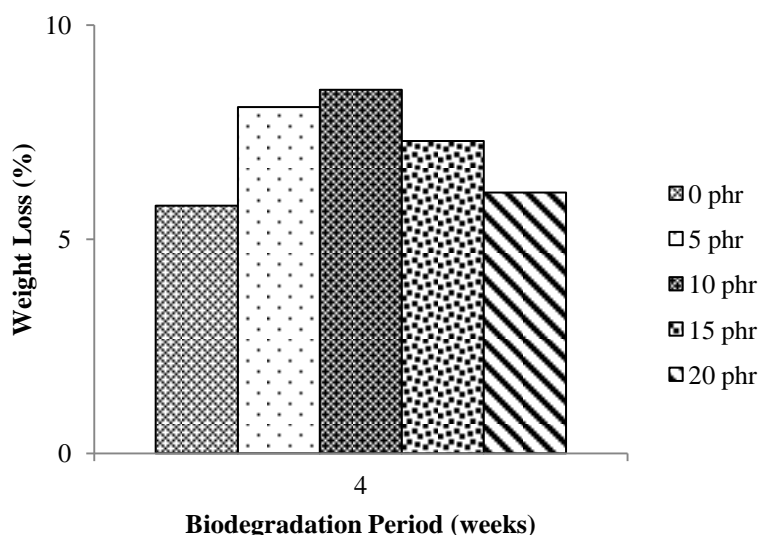
Fig 3: The effect of filler of NR latex films biodegradation, 4th week.

Fig. 3 shows that after 4 week of hanging samples at open air, film with 0 phr loading shows the least weight loss. Increasing filler load to 5 phr and 10 phr will increase the weight loss. Further increase of filler loading to 15 phr and 20 phr will cause the samples to become brittle and the weight loss decrease compare to 10 phr loading. Small and discontinuous surface crack can be observed on 15 phr and 20 phr due to attack of ozone. The small surface crack were discontinuous because while the crack grows, it will encounter inert particle of filler and prevent the crack to grow further [8].

4. CONCLUSION

NR latex films with 0 phr loading didn't show significant weight loss. Increase of filler loading until 10 phr will increase the weight loss significantly, but further increase in filler will decrease the weight loss, but the films become more brittle.

5. REFERENCES

1. Blackley, D.C. (1997). *Polymer Latices Science and Technology*. London: Chapman & Hall. 1.
2. Kent, James A. (2007). *Kent and Riegel's Handbook of Industrial Chemistry and Biotechnology* (11th ed.). New York: Springer. 696.
3. Kolybaba, M. et al. (2003). *Biodegradable Polymer: Past, Present, and Future*. ASAE Paper No. RRV03-0007.
4. Tillotson. (2005). *Ozone Can Cause Serious Problems for Natural Rubber Latex Gloves*. Technicare Bulletin, 1-3.
5. Anhwange, B.A. et al. (2009). *Chemical Composition of Musa Sapientum (Banana) Peels*. EJEAFChe, 8(6), 437-442.
6. Zyska, B.J. (1981). *Rubber, In Rose A.H. ed., Microbial biodegradation*. New York: Academic Press, Inc.
7. *Hamed, Gary R. Materials and Compounds. Retrieved 28 January 2012, from: www.gupta-verlag.de/media/bookshop/rehearsal/extract_06.pdf*
8. Vinod, V.S. et al. 2002. *Degradation Behavior of Natural Rubber-Aluminium Powder Composites: Effect of Heat, Ozone and High Energy Radiation*. Poly. deg. stab 75, 405-412.

Experimental study and numeric modeling of the influence to the austenit rate on the tenacityof a welded joint in stainless steel

B. Bouchouicha[1,*], M. Zemri[1], A. Ghazi[1], M. Mazari[1], B. Ould chikh[3], M. Benguediab[1], and A. Imad[2]

[1]Laboratory of Materials and reactive systems LMSR, engineering, Faculty of Science of the engineer, University Djillali Liabes Adresse: BP 89   Sidi Bel Abbés 22000 ALGERIA
[2]Laboratory of Mechanics of Lille LML France
[3]Laboratory LSTE, university of Mascara Algeria

Corresponding author : benattou_b@yahoo.fr

Abstract: *This work is about the experimental and numeric study of the mechanical behavior of a welded joint using TIG welding process of austenitic stainless steels 316L. Generally, the mechanical properties characteristics depend mainly on two parameters: the quality of weld metal and the quality of gaseous protection. The observation made and the results obtained from different mechanical tests had been correlated the arm is to be able to propose of austenitic stainless steels 316L containing a high concentration of chrome and lower concentration of nickel in order that a fraction of ferrite can stabilized during solidification.*

Key-words: Welding, ferrite, toughness, austenite, austenitic stainless steel 316L

1.   INTRODUCTION

Several recent works [1] showed that the weld joints of austenitic stainless steel are known as source of damage and defects with respect to other steels [2] .This damage results from microcavities and development of micro-cracks due to the ability of deformation and resistance to mechanical stress of the weld metal with bad fusion protection [3].

The particularity of the composition of the base metal comes from mechanical properties seeked in the case of optimal use of work and environmental conditions. The weld metal used for welding austenitic-stainless steels 316L must be austeno-ferritie because it presents a higher tensile resistance to fracture than that of the base metal because of the existence of ferrite and the mechanical characteristics of the HAZ has the same evolution as in the case of austenitic steels [4].

In general, the agreement has been found in literature on the 17% of ferrite concentration in weld joint, to avoid cracks during heating and more than 8% to limit the structural evolution of the weld by maintaining to high temperature [5].

The objective of this work concerns the study of the global mechanical behaviour of 316L austenitic- stainless steel weld joint obtained by TIG welding process which depends on two parameters: The quality of the weld metal and the quality of gas of protection. Three qualities of weld metal have been used (UP-CNM 18 16 noted WM1), (SG- X2/CNM 19 12 noted WM2) and (SG- X12/CNM 19 10 noted WM3) and protection to the argon gas were used.

2. MATERIALS AND EXPERIMENTAL PROCEDURES

2.1. Materials

The material used in this investigation is an austenitic stainless steel 316L whose chemical composition and the mechanical characteristics are given in Table 1.

Table 1: Chemical composition and the mechanical characteristics of stainless steel 316L.

Material	Chemical composition						Mechanical properties				
	%C	%Si	%Mn	%Cr	%Ni	%Mo	Re (N/mm²)	Rm (N/mm²)	A (%)	k	n
316L	0,028	0,52	1,8	16,3	12,4	2,2	225	485	40	1169	0,608
WM1	≤0,045	0,5	-	18	12,5	2,5	210	440	34	936	0,402
WM2	≤0,040	0,7	-	19	11,5	2,8	210	430	35	1154	0,501
WM3	≤0,045	0,4	-	19	11	2,2	250	550	35	1180	0,55

2.2. Weld metal

The weld metal has been chosen affect the ferrite concentration at the welded joint. Three products of weld metal have been used with different ferrite concentration: from 0 to 55%. During weldments of austenitic stainless steel 316L, the ferrite concentration sought in the welded joint is 8 to 19% [6]. It is well-known that concentration greater than 19% this may cause ferrite interalloyed network, which decreases the resistance to corrosion of the welded joint. Low concentrations of ferrite increase the possibilities of cracking due to the difference of expansion coefficients of the base and weld metals. The chemical composition and the mechanical characteristics of the three weld metals are given in table 1. The protector gas prevent the penetration of the air and around the fusion zone of the weld during the pipe welding it is generally necessary to use internal atmospheric protection. This protection is required in order to obtain a good penetration and aspect with no oxidation [7].

3. RESULTS AND DISCUSSIONS

3.1. Tensile test

Tensile tests were conducted at the laboratory LML (Mechanic Laboratory of Lille). For the determination of the conventional and rational features of traction, the tests have been done to ambient temperature on specimens appropriated in accordance with the norms AFNOR A03-151 and A03-351. All the tests had been conducted on electro-hydraulic universal machine with IBERTEST control with a strain capacity of 4000 daN and 3300 daN as dynamic capacity. The speeds of applied solicitation during the test are of:

- 12 mm/s for the determination of $R_{0,2}$ (control distortion)
- 0,5 mm/min for the rational curve
- 25 mm/min for the determination of R_m (control displacement)
The results obtained are summarized in table 1 and represented in Fig. 1.
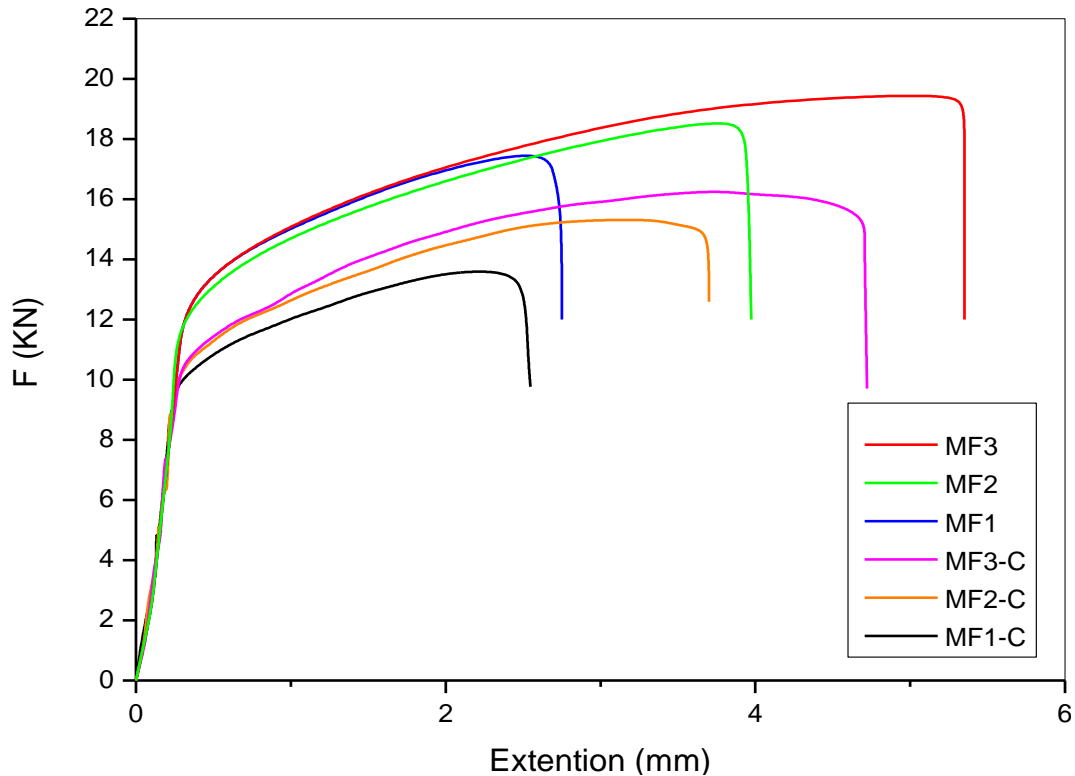
Fig. 1: Curve of traction (strength displacements) of the different specimens.

The tensile resistance (530 N/mm^2) is really higher than the minimum resistance. The welded joints, with the weld metal exempt of ferrite increases the welds ductility (A=20%). The ferrite increases the ductility of the welding. Argon gas protection gives a better mechanical characteristics, and this whatever the weld metal.

3.2.   Hardness measurement (Hv)

These hardness tests aim to determine if the filiations of hardness in welded joint was regular or on the contrary it presents hardenings, the results obtained are represented in Fig. 2. The obtained measures show hardness welded specimens with weld metal exempt of ferrite in the other hand in the other cases there is regular uniform hardness in particular for specimen welded using SG- X12/CNM 19 10 as weld metal with Helium gas protection because it presents a lower (ΔHv min) which is recommended [8] .
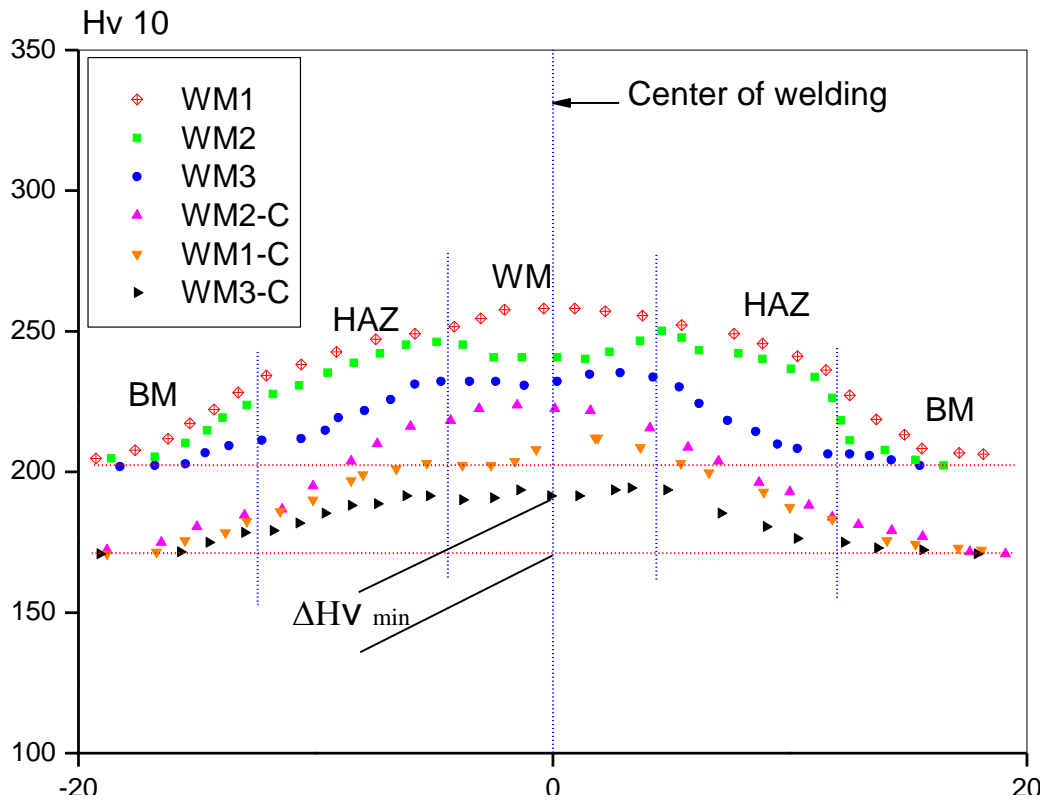
Fig. 2: Evolution of hardness in the three areas of the weld.

3.2. Toughness testing J_{IC}

The tests of resistance to the ductile rip have been achieved on a machine trial servohydraulique having a maximal capacity of 400 kN, piloted in servitude of position. The piloting of the machine and the acquirement of the data are done by a microordinateur while using the program (Instron Fast Track J_{IC}), who is part of a family of programs of application of tests of materials written for tests of specific material done on the systems of tests of Instron. These tests have been done to the ambient air on specimens SENB10 type (bending three points of BxB section) taken in the TL direction of the welding joint. The test device is presented in Fig. 3.

Fig. 3: The test device bending three points.

The remarks that one can make to the exam of these curves are the following:

- A plastic instability limited occurring after the peak of the loading curve and absence of the ductile landing, of or the existence of a strong structural heterogeneity, what drives to features of fragile rupture for the specimens exempt or containing a rate reduces of ferrite. This phenomenon is linked to the presence of fragile areas near front of the crack and extortions lamellar especially for specimens corroded.
- Presence of ductility, therefore the existence of a structural homogenization, this leads to the characteristics of ductile fracture to the specimens containing a high rate of ferrite.

The evolution of the integral J in relation to the extension of the crack (J - has) is shown in Figure 4. The data points are plotted from the beginning of the test, but only the data points located between the lines of exclusion from 0.2 mm and 1.5 mm are considered to be valid. J_{IC} is determined to the point where the curve cuts the line of shift of 0,2 mm (E318 norm of the ASTM).The remarks that one can make to the exam of these curves are the following:

The lowest values of the parameter J0, 2 obtained are observed for the specimens exempt or containing a reduced rate of ferrite (crude and corroded), on the other hand the highest values are observed for the specimens containing a high rate of ferrite. Then one notes whereas for the specimens containing a high rate of ferrite, the tenacity is 20% more important than in the other cases, same remark for the corroded specimens.
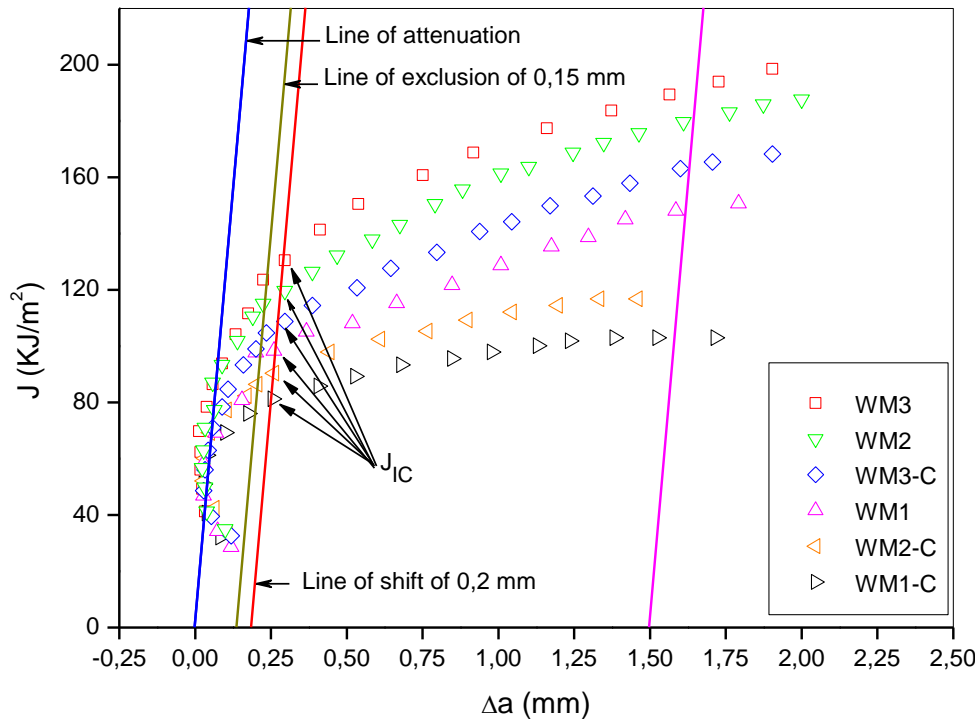
Fig. 4: Curves (J-Δa) of the different specimens.

We noticed that there is increasing values of relative permeability welds in the specimens type (MA3). This increase is due to an increase in the rate of ferrite. These results have been confirmed while using the representational zones of every contribution metal on the diagrams of Schaeffer [9]. The gotten results are represented on the Table 2.

Table 2: Rate of ferrite in the different specimens.

Weld Metal	Dilution rate	Effective ferrite (%)
MF1	27	0
MF2	48	$5 \div 7$
MF3	58	$15 \div 19$

4. NUMERICAL MODELING

The simulations test failure implemented experimentally were carried out using the finite element code « ABAQUS V.6.5 ». The analysis is made with plane deformation; we chose to conduct a preliminary numerical approach by introducing the law elastoplastic behavior. The specimen modeled is the SENB type (bending three points). The mesh is done using quadrilateral mesh to 8 nodes that can treat the condition of plane deformation (CPS8). In the bottom of crack, it is particularly refined for modeling local approach. The evaluation of the J will be on full contours 6, as a/w = 0,5. The regressions of mesh are regular in order to avoid any sudden change in mesh size and the elements too distorted (figure 5).

491
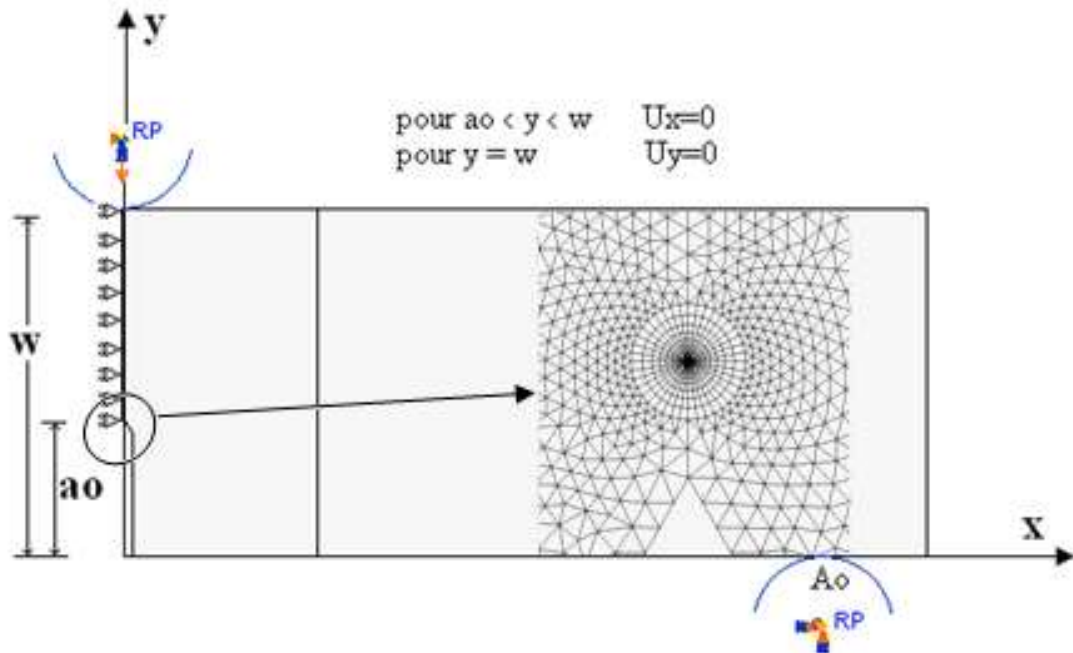
Fig. 5: Mesh case of a half specimen SENB.

4.1.   Evolution load/displacement

The numeric evolution of the load according to the displacement imposed for the different configurations is illustrated by the figure (6), we have drawn the following information:

- A good agreement between the experimental and numerical results is noticed in the elastic part of these curves for the different configurations. The difference appears beyond the elastic domain, this phenomenon is related primarily to differences in the laws of behavior of these materials.
- The relative difference between the curve of the weld metal with a high rate of ferrite and the same corroded metal is low (about 12% for d=2mm). By contrast, for other configurations, It is important (about 30% for the same advanced). The rate of ferrite seems therefore govern the global behavior of this material.
- Otherwise, one notes that the report of the load limits P(MF3)/P(MB), is roughly equal to the rate of mismatching M, given by the report (Re MF3)/(Re MB) (in our case M = 1,5).
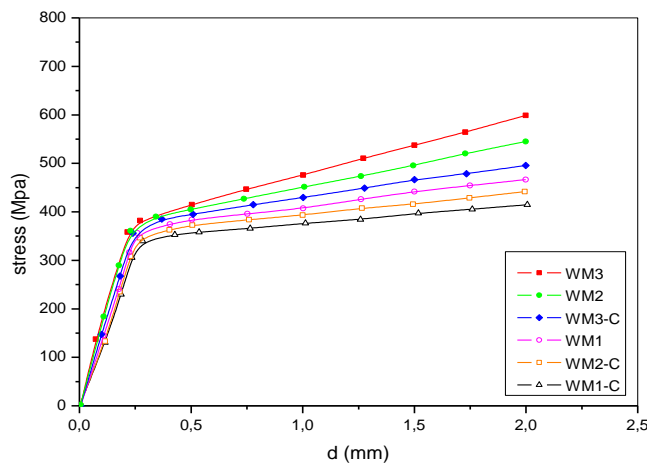
Fig. 6: Evolution load/displacement.

4.2. Evolution of the opening to the tip of the crack (CTOD)

The forecast CTOD according to the displacement d is presented by Figure 7. This evolution shows that the opening loan of the bottom of the crack is nearly the same in the different studied configurations.
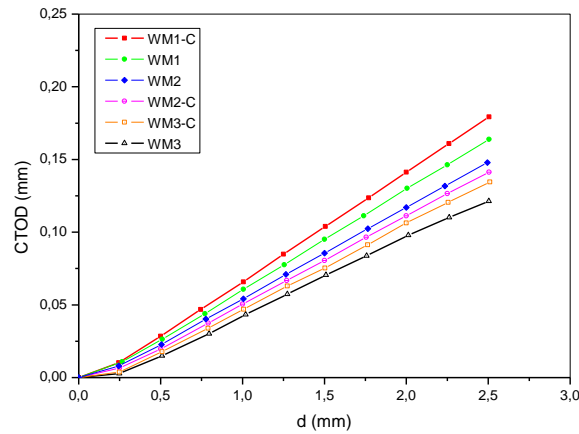
Fig. 7: Evolution of the CTOD according to the imposed displacement d.

4.3. Evolution of the integral J

The evolution of the J integral for the different configurations is presented in Figure 8. The different cases give tenacity to the identical beginning for weak values of the displacements, and a relative evolution for more important displacements. The gap between the J weld metal exempt and containing a high rate of ferrite for d = 2 mm is almost double, same gap is noticed between the two corroded components. This same evolution, Shows that there is a small gap between the values calculated numerically and experimentally determined.
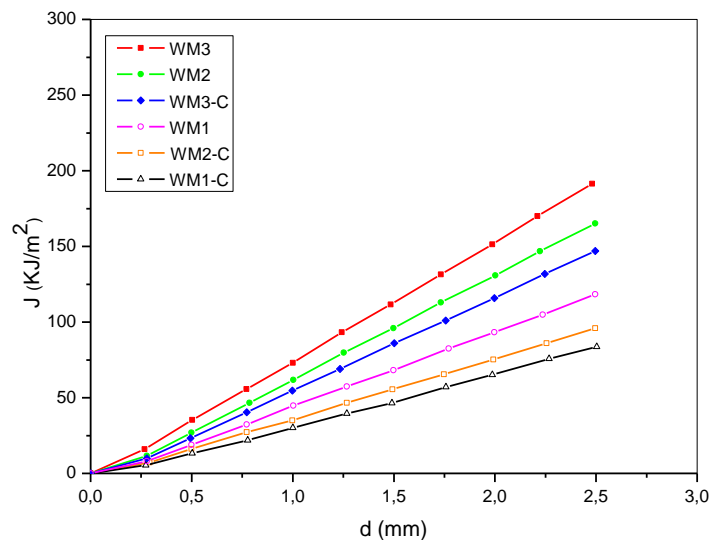
Fig. 8: Evolution of the J according to the imposed displacement d.

5.   CONCLUSION

From the experimental investigations carried out to study the global mechanical behaviour of a welded joint using TIG welding process (tungsten inert gas) of austenitic stainless steels 316L, the following conclusions have been drawn:

For TIG welding, it is preferred for 316L austenitic stainless steel to have a higher concentration in Chrome (Cr) and lower concentration of Nickel (Ni) in order for a ferrite fraction to be stabilized during solidification. The adequate solution will be the use of weld metal whose characteristics are closer to the dispersion band of the mechanical properties of the base metal and which presents austenitic deposit of about 18% of ferrite. If the dilution rate is 58% during welding, the structure of the weld will have about 15% of concentration of ferrite. This austenito-ferrite joint presents a better resistance and good resistance to intercristal corrosion.

Numerical modeling has highlighted the complexity of the characterization of the ductile tearing in the case of welded joints. This work has enabled us to conclude that the mechanical properties of the welded joint containing significant levels of ferrite, in the case of a major rate Overmatching, have a dominant effect on the global behavior of such structures

6.   REFERENCES BIBLIOGRAPHIC

1.   G. Balalchandran, M. L. Bhatia, (2001): Some Theoretical Aspects on Designing Nickel Free High Nitrogen Austenitic Stainless Steels, ISIJ Int., Vol. 41:9, pp. 1018-1027.
2.   YOUNG JY, Lawrence FV. (1985): Analytical and graphical aids for the fatigue design of weldments. Fatigue Fract. Engng. Mater. Struct.; 8(3); 223-41.
3.   WALLIN K., (1994): New Improved Methodology for Selecting Charpy Toughness Criteria for Thin High Strength Steels, IIW Doc. N° X-1290-94, IIW Annual Assembly, Beijing,
4.   Suutala N., Takalo T., Moisio T., (1999): The relationship between solidification and microstructure in austenitic and austenitic ferritic stainless steel welds, Metallurgical Transactions A, vol .10 A, pp.512-514,
5.   Gill T.P.S., Shankar V, Pujar M.G ., Rodriguez P ., (1995): Effect of composition on the transformation of delta-ferrite to 6 in type 316 stainless steel weld metals, Scripta Metallurgica, vol . 32, N°10, pp.]595-1600.
6.   HARRIES D.R.,(1981): Physical metallurgy of Fe-Cr-Ni austenitic steels, in: Mechanical behaviour and nuclear applications of stainless steel at elevated temperatures, Varese, p 1/1-1
7.   Chen M .H ., Chou C .P ., (1999): Effect of thermal cycles on ferrite content of austenitic stainless steel, Science and technology of welding and joining, vol . 4, n°1, pp. 58-62.
8.   DEVAUX .J.C, G. MOTTET, P. BALLADON and A PELLISSIER-TANON, (1987). ((Calibration of the parameters of a ductile fracture damage mode1 on an austenitic-femtic duplex welded joint », Nuclear Engineering and Design, Vol. 105, PP. 13 1-138,
9.   SCHOEFER E.A., (1976): Constitution Diagram for Stainless Steel Castings, Metal Progress,

Rheological Behaviour of Low Density Polyethylene/Palm Kernel Shell Composites:

Effect of Eco-degradant

B. Y. Lim[*] , H. Salmah, and P. L. Teh
School of Materials Engineering,
Universiti Malaysia Perlis,
Taman Muhibah, 02600 Jejawi, Perlis, Malaysia

Corresponding email: bying425@yahoo.com

Abstract: *A rheological study of the palm kernel shell filled low density polyethylene composites with and without eco-degradant had been performed with capillary rheometer. The effect of filler loading on the rheological properties of the composites was studied in the range of 0-40 php. The testing was carried out at a temperature range of 180 to 210 ºC and a shear rate range of 50 to 5000 s^{-1}. The shear viscosity of the composites was increased with increasing filler loading. At similar filler loading, high temperature had decreased the shear viscosity of the composites. The composites with eco-degradant were found to have better flowability and lower viscosity.*

Keywords: low density polyethylene, palm kernel shell, eco-degradant, rheology

1. INTRODUCTION

Low density polyethylene (LDPE) is one of the petroleum based thermoplastic that is light weight, low cost and can be process easily. It is widely used as packaging materials, protecting films and carrier bags. The increasing usage of the non-degradable LDPE has led to environmental pollution and municipal solid waste management. The incorporation of the fillers into polymeric matrix is one of the ways to reduce the polymer usage.

There has been a growing interest in the use of natural fillers in producing composites. The natural fillers offer better options compare to the inorganic fillers which are usually high cost. The natural fillers possess several advantages such as low cost, light weight, non toxic, non abrasive to processing machines and able to degrade slowly [1]]. The commonly used natural fillers are wood fibres and flour, kenaf fibres, henequen fibres, jute and etc [1-4]. Malaysia as the main oil palm country produces large quantity of palm kernel shell. Palm kernel shell is hard stony endocarps that surround the kernel. It is produced annually in large quantity and usually been burnt as waste material. Thus, it has high potential to be used as natural filler in polymeric composites due to its high availability low cost.

The processability of polymeric materials is strongly dependant on their rheological properties. Good understanding on rheological properties of the materials helps to optimise the process conditions and maximize the product performances. However, addition of fillers will alter the rheological properties of the compounds and result in change of processability. Hence, the study of the melt flow properties of filled polymer systems is important to study the mechanism by which addition of fillers to polymers influences the original polymers and to determine those combinations in which such effects occurs [5]. Generally, the presence of filler in thermoplastic and elastomers increase the melt viscosity and may result in unusual

rheological effects. The rheological studies of polymeric composites have been carried out extensively by these workers [6-12].

In this study, the rheological behaviour of palm kernel shell filled low density polyethylene composites was investigated. The effect of temperature, palm kernel shell loading and presence of eco-degradant on the melt flow behaviour of the composites were evaluated.

2.   EXPERIMENTAL

2.1 Materials

The LDPE was supplied by Titan Chemical, Johor, Malaysia with density of 0.922 g/cm^3 and MFI of 0.33g/10min. The palm kernel shell that used as fillers was obtained from Malpom Oil Palm Processing, Nibong Tebal, Malaysia. The palm kernel shell was cleaned and dried at 80 ºC for 24 hours to evaporate the moisture content. Then it was crushed into powder form and sieved. The average particles size of 75 μm was measured by using Malvern particle size analyzer. The eco-degradant was supplied by Behn Meyer Polymers Manufacturing Sdn. Bhd. It is light brown free flowing pellets with density of 0.940 kg/m^3.

2.2   Composites Preparation

Composites were prepared by using a Z-Blade mixer at temperature of 180 ºC and rotor speed of 50 rpm. The LDPE were loaded into the mixing chamber for 5 minutes. After 5 minutes, filler was added and mixing continued for 10 minutes. The total mixing time of composites was 15 minutes. Finally, the composites were removed from the mixing chamber and pressed into thick round pieces. For the preparation of composites with eco-degradant, LDPE and eco-degradant were charged into the mixing chamber for 5 minutes until they completely melt. Then the filler was added and mixing continued for 10 minutes. Hot press procedures involved preheating at 180 ºC for 9 minutes followed by compressing for 6 minutes and subsequent cooling under pressure for 4 minutes. The formulation of the LDPE/PKS composites with and without eco-degradant is shown in Table 1.

Table 1: Formulation for LDPE/PKS composites with and without eco-degradant.

Materials	Without eco-degradant	With eco-degradant
LDPE (php)	100	100
PKS (php)	0, 10, 20, 30, 40	10, 20, 30, 40
Eco-degradant (php)*	-	5

* 5 php based on weight of LDPE

2.3   Rheological measurements

The rheological testing was carried out by using Alpha Technologies LCR C7001 capillary rheometer. The capillary has an angle of entry of 90 °C and barrel diameter of 9.55 mm. The die with length to diameter (L/D) of 30 was selected. By using shear rate in the range of 50-5000 sec^{-1}, different shear viscosities were obtained from single charge of material. The composites samples were cut into small size of 2mm x 2mm x 1mm and charged into the barrel. The sample was compacted in the barrel by using charging tool to avoid air bubbles. After a residence time of 6 min, the composites melt was extruded through

the long die at different plunger speed. The testing was carried out at temperature range of 180 to 210 °C with the initial plunger position kept constant at 100 cm.

2.4. Melt flow index (MFI) test

The melt flow indexes of the composites with different filler loading were measured with a melt flow indexer. The measuring technique of MFI is according to ASTM D1238. The die length and the die diameter were 8.000 mm and 2.095 mm respectively. The entry angle was 180°. After a residence time of 6 min, the melt was extruded through the die. The testing temperature was varied from 190 °C to 210 °C with the load of 2.16 kg.

A relationship between shear stress (τ_w) and apparent shear rate (γ_a) at the wall can be written as follow:

$$\tau_w = \frac{FR}{2\pi R_P^2 L}$$

(1)

$$\gamma_a = \frac{4Q}{\pi R^3}$$

(2)

$$Q = \frac{m}{t \times \rho}$$

(3)

$$\eta = \frac{\tau}{\gamma}$$

(4)

where R = barrel radius, R_P = die radius, L = die length, , F = load, Q = flow rate, t = time, ρ = density and η = viscosity.

The Arrhenius equation is shown as below:

$$\eta_a = A \exp (E/RT)$$

(5)

where A is the constant related to melt viscosity, E is the activation energy of viscous flow and R is the universal gas constant.

3.   RESULTS AND DISCUSSION

Fig. 1 shows the effect of shear rate on the shear viscosity of the LDPE/PKS composites at different filler loading at 180 °C. The graph shows that all the LDPE/PKS composites system exhibited pseudoplastic behaviour. At a specific temperature, the LDPE/PKS composites at different filler loading show decreasing viscosity as the shear rate increased. At low shear rate, the filler are disoriented. The probability of filler-filler collision and friction is much higher for these disoriented filler. However, at higher shear rate, these filler to filler collisions are diminished because of the alignment of fillers along the capillary axis [9].

The filler loading of PKS in the composites affects the viscosity of the LDPE/PKS composites. The composites with higher filler loading, (40 php) of PKS, exhibited higher viscosity compared to that of the composites with lower filler loading, (10 php) of PKS. The presence of filler will disturb the normal flow of the composites melt and hinder the mobility of chain segment in flow [13,14]. As more filler was added into the composites, the flow of the composites melt was disturbed and the resistance to flow of the composites became higher.
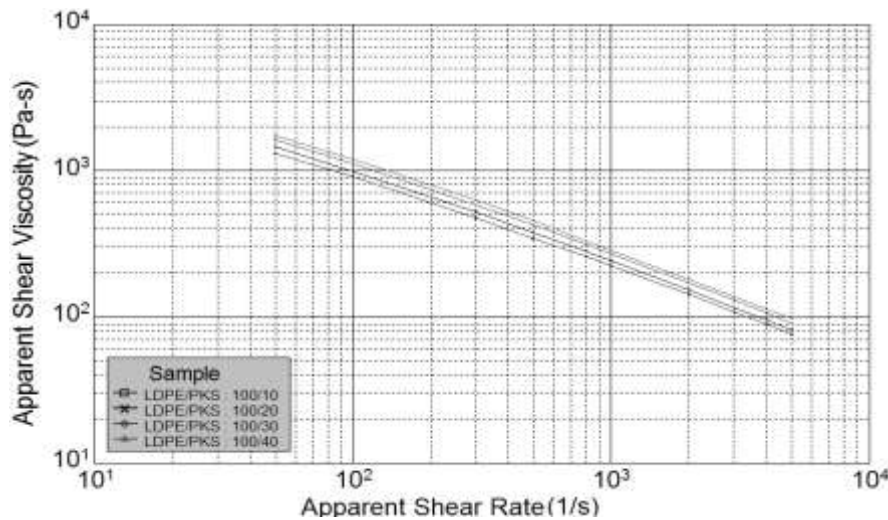
Fig. 1: The shear viscosity of the untreated LDPE/PKS composites at different shear rate and filler loading at 180 ℃.

The rheological properties of the composites are not only affected by its filler loading but also the processing temperature. Figure 2 shows the effect of temperature on the LDPE/PKS composites at 20 php of PKS. The shear viscosity of the composites decreased with the increasing of the shear rate at the temperature range from 180 to 210 ℃. At similar shear rate, high temperature tends to decrease the shear viscosity of the LDPE/PKS composites. This is attributed to the accelerated molecular motions due to availability of greater free volume and decreasing entanglement density and weak intermolecular interaction.
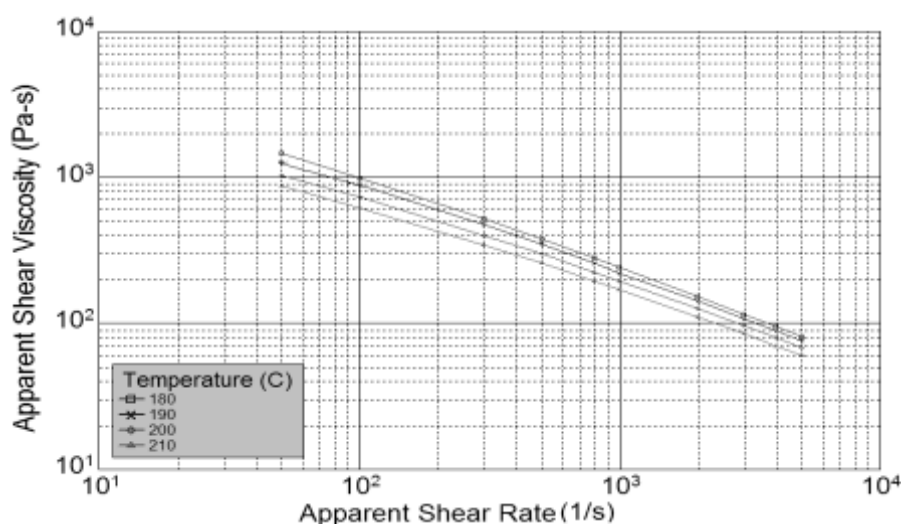
Fig. 2: The shear viscosity of the untreated LDPE/PKS composites at different shear rate and filler loading.

The effect of eco-degradant on the shear stress of the LDPE/PKS composites with 20 and 40 php filler loading respectively at 180 ℃ was showed at Fig. 3. At similar temperature

and filler loading, the LDPE/PKS composites with eco-degradant exhibited lower shear stress compared to that of the composites without eco-degradant. The presence of the ecodegrdant was able to establish better interfacial bonding between the PKS and the LDPE polymeric matrix. As a result, the LDPE/PKS composites with eco-degradant can flow more easily compared to the composites without eco-degradant by showing lower shear stress at the particular shear rate. The presence of eco-degradant enhanced the flowability of the LDPE/PKS composites through lower the shear viscosity the composites.
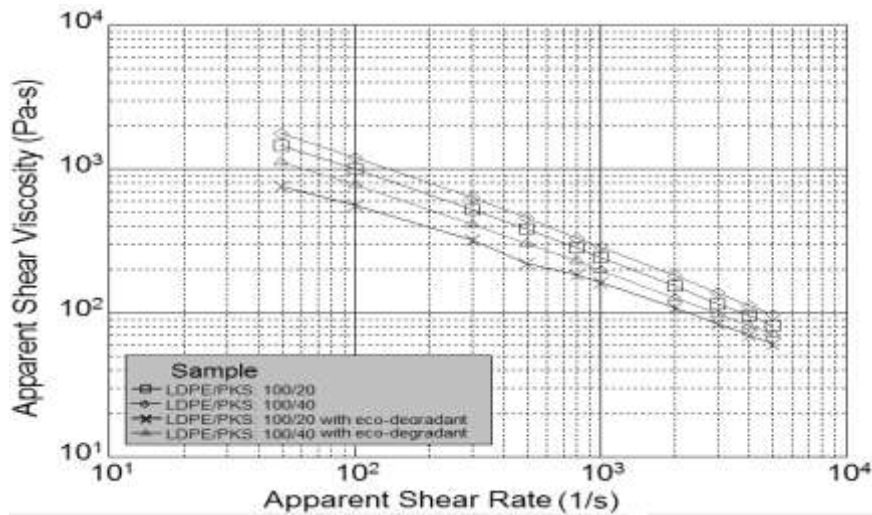
Fig. 3: The shear viscosity of the LDPE/PKS composites with and without eco-degradant at different shear rate and filler loading at 180 °C.

Fig. 4 shows the effect of temperature on the apparent viscosity of LDPE/PKS composites. Arrhenius plot at constant shear rate with the load of 2.16 kg were made to find out the influence of temperature on viscosity composites. The ln apparent viscosity of the LDPE/PKS composites with and without eco-degradant increased with increasing reciprocal absolute temperature $(1/T)$. A linear relationship was obtained between them. This indicates that the dependence of the shear viscosity of LDPE/PKS composites on temperature obeys the Arrhenius equations as shown in Equation 5. At same temperature, the addition of filler into LDPE increased the viscosity of the composites. The trend was true for all the composites at different temperature. At similar filler loading, the LDPE/PKS composites with eco-degradant showed lower apparent viscosity compared to the composites without eco-degradant.
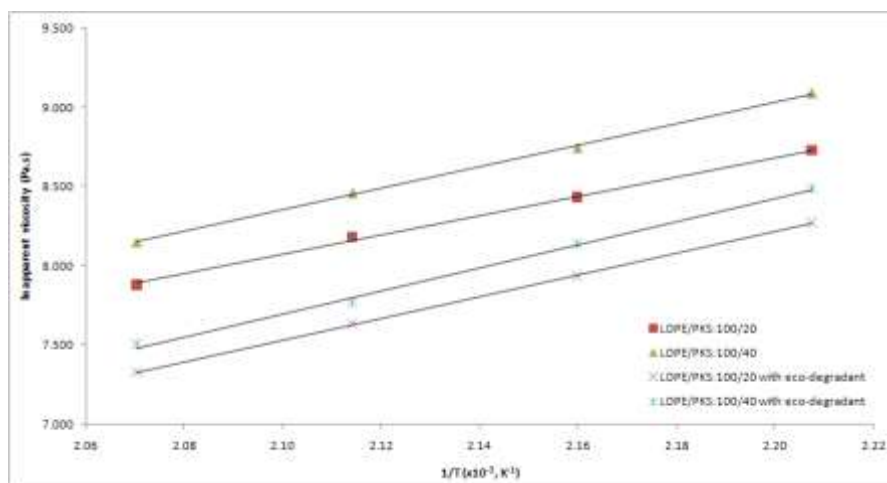
Fig. 4: The apparent viscosity on temperature of LDPE/PKS composites with and without eco-degradant.

Tables 2 lists the values of A and E of the LDPE/PKS composites with and without eco-degradant. The activation energy, E of a material provides important information on the sensitivity of material towards changes in temperature. The higher the activation energy the more temperature sensitive is the material. The results in Table 2 showed that the addition of filler into LDPE increased the activation energy of composites. The more filler added, the higher was the activation energy. However, at similar filler loading, the addition of eco-degrdant into LDPE/PKS composites increased its activation energy. The LDPE/PKS composites with eco-degradant were more temperature sensitive compared to the one without eco-degradant.

Table 2: Values of A, E and R_0 of LDPE/PKS composites melt with and without eco-degradant.

Filler loading (phr)	A	E (kJ/mol)	R_0
LDPE/PKS:100/20	0.0086	50.7658	0.999
LDPE/PKS:100/40	0.0028	56.3086	0.997
LDPE/PKS:100/20 with eco-degradant	0.0010	56.9484	0.999
LDPE/PKS:100/40 with eco-degradant	0.0050	60.4137	0.996

4.   CONCLUSIONS

The rheological properties of the LDPE/PKS composites were affected by the filler loading and processing temperature. At higher filler loading of the composites, the composites exhibited lower shear viscosity as the presence of filler will disturb the flowablity of the composites. On the other hand, the shear viscosity of the LDPE/PKS composites decreased as the temperature increased, which was attributed to the accelerated molecular motions. The LDPE/PKS composites with eco-degradant possessed lower shear stress compared to that of the composites without eco-degradant. The presence of eco-degradant was able to improve the flowablity of the LDPE/PKS composites. The apparent viscosity of the composites followed the Arrhenius equation and the activation energy of the composites melt was increased with filler loading. At similar filler loading, the addition of eco-degrandat into LDPE/PKS composites increased the activation energy.

5.   REFERENCES

1.   Thiruchitrambalam, M., Athijayamani, A., Sathiyamurthy, S. and Thaheer, A. S. A. (2010). A Review on the Natural Fiber-Reinforced Polymer Composites for the Development of Roselle Fiber-Reinforced Polyester Composite. *J. Nat. Fibers.*, 7(4), 307-323.

2.   Herrera-Franco, P. J. and Valadez-Gonzalez, A. (2005). A study of the mechanical properties of short natural-fiber reinforced composites. *Composites, Part B*, 36(8), 597-608.

3.   Morreale, M., Scaffaro, R., Maio, A. and La Mantia, F. P. (2008). Effect of adding wood flour to the physical properties of a biodegradable polymer. *Composites, Part A*, 39(3), 503-513.

4. Behjat, T., Russly, A. B., Luqman, C. A., Nor Azowa, I. and Yus, A. Y. (2009). Thermal properties of low density polyethylene - filled kenaf cellulose composite. *Eur. J. Sci. Res.*, 32(2), 223-230.

5. Yang, W., Liu, Z. Y., Shan, G. F., Li, Z. M., Xie, B. H. and Yang, M. B. (2005). Study on the melt flow behavior of glass bead filled polypropylene. *Polym. Test.*, 24(4), 490-497.

6. Li, T. Q. and Wolcott, M. P. (2004). Rheology of HDPE-wood composites. I. Steady state shear and extensional flow. *Composites, Part A*, 35(3), 303-311.

7. Mohanty, S., Verma, S. K. and Nayak, S. K. (2006). Rheological characterization of PP/Jute composite melts. *J. Appl. Polym. Sci.*, 99, 1476-1484.

8. Mohanty, S. and Nayak, S. K. (2007). Rheological characterization of HDPE/sisal fiber composites. *Polym. Eng. Sci.*, 47(10), 1634-1642.

9. Kalaprasad, G. and Thomas, S. (2003). Melt rheological behavior of intimately mixed short sisal–glass hybrid fiber-reinforced low-density polyethylene composites. II. Chemical modification. *J. Appl. Polym. Sci.*, 89(2), 443-450.

10. Liang, J. Z. (2009). Effects of Extrusion Conditions on Melt Viscoelasticity during Capillary Flow of Low-Density Polyethylene. *J. Thermoplast. Compos. Mater.*, 22(1), 99-110.

11. Dong, A., Yin, Q., Xie, J., Li, D. and Yin, Y. (2009). Rheological behavior of LDPE/CaCO3 blends containing EAA. *Polym. Compos.*, 30(9), 1212-1217.

12. Wu, G., Song, Y., Zheng, Q., Du, M. and Zhang, P. (2003). Dynamic rheological properties for HDPE/CB composite melts. *J. Appl. Polym. Sci.*, 88(9), 2160-2167.

13. George, J., Janardhan, R., Anand, J. S., Bhagawan, S. S. and Thomas, S. (1996). Melt rheological behaviour of short pineapple fibre reinforced low density polyethylene composites. *Polymer*, 37(24), 5421-5431.

14. Mohanty, S. and Nayak, S. K. (2006). Mechanical and Rheological Characterization of Treated Jute-HDPE Composites with a Different Morphology *J. Reinf. Plast. Compos.*, 26(13), 1419-1439.

Structural Properties of Nanocrystalline CdS Thin Films Using Sol-Gel Method for Solar Cells Applications

Abdulwahab. S. Z. Lahewil[1,*], Y. Al-Douri[1], U. Hashim[1], and N. M. Ahmed[2]

[1]Institute of Nano Electronic Engineering, University Malaysia Perlis, Kangar, Perlis, Malaysia
[2]School of Physics, Universiti Sains Malaysia, 11800 USM, Penang, Malaysia

*Corresponding author: alkmatys@yahoo.com

Abstract: *Nanocrystalline CdS thin films were prepared using Sol gel method. The CdS films were found to be nanocrystallined with hexagonal structure. XRD displays pattern for different annealing temperature. The structural properties are investigated using XRD. The obtained results are in agreement with other experimental and theoretical values.*

Keywords: Nanocrystalline, cadmium sulphide, sol-gel method; Solar cells.

1.   INTRODUCTION

Cadmium sulphide (CdS) nanocrystalline thin films were used as window material for CdS/CdTe solar cells continues as a subject of intense research due to its potential application in solar cells. CdS with hexagonal structure is highly favourable for solar cells application as a window layer because of it has suitable band gap and stabile. CdS is one of the important materials for application in electrooptical devices such as laser materials, transducers, photoconducting cells, photosensors, optical wave-guides and non-linear integrated optical devices [1]. The II–VI semiconductor nanocrystals exhibit interesting properties. This size dependence and the emergence of a discrete electronic structure from a continuum of levels in the valence and conduction bands of the bulk semiconductor result.

CdS thin films have been prepared using various techniques such as electro deposition [2], screen printing [3], physical vapour deposition [4], spray pyrolysis [5], molecular beam epitaxy [6], chemical bath deposition [7], successive ionic layer adsorption and reaction [8], sonchemical [9] and spin coating method [10].

Sol-gel method is more suitable to prepare optical materials as it permits molecular-level mixing and processing of the raw materials and precursors at relatively lower temperature and produces nano-structured bulk, powders and thin films [11]. Sol-gel is a very attractive method to produce CdS films for photovoltaic applications for which large-area devices are required at low cost. It also does not limit the choice of the substrate material. In this work, we report the preparation of nanocrystalline CdS films using sol-gel spin coating method and investigate the structural properties of the prepared thin films.

2.   EXPEIMENTAL PROCESS

Polyethylene glycol (PEG) sol was prepared by mixing 0.7 ml of PEG and 9.5 ml of ethanol and 0.6 ml of acetic acid under stirring for one hour. Cadmium nitrate 0.4 mol/L and thiourea 0.5 mol/L were dissolved in 15 ml ethanol with stirring for one hour also. The

prepared solution was slowly added to the PEG sol with vigorous stirring for 5 hours. To obtained the final sol thin films. The spin coating technique was used to obtain the thin films ready to be used by glass substrates with rotated at a speed of 800 rpm for 30 second for all samples. The last steps were the annealing, samples at different temperature (100, 200, 300 and 400 ^{O}C). The X-ray diffraction XRD studies have been carried out using Panalytical X-ray XRD diffractmeter.

3.   RESULT AND DISCUSSION

3.1   X-ray diffraction

The structural properties of the spin coated CdS films have been investigated by X-ray diffraction (XRD) technique as the shown in Fig 1, prepared by spin coating method and annealed at 100, 200, 300, and 400 ^{o}C for 30 minutes. The x-ray diffraction pattern exhibits peaks at 26.32^{o} and 43.59^{o} corresponding to the (002) and (110) directions respectively. The diffraction pattern of CdS film annealed at 400 ^{o}C exhibits two more additions peaks at 24.66^{o} and 28.22^{o} corresponding to (100) and (101) planes respectively. All these peaks correspond to the hexagonal phase. The existence of small peaks in the X-ray diffractogram reveals the formation of nanocrystalline CdS films. The peaks are not sharp indicating that the average crystallite size is small. Due to size effect, the peaks in the diffraction pattern broaden and their widths become large as the particles become smaller. The crystalline is improved due to the increasing annealing temperature.

The average size of grain has been obtained from the x-ray diffraction pattern using the Scherrer̕s formula:

$$D = k \lambda / \beta \cos \theta \qquad (1)$$

Where D is the grain size, k is the constant taken to be 0.94; β is the full width at half maximum (FWHM) and λ is the wave length of the x-rays = Cu (1.54060). The obtained grain size values of the annealed CdS films are given in Table 1. It is seen that crystallite size of CdS increases from 5.0 nm to 8 nm as the annealing temperature increased from 100 to 400 ^{o}C. So it is found that nanocrystalline CdS films with particle size 10 nm has been prepared using sol-gel spin coating method.
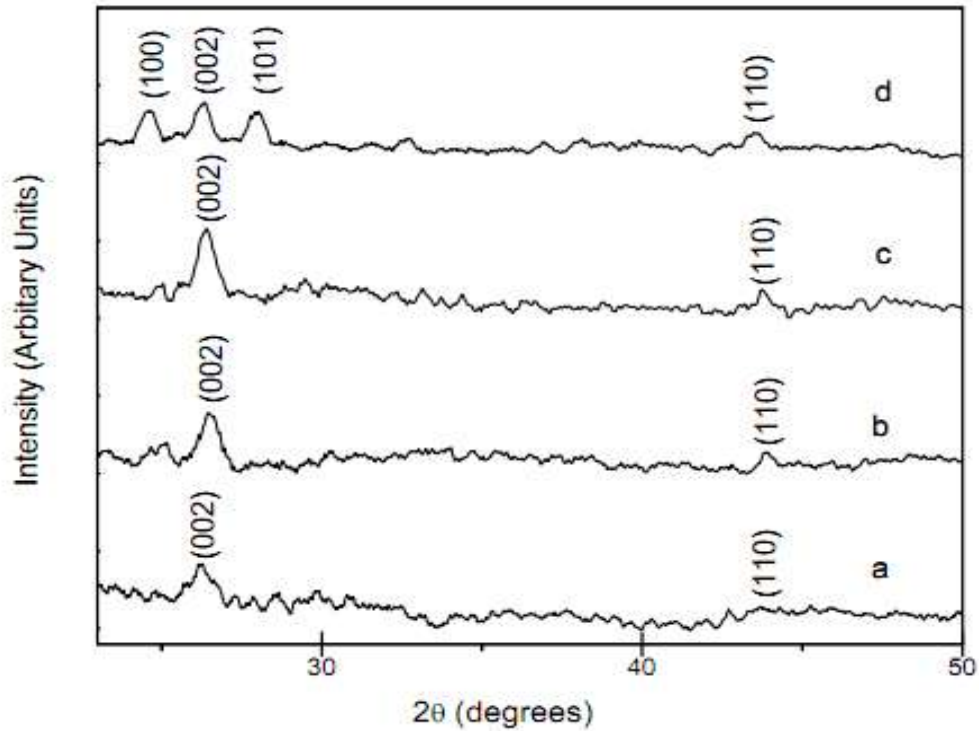
Fig. 1: X-ray diffraction pattern of films annealed at different temperature a) 100, b) 200 ^{o}C, c) 300 ^{o}C and d) 400 ^{o}C.

Table 1: Particle size from XRD for CdS films annealed at different temperatures.

Annealing temperatures (^{o}C)	Particle size from XRD (nm)
100	5.0
200	5.9
300	6.7
400	8.0

3.2   SEM characterization

Scanning electron microscopy is a convenient technique to study the microstructure of thin films. Fig. 2:, shows the surface morphology of CdS thin films annealed at 100, 200, 300 and 400 ^{O}C observed by SEM. From the images, it is observed that the annealed films are not uniform throughout all the images. But the film without any void, pinhole or cracks and that they cover the substrates well. From the Figure, we clearly observe the small nanosized grains some amorphous phase of CdS thin films. From these images, it can be seen that the grain sizes of the films are not uniform.
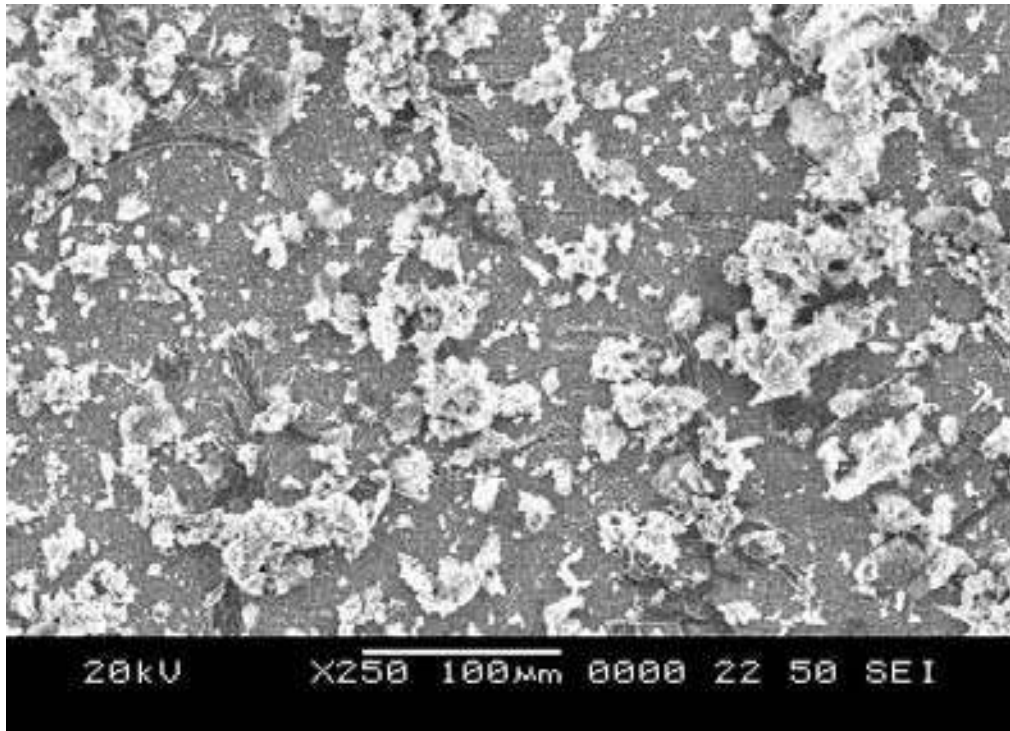
(a)
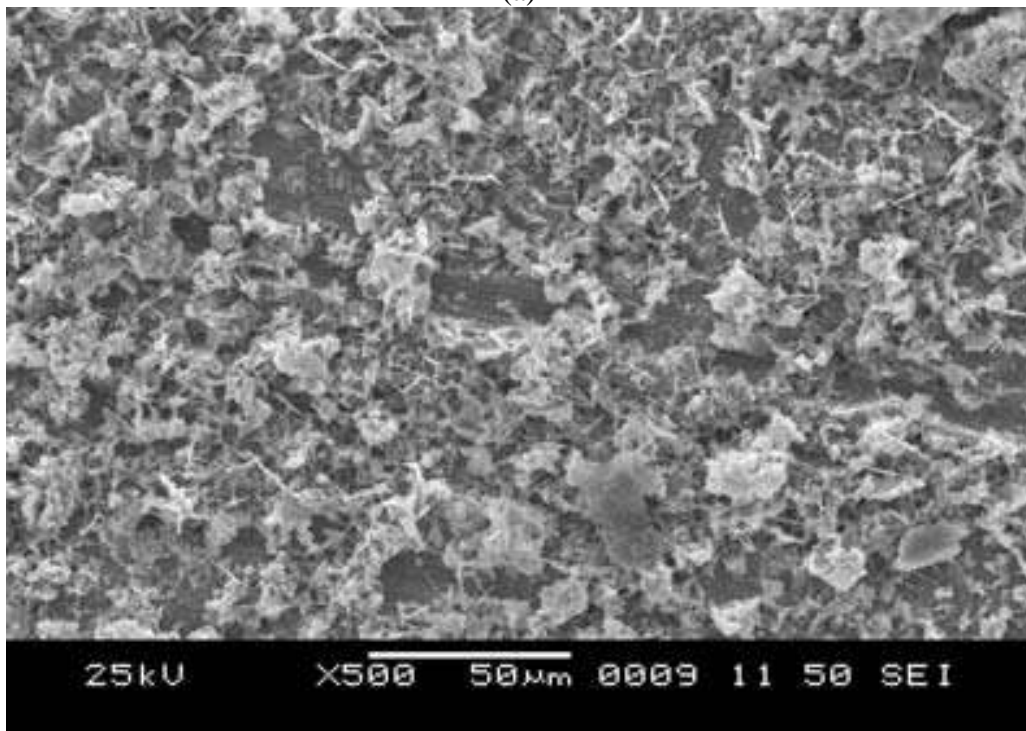
(b)
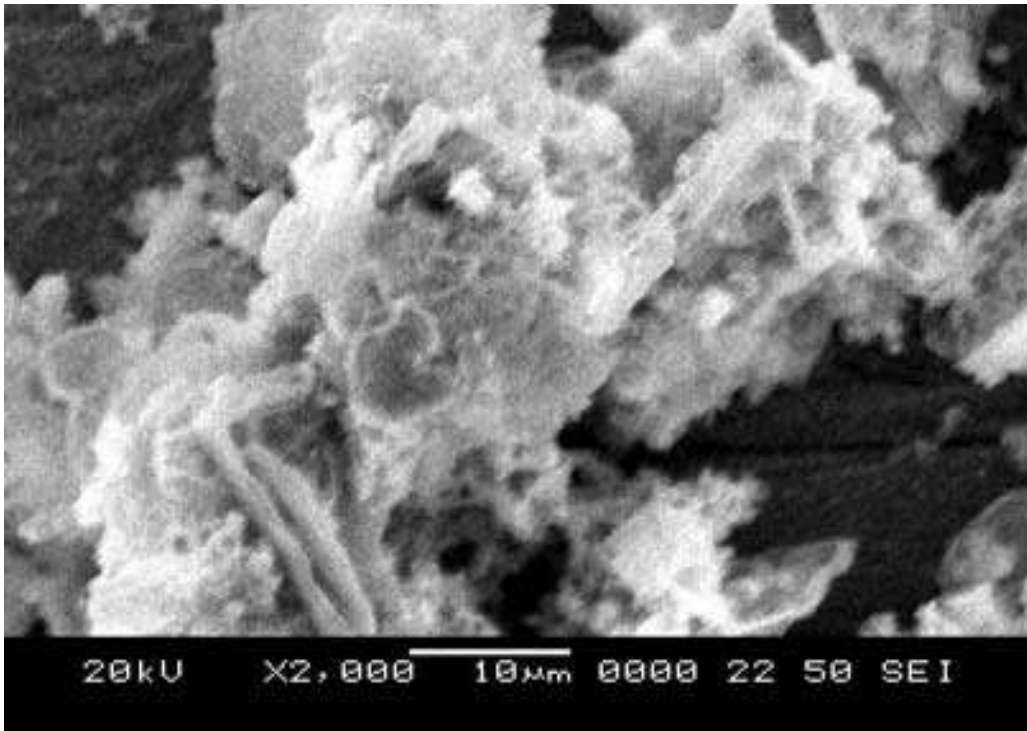
(c)
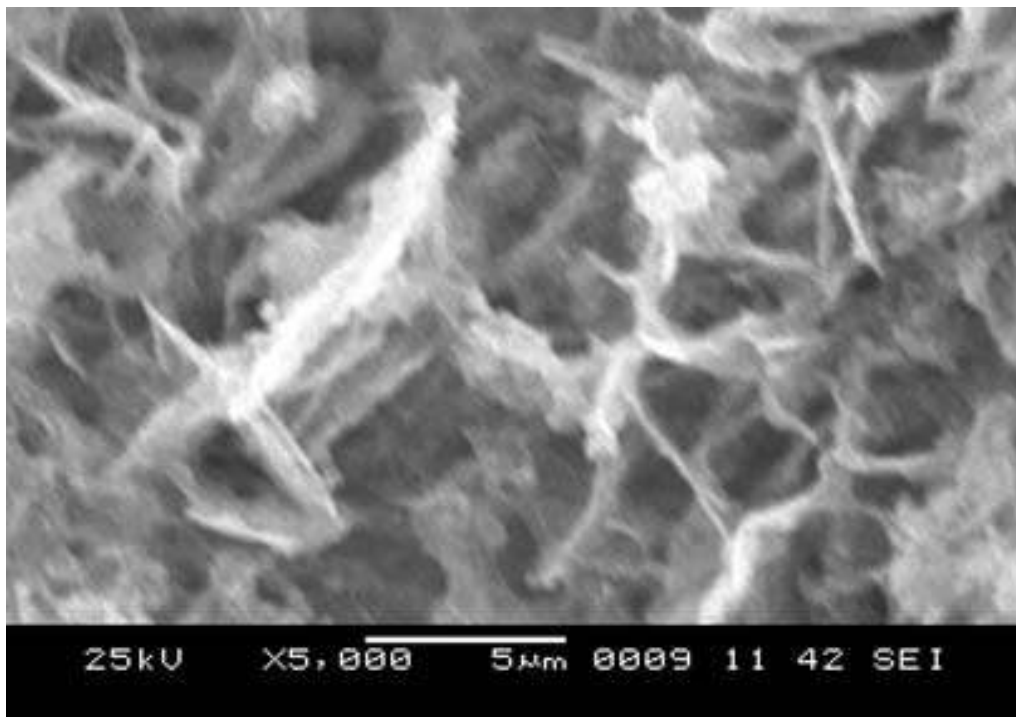
(d)

Fig. 2: SEM of CdS nanocrystalline films at different temperatures and magnitudes
a)   100, b) 200, c) 300 and d) 400 ^{O}C.

4.   CONCLUSION

Nanocrystalline CdS films have been prepared by sol-gel spin coating method. The XRD is studied revealed the formation of small grains having a size of 5.0 to 8.0 nm basing on the annealing temperature and resulting in the formation of CdS. SEM studies show presence of long tubes and irregular distributions of particles.

5. REFRENCES

1. A. Romeo, D. L. BaKtzner, H. Zogg, C. Vignali, A. N. Tiwari. 2011. Infuence of CdS growth process on structural and photovoltaic properties of CdTe/CdS solar cells. *Solar Energy Materials & Solar Cells,* **67**, pp 311-321.

2. P. J. Sebastian, M. E. Calixt. 2000. Porous CdS:CdO composite structure formed by screen printing and sintering of CdS in air. *Thin Solid Films,* **360,** pp 128-132.

3. D. P. Amalnerkar. 1999. Photoconducting and allied properties of CdS thick films. *Materials chemistry and physics*. **60,** pp 1-21.

4. D. kim, B. E. McCandless, S. S. Hegedus, R. W. Birkmire. 2007. Cu_x S back contact for CdTe solar cells. *Revista Mexicana de fisica*. **1**, 5-8.

5. H. Metina, S. Eratb, S. Durmus, M. Arid. 2010. Annealing effect on CdS/SnO2 films grown by chemical bath deposition. *Applied Surface Science*, **256**, pp 5076-5081.

6. J. W. Choi, A. Bhupathiraju, M. A. Hasan, J. M. Lannon, J. 2009. Characteristics of brush electrodeposited CdS films. *Chalcogenide, Letters*, **6,** pp 483-490.

7. M. A. Mahdi, Z. Hassan, S. S. Ng, J. J. Hassan, S. K. M. Bakhori. 2012. Structural and optical properties of nanocrystalline CdS thin films prepared using microwave-assisted chemical bath deposition. *Thin solid films*, pp 1-8.

8. B. Pradhana, A. K. Sharmab, A. K. Ray. 2007. Conduction studies on chemical bath – deposited nanocrystalline CdS thin films. *Journal of Crystal Growth*, **304**, pp 388-392.

9. S. M. Reda. 2008. Synthesis and optical properties of CdS quantum dots embedded in silica matrix thin films and their applications as luminescent solar concentrators. *Acta Material,* **56**, pp 259.

10. G. T. Pan, T. F. R. Shen, M. H. Lai, R. C. Juang, T. C. K. Yang. 2011. The preparation and characterizationof CdS1_xTex semiconductor films for hydrogen production by the chemical bath deposition method. *Solar Energy Materials & Solar Cells,* **95**, pp 2524–2530.

11. S. Gorer, G. Hodes, Y. Sorek, R. Reisfeld. 1997. Crystal phase transformation in sol-gel films of nanocrystalline CdSe and CdS. *Materials Letters,* 31, pp 209-214.

Preparation and Properties of Nanocomposite Foams based on Layered Silicate/Natural Rubber (NR)/Ethylene-Vinyl Acetate (EVA)

A. Masa[1], N. Karee-uma[1], A. Kaesaman[1], C. Thongpin[2], and N. Lopattananon[1,*]

[1]Center of Excellence in Natural Rubber Technology (COE-NR), Department of Rubber Technology and Polymer Science, Faculty of Science and Technology, Prince of Songkla University, Pattani 94000, THAILAND
[2]Faculty of Engineering and Industrial Technology, Silpakorn University, Nakhon Pathom 73000, THAILAND

[*]Corresponding author: lnatinee@bunga.pn.psu.ac.th

Abstract: *Nanocomposite foams based on natural rubber (NR)/ethylene-vinyl acetate (EVA) blends with a ratio of 40/60 were prepared by melt mixing in an internal mixer and compounding on two roll-mill at 70 ^{o}C, followed by compression molding. Effect of nanoclay (Na-MMT) contents (2-10 phr) on cure, tensile and morphological properties was studied. The X-Ray diffraction (XRD) results showed that the nanoclay was intercalated. The addition of clay into EVA/NR blends decreased foam density and improved cell morphology. The present work suggested that the production of nanocomposite foams with low density and acceptable strength was obtained at 5 phr nanoclay.*

Keywords: Natural rubber, ethylene-vinyl acetate, nanocomposite, foam, mechanical properties

1. INTRODUCTION

Polymeric foams is widely used in various applications, due to its low density, buoyancy, cushioning performance, impact damping, thermal and acoustic insulation properties, good energy absorption, and low cost. The most common to manufacture foams is through latex form. Alternatively, rubber foams can be produced through solid form. Foamed polymers, which made from dry rubber, are generally made up of solid phase and gas phase, produced by using either chemical or physical blowing agent. Ethylene-vinyl acetate copolymer (EVA) is one of the most widely used polymers for manufacturing foamed products. Because EVA has low strength and flexibility, therefore it was often blended with other polymers such as natural rubber [1] and EtBC (ethylene-1-butene copolymer) [2,3] to improve the mechanical properties. Reinforcing fillers are usually added in the foam to increase certain properties. Recently, the incorporation of nano-size filler, that is nanoclay or layered silicate, as reinforcing filler in polymer to produce low density nanocomposite foams with improved morphology and mechanical properties was reported. [3,4] In this work, EVA/NR blend foams with blend composition of 60/40 %wt were prepared using Azodicarbonamide (ACD) as blowing agent. Nanoclay was used as a reinforcing filler. The effect of nanoclay content on foam properties was studied.

2. EXPERIMENTAL METHODS

EVA pellet (POLENE Co., Ltd., Thailand) and NR (Khokpho-Maelarn, Pattani, Thailand) were firstly melt-mixed in an internal mixer at a temperature of 70 ^{o}C with rotor speed of 60 rpm. Next, sodium montmorillonite (Na-MMT; Kunipia-F) (Kunimine Industries

CO., LTD., Japan) (2-10 phr) and other additives were added. The obtained EVA/NR blend masterbatchs were compounded with ADC, dicumyl peroxide (DCP) and trimethylol propane trimethacrylate (TMPTMA) on a two-roll mill. The blends were kept at room temperature for 24 hours and then hot-pressed at 160 ^{o}C to obtain EVA/NR foams. The foams were cut into test-specimens for density, mechanical property, XRD and SEM characterizations.

2.1   Measurements

Cure characteristics were studied using an Oscillating Disk rheometer (ODR 2000, Monsanto Inc.) according to ASTM D224 at temperature of 160 ^{O}C for 30 min.

The X-ray diffraction (XRD) studies were performed by using a Rigaku (TTRAXIII) X-ray diffractometer. The X-ray beam was nickel-filtered CuKα (wave length = 0.154nm). Data were obtained for a 2θ range of 1-10°.

The cell structure of the nanocomposite foams was observed with FEI Quanta 400 scanning electron microscope (SEM). The SEM analysis was carried out on frozen-cut samples, coated with thin layer of gold by using Sputter coater.

Density of foams was characterized by mean of mass to volume ratio of sample according to ASTM D1622-03.

The tensile properties of the NR/EVA foams were perform using universal tensile testing machine (HOUNFIELD H10KS) at room temperature. The crosshead speed was 500 mm/min. Five replicates of dumb-bell shaped specimens were measured and the data were averaged.

3.   RESULTS AND DISCUSSION

The cure characteristics of NR/EVA nanocomposite foams produced at 160 ^{O}C with different nanoclay contents are shown in Table 1. Scorch (T_{s1}) and cure times (Tc_{90}) are measure of time at onset of vulcanization and at 90% of complete cure. The minimum torque (M_L) is related to initial viscosity of rubber compounds. It can be seen from Table 1 that the T_{s1}, Tc_{90} and M_L of blend 40/60 NR/EVA compounds were independent of nanoclay loading. However, the maximum torque (M_H) increased with increasing nanoclay content. This means that the stiffness of the rubber blend foam increased, due to the restriction of rubber chain mobility upon addition of reinforcing clay.

Table 1: Cure characteristics of NR/EVA blend nanocomposite foams containing different nanoclay content.

Na-MMT Content (phr)	T_{s1} (min)	T_{c90} (min)	M_L (dN.m)	M_H (dN.m)
0.0	1:15	11:04	1.13	4.31
2.0	3:01	11:37	1.73	4.32
4.0	2:23	12:15	0.78	4.49
5.0	2:48	13:38	0.75	4.45
8.0	2:04	11:57	0.96	4.90
10.0	2:49	13:22	1.19	4.99
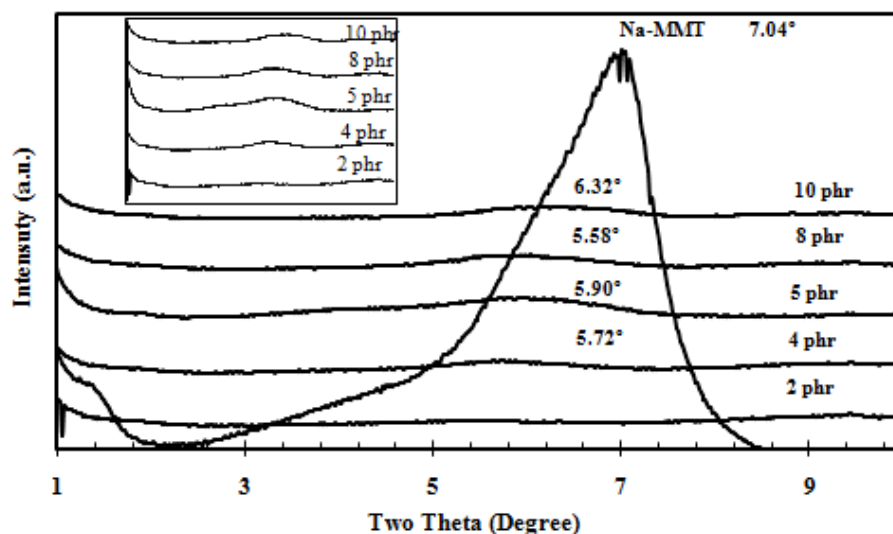
Fig. 1: XRD patterns of nanoclay (Na-MMT) and 60/40 EVA/NR nanocomposite foams containing different nanoclay contents.

Fig. 1 shows XRD patterns of Na-MMT and 60/40 EVA/NR nanocomposite foams. The Na-MMT showed typical strong diffraction peak at $2\theta = 7.04°$, corresponding to clay interlayer distance of 1.25 nm. For the nanocomposite foams (with 4-10 phr clay loading), the peak corresponding to clay interlayer were shifted to lower angle (5.58 - 6.32°), indicating that interlayer spacing was increased to 1.39 – 1.64 nm because the clay was intercalated by rubber chains. However, no diffraction peak due to clay interlayer was observed for 2 phr nanocomposite, indicating exfoliated and/or intercalated disordered clay structures.

SEM photomicrographs of 60/40 EVA/NR nanocomposite foams are shown in Fig. 2. The blend foams showed a closed-cell structure. The number of foam cell increased with increasing nanoclay, and the cell size increased with clay content upto 5 phr. This was because the nanoclay acted as nucleating agent, [3,5] facilitating foam formation. However, at higher clay loading (10 phr), the cell size appeared to decrease and the distribution of foam cells was not uniform. Some large cells were also apparently seen to disperse together with smaller cells. The non-uniform cell distribution was probably due to aggregation of nanoclay as shown in Fig. 2. The effect of nanoclay content on foam density of EVA/NR blends is shown in Fig. 3.
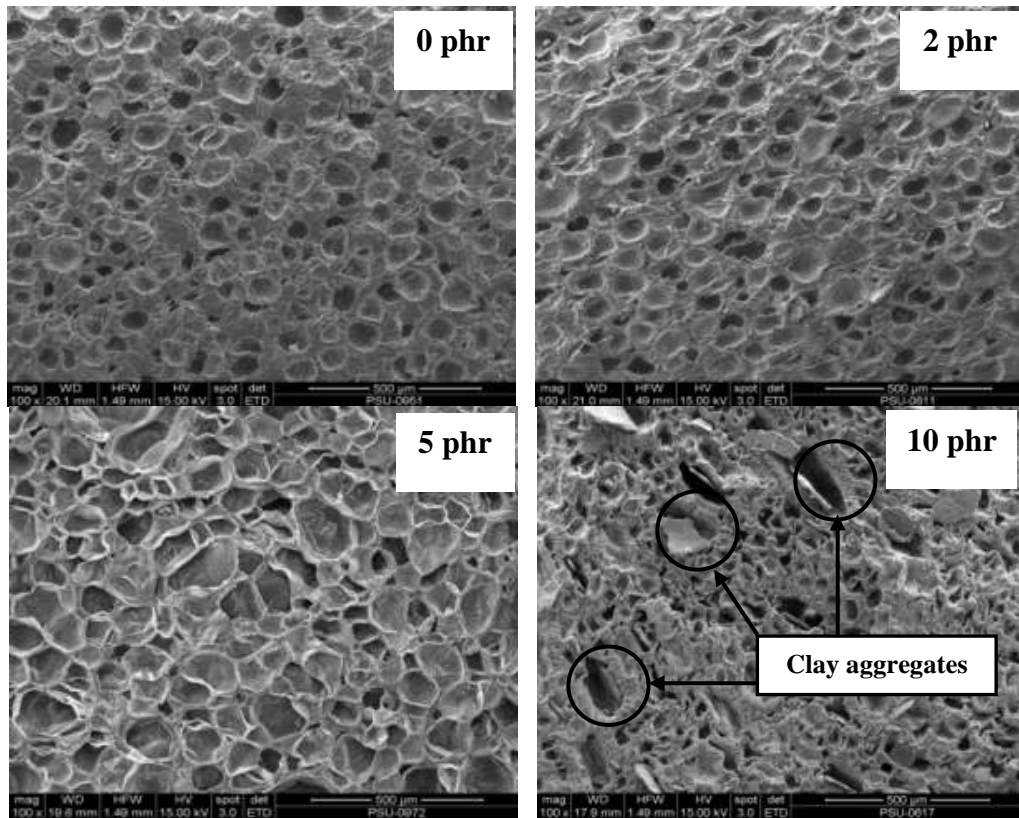
Fig. 2: SEM images of 60/40 NR/EVA blend nanocomposite foams containing different nanoclay contents.
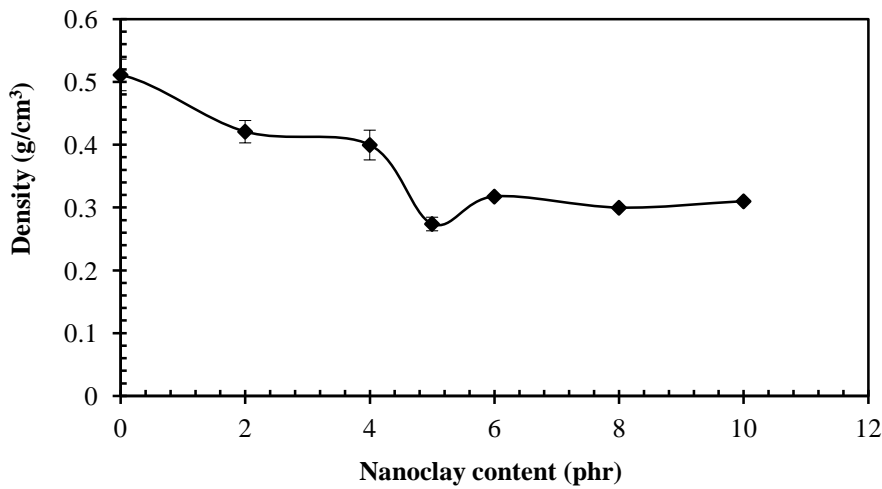
Fig. 3: Density of 60/40 NR/EVA blend nanocomposite foams containing different nanoclay contents.

From Fig. 3, the foam density decreased with increasing nanoclay content up to 5 phr, after which the density slightly increased and remained unchanged. The decrease in foam density was because more cells was formed in the blend due to the presence of nanoclay, leading to more gas present in the blend nanocomposites. At higher clay loading (6-10 phr), however, the poor dispersion of nanoclay caused by clay agglomeration may contribute to the increase in density of blend nanocomposite foam.
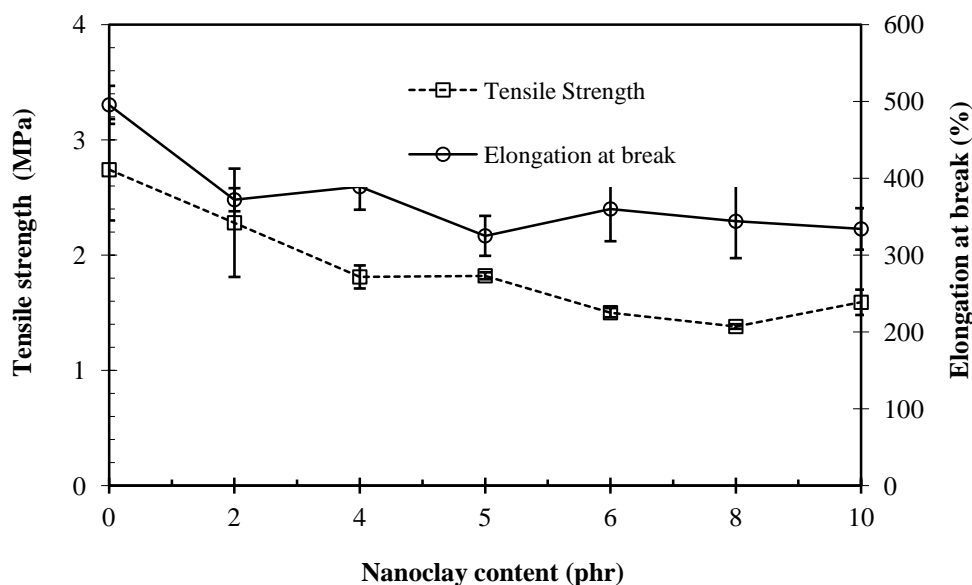
Fig. 4: Tensile properties of 60/40 NR/EVA blend nanocomposite foams containing different nanoclay contents

Fig. 4 shows tensile strength and elongation at break of the EVA/NR blend nanocomposite foams. Both tensile properties decreased with increasing clay content and became constant at clay content greater than 5 phr. It was reported that the mechanical strength of nanocomposite foams strongly depends on cell morphology and foam density. [5] Therefore, the tensile strength and elongation at break decrease in proportion to a decrease of foam density (Fig. 3). However, the addition of clay over 5 phr did not further decrease the foam density, leading to constant values of strength and elongation at break.

4.   CONCLUSION

Effect of nanoclay contents (2-10 phr) on the properties of EVA/NR nanocomposite foams was studied. XRD results showed that the nanoclay was intercalated. The addition of clay into EVA/NR blends decreased foam density and improved cell morphology. The present work suggested that the production of nanocomposite foams with low density and acceptable strength was obtained at 5 phr nanoclay.

5.   ACKNOWLEDGEMENT

6.   REFERENCES

1.   Kim, D. W., Park, K. W., Chowdhury, S. R. and Kim, G, H. (2006). Effect of Compatibilizer and Silane Coupling Agent on Physical Properties of Ethylene Vinyl Acetate Copolymer/Ethylene-1-Butene Copolymer/clay Nanocomposite Foams. *J. Appl. Polym. Sci.*, 102(4), 3259-3265.
2.   Park, W. K., Chowdhury, R. S., Park, C. C. and Kim, H. G., (2007). Effect of dispersion state of organoclay on cellular foam structure and mechanical properties of

ethylene vinyl acetate copolymer/ethylene-1-butenecopolymer/organoclay nanocomposite foams. *J. Appl. Polym. Sci.*, 104(6), 3879-3885.

3. Fu, J. and Naguib, H. E., (2006). Effect of Nanoclay on the Mechanical Properties of PMMA/Clay Nanocomposite Foams. *Journal of Cellular Plastics*, 42, 325-342.

4. Xin, Z. X., Zhang, Z. X., Pal, K., Kang, D. J., Lee, S. H. and Kim, J. K. 2009. Effects of Waste Ground Tire Powder (WGRT) and Chemical Blowing Agent Content on the Cell Morphology and physicomechanical Properties of Injection-Molded Polypropylene /WGRT Foams, *Journal of Vinyl & Additive Technology*, 15: 275-280.

Effect of Polypyrrole on the Morphology, Mechanical and Electrical Properties of High Density Polyethylene/Montmorillonite Nanocomposites

Khatereh Abron, Mat Uzir B. Wahit*, and Sobhan Bahraeian

[1]#904, U3A, Perdana, Universiti Teknologi Malaysia, Skudai, Johor, Malaysia

[2]Polymer Engineering Department, Faculty of Chemical Engineering, Universiti Teknologi Malaysia, 81310 UTM Skudai, Johor, Malaysia

*Corresponding author: mat.uzir@cheme.utm.my

Abstract: *Polypyrrole (PPy) was incorporated into high density polyethylene grafted maleic anhydride (HDPE-g-MAH) /montmorillonite(MMT) nanocomposites by using melt mixing followed by compression molding. PPy concentration varied in the range of 5-20% by weight in nanocomposites. The effect of PPy concentration on morphology, mechanical and electrical properties of nanocomposites was investigated. The result of tensile test shows that addition of PPy has increased the Young's modulus and tensile strength; but it has exhibited average decrease in percentage elongation at break. Two probe conductivity measurements have indicated that raising the amount of PPy increases the conductivity of nanocomposites. The result of X-Ray Diffraction (XRD) and Scanning Electron Microscopy (SEM) indicate that HDPE-g-MAH has good compatibility with MMT and PPy chains.*

Keywords: Conducting polymer, polypyrrole, high density polyethylene, montmorillonite

1.   INTRODUCTION

Conducting polymers as a material with magnetic and electrical properties has been attracted many researches. During the last decade, the study on inherently conductive polymers such as polyaniline (PANi), polypyrrole (PPy) and polythiophene (PTh) have been increased significantly due to their advantageous morphological and structural properties. Among intrinsically conductive polymers, polypyrrole (PPy) has many unique properties like simple synthesis, high flexibility in the process and good stability and mechanical properties [1,2].

High density polyethylene (HDPE) is a thermoplastic with significant mechanical properties which due to its availability and competitive cost is one of the most popular polymers. In spite of wide applications of HDPE in daily life its thermal stability is poor and also it is an insulating polymer. The approach to the enhancement of thermal stability based on the use of polymer nanocomposite has been developed in the last years [3].

Polymer nanocomposites are moderately new group of materials that poses a wide range of properties. The combination of nano sized particle and big interfacial area can strongly influence the nanocomposites behavior [4]. By applying layered silicates as a reinforcing agent nanocomposites can be designed with a wide range of properties. Montmorillonite (MMT) is important nanofiller which cause to significant improvement in optical, electric, mechanical, thermal, flammability, dimensional and barrier properties [5]. Zhou et al. (2005) reported that inorganic MMT and polyethylene have different characterization. In order to improve the compatibility between PE and MMT, polyethylene grafted maleic anhydride was used. Grafting polyethylene has polar groups in its backbone

and this helps to improve the compatibility between PE and MMT. By addition of MMT to HDPE, thermal stability and the mechanical properties can be increased but there was no improvement in electrical conductivity of nanocomposite. The attribution of PPy as regarding to its high conductivity is to form a conductive nanocomposite [6].

Conducting polymer-based composites are new materials. Many researchers have studied on the conductive nanocomposites based on polypyrrole. (Pavlinec et al., 1997). Boukerma et al. (2005) reported that the blend of PPy/MMT is suitable filler for improving the conducting and mechanical properties of insulating polymer matrices [7, 8]. Elyashevich et al. (2003) found that HDPE/PPy composites have high thermal stability. PPy layer can increase all mechanical characteristics of PE/PPy at PPy content less than 20%. They reported that at further increase of PPy, the breaking strength and break elongation start to decrease [9].

2.   EXPERIMENT

2.1   Chemicals and reagents

High density polyethylene (HDPE) and High density polyethylene grafted maleic anhydride (HDPE-g-MAH) used in this study was purchased from Petrochemicals (Malaysia). Montmorillonite (MMT) which was used as organoclay filler has a grade of 1.30p from a nano clay Company. Pyrrole monomer with a density of 0.97g/cm^3 at 20°C and a melting point of -24°C was purchased from Merck Company. Sodium dodecylbenzene sulfonate (DBSNa) as a surfactant was from Acros Organic Company and has a grade of 88%. Iron (III) Chloride Hexahydrate ($FeCl_3.6H_2O$) which was used as an oxidant was purchased from Qrec Company.

2.2   Polypyrrole Synthesis

3.48 gr DBSNa was dissolved in 100 cc H_2O and (0.1 mol) 27.03 gr $FeCl_3.6H_2O$ also dissolved in 100cc water and mixed together. After 15 minutes stirring in 0°C, 0.15 mol (10.4 cc) monomer of pyrrole was dissolved in 50cc of H_2O and drop wised during 20 minutes to mixture. The black powder of polypyrrole filtered and washed off with water and dried for 8 hours in an oven at 60°C temperature. The conductivity of synthesized PPy was around 3.18 S/cm.

2.3   Blending

HDPE/MMT/HDPE-g-MAH/PPy nanocomposites were prepared based on Table 1 designation by internal mixer at temperature of 170°C and screw revolution of 15 rpm. After blending the materials, compression molding was applied to prepare samples at temperature of 170° C.

Table 1: Blends composition and their designation.

Samples	HDPE (%)	PPy (%)	HDPE-g-MAH (%)	MMT (phr)
1	95	0	5	4.8
2	90	5	5	4.8

3	85	10	5	4.8
4	80	15	5	4.8
5	75	20	5	4.8

2.4   Characterization

To characterize and evaluate the samples different experiments were applied. XRD was conducted to study the intercalation of MMT in the matrix. It was performed with the Siemens 500 X-ray diffractometer by using Cu-WL anode in 2-Theta range between 1.5° to 10° and the voltage used was 40 kv. Electrical conductivity of synthesized PPy was measured by using two probe tests. The current is supplied from Tektronix PS280 DC Power Supply. The SEM study was meant to observe the distribution of MMT and PPy particles in the nanocomposite. This evaluation carried out by Phlips ZL40 Scanning Electron Microscopy. Tensile test was carried out according to ASTM D638 by using Universal Testing Machine Model 5567, Instron Co. The measurements tensile modulus, tensile strength and elongation at break were obtained under ambient condition.

3.   RESULTS AND DISSCUSSION

3.1   X-ray diffraction (XRD)

XRD results of HDPE/PPy/MMT nanocomposites are shown in Figure 1 and Table 2. The shift of MMT angles to lower amount is attributed to the presence of maleated HDPE and PPy which intercalated between the layers of MMT thus, the interlayer distance was enlarged. Therefore, it can be said that HDPE-g-MAH had good compatibility with MMT and also the rigid PPy chains as it can diffuse into MMT layers. Rizvi *et al*., (2009) also reported similar result and stated that the growth of *d*-spacing show the MMT layers are further intercalated by PPy [10]. These results indicated the formation of HDPE/MMT/PPy nanocomposites. The calculated d-spacings of MMT in HDPE/MMT and HDPE/PPy/MMT nanocomposites are shown in Table 2.
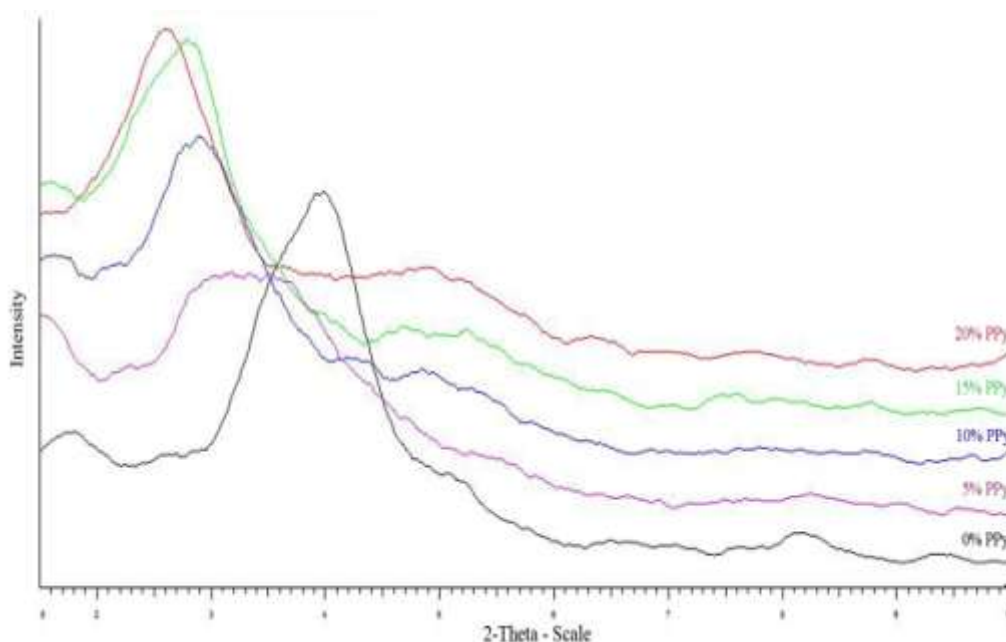
Fig. 1: XRD pattern of HDPE/MMT/PPy with different amount of PPy

Table 2: The 2θ angle and d-spacing of MMT for HDPE/HDPE-g-MAH/PPy/MMT nanocomposites with different content of PPy.

Samples	HDPE (wt %)	HDPE-g-MAH (wt %)	PPy (wt %)	MMT (phr)	2θ	d-spacing (nm)
PPy	0	0	100	0	22	0.5
MMT	0	0	0	100	4.1	2.1530
0%PPy	95	5	0	4	3.96	2.2284
5%PPy	90	5	5	4	3.43	2.5726
10%PPy	85	5	10	4	3.43	2.5726
15%PPy	80	5	15	4	2.79	3.1562
20%PPy	75	5	20	4	2.60	3.3944

3.2 Scanning Electron Microscopy (SEM)

SEM was used to illustrate the morphological properties of HDPE/MMT nanaocomposite in presence of PPy. The SEM image of HDPE/MMT and HDPE/MMT/10%PPy is presented in Figure 2 and 3 with Globular particles of PPy in dimensions between 10-20 micrometers.
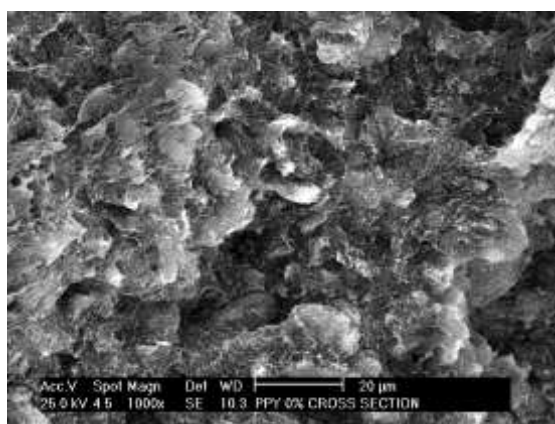
Fig. 2: HDPE/MMT cross section   Fig. 3: HDPE/MMT/10%PPy cross section
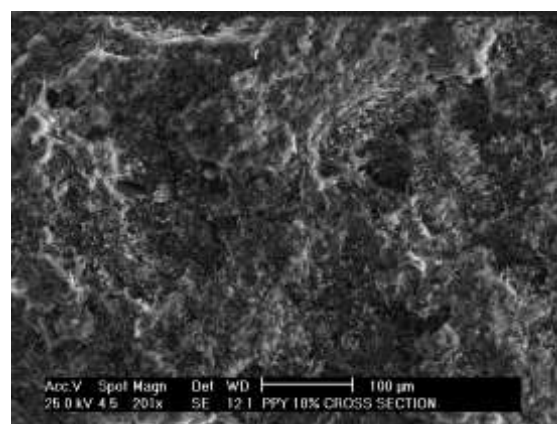
The color of HDPE/MMT with PPy is darker and improvement in dispersion of PPy in the matrix can be observed. It can be seen that the surfaces of matrix become smoother with increasing content of PPy due to destruction of HDPE structure. Similar result was also reported by other researchers that showed that PPy was situated on the surface of HDPE and the deposition does not form a homogenous pattern [9, 12]. Omastova *et al*., (2003) also reported that, the sand-like color of MMT particles change to grey or black in the presence of PPy. Depending on the amount of PPy color changing is higher [13].

3.3 Conductivity

The resistivity values of HDPE/MMT with various amount of PPy are shown in Table 3. The resistivity of nanocomposites without PPy was around 15.58 GΩ and upon the addition of 5% PPy to nanocomposites the resistivity decreased to 9.504 GΩ. Although it is clear that the addition of higher amount of PPy decreases the resistivity of nanocomposites

further addition up to 20% does not change the resistivity. The blend with 20% PPy presents the lowest resistivity (880 MΩ) with a large difference compared to other nanocomposites.

Table 3: Resistivity and conductivity of different HDPE/HDPE-g-MAH/MMT/PPy blends.

HDPE/HDPE g MAH/MMT/PPy	PPy (%)	Resistivity (GΩ)	Conductivity (S/cm)
28.5/1.5/1.2/0	0	15.58	6.41×10^{-11}
27/1.5/1.2/1.5	5	9.504	1.052×10^{-10}
25.5/1.5/1.2/3	10	5.784	1.728×10^{-10}
24/1.5/1.2/4.5	15	2.120	4.716×10^{-10}
22.5/1.5/1.2/6	20	0.880	1.136×10^{-9}

Ong et al. (2008) also stated that the presence of small amounts of PPy can increase the conductivity of blend. The conductivity of PE is around 10 -16 s/cm, so the low conductivity of the composite is due to a very small amount of conductivity in the matrix [14].

3.4   Mechanical Test

In this study, mechanical properties of HDPE/MMT/PPy nanocomposites were investigated by tensile test. The different amount of PPy into matrix has been changed tensile properties of nanocomposites. The changes in tensile strength, modulus and elongation at break with increasing content of PPy are shown in Table 4.

Table 4: Elongation at break, tensile strength, Young's modulus values for HDPE/MMT nanocomposites with differtent content of PPy.

PPy content (W%)	Elongation at break (%)	Tensile strength (MPa)	Young's modulus (MPa)
0	2.294	17.9	64.90
5	2.136	19.3	68.23
10	1.945	20.4	71.34
15	1.743	21.5	75.52
20	1.632	22.4	78.64

According to table it can be observed that tensile strength of HDPE/ MMT increased by growing amount of PPy in it. Adding PPy to nanocomposites conducted to have stiffer material due to the stronger interfacial adhesion between nanocomposite and the PPy chains. Addition of PPy, causes to decrease elongation at break of nanocomposites. As the amount of PPy increase in the matrix of HDPE/MMT the percentage of decrease reaching to its lowest value in nanocomposite with 20% PPy. The reason for it is maybe incorporation of PPy into HDPE/MMT matrix cause to disruption of polymer matrix and prevents elongation of HDPE matrix.

It can be observed in Table the Young's modulus of blends increased slowly by addition of PPy. Addition of PPy restricted the chain mobility due to rigidity of this polymer. Thus, as PPy contents increased the blends became more rigid and the chain mobility became more restricted, and resulted in high modulus properties. The incorporation of PPy into HDPE has led to an increase in the modulus of the composites because PPy powder is stiffer than the matrix in which they are dispersed.

Aydinli *et al*., (1998) reported decrease in elongation at break in the blend of PE and PPy. Incorporation of PPy into matrix causes disruption of polymer matrix. Due to weak

interaction between PPy and matrix, addition of PPy cause to decrease in percentage of strain at break value. Increase in Youngs modulus show that PPy enhanced then stiffness of the nanocomposite [15].

4.   CONCLUSION

Polypyrrole was synthesized by chemical method using FeCl3 as an oxidant and DBSNa as the surfactant. The electrical conductivity measurement has shown that electrical conductivity of PPy is 3.18 S/cm. PPy improves mechanical and electrical properties of HDPE/MMT nanocomposites. Based on tensile results PPy improved tensile strength and Youngs modulus of HDPE/MMT nanocomposites. The electrical conductivity measurements have shown that incorporation of PPy increases the conductivity of the nanocomposites up to orders of 5 Scm-1.

5.   REFERENCES

1.   Schulz B, Orgzall I, Díez I, Dietzel B, Tauer K.(2010). Colloids and Surfaces A : Physicochemical and Engineering Aspects Template mediated formation of shaped polypyrrole particles. *Colloids and Surfaces*. 354:368-376.
2.   Hatchett DW, Josowicz M.(2008). Composites of Intrinsically Conducting Polymers as Sensing Nanomaterials. *Inorganic Chemistry*. 746-769.
3.   Lomakin SM, Novokshonova L a, Brevnov PN, Shchegolikhin AN.(2007) Thermal properties of polyethylene/montmorillonite nanocomposites prepared by intercalative polymerization. Journal of Materials Science. 43(4):1340-1353.
4.   Zhou Z, Zhai H, Xu W, (2006). Preparation and characterization of polyethylene-g-maleic anhydride–styrene/montmorillonite nanocomposites. *Journal of Applied Polymer Science.* 101(2):805-809.
5.   Araújo EM, Barbosa R, Morais CRS. (2007). Effects of organoclays on the thermal proccesing of PE / CLAY nanocomposites. *Journal of Thermal Analysis*. 90:841-848.
6.   Zhou Z, Zhai H, Xu W, et al. (2005) Preparation and Characterization of Polyethylene-g-Maleic Anhydride – Styrene / Montmorillonite Nanocomposites. *Polymer*.
7.   Pavlinec J, Simon F.(1997). Synthesis, Electrical Properties and Stability of Polypyrrole-Containing Conducting Polymer Composites. *Polymer International*. 43.
8.   Boukerma K, Piquemal J-Y, Chehimi MM. (2005). Synthesis and interfacial properties of montmorillonite/polypyrrole nanocomposites. *Polymer*. 47(2):569-576.
9.   Elyashevich GK, Rosova EY, Sidorovich AV, Kuryndin IS, Trchov M.(2003). The effect of a polypyrrole coating on the thermal stability of microporous polyethylene membranes. *European Polymer Journal*. 39:647-654.
10.   Rizvi TZ, Shakoor A. (2009). Electrical conductivity and dielectric properties of polypyrrole / Na^+ – montmorillonite (PPy / Na^+ – MMT) clay nanocomposites. *Journal of Physics*. 095415.
12.   Elyashevich GK, Rosova EY, Andreeva DV. (2004). New Composite Systems on the Base of Polyethylene Porous Films Covered by Polypyrrole and Polyacrylic Acid. *Polymer*.

13.   Omastova M. (2003). Synthesis and structural study of polypyrroles prepared in the presence of surfactants. *Synthetic Metals.* 138(3):447-455.
14.   Ong CK, Ray S, Cooney RP, Edmonds NR, Easteal AJ.(2008). Preparation and Characterization of Composites of Polyethylene with Polypyrrole-Coated Wollastonite. Composites. 110:632-640.
15.   Aydinli B, Toppare L, Tinc T. (1998). A Conducting Composite of Polypyrrole with Ultrahigh Molecular Weight Polyethylene Foam. *Polymer*. 1843-1850.

Compressive Strength and Rapid Chloride Penetration of Engineered Cementitious Composites (ECC) with Palm Oil Fuel Ash (POFA)

Nurdeen M. Altwair[1, 2], Megat A. Megat Johari[1,*], and Syed F. Saiyid Hashim[3]

[1]School of Civil Engineering, Engineering Campus, Universiti Sains Malaysia, 14300 Nibong Tebal, P. Pinang, Malaysia
[2]Civil Engineering Department, Faculty of Engineering, Al-Margab University, Al-Khoms, Libya
[3]School of Materials and Mineral Resources Engineering, Engineering Campus Universiti Sains Malaysia, 14300 Nibong Tebal, P. Pinang, Malaysia

*Corresponding author: cemamj@eng.usm.my, mgtazmi@yahoo.com

Abstract: *The objective of this study is to investigate the effects of using different proportions of high fineness treated POFA on compressive strength and rapid chloride penetration of Engineered Cementitious Composites (ECC). ECC was prepared using various ratios of POFA ranging from 0 to 1.2 from the mass of cement. Water-binder ratios of 0.33, 0.36 and 0.38 were used. A polyvinyl alcohol (PVA) fiber was used at a moderate volume fraction of 2%. The results of RCPT test reveal that the resistance to chloride penetration of ECC containing POFA was significantly improved. The charge passed was gradually reduced with the addition of more amount of POFA. The results also indicate that at 28 and 90 days, increasing the POFA/C ratio up to 0.2 led to an increase in the ECC compressive strength.*

Keywords: Compressive strength, RCPT test, POFA, ECC

1.   INTRODUCTION

At the beginning of the 1990s, Li et al. from the University of Michigan have investigated a composite material known as engineered cementitious composite (ECC). The ECC is a fiber-reinforced material that supports a microstructure design guided by micromechanical criteria[1]. This composite is used mostly at 2% or less by volume, although the composite is designed for structural applications[2]. The most important characteristic of an ECC is its tensile ductility with strain capacity in the range of 3%–7%[3, 4]. An ECC also exhibits a strain capacity 500–600 times higher than normal concrete[5]. During strain-hardening, the multiple cracks are limited to approximately 60 μm to 80 μm[6] or 100 μm to 200 μm[7].

Coarse aggregates are eliminated in the mixture design of ECC, resulting in the usage of greater cement content compared with normal concrete. High cement content generally introduces higher shrinkage, heat of hydration, and cost. Moreover, Cement production is an energy intensive process which also has an important effect on the environment. Producing one ton of cement produces 0.5 tons of chemical CO_2, in a reaction that takes place at 1450 °C. An additional 0.4 ton of CO_2 is given off as a result of the burning of carbon fuel to provide this heat[8, 9]. To put it simply, one ton of cement produced equals one ton of CO_2 released and as a result of this production 1.6 billion tons of CO_2 is released each year which is estimated at approximately 7% of the CO_2 production worldwide[10, 11].

521

A reasonable solution for these problems is via the substitution of larger portions of the cement in ECC with industrial wastes or by-products as supplementary cementitious materials without sacrificing its mechanical properties in general, particularly its ductility. Palm oil fuel ash (POFA) is one such material that is being used as partial cement replacement. Several studies have found that POFA has pozzolanic properties[12-15]. The partial replacement of Portland cement (PC) with POFA can lower the production costs, as well as improve the engineering properties and durability of concrete. Furthermore, POFA can increase the eco-friendliness of concrete, contributing to a healthier and more sustainable environment.

The main objective of the work presented herein is to investigate the effects of treated palm oil fuel on compressive strength and rapid chloride permeability (RCPT) of ECC at high volume ash.

2. EXPERIMENTAL PROGRAM

2.1 Materials

The mix proportions used in this paper are listed in Table 1, where POFA/C and w/b ratios range from 0 to 1.2 and 0.33 to 0.38, respectively.

Table 1: Mixture properties of ECCs.

Mix ID	C/C	S/C	POFA/C	SP/C	HPMC/C	Fiber*
w/b= 0.33						
Ma1	1	0.8	0	0.022	0.001	0.02
Ma2	1	0.8	0.2	0.02	0.001	0.02
Ma3	1	0.8	0.4	0.022	0.001	0.02
Ma5	1	0.8	0.8	0.025	0.001	0.02
Ma6	1	0.8	1.2	0.03	0.001	0.02
w/b = 0.36						
Mb1	1	0.8	0	0.019	0.001	0.02
Mb2	1	0.8	0.2	0.018	0.001	0.02
Mb3	1	0.8	0.4	0.019	0.001	0.02
Mb5	1	0.8	0.8	0.021	0.001	0.02
Mb6	1	0.8	1.2	0.027	0.001	0.02
w/b = 0.38						
Md1	1	0.8	0	0.015	0.001	0.02
Md2	1	0.8	0.2	0.017	0.001	0.02
Md3	1	0.8	0.4	0.018	0.001	0.02
Md5	1	0.8	0.8	0.02	0.001	0.02
Md6	1	0.8	1.2	0.025	0.001	0.02

*PVA fiber is by volume fraction, and all others are by weight parts.

Table 2: Chemical compositions of Type I cement, silica sand and treated POFA.

Chemical constituents (%)	Type I cement	Silica sand	Treated POFA
SiO_2	20.90	99.2	66.91
Al_2O_3	5.27	0.02	6.44
Fe_2O_3	3.10	0.01	5.72
CaO	62.80	-	5.56
MgO	1.52	-	3.13
Na_2O	0.16	-	0.19
K_2O	0.63	-	5.20
SO_3	2.73	-	0.33
P_2O_2	0.13	-	3.72
LOI	0.87	-	2.30

Untreated POFA was collected from the plant of United Oil Palm Industries Sdn. Bhd. in Nibong Tebal, Penang, Malaysia. The POFA was dried in an oven at 100 °C for 24 hrs and then sieved using a set of sieves (3 mm, 600 µm, and 300 µm) to remove unburned fiber or shells that are coarser than 300 µm. Then, the ash was ground by a ball mill to reduce the particle size to improve reactivity (ground POFA). To remove unburned carbon and prevent glassy phase crystallization, as well as particle agglomeration, that affect the pozzolanic properties, POFA was heated using low heat treatment at 450 °C for 90 min. The average particle sizes of untreated and treated POFA were approximately 2.87 and 2.99 µm, respectively. The specific surface area of treated POFA was approximately 6200 cm^2/g. The chemical composition of POFA is tabulated in Table 2. The chemical compositions of the Type I cement, silica sand, and treated POFA are tabulated in Table 2. An ASTM C494 Type

F high-range water-reducing admixture and a dry viscosity enhancing agent, hydroxypropylmethylcellulose (HPMC) were used to modify the workability and to achieve consistent rheological properties in the fresh matrix for better fiber distribution. Polyvinyl alcohol (PVA) fiber was used at a moderate volume fraction of 2 %. The fiber was surface-coated with oil (1.2 % by weight) to reduce the fiber/matrix interfacial bond strength[16]. Silica sand was used as fine aggregates with an average and maximum grain sizes of 110 μm and 200 μm, respectively.

2.2 Test Procedure

To evaluate the compressive strength properties of POFA-ECC specimens, the test was carried out on the mixtures which are shown in Table 1. The fresh mixtures were cast into a beam with the dimension of 160 mm × 50 mm × 50 mm, after one day curing in moulds covered with plastic paper, the specimens were cured in a water tank at room temperature (23±2°C) for periods according to the needs. The durations of the test were 3, 28 and 90 days. After each specific period to test, the beam specimen was cut into three cubes with the dimension of 50 mm×50 mm ×50 mm using a concrete cuter. The test was performed using a 100 kN AG-X series Shimadzu Universal Testing Machine. The compressive strength is measured at a constant loading rate of 21 MPa/min which was obtained by averaging the results of three measurements.

RCPT was performed on specimens in accordance with ASTM C1202-05 and AASHTO T277-97. Three specimens per mixture at the ages of 28 and 90days were tested. The specimen of 100 mm in diameter and 50mm thick were cut from 100mm x 200mm ECC cylinders. The specimen was placed in *vacuum desiccator* for three hours. After three hours, the specimen was submerged in deaerated water and then the pump was allowed to run for additional one hour. Finally air was allowed to re-enter *desiccator* and the specimen was then removed and immersed in water to soak for 18 hours. The specimens were placed between the cathode and anode cells. The anode cell was filled with 250 ml 0.3 N NaOH solution and the cathode cell was filled with 250 ml 3% NaCl solution. A current of 60 ± 0.1 V was applied across the end of the specimens for 6 hours, and record initial current reading. The total charge passed in coloumb was obtained by integrating the current with time and used as an index to evaluate the penetration of chloride ions in cement-based composites.

3. RESULTS AND DISCUSSION

3.1 Compressive Strengths of ECC

The average compressive strength at 3, 28 and 90 days of ECC mixtures which were grouped according to w/b ratio into 3 gropes are listed in Table 3. The compressive strength of the composites containing the same amount of POFA with different w/b ratios were tended to be lower as w/b ratios increase from 0.33 to 0.38 (Table 3). It can be noticed that as w/b increases from 0.33 to 0.38, the compressive strength of the composites without POFA decrease to about 4%, 7.8% and 12.7 % at 3, 28 and 90 days respectively. When POFA/C=0.4, it can be easily observed that an increase in w/b results in a decrease in compressive strength with of 36 %, 13% and 5% after 3, 28 and 90 days, respectively. At the same w/b ratio, the compressive strength of the composites which have POFA/C = 1.2 tend to decrease by 19%, 24% and 18 % at 3, 28 and 90 days, respectively. The instability of the percentage decrease of compressive strength could be attributed to the negative effect

of w/b ratio was higher at 28 days. In general, the added water affected the matrix/PVA interface, which resulted in a loss of compressive strength.

Table 3: Compressive properties and chloride permeability of ECC with different w/b and POFA/C.

Mix ID	Compressive strength (MPa)			Compressive strain after 28 d (%)	RCPT (Coulomb)	
	3 d	28 d	90 d		28 d	90 d
w/b= 0.33						
Ma1	28.25	39.52	46.42	1.041	6700	5162
Ma2	28.42	43.15	50.52	-	-	
Ma3	25.82	40.55	45.65	0.826	2556	1447
Ma5	24.8	39.21	44.63	-	2302	712
Ma6	21.63	37.3	42.42	1.34	1941	577
w/b= 0.36						
Mb1	27.22	37.35	43.25	1.21	7112	6595
Mb2	26.26	37.72	43.31	-	-	-
Mb3	20.89	39.83	42.15	0.86	2915	1598
Mb5	18.89	36.53	40.01	-	2520	828
Mb6	19.94	32.82	36.67	1.429	2139	631
w/b= 0.38						
Md1	27.02	36.65	41.17	1.305	8240	6914
Md2	26.1	36.69	42.102	-	-	-
Md3	18.98	35.6	43.33	1.19	3003	1642
Md5	17.29	31.91	36.07	-	2603	957
Md6	18.13	30.02	35.36	1.402	2352	683
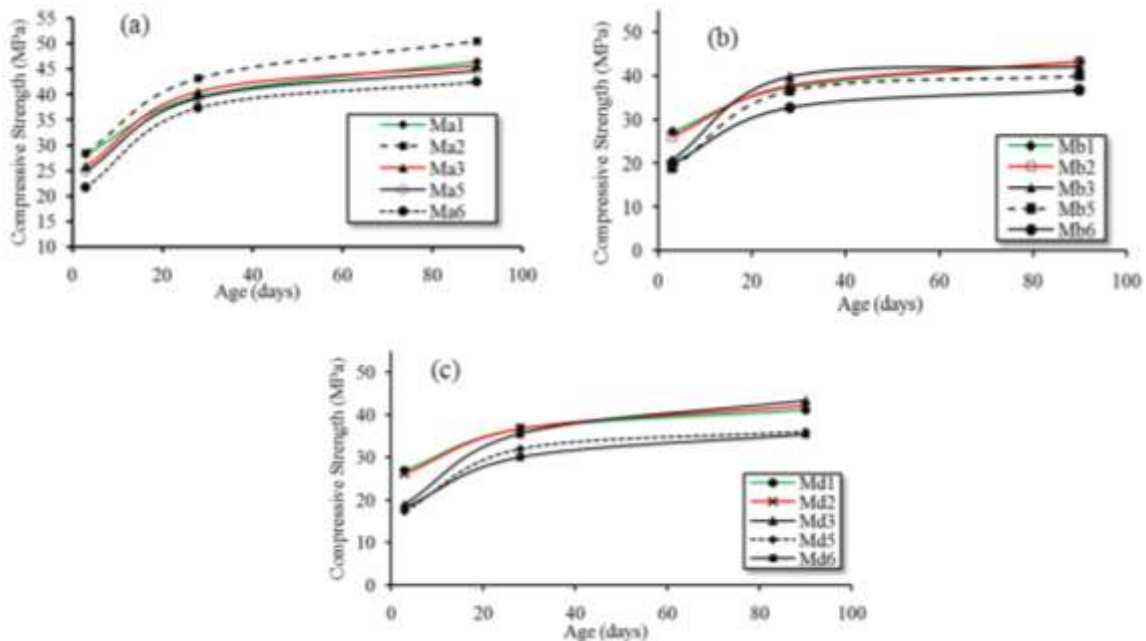
Fig. 1: Effect of POFA/C on compressive strength of ECCs with: (a) w/b= 0.33; (b) w/b= 0.36; (c) w/b= 0.38.

The results obtained indicate that increase POFA/C ratio up to 0.2 with w/b ratio ranging from 0.33 to 0.38 at 28 and 90 days lead to an increase in the ECC compressive strength, but that does not lead to a significant change in compressive strength at age of 3 days as compared to OPC-ECC. For example, with w/b ratios 0.33 and 0.38, at 28 days, the compressive strengths of mixes containing POFA/C of 0.2 (Ma2 and Md2) were about 109% and 101% of that of the OPC-ECC (Ma1 and Md1), respectively, as well as 108% and 102% at 90 days (Fig1a and 1c), which may be due to additional amount of calcium silicate hydrate formed as a result of pozzolanic reaction. This demonstrates that ground

POFA at this ratio is considered a beneficial ingredient for long term strength development due to its pozzolanic properties as well as small particle size of POFA increased the compressive strength by the filler effect. At w/b ratios of 0.33 and 0.38, the compressive strengths of Ma3 and Md3 were 102% and 97% of OPC composites, respectively at 28 days; and 98% and 105%, respectively, at 90 days (Fig. 1a and 1c). The results of compressive strength of POFA-ECC mixes show the compressive strength of POFA-ECC mixtures with POFA/C ratio more than 0.8 decreases with increasing POFA content due to the dilution effect. However, even at approximately 55% addition of cement by POFA (POFA/C = 1.2) and w/b ratio= 0.38, the compressive strength of POFA-ECC at 28 days can still reach 30.02 which exceeds the normal compressive strength for normal concrete (30 MPa).

At w/b ratio of 0.33, the compressive strain of Ma6 at failure was 0.013 which is more than compressive strain of Ma1 (0.0104). In addition, as w/b ratio increased to be 0.38, the compressive strain of Md6 was 0.014, which is also more than the compressive strain of composite without POFA (0.013). This indicates that as the POFA/C ratio is greater than 0.8, the POFA-ECC has better deformation capacity than the others. On the other hand, greater water content resulted in a significant increase in the compressive strain, i.e., at each POFA/C ratio, the results revealed the general increasing compressive strain occurred when the water-the binder ratio increases from 0.33 to 0.38 (Table 3). In addition, the failure mode of the POFA-ECC composites with POFA/C more than 0.8 was much more ductile compared to the OPC-ECC composite (Fig. 2). ECC samples are failed under compressive load through lateral tensile expansion. This lateral expansion was partially restrained by the internal PVA fiber, thus allowing for a more ductile failure than may be expected. When the load reached its peak point, the cracks propagated through the section and divided the specimen into three or more parts. However, the fibers still linked the fragments and prevented them from separation and the separated parts stuck together under the residue load[17].
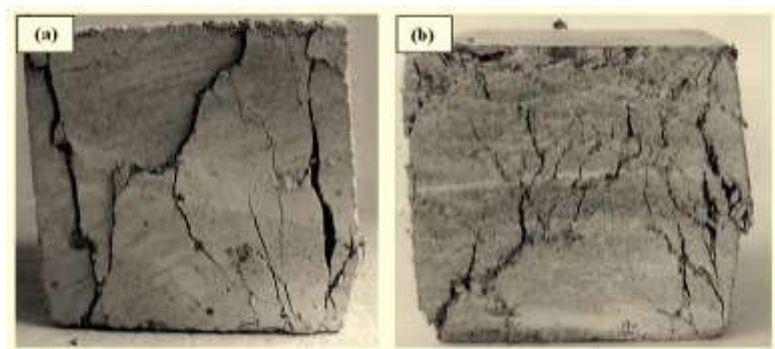
Figure 2: Pattern of failure: (a) Ma1; (b) Md6, fiber bridging is clearly evident.

3.2   Resistance to Chloride Ion Penetration

The ASTM C 1202-05[18] rapid chloride ion penetration test results of ECC mixtures obtained at 28 and 90 day-old specimens are given in Table 3.
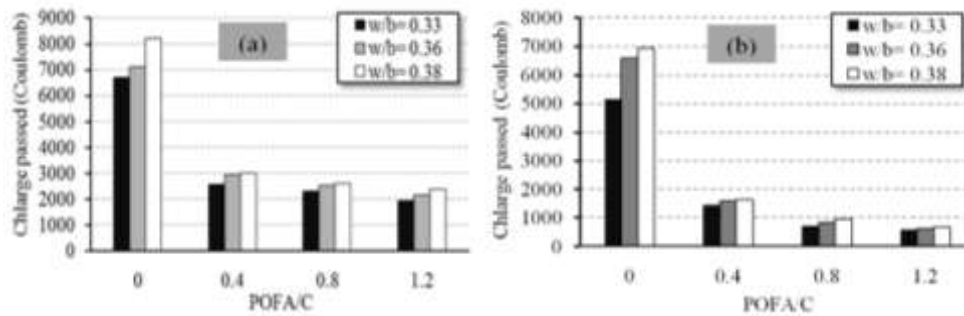
Figure 3: Relationship between charge passed and POFA/C ratio of ECC mixtures with different w/b ratios at age: (a) 28 days; (b) 90 days.

From Figures 3a and 3b, it is clear that as w/b ratio increases, the total charge value of all ECC specimens significantly increases. Expected trends in the results appear at 28 days. One such obvious trend is increased chloride penetration of OPC-ECC mixtures as w/b ratio increasing from 0.33 to 0.0.38 by 23%. The charge passed through the specimens also decreased substantially by about 33% at 90 days. As a result of increasing w/b ratio, it is also observed that the mixtures containing 0.4 POFA-cement ratio have 17% and 13% increase in the chloride penetration at 28 and 90 days, respectively. Meanwhile, the percentage increase in the chloride penetration values of POFA-ECC with 1.2 POFA/C is lower than the OPC-ECC spacemen; where it was about 21% and 18 % at 28 and 90 days, respectively. At 90 days, however, the percentage of an increase in the chloride penetration values due to increasing the w/b ratio is low after 90 days for the mixtures contained POFA. This observation apparently is explained by the fact that the POFA is much more effective at the delayed age. Generally, increasing the RCPT values with an increase the water-binder ratio is in agreement with previous study conducted by [19].

Figures 3a and 3b show the inverse relationship between penetration of chloride ions and POFA content at 28 and 90 days. As seen in the both figures, the rapid chloride ion penetration decreases with increasing age of ECC specimens. For the w/b ratio of 0.33, 36 and 0.38, the total charge passing through the OPC-ECC specimens decreases about 22 %, 7 % and 16 %, respectively, between 28 and 90 days. In addition, after 90 days of curing time, there is a distinct improvement in chloride penetration reduction in the POFA-ECC. However, with POFA/C= 1.2, the reduction of the chloride penetration between 28 and 90 days was about 70%, 70.5 and 70.9% at w/b of 0.33, 0.36 and 0.38, respectively. Comparing with ECC mixtures to each other at 28 and 90 days, it can be concluded that the high delayed reaction of POFA at 90 days is evident by the high decrease in chloride penetration with an increase in the curing time.

As shown in Fig. 3a, for 0.33 w/b ratio and age of 28 days, adding 1.2 of POFA caused a decrease of about 71% in RCPT value compared to OPC-ECC. At the same w/b and POFA/C, the reduction was about 89% after 90 days (Fig. 3b). At 28 and 90 days, the addition of POFA reduces the total charge passed values by approximately 61% and 71% respectively, when POFA/C equaling 0.4. For w/b ratio of 0.38, the total charge going through the POFA-ECC specimens containing 1.2 POFA/C ratio decreases by nearly 72% and 90% at 28 and 90 days, respectively. While, for the w/b ratio of 0.38; the POFA-ECC with POFA/C ratio of 0.4 had lower RCPT values than OPC-ECC specimens, which are decreased by about 63 % and 76% at 28 and 90 days, respectively.

The matrix of ECC specimens contains more pore structure and less dense are more likely to passage the largest amount of chloride ions. Therefore, as mentioned above, ECC mixtures containing the high amount of POFA showed the best performance among the

other specimens in the rapid chloride penetration. The total charge passed decreased with the addition of POFA contents because of the dense microstructure and the filling effect of pozzolanic products. The pozzolanic reaction may lead to lower amount of capillary pores and blocking of the pores [20]. The addition of POFA, that particles are finer than those of OPC (the palm oil fuel ash used in this study had average particle size equal to 2.99 μm) causes segmentation of large pores and increases the number of nucleation sites for precipitation of the hydration products of the cementitious past (cement paste or/and POFA-cement paste)[21-24]. Therefore, this mechanism makes the paste of POFA-cement extra homogeneous and denser.

4.   CONCLUSION

Based on the results presented earlier on the study, the following conclusions are offered:
1.   The compressive strength of POFA-ECC mixtures in the early age was gained slowly. However, the increase in compressive strength of POFA-ECC seems in significant after 28 days. In addition, the compressive strength of composites was tended to be lower as w/b ratio increased from 0.33 to 0.38.
2.   The compressive strength gain rate of composites which had POFA/C of 0.2 at all w/b ratios after 28 days tends to be higher compared to OPC-ECC. At POFA/C equals 1.2 and w/b equals 0.38; however, the compressive strength at 28 days and can be still reach 30.02 MPa, which is the normal strength for concrete in many applications. Furthermore, high palm oil fuel ash tends to give better deformation capacity. The failure mode of the POFA-ECC composites with POFA/C more than 0.8, was much more ductile. Generally, POFA-ECC with deferent compressive strength can be chosen for use in various applications.
3.   For all ECC mixtures, the rapid chloride ion penetration decreases with age. In addition, increase w/b ratio tends to increase the total charge passed and the negative effect caused by the increase in the w/b ratio was lower with increasing the amount of POFA.
4.   The incorporations of treated POFA significantly improve the resistance to chloride penetration. Test results also indicate that delayed reaction of POFA is evident by the high decrease in chloride penetration with an increase in the curing time. Based on ASTM C 1202-05[18], the mixtures containing palm oil fuel ash can be considered as mixtures of low penetration.

5.   ACKNOWLEDGMENT

6.   REFERENCES

1.   Kanda T & Li VC (1998) Multiple cracking sequence and saturation in fiber reinforced cementitious composites. Concrete Research and Technology 9(2):19-33.
2.   Li VC & Kanda T (1998) Engineered cementitious composites for structural applications. Journal of Materials in Civil Engineering 10(2):66-69.
3.   Li VC (2002) Advances in ECC research. ACI SPECIAL PUBLICATIONS 206:373-400.
4.   Cai XR, Fu BQ, & Xu SL (2011) The Apparent Density, Tensile Properties and Drying Shrinkage of Ultra High Toughness Cementitious Composites. Advanced Materials Research 261:223-227.
5.   Li VC (2003) On engineered cementitious composites (ECC). Journal of Advanced Concrete Technology 1(3):215-230.
6.   Wang S & Li VC (2005) Polyvinyl alcohol fiber reinforced engineered cementitious composites: material design and performances. (Citeseer), pp 65-74.
7.   Fischer G, Stang H, & Dick-Nielsen L (2007) Initiation and development of cracking in ECC materials: Experimental observations and modeling". pp 1517-1522.
8.   Altwair NM & Kabir S (2010) GREEN CONCRETE STRUCTURES BY REPLACING CEMENT WITH POZZOLANIC MATERIALS TO REDUCE GREENHOUSE GAS EMISSIONS FOR SUSTAINABLE ENVIRONMENT. 6th International Engineering and Construction Conference (IECC'6), Cairo, Egypt, June 28-30.
9.   Davidovits J (1994) Global warming impact on the cement and aggregates industries. World Resource Review;(United States), 6,(CONF-940422).
10.   Mehta PK (2001) Reducing the environmental impact of concrete. Concrete international 23(10):61-66.
11.   Malhotra V (1999) Making concrete" greener" with fly ash. CONCRETE INTERNATIONAL-DETROIT- 21:61-66.
12.   Rukzon S & Chindaprasirt P (2009) An Experimental Investigation of the Carbonation of Blended Portland Cement Palm Oil Fuel Ash Mortar in an Indoor Environment. Indoor and Built Environment 18(4):313-318.
13.   Awal A & Hussin MW (1997) The effectiveness of palm oil fuel ash in preventing expansion due to alkali-silica reaction. Cement and Concrete Composites 19(4):367-372.
14.   Tangchirapat W, Tangpagasit J, Waew-kum S, & Jaturapitakkul C (2003) A new pozzolanic material from palm oil fuel ash. KMUTT Res. Dev. J 26(4):459-473.
15.   Altwair NM, Johari MAM, & Hashim SFS (2011) Strength Activity Index and Microstructural Characteristics of Treated Palm Oil Fuel Ash. International Journal of Civil & Environmental Engineering11(5):100-107.
16.   Li VC, Wu C, Wang S, & Saito T (2002) Interface Tailoring for Strain-Hardening PVA-ECC. ACI materials journal 99(5):463-472.
17.   Xu B, Toutanji HA, Lavin T, & Gilbert JA (2011) Characterization of Poly (vinyl Alcohol) Fiber Reinforced Organic Aggregate Cementitious Materials. Key Engineering Materials 466:73-83.
18.   ASTM (2005) Standard test method for electrical indication of concrete's ability to resist chloride ion penetration, C 1202-05.
19.   Sengul O & Tasdemir MA (2009) Compressive Strength and Rapid Chloride Permeability of Concretes with Ground Fly Ash and Slag. Journal of materials in civil engineering 21:494.

20. Li S & Roy DM (1986) Investigation of relations between porosity, pore structure, and C1-diffusion of fly ash and blended cement pastes. Cement and Concrete Research 16(5):749-759.

21. Goyal A, et al. (2007) Synergic Effect of Wheat Straw Ash and Rice-Husk Ash on Strength Properties of Mortar. Journal of Applied Sciences 7:3256-3261.

22. Isaia GC, Gastaldini ALG, & Moraes R (2003) Physical and pozzolanic action of mineral additions on the mechanical strength of high-performance concrete. Cement and Concrete Composites 25(1):69-76.

23. Chindaprasirt P, Chotetanorm C, & Rukzon S (2011) Use of Palm Oil Fuel Ash to Improve Chloride and Corrosion Resistance of High-Strength and High-Workability Concrete. Journal of materials in civil engineering 23:499.

24. Mehta PK (1987) Studies on the mechanisms by which condensed silica fume improves the properties of concrete: durability aspects. in Proceedings of international workshop on condensed silica fume in concrete, Ottawa, p. 1–17.

The Effect of pH on Zinc Phosphate Coating Morphology and its Corrosion Resistance on Mild Steel

Khalid Abdalla [1,2], Azmi Rahmat [1], and A. Azizan [1,*]

[1] School of Material and Mineral Resources Enginerring, Engineering Campus, Universiti sains malaysia, 14300 Nibong Tebal, Pulau Penang, Malaysia
[2] Faculty of Engineering, Omar-Almukhtar university, Al-Bayda, Libya

*Corresponding author: azizan@eng.usm.my

Abstract: *Zinc phosphate coating is commonly used for corrosion protection of metallic materials, mainly mild steel. In this study, influence of the pH of phosphating bath on zinc phosphate coating properties on mild steel was investigated via scanning electron microscopy (SEM), and energy-dispersive X-ray (EDX). The corrosion resistance of the coating was evaluated by polarization curves (anodic and cathodic) in a 3.5% NaCl solution. The results showed that better surface coverage and corrosion resistance for the steel phosphated at pH 2.75.*

Keywords: Phosphating, zinc phosphate, corrosion resistance, mild steel

1.   INTRODUCTION

Zinc phosphating (ZPO) is a conversion coating treatment that has been used for many years in the industry as surface preparation for paint coating to increase adhesion and corrosion resistance [1–5]. There are many phosphating systems which have been proposed, but iron phosphate, manganese phosphate and zinc phosphate are three of the most common coatings used for steel corrosion protection [6]. The type of coating used depends on the application of phosphated material. For corrosion protection and wear resistance, the phosphate coating should be compact, finely-structured and firmly adhered to the metal surface [7].

The performance of phosphate coating on steel depends on the fraction of the total surface area covered by the deposit. This coverage fraction is influenced by parameters such as chemical composition of ZPO bath, surface morphology of the deposit, and operating conditions of ZPO process in particular pH and temperature [8,9]. The reaction mechanism of the coating process is a pH controlled and depends on the dissolution of substrate at local anodic sites (pH 2–3.5) and the deposition of insoluble phosphate coating initiates at local cathodic sites [10]:

$$Fe \rightarrow Fe^{2+} + 2\ e^{-} \quad \text{(anodic reaction)}$$

(1)

$$2\ H^{+} + 2\ e^{-} \rightarrow H_2\uparrow \quad \text{(cathodic reaction)}$$

(2)
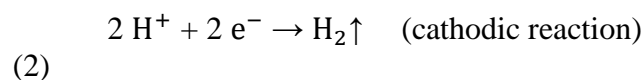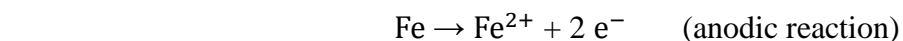
The reduction of the hydrogen ions at the cathodic sites results in an increase in the local pH at the metal-bath interface and in turn drives the precipitation of insoluble zinc phosphate crystals [11,12]. The formation of the insoluble phosphate coating followed by the reactions:

530

$$H_3PO_4 \rightleftharpoons H^+ + H_2 PO_4^- \rightleftharpoons 2H^+ + H PO_4^{-2} \rightleftharpoons 3H^+ + PO_4^{3-}$$

(3)

$$3Zn^{2+} + 2 PO_4^{3-} + 4H_2O \rightarrow Zn_3 (PO_4)_2 .4H_2O \ \text{(hopeite)}$$

(4)

$$2Zn^{2+} + Fe^{2+} + 2 PO_4^{3-} + 4H_2O \rightarrow Zn_2 Fe(PO_4)_2 .4H_2O \ \text{(phosphophylite)}$$
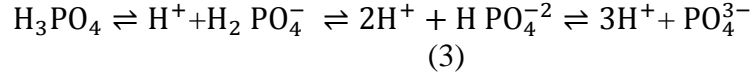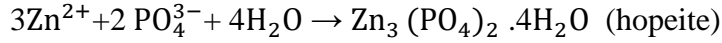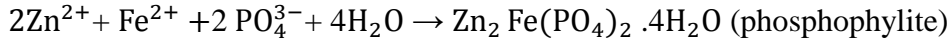
(5)

The coating process starts in a definitely acidic state, but the deposition of insoluble phosphate requires the pH at the metal-solution interface to be increased well into the basic range due to H_2 evolution at cathodic sites [13]. This process reveals that the coating reaction is pH controlled and the coating formation and properties may change accordingly to starting pH of the phosphating solution. Therefore, the aim of this work is to study the influence of the pH of a zinc phosphating bath on the coating deposition and properties on mild steel. The surface morphology and composition of the phosphate layer were analyzed using scanning electron microscopy (SEM), and energy-dispersive spectroscopy (EDS). The corrosion behavior of the coated samples was examined by anodic and cathodic polarization curves in a 3.5% NaCl solution.

2.   EXPERIMENTAL

2.1.   Sample preparation

Mild steel samples with 15 mm×10 mm×2 mm dimensions were used in the study; the chemical composition is given in Table 1. The substrates were mechanically polished with a series of SiC papers up to 600 grits. The samples were then subjected to ultrasonic cleaning in acetone and rinsed with deionized water. The cleaned specimens were then immersed in a phosphating bath (composition in Table 2) for 5 min at different pH values, and then rinsed and dried using compressed air. The pH adjustment was done by adding 50% NaOH solution. For the determination of the phosphate coating weight per unit area, the phosphate coating was solubilized in a 5% chromium trioxide solution for 15 min at 70 °C.

Table 1: Chemical composition of the mild steel substrate.

Element	Composition (wt. %)
C	0.16
Al	0.07
Si	0.168
Mn	0.18
P	0.025
Cu	0.09
Fe	balance

The phosphate coating weight per unit area was calculated according to the following equation:

$$W = (W_1 - W_2)/A$$

where W is the phosphate coating weight per unit area, W_1 is the specimen weight after phosphating, W_2 is the specimen weight after the coating was eliminated, and A is the surface area exposed to the phosphating bath.

Table 2: Operating conditions and chemical composition of the phosphating bath.

Bath composition	(g/L)	Operating conditions
H_3PO_4 (85%)	15	T = 55±3 °C
ZnO	2.5	pH = 1.75~ 2.75
HNO_3 (70%)	25	
NaF	0.66	

2.2.   Characterization of phosphate coating

The surface morphology and composition of the phosphate coating were assesed by SEM using a Zeiss Supra Model 35VP and EDS. The corrosion resistance of the phosphated substrates was evaluated by potentiodynamic polarization (anodic and cathodic curves) measurements using a potentiostat/frequency response analyzer (AUT 71943, Autolab Instruments). A 3.5% NaCl solution, maintained at 25±2 °C, was used as the electrolyte medium. The coated steel with an area 1.5 cm^2 was used as the working electrode, whereas a silver/silver chloride electrode and a platinum wire were used as the reference and counter electrodes, respectively. The scan rate for polarization was 1 mV/s with a potentail range of -1 to 0 V.

3.   RESULTS AND DISCUSSION

3.1.   Coating morphology and composition

The SEM micrographs of the bare steel surface and of the zinc phosphate coatings obtained from baths with different pH values are shown in Fig. 1. It is seen that when samples were phosphated in the ZPO bath with pH 1.75, small cubic particles of phosphate crystals formed on the substrate surface which did not cover the entire substrate (Fig. 1(B)). When the pH was 2.25, the deposition rate of the zinc phosphate was increased and the crystals became finer. As the pH of the bath reached to about 2.75, the coating became more compact and the substrate was almost fully covered by zinc phosphate crystals (Fig. 1(D)). This could be explained by the fact that, in the strong acidic phosphating bath (pH < 2) the local pH at metal-bath interface was not increased well into the basic range, due to the strong acidity of the bath, and this delayed the formation of the phosphate coating. When the pH of the ZPO bath was 2.75, the local pH was increased well into the basic range due to H$_2$ evolution at micro cathodic sites and in turn resulted in a good precipitation of phosphate crystals on the metal surface.
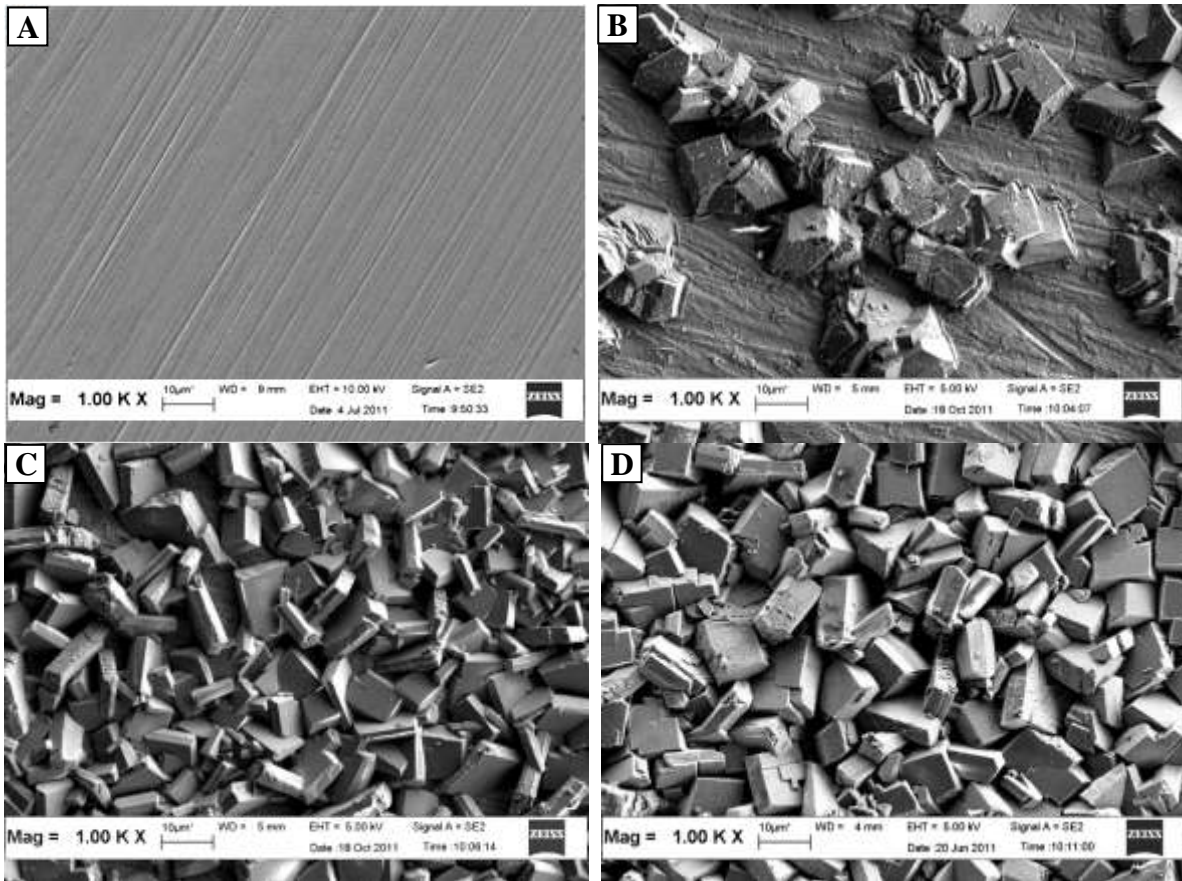
Fig. 1: SEM Images of the steel substrate surface (A) and of the zinc phosphate coatings obtained from baths with different pH values: (B) 1.75, (C) 2.25 and (D) 2.75.

The chemical compositions of the phosphate coatings obtained from EDS analysis are shown in Table 3. The phosphate layers mainly contained zinc, iron, and phosphorus. The high content of Fe (54 %) appeared on the coating, when the pH of the phosphating bath was 1.75, is mainly due to the metallic substrate and high porosity of the coating itself. When the pH of the bath was increased to 2.25 and 2.75, the content of Fe decreased to about 27.51% and 20% respectively, indicating that more phosphate deposition has covered the metallic substrate.

Table 3: Chemical composition of the different phosphate coatings.

Element	Composition (wt. %)		
	pH = 1.75	pH = 2.25	pH = 2.75
O	18.27	27.93	31.84
Zn	18.76	30.78	33.61
P	08.74	13.78	13.97
Fe	54.23	27.51	20.58

3.2. Phosphate coating weight

Fig. 4 shows the average coating weights obtained from various ZPO baths with different pH values. It is seen that the increase of pH from 1.5 to 2.5 causes an increase of the coating weight from 1.3 g/m^2 to about 6.2 g/m^2, indicating that the pH of the phosphating bath has a strong effect on the formation and characteristics of the phosphate film. After that

no further significant change in the coating weight as the pH increases. These results are consistent with SEM observation, which indicate high deposition and coverage of zinc phosphate coating with pH 2.75.
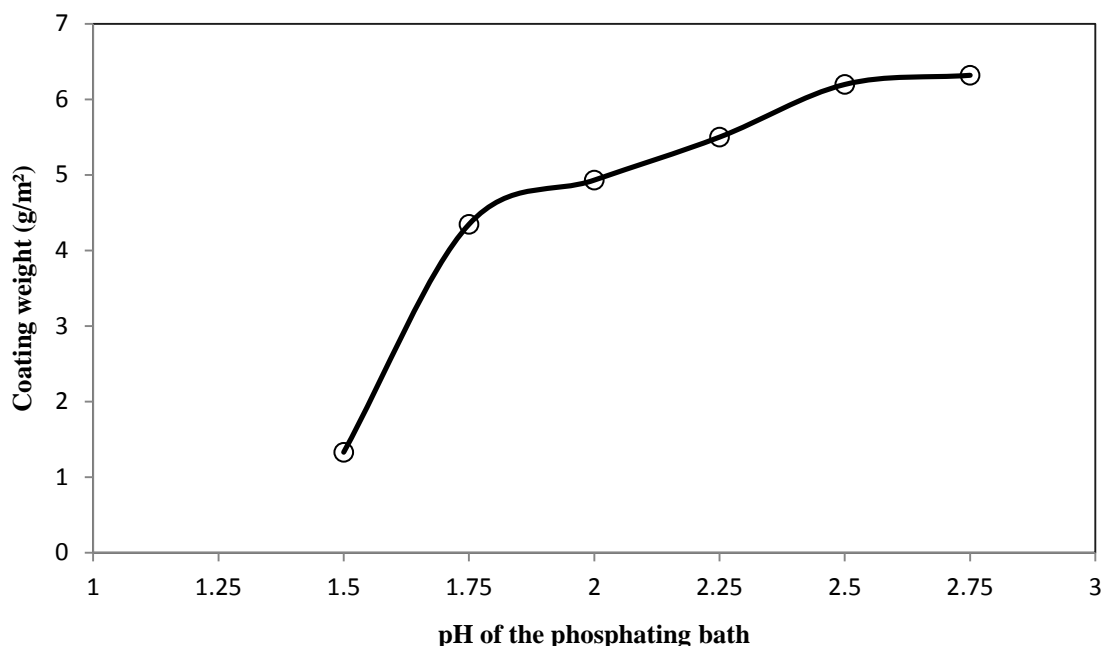
Fig. 2: Variation of the phosphate coatings weights obtained from the baths with different pH values.

3.3.   Electrochemical characterization

Polarization curves for the bare steel and phosphated samples obtained from baths with different pH values   are presented in Fig. 3. The corresponding corrosion potential (E_{cor}) and corrosion current density ($i_{corr.}$) obtained from the polarization curves by Tafel extrapolation method are listed in Table 4. The cathodic reaction in the polarization curves corresponds to hydrogen evolution, and the anodic reaction relates to the corrosion resistance of the phosphate layer [14]. It is seen that the corrosion current density decreased from 7.13 $\mu A/cm^2$ of the bare steel to about 6.35 $\mu A/cm^2$ ~ 1.06 $\mu A/cm^2$ of the phosphated samples. In the same time, the corrosion potential of the phosphate coatings shifted positively about 195 mV compared with that of mild steel substrate. Moreover, as the pH increased from 1.75 to 2.275, the corrosion current density decreased and the corrosion potential shifted to nobler values (in positive direction). These results indicate that the corrosion resistance of the mild steel significantly increased due to the surface passivation and barrier properties of the phosphate layer. In addition, higher passivation of phosphate coating was obtained with pH 2.75. This higher passivation, which can be understood from the anodic branch of the polarization curves, can be attributed to the wider coverage of the phosphate layer that formed with pH 2.75 as observed in SEM micrographs.

534
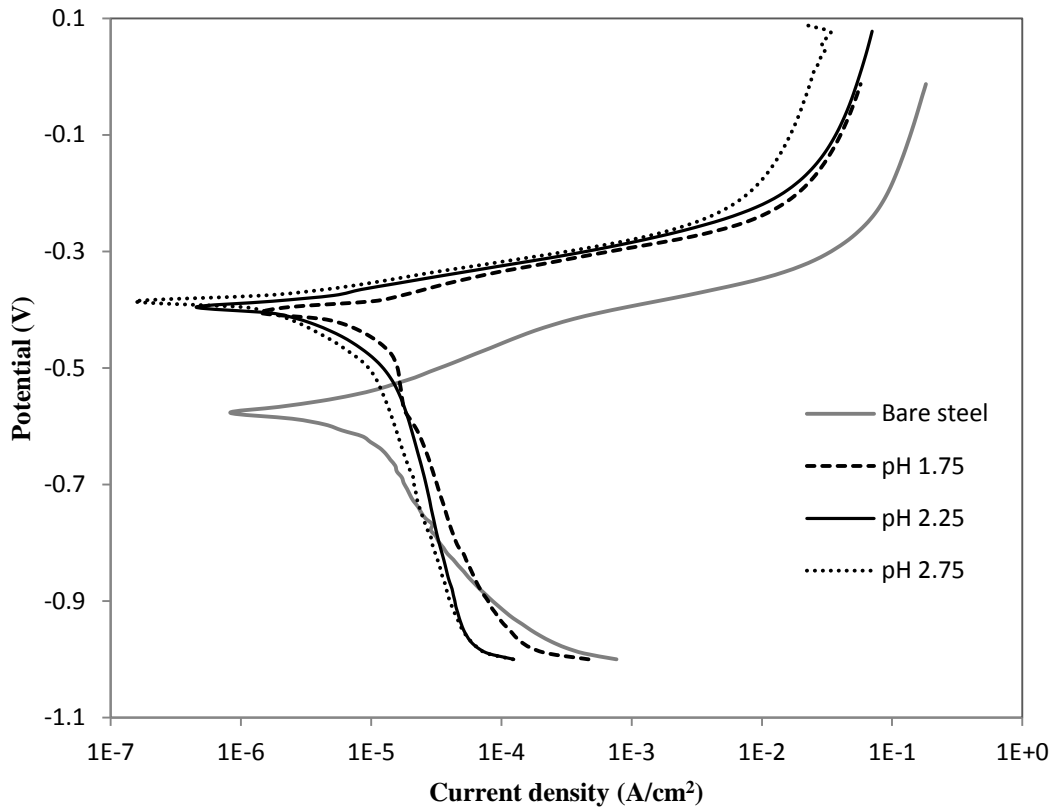
Fig. 3: Polarization curves for bare steel and the phosphated samples obtained from the baths with different pH values.

Table 4: Corrosion potential (E_{cor}), and corrosion current density (i_{cor}) evaluated by potentiodynamic polarization studies.

Treatment	E_{cor} (mV)	i_{cor} (μA/cm^2)
Bare steel	-576	7.13
Coating obtained from the bath pH 1.75	-399	6.35
Coating obtained from the bath pH 2.25	-391	1.75
Coating obtained from the bath pH 2.75	-381	1.06

4.   CONCLUSIONS

The surface morphology, composition and corrosion resistance of zinc phosphate coating on mild steel substrate have been invistigated as a function of pH of the phosphating bath. It was found that the pH of the phosphating bath has strongly effects on deposition and chracteristics of the phosphate coating. The compact and dense phosphate coating were formed in the phosphating bath with pH = 2.75. Polarization measurement in a 3.5% NaCl solution showed that increase in the pH of the phosphating bath caused increase in the corrosion resistance of phosphated samples. The highest increase in the corrosion resistance was observed in the phosphating bath with pH 2.75.

5.   ACKNOWLEDGEMENT

6. REFERENCES

1. T.S.N. Sankara Narayanan. (2005). Surface pretreatment by phosphate conversion coatings – a review. Rev. Adv. Mater. Sci., 9, 130–132.
2. R. Amini, A.A. Sarabi. (2011). The corrosion properties of phosphate coating on AZ31 magnesium alloy: The effect of sodium dodecyl sulfate (SDS) as an eco-friendly accelerating agent. Appl. Surf. Sci., 257, 7134.
3. E.P. Banczek, P.R.P. Rodrigues, & I. Costa. (2006). Investigation on the effect of benzotriazole on the phosphating of carbon steel. Surf. Coat. Technol., 201, 3706.
4. L.Y. Niu, Z.H. Jiang, G.Y. Li, C.D. Gu, & J.S Lian. (2006). A study and application of zinc phosphate coating on AZ91D magnesium alloy. Surf. Coat. Technol., 200, 3021.
5. L.C. Deepa, S. Sathiyanarayanan, C. Marikkannu, & D. Mukherjee. (2003). Effect of divalent cations in low zinc ambient temperature phosphating bath. Anti-Corros. Methods Mat., 50(4), 286.
6. Chao-Min Wang, Han-Chih Liau, & Wen-Ta Tsai. (2006). Effects of temperature and applied potential on the microstructure and electrochemical behavior of manganese phosphate coating. Surf. Coat. Technol., 201, 2994.
7. Bi-lan Lin, Jin-tang Lu, & Gang Kong. (2008). Synergistic corrosion protection for galvanized steel by phosphating and sodium silicate post-sealing. Surf. Coat. Technol., 202, 1831.
8. G. Y. Li, J. S. Lian, L. Y. Niu, & Z. H. Jiang. (2006). Influence of pH of Phosphating Bath on the Zinc Phosphate Coating on AZ91D Magnesium Alloy. Adv. Eng. Mater., 6(1-2), 123–127.
9. C. H. S. B. Teixeira, E. A. Alvarenga, W. L. Vasconcelos & V. F. C. Lins. (2010). Effect of porosity of phosphate coating on corrosion resistance of galvanized and phosphate steels Part I: Measurement of porosity of phosphate. Mater. Corros., 61(9999), 1.
10. E. Klusmann, & J.W. Schultze. (2003). pH-Microscopy: technical application in phosphating solutions. Electrochim. Acta 48, 3325–3326.
11. A.S. Akhtar, D. Susac, P. Glaze, K.C. Wong, P.C. Wong, & K.A.R. Mitchell. (2004). The effect of Ni^{2+} on zinc phosphating of 2024-T3 Al alloy. Surf. Coat. Technol., 187, 208.
12. Zhang Shenglin. (2009). Study on phosphating treatment of aluminum alloy: role of yttrium oxide. J. Rare Earthes, 27,469.
13. A.S. Akhtar, K.C. Wong, & K.A.R. Mitchell. (2006). The effect of pH and role of Ni^{2+} in zinc phosphating of 2024-Al alloy Part I: Macroscopic studies with XPS and SEM. Appl. Surf. Sci., 253, 494.
14. G.Y. Li, J.S. Lian, L.Y. Niu, Z.H. Jiang, & Q. Jiang. (2006). Growth of zinc phosphate coatings on AZ91D magnesium alloy, Surf. Coat. Technol., 201, 1818.

Biodegradable Film Based on Polyethylene/Rice Brain: Mechanical Properties

Mohd Zul Halmy Saadan[*] and Zurina Mohamad

Department of Polymer Engineering, Faculty of Chemical Engineering, Universiti Teknologi Malaysia, 81310 UTM Skudai, Johor, Malaysia.

*Corresponding author: zulhalmy87@gmail.com

Abstract: *In this study, rice bran was blended with Low Density Polyethylene (LDPE) with different compositions (2% - 4%). Twin screw extruder was introduced to produce LDPE/rice bran biodegradable compound while the film sample was prepared by blow film machine. The rice bran incorporation was influenced physical and mechanical properties of LDPE. Tensile and tear test were carried out to obtain the mechanical properties of the film. The results show, mechanical properties such as tensile strength and elongation at break decreased as the percentage of rice bran increased. Incorporation of rice bran in LDPE film also affected on the morphology of these blends which determined by using Scanning electron microscopy (SEM).*

Keywords: Biodegradable film, rice bran, natural filler, LDPE film

## 1.	INTRODUCTION

Every year, 125 million tons of plastic are used around the world especially in manufacturing industries. The plastics such as high density polyethylene (HDPE), low density polyethylene (LDPE) and polypropylene (PP) are widely use due to their properties such as light weight, material costs, mechanical properties and easy processibility. But, the problem is to manage the plastic waste because it takes a long time to degrade or cannot be degrade properly. Other can degrades into substances that are hazardous and polluting. Therefore, the recycling method was taken place to minimize these problems. But, the problem of recycling method of these materials has become an important issue for economic and environmental reasons [1,2]. In addition, only a small percentage of plastic waste is recyclable and most of them are end up in the municipal landfill. Therefore, it more better if the plastics can be degraded into safe by-products under normal composting conditions or natural environment [3].

Biodegradable plastic is very popular which will decompose in nature aerobic and anaerobic. Therefore, the solutions to tackle the problem of plastic waste management are the production of environmental friendly degradable polymers especially in the packaging applications [4]. In addition, the advantages of using biodegradable products are eco-compatible, relatively inexpensive and environmental friendly. Today, there have been demands to used biodegradable polymer to replace the increasing use of non-biodegradable polymer [5]. There are many renewable sources are used to produce biodegradation polymer product such as starch, chitosan, wool and silk. Incorporating the different additives such as starch to enhance the biodegradability plastic like LDPE [6,7].

Rice bran is a byproduct of the rice milling process during the spread the brown rice to white rice. The outer brown layer was called rice bran is composed of the rice germ and several sub layers which account for approximately 8% by weight of paddy rice and contain

over 60% of the nutrients found in each kernel of rice. The nutrients have been claimed in rice bran such as protein, fat and high potential as a raw material for the preparation of functional foods or nutraceuticals [8]. Malaysia is one of most countries in Asian producing rice and also produces rice bran. Market demand of rice bran in Malaysia is quite low so that most of rice bran going to waste.

Thus, this aim of study was to determine biodegradable film based on Low Density polyethylene (LDPE) with different contents of rice bran. Both of materials were blended using twin screw extruder and blow film machine. The mechanical properties such as tensile strength, percentages of elongation at break and tear strength were determined.

2.   EXPERIMENTAL

2.1   Materials

LDPE (LDF260GG; density: 0.918 g/cm^3) was purchased from TITAN Chemical, Malaysia. Rice bran was purchase from local rice mills (Kelantan).

2.2   Extrude and blow film procedure

Rice bran was dried in oven at 60°C for 24 hour before using. Then, LDPE and rice bran was blended with different concentration of rice bran (2 - 4%) by using Twin screw extruder with temperature range of 150°C - 190°C while the speed was 50 rpm. The compound was pelletized by using pelletizer. The pellet of compound was blowing into film by using blow film machine (Tai King 42440) with temperature range 120°C - 150°C and the speed by 400 rpm.

2.3   Mechanical properties testing

Mechanical properties for biodegradable film of LDPE/Rice bran such as tensile strength and percentages of elongation at break was measured by using Lloyd Instruments testing machine. This speed of the machine was setting at 50 mm/min and the sample film was preparing in rectangular or strip uniform as ASTM D 882. For tear strength, Elmendorf tearing tester was used according to ASTM D 1004.

3.   RESULTS AND DISCUSSION

3.1   Mechanical properties

3.1.1   Tensile test and tear test
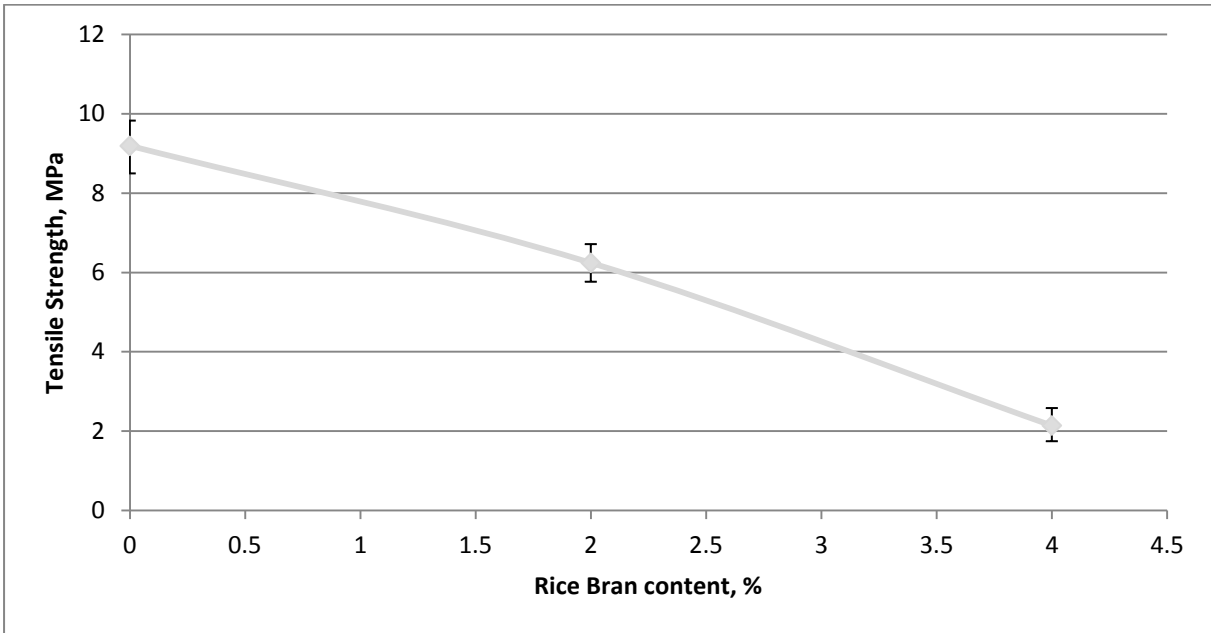
Fig. 1: Effect of rice bran concentration on tensile Strength for biodegradable Film of LDPE/Rice bran.
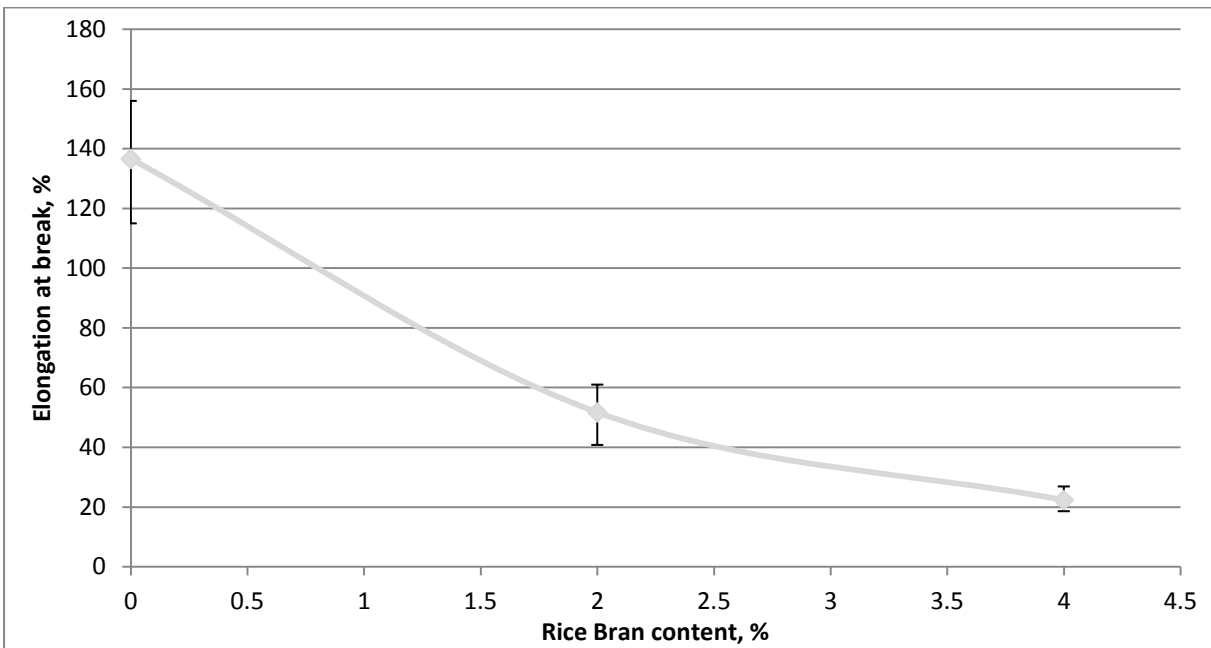
Fig. 2: Effect of rice bran concentration on percentage of elongation at break for biodegradable Film of LDPE/Rice bran.
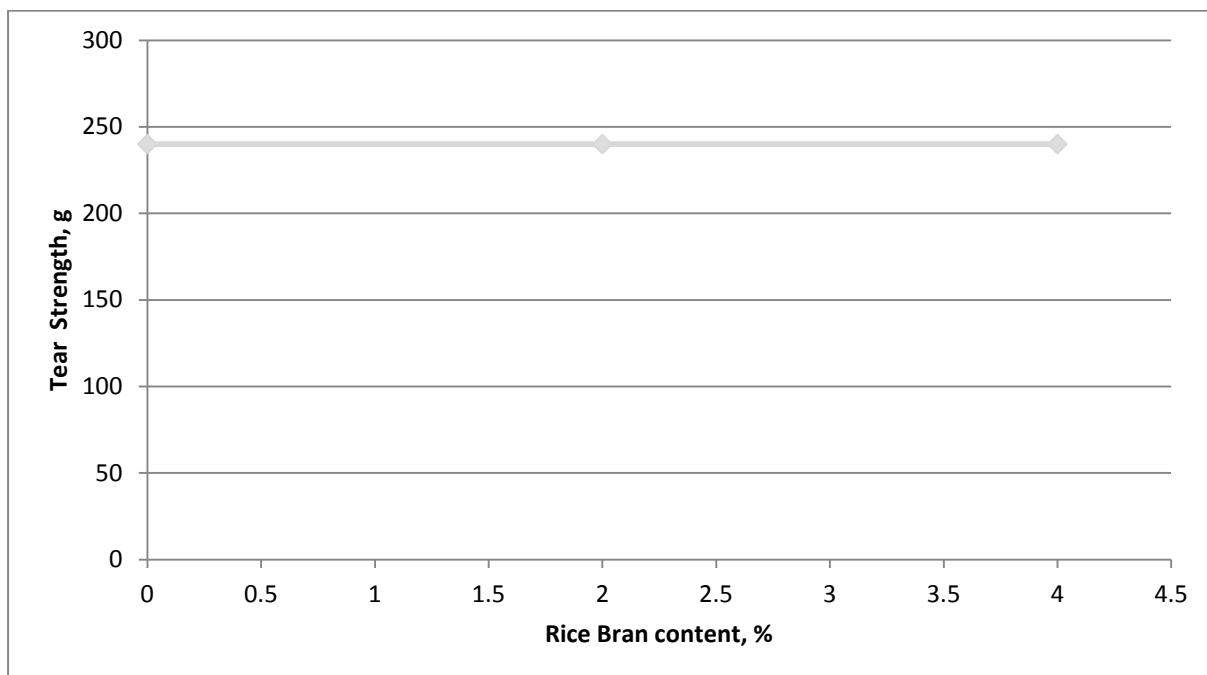
Fig. 3: Effect of rice bran concentration on tear strength for biodegradable Film of LDPE/Rice bran.

Figure 1 and Figure 2 shows the tensile strength and percent elongation at break of LDPE/Rice bran film at different concentration of rice bran (0% to 4%). From these Figure, it can be seen that both of the tensile strength and percent elongation were decrease linearly with the increasing of Rice bran content. The reduction of tensile strength and elongation at break might be due to the formation of clumps which cause improper stress transfer across the LDPE/rice bran film. This similar finding was also reported by George et al. [9]. In addition, the tensile strength also decreased because the stress on the continuous phase increased with the increase in percentage of rice bran in LDPE content. As the filler loading (rice bran) increased until 4 % the percent elongation was decreased by 83 %. At higher loading, rice bran tends to accumulate and agglomerate within the polymer matrix and also reduce the mobility of polymer chains thus reduced the percent of elongation at break. In the Torres et al. [4] studied was reported that addition banana starch into LDPE film was decreasing of mechanical properties. Raj et al. [10] and Garg & Jana [11] also reported that the incorporation of starch in LDPE film decreased the mechanical properties such as tensile strength and percent elongation. This is due to incompatibility of starch with LDPE which changing the morphology or low interfacial interaction between two phase. Other researcher like Pedroso and Rosa [12] have been reported the reduction of percent elongation at break with addition corn starch into LDPE content. The addition of an immiscible phase to a ductile matrix material usually significantly decreases the elongation at break. Furthermore, there is no chemical interaction between starch and LDPE, starch incorporation produced discontinuity in the matrix resulting in lower elongation. Figure 3 shows the effect of rice bran concentration on tear strength for biodegradable film of LDPE/rice bran. It is revealed that the incorporation of rice bran in LDPE film was not affected at LDPE/rice bran film. Tear strength was measured of resistance to failure of material when it was subjected to continue stretching. As increased in tear strength show increases the resistance for crack propagation. In this case it no different in tear strength which show that rice bran is not giving any resistant for crack propagation due to it particulate nature and small amount use in LDPE/rice bran film.

3.2   Morphology

(a)

(b)

(c)
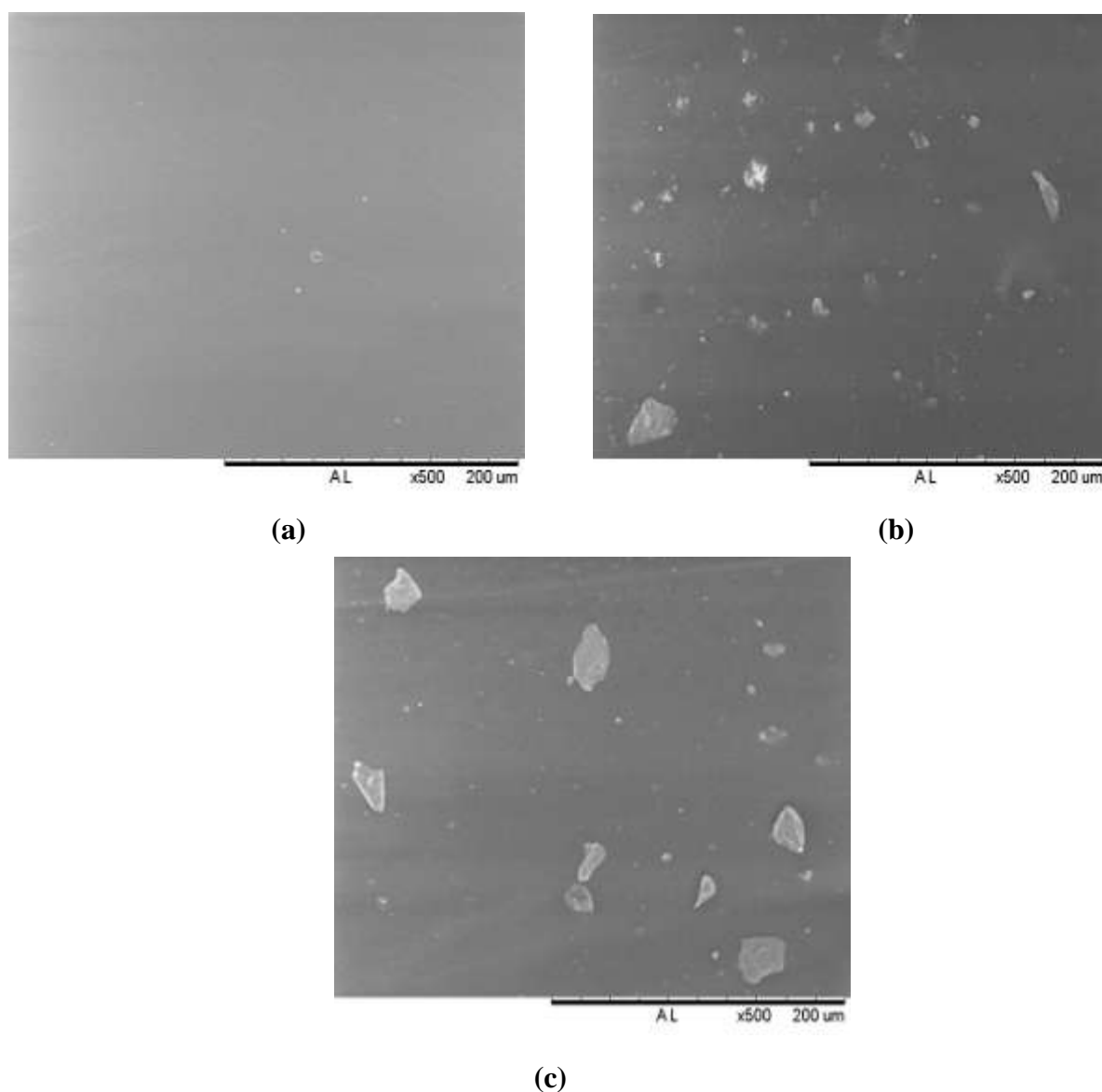
Fig. 4: SEM of LDPE/rice bran film: (a) LDPE (500X); (b) 2% rice bran in LDPE film (500X); (c) 4% rice bran in LDPE film (500X).

Figure 4(a – c) shows the morphology of LDPE/rice bran film which analyze by using Scanning electron microscopy (SEM). Figure 4(a) show the morphology of LDPE is very homogeneous and structure chain was uniform. Figure 4(b and c) show the images of rice bran domains dispersed in LDPE matrix. At 2% rice bran, the dispersion and distribution of rice bran seem to be uniform. While for 4% rice bran was not mixed homogenous with LDPE matrix so that the granules are grouped together leading to the formation of clumps. This is possibly due to the hygroscopic nature of rice bran. This because rice bran is hydrophobic while LDPE is hydrophilic so that it immiscible or non-homogenous. Furthermore, lack of interfacial adhesion between LDPE and rice bran also lead to reduction of mechanical properties of LDPE/rice bran film. From the previous studies of LDPE blend with starch show increasing the concentration starch will contribute to lack of adhesion between filler and matrix so that it become poor interfacial interaction [12]. As the starch content increased, filler–filler interactions also increased. This could also account for the deterioration in

physical properties since the transfer of stress from the matrix to the filler was less effective because a lack of interfacial adhesion between matrix and filler.

4. CONCLUSION

The mechanical properties such as tensile strength and elongation at break of LDPE/rice bran film decreased with increased in rice bran concentration. Tear strength was not affected by the addition rice bran in LDPE/rice bran film. Morphology studied reveal that the clump formations exist at 4% rice bran loading in LDPE/rice bran film which affected the mechanical properties.

5. ACKNOWLEDGEMENT

6. REFERENCES

1. Pracella, M., Pazzagli, F., & Galeski, A. (2002). Reactive compatibilization and properties of recycled poly(ethylene terephthalate)/polyethylene blends. *Polymer Bulletin, 48*(1), 67-74.
2. Ishiaku, U. S., Pang, K. W., Lee, W. S., & Ishak, Z. A. M. (2002). Mechanical properties and enzymic degradation of thermoplastic and granular sago starch filled poly(ε-caprolactone). *European Polymer Journal, 38*(2), 393-401.
3. Aburto, J., Thiebaud, S., Alric, I., Borredon, E., Bikiaris, D., Prinos, J., et al. (1997). Properties of octanoated starch and its blends with polyethylene. *Carbohydrate Polymers, 34*(1–2), 101-112.
4. Torres, A. V., Zamudio-Flores, P. B., Salgado-Delgado, R., & Bello-Pérez, L. A. (2008). Biodegradation of low-density polyethylene-banana starch films. *Journal of Applied Polymer Science, 110*(6), 3464-3472.
5. Tudorachi, N., Cascaval, C. N., Rusu, M., & Pruteanu, M. (2000). Testing of polyvinyl alcohol and starch mixtures as biodegradable polymeric materials. *Polymer Testing, 19*(7), 785-799.
6. Arvanitoyannis, I., & Biliaderis, C. G. (1998). Physical properties of polyol-plasticized edible films made from sodium caseinate and soluble starch blends. *Food Chemistry, 62*(3), 333-342.
7. Kim, M., Pometto, A. L., Johnson, K. E., & Fratzke, A. R. (1994). Degradation studies of novel degradable starch-polyethylene plastics containing oxidized polyethylene and prooxidant. *Journal of Polymers and the Environment, 2*(1), 27-38.
8. Wanyo, P., Chomnawang, C., & Siriamornpun, S. (2009). Substitution of Wheat Flour with Rice Flour and Rice Bran in Flake Products:Effects on Chemical, Physical and Antioxidant Properties. *World Applied Sciences Journal, 7*(1), 49-56.
9. George, J., Kumar, R., Jayaprahash, C., Ramakrishna, A., Sabapathy, S. N., & Bawa, A. S. (2006). Rice bran-filled biodegradable low-density polyethylene films: Development and characterization for packaging applications. *Journal of Applied Polymer Science, 102*(5), 4514-4522.

10. Raj, B., K, U. S., & Siddaramaiah. (2004). Low density polyethylene/starch blend films for food packaging applications. *Advances in Polymer Technology, 23*(1), 32-45.

11. Garg, S., & Jana, A. K. (2006). Effect of Starch Blends on Mechanical Properties of Low Density Polyethylene (LDPE) Film. *Indian Chemical Engineering 48*(3).

12. Pedroso, A. G., & Rosa, D. S. (2005). Mechanical, thermal and morphological characterization of recycled LDPE/corn starch blends. *Carbohydrate Polymers, 59*(1), 1-9.

The Investigation of Morphological Characteristics of Porous Anodic Alumina Generated by Electrochemical Etching

L.K. Tan[1,*], F.K. Yam, K.P.Beh, Z. Hassan

[1]Nano-Optoelectronics Research and Technology Laboratory, School of Physics, Universiti Sains Malaysia, 11800 Penang, Malaysia

*Corresponding author: tlk-1312@hotmail.com

Abstract: *Porous anodic alumina (PAA) samples were fabricated by using commercially available aluminium sheet. Anodization was performed in 0.3M oxalic acid at different voltages (i.e 10V, 20V, 30V, 40V, 50V) and the morphology of the samples was investigated. The changes before and after pore widening process were also studied. From scanning electron microscopy images, the pore size was found to be voltage dependent. Also, scanning electron microscopy images revealed that 40V is the most preferable anodization voltage to produce the good ordering of pore structure. In addition, the pore size was widened after immersing in phosphoric acid.*

Keywords: Porous anodic alumina; voltage; anodization; pore widening; morphology.

1. INTRODUCTION

Over the last decade, porous anodic alumina (PAA) has been investigated extensively due to its unique self-organized hexagonal pore arrays with a semispherical alumina barrier layer formed between the pore bottom and the Al substrate. These uniformity and periodicity of pore arrays make PAA highly suitable for the template-based synthesis of nanostructures [1,2] which later can be tailored into various devices [3].

Formation of PAA is generally accomplished by electrochemical etching, namely the anodization process where the Al is connected to the anode. In recent years, various anodization processes such as mild anodization [4], hard anodization [5], pulse anodization [6] and two-step anodization [7] have been proposed to fabricate the self-ordering PAA. In fact, the self-ordering PAA is controllable through anodization conditions, including anodization voltage, anodization duration, temperature and the types of electrolytes [8].

In the present study, we investigated the effect of anodization voltage on the morphological properties of PAA in an acidic electrolyte using low cost, impure aluminium sheet as the starting material. Apart from that, we also examined the structural changes of the deposited PAA after pore widening process.

2. EXPERIMENTAL

PAA was generated by means of electrochemical anodization using the commercially available aluminium sheet. Prior to the anodization, mechanical polishing was applied on the aluminium sheet. The polished aluminium sheet was then anodized in oxalic acid with 0.3M concentration at voltages of 10V, 20V, 30V, 40V and 50V for 45 minutes. In this experiment, copper was employed as the electrode and a small volume of glycerol was added into the electrolyte in order to reduce the ions mobility. Finally, a post-treatment, pore widening process was performed by immersing the as-grown PAA samples in 1M of phosphoric acid

for 20 minutes. Morphological and structural changes of the resulting PAA samples were characterized by using scanning electron microscopy (SEM).

3.   RESULTS AND DISCUSSION

3.1   Effect of DC Voltage on the Surface Morphology

Fig. 1 shows the SEM micrographs of PAA anodized at different DC voltages with constant increment of 10V. By comparing the SEM images from Fig. 1(a) to Fig. 1(e), it is noted that the pore diameter is dependent on the DC voltage. In other words, the pore size increases with increasing DC voltage. The pore formation initiated at DC voltage of 20V with a rough surface as shown in Fig. 1(b). Interestingly, the surface of PAA sample becomes smoother with more uniform pore distribution at DC voltage of 40V which is believed the optimum anodization voltage for the highly ordered PAA [3]. In our case, there are no highly ordered honeycomb nanopore arrays formed as those existed in PAA obtained from high purity aluminium. This indicates that the purity of aluminium is the main factor in contributing the self-ordering nanostructures of PAA.

On the other hand, when the voltage is increased to 50V, the surface morphology of PAA sample is totally different compared to the other anodization voltages. As shown in Fig. 1(e), the pores are not uniformly distributed and they are arranged in irregular pattern. Besides, the pores vary inconsistently in size and they are appeared to be non-circular in shape. Also, it can be seen that the pore diameter is obviously larger than the PAA samples obtained at lower voltages. This phenomenon is associated with the higher etching rate at higher anodization voltage [9]. However, the pores formed at 50V are not well arranged. Instead, it seems to be merged with neighbouring pores which is undesired condition and subsequently damages the nature structure of PAA.
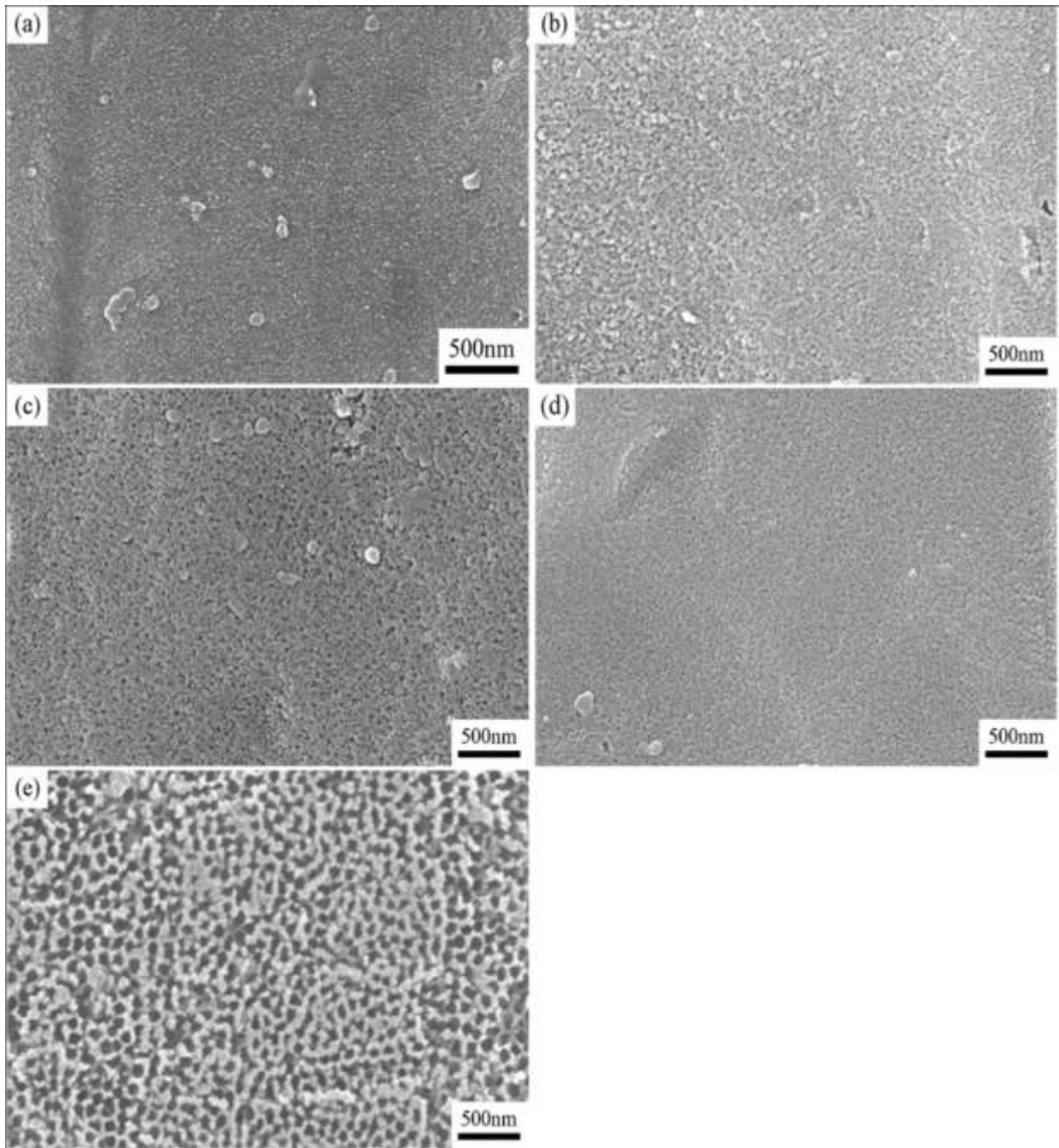
Fig. 1: SEM micrographs of PAA anodized at voltage of (a) 10V (b) 20V (c) 30V (d) 40V and (e) 50V

3.2 Structural Changes of As-grown PAA after Pore Widening Treatment

In order to obtain larger pores, the pores were widened by immersing the PAA samples into solution of phosphoric acid. Fig. 2 shows the SEM micrographs of PAA's pore structure fabricated at various DC voltages after the pore widening process. It is expected that the pore size increases with the acid treatment. Comparing Fig. 1 and Fig.2, the widened pores can be seen clearly as shown in Fig. 2(a) to Fig. 2(d). Fig. 1(a) to Fig. 1(c) shows the same surface morphology as the pre-treatment with rough surfaces on PAA samples. The only difference is the pores are opened wide after treatment. The pore structure of PAA fabricated at 40V after treatment shows the smoother surface with more evenly pore distribution as well as more consistent pore diameter. However, the PAAs here also show no

hexagonal pore ordering which is expected in the fabrication of PAA. Therefore, it can be concluded that the pore arrays contain a large amount of rotational defects [8].
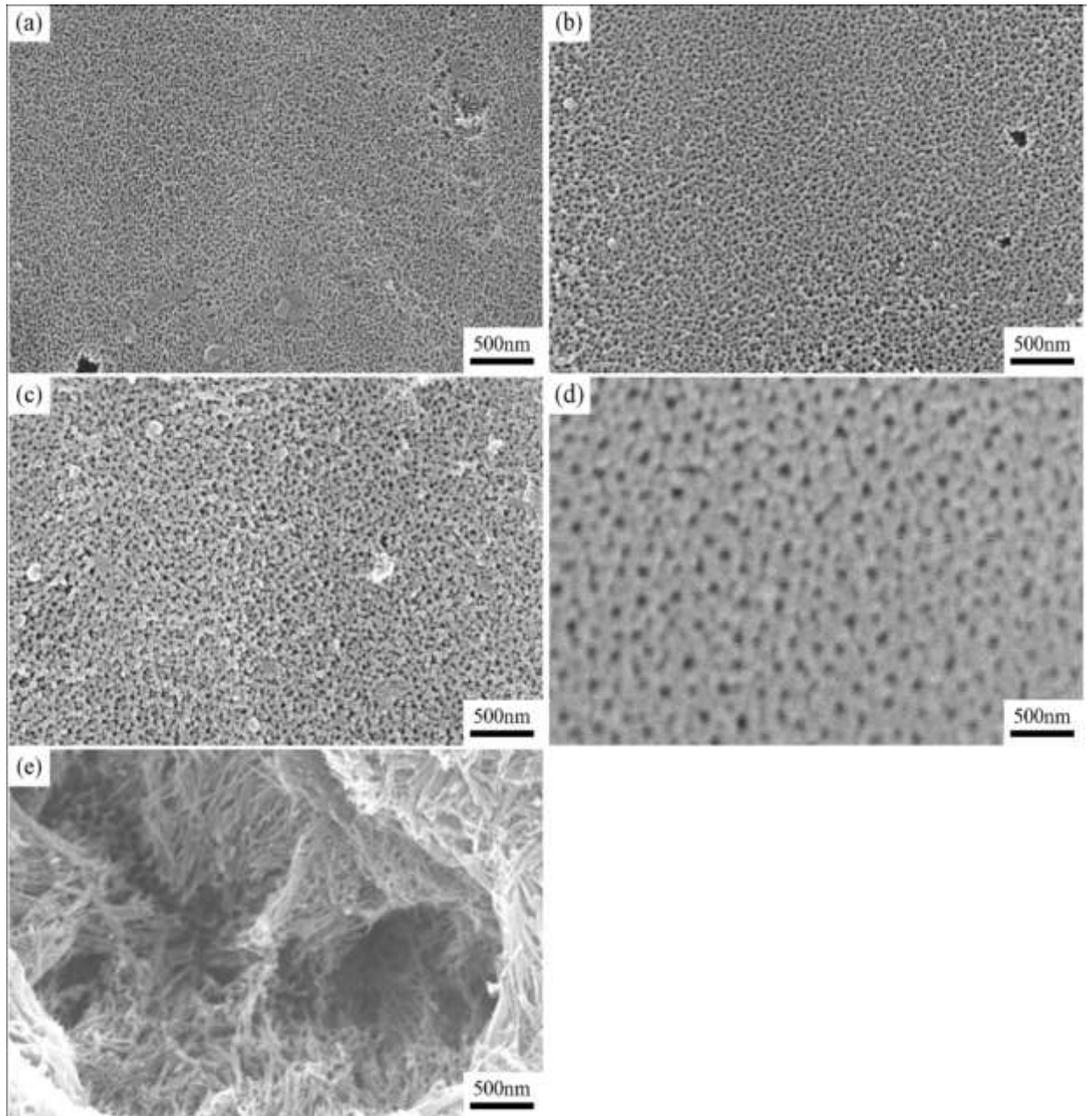
Fig. 2: SEM micrographs of PAA after pore widening treatment at DC voltage of (a) 10V (b) 20V (c) 30V (d) 40V and (e) 50V

Unexpectedly, the pore structure of PAA at 50V has been destroyed and it is appeared to be wire-like structure as shown in Fig. 2(e). To explain the mechanism of nanowires formation, a schematic diagram is illustrated in Fig. 3. The presence of the naowires is believed due to the fracture of PAA occurred along the breakage line which subsequently breaks into individual nanowires. Xiao et al. reported that nanowires are formed when all or most of the walls of PAA between its neighbours break during the homogeneous expansion of the pores [10]. The pore structure will be damaged and broken with increasing etching time.
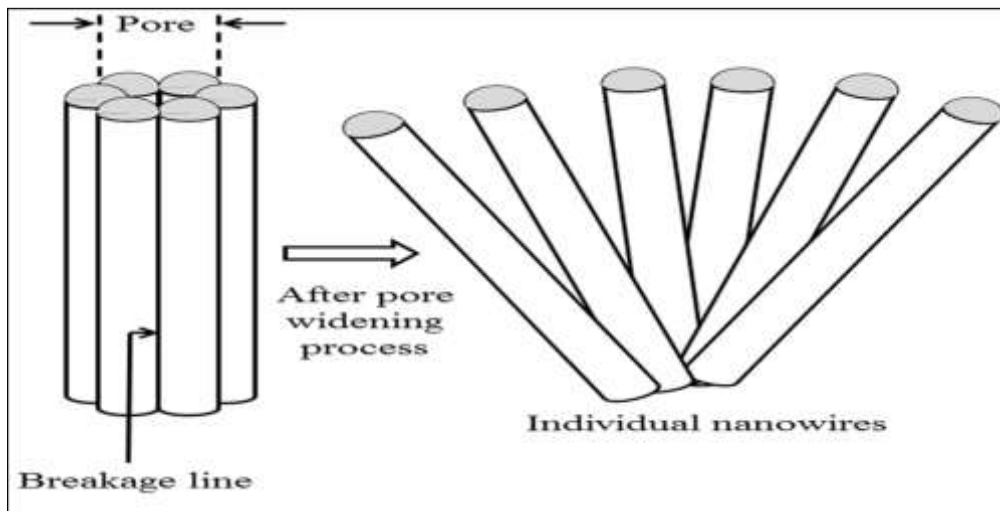
Fig. 3: Schematic representation of mechanism of nanowires formation

Fig.4 shows the variation of average pore diameter at anodization voltage of 10V, 20V, 30V and 40V after the pore widening treatment. This plotted graph clearly demonstrates the pore diameter increases linearly with the greater anodization voltage. As can be seen in Fig. 4, the average pore diameter varies approximately in the range of 25nm to 45nm which is the medium pore size for oxalic acid electrolyte. At voltage of 40V, it shows the greatest pore diameter of about 45nm which is in close agreement with the pore diameter reported by Lo and Budiman [8]. Hence, it can be said that the anodization voltage enhanced the dissolution/etching rate making the pore size dependent on the anodization voltage.
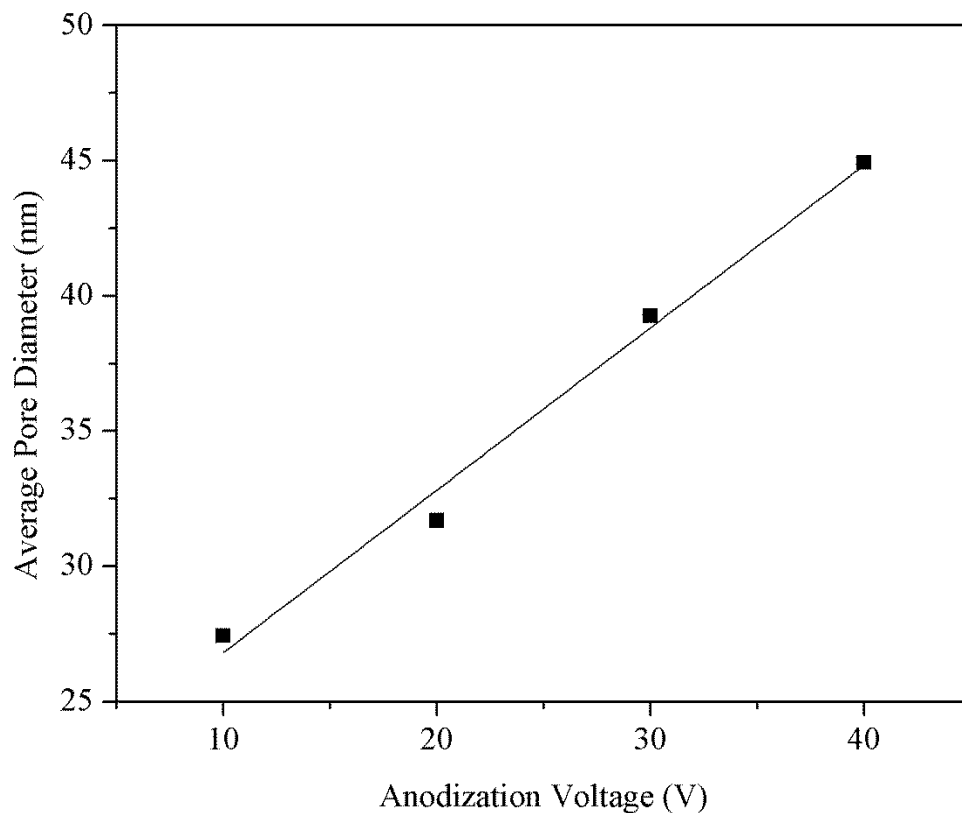
Fig. 4: Variation of average pore diameter as a function of anodization voltage after pore widening treatment

4.   CONCLUSION

In summary, we have successfully synthesized the PAA by using commercial aluminium sheet in 0.3M oxalic acid. The SEM images revealed that the pore size is dependent on the anodization voltage. The PAA anodized at voltage of 40V showed the most uniform pore distribution with no hexagonal pore ordering. With pore widening process, the pores in all the samples were obviously widened. Surprisingly, nanowires were observed after pore widening process at voltage of 50V.

5.   ACKNOWLEDGEMENTS

6.   REFERENCES

1.   Zhang, R., Jiang, K.M., Chen, D.L., & Ding, G.Q. (2009). Indium oxide nanorods and nanowires on porous anodic alumina. *Materials Letters.,* 63, 1044-1046.

2.   Cheng, G.S., Chen, S.H., Zhu, X.G., Mao, Y.Q., & Zhang, L.D. (2000). Highly ordered nanostructures of single crystalline GaN nanowires in anodic alumina membranes. *Materials Science & Engineering A.,* 286, 165-168.

3.   Masuda, H. & Fukuda, K. (1995). Ordered metal nanohole arrays made by a two-step replication of honeycomb structures of anodic alumina. *Science.,* 268, 1466-1468.

4.   Kirchner, A., Mackenzie, K.J.D., Brown, I.W.M., Kemmitt, T., & Bowden, M.E. (2007). Structural characterization of heat-treated anodic alumina membranes prepared using a simplified fabrication process. *Journal of Membrane Science.,* 287(2), 264-270.

5.   Schwirn, K., Lee, W., Hillebrand, R., Steinhart, M., Nielsch, K., & Gosele, U. (2008). Self-ordered anodic aluminum oxide formed by H_2SO_4 hard anodization. *American Chemical Society Nano.,* 2(2), 302-310.

6.   Lee, W., Schwirn, K., Steinhart, M., Pippel, E., Scholz, R., & Gosele, U. (2008). Structural engineering of nanoporous anodic alumina oxide by pulse anodization of aluminium. *Nature Nanotechnology.,* 3, 234-239.

7.   Li, Y., Ling, Z.Y., Chen, C.C., & Wang, J.C. (2008). Fabrication of novel porous anodic alumina membranes by two-step hard anodization. *Nanotechnology.,* 19, 225604-225609.

8.   Lo, D., & Budiman R.A. (2007). Fabrication and characterization of porous anodic alumina films from impure aluminum foils. *Journal of Electrochemical Society.,* 154(1), C60-C66.

9.   Jessensky, O., Muller, F., & Gosele, U. (1998). Self-organized formation of hexagonal pore arrays in anodic alumina. *Applied Physics Letters.,* 72(10), 1173-1175.

10. Xiao, Z.L., Han, C.Y., Welp, U., Wang, H.H., Kwok, W.K.,Willing, G.A., Hiller, J.M., Cook, R.E., Miller, D.J., & Crabtree, G.W. (2002). Fabrication of alumina nanotubes and nanowires by etching porous alumina membranes. *Nano Letters.,* 2(11), 1293-1297.

Sol-gel titania and silica coating on steel for corrosion protection

S Sangsuk[1,*], K Saengkiettiyut[2], P Laiwan[3]

[1,2] Metallurgy and Materials Science Research Institute, Chulalongkorn University, Phayathai Road, Pathumwan, Bangkok, Thailand 10330

[3] Department of Industrial Chemistry, Faculty of Science, Chiang Mai University, Huay Keaw Road, Muang District, Chiang Mai, Thailand 50200

*Corresponding author: supin.t@chula.ac.th

Abstract: *Titania and silica sol coatings have been developed for corrosion protection of steel by dip coating technique. The two layers of coating on steel were titania and silica sol-gel for the first and the second layer, respectively. The coated steel was fired in air atmosphere at 400^oC for 5 min. The coating characteristics of coated steel samples were investigated by optical microscopy and scanning electron microscopy. Corrosion resistance properties of the sol-gel coating were studied by electrochemical method. Potentiodynamic polarization curves of the coated samples indicated improvement of the corrosion resistance.*

Keywords: sol-gel, titania, silica, steel, corrosion

1. INTRODUCTION

Sol-gel process is a ceramic synthesis technique by preparation of sol, gelation of sol, followed by drying, thermal decomposition of organic species, densification of the gel network and finally crystallization into the desired crystal structure. The sol-gel process is used to prepare metal oxide in various forms such as powder, fiber, membranes including film and coating. Film and coatings represent the earliest commercial application of the sol-gel technology. For protective film, sol-gel coating is an effective method for corrosion protection of metals because the coating increases the corrosion potential and decreases the corrosion rate. For example, stainless steel was coated with sol-gel silica [1], zirconia or alumina. In the case of titanium dioxide, it is mostly used in catalyst. Very few TiO_2 films have been reported as protective coating on stainless steel substrate [2]. In our previous work, steel coating with sol-gel titania showed a higher corrosion potential and lower corrosion rate than steel without coating. Therefore the objective of this work is to enhance corrosion resistance of steel by coating two layers of sol-gel film, i.e. titania- silica film.

2. EXPERIMENTAL PROCEDURE

The titania sols were prepared using titanium diisopropoxide bisacetylacetonate (TIAA) and 1,3 propanediol as chemical precursors [3]. The silica sols were prepared by hydrolysis and condensation of tetraethylorthosilicate (TEOS) in the presence of an acidic catalyst. The steel sheets, which were cleaned with ethanol, were used as substrates. The steel substrates were coated using dip coating technique. The two layers of coating on the top of the steel surface are sol-gel titania for the first layer and sol-gel silica for the second layer. The coated steel was fired at 400^oC for 5 min in an open-to-air oven. The coating characteristics of coated steel samples were carried out using optical microscopy and scanning electron microscopy (SEM). Corrosion resistance properties of the sol-gel coatings were studied by potentiostat. A platinum rod and a saturated calomel electrode were used as

counter and reference electrode, respectively. Corrosion experiments were carried out on samples with and without coating in 3.5 wt% NaCl solution by fitting the data to the NOVA 1.7 program, corrosion potential and corrosion current density were determined.

3. RESULT AND DISCUSSION

3.1 Coating characteristics

Titania-silica gel film coating on steel surface after dip coating is shown in Fig.1. It shows a smooth surface without crack.
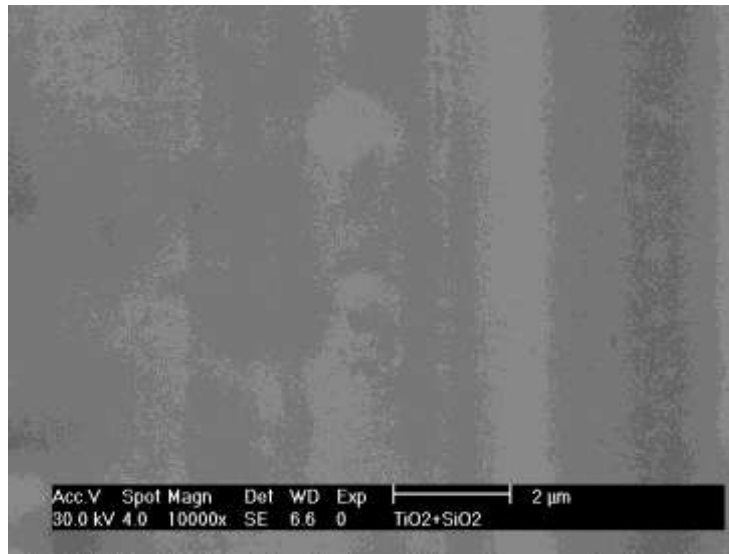
Figure 1 SEM micrograph of TiO_2 - SiO_2 gel coating on steel before firing at $400^{o}C$.

After firing at $400^{o}C$, optical micrograph shows different colors in 3 areas on the steel surface, i.e. uncoated, coated with titania film, and coated with silica areas. The thicker film represented darker color (Fig.2). SEM observation, Fig. 3, shows the formation of a crack free surface.
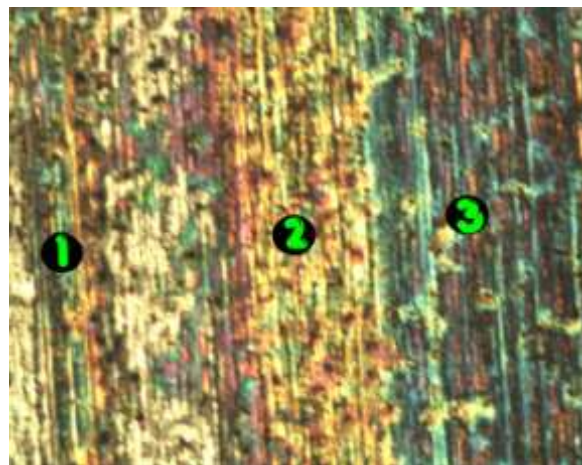
Figure 2 Optical micrograph of TiO_2-SiO_2 film coating on steel after firing at $400^{o}C$. (1 = bare steel surface, 2 = titania film and 3= silica film).
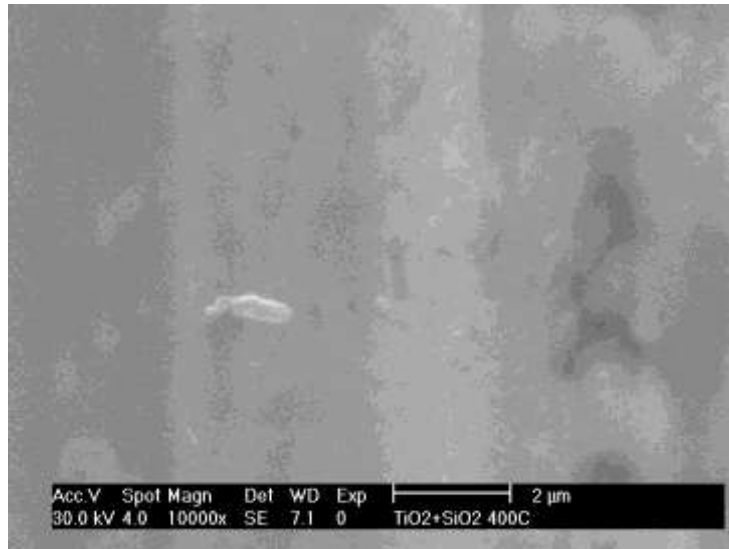
Figure 3 SEM micrograph of TiO_2-SiO_2 film coating on steel after firing at 400^oC.

In the case of steel without coating, the steel surface after firing at 400^oC shows distribution of needle crystal (Fig. 4). It is possible that the crystal on steel surface is iron oxide because of oxidation of steel at elevated temperature [4].
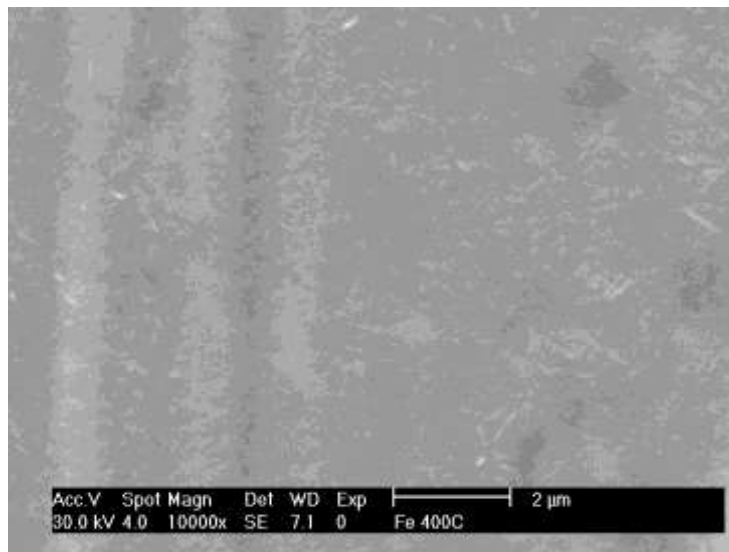
Figure 4 SEM micrograph of bare steel after firing at 400^oC.

3.2 Corrosion Test

The polarization curves (Fig.5) of sol-gel coating was different from that of the bare steel substrate. The coated samples with titania film and titania-silica film increased the corrosion potential.
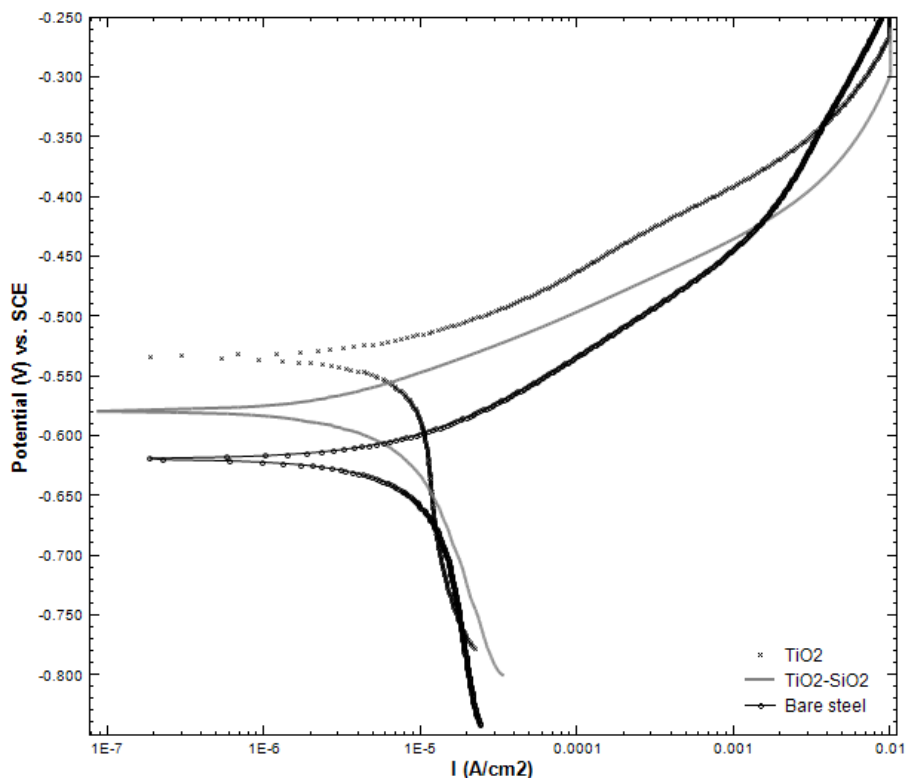
Figure 5 Polarization curves in 3.5 wt% NaCl solution for bare steel, steel with TiO_2 film, and steel with TiO_2 -SiO_2 film.

Table 1 Corrosion parameter estimated from potentiodynamic polarization curves for samples in 3.5 wt% NaCl solution.

	Bare steel	Steel with TiO_2	Steel with TiO_2 -SiO_2
E_{corr} (V)	-0.610	-0.531	-0.572
I_{cor} ($\mu A/cm^2$)	14.95	13.32	5.74
Corrosion rate (mm/y)	0.173	0.155	0.067

From the results in Table 1, titania film slightly decreased the corrosion rate of steel samples. After coating silica film on the top of titania film, we found that titania-silica film much increased the corrosion resistance. This finding was in agreement with Thim et al. (2000) who showed that an increasing number of coating films increased the film thickness. Then the thicker film showed a higher corrosion protection than the thinner film.

.

4. CONCLUSION

Two types of sol i.e. titania and silica sol were used for dip coating on steel. The steel with titania-silica film showed a slightly higher corrosion potential and much lower corrosion rate than the steel without coating.

5. ACKNOWLEDGEMENTS

6. REFERENCES

1. Vasconcelos, D.C.L., Carvalho, J.A.N., Mantel, M. & Vasconcelos, W.L. (2000). Corrosion resistance of stainless steel coated with sol-gel silica. *Journal of Non-Crystalline Solid*, 273: 135-139.
2. Wang, D., & Bierwagen, G.P. (2009). Sol-gel coatings on metals for corrosion protection. *Progress in Organic Coatings*, 64, 327-338.
3. Tangwiwat, S. & Milne, S.J. (2005). Barium titanate sols prepared by a diol-based sol-gel route. *Journal of Non-Crystalline Solid*, 351, 976-980.
4. Szpunai, J. A. & Kim, B-K. (2007). High temperature oxidation of steel; new description of structure and properties of oxide. Materials Science Forum, 539, 223-227.
5. Thim, G.P., Oliveira, M.A.S., Oliveira, E.D.A. & Melo, F.C.L. (2000). Sol-gel silica film preparation from aqueous solution for corrosion protection. *Journal of Non-Crystalline Solid*, 273: 124-128.

Development of alginate microspheres of nitrendipine for nasal delivery

S. B. Patil[1,*], K. K. Sawant[2]

[1]Shri Neminath Jain Brahmacharyashram's, Shriman Sureshdada Jain College of Pharmacy (PG course), Neminagar, Chandwad, Dist. Nashik- 423 101 (Maharashtra), India
[2]New Drug Delivery Systems Laboratory, TIFAC Center of Relevance and Excellence in NDDS, Pharmacy Department, The M. S. University of Baroda, Fatehgunj, Vadodara- 390002, (Gujarat), India

*Corresponding author: sbpatil_99@rediffmail.com

Abstract: *The present study was aimed at development and in vitro evaluation of mucoadhesive alginate microspheres of nitrendipine for nasal delivery to avoid first pass metabolism and to improve the therapeutic efficacy in treatment of the hypertension and angina pectoris. The microspheres were prepared by water-in-oil (w/o) emulsification followed by cross linking with calcium chloride. The prepared microspheres were evaluated for various in vitro parameters like particle size, entrapment efficiency, mucoadhesion, drug release, and histology studies. The results clearly indicated promising potentials of alginate microspheres for delivering nitrendipine intranasally and could be viewed as a potential alternative to conventional dosage forms.*

Keywords: Microspheres, sodium alginate, nitrendipine, nasal delivery

1. INTRODUCTION

In the past decade, the use of the nasal cavity as a route for drug delivery has been an area of great interest to the pharmaceutical industry, especially for systemically acting drugs that are difficult to deliver via routes other than injection. The nasal route appears to be an ideal alternative to the parenterals for administering drugs intended for systemic effect, in view of the rich vascularity of the nasal membranes and the ease of intranasal administration. Besides avoidance of hepatic first pass elimination, the rate and extent of absorption and the plasma concentration versus time profile are relatively comparable to those obtained by IV medication [1].

The use of microsphere-based therapy allows drug release to be carefully tailored to the specific treatment site through the choice and formulation of various drug–polymer combinations. The total dose of medication and the kinetics of release are the variables, which can be manipulated to achieve the desired result. Using innovative microencapsulation technologies, and by varying the polymer ratios, molecular weight of the polymer, etc., microspheres can be developed into an optimal drug delivery system which will provide the desired release profile. Microsphere based systems may increase the life span of the drug encapsulated and control the release of the drugs. Being small in size, microspheres have large surface to volume ratios and can be used for controlled release of insoluble drugs [2].

Nitrendipine is a lipophilic, calcium channel blocker used in the treatment of hypertension, has very poor absolute bioavailability (10–20%) due to extensive first pass metabolism [3]. Sodium alginate is a hydrophilic, biodegradable, biocompatible, mucoadhesive, nontoxic polymer and is widely used as carrier for sustained and controlled drug delivery systems. Hence, present study was aimed at avoidance of first pass metabolism of nitrendipine by preparing alginate microspheres for nasal administration.

2. MATERIALS AND METHODS

2.1   Materials

Nitrendipine (NTD) was a gift sample from USV Limited, Mumbai, India. Sodium alginate, liquid paraffin (light), calcium chloride, Span 80[®] was procured from S. D. Fine Chemicals, Mumbai, India. A dialysis membrane (cut-off Mw 12000) was procured from Hi Media, India. All other chemicals and reagents used in the study were of analytical grade.

2.2   Preparation of Microspheres

The emulsification method was utilized for the preparation of microspheres followed by cross linking with calcium chloride [4,5]. NTD was dispersed in an aqueous solution containing 3% w/v sodium alginate. The aqueous phase was emulsified in light liquid paraffin containing 2% (v/v) Span 80 in the ratio 1:10 using a Eurostar (IKA Labortechnik, Germany) high speed stirrer at 1200 rpm for 60 min. Calcium chloride solution (2%) in a mixture of methanol and isopropyl alcohol (2:3) was added drop wise and the dispersion was stirred for another 10 min. Microspheres were collected by filtration in vacuum, washed with isopropyl alcohol thrice and finally air dried at room temperature.

2.3   In Vitro Evaluation of Microspheres

2.3.1   Particle Size

Particle size was determined by the principle of laser light scattering on a particle size analyzer (Malvern Mastersizer 2000, Malvern Instruments, UK). The dispersion of microspheres was added to the sample dispersion unit containing the stirrer and stirred in order to reduce the aggregation between the microspheres and the laser obscuration range was maintained between 3–15%. The average volume mean particle size was measured after performing the experiment in triplicate.

2.3.2   Scanning Electron Microscopy (SEM)

The shape and surface characteristics of the microspheres were determined by scanning electron microscopy (JSM 5610 LV, Jeol Datum Ltd., Japan). The samples were mounted directly onto the SEM sample holder using double-sided sticking tape and images were recorded at the required magnification at the acceleration voltage of 5 kV.

2.3.3   Entrapment Efficiency

The microspheres were evaluated for entrapment efficiency by dissolving them in phosphate buffer pH 6.2 containing 1% Tween 80 and analyzing at 355 nm on UV spectrophotometer (Shimadzu UV1610, Japan). It was confirmed from preliminary UV studies that the presence of dissolved polymers did not interfere with the absorbance of the nitrendipine at 355 nm.

2.3.4   In Vitro Mucoadhesion

Adhesion number was determined by using the sheep nasal mucosa [6,7]. The microspheres were placed on sheep nasal mucosa after fixing to the polyethylene support. The mucosa was then placed in the dessicator to maintain at > 80% RH at room temperature for 30 min to allow the polymer to hydrate and to prevent drying of the mucus. The mucosa was then observed under a microscope and the number of particles attached to the particular area was counted. After 30 min, the polyethylene support was introduced into a plastic tube cut in circular manner and held in an inclined position at an angle of 45^0. Mucosa was washed thoroughly at flow rate of 1 mL min^{-1} for 5 min with phosphate buffer pH 6.2. Tissue was again observed under a microscope to see the number of microspheres remaining in the same field area.

The adhesion number was determined by the following equation:

$$N_a = N/N_0 \text{ X } 100 \qquad\qquad (1)$$

Where N_a is adhesion number, N_0 is total number of particles in a particular area and N is number of particles attached to the mucosa after washing.

2.3.5 In Vitro Drug Release

It was carried out by using Franz diffusion cell containing phosphate buffer pH 6.2 and 1% Tween 80. A dialysis membrane (cut-off Mw 12 000, Hi Media, India) was used to keep the microspheres (5 mg) on the donor side, which allowed free diffusion of nitrendipine to the receptor compartment containing 20 mL phosphate buffer solution pH 6.2 (within the pH range in nasal cavity) and maintained at 37 ± 1^0C. The receptor compartment was stirred with a magnetic stirring bar. At scheduled time intervals, aliquots (1 mL) were withdrawn from receptor cell and replaced with the same volume of fresh medium and aliquots were analyzed spectrophotometrically at 355 nm.

2.3.6 Differential Scanning Calorimetry (DSC)

DSC (Mettler Toledo DSC 822) was performed on placebo microspheres, drug-loaded microspheres and plain NTD. Samples were heated from 20 to 300 ^{0}C at the heating rate of 10 ^{0}C min $^{-1}$ in nitrogen atmosphere (flow rate, 20 mL/min).

2.3.7 X- ray diffraction (XRD) studies

The X-RD patterns of placebo microspheres, plain NTD, and drug-loaded microspheres were recorded using X-ray diffractometer (Bruker AXS D8 Advance). The samples were mounted on a sample holder and X-RD patterns were recorded in the range of $3–50^0$ at the speed of 5^0 min^{-1}.

2.3.8 Histology studies

The nasal mucosa tissues were carefully removed from the nasal cavity of sheep obtained from the local slaughterhouse. Histopathological evaluation of tissue incubated in phosphate buffer (pH 6.2) after collection was compared with tissue incubated in the diffusion chamber of Franz cell with microsphere formulations. Tissue was fixed in 10% buffered formalin (pH 6.2), routinely processed and embedded in paraffin. Paraffin sections were cut on glass slides and stained with hematoxylin and eosin (HE). The sections were examined by light microscopy, to examine the morphological changes to the tissue during in vitro permeation study by a pathologist blinded to the study [8].

3. RESULTS AND DISCUSSION

3.1 Particle Size

The size of the microspheres prepared in this study was in the range of 22.68 – 48.95 μm, which is favorable for intranasal absorption. Preliminary studies showed that as the concentration of polymer was increased, the particle size also proportionally increased.

3.2 Scanning Electron Microscopy (SEM)

The microspheres had a slight smooth surface and were found to be discrete and spherical in shape (Fig. 1). SEM was used to investigate the physical appearance of the NTD loaded alginate microparticles.
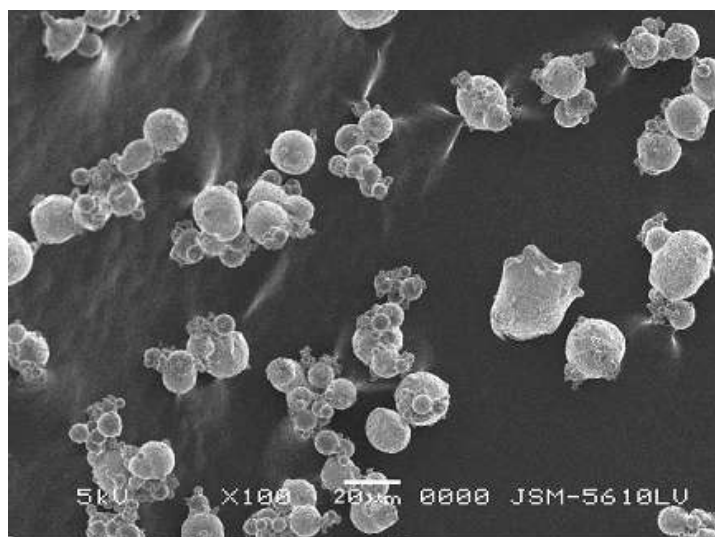
Figure 1. SEM Photograph of alginate microspheres

3.3 Entrapment Efficiency

The % entrapment efficiency was found to be in the range between 42.12 and 63.42. The % entrapment efficiency showed a dependence on drug loading, amount of cross linking agent and time of cross linking. The formulations loaded with higher amount of drug exhibited higher encapsulation efficiencies. The encapsulation efficiency, however, showed an inverse relationship with increasing calcium chloride concentration and cross linking time. Both these factors lead to an increase in cross link density, which will reduce the free volume spaces within the polymer matrix and hence, a reduction in encapsulation efficiency is observed.

3.4 In Vitro Mucoadhesion

The results of *in vitro* mucoadhesion showed that all the batches of microspheres had satisfactory mucoadhesive property ranging from 69.24 to 83.67% and could adequately adhere on nasal mucosa. The results also showed that with increasing polymer ratio, higher mucoadhesion percentages were obtained. This could be attributed to the availability of higher amount of polymer for interaction with mucus. Increase in calcium chloride concentration and cross linking time decreased the mucoadhesive property of the microspheres.

3.5 In Vitro Drug Release

All the batches of the microspheres released around 90% of drug in 8 hr. The release pattern showed a slow and controlled release phase resulting from the controlled diffusion of entrapped drug. *In vitro* drug release proportionally increased with increasing the drug concentration. With an increase in the cross linking agent concentration, a respective decrease in the rate and extent of drug release was observed [9].

3.6 Differential Scanning Calorimetry (DSC)

DSC thermograms of pure nitrendipine, placebo alginate microspheres and nitrendipine loaded alginate microspheres are displayed in Fig. 2. Thermogram of nitrendipine showed a sharp peak at 159 ^{0}C due to melting of the drug, but in case of nitrendipine loaded microspheres, no characteristic peak was observed at 159 ^{0}C, implying that there are no free Nitrendipine crystals in the system i.e. the microspheres exhibited thermic behaviour characteristic of amorphous substances.
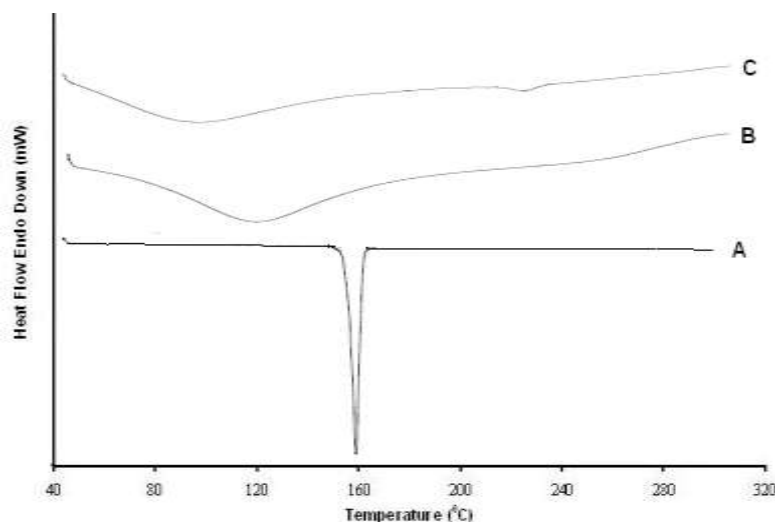
Figure 2. DSC thermograms of (A) pure NTD; (B) placebo microspheres; (C) drug loaded microspheres.

3.7 X- ray diffraction (XRD) studies

The XRD spectra recorded for plain NTD (A), placebo alginate microspheres (B) and NTD loaded alginate microspheres (C) are presented in Fig. 3. NTD showed characteristic intense peaks at 2θ of 9.99^0, 11.33^0, 13.09^0, 23.80^0, 24.30^0, 27.45^0 and 28.70^0. However, these peaks were not observed in the NTD loaded microspheres. This indicates that drug particles are dispersed at molecular level in the polymer matrix.
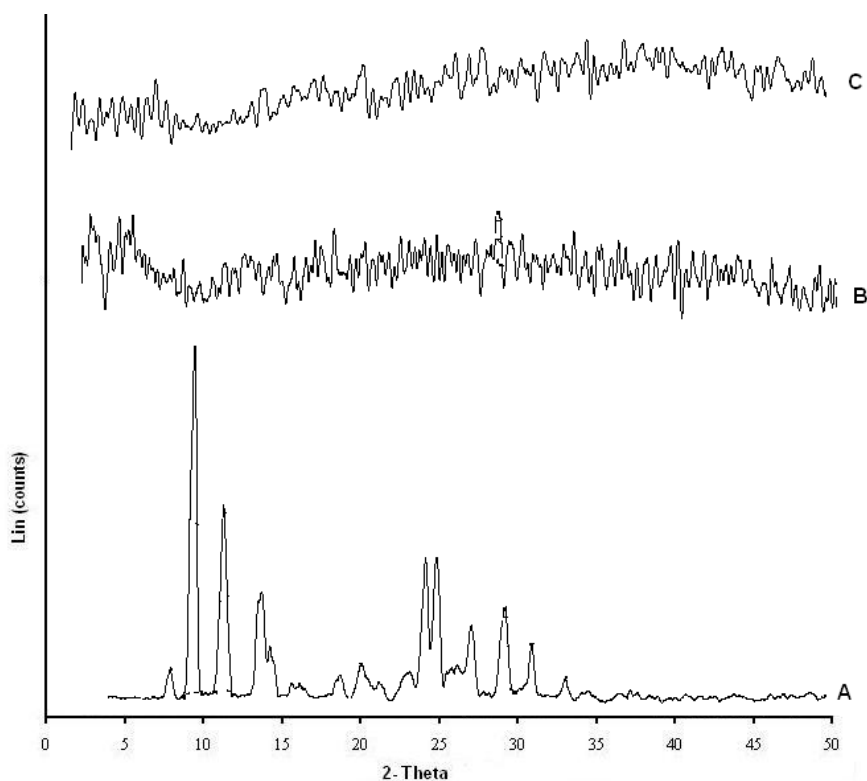
Figure 3. Powder X-ray diffraction patterns of (A) pure NTD; (B) placebo microspheres; (C) NTD loaded microspheres

3.8 Histology studies

The histology of nasal mucosa for control and treated with alginate microspheres is shown in Fig. 4. The microscopic observations indicated that the optimized formulation had no significant effect on the microscopic structure of sheep nasal mucosa. The surface epithelium lining and the granular cellular structure of the nasal mucosa were totally intact. Thus, the microsphere formulation seems to be safe with respect to nasal administration.
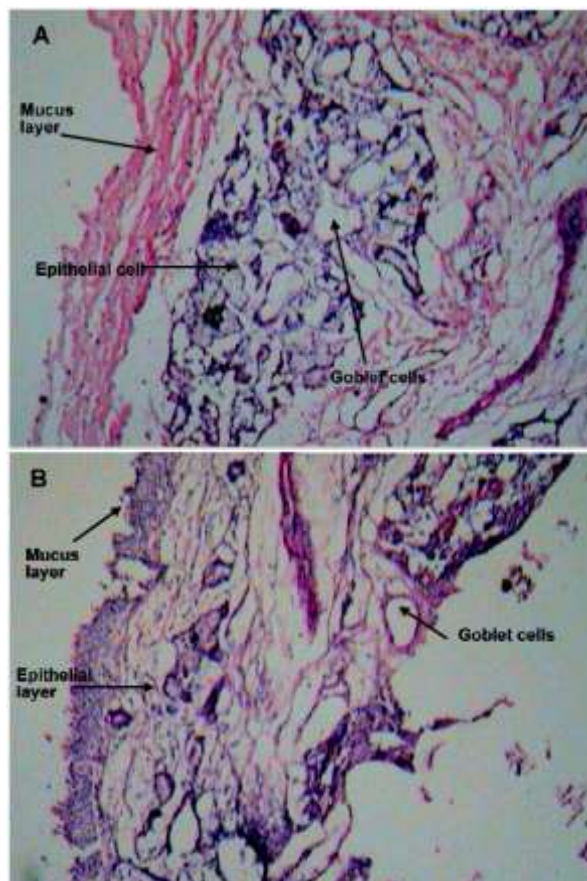
Figure 4. Histology evaluations of sections of sheep nasal mucosa. (A) Control mucosa; (B) Mucosa treated with microsphere formulation

4. CONCLUSION

The alginate microspheres can be prepared by emulsification-cross linking method with particle size range of 22.68 – 48.95 μm, which is favorable for intranasal absorption. These microspheres could be used to deliver nitrendipine following nasal administration to avoid first pass metabolism and to improve the therapeutic efficacy in the treatment of hypertension and angina pectoris.

5. REFERENCES

1.   Illum, L.   (2003). Nasal drug delivery-possibilities, problems and solutions. J. Controlled Rel., 87, 187–198.
2.   Sinha, V. R., Singla, A. K., Wadhawan, S., Kaushik, R., Kumria, R., Bansal, A. K., Dhawan, S. (2004). Chitosan microspheres as a potential carrier for drugs. Int. J. Pharm. 274, 1–33.
3.   Rang, H. P., Dale, M. M., Ritter, J. M., Moore, P. K. (2003). The vascular system. In: *Pharmacology*, 5th Edition, Churchil Livingstone, Edinburgh, pp-173-180.

4.   Rastogi, R., Sultana, Y., Aqil, M., Ali, A., Kumar, S., Chuttani, K., Mishra, A. K. (2007). Alginate microspheres of isoniazid for oral sustained drug delivery. Int. J. Pharm., 334, 71-77.

5.   Patil, S. B., Sawant, K. K. (2009). Development, optimization and in vitro evaluation of alginate mucoadhesive microspheres of carvedilol for nasal delivery. J. Microencapsul., 26(5), 432-443.

6.   Ranga Rao, K.V., Buri, P. (1989). A novel in situ method to test polymer and coated microparticles for bioadhesion. Int. J. Pharm., 52, 265–270.

7.   Patil, S. B., Murthy, R.S.R. (2006). Preparation and in vitro evaluation of mucoadhesive chitosan microspheres of amlodipine besylate for nasal administration. Ind. J. Pharm. Sci., 8, 64–67.

8.   Majithiya, R. J., Ghosh, P. K., Umrethia, M. L., Murthy, R. S. R. (2006). Thermoreversible-mucoadhesive gel for nasal delivery of sumatriptan. AAPS Pharm. Sci. Tech., 7(3), Article 67.

9.   Thanoo, B. C., Sunny, M. C., Jayakrishnan, A. (1992). Cross-linked chitosan microspheres: preparation and evaluation as a matrix for the controlled release of pharmaceuticals. J. Pharm. Pharmacol., 44, 283-286.

The Influence of Flame Retardant Material on the Mechanical Properties of Polylactic Acid/Kenaf/Polyethylene Glycol Green Biocomposite

Nur Faseha Shukor[1], Azman Hassan[2], Munirah Mokhtar[3]

[1]Enhanced Research Polymer Group, Universiti Teknologi Malaysia, Johor, Malaysia
[2]Research Management Centre, Universiti Teknologi Malaysia, Johor, Malaysia
[3] Enhanced Research Polymer Group, Universiti Teknologi Malaysia, Johor, Malaysia

*corresponding author: fasehashukor@gmail.com

Abstract: *This paper investigates and compares the performance of polylactic acid (PLA)/kenaf (K)/polyethylene glycol (PEG) composites and PLA/K/PEG/AP 760 (flame retardant) in terms of mechanical properties. Test specimens were prepared by dry blending, twin screw extrusion and compression molding. PEG in this study was used as a plasticizer in the composite. Mechanical testing was performed to determine the optimum blend ratio of PLA/K/PEG blend. All results were compared to a pure PLA matrix sample. The flexural strength and modulus of PLA/K/PEG composites decreased with increasing in PEG content while impact strength increased probably due to plasticization effect. When flame retardant was added to PLA/K/PEG composites, both flexural and impact strength of composites was decreased. This is due to poor compatibility of flame retardant and composite.*
Keywords : plasticizer, flame retardant

Introduction

or over 3000 years, natural fibers have been used as reinforcement to materials. Currently they have been employed in combination with plastics. Natural fiber reinforced composites is an emerging area in polymer science. There are many types of natural fibers that have been investigated for use in plastics including flax, hemp, jute, straw, wood fiber, rice husks, wheat, barley, oats, rye, cane (sugar and bamboo), grass reeds, kenaf, ramie, oil palm empty fruit bunch, sisal, coir, water hyacinth, pennywort, kapok, paper-mulberry, raphia, banana fiber, pineapple leaf fiber and papyrus. Composites are materials that comprise strong load carrying material (known as reinforcement) imbedded in weaker material (known as matrix). Reinforcement provides strength and rigidity, helping to support structural load. The matrix or binder (organic or inorganic) maintains the position and orientation of the reinforcement.

Sustainability, industrial ecology, eco-efficiency, and green chemistry are guiding the development of the next generation of materials, products, and processes. Using natural fibers with polymer based on renewable resources will allow many environmental issues to be solved. These natural fibers are low cost fibers with low density and high specific properties. These are biodegradable and non-abrasive. The natural fiber composites offer specific properties comparable to those of conventional fiber composites. Natural fibers, as reinforcement, attracted the attention of researches because of their advantages over other established materials. They are fully biodegradable, environmental friendly, abundantly available, renewable and cheap. By using biodegradable polymers as matrices, natural fiber-reinforced plastics are the most environmental friendly materials, which can be composed at the end of their life cycle.

The main target development of natural fiber reinforced green biocomposites is to achieve a good combination of properties and processability at a moderate cost as natural fibers has increasingly gained importance in the thermoplastic industry. Natural/biofiber composites (bio-composites) are emerging as a viable alternative to glass fiber reinforced

composites especially in automotive and building product applications. By embedding biofibers with renewable resource-based biopolymers such as cellulosic plastics; polylactides; starch plastics; polyhydroxyalkanoates (bacterial polyesters); and soy-based plastics, the so-called green biocomposites are continuously being developed [1].

Polylactic acid (PLA) is a rigid thermoplastic polymer that can be semicrystalline or totally amorphous, depending on the stereopurity of the polymer backbone. PLA is the first commodity polymer produced from annually renewable resources [2]. Some of the environmental benefits of PLA are low energy to produce and reduced green house gas production. PLA is a unique polymer that in many ways behaves like polyethylene terephthalate (PET), but also performs a lot like polypropylene (PP), a polyolefin. Ultimately it may be the polymer with the broadest range of applications because of its ability to be stress crystallized, thermally crystallized, impact modified, filled, copolymerized, and processed in most polymer processing equipment. It can be formed into transparent films, fibers, or injection molded into blowmoldable preforms for bottles, like PET. PLA also has excellent organoleptic characteristics and is excellent for food contact and related packaging applications.

A study conducted by Graupner et al. (2009) [3] describes the production and the mechanical characteristics of composites made completely of renewable raw materials. Various characteristics of composites with different kinds of natural fibers like hemp, kenaf, cotton and man-made cellulose fibers (Lyocell) were processed with a fiber mass proportion of 40% and PLA by compression molding. Additionally, composites were made of fiber mixtures (hemp/kenaf, hemp/Lyocell). All the composites were tested for tensile strength, elongation at break, Young's modulus and Charpy impact strength. The result showed that kenaf and hemp/PLA composites had very high tensile strength and Young's modulus while cotton/PLA showed good impact resistance. Lyocell/PLA composites showed high tensile strength and Young's modulus with high impact strength. These results varied markedly depending on the characteristics of the raw fibers and fiber bundles and fiber mixtures used.

During the period up to about 1970-1980, the established durable and flame retardant treatments for cotton and wool fibres as well as those additives and comonomers introduced into both regenerated (e.g. viscose) and synthetic (notably polyester, polypropylene and the modacrylics) fibres during manufacture were synthesized and developed into commercially-acceptable products [4]. Flame retardants have been used in polymers to reduce the flammability of plastics, building materials, fabric and papers. In recent years, organophosphate flame retardants were used as substitutes for Brominated Flame Retardants [5].

Therefore, this paper will focus on investigation of PLA/K/PEG and PLA/K/PEG/AP 760 composites and compares them on mechanical properties.

Experimental

Materials

The matrix polymer that has been used in this study was polylactic acid (PLA) from grade 3001D from NatureWorks, USA (bulk density: 1.24 g/cc). The kenaf core fiber (K) that was approximately 2mm in size was obtained from Innovative Pultrusion Sdn,Bhd and were no chemically treated prior to processing. In this study, polyethylene glycol (PEG) was added in the composite formulations to plasticize PLA. PEG (PEG 600) with a weight-average M_w 600

g/mol, density of 1.126 g/cm^3 from Acros Organics, Belgium. Flame retardant used in this study was Exolit AP 760 from Carliant.

Melt compounding of the composite

Before melt compounding process, PLA, PEG, K and AP 760 were mixed in a high speed rotor mixer for 15 minutes to achieve homogeneous mixing. Melt compounding of the composites was done in a laboratory-size, counter-rotating twin-screw extruder (Brabender Plasticoder PL 2000, Germany), with a screw speed of 50rpm and temperature zones were fixed at 180, 190, 200, 210°C. The K and PEG content was fixed at 25wt% and 15wt% respectively while for AP 760, the flame retardant content varied from 0 to 20 phr. Composites were pelletized for further compression molding in order to prepare samples for characterization. Flexural and impact test specimens were prepared by hot press process. The material was preheated for 3 minutes at 190°C followed by compressing at the same temperature for another 6 minutes and lastly cooling down to room temperature under pressure by using water cooling machine.

Flexural Test

The flexural test was conducted according to the ASTM D790 standard test method by using the Instron machine model 5567. The samples were tested under a crosshead speed of 3mm/min and the support span for flexural testing was 50 mm. The result values for flexural strength and flexural modulus was determined from the average of seven specimens.

Izod Impact Test

The Izod impact strength was measured under the ASTM D256 standard test method. The Izod Impact Test was carried out at room temperature. The purpose of this testing was to determine the pendulum impact resistance of notched specimen of plastic. The thickness of each sample was determined and the impact strength reported was the average of ten specimens.

Results and Discussion

Mechanical Testing of PLA/K/PEG composites

Figure 1 and Table 1 shows the mechanical properties for pure PLA and PLA/K/PEG composites. It is clear from Figure 1 (a) that the addition of plasticizer into pure PLA and PLA/K resulted in a significant decrease in flexural strength. This decrease is probably due to the presence of PEG as plasticizer that somehow interferes the interaction between PLA and K in the composites. Similar observation was reported by Oksman et al. [6] who attributed the decrease in tensile stress as well as modulus was due to the effect of triacetin as plasticizer.

As shown in Figure 1 (b), addition of kenaf fiber in PLA resulted in higher flexural modulus. The increment of flexural modulus with the addition of natural fiber was expected since a stiffer material is introduced into the polymer matrix [7]. It can be seen that the flexural modulus of composites is insignificant decreased when PEG content increased. This is because of the plasticization effect.

Figure 1 (c) shows that improvement in impact strength when the amount of PEG added increased. The composite contains 15wt% PEG was selected for further analysis because in our preliminary study showed that this formulation has the optimum properties.
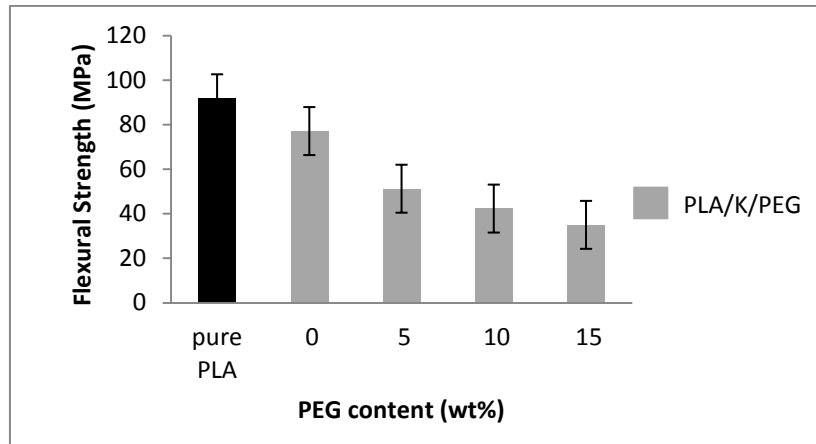
(a)
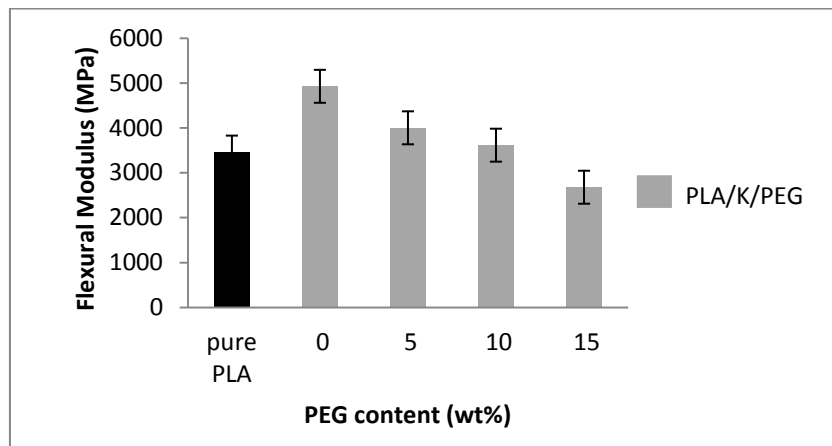
(b)
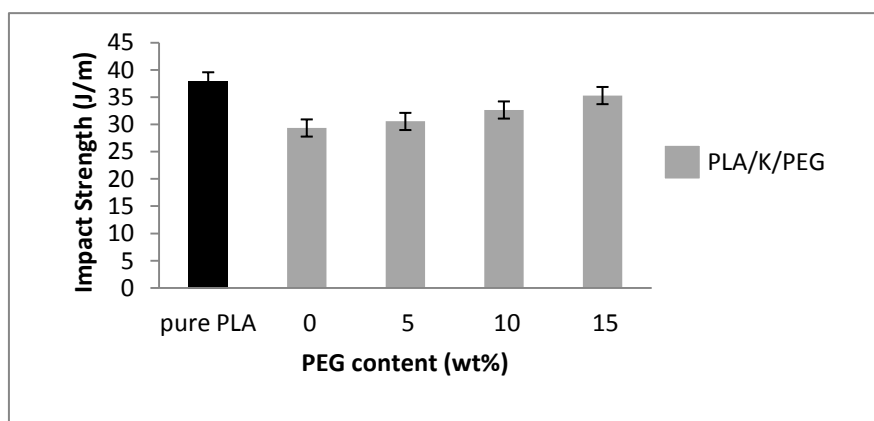
(c)

Figure 1 – (a) flexural strength, (b) flexural modulus, and (c) impact strength of pure PLA and PLA/K/PEG composites at various PEG contents.

Mechanical Testing of PLA/K/PEG/AP 760 green biocomposites

In this second study, the (K) and PEG content were fixed at 25 wt% and 15wt% respectively. Figure 2 (a) shows the addition of flame retardant decreased the flexural strength of PLA/K/PEG/AP 760 biocomposites. The decrease in flexural modulus suggests that PLA/K/PEG and AP 760 are not compatible due to poor interfacial interaction between the two components. Similar reason can be applied to explain the decrease in impact strength of the composite (Figure 2 (c)).

However, addition of AP 760 causes only a slight decrease in flexural strength (Figure 2 (a)). It shows that addition of AP 760 does not affect the strength of the composite at all. Deterioration of the mechanical properties of polymer composites with the addition of flame retardant were also reported by other researcher group [8,9].
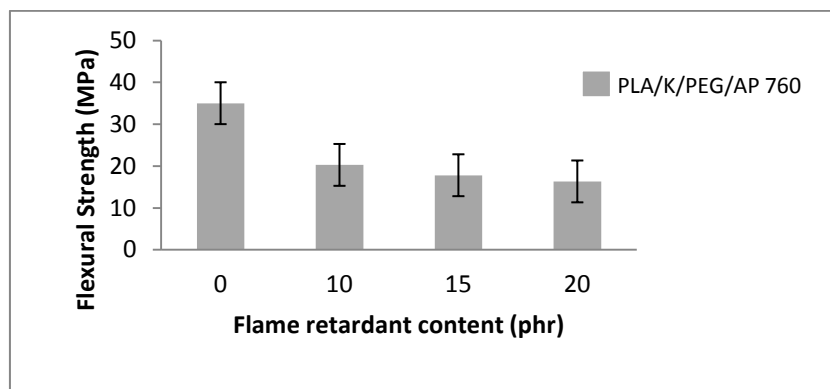
(a)
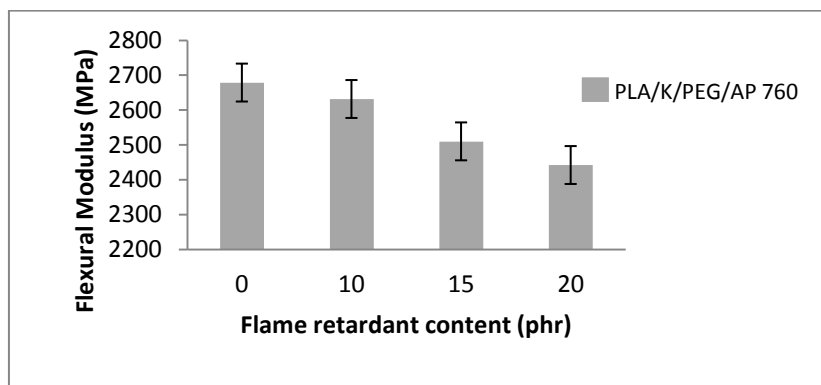
(b)
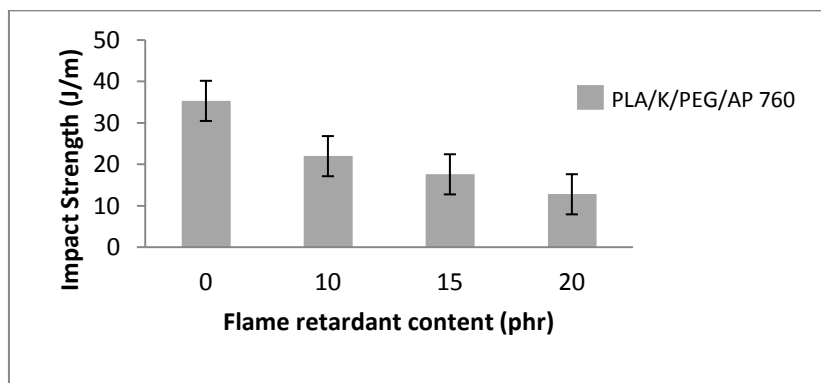
(c)

Figure 2 – (a) flexural strength, (b) flexural modulus, and (c) impact strength of PLA/K/PEG/AP 760 green biocomposites at various flame retardant contents.

Summary of mechanical properties of PLA/K/PEG and PLA/K/PEG/AP 760 green biocomposites

Table 1 Mechanical properties of PLA and its composites

Materials	Flexural Modulus (GPa)	Flexural Strength (MPa)	Impact Strength (J/m)
PLA	3.50±0.20	92±1.25	38.09±8.35
PLA/K/PEG			
i) 0 wt% PEG	4.90±0.30	77±2.81	29.36±4.38
ii)5 wt% PEG	4.00±0.40	51±2.76	30.56±1.21
iii)10wt% PEG	3.62±0.60	42±2.61	32.66±1.14
iv)15wt% PEG	2.68±0.90	35±1.76	35.31±1.98
PLA/K/PEG/AP 760			
i) 0 phr AP 760	2.68±0.90	35±1.76	35.31±1.98
ii)10 phr AP 760	2.63±1.00	20.3±3.38	21.98±3.12
iii)15 phr AP 760	2.51±0.57	17.8±2.33	17.60±2.75
iv)20 phr AP 760	2.44±0.86	16.3±3.30	12.79±4.37

Conclusions

The results of this study could be summarized as follows:

The flexural strength and modulus of plasticized PLA/K composites decreased with increasing of PEG content. PLA is compatible and can interact with K. The presence of PEG as plasticizer might have disturbed the fiber-matrix interaction in the PLA/K/PEG composites. However, the presence of PEG had slightly improved the impact strength of the composites due to the effect of plasticization.

Adding flame retardant material into PLA/K/PEG composites has reduced the mechanical properties of the composites in terms of strength and modulus. This is because of poor compatibility between the added flame retardant and composites.

References

1. Masud S.Huda, Lawrence T.Drzal, Amar K.Mohanty, Manjusri Misra (2008). Effect of fiber surface treatments on the properties of laminated biocomposites from poly(lactic) acid (PLA) and kenaf fibers. Composites Science and Technology 68:424-432.

2. David E.Henton, Patrick Gubber, Jim Lunt, Jed Randall (2005). Polylactic Acid Technology. Book ofNatural Fiber, biopolymers, and biocomposites, Chapter 16:527-578.

3. Nina Graupner, Axel S.Herrmann, Jorg Mussig (2009). Natural and man-made cellulose fiber reinforced polylactic acid (PLA) composites: An overview about

mechanical characteristics and application areas. Composites:Part A 40:810-821.

4. A.Richard Horrocks (2011). Flame retardant challenges for textile and fibers: New chemistry versus innovatory solutions. Polymer Degradation and Stability 96:377-392.

5. Y.ni, K.Kumagai, and Y.Yanagisawa. Optimum Additive Level of Organophosphate Flame Retardants in Materials.

6. K. Oksman, M.Skifvars, J.-F. Selin (2003). Natural fibers as reinforcement in polylactic acid (PLA) composites. Composites Science and Technology 63:1317-1324

7. Zampaloni M, Pourboghrat F, Yankovich SA, Redgers BN, Moore J, Drzal LT, Mohanty AK, Misra M (2007). Kenaf natural fiber reinforced polypropylene composites: a discussion on manufacturing problems and solutions. Composites A 38(6):1569-1580.

8. M. Sain, S.H Park, F. Suhara, S.Law (2004). Flame Retardant and Mechanical Properties of Natural Fiber-PP Composites containing Magnesium Hydroxide. Polymer Degradation and Stability 83:363-367.

9. Nittinat Suppakarn, Kasama Jarukumjorn (2009). Mechanical properties and flammability of sisal/PP composites: Effect of flame retardant type and content. Composites B 40:613-618.

Structural Studies of GaN-nanowires Grown at Different Ammonia Flow Rate

K.P. Beh*, F.K. Yam, L.L. Low, Z. Hassan

Nano-Optoelectronics Research and Technology Laboratory, School of Physics,
Universiti Sains Malaysia, Penang, Malaysia

*Corresponding author. E-mail address: kpbeh@hotmail.com

Abstract*: Gallium nitride (GaN) nanowires were grown iron coated sapphire substrates using chemical vapour deposition method. The nanowires have diameter ranging from 40nm to 440nm and length up to several ten of microns. The diameter distribution of the nanowires was affected by the flow rate of ammonia, with lower flow rate yielding greater diameter. The N/Ga ratio obtained from energy dispersive x-rays decreased with increasing ammonia flow. X-ray diffractometry revealed hexagonal wurtzite GaN, in addition to several peaks belonged to iron-related compounds. Immersion of GaN in sulphuric acid bath removed such compounds.*
Keywords: Gallium nitride; Nanowires; Structural properties; Morphology; X-ray diffraction

1.   INTRODUCTION

Gallium nitride (GaN) is a wide bandgap semiconductor material used in variety of applications such as optoelectronics, high-powered electronics, and biosensing circuits. In optoelectronics applications, GaN, with bandgap of 3.4eV, is useful in fabricating ultra-violet (UV) based lighting and photosensing devices. [1].

Low dimensional (LD) semiconductor material such as nanodots (0D), nanowires (1D), and nanoribbons (2D) gained much attention as they have unique properties which make them superior compared to their bulk counterparts. With the reduction in terms of sizes these LD materials can be used as building blocks for more complex devices [2, 3].

One of the widely studied LD semiconductor materials is GaN nanowires. GaN nanowires have unique properties that excelled in optoelectronics field compared to its bulk counterparts. GaN nanowires possessed lower dislocation defects which enable the production of high quality optoelectronics devices. GaN nanowires based rectifiers, LEDs, and photodetectors have been made and exhibited superior performance [4-6].

GaN nanowires can be fabricated using chemical vapour deposition (CVD) method. The growth of GaN was made simple by using vapour-liquid-solid (VLS) mechanism. Such growth requires metal-catalyst that acted as nucleation sites for nanowires growth. Commonly used metal-catalysts are Au, Fe, and Ni [6-11]. CVD growth of GaN nanowires has allowed high quality and purity nanowires to be grown by varying parameters such as temperature, precursor flow rate, and growth duration [7, 8, 11]. One of the essential precursors that commonly used is ammonia. Ammonia, when heated at elevated temperature, dissociated into active nitrogen species that will react with gallium precursor to form GaN [1, 2, 11, 12]. Being a key component in producing GaN, it is essential that ammonia requires optimum control in order to produce high quality GaN. As ammonia exists in gaseous form, the flow rate of ammonia is an important parameter for researchers to consider.

In this work, the growth of GaN nanowires was done using CVD method. Fe-catalyst was used to promote VLS growth of the nanowires. The flow rate of ammonia was varied in

order to investigate the growth effects. Post treatment of GaN nanowires was done by immersing it in acidic bath. The effects of such process were investigated.

2. EXPERIMENTAL DETAILS

2.1 Deposition of Fe-catalyst

A 3-inch in diameter sapphire substrate was cleaned sonically in alcohol solution. Next, the deposition of Fe-catalyst on the substrate was done using a vacuum thermal evaporation system (Edwards, Auto 306). The chamber was pumped down to 7.5×10^{-4} mbar prior deposition. Fe_2O_3 powder was used as the precursor for Fe-catalyst. As the current ramped up, the Fe_2O_3 powder decomposed, leaving Fe deposited on the substrate. The substrate was taken out after venting the chamber.

2.2 Growth of GaN nanowires

The Fe-coated sapphire was cleaved into square pieces with length of 6.35mm. A 3-zone horizontal tube furnace was ramped to 1050˚C initially, after that the zone that near the gas input was further ramped up to 1100˚C. Gallium oxide powder (Sigma Aldrich, 99.98%, Ga_2O_3) was used as the gallium precursor while ammonia gas (NH_3, MOX, 99.98%) was used as the nitrogen precursor. In this work, the flow rate of NH_3 was set to be at 250, 150, and 100 sccm, the designation for these samples will be S1, S2, and S3 respectively. The Fe-coated sapphire substrates and Ga_2O_3 powder was placed in an alumina boat and placed downstream in the 1050˚C zone. NH_3 gas was introduced into the furnace gradually and the process lasted for 30 minutes. After that N_2 gas was used to purge the system and the alumina boat was removed from the furnace. A yellowish powdered film was observed on the substrate. Sample S1 were immersed in 4.3M H_2SO_4 for 5 and 20 minutes (denoted as S1#05 and S1#20 respectively) to remove the Fe-catalyst.

2.3 Characterizations

The morphological aspects of the samples were screened using scanning electron microscopy (SEM), while the elemental compositions of the samples were determined using energy dispersive x-ray (EDX) method. The structural aspects of the samples were characterized using high resolution x-ray diffractometry (HR-XRD).

3. RESULTS AND DISCUSSIONS

The growth of GaN nanowires was based on catalytic growth, hence VLS mechanism. Several reactions occurred during growth. Upon heating the substrate, the iron film breaks down into minute droplet, which acted as nucleation sites for nanowires growth. Ammonia gas, upon heated at 1050˚C, dissociated into hydrogen and active nitrogen species [2].

$$2NH_3(g) \rightarrow 3H_2(g) + N_2(g) \qquad (1)$$

The generated hydrogen served as a reduction agent for Ga_2O_3. The reduction of Ga_2O_3 yield Gallium (I) oxide (Ga_2O) vapour, which will be absorbed by the iron droplets. Since ammonia gas was introduced into the growth chamber continuously, un-dissociated ammonia, as well as excess hydrogen and active nitrogen species were present. Ga_2O vapour that absorbed by the iron droplets could be reduced further into its constituent element. Hence, iron-gallium alloy was generated. Further absorption of such species as well as active nitrogen into the droplet will yield Fe-Ga-N alloy. When the droplet was saturated, GaN will precipitate out of the droplet. The precipitated GaN will present itself in the form of a wire, thus GaN nanowires

were formed. Eq. (2) and Eq. (3) showed the involved chemical reaction occurred in the formation of GaN nanowires.

$$Ga_2O_3(s) + 2H_2(g) \rightarrow Ga_2O(g) + 2H_2O(g) \qquad (2)$$

$$Ga_2O(g) + 2H_2(g) + N_2(g) \rightarrow 2GaN(s) + 2H_2O(g) \qquad (3)$$
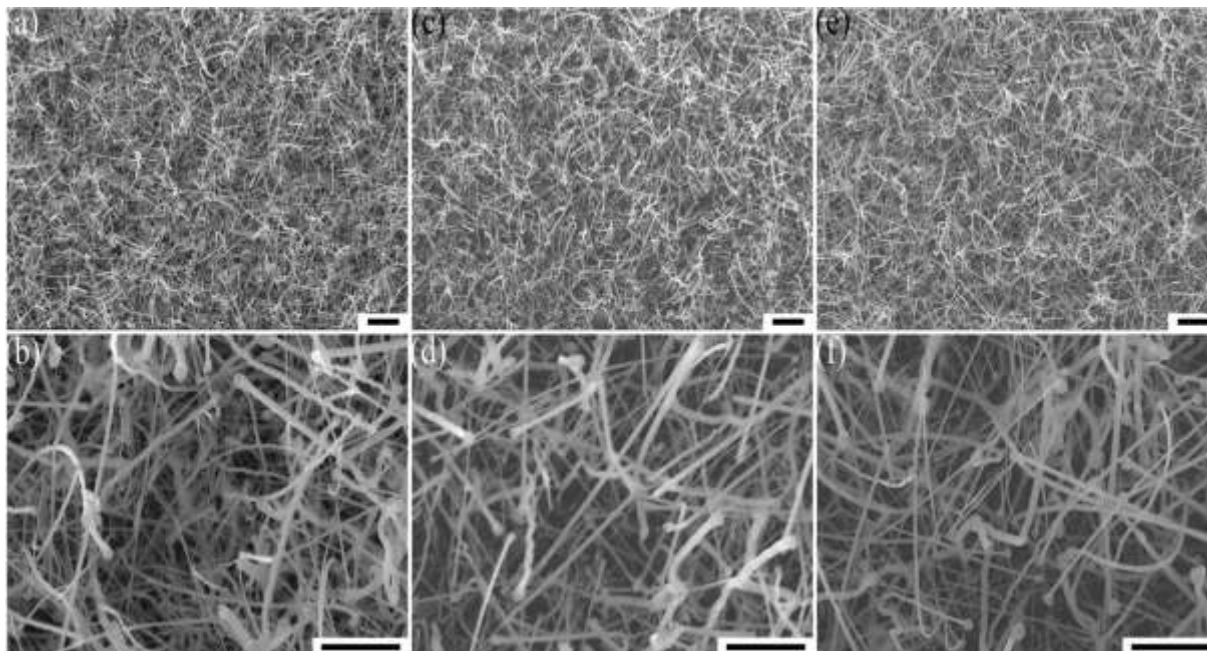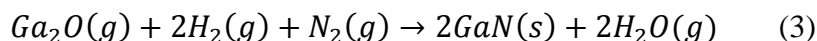
Fig. 1: SEM images of GaN nanowires. Sample S1 is Fig. 1(a, b); Sample S2 is Fig. 1(c, d); Sample S3 is Fig. 1(e, f). The scale bar for Fig. 1(a, c, d) is 10μm, while that of Fig. 1(b, d, f) is 5μm.

The surface morphologies of the GaN nanowires were shown in Fig. 1. It is discernable that the surface of the substrates was covered with densely packed GaN nanowires. The length of the nanowires was several tens of microns, while that of diameter were widely distributed. In sample S1, nanowires with diameter ranging from 65.8nm to 250nm could be observed. Majority of the nanowires in S1 have diameter ranged from 100nm to 200nm. For sample S2, the number of nanowires with diameter less than 100nm was less observed, with majority of the nanowires having diameter greater than 160nm. The diameter distribution for sample S3 was nearly identical to S2, but the number of large nanowires (~200nm to 500nm) could be observed. Some of the larger nanowires were straight, while some have jagged segments, suggesting the presence of strain during growth.

The large distribution in terms of diameter observed in all samples may due to the state of the catalyst during growth. As iron-gallium eutectic alloy were formed, some of these droplets coalesced into larger droplets, which also obeyed the VLS mechanism, thus larger nanowires were grown. In addition, such distribution was obtained under different ammonia flow, which suggested that the size of the nanowires can be manipulated by varying the flow. A plausible reasoning would be the interaction of ammonia towards both catalyst and gallium source. As more ammonia was introduced into the growth chamber, large amount of Ga_2O was generated, subsequently alloyed with iron to become iron-gallium eutectic alloy. The alloy can be saturated at a higher rate when more ammonia was introduced, thus reducing the probability of alloy droplets coalesced together.
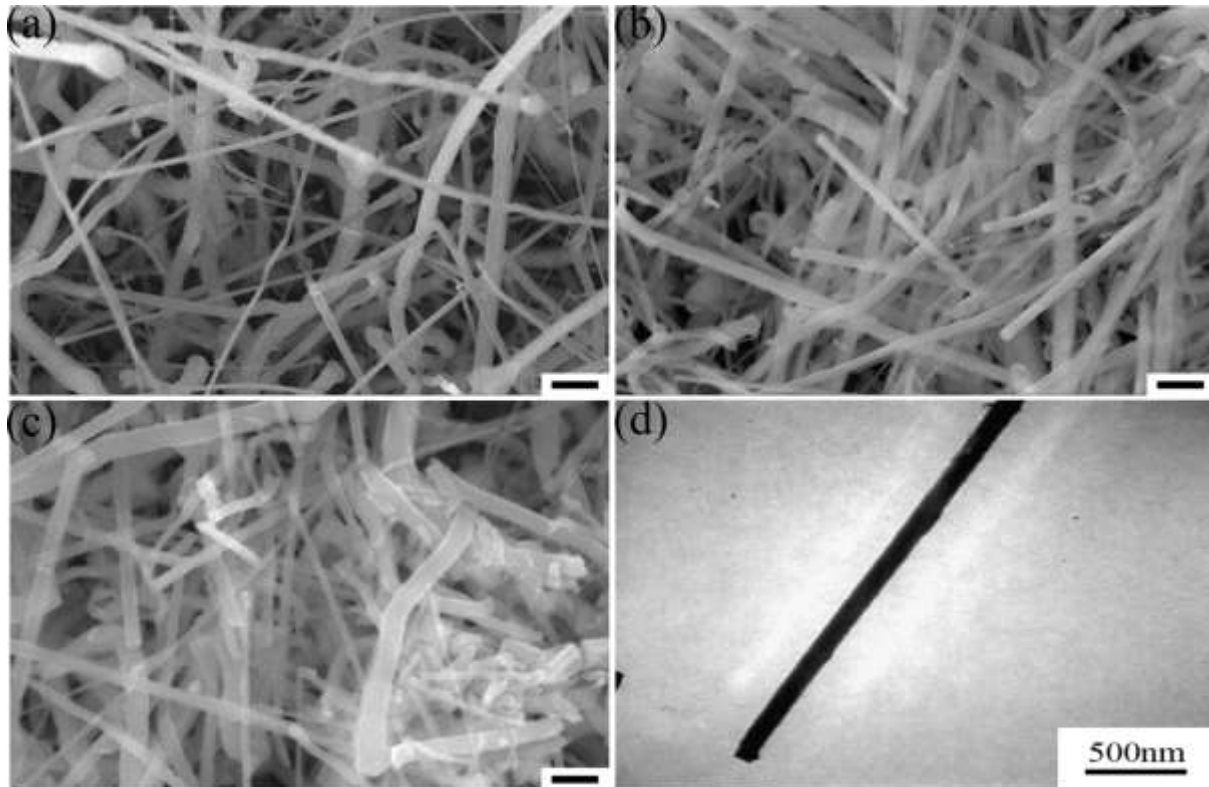
Fig. 2: Micrographs of S1 (a) untreated, (b) immersed in H_2SO_4 for 5 minutes (S1#05), (c) immersed in H_2SO_4 for 20 minutes (S1#20), (d) TEM image of S1#05. The scale bar in (a, b, c) is 1μm.

One notable feature observed in the GaN nanowires in Fig. 1 was each end of the nanowires was terminated by a droplet, which was the catalyst. Sample S1 was chosen for further treatment, i.e. by immersing it in H_2SO_4 in order to remove the catalyst head. In Fig. 2, the catalyst droplet was absent, suggesting the catalyst is vulnerable to acidic etch. However, in Fig. 2(b), remnants of the catalyst could still be observed in larger nanowires, although absent in smaller nanowires. The removal of the residue iron catalyst would require more time. In addition, Fig. 2(d) shows TEM image of the treated nanowire (S1#05). The catalyst droplet was absent and the interior was solid, which signifies such growth produced nanowires rather than nanotubes.
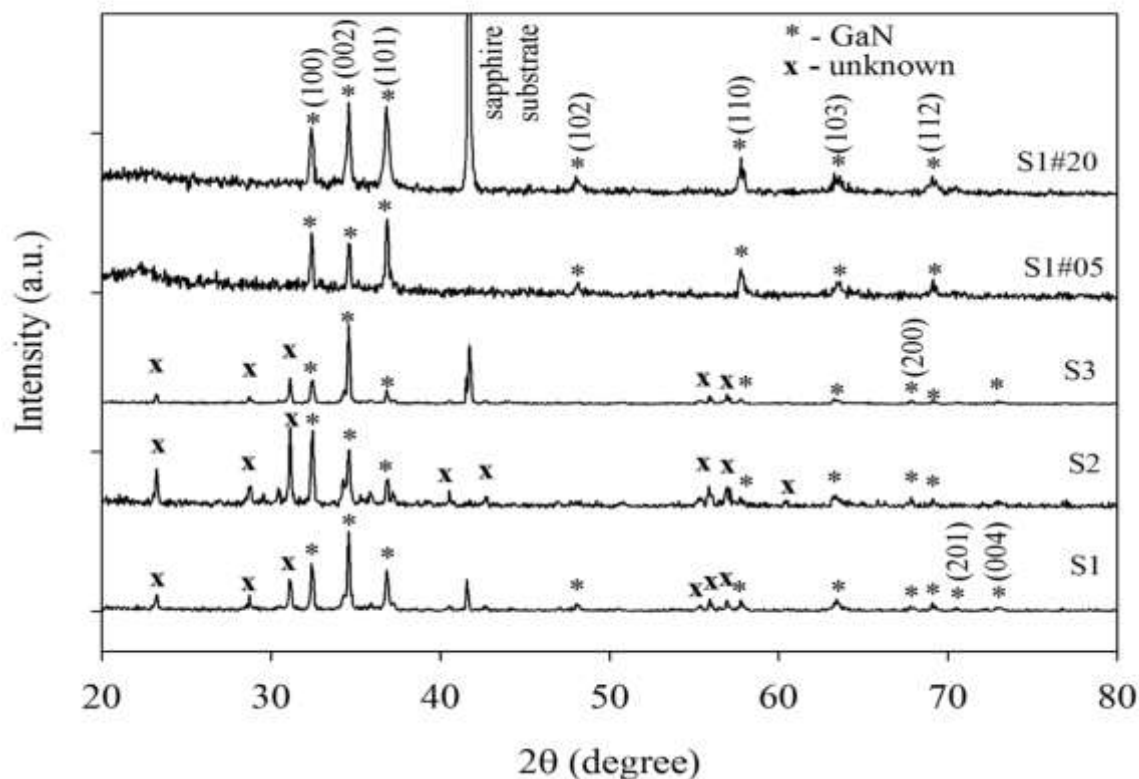
Fig. 3: XRD patterns of the GaN nanowires.

The structural properties of the GaN nanowires were assessed by x-ray diffraction method, with the results displayed in Fig. 3. From the patterns, the obtained GaN nanowires have hexagonal wurzite structure. For sample S1, S2, and S3, additional peaks that don't belong to GaN appeared. It is possible that those peaks were contributed by the catalyst and its related compound, since iron can undergo oxidation and nitridation process during growth besides alloying with gallium. However, since these iron-related compounds exhibit polymorphism, in addition having different oxidation state, the "unknown" peaks marked in Fig. 3 would be difficult to be indexed. When sample S1 is immersed in H_2SO_4, those "unknown" peaks become absent for sample S1#05 and S1#20. Thus it is highly probable that the unknown peaks were attributed to the iron-related compound, since such compound is vulnerable towards H_2SO_4. In addition, this also displayed the chemical resistance of GaN nanowires. The absence of the additional peaks would not indicate all iron-related compounds were consumed by H_2SO_4, as the sensitivity of the measuring instrument would have to be accounted for.

Additional information about the GaN nanowires was obtained from Fig. 3 using suitable equations [13, 14]. One important aspect would be the lattice constant (c and a for hexagonal wurtzite GaN). All samples have similar c and a, i.e. 5.184Å and 3.191Å respectively. These values were in consistent with those reported in the literature [6]. In addition the grain size of the GaN nanowires was calculated using Scherrer's equation. The grain size for the untreated GaN was 41.58nm, while that of treated GaN was 33.28nm. Although the grain size was reduced, which would suggest defects generated within GaN nanowires during immersion in H_2SO_4, it displayed time-independent behavior in this study. One plausible reason for the reduction of grain size would be the tip of the nanowires experienced stress relieve as the catalyst droplet being dissolved.

571
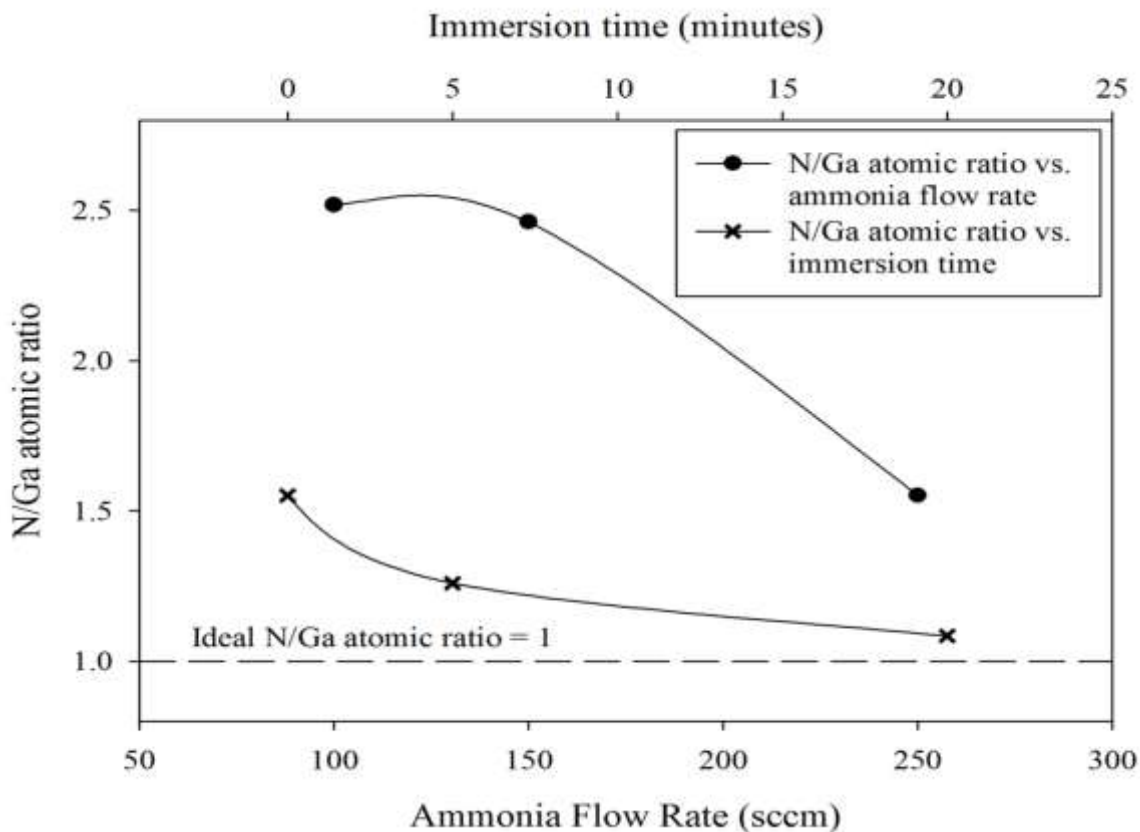
Fig. 4: EDX analysis of the GaN nanowires.

EDX method was used to determine the composition of elements present in a sample. In this work, the atomic composition of nitrogen and gallium were studied. The study of atomic ratio of nitrogen to gallium derived from EDX analysis towards the effects of ammonia flow rate and H_2SO_4 immersion time was displayed in Fig. 4. When the N/Ga atomic ratio was plotted against ammonia flow rate, it is discernable that the ratio decreased when more ammonia was introduced into the growth chamber. The larger N/Ga ratio signified that less Ga_2O_3 reacted with ammonia and its dissociated species as indicated in Eq. (2, 3). The excess amount nitrogen species would have reacted with the catalyst, thus the appearance of addition peaks in Fig. 3. It is desired that the ideal N/Ga atomic ratio valued at 1 (unity), which attributed to perfect GaN crystal. However, due to the presence of native defects and other un-accounted growth parameters, it is rather difficult to obtain unity N/Ga atomic ratio.

The immersion of GaN nanowires in H_2SO_4 at different time resulted in the decrease of N/Ga atomic ratio, with that valued 1.08 for sample S1#20. This method revealed that by removing other impurities present in GaN nanowire, a more precise N/Ga ratio could be determined. However, the N/Ga atomic ratio for sample S1#20 still greater than unity, in addition residual iron was detected by EDX. Thus, the excess nitrogen may have reacted with iron. Nevertheless, the immersion of GaN in H_2SO_4 would yield higher purity.

4.   CONCLUSION

The study of the morphological and structural properties of GaN under different ammonia flow rate and its post-treatment effects were done. Smaller diameter of GaN

nanowires were obtained in higher ammonia flow. When immersed in H_2SO_4, the catalyst droplet at the end of the nanowires dissolved away. This is in consistent with the XRD patterns, where only GaN peaks were detected. In addition, XRD patterns revealed the obtained GaN nanowires were hexagonal wurtzite in structure. There was a reduction in grain size for the treated GaN nanowires. The N/Ga atomic ratio decreased with increasing ammonia flow rate as well as immersion time.

ACKNOWLEDGEMENT

REFERENCES

1. Feng Zhe Chuan (2008). *III-Nitride Devices and Nanoengineering.* London: Imperial College Press.
2. Rao C.N.R., Deepak F.L., Gundiah Gautam, Govindaraj A. (2003). Inorganic nanowires. *Prog. Solid State Ch.*, 31, 5-147.
3. Grace Lu Jia, Chang Paichun, Fan Zhiyong (2006). Quasi-one-dimensional metal oxide materials – Synthesis, properties and applications. *Mat. Sci. Eng. R*, 52, 49-91.
4. Zhong Zhaohui, Qian Fang, Wang Deli, Lieber Charles M. (2003). Synthesis of p-Type Gallium Nitride nanowires for electronic and photonic nanodevices. *Nano Lett.*, Vol. 3, No. 3, 343-346.
5. Lee Jae-Woong, Moon Ju-Kyeong, Ham Moon-Ho, Myoung Jae-Min (2008). Dieletrophoretic assembly of GaN nanowires for UV sensor applications. *Solid State Commun.*, 148, 194-198.
6. Stern E. et al. (2005). Electrical characterization of single GaN nanowires. *Nanotechnology*, 16, 2941-2953.
7. Low L.L., Yam F.K., Beh K.P., Hassan Z. (2011). The influence of Ga source and substrate position on the growth of low dimensional GaN wires by chemical vapour deposition. *Appl. Surf. Sci.*, 257, 10052-10055.
8. Low L.L., Yam F.K., Beh K.P., Hassan Z. (2011). The influence of growth temperatures on the characteristics of GaN nanowires. *Appl. Surf. Sci.*, 258, 542-546.
9. Wang Ying, Xue Chengshan, Zhuang Huizhao, Wang Zouping, Zhang Dongdong, Huang Yinglong, Liu Wenjun (2009). Synthesis and characterization of GaN nanowires. *Appl. Surf. Sci.*, 255, 7719-7722.
10. Gottschalch V., Wagner G., Bauer J., Paetzelt H., Shimow M. (2008). VLS growth of GaN nanowires on various substrates. *J. Cryst. Growth*, 310, 5123-5128.
11. Cai X.M., Djurišić A.B., Xie M.H. (2006). GaN nanowires: CVD synthesis and properties. *Thin Solid Films*, 515, 984-989.
12. He Maoqi, Zhou Peizhen, Noor Mohammad S., Harris Garry L., Halpern Joshua B., Jacobs Randy, Sarney Wendy L., Salamanca-Riba Lourdes (2001). Growth of GaN nanowires by direct reaction of Ga with NH_3. *J. Cryst. Growth*, 231, 357-365.

13. Cullity B.D. (1956). *Elements of X-ray Diffraction*. United States of America: Addison-Wesley Publishing Company Inc.

14. Yam F.K., Hassan Z. (2008). InGaN: An overview of the growth kinetics, physical properties and emission mechanism. *Superlattice Microst.*, 43, 1-23.

The Optical Characteristics of N:TiO$_2$ Thin Film Synthesized via Simple Chemical Vapour Deposition Route

S.W. Ng*, F.K. Yam, S.S. Tneh, Z. Hassan

Nano-Optoelectronics Research and Technology Laboratory, School of Physics, Universiti Sains Malaysia, 11800 Penang, Malaysia

*Corresponding author: sw.ng@live.com

Abstract: *In this work, we present the study of optical characteristics of nitrogen doped titanium dioxide (N:TiO$_2$) thin film. N:TiO$_2$ thin film has been synthesized on glass substrate via atmospheric pressure chemical vapour deposition (AP-CVD) by using titanium tetrachloride (TiCl$_4$) as precursor. Semi-transparent yellowish surface could be observed on the sample. X-ray diffraction measurement shows that the sample consists of anatase crystalline phase. The optical properties were determined by spectrophotometer measurement in ultraviolet-visible wavelength region under transmittance mode. Swanepoel's envelope method was employed to evaluate the optical constants of N:TiO$_2$ thin film and optical band gap was determined through Tauc plot.*

Keywords: nitrogen doped titanium dioxide; thin film; atmospheric pressure chemical vapour deposition; Swanepoel's envelope method; optical characteristics

1. INTRODUCTION

Titanium dioxide (TiO$_2$) is a wide band gap semiconductor with unique photocatalytic properties and high potential in water splitting applications. TiO$_2$ is favourable in optical devices due to their good transmittance in visible region, high refractive index and good chemical stability. Hence TiO$_2$ is one of the most widely studied transition metal oxides in recent years [1-3].

Photocatalytic activity of a material is affected by electron-hole pair lifetime, electron mobility, surface area and the band gap of the material. The band gap of TiO$_2$ depends on its crystalline phases, anatase at 3.2eV and rutile at 3.0eV. Despite the band gap of anatase is larger, photocatalytic activity of TiO$_2$ anatase phase is reported to be higher than its rutile phase. Hence efforts have been made to decrease the band gap energy of TiO$_2$ through metal or non-metal doping [3-6].

TiO$_2$ exists in several forms such as powder, thin film and nanostructures. However various physical characterizations are difficult to be carried out on powder based sample, whereas for nanostructured TiO$_2$, homogeneity and surface roughness of the sample have to be considered. Therefore thin film is a preferable choice in optical investigations [1,7-8].

Several commonly reported methods of deposition of TiO$_2$ thin film are sol-gel, anodization, direct current (DC) magnetron sputtering, radio frequency (RF) magnetron sputtering, electron beam evaporation and chemical vapour deposition (CVD)[1, 5-6, 8-9]. In this work, we employed a simple CVD method which features low cost and simple experimental setup. Atmospheric pressure and air which acted as carrier gas was utilized to deposit TiO$_2$ thin film together with nitrogen doping on glass substrate in a short duration and low substrate temperature.

2. EXPERIMENTAL DETAILS

2.1 Fabrication of N:TiO$_2$ Thin Film

CVD chamber was pre-heated to less than 500°C for 1 hr to remove any possible contaminant in the chamber. Glass substrate was pre-cleaned with ethanol and was rinsed with deionized (DI) water to remove the organic residue. The substrate was then placed in the chamber and was left to achieve thermal equilibrium with the chamber. Titanium tetrachloride (TiCl$_4$) and ammonium acetate (CH$_3$COONH$_4$) of 1:1 volume ratio were used as precursor for titanium (Ti) and nitrogen (N) dopant, respectively. Horizontal laminar flow of air at controlled humidity of 80-90% was acted as carrier gas. The deposition process was done in atmospheric pressure for less than 1 min. After the process, the sample was cooled to room temperature and rinsed with DI water.

2.2 Characterization of N:TiO$_2$ Thin Film

The crystal structure of the as deposited N:TiO$_2$ thin film was determined by High-resolution X-ray diffractometer (HRXRD) (PANalytical X'Pert PRO MRD PW3040). The settings were 40 kV, 30 mA with CuK$_{\alpha 1}$ radiation of wavelength 0.154 nm. The surface morphology and elemental analysis were done by scanning electron microscopy (SEM) (Jeol JSM-6460/LV) and energy dispersive X-ray spectroscopy (EDX) attached to SEM, respectively. Optical properties of the sample were characterized by ultraviolet-visible spectrophotometer (U-2000 Hitachi).

3. RESULTS AND DISCUSSION

3.1 Structural and Surface Morphology

The as-synthesized N:TiO$_2$ sample is yellowish semi-transparent as observed by naked eye. This observation agrees with the N doped TiO$_2$ thin film or nanostructured samples obtained by other researchers. TiO$_2$ thin film is supposed to be transparent or opaque white in colour according to several reports. Further, the increase of colour intensity signifies the increase of doping intensity because the colour of a solid is determined by the position of its absorption edge [5]. Herein our sample on transparent glass substrate has transformed into yellowish colour as shown in Fig. 1 (a).
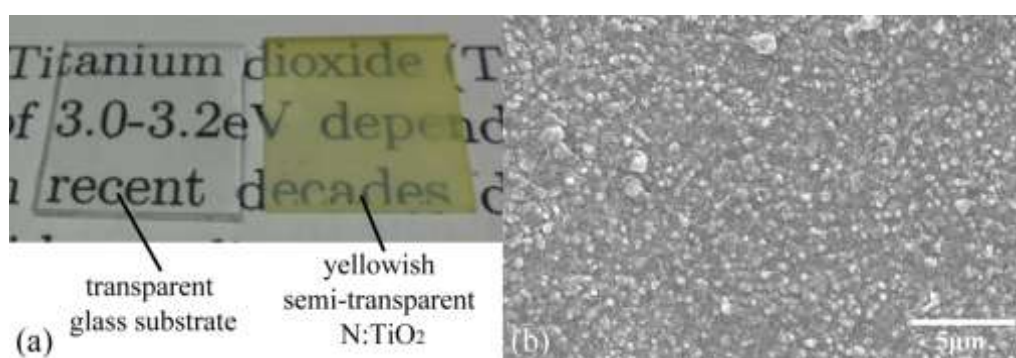
Fig. 1 (a) Comparison of transparent glass substrate with as-synthesized N:TiO$_2$ (b) SEM image of homogeneous surface of as-synthesized N:TiO$_2$

However it is of our interest to look at the sample surface in microscopic scale. A homogeneous surface on the entire as-synthesized N:TiO$_2$ is displayed in Fig. 1(b) and the elements exist on the sample is shown in table 1. From the analysis, it is observed that the

sample contained of rich Ti and O element which could possibly be TiO_2. The tiny amount of Cl could be originated from $TiCl_4$ precursor used during the deposition process and the presence of Si is due to the nature of glass substrate. In additional, no trace of N indicates that the sample was appropriately doped.

Table 1 EDX analysis of N:TiO_2

Element	Atomic Percentage (%)
Titanium (Ti)	35.08
Oxygen (O)	62.84
Chlorine (Cl)	0.60
Silicon (Si)	1.48

In order to confirm the crystalline phases of TiO_2 thin film, the sample was thermally treated at 400^oC for 2 hrs under air ambient in tube furnace prior to XRD measurement. The XRD pattern is depicted in Fig. 2.
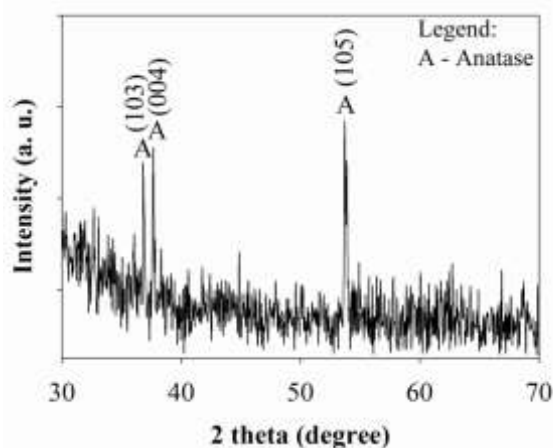
Fig. 2 XRD pattern of N:TiO_2 after thermal treatment

Three prominent peaks situated at 36.9^o, 37.7^o and 53.7^o were assigned as anatase (103), (004) and (105), respectively. No other peaks were observed suggests that the sample consists of only TiO_2 in polycrystalline anatase phases.

3.2 Optical Properties

The homogeneity and the quality of the N:TiO_2 thin film were investigated. The transmittance spectrum of the sample and of the blank glass substrate is presented in Fig. 3 (a). The interference fringes of the incident beam on the homogeneously deposited thin film have resulted in adjacent maxima and minima in transmittance spectrum. Hence the optical constants of the thin films could be calculated by using Swanepoel's envelope method [1, 10].
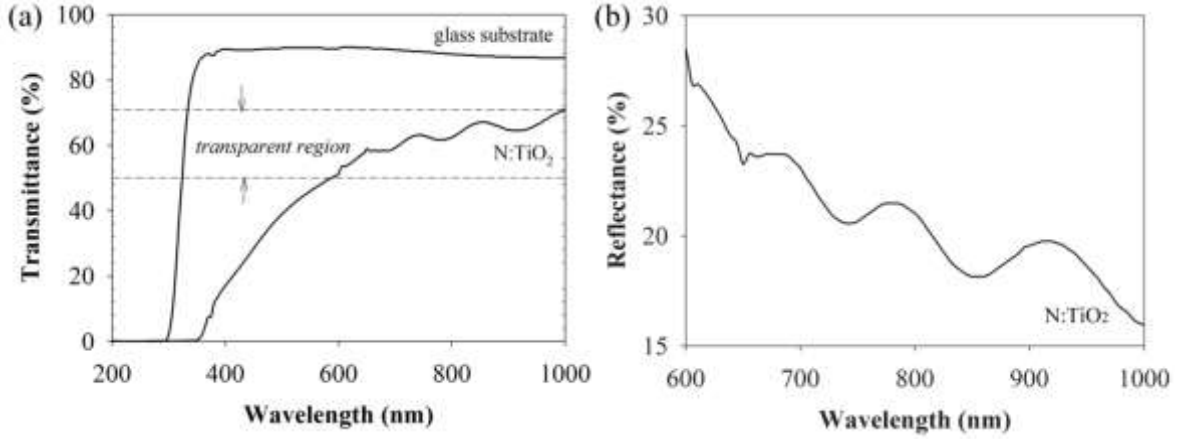
Fig. 3 (a) Transmittance spectrum of glass substrate and N:TiO$_2$ sample (b) Reflectance spectrum of N:TiO$_2$ at highly transparent region calculated through transmittance spectrum.

At highly transparent region, transmittance, T

$$T = (1-R)^2 \tag{1}$$

Where R is the reflectance of the thin film.

The calculated reflectance of N:TiO$_2$ sample is plotted against wavelength in Fig. 3(b).

Based on the envelope pattern in Fig. 3, transmittance at maxima, T_M and minima, T_m, the refractive index, n can be determined through eq. 2

$$n = [N + (N^2 - s^2)^{\frac{1}{2}}]^{\frac{1}{2}} \tag{2}$$

Where $N = 2s\dfrac{(T_M - T_m)}{T_M T_m} + \dfrac{(s^2 + 1)}{2} \tag{3}$

And s is the refractive index of glass substrate.

While the refractive index of glass substrate, s can be obtained through eq. 4

$$s = \frac{1}{T_s} + \left(\frac{1}{T_s^2} - 1\right)^{\frac{1}{2}} \tag{4}$$

And T_s is the transmittance of substrate.

The thickness of the thin film, d were calculated by eq. 5 and the N:TiO$_2$ film is 1.9μm thick.

$$d = \frac{\lambda_1 \lambda_2}{2(\lambda_1 n_2 - \lambda_2 n_1)} \tag{5}$$

Where n_1 and n_2 are refractive indices at two adjacent maxima (or minima) at λ_1 and λ_2, respectively.

Subsequently, the absorption coefficient, α can be obtained by eq. 6

$$\alpha = -\frac{1}{d} \ln T_{film} \tag{6}$$

Where T_{film} is the transmittance of the N:TiO$_2$ film.

The extinction coefficient, k is given by eq. 7

$$k = \frac{\alpha \lambda}{4\pi} \tag{7}$$

The variations of refractive index, n, and extinction coefficient, k with respect to various wavelengths are plotted in Fig. 4.
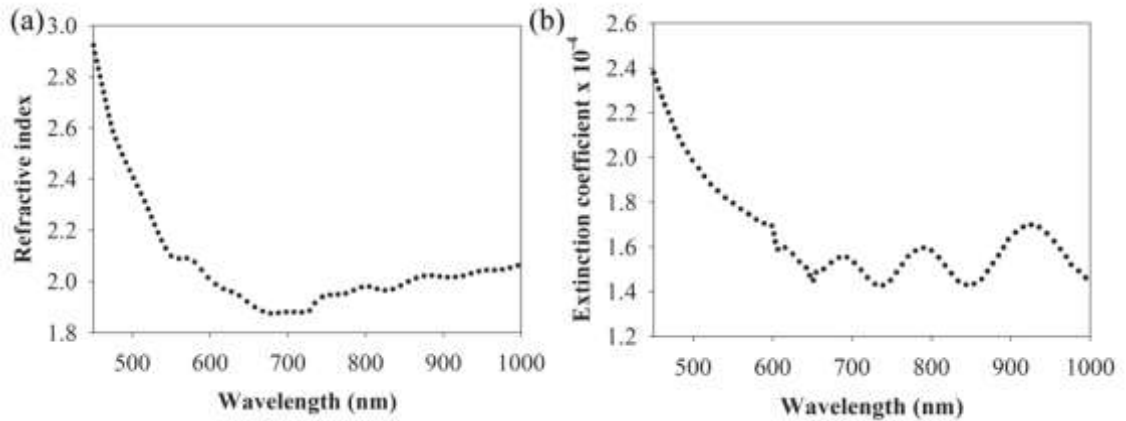
Fig. 4 (a) Refractive index (b) Extinction coefficient of N:TiO$_2$ with respect to wavelength.

Despite the thickness of the film was found to be nearly 1.9μm, the transparency of the sample as seen in Fig. 1(a) is supported by up to 50 to 71% of transmittance in the visible and infrared region of electromagnetic spectrum as shown in Fig. 3 (a). The increase of transmittance leads to the decrease of refractive index. The refractive index for wavelength ranging from 550 to 1000nm as observed in Fig. 4 (a) falls in the range of 1.8 to 2.1, particularly 1.96 at 632nm. Comparing the commonly reported refractive index of anatase TiO$_2$ which is 2.3 to 2.5 [1-2, 8], the refractive index of our sample appeared to be lower. This could be due to the fabrication method of our sample. The carrier gas of this experiment was air which consists of approximately 20% of oxygen only. This oxygen content is significantly lower than the work that uses carrier gas which consists of high oxygen content. Similar work has been reported by Stamate et. al that refractive index of TiO$_2$ films deposited by DC magnetron sputtering method, varied with different gas flow rate which consist of mixture of argon and oxygen. At lower flow rate, the refractive index was significantly lowered to around 2.0 compare to 2.3 at higher flow rate, both recorded at 632nm [2]. In addition, our work was done under atmospheric pressure at temperature less than 500°C, with the total deposition time less than 1 min. Hence there was no sufficient time and energy to break the O-O bond in oxygen compare to plasma-enhanced CVD which provides high bombardment energy under low pressure. Moreover, Ghamsari et. al has observed refractive index less than 1.96 at 632nm for their nanostructured TiO$_2$ thin film fabricated through sol-gel method [8].

The calculated absorption coefficient, α, values earlier can be extended in Tauc equation expressed in eq. 8 to determine the optical band gap of the N:TiO$_2$ thin film.

$$\alpha h\upsilon = A(h\upsilon - E_g)^m \tag{8}$$

Where h is planck constant or $h\upsilon$ is photon energy in electron volts (eV), E_g is optical band gap, A is an optical constant that depends on the properties of the material and m value is a constant that depends on the type of electronic transition. In our case, m value is taken as 2 for indirect allowed transitions. Based on Tauc equation, Tauc plot of the N:TiO$_2$ is presented in Fig. 5.

579
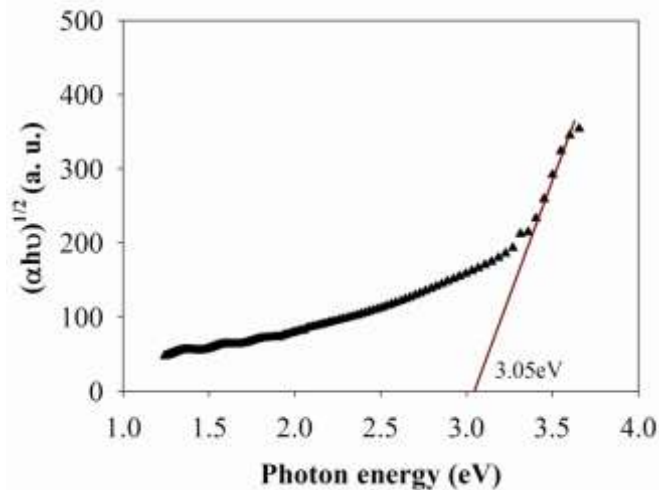
Fig. 5 Tauc plot of N:TiO$_2$ thin film for indirect transition

The optical band gap of N:TiO$_2$ thin film for indirect transitions is 3.05eV. The reported indirect band gap lies in between 3.1 to 3.3eV [1, 3-4, 11]. Comparing the band gap of our sample in Fig. 5, nitrogen doping has caused a slight shift of ~5% to 3.05eV.

The band gap of TiO$_2$ has been successfully reduced by doping with nitrogen yet maintains its anatase crystalline structure. The lower band gap energy is believed to be able to enhance the photocatalytic reaction of TiO$_2$ in ultraviolet and visible light region. This is particularly important because at current stage TiO$_2$ is active only in ultraviolet region, it is in hope that TiO$_2$ will be able to absorb a considerable part from visible light region [4, 6]. The increase of nitrogen doping content could possibly further decrease the bang gap of TiO$_2$ thin film which will be further investigated in the future.

4.   CONCLUSION

Nitrogen doping was introduced to TiO$_2$ simultaneously during the deposition of TiO$_2$ thin film by simple CVD system. The as-synthesized sample presents a yellowish semi-transparent outlook. Structural investigation has confirmed that the deposited TiO$_2$ is comprised of polycrystalline anatase phase. Optical investigation has showed that the sample is highly transparent despite the calculated film thickness is 1.9μm. Based on Swanepoel's envelope method, optical constants such as refractive index, absorption coefficient and extinction coefficient were calculated. The lower refractive index of 1.96 at 632nm was attributed to the lower oxygen content in carrier gas during the fabrication process. Optical band gap of indirect allowed transitions was obtained from Tauc plot. The band gap of 3.05eV of N:TiO$_2$ indirect transitions is lower than the reported ~3.2 eV of anatase TiO$_2$.

5.   ACKNOWLEDGEMENTS

6. REFERENCES

1. Martin Nicolas, Rousselot Christophe, Rondot Daniel, Palmino Franck, Mercier Rene. (1997) *Thin Solid Films*. 300, 113-121
2. Stamate M., Vasan I., Lazar G., Caraman I., Caraman M. (2005) Optical and surface properties TiO_2 thin films by DC magnetron sputtering method. *J. Optoelectron. Adv. M.* 7, 771-774
3. Slav A. (2011) Optical characterization of TiO_2-Ge nanocomposite films obtained by reactive magnetron sputtering. *Dig. J. Nanomater. Bios*, 6, 915-920
4. Hong Yong Cheol, Bang Chan Uk, Shin Dong Hun, Uhm Han Sup. (2005) Band gap narrowing of TiO_2 by nitrogen doping in atmospheric microwave plasma. Chem. Phys. Lett., 413, 454-457
5. Liu Shouxin, Chen Xiaoyun, Chen Xi. (2006) Preparation of N-doped visible-light response nanosize TiO_2 photocatalyst using the acid-catalyzed hydrolysis method. *Chin. J. Catal.* 27, 697-702.
6. Zachariah A., Baiju K. V., Shukla S., Deepa K. S., James J., Warrier K. G. G. (2008) Synergistic effect in photocatalysis as observed for mixed-phase nanocrystalline titania processed via sol-gel solvent mixing and calcinations. *J. Phys. Chem. C.* 112, 11345-11356
7. Gonzalez A. E. Jimenez, Santiago S. Gelover. (2007) Structural and optoelectronic characterization of TiO_2 films prepared by using the sol-gel technique. *Semicond. Sci. Technol.* 22, 709-716
8. Ghamsari M. Sasani, Bahramian A. R. (2008) High transparent sol-gel derived nanostructured TiO_2 thin film. *Mater. Lett.* 62, 361-364
9. Kuo Dong-Hau, Shueh Cheng-Nan. (2003) Growth and properties of $TiCl_4$ derived CVD titanium oxide films at various CO_2/H_2 inputs. *Chem. Vapor. Depos.* 9, 265-271
10. Swanepoel R. (1983) Determination of the thickness and optical constants of amorphous silicon. *J. Phys. E: Sci. Instrum.* 16, 1214-1222
11. Valencia Sergio, Marín Juan Miguel, Restrepo Gloria (2010) Study of the bandgap of synthesized titanium dioxide nanoparticules using the sol-gel method and a hydrothermal treatment. *The Open Materials Science Journal.* 4, 9-14

Preparation and Microwave Absorption Properties of NiZn Ferrite Nanoparticles Filled Thermoplastic Natural Rubber Nanocomposite

Moayad Husein Flaifel[1,*], Sahrim Hj Ahmad[1], Mustaffa Hj Abdullah[1], Ayman A. El-Saleh[2]

[1]School of Applied Physics, Faculty of Science and Technology,
Universiti Kebangsaan Malaysia, 43600 Bangi, Selangor, Malaysia
[2]Faculty of Engineering (FOE), Multimedia University (MMU), Jalan Multimedia, 63100 Cyberjaya, Selangor, Malaysia

*Corresponding author: physci2007@hotmail.com

Abstract: *In this research nanocomposite was prepared from high density polyethylene, natural rubber and liquid natural rubber in a ratio of 70:20:10, which was impregnated with various filler loading of NiZn ferrite nanoparticles and compounded by melt blending technique. The measurement of relative complex permittivity, relative complex permeability, and reflection loss were carried out using vector network analyzer to determine the microwave absorption characteristics of the samples in the frequency range of 0.5-12 GHz. The results showed multi-absorbing peaks characteristic with a great enhancement attained for 12 wt% nanocomposite at a sample thickness of 7mm in the X-band frequency.*

Keywords: Microwave absorbing materials (MAMs), NiZn ferrite, Thermoplastic natural rubber (TPNR), Reflection loss (R_L).

1. INTRODUCTION

Microwave absorbing materials (MAMs) derive its importance from the widespread applications that they are involved in. Hazards and environmental pollution associated with the vast utilization of electrical and electronic devices [1] as well as the increasing improvement of radar technology in military applications being as a countermeasure to stealth technology [2, 3], are considered to be the major challenges that must be taken into account when developing MAMs.

Magnetic polymer nanocomposite (MPNCs) materials being one class of nanocomposites demonstrate themselves as a competent candidate to be employed in electromagnetic interference suppression or EMI shielding [4, 5] and in microwave absorption [6, 7] due to their merit of combining the characteristics of both dielectric and magnetic materials [8].

The effect of incorporation of MNPs into polymeric matrix was evident on the overall MPNCs characteristics, particularly, on the enhancement of its microwave absorption properties [9, 10]. However, very few researches have discussed the importance of MPNCs in microwave absorption using TPNR as a matrix. In our work, MPNCs has comprised of TPNR matrix which is a combination of NR, LNR and HDPE as well as NiZn ferrite nanoparticles. The selection of NR and HDPE to form TPNR matrix was made due to their cost effectiveness, light weight, high flexibility and mouldability, the demand of low energy for processing and their capability of being produced in high amounts [11, 12], while opting for NiZn ferrite nanoparticles as a magnetic filler was due to their unique properties such as; low production cost, high electrical resistivity,

582

good chemical stability, mechanical hardness [13] and their capability of absorbing EM wave caused by their large electric or magnetic loss due to their natural resonance phenomena.

2. MATERIALS AND METHODS

2.1 Materials

NiZn ferrite nanoparticles ($Ni_{0.5}Zn_{0.5}Fe_2O_4$) which have a powder form with 98.5% purity and 10-30 nm average particle size was supplied by Nanostructured & Amorphous Materials Inc, USA. Natural rubber (NR) was supplied by Rubber Research Institute of Malaysia (RRIM). High density polyethylene (HDPE) was supplied by Titan Chemicals Corporation Sdn. Bhd.

2.2 Preparation

NiZn ferrite nanoparticles with 4, 8, 12 wt% loading were introduced to thermoplastic natural rubber (TPNR) matrix by melt compounding technique. This method has proven to be economical, simple as it uses conventional processing equipment and environmentally friendly as it doesn't require any solvents [14].

TPNR matrix was comprised of high density polyethylene (HDPE), natural rubber (NR) and liquid natural rubber (LNR) in a ratio of 70:20:10. LNR function was to compatibilize between the two phases of polymers. Indirect technique was implemented in which LNR and NiZn ferrite NPs were pre-mixed before being blended with NR and HDPE. Thus, NR was first added to Thermo-Haake Polylab internal mixer (Model Rheomix 600P) followed by gradual pouring of pre-mixed blend of LNR and NiZn ferrite nano-powder, and finally HDPE was introduced. The nanocomposite was blended at a temperature of 140 ^{O}C for about 13 minutes at a rotation speed of 100 r.p.m.

After the completion of the blending process, the samples were removed from the mixer and moulded into toroidal shape samples with 6.9 mm diameter (inner diameter = 2.9 mm, outer diameter = 4 mm) using injection moulding instrument (Model Ray-Ran).

2.3 Characterization

The complex permittivity ε^*, complex permeability μ^* and microwave absorption characteristics of TPNR matrix and NiZn-TPNR nanocomposite of different filler content were measured in frequency range of 0.5-12 GHz by transmission/reflection method using microwave vector network analyzer (Model Anritsu 37247D) with GPC-7mm coaxial line.

Firstly, the instrument was calibrated by measuring the complex permittivity and permeability of air in order to remove all errors originated due to the directivity, source match, load match, isolation and frequency response in both the forward and reverse measurements. Then the sample was closely inserted and positioned in the middle of the sample holder (needle-like) between the inner and outer conductors of the GPC-7mm coaxial line, and thereafter microwave energy propagated by a TEM (transverse electric and magnetic wave) mode was incident on the nanocomposite sample. For the purpose of measuring reflection parameter, either face of the sample was terminated by a short-circuited perfect conductor with a golden face.

3. RESULTS AND DISCUSSION

Electromagnetic waves incident on MAMs can be completely absorbed and then dissipated to heat by the concept of Joule effect through magnetic and dielectric losses. Complete absorption is a goal of which most researchers are fond of to obtain. This absorption is expressed in terms of attenuation constant (Γ) and reflection loss (R_L) which both are indications of the effectiveness of MAMs [15].

The reflection loss minimum or the dip in R_L is equivalent to the occurrence of minimum reflection of the microwave power for a particular thickness. The lower R_L implies better absorption properties. Therefore, in many cases the performance of the absorber is evaluated by comparing frequency range where the R_L is below a certain limit (e.g., 10 or 20 dB). However, according to sunny & Kurian [15], the ideal microwave absorber should have a R_L of at least −20 dB.

In the case of a metal-backed single-layered absorber, the value of the R_L is dependent on the measured values of complex permittivity and permeability of a material through the following relations;

$$R_L = -20 \log_{10}|\Gamma| \qquad (1)$$

$$\Gamma = \frac{(Z_{in} - Z_0)}{(Z_{in} + Z_0)} \qquad (2)$$

$$Z_{in} = Z_O \sqrt{\frac{\mu_r^*}{\varepsilon_r^*}} \tanh[\gamma t] \qquad (3)$$

Where; R_L: is the reflection loss, Γ: is the reflection/attenuation coefficient, Z_{in}: is the input impedance at the air − material interface $Z_0 = \sqrt{\frac{\mu_0}{\varepsilon_0}} = 377\Omega$ is the intrinsic impedance of free space, $\gamma = \frac{\left[j\omega\sqrt{(\mu_r^* \varepsilon_r^*)}\right]}{c}$ is the propagation factor in the EM wave absorber material, ε_r^* and μ_r^* are relative complex permittivity and permeability respectively, *tanh* is the hyperbolic tangent function and *t* is the thickness of the absorber.

From the above equations, there are some characteristic frequencies at which R_L takes place and related to what is known as impedance matching condition which is determined by the combinations of the six parameters $\varepsilon', \varepsilon'', \mu', \mu'', \lambda$ and t [9]. However, other than the above mentioned phenomena, filler content and matrix permittivity were also reported to have significant effect on the characteristics of the absorber.

To assess the microwave absorption effectiveness of our prepared NiZn-TPNR nanocomposite with different ferrite content, the variation of the minimum reflection loss (R_L) for TPNR and NiZn-TPNR nanocomposites containing 4, 8 and 12 wt% ferrite loading at the thickness of 7 mm is illustrated in Fig. 1.
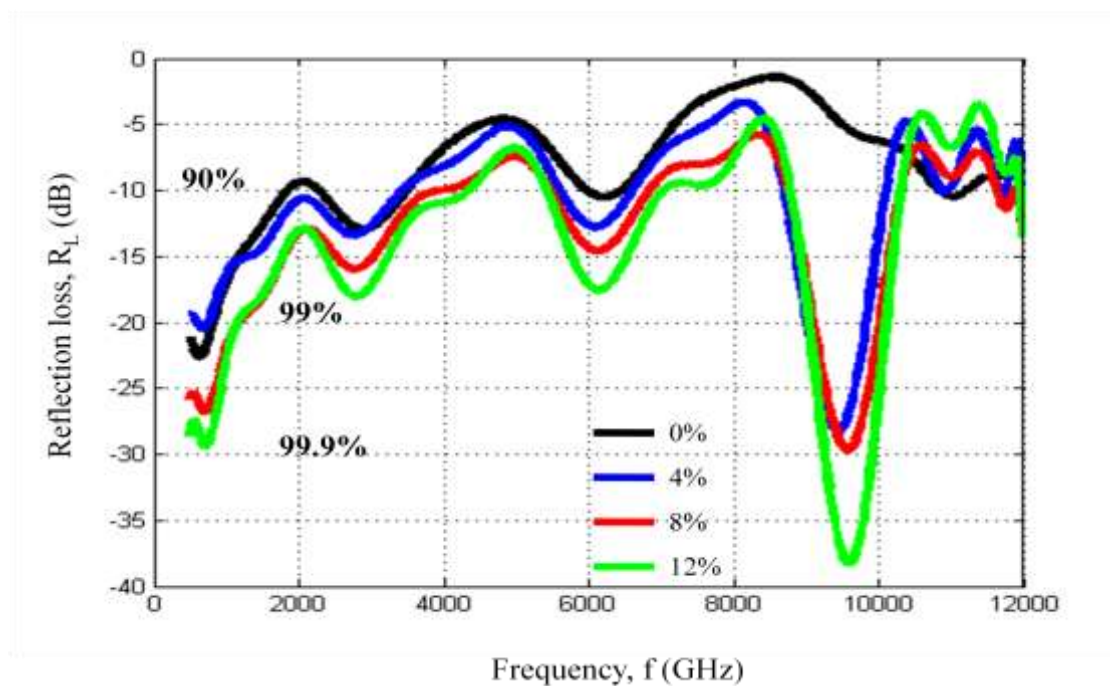
Fig. 1 Effect of filler content on the reflection loss R_L values of all attenuation dips for NiZn-TPNR nanocomposite with an optimum sample thickness of 7 mm

This plot is quite revealing in several ways. First, multi absorbing peaks or dips appeared in the plot are not expected according to the impedance matching conditions. Two matching conditions appear usually for ferrites materials, where one occurs when $\varepsilon_r^* = \mu_r^*$ for zero reflection and second one takes place due the geometrical cancellation of the incident and reflected waves at the surface of the absorber provided that the sample's thickness equals to odd number multiple of quarter of the propagating wavelength in the material [16]. However, from the literature, very few had reported on multi absorbing peaks behaviour in our studied frequency range [17]. Such kind of behaviour could be ascribed to different mechanisms. In general, the simultaneous and synergistic effect of both dielectric and magnetic losses could be mainly the cause behind such behaviour. In another word, we believe that the significant interaction between NiZn ferrite NPs and the TPNR matrix had resulted in unexpected absorption behaviour. Furthermore, the damping parameter (α) could be one of the reasons behind the creation of many peaks in our studied frequency range. It was reported by Bregar [8] that larger value of damping coefficient could significantly broaden the ferromagnetic resonance and hence create strong subsequent absorption peaks at higher frequencies. Another reason could be due to TPNR matrix permittivity value which prompted the creation of multi absorption peaks in the stipulated frequency range.

Secondly, a remarkable notice from Fig. 1 has highlighted on the reflection loss dips in three different frequency bands S, C and X to which many electronic and military applications are related. It is apparently seen that there were three absorption peaks corresponding to the former mentioned bands in which the bandwidth range for each has attained absorption of ≤ -10 dB.

585

At relative lower frequency in the S-band and moderate frequency in the C-band, the R_L dip has increased and its position was observed to shift to lower frequencies with increasing ferrite content in the nanocomposite. The minimum R_L value was achieved for 12 wt% sample at 7mm with values -18.00 and -17.6 at 2.8 and 6.1 GHz respectively. However, at higher frequency the R_L dip has also increased and reached to -38.3 at 9.6 GHz for the same sample, but its position was noticed to shift to higher frequency which is attributed to the enhancement of anisotropy field with increasing ferrite content. Furthermore, the bandwidth range in which minimum absorption was ≤ -10 dB, has increased in the S and C bands but remained constant in the X-band.

The estimated enhancement of the R_L dip of the 12 wt% NiZn- TPNR nanocomposite in S and C bands was significant when comparing it to the R_L values obtained for TPNR sample in the same bands. The estimated improvement of the R_L value for TPNR matrix in S and C bands was determined to be 17 and 29% respectively when 12 wt% of NiZn ferrite was added to the matrix. This enhancement of the R_L dip might be ascribed to the synergistic interaction of dielectric loss through interface polarization and multi scattering with magnetic loss through magnetocrystalline anisotropy and shape anisotropy [18]. On the other hand, the R_L value obtained in the X-band was considered to be of tremendous achievement since no R_L dip was detected for the TPNR matrix in this frequency band. This can be attributed to the non-magnetic behaviour of the TPNR matrix previously mentioned as the occurrence of the R_L minimum in this frequency band was owed to the relative complex permeability and its effect on the ferromagnetic resonance.

The variation of the minimum reflection loss R_L with sample thickness for TPNR matrix and NiZn-TPNR nanocomposite of 12wt% NiZn ferrite loading measured in the frequency range of 0.5-12 GHz is illustrated in Fig. 2 and Fig. 3 respectively. In case of Fig. 2, two peaks were observed in the S and C bands where it might be due to the relative complex permittivity contribution of the TPNR matrix. It is clearly seen that the microwave absorbing peaks in both frequency bands moved to higher frequency when sample thickness was below 7 mm. However, the R_L minimum dropped off with increasing of sample thickness.
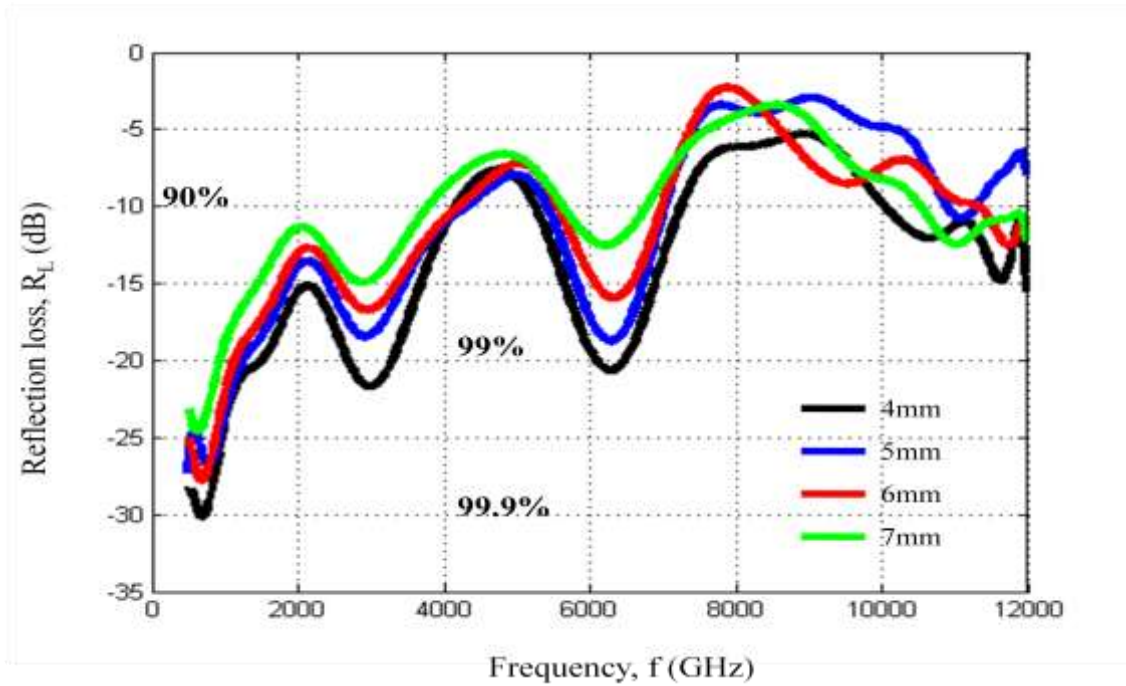
Fig. 2 Reflection loss dependence on the frequency for 0% NiZn-TPNR nanocomposite of 4,5,6,7 mm sample thicknesses
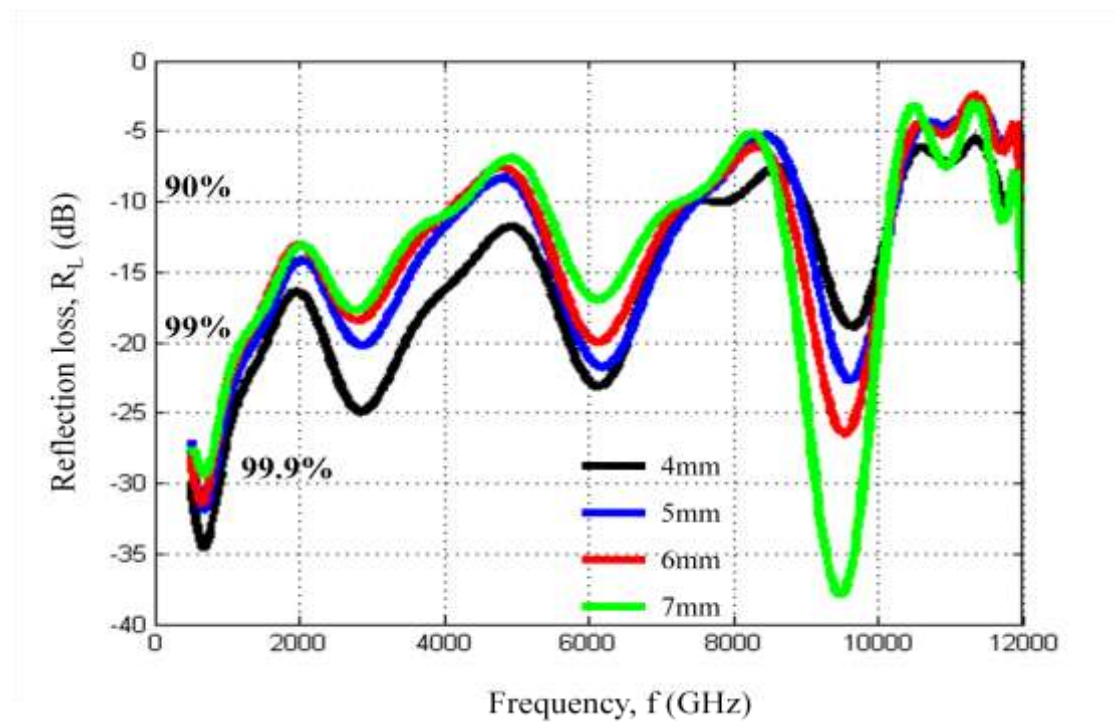
Fig. 3 Reflection loss dependence on the frequency for 12% NiZn-TPNR nanocomposite of 4,5,6,7 mm sample thicknesses

As depicted in Fig. 3, it is proven that unlike the former plot specified for the TPNR matrix, the current results of this figure exhibited a shift in the R_L dip into lower frequency above sample thickness of 4mm in the S-band and the absorbing peaks diminished with increasing sample thickness. However, in C-band the absorbing peaks shifted to higher frequency and its strength has decreased with increasing sample thickness. Interestingly, for the

587

situation in the X-band frequency range, the position of the absorbing peaks has shifted to lower frequency with increasing thickness as it is a conclusive pattern of the quarter wavelength principle [19], but in this time the strength of the R_L minimum has increased with increasing sample thickness.

4.   CONCLUSION

Microwave absorption properties of all nanocomposites samples were determined through the evaluation of refection loss as a function of frequency. The results showed multi absorbing peaks behaviour in the mentioned range. Larger value of damping coefficient (α) as well as simultaneous and synergistic effect of both dielectric and magnetic losses could be mainly the cause behind such behaviour. The influence of NiZn ferrite was reported to enhance the absorption properties of TPNR matrix in all frequency bands especially in the X-band with a R_L minimum of -38.3 dB at 9.6 GHz for 12 wt% sample at 7mm thickness. Further, the operating bandwidth frequency was also affected by the addition of NiZn ferrite into TPNR matrix in S and C bands, but had left no mentioned sign in the X-band frequency. The shift in the R_L peak positions which was observed as a result of different NiZn ferrite loading and various sample thicknesses was believed to be due to different effects such as; the increase in the values of $\mu^{'}$ and $\mu^{''}$ or enhancement of anisotropy field.

5.   REFERENCES

1.   Y. Feng, T. Qiu, C. Shen & X. Li, in: Microwave Conference Proceedings, 2005. APMC 2005. Asia-Pacific Conference Proceedings, (2005).
2.   P.C. Kim & D.G. Lee. (2009). Composite sandwich constructions for absorbing the electromagnetic waves. *Composite Structures*. 87 (2), 161-167.
3.   L.C. Folgueras, E.L. Nohara, R. Faez & M.C. Rezende. (2007). Dielectric microwave absorbing material processed by impregnation of carbon fiber fabric with polyaniline. *Materials Research*. 10 (1), 95-99.
4.   J. Alam, U. Riaz & S. Ahmad. (2007). Effect of ferrofluid concentration on electrical and magnetic properties of the Fe_3O_4/PANI nanocomposites. *Journal of Magnetism and Magnetic Materials*. 314 (2), 93-99.
5.   S. Sindhu, S. Jegadesan, A. Parthiban & S. Valiyaveettil. (2006). Synthesis and characterization of ferrite nanocomposite spheres from hydroxylated polymers. *Journal of Magnetism and Magnetic Materials*. 296 (2), 104-113.
6.   J.R. Liu, M. Itoh & K. Machida. (2006). Magnetic and electromagnetic wave absorption properties of α-Fe/Z-type Ba-ferrite nanocomposites. *Applied physics letters*. 88 (6), 062503-062503-062503.
7.   I. Kong, S. Hj Ahmad, M. Hj Abdullah, D. Hui, A. Nazlim Yusoff & D. Puryanti. (2010). Magnetic and microwave absorbing properties of magnetite-thermoplastic natural rubber nanocomposites. *Journal of Magnetism and Magnetic Materials*. 322 (21), 3401-3409.
8.   V.B. Bregar. (2004). Advantages of ferromagnetic nanoparticle composites in microwave absorbers. *Magnetics, IEEE Transactions on*. 40 (3), 1679-1684.
9.   D.Y. Kim, Y.C. Chung, T.W. Kang & H.C. Kim. (1996). Dependence of microwave absorbing property on ferrite volume fraction in MnZn ferrite-rubber composites. *Magnetics, IEEE Transactions on*. 32 (2), 555-558.

10. T.-H. Hsieh, K.-S. Ho, C.-H. Huang, Y.-Z. Wang & Z.-L. Chen. (2006). Electromagnetic properties of polyaniline/maghemite nanocomposites: I. The effect of re-doping time on the electromagnetic properties. *Synthetic Metals*. 156 (21-24), 1355-1361.

11. M. Anantharaman, K. Malini, S. Sindhu, E. Mohammed, S. Date, S. Kulkarni, P. Joy & P. Kurian. (2001). Tailoring magnetic and dielectric properties of rubber ferrite composites containing mixed ferrites. *Bulletin of Materials Science*. 24 (6), 623-631.

12. I. Grigoriadou, K.M. Paraskevopoulos, K. Chrissafis, E. Pavlidou, T.G. Stamkopoulos & D. Bikiaris. (2011). Effect of different nanoparticles on HDPE UV stability. *Polymer Degradation and Stability*. 96 (1), 151-163.

13. S. Singhal, S.K. Barthwal & K. Chandra. (2006). Structural, magnetic and Mössbauer spectral studies of nanosize aluminum substituted nickel zinc ferrites. *Journal of Magnetism and Magnetic Materials*. 296 (2), 94-103.

14. D.W. Chae & B.C. Kim. (2007). Thermal and rheological properties of highly concentrated PET composites with ferrite nanoparticles. *Composites Science and Technology*. 67 (7-8), 1348-1352.

15. V. Sunny, P. Kurian, P. Mohanan, P.A. Joy & M.R. Anantharaman. (2010). A flexible microwave absorber based on nickel ferrite nanocomposite. *Journal of Alloys and Compounds*. 489 (1), 297-303.

16. A.N. Yusoff & M.H. Abdullah. (2004). Microwave electromagnetic and absorption properties of some LiZn ferrites. *Journal of Magnetism and Magnetic Materials*. 269 (2), 271-280.

17. Z. Wang, H. Bi, J. Liu, T. Sun & X. Wu. (2008). Magnetic and microwave absorbing properties of polyaniline/γ-Fe2O3 nanocomposite. *Journal of Magnetism and Magnetic Materials*. 320 (16), 2132-2139.

18. A. Ohlan, K. Singh, A. Chandra & S. Dhawan. (2008). Microwave absorption properties of conducting polymer composite with barium ferrite nanoparticles in 12.4–18; GHz. *Applied physics letters*. 93 (5), 053114-053114-053113.

19. A. Yusoff, M. Abdullah, S. Ahmad, S. Jusoh, A. Mansor & S. Hamid. (2002). Electromagnetic and absorption properties of some microwave absorbers. *Journal of Applied Physics*. 92 876.

Improving the mechanical properties of Mg-3Al-5.6Ti composite through nano-Al_2O_3 addition with recrystallization heat treatment

S. Sankaranarayanan*, S. Jayalakshmi, and M. Gupta

Department of Mechanical Engineering, National University of Singapore (NUS)
9 Engineering Drive 1, Singapore

*Corresponding author: seetharaman.s@nus.edu.sg

Abstract: *In the current study, the role of nano-Al_2O_3 addition to Mg-3Al-5.6Ti composite and subsequent recrystallization heat treatment in improving the mechanical properties is investigated. Mg composites, (i) Mg-5.6Ti-3Al, with (3wt% Al and 5.6wt% Ti) and (ii) Mg-5.6Ti-3Al-2.5Al_2O_3, with (3wt% Al, 5.6wt% Ti and 2.5wt% Al_2O_3) were synthesized through the disintegrated melt deposition technique (DMD) followed by hot extrusion. Mg-5.6Ti-3Al-2.5Al_2O_3 composite was then subjected to recrystallization heat treatment at 200ºC for 5 hours. Mechanical properties evaluation of the developed Mg composites indicated a significant improvement in microhardness and tensile properties when compared to pure Mg and Mg-3Al-5.6Ti. Microstructural characterization revealed significant grain refinement and uniform distribution of reinforcements / second phases in the developed Mg composites due to hybrid reinforcement additions and heat treatment. In case of as-extruded Mg-5.6Ti-3Al-2.5Al_2O_3 composite, the strength improvement occurred at the expense of ductility while for heat treated composite, the increase in strength properties was accompanied by an increase in ductility. Based on the processing-structure-property correlation, it was identified that the presence of hard reinforcements / intermetallics in Mg matrix contributes to the improvement in strength properties while the stress relaxation during heat treatment contribute to the ductility enhancement.*

Keywords: Magnesium, Heat treatment, Mechanical Properties, SEM, Fractography

1. INTRODUCTION

The research and development of magnesium (Mg)-based materials are focused more towards making them the best replacement to Aluminium (Al), as Mg is ~ 35% lighter than Al and exhibits properties comparable to that of Al. The advantages of Mg as engineering material include excellent machinability, damping capacity and castability [1, 2]. But the low elastic modulus and elevated strength properties of Mg restricts its extended usage in critical engineering applications. To overcome these limitations, hard ceramic reinforcements such as SiC, Al_2O_3 are added to Mg which often results in the ductility reduction [1, 2]. The available literature reveals that addition of nanoscale particulate reinforcements results in simultaneous improvement in strength and ductility of Mg materials [1]. Similar results are also observed for Mg composites with insoluble metallic reinforcements [1]. Further, the positive influence of addition of hybrid reinforcements on the mechanical properties of the Mg–composites has been recently identified [3]. In composite development methodology involving secondary processing such as extrusion, the failure of the composite under loading is initiated by the crack formation at the interface owing to the stress attributing to the difference in thermal expansion coefficients

between the matrix and reinforcements. In such cases, heat treatment near the recrystallization temperature results in the stress relaxation at the interface and improves the mechanical properties [4].

In order to study the role of nano-reinforcement addition and heat treatment, the following Mg composites (i) Mg-5.6Ti-3Al, with (3wt% Al and 5.6wt% Ti) particulates, and (ii) Mg-5.6Ti-3Al-2.5Al$_2$O$_3$, with (3wt% Al, 5.6wt% Ti and 2.5wt% Al$_2$O$_3$) were synthesized through the disintegrated melt deposition technique (DMD) followed by hot extrusion and Mg-5.6Ti-3Al-2.5Al$_2$O$_3$ composite is then subjected to recrystallization heat treatment at 200°C for 5hours. The physical, microstructural and mechanical properties of the developed composites were evaluated in order to study the effect on the microstructure and mechanical properties.

2. EXPERIMENTAL PROCEDURE

MATERIALS

Mg turnings of > 99.9% purity (ACROS Organics, USA), was used as the matrix material. Elemental Ti particulates of particle size < 140 μm (purity 98%) supplied by Merck, Al particulates of average particle size ~15 μm (purity 98%) supplied by Alfa Aesar were used as metallic additions. Nano Al$_2$O$_3$ particulates of average particle size ~50 nm (purity 99%) supplied by Baikowsi was used as the ceramic reinforcement.

MELTING, CASTING AND EXTRUSION

The Mg-based materials were prepared using the DMD technique [3]. Mg turnings together with the reinforcements/alloying additions were heated in a graphite crucible to 1023 K in an electrical resistance furnace, under inert argon gas atmosphere. The superheated molten slurry was stirred for 5 min at 460 to facilitate uniform distribution of the reinforcements/intermetallics in the Mg-matrix. Following stirring, the melt was then released through a 0.01 m diameter orifice at the base of the crucible and it was disintegrated by two jets of argon gas. The disintegrated melt slurry was subsequently deposited onto the steel mould to obtain an ingot of 0.04 m diameter. The synthesis of pure Mg was carried out in a similar fashion, except that no alloying elements were added. The obtained ingot was then machined to a diameter of 0.036 m and soaked at 400 °C for 1 hour to perform hot extrusion at 350 °C resulting rods of diameter 8 mm. Further characterization studies were conducted on the extruded rods. The Mg-5.6Ti-3Al-2.5Al$_2$O$_3$ composite is then subjected to recrystallization heat treatment at 200°C for 5hours.

MATERIALS CHARACTERIZATION

Standard tests were conducted on the as-polished samples cut from the extruded rods of developed materials to determine the density [3]. The grain morphology and the distribution of second phases in Mg matrix were studied on the as-polished samples using a Hitachi S-4300 FESEM equipped with EDS, an Olympus metallographic optical microscope and Scion image analysis software. Shimadzu LAB X XRD-6000 diffractometer was used to carry out the X-ray diffraction analysis on the developed Mg materials. The microhardness measurements were carried out on the as-polished samples of developed materials using Matsuzawa MXT 50 automatic digital Microhardness tester based in accordance with ASTM standard E3 84-99.

Standard ASTM test method E8M-96 was conducted on the test samples using a fully automated servo-hydraulic mechanical testing machine, to determine the tensile properties of developed materials before and after heat treatment. The fractured surfaces of Mg-materials after tensile test were studied using the Hitachi S-4300 FESEM.

3.   RESULTS AND DISCUSSION

The visual observation of the surfaces of the developed as-cast Mg-ingots and extruded Mg-rods indicates no macrostructural defects. From the experimental density values (Table 1), it can be seen that near-dense materials have been developed and the porosity level is relatively low (< 0.1%) in all the samples. This confirms the suitability of processing parameters used in the study.

Table 1 – Results of density and microstructural measurements.

S. No.	Material	Th. Density (g/cc)	Exp. Density (g/cc)	Porosity (%)	Grain Size (μm)
1	Mg-5.6Ti-3Al	1.8221	1.7655 ± 0.0064	0.03	8.5 ± 1.53
2	Mg-5.6Ti-3Al-2.5Al$_2$O$_3$	1.8474	1.7685 ± 0.0324	0.06	6.3 ± 1.01
3	Mg-5.6Ti-3Al-2.5Al$_2$O$_3$ (HT)	1.8474	1.7740 ± 0.0101	0.04	8.2 ± 2.27

The microstructure and x-ray studies reveal the presence of Ti and Mg$_{17}$Al$_{12}$ intermetallic in Mg-5.6Ti-3Al, and Ti, nano-Al$_2$O$_3$ and Mg$_{17}$Al$_{12}$ in Mg-5.6Ti-3Al-2.5Al$_2$O$_3$ and Mg-5.6Ti-3Al-2.5Al$_2$O$_3$ (HT) as shown in Fig.1 (a-d) and Table 1. The results from grain size measurements reveal significant grain refinement in the case of Mg-5.6Ti-3Al-2.5Al$_2$O$_3$ when compared to Mg-5.6Ti-3Al (Table 1). The grain refinement as observed in Fig.1 (a-d) is attributed to the presence of hard reinforcements and other second phase intermetallics [5]. Post heat treatment, the observed grain size (Fig.2) of Mg-5.6Ti-3Al-2.5Al$_2$O$_3$ (HT) appeared to be larger when compared to Mg-5.6Ti-3Al-2.5Al$_2$O$_3$ without heat treatment. The grain growth in Mg-5.6Ti-3Al-2.5Al$_2$O$_3$ (HT) is attributed to the stress relaxation while heat treatment [6].
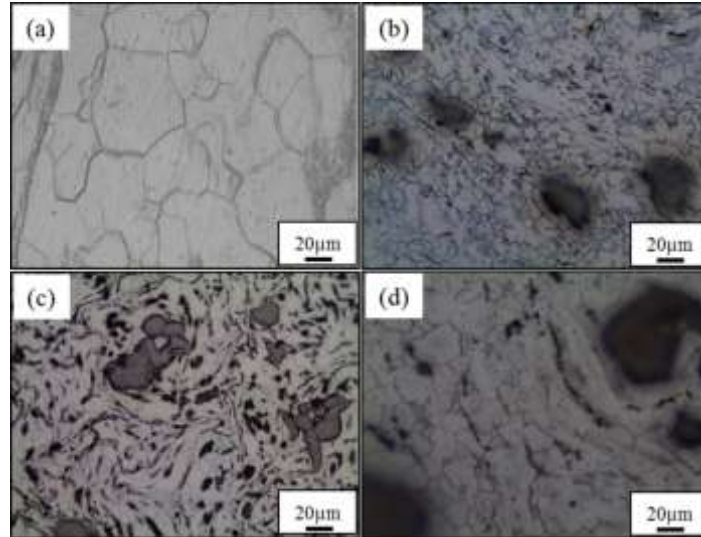
Fig. 1 – Grain morphology of (a) pure Mg, (b) Mg-5.6Ti-3Al, (c) Mg-5.6Ti-3Al-2.5Al$_2$O$_3$ and (d) Mg-5.6Ti-3Al-2.5Al$_2$O$_3$ (HT).
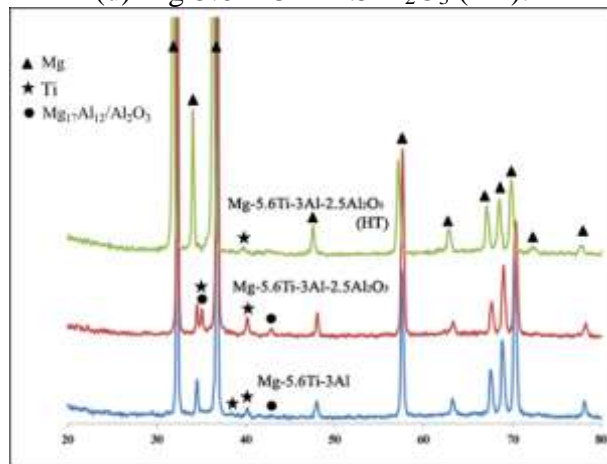
Fig. 2 – Results of X-ray diffraction studies conducted on developed Mg composites.

The hardness values from microhardness measurements (Fig.2) indicate an improvement in microhardness values in all the developed composites when compared to pure Mg. An improvement of ~30% occurred in Mg-5.6Ti-3Al-2.5Al$_2$O$_3$ and ~20% in Mg-5.6Ti-3Al-2.5Al$_2$O$_3$ (HT) when compared to Mg-5.6Ti-3Al. The improvement in hardness value attributes to the presence of harder Al$_2$O$_3$ (~2.2 GPa) [7]. The hardness value is found to reduce in the case of Mg-5.6Ti-3Al-2.5Al$_2$O$_3$ (HT) when compared to Mg-5.6Ti-3Al-2.5Al$_2$O$_3$ due to the stress relaxation and grain growth upon heat treatment [6].

The results from tensile tests indicate a significant improvement in the strength properties of Mg incorporated with hard metallic and metallic/ceramic elements (Fig. 3). The improvement in mechanical properties of Mg-composites when compared to pure Mg can be ascribed to the following strengthening effects: (i) thermal misfit between matrix and reinforcements / intermetallics, (ii) grain refinement, (iii) the morphology of the Ti-particles, wherein the sharp-edged particles contribute to higher dislocation density due to the increased stress concentration at the pointed corners [8]. Also the presence of harder reinforcements/second phases in Mg matrix eventually increases the load carrying capacity thus improving the strength much significantly [9]. While the improvement in strength properties in Mg-5.6Ti-3Al-2.5Al$_2$O$_3$ occurred at the expense of ductility, significant improvement in ductility with little effect on

strength properties took place in the case of Mg-5.6Ti-3Al-2.5Al$_2$O$_3$ (HT). The reduction in thermal residual stress upon heat treatment has resulted in the improvement in tensile ductility of Mg-5.6Ti-3Al-2.5Al$_2$O$_3$ (HT). This also effectively improves the matrix-reinforcement/intermetallic interface which is evident from the micrographs showing the distribution of second phases [10].
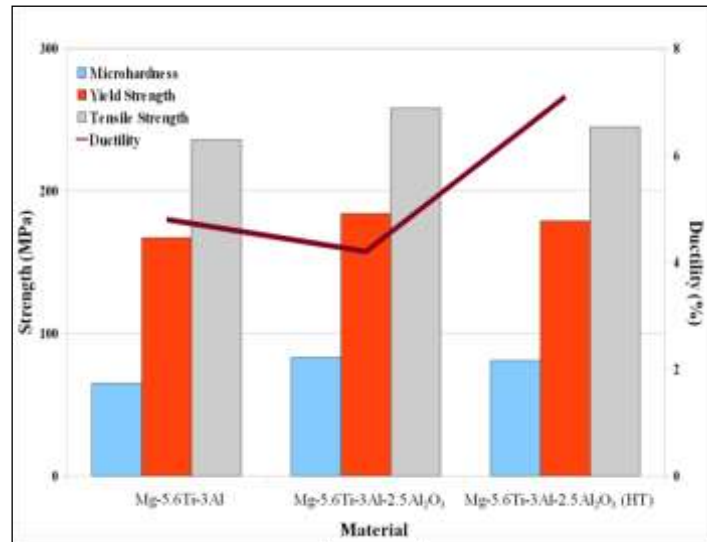
Fig. 3 - Variation in Strength and Microhardness of developed Mg-composites.

The fracture surface analysis of composite samples failed under tensile loading indicates a mixed mode fracture with particulate debonding (Fig. 4(b & c)) observed in Mg-5.6Ti-3Al and Mg-5.6Ti-3Al-2.5Al$_2$O$_3$ while mixed mode fracture with relative plastic deformation and good interfacial bonding (Fig. 4(d)) observed in Mg-5.6Ti-3Al-2.5Al$_2$O$_3$ (HT) while the fracture mode of pure Mg under tension is through cleavage (Fig. 4(a)) [10].
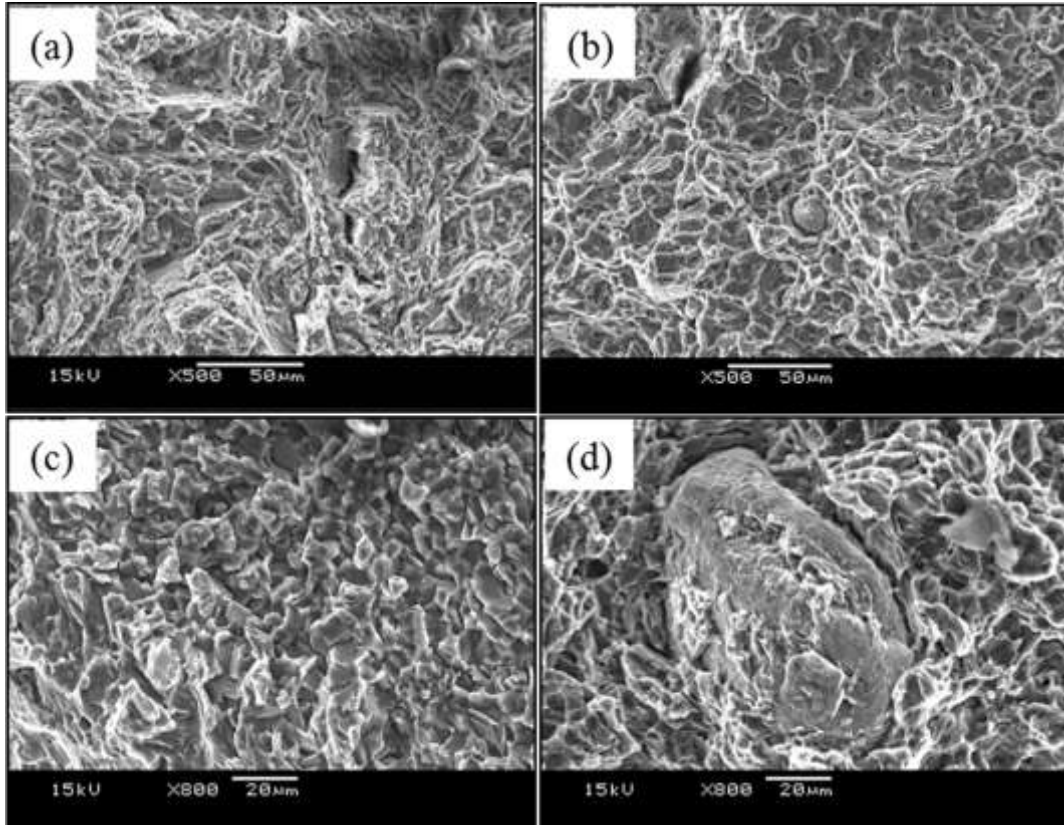
Fig. 4 - Tensile fractographs of (a) Mg (b) Mg-5.6Ti-3Al, (c) Mg-5.6Ti-3Al-2.5Al$_2$O$_3$ and (d) Mg-5.6Ti-3Al-2.5Al$_2$O$_3$ (HT)

4.   CONCLUSIONS

  i.   DMD technique can successfully synthesize magnesium composites.
 ii.   The inherent properties of metallic and ceramic reinforcements such as Ti, Al and Al$_2$O$_3$ respectively such as hardness, ductility, structural compatibility with Mg and the good wettability of Ti and Mg results in the enhancement of strength and ductility in Mg composites under tensile loads.
iii.   Addition of nano Al$_2$O$_3$ to Mg-5.6Ti-3Al results in the improvement in strength properties and hardness at the expense of ductility. The stress relaxation, grain growth and uniform distribution of finer intermetallics and second phases attributes to the improvement in ductility in case of Mg-5.6Ti-3Al-Al$_2$O$_3$ after heat treatment.

5.   REFERENCES

[1]   M Gupta and Sharon Nai. Magnesium, magnesium alloys and magnesium composites. John Wiley 2011.
[2]   S.F. Hassan, M. Gupta, Effect of submicron size Al2O3 particulates on microstructural and tensile properties of elemental Mg, Journal of Alloys and Compounds 457 (2008) 244–250.
[3]   S. Sankaranarayanan, S. Jayalakshmi, M. Gupta, Effect of ball milling the hybrid reinforcements on the microstructure and mechanical properties of Mg–(Ti + n-Al2O3) composites, Journal of Alloys and Compounds 509 (2011) 7229–7237.
[4]   S. Ugandhar, M. Gupta S.K. Sinha. Enhancing strength and ductility of Mg/SiC composites using recrystallization heat treatment. Compos. Struct. 2006; 72: 266–272.
[5]   G E Dieter. Mechanical Metallurgy; Mc Graw-Hill, USA 1986.

[6] S. C. V. Lim and M. Gupta, Enhancing modulus and ductility of Mg/SiC composite through judicious selection of extrusion temperature and heat treatment, Materials Science and Technology June 2003 Vol. 19 803.

[7] S.F. Hassan, M. Gupta, Development of high performance magnesium nano-composites using nano-Al2O3 as reinforcement, Materials Science and Engineering A 392 (2005) 163–168.

[8] Shuyi Qin, Changrong Chen, Guoding Zhang, Wenlong Wang, Zhongguang Wang. The effect of particle shape on ductility of SiCp reinforced 6061 Al matrix composites. Mater. Sci. Eng. A 1999; 272: 363–370.

[9] D J Lloyd. Particle reinforced aluminium and magnesium matrix composites. Int. Mater. Review. 1994; 39(1): 1–23.

[10] S. Sankaranarayanan, S. Jayalakshmi, M. Gupta. Effect of addition of mutually soluble and insoluble metallic elements on the microstructure, tensile and compressive properties of pure magnesium. Mater. Sci. Engg. A 2011; 530: 149-160.

ACKNOWLEDGMENT

Investigation effect of hafnium addition on the microstructure of IN-738LC Nickel base superalloy

Ali Akbar Saghafi[1,*], Jamshid Aghazade Mohandesi[1], Mahmood Nili Ahmadabadi[2]
and Hamid Reza Alizade[3]

[1]Faculty of mining and material engineering, Amirkabir University of Technology, Tehran, Iran
[2]Faculty of material science and engineering, University of Tehran,Tehran,Iran
[3] Mapna turbine blade engineering and manufacturing, Karaj, Iran

*Ali Akbar Saghafi: saghafi.aa66@gmail.com

Abstract: *In this work the effect of hafnium addition on the microstructure of IN-738LC nickel base superalloy have been studied using metallographic and electron microscopic techniques. Vacuum Arc remelting has been utilized in order to add excess amount of Hafnium at different percentages. Results show that hafnium addition can change carbides morphology, composition and distribution. Addition of Hafnium moderately increases the hardness that it related to the formation of hafnium rich carbides and Ni-Hf intermetallic compounds.*

Keywords: IN-738LC, Hafnium, Microstructure, Hardness

1. INTRODUCTION

Addition of hafnium was found to be very effective in improvement of creep behaviour in nickel base superalloys by promoting a more viable grain boundary structure. Hafnium has high solubility in γ' relative to γ**Error! *Bookmark not defined*.**[1], strengthens the γ' and is an extremely active carbide former. Although generally accepted that a controlled amount of $M_{23}C_6/M_6C$ particles are advantageous at grain boundaries to inhibit its sliding, nevertheless an extensive interconnected series of such particles permits rapid crack propagation. Excessive amount of the ratio: $M_{23}C_6/M_6C$ particles at grain boundary can be inhibited by hafnium, which reacts with the carbon freed by MC breakdown and results in a secondary stable MC (predominantly HfC) precipitated as finely divided random particles[2]. It has been shown that hafnium replaces titanium, tantalum, tungsten, molybdenum and niobium in the interior of MC carbides in different alloys[3]. Further, during solidification, strong partitioning of hafnium to the γ' results in a convoluted γ'-γ structure in the grain boundary area that inhibits rapid crack propagation and retard grain boundary sliding and separation during creep and gives in higher stress-rupture life for hafnium-modified alloys[4]. Also hafnium has an added advantage of increasing the oxidation resistance of the base alloy. However, its high reactivity causes an added "adventure", creating difficult (but controllable) problems during ingot melting and component processing. Beside hafnium is a strong oxygen, nitrogen, and sulfur scavenger[2].

While most minor elements are added up to the amounts much less than 0.1%, hafnium is found at levels from about 0.5% to nearly 2.0%. Customary levels might be 0.5% for polycrystalline cast nickel-base superalloys[5] to 1.5% for columnar grain directionally solidified cast nickel-base superalloys. In this article effect of different amounts of hafnium addition on the microstructure of In-738 have been studied

2. MATERIAL AND EXPERIMENTAL PROCEDURE

Vacuum induction melted In-738 samples have been sand blasted and then grinded. After grinding, vacuum arc remelting has been used in order to add excess high purity hafnium to the base alloy. The amount of superimposed hafnium in the different samples stated in Table 4. The purity of added hafnium was 99.99%.

Table 4) The percentage of primary material in different sample charges

Sample No.	1		2		3	
	Weight (gr)	Weight%	Weight (gr)	Weight%	Weight (gr)	Weight%
IN-738LC	31.7	100	33.5	99.41	38	98.45
Hafnium	0	0	0.2	0.59≈0.6	0.6	1.55≈1.5

After VAR processing, single and double solution treatment has been used in order to homogenize the microstructure. Figure 3 shows the time- temperature- pressure graph for both solution treatments.

Metallographic investigations on the as-cast and heat treated samples, has been done using optical and electron microscope. Figure 5-6 show microstructure of different samples. Rockwell C Hardness test was conducted on the as-cast and solution treated samples. The results presented in Figure 4.
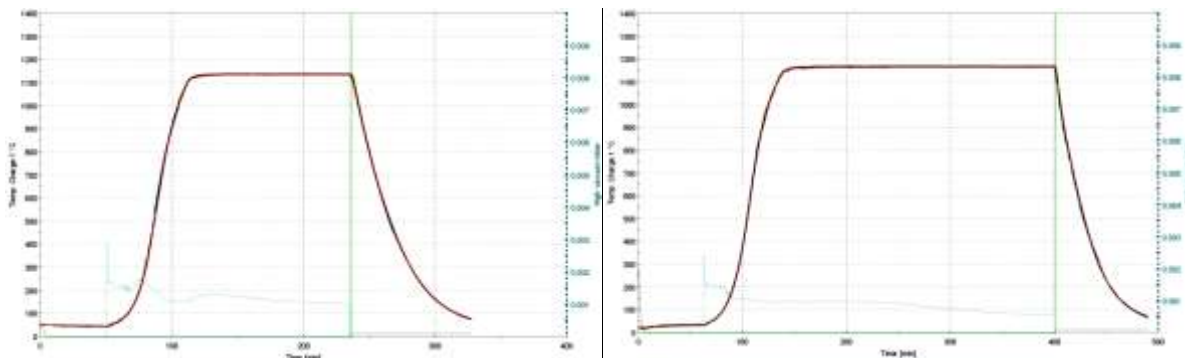
Figure 3) Time- Temperature- Pressure cycle during first (left picture) and second (right) solution treatment

598
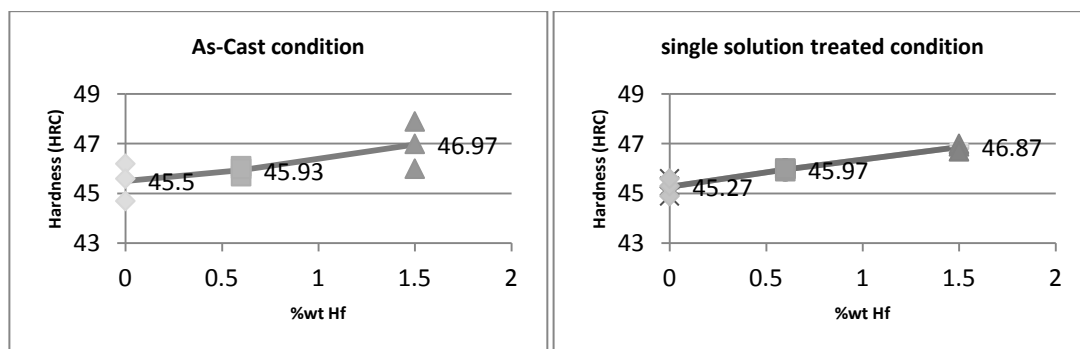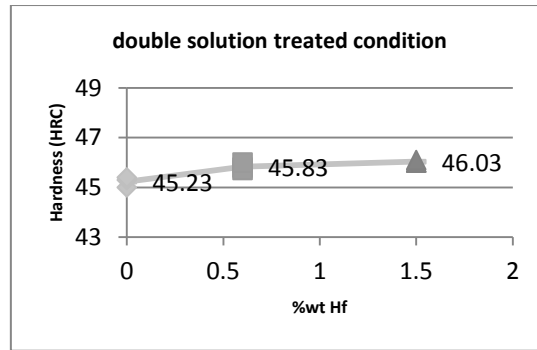
Figure 4) Results of hardness test in As-Cast and Solution treated condition

3. RESULT AND DISCUSSION

3.1 Microstructure of Different Alloys In The As-Cast Condition

The microstructure of different alloys before heat treatment is shown in Figure 5. Figure 5-a, shows the microstructure of hafnium free IN-738LC. It is evident that there are some segregation phases at dendrite boundaries. These regions could be also seen in IN-738LC doped with 0.6 and 1.5 Wt pct hafnium (Figure 5-b and c). In hafnium free alloy, these area contain γ, $\gamma^{'}$ and carbide islands however in hafnium bearing alloys, these zones encompass γ, $\gamma^{'}$ and Ni_xHf intermetallic compounds[3]. Zheng et al[6] reported an observation of Ni_5Hf in the hafnium-bearing nickel base superalloys; nevertheless Yoshinori et al[7] found Ni_7Hf_2 type intermetallic compounds in their study. Also Yoshinori et al[7] and Sellamuthu et al[8] expressed that hafnium segregates at liquid stage. Because of segregation of intermetallic phases at dendrite boundaries in this study, it could be concluded that they formed at final step of solidification from the remainder liquid. Electron micrograph analysis show that these hafnium rich compounds are of Ni_7Hf_2 type.
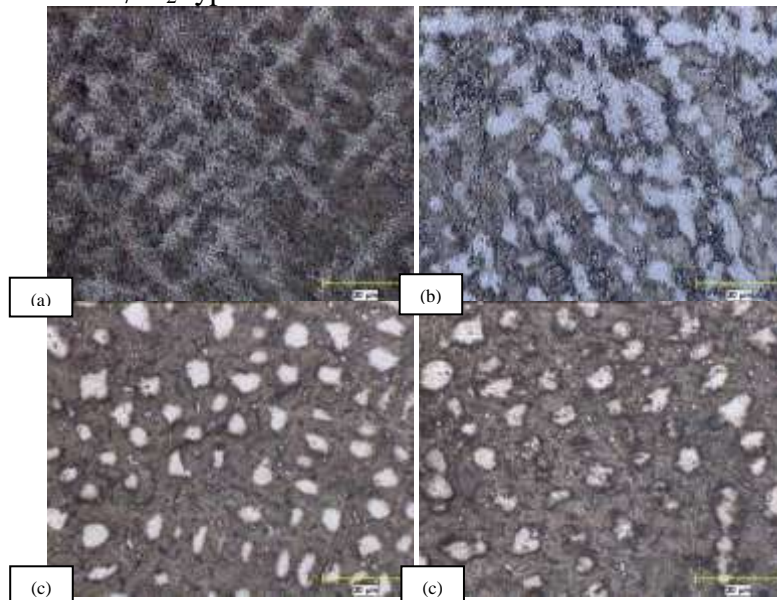
Figure 5) microstructure of different alloys in the as-cast condition. a) Hafnium free alloy, b) 0.6 wt pct hafnium added alloy, c) 1.5 wt pct hafnium added alloy

3.2 Effect of First and second Solution Treatment

Figure **6** shows the microstructure of samples after first solution treatment. It is clear that solution treatment decreases segregations in all three compositions; however there are little differences in the reformed phases. In hafnium free alloy (

Figure **6**-a), carbides are formed at two morphologies. Chinese script carbides at the grains (A) and discontinuous carbides at grain boundaries (B). The discontinuous carbides at grain boundaries are the $M_{23}C_6$-type carbides that results from the decomposition of MC-type carbides during solution treatment. The partitioning of different elements in carbides in hafnium free alloy is shown in Figure 7. It could be seen that tantalum and titanium partitions at the carbide.

There isn't an obvious difference in the amount of $M_{23}C_6$ carbides in the alloy doped with 0.6 Wt pct hafnium (

Figure **6**-b) in comparison with hafnium free alloy; In the grains, discrete plate like and angular carbides are formed after solution treatment. Also a large amount of eutectic phases formed in grain boundaries that encompass $M_{23}C_6$ carbides. This morphology shows that although ordinary solution treatment is suitable for homogenization of hafnium free alloy, it's not appropriate for dissolution of detrimental phases. Therefore secondary solution treatment has to be performed to dissolve these phases.

Figure 8 shows the partitioning of elements in the IN-738LC+0.3% Hf. It could be seen that hafnium doesn't have an obvious aggregation in carbides; however in the IN-738LC+1.5% Hf, hafnium aggregation in carbide is very clear. this could be related to high solubility of hafnium in the γ' phase (about 7% at) causing a little amount of free hafnium that partitions in carbide. Increases in hafnium content, enhances the presence of hafnium in carbides. Titanium content in carbides of IN-738LC+1.5Hf is lesser than other compositions. It shows that hafnium replaces titanium in the alloy.

In the alloy doped with 1.5wt% hafnium (

Figure **6**-c), the morphology of carbides, changes both in the grains and at grain boundaries. In the grains, well distributed angular carbides are formed after solution treatment. Elemental map from these carbides (Figure 9) shows that they are hafnium rich. Also it shows that tantalum is another element that take part in the formation of carbides in this alloy. In the alloys with zero and 0.6% hafnium, carbides are the titanium rich type.

It could be seen in the

Figure 6 **that the amount of $M_{23}C_6$-type carbides at grain boundaries in 1.5 wt pct hafnium alloy is smaller than similar carbides in hafnium free alloy. This may be related to free carbon that liberated from MC-type carbide decomposition. The composition of MC-type carbides in hafnium free alloy consists of element such as titanium and tantalum except hafnium; however in hafnium containing alloy, MC-type carbides are rich in hafnium. The high melting point (**

Table 5) and low heat of formation (Figure 10) results in the greater stability of HfC carbides rather than other carbides. Therefore decomposition of HfC is lesser than other carbides and thus the resultant free carbon is also lesser. Accordingly there is a lower tendency to form $M_{23}C_6$-type carbide in the hafnium containing alloy.
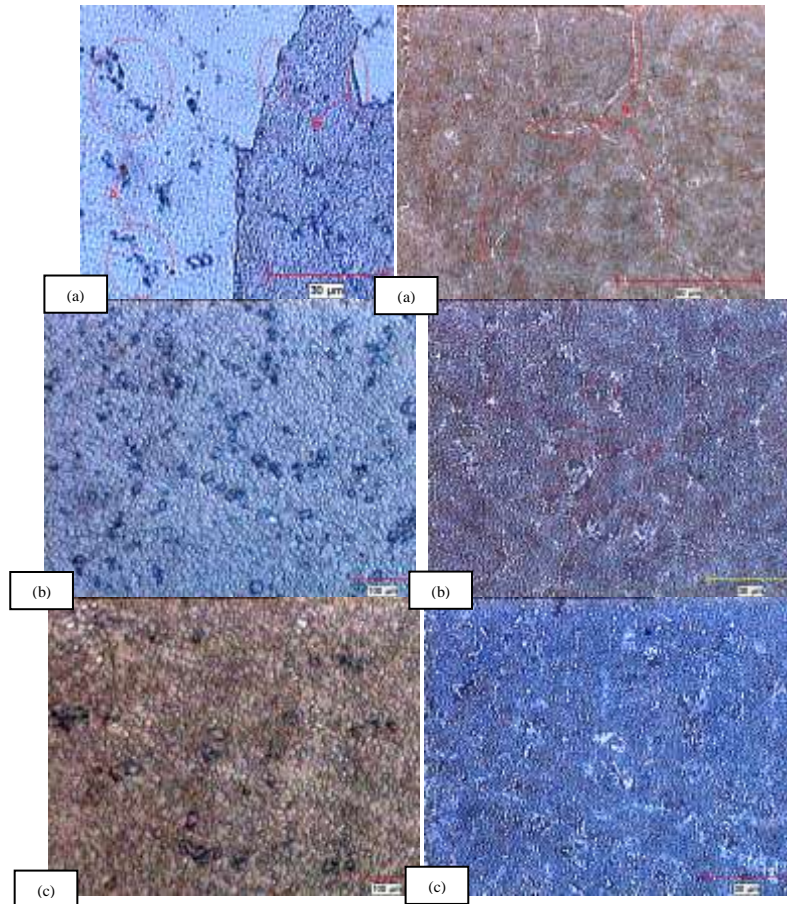
Figure 6) microstructure of different alloys after single solution treatment a) hafnium free alloy. A= Chinese script carbides at the grains. B= discontinuous carbides of M$_{23}$C$_6$ type at grain boundaries, b) 0.6 wt pct added hafnium alloy. C= grain boundary eutectic, c) 1.5 wt pct added hafnium alloy
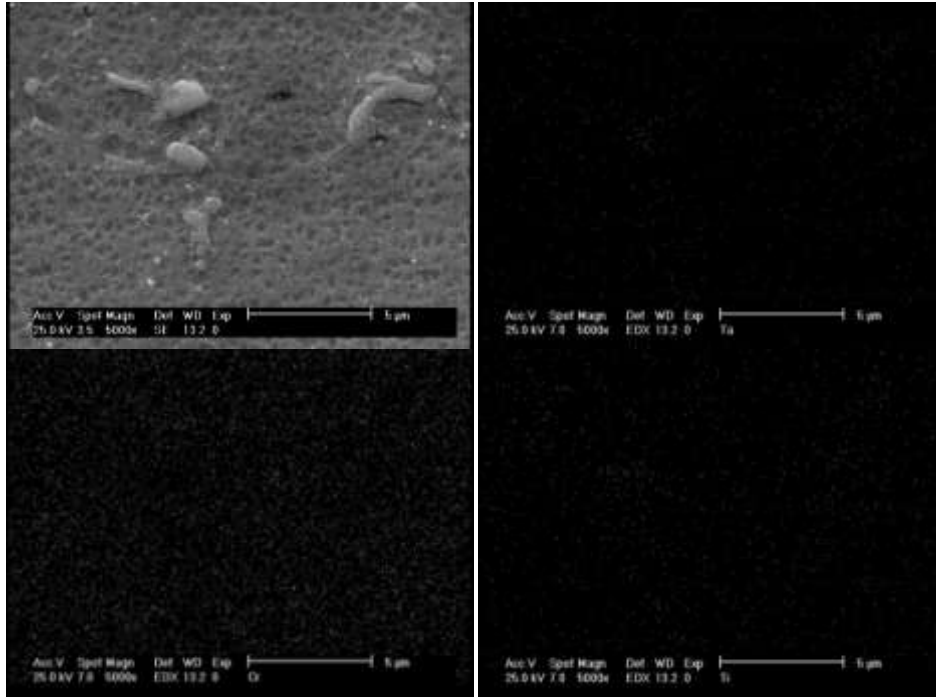
Figure 7) Elemental image from hafnium free IN-738LC, solution treated at 1120 ^{0}C for 2 h
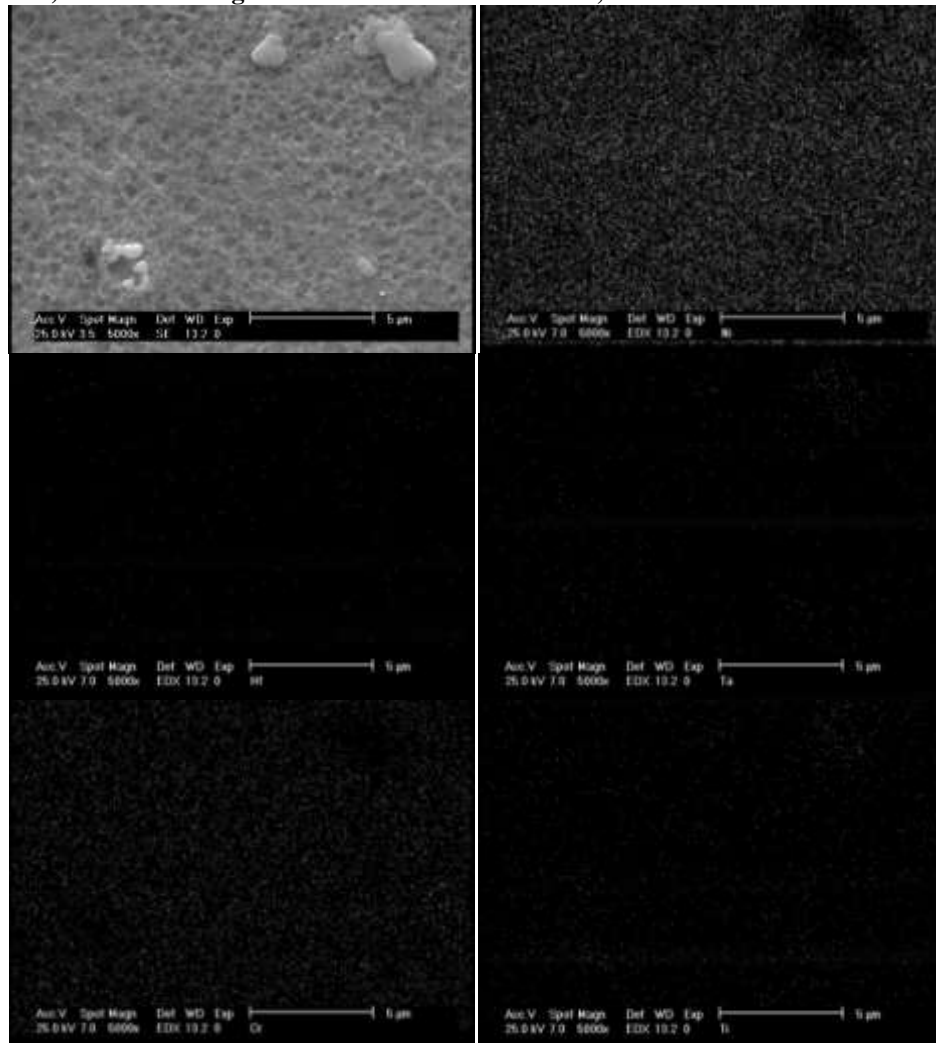
Figure 8) Elemental image from IN-738LC+0.6%Hf, solution treated at 1120 ^{0}C for 2 h

Figure 9) Elemental image from IN-738LC+1.5%Hf, solution treated at 1120 ^{0}C for 2 h

Table 5) Bonding energy and melting point of interstitial carbides and their host metal[9]

Carbide	Bonding Energy E_0, eV	Melting point (^{0}C)	
		Carbide	Metal
TiC	14.66	3067	1660
ZrC	15.75	3420	1850
HfC	17.01	3928	2230
VC	13.75	2830	1890
NbC	16.32	3600	2468
TaC	16.98	3950	2996
Cr$_3$C$_2$	-	1810	1865
Mo$_2$C	-	2520	2620
WC	-	2870	3410
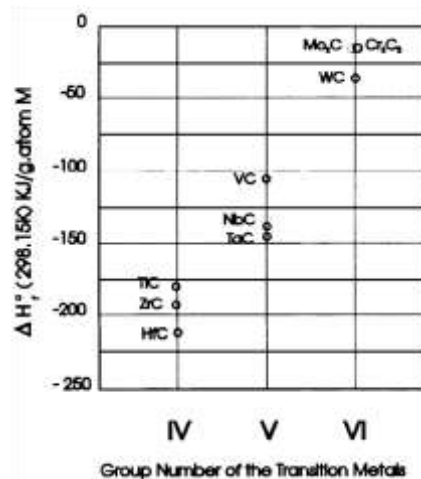
Figure 10) Heat of formation of interstitial carbides[9]

Microstructure of alloys after secondary solution treatment shows similar carbide morphology and distribution in all three compositions. Also no eutectic phase was observed by optical microscopy, indicating that the present time and temperature combination is suitable scheme for secondary solution treatment.

Figure 11) microstructure of different alloys after double solution treatment a) hafnium free alloy, b) 0.6 wt pct added hafnium alloy, c) 1.5 wt pct added hafnium alloy

3.3 Hardness Test

The hardness of the as-cast specimen increases moderately by increasing the amount of hafnium. Seemingly due to formation of hafnium rich intermetallic compounds and carbides. However by conducting single solution treatment the scatter of the results decreases considerably and further decrease maybe achieved upon second solution treatment. This is due to the effect of partial and complete homogenization of the microstructure in the single and double solution treated specimen.

4. CONCLUSION

The present study shows that hafnium addition influences carbide composition, morphology and distribution in IN-738 alloy:
1) Hafnium effectively replaces titanium rather than other elements in the MC type carbides.
2) Hafnium addition increases amount of eutectic phases in the alloy.

604

3) Single solution treatment of IN-738LC superalloy, is not adequate for dissolution of harmful phases in hafnium bearing alloys and a secondary solution treatment is recommended.

4) Hafnium addition moderately increases the hardness of as-cast specimen. The scatter of the results is eliminated by conducting single solution treatment and further improvement maybe achieved by double solution treatment.

5. REFRENCE

1. Raghavan, V., *Al-Hf-Ni (Aluminum-Hafnium-Nickel).* Journal of Phase Equilibria and Diffusion, 2006. **27**(5): p. 491-492.

2. Spilling, P.D. and J.W. Martin, *Precipitation of HfC in MM-002.* Metallography, 1982. **15**(1): p. 63-71.

3. Dahl, J., W. Danesi, and R. Dunn, *The partitioning of refactory metal elements in hafnium-modified cast nickel- base superalloys.* Metallurgical and Materials Transactions B, 1973. **4**(4): p. 1087-1096.

4. Kotval, P., J. Venables, and R. Calder, *The role of hafnium in modifying the microstructure of cast nickel-base superalloys.* Metallurgical and Materials Transactions B, 1972. **3**(2): p. 457-462.

5. Hou, J.S., et al., *Effect of hafnium on creep behavior of a corrosion resistant nickel base superalloy.* Materials Science and Engineering: A, 2010. **527**(6): p. 1548-1554.

6. Yunrong, Z. and C. Yulin, *Phase transformations in hafnium-bearing cast nickel base superalloys*, in *Superalloys* 1980. p. 465-472.

7. Murata, Y., R. Ninomiya, and N. yukawa, *A nickel-hafnium intermetallic compound and its transformation in a hafnium-doped nickel-base superalloy.* Scripta metallurgy, 1988. **22**: p. 21-26.

8. Sellamuthu, R., H. Brody, and A. Giamei, *Effect of fluid flow and hafnium content on macrosegregation in the directional solidification of nickel base superalloys.* Metallurgical and Materials Transactions B, 1986. **17**(2): p. 347-356.

9. Pierson, H.O., *Handbook of Refractory Carbides and Nitrides*, 1996, William Andrew Publishing/Noyes.

YCT COMPUTER

Parit Buntar

PUSAT JUALAN / SERVIS KOMPUTER

Sales & service

30, Jln Wawasan 1, Tmn Wawasan Jaya, 34200 Parit Buntar, Perak.
Tel : 05-7166012   Fax : 05-7168791   H/p : 012-4300214

PUSAT KOMPUTER P M I

Abdul Malik Ahmad
(Adv. Dip. In Comp. Sc. U.K.)
H/P: 012-4026786
malikahm@tm.net.my

20A, Jalan Keli, Taman Kerian Permai,
34200 Parit Buntar, Perak Darul Ridzuan.
Tel: 05-7166786
Fax: 05-7171943

N G Optical Centre

HQ: No. 21, Persiaran Shahbandar,
Pusat Bandar Baru, 34200 Parit Buntar, Perak.
Tel: 05-7165495, 016-4424858

Branch: Lot Pt 140, Jalan Perusahaan 1,
Kawasan Perindustrian Simpang Lima,
34200 Parit Buntar, Perak. (Econsave)
Tel: 016-4124858

LCW SPORT CENTRE

Ang Boon Chai
(Director)
H/P: 012-7708084

No 9, Jalan Perwira, Pusat Bandar,
34200 Parit Buntar, Perak Darul
Ridzuan, Malaysia.

Beauty World
Facial & Slimming Centre

Kelly Low
(Beauty consultant)
H/P: 016-4145420

No. 18A, Tingkat Atas, Jalan Keli,
Taman Kerian Permai, 34200, Parit Buntar.
Tel: 05-7169979

ScienceGates
Partners in science

Quantachrome INSTRUMENTS

Instruments for Particles & Porous Materials Characterization:
- Pore Size and Surface Area Analyzers
- Porometer
- Mercury Porosimetry Analyzer
- True Density Analyzer
- Water Vapor Sorption Analyzer

XRF scientific

- Fusion Machines (Gas & Electric)
- Platinum Ware
- High Temperature Furnaces

ROCKLABS

- Ring Mill
- Jaw Crusher

Glen Creston

- McCrone Micronising Mill

PreeKem

- Microwave Digestion System